I. R. IRAN

ISSN: 1728-1431
e-ISSN: 1735-9244

International Journal of Engineering

Journal Homepage: www.ije.ir

MERC

TRANSACTIONS A: Basics

Volume 34, Number 10, October 2021

Materials and Energy Research Center

In the Name of God

INTERNATIONAL JOURNAL OF ENGINEERING
Transactions A: Basics

International **J**ournal of **E**ngineering *Transactions A: Basics* (ISSN 1728-1431) (EISSN 1735-9244)
International **J**ournal of **E**ngineering *Transactions B: Applications* (ISSN 1728-144X) (EISSN 1735-9244)
International **J**ournal of **E**ngineering *Transactions C: Aspects* (ISSN 2423-7167) (EISSN 1735-9244)
Web Sites: www.ije.ir & www.ijeir.info E-mails: ije.editor8@gmail.com, Tel: (+9821) 88771578, Fax: (+9821) 88773352
Materials and Energy Research Center (MERC)

ISSN: 1728-1431, e-ISSN: 1735-9244

International Journal of Engineering, Volume 34, Number 10, October 2021

CONTENTS:

ISSN: 1728-1431, e-ISSN: 1735-9244

International Journal of Engineering, Volume 34, Number 10, October 2021

International Journal of Engineering

Journal Homepage: www.ije.ir

Semi-augmented Reality, A Novel Approach to Improve Customer Safety in Pre-sale Process of under Construction Buildings

A. Alvanchi*, N. Didehvar, M. Jalilehvand, P. Adami, S. Shahmir

Department of Civil Engineering, Sharif University of Technology, Tehran, Iran

PAPER INFO

Paper history:
Received 15 May 2021
Received in revised form 24 June 2021
Accepted 25 June 2021

Keywords:
Augmented Reality
Virtual Reality
Building Construction
Safety
Marketing

ABSTRACT

Effective marketing is quite vital in many building construction projects that depend on the pre-sale cash in-flow. However, the unsafe condition of the under-construction projects postpones in-person customer visits to the completion date and complicates the marketing process. This safety concern is especially critical for the upper floor units. Although virtual tours of the buildings are used to show the project specifications, they do not convey the impression that customers receive in the real ambiance of in-person visits. This research proposes a novel method called semi-augmented reality to address the safety issue of the under-construction projects during the marketing process. In this method, lower floor apartment units are safeguarded for the customer's visits to give an accurate impression of the building's condition. Virtual models of the upper floor apartments are linked to a similar safeguarded unit on the lower floor to augment the existing deviations between lower and upper floor units. The capability of the method was successfully tested in an experimental case. The participating real estate agents in the test found the method beneficial for the customers' safety, attracting their attention, facilitating the decision-making process, and increasing their convenience. This method introduces a new approach to the building pre-sale marketing process. Similar techniques are expected to emerge shortly.

doi: *10.5829/IJE.2021.34.10a.01*

NOMENCLATURE

2D	2-Dimensional	PPE	Personal Protective Equipment
3D	3-Dimensional	QR code	Quick Response code
AR	Augmented Reality	SAR	Semi-Augmented Reality
BIM	Building Information Modeling	VR	Virtual Reality
IFC	Industry Foundation Class		

1. INTRODUCTION

Many researchers and practitioners have highlighted the integral impact of adopting an effective marketing approach in the construction industry in different parts of the world [1-5]. Adopting proper communication tools with clients [4, 6] and satisfying the clients' needs [7-9] are fundamental elements of practical marketing approaches in the building construction industry. Since pre-sale customers purchase products that are not entirely built yet, improving these two essential elements can substantially enhance the entire marketing process.

In recent years, advanced technologies, such as augmented reality (AR) and virtual reality (VR) technologies have proven themselves as effective marketing tools [10]. They are likely to change the marketing industry soon [11]. AR and VR are two digital information visualization techniques that rapidly grew in the shadow of the recent advances in information technology [12]. "Virtual reality refers to computer technologies that use software to generate the realistic images, sounds, and other sensations that represent an immersive environment and simulate a user's physical presence in this environment" [13]. Augmented reality is a variation of virtual reality [14], representing a direct or

*Corresponding Author Institutional Email: alvanchi@sharif.edu (A. Alvanchi)

Please cite this article as: A. Alvanchi, N. Didehvar, M. Jalilehvand, P. Adami, S. Shahmir, Semi-augmented Reality, A Novel Approach to Improve Customer Safety in Pre-sale Process of under Construction Buildings, International Journal of Engineering, Transactions A: Basics, Vol. 34, No. 10, (2021) 2198-2205

indirect view of the real physical world created by adding computer-generated virtual information [15]. Currently, consumer-based AR and VR computer applications form an inseparable part of marketing processes in many organizations [16].

Marketing tools are typically designed to attract potential customer's attention and educate them about the benefits and specifications of the products. AR- and VR-based tools have presented themselves more in favor of various businesses' customers than traditional marketing tools [12]. In a survey conducted by Szymczyk [17], 26% of senior market specialists mentioned AR and VR technologies as the most effective marketing tools in the future. AR and VR have been applied in various forms in marketing processes. Their sample applications include virtual and interactive product preview in public places [18, 19], wearing virtual clothes [20], virtual project tours [21], virtual shopping malls [22], presenting tourist attractions [23], and augmenting items in the museum [24, 25]. AR creates high purchasing pleasure and confidence in the customers [26]. AR and VR technologies are also emerging in building marketing. They are utilized for enhanced sales efficiency through virtual home touring, facilitated sight-unseen purchases, improved fix and flips rehabilitation, enhanced rental marketing, and improved tenant communication [27].

Meanwhile, the construction industry is considered among the most unsafe sectors in the world [28-30]. The construction industry accommodates 7% of the workforce globally; however, 30-40% of work-related casualties happen in this industry [31]. This rate represents five times the global average [32]. The high rates of safety incidents in the construction industry are regardless of various mandatory personal protective equipment (PPE) used and new methods and tools introduced to enhance the safety of the construction sites [33]. However, in recent years, modern technologies and tools have helped many developed economies considerably improve safety in their construction projects [34]. Advanced technologies, such as computer simulation [35, 36], integrated design approaches [37], and AR and VR technologies [38] have enhanced the safety of the construction sites .

According to the review article presented by Li, Yib [38], applications of AR and VR techniques in the construction safety methods are divided into three folds, including 1) "safety planning" through hazard identification and assessment before construction begins, 2) "safety training" by visualizing the actual work conditions and providing safety tips to the, and 3) "safety inspection" through easy access to the detailed 3-dimensional (3D) view of the job-site. A review of the past research shows that the focus of different developed safety tools in the construction, including AR- and VR-based tools, is on the construction crew. No research effort was found to address the existing safety concern for the under-construction building's customers. It should be noted that the untrained and inexperienced job-site visitors, such as pre-sale consumers of the building, bear a higher risk than the safety-educated and experienced construction workers. This safety concern is especially highlighted for the upper floor apartment units. The increased risk of the customers' in-person visits during the construction period is a concern that postpones customers' visits until the project's completion date. Meanwhile, in the final stages of a building project only limited and cosmetic changes can be made to the building and it is challenging to address the clients' particular needs. In this perspective, marketing approaches that consider the safety of customers during the in-person visits of the buildings are required to facilitate the marketing process and enhance the customers' satisfaction.

This research proposes a novel method to address the need for a safe and effective marketing method in pre-sale building marketing. The focus of the proposed method is on multi-story apartment building projects. The research utilizes a novel form of AR and VR technologies, called semi-augmented reality (SAR), to create a safe and effective in-person site visit experience for the customers with augmented reality details for the under-construction building parts. Following, section 2 presents the marketing paradigm of the multi-story apartment buildings. In section 3, the details of the proposed method are explained. Following that, in section 4, specifications of the implemented SAR tablet/ smartphone application in the research are outlined. Different steps that were taken to apply and test capabilities of the developed application to a sample seven-story apartment building come in section 5. Finally, section 6 concludes the research results and achievements.

2. MARKETING PARADIGM IN MULTI-STORY APARTMENT BUILDINGS

In contrast to typical family house construction projects, the construction of many multi-story residential apartment buildings commences without a sale contract with the clients. An investor invests initial money in the building construction and gradually complements its investment by selling a number of under-construction apartment units to the pre-sale customers. Here, the construction period is essential for the project managers and their real estate agents to accomplish their marketing chores properly, find clients for pre-sale units, and guarantee the required inflow. The unsafe construction environment creates a challenging condition and prevents real estate agents from correctly showing the apartments' specifications to the customers. It is especially the case for the upper floor apartment units where visitors need to

use incomplete and unsafe stairways to reach their desirable units. In recent years, virtual 3D models of the buildings have created a significant enhancement in the marketing process for presenting the building's specifications to the customers. The property owners, customers, real estate agents, and other stakeholders benefit from these virtual 3D models [39]. It should be noted that the 3D models do not replace the experience of the customers to walk through their desirable units, feeling the spaces, and observe the outside views. In-person site visit experience can increase the customers' confidence in the project and increase the chance that the customer steps forward and purchases the apartment. Furthermore, after the apartment purchase and during the construction period, site visits can help the clients proactively contribute to the final specifications of the building, customize it to their needs, and enhance their satisfaction.

In many apartment buildings, apartment units on different floors share similar layout plans. One solution followed by constructors and real estate agents to conquer the unsafe condition of the upper floor units is to prepare safeguarded model units on the ground or the first floor of the building. Pre-sale building customers are directed to visit the safeguarded model units with similar directions and layout plans during their site visits. In this approach, the prepared model units share similar plans and directions with the desired higher-level units; the customers can experience the real space, dimensions, and environment in the unit. However, it should be noted that specific details can drastically change on different floors. Building components such as vertical risers, structural column diameters, finishing details, natural light, building façade, and exterior views can vary from one floor to the other. Existing differences between lower and upper floors can even sometimes mislead the customers. Customers might interest in specific elements of the apartment building in the safe model units that do not exist on the upper floors. It is also possible that specific features in the model units, that do not exist in the upper floor units, discourage the customers from the deal. The proposed SAR method also addresses these concerns.

3. PROPOSED METHOD

The scope of the proposed method is the projects with similar plans in several floors. In the proposed method, virtual 3D models of the units on the higher floors, with increased safety concerns for the customers' in-person visits, are linked to the real environment of similar units on the lower floors. Therefore, clients can experience the real areas, spaces, and dimensions of their desirable upper floor units while walking in the safeguarded model units. Since the developed virtual model of the desired unit is linked to similar elements in the safeguarded model unit, the customer can simply distinguish the differences. Modified corners, different outside views, and changes in the window sizes are distinguishable in the virtual 3D model of the desired upper floor units. This approach to the virtual model demonstration is called semi-augmented reality (SAR) since the virtual model is linked to similar, not the exact, building elements. This approach also helps customers to get quick SAR tours in different nominated units on multiple floors and compare their features. While the customers' visits are done during the building's construction period, the safeguarded model unit also might still be incomplete. The developed SAR tool can also be used for the augmented visit of the model unit itself. The use of SAR-based tools helps customers to observe the designed completion for different components and, if possible, contribute to the building design according to their needs. Currently, the development of building information modeling (BIM) has become a trend in the construction of many apartment buildings [40].

Therefore, the 3D models of buildings are accessible in building projects with no additional cost. With the aid of the existing software packages, BIM-based 3D models of the building can be used for SAR-based model development with minimal cost. The developed SAR models need to be installed on mobile devices such as tablets and smartphones to be used on site. Figure 1 illustrates different parts of the proposed SAR-based marketing method. Figure 1 contains two parts, a and b. Figure 1(a) shows the schematic view of the SAR concept, and Figure 1(b) displays the step-by-step view of the proposed method.

4. IMPLEMENTATION OF PROPOSED METHOD

The proposed method was implemented in the form of a mobile application using AR Software in collaboration with a collaborating construction company. The industry foundation class (IFC) [41] files of the buildings were

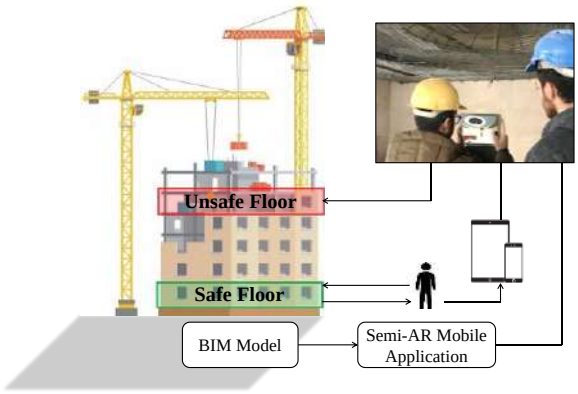

(a) Schematic view of the SAR concept

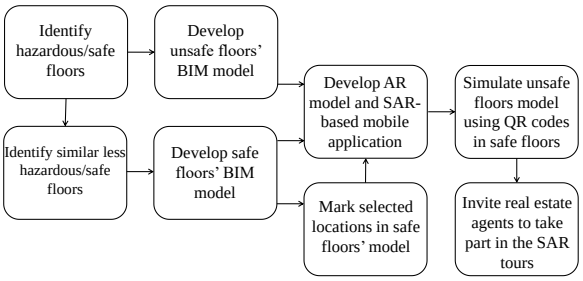

(b) Stages to develop SAR-based marketing method

Figure 1. Different parts of the proposed SAR-based marketing method

Figure 2. Scanning QR code to link an upper floor unit to the corresponding elements of the model unit

Figure 3. Under-construction condition of the building's stairway and elevator

Figure 4. Real estate agents participated in the SAR application capability test in the real building project case

used for the development of the 3D models of the building in the application. The developed application supported all VR, AR, and SAR views of a building. The VR view was the default view of the developed package. The VR view could be utilized for marketing purposes in on-site or off-site locations. Quick response (QR) codes [42] were used for triggering the AR and SAR views of the building. The QR codes of different apartment locations, such as the center of the living room, center of the master bedroom, corner side of the kitchen, and the front of the main entrance, could be created for different apartment units located on different floors. These QR codes could be scanned for linking the AR or SAR views to the desirable building components regardless of the clients' current floor. Figure 2 represents how a QR code print was scanned by the developed SAR package installed on a tablet to link the virtual models of an upper floor unit to the corresponding elements of the model unit. The customers could then use this mobile application to navigate current and prospective details of the apartment units. The customers could zoom in, zoom out, and calibrate the camera during their SAR experience when required.

5. EXPERIMENTAL CASE

To test the potential capabilities of the proposed method, it was applied to a real under-construction seven-story residential apartment building case in the central part of Tehran (Iran). Following, the case study experiment specification is explained, and the achieved results are presented and discussed.

5. 1. Case Study Specification Each floor of the studied case had two two-bedroom residential apartment units. At the time of the experiment, interior finishing activities of the building construction had just been commenced; the majority parts of the building's finishing works were missing. The stairways were still under construction and unsafe to use. The elevator was not installed as well. Figure 3 presents the condition of the stairway and the elevator shaft at the time of the experiment. The current condition was not appropriate for taking customers to the upper floors. The BIM models of the building, developed by the collaborative construction company, were used for customizing the developed SAR mobile package for the case. Members from the design and construction groups assisted the research team in finalizing the SAR package of the building. Ten active real estate agents in the region with an average work experience of 16 years were contacted to participate in the capability test experiment of the developed SAR package for the case. All participants indicated that they would prefer to set visits for the potential building customers as the primary marketing

practice for under-construction buildings. Eight agents indicated they have past experiences working with AR and VR technologies. However, none of them used AR or VR technologies as a regular practice in their marketing process. Six agents were also using 2D drawings to explain the specifications of the building for the customers as a common practice. Four agents had faced issues during the in-person customers' site visits. Figure 4 illustrates one of the agents using the developed SAR package during the experiment.

The objective of this experiment was to test the potential benefits SAR could bring to the marketing process during the construction period of the building. The test was separately performed for each agent and was divided into two parts. First, participants walked through the model unit on the first floor and observed the AR model of this apartment on the tablet using the developed SAR package. In this part of the experiment, real estate agents could monitor the finishing condition of the incomplete parts of the building. Figure 5 compares the actual view of the ceiling of the model unit on the first floor (Figure 5 (a)) linked to the prospective virtual view of the ceiling (Figure 5 (b)). In the second part of the experiment, the agents were guided to observe the SAR model of the seventh floor's apartment unit in the tablet while standing in the model unit. In this part of the experiment, the participants could observe the prospective virtual views of the seventh-floor unit linked to the corresponding actual components in the model unit on the first floor. The differences between the first and seventh-floor apartments' layouts and outside views were distinguishable through the SAR package. Figure 6 presents the actual view of the living room corner of the first floor (Figure 6 (a)) and a virtual view of the corresponding scene on the seventh floor (Figure 6 (b)). Here, the real estate agents could notice that the under-construction column in the middle of the living room of the model unit does not exist in the finishing condition of the seventh-floor unit. Furthermore, the protruding column on the right-side wall of the model unit fades in the finishing condition of the seventh floor.

5. 2. Experiment Result After the experiment, participating real estate agents answered several questions regarding their experience with SAR-based tools. Nine participants identified the SAR-based tool as beneficial for improving customers' safety, attracting customers, helping customers to decide accurately, and increasing customers' convenience during their site visits. In addition, seven agents identified the SAR as a beneficial tool for building the customers' confidence in the building's quality. However, only five agents identified SAR as a helpful tool for reducing the in-person site visit duration since they need time to set up the application for each customer. In general, all participants found SAR a helpful tool in their marketing process and indicated that they are interested in using the proposed method in their day-to-day marketing activities. Figure 7 shows the experiment's outcome and the potential benefits of the SAR-based method identified by participants. The achieved result of the investigation revealed the benefits of the proposed SAR method for improving different pre-sale marketing processes of the under-construction apartment buildings. Although the developed SAR application was at the preliminary stage with limited features, all participants indicated their desire to start using it in their marketing activities. Commercial development of the SAR application, with user-friendly and advanced features, can enhance the applicability of the SAR method in the pre-sale marketing practices.

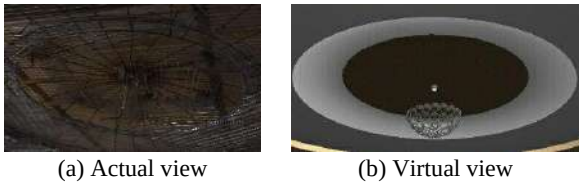

(a) Actual view (b) Virtual view

Figure 5. Linked views of the actual and virtual models of the ceiling in the model unit on the first floor

(a) Actual view of the living room on the first floor (b) Virtual view of the living room on the seventh-floor

Figure 6. SAR view of the seventh-floor unit's living room corner was observed in the model unit on the first floor

6. CONCLUSION

The emergence of the new AR- and VR-based technologies has evolved the marketing processes of many business sectors from different perspectives. The

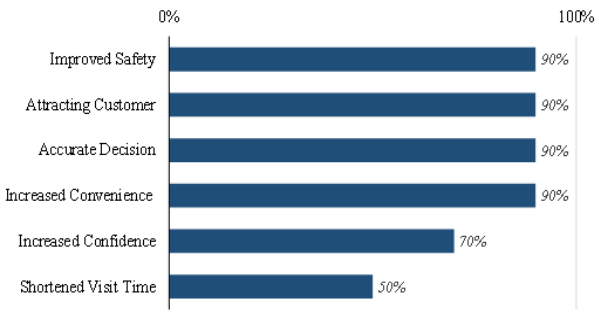

Figure 7. Potential benefits of the SAR-based method identified by participants

construction industry is a big industry with its specific marketing requirements. The unconfined nature of the construction jobs creates a high risk of incidents and hazards in construction projects and endangers the customers' safety during the marketing process. The complex combination of various building components and the long duration of building projects require proper marketing methods to attract customers' confidence and satisfaction. This research proposed a new AR/VR-based method called semi-augmented reality (SAR) to address the specific needs of pre-sale marketing in multi-story apartment buildings. The proposed method aims to enhance building customers' safety, contribution, and satisfaction. Safety concern of the construction operations has encouraged many researchers to study the new techniques and technologies for safety improvement in the construction industry. The focus of these research efforts, however, has been on the construction crew. In this perspective, this research is among the first research efforts to address the safety of pre-sale customers during the building's construction period. The SAR method can also provide a platform for collecting the customer's particular needs in building projects and consider them in the final product. It is expected that this approach can directly contribute to the customer's satisfaction. The achieved results of the experimental case also demonstrated high potentials for the proposed SAR method. Various applications of AR/VR-based tools have been introduced and used in the construction industry in recent years. However, the proposed SAR method leverages AR/ VR technology capabilities in a novel setting to address the current needs of the construction industry.

The proposed method in this research was implemented in an under-construction apartment building in Tehran, and some real estate agents participated in SAR tours. The performed investigation demonstrates the potential benefits of the proposed SAR method.

90% of the participants declared that this method could:

- improve customers' safety;
- attract customers;
- help customers to decide accurately;

70% of them mentioned that the technique could:

- increase customers' convenience during their site visits;

and only 50% of the participants said that SAR method could:

- be as a beneficial tool for building the customers' confidence in the building's quality.

The implemented SAR-based tool and the results achieved in the experiments might have been affected by the specific regional conditions of the apartment building marketing in Tehran. Further investigations are encouraged in other locations to test the applicability of the proposed SAR method in other regions. Also, the proposed method is applicable in apartments with similar plans on different floors. As future research, it is suggested to investigate the usefulness and applicability of the SAR method in other kinds of buildings.

7. ACKNOWLEDGEMENT

Authors would like to express their appreciation to Mr. Shiri and Ms. Sayanjali, who generously provided their support to the research team during the method implementation and the case study.

8. REFERENCES

1. Birhanu. B, "The effect of integrated marketing communication on sales performance: A case study of selected real estate companies in Addis Ababa". (2020), St. Mary's University.
2. Mokhtariani. M, Sebt. M. H, and Davoudpour. H, "Construction marketing: developing a reference framework", ***Advances in Civil Engineering***. (2017), Article ID 7548905 DOI: 10.1155/2017/7548905.
3. Liu. Z, Huang. S. S, Hallak. R, and Liang. M, "Chinese consumers' brand personality perceptions of tourism real estate firms". ***Tourism Management***, Vol. 52, (2016), 310-326, DOI: 10.1016/j.tourman.2015.06.022.
4. Yankah. J. E, and Dadzie. D. K, "Marketing Construction Business: Problems, Prospects and Strategies". ***Marketing***, Vol. 7, No. 29, (2015), 182-192.
5. Maira. D, "Online Marketing Issues of Real Estate Companies: A Case of Latvia". ***Baltic Journal of Real Estate Economics and Construction Management***, Vol. 3, No. 1, (2015), 130-139, DOI: 10.1515/bjreecm-2015-0013.
6. Mandica. T, Mackova. D, Mesaros. P, and Spisakova. M, "Impact model of communication and marketing tools for the promotion of family houses built by modern methods of construction". ***International Journal of Applied Engineering Research***, Vol. 12, No. 21, (2017), 11749-11759.
7. Naranjo. G, Pellicer. E, and Yepes. V, "Marketing in the construction industry: State of knowledge and current trends". Dyna, Vol. 78, No. 170, (2011), 245-253.
8. Cicmil. S, and Nicholson. A, "The role of the marketing function in operations of a construction enterprise: misconceptions and paradigms". ***Management Decision*** Vol. 36, No. 2, (1998), 96-101, DOI: 10.1108/00251749810204179.
9. Smeal, A. and P. Colwell, "A comparison of real estate marketing systems: theory and evidence". ***Journal of Real Estate Research***, Vol. 10, No. 5, (1995), 583-599, DOI: 10.1080/10835547.1995.12090804.
10. Feng. Y, and Mueller. B, "The State of Augmented Reality Advertising Around the Globe: A Multi-Cultural Content Analysis". ***Journal of Promotion Management***, Vol. 25, No. 4 (2019), 453-475, DOI: 10.1080/10496491.2018.1448323.
11. Kannan. P, "Digital marketing: A framework, review and research agenda". ***International Journal of Research in Marketing***, Vol. 34, No. 1, (2017), 22-45, DOI: 10.1016/j.ijresmar.2016.11.006.
12. Billinghurst. M, Clark. A, and Lee. G, "A Survey of Augmented Reality". Foundations and Trends® in Human–Computer Interaction, Vol. 8, No. (2-3), (2015), 73-272, DOI: 10.1561/1100000049.

13. Parvinen. P, Hamari. J, and Pöyry. E, "Introduction to Minitrack: Mixed, Augmented and Virtual Reality". in 51st Hawaii International Conference on System Sciences (2018), DOI: 10.24251/hicss.2018.172.
14. Azuma. R. T, "A Survey of Augmented Reality". In Presence: Teleoperators and Virtual Environments, Vol. 6, No. 4, (1997), 355-385, DOI: 10.1162/pres.1997.6.4.355.
15. Carmigniani. J, Furht. B, Anisetti. M, Ceravolo. P, Damiani. E, and Ivkovic. M, "Augmented Reality Technologies, Systems and Applications", ***Multimedia Tools and Applications***, Vol. 51, (2011), 341-377, DOI: 10.1109/ISIE.2008.4676964.
16. Brohm. D, Domurath. N, Glanz-Chanos. V, and Grunert. K. G, "Future trends of augmented reality". In Augmented reality for food marketers and consumers, (2017), 1681-1685, DOI: 10.3920/978-90-8686-842-1_6.
17. Szymczyk. M, "CMO's Select Augmented Reality as Future Trend for Marketing." Zugara. Retrieved February 3, 2020, from http://zugara.com/cmos-select-augmented-reality-future-trend-marketing, (2015).
18. Javornik. A, "[Poster] classifications of augmented reality uses in marketing". in IEEE. 2014. Mixed and Augmented Reality-Media, Art, Social Science, Humanities and Design (ISMAR-MASH'D), (2014), IEEE International Symposium, DOI: 10.1109/ISMAR-AMH.2014.6935441.
19. Van Krevelen. D. W. F, and Poelman. R, "A survey of augmented reality technologies, applications and limitations". ***International Journal of Virtual Reality***, Vol. 9, No. 2, (2010), DOI: 10.20870/ijvr.2010.9.2.2767.
20. Yuen. S. C. Y, Yaoyuneyong. G, and Johnson. E, "Augmented reality: An overview and five directions for AR in education". ***Journal of Educational Technology Development and Exchange***, Vol. 4, No. 1, (2011), 11, DOI: 10.18785/jetde.0401.10.
21. Agarwal. S, "Review on application of augmented reality in civil engineering". in International Conference on Inter Disciplinary Research in Engineering and Technology. (2016).
22. Van Kerrebroeck. H, Brengman. M, and Willems. K, "Escaping the crowd: An experimental study on the impact of a Virtual Reality experience in a shopping mall". ***Computers in Human Behavior***, Vol. 77, (2017), 437-450, DOI: 10.1016/j.chb.2017.07.019.
23. Moorhouse. N, Jung. T, and tom Dieck. M. C, "The marketing of urban tourism destibations through virtual reality: tourism marketers' perspectives". in 8th advances in hospitality and tourism marketing and management (AHTMM) (2018).
24. Trunfio. M, Magnelli. A, Della Lucia. M, Verreschi. G, and Campana. S, "Augmented and virtual reality in cultural heritage: enhancing the visitor experience and satisfaction at the area Pacis museum in Rome, Italy". in 8th advances in hospitality and tourism marketing and management (AHTMM). (2018).
25. He. Z, Laurie. W, and Xiang. R. L, "When art meets tech: "The role of augmented reality in enhancing museum experiences and purchase intentions". ***Tourism Management***, Vol. 68, (2018), 127-139, DOI: 10.1016/j.tourman.2018.03.003.
26. Brengman. M, Willems. K, and Van Kerrebroeck. H, "Can't touch this: the impact of augmented reality versus touch and non-touch interfaces on perceived ownership". ***Virtual Reality***, Vol. 23, No. 3, (2019), 269-280, DOI: 10.1007/s10055-018-0335-6.
27. Ullah. F, Sepasgozar S. M, and Wang. C, "A systematic review of smart real estate technology: Drivers of, and barriers to, the use of digital disruptive technologies and online platforms". ***Sustainability***, Vol. 10, No. 9, (2018), 3142, DOI: 10.3390/su10093142.
28. Zhou. Z, Goh. Y. M, and Li. Q, "Overview and analysis of safety management studies in the construction industry". ***Safety Science***, Vol. 72, (2015), 337-350, DOI: 10.1016/j.ssci.2014.10.006.
29. Sunindijo. R. Y, "Improving safety among small organisations in the construction industry: Key barriers and improvement strategies". ***Procedia Engineering***, Vol. 125, (2015), 109-116, DOI: 10.1016/j.proeng.2015.11.017.
30. Fang. D, Wu. C, and Wu. H, "Impact of the supervisor on worker safety behavior in construction projects". ***Journal of Management in Engineering***, Vol. 31, No. 6, (2015), 04015001, DOI: 10.1061/(ASCE)ME.1943-5479.0000355.
31. Sunindijo. R. Y, and Zou. P. X, "Political skill for developing construction safety climate". ***Journal of Construction Engineering and Management***, Vol. 138, No. 5, (2012), 605-612, DOI: 10.1061/(ASCE)CO.1943-7862.0000482.
32. US Bureau of Labor Statistics (BSL), "National census of fatal occupational injuries in 2017". United States Department of Labor, Bureau of labor statistics, (2018), 7.
33. Choudhry. R. M, and Fang. D, "Why operatives engage in unsafe work behavior: Investigating factors on construction sites". ***Safety Science***, Vol. 46, No. 4, (2008), 566-584, DOI: 10.1016/j.ssci.2007.06.027.
34. Zou. P. X, and Sunindijo. R. Y, "Strategic safety management in construction and engineering". (2015), Wiley Online Library, DOI: 10.1002/9781118839362.
35. Baniassadi. F, Alvanchi. A, and Mostafavi. A, "A simulation-based framework for concurrent safety and productivity improvement in construction projects". ***Engineering, Construction and Architectural Management***, (2018), DOI: 10.1108/ECAM-12-2017-0266.
36. Marzouk. M, and Ali. H, "Modeling safety considerations and space limitations in piling operations using agent based simulation". ***Expert Systems with Applications***, Vol. 40, No. 12, (2013), 4848-4857, DOI: 10.1016/j.eswa.2013.02.021.
37. Malekitabar. H, Ardeshir. A, Sebt. M. H, and Stouffs. R, "Construction safety risk drivers: A BIM approach". ***Safety Science***, Vol. 82, (2016), 445-455, DOI: 10.1016/j.ssci.2015.11.002.
38. Li. X, Yi. W, Chi. H. L, Wang. X, and Chan. A. P, "A Critical Review of Virtual and Augmented Reality (VR/AR) Applications in Construction Safety". ***Automation in Construction***, Vol. 86, (2018), 150-162.
39. Takin. M, Peng. J, Sepasgozar. S. M. E, and Ebrahimi. H, "A Framework for Using Advanced Visualization Tools for Residential Property Management". in ISARC. Proceedings of the International Symposium on Automation and Robotics in Construction. (2017). IAARC Publications, DOI: 10.3390/su10093142.
40. Sacks. R, Eastman. C, Lee, G. and Teicholz. P, "BIM handbook: A guide to building information modeling for owners, designers, engineers, contractors, and facility managers". (2018), John Wiley & Sons.
41. ISO, "ISO 16739-1:2018, Industry Foundation Classes (IFC) for data sharing in the construction and facility management industries — Part 1: Data schema". (2018), The International Organization for Standardization.
42. Coleman. J, "QR codes: what are they and why should you care?" Kansas Library Association College and University Libraries Section Proceedings, Vol. 1, (2011), 16-23, DOI: 10.4148/culs.v1i0.1355.

Persian Abstract

چکیده

بازاریابی اثربخش در بسیاری از پروژه‌های ساختمانی امری بسیار حیاتی است که می‌تواند جریان نقدی ورودی حاصل از پیش‌فروش آن پروژه را ایجاد کند. با این وجود، شرایط ناامن پروژه‌های در حال ساخت، مراجعه حضوری مشتری را به زمان اتمام پروژه موکول می‌کند و روند بازاریابی را پیچیده می‌کند. این مسئله به ویژه برای واحدهای طبقات فوقانی بسیار پراهمیت است. باآن‌که از تورهای مجازی ساختمان برای نشان دادن مشخصات پروژه استفاده می‌شود، اما احساسی را که مشتریان در محیط واقعی بازدیدهای حضوری دریافت می کنند، منتقل نمی‌کند. این پژوهش روشی جدید به نام شبه واقعیت افزوده را برای افزایش ایمنی پروژه‌های در حال ساخت در طی فرآیند بازاریابی پیشنهاد می‌دهد. در این روش، واحدهای آپارتمانی طبقه پایین برای بازدید مشتری کاملا ایمن می‌شوند تا بازدید مشتری انجام شود و برداشت دقیقی از وضعیت ساختمان داشته باشد. سپس مدل مجازی آپارتمان‌های طبقه فوقانی به واحد ایمن مشابه در طبقه پایین متصل می‌شود تا تفاوت‌های موجود بین واحدهای طبقه پایین و طبقه بالا مشاهده شود. قابلیت این روش در یک مورد تجربی با موفقیت مورد آزمایش قرار گرفته است. نمایندگان آژانس‌های املاک و مستغلات شرکت کننده در این آزمون، روش ارائه‌شده را برای افزایش ایمنی مشتریان، جلب توجه آن‌ها، تسهیل روند تصمیم‌گیری و افزایش راحتی آن‌ها مفید دانستند. این روش رویکرد جدیدی را در روند بازاریابی پیش‌فروش پروژه‌های ساختمانی معرفی می‌کند. انتظار می‌رود که تکنیک‌های مشابه در آینده‌ای نزدیک ظهور کنند.

IJE TRANSACTIONS A: Basics Vol. 34, No. 10, (October 2021) 2206-2212

International Journal of Engineering

Journal Homepage: www.ije.ir

Soil Shrinkage Characterization of Low Plasticty Soil using Digital Image Analysis Process

A. G. Sharanya*[a], M. Heeralal[a], T. Thyagaraj[b]

[a] *Department of Civil Engineering, National Institute of Technology, Warangal, India*
[b] *Department of Civil Engineering, Indian Institute of Technology, Madras, India*

PAPER INFO

Paper history:
Received 27 March 2021
Received in revised form 18 June 2021
Accepted 25 June 2021

Keywords:
Water-retention
Low-plasticity Soil
Shrinkage Characterization
Unsaturated Soil
Digital Image Analysis
Volumetric Strain

ABSTRACT

The purpose of this paper is to understand the shrinkage behaviour of low plasticity soil, which is prevalent in Warangal, India. In this study, the shrinkage mechanism and behaviour with suction variation are characterised and described using simple and reliable experimental approaches. The findings concern the changes in suction, water content, and void ratio of soil that has been air-dried from full saturation to dryness. The proposed framework employs two simple processes: one to calculate the suction potential and the other to characterise the shrinkage mechanism. The study also highlights the use of ImageJ software to capture sample shrinkage using digital image processing (DIP). The findings confirm the absence of macro pores, and the effects of capillary suction on the shrinkage response are reiterated in volume change studies using suction as a stress-state variable.

***doi**: 10.5829/ije.2021.34.10a.02*

1. INTRODUCTION

There is extensive research to understand the volume change of expanding clay minerals. The soils of low plasticity are considered to be less prone to hydration or desoprtion and thus often neglected in volume change characterization. There are many field applications of locally available low plasticity soils, and there is no insight into the behavior of soil during desiccation [1]. There are limited works that have put emphasis on the impact of drying pertaining to geotechnical engineering application [2]. During the construction phase and the service life, compacted soil layers tend to remain in unsaturated state. This consideration necessitates the inclusion of suction existing between the soil pore spaces contributed by the water to understand the-thermo-hydro-mechanical behavior [3, 4]. Based on the recognition that suction is a function of water content, shrinkage analysis in the framework of suction change and the volume of void variation has been examined by number of researchers [4-6]. The plastic strain accumulation of soil deformation under the effect of mechanical loading and the suction induced stress has been studied to incorporate constitutive relationship by numerous experimental works [7, 8]. The complex nature of soil pore structure and the physical significance of understanding the suction potential of engineered soils is explained in terms of soil water characteristic curve (SWCC) [9]. In order to determine the shrinkage character of soil from its initial state to dryness, the experimental works required the simultaneous measurements of volume changes and the water content changes [10]. The volume change will be expressed as the quantification of the void ratio induced by changing the water content subjected to various methods of drying. The water content reduction and the subsequent pore void changes are represented as the soil ashrinkage curve (SSC) [11].

The measurement of moisture change in the course of drying is very easy and can be done with the help of weight change. The complexity of framing the SSC lies in the accurate measurement of the volume of void change. The measurement of the volume change in the laboratory has progressed from the use of fluid

*Corresponding Author Institutional Email: sharanyaag@student.nitw.ac.in (A. G. Sharanya)

Please cite this article as: A. G. Sharanya, M. Heeralal, T. Thyagaraj, Soil Shrinkage Characterization of Low Plasticty Soil using Digital Image Analysis Process, International Journal of Engineering, Transactions A: Basics, Vol. 34, No. 10, (2021) 2206-2212

displacement method with various types of fluids to the advanced method of 3D modeling using photogrammetric techniques.

The use of direct methods such as water or mercury displacement, saran resin coating, use of kerdane oil, toluene coating, rubber balloon method and flexible tape or Vernier caliper to measure the dimensional change has been widely studied [12, 13]. All these procedures have been applied primarily on soil samples obtained as clods. It has been observed that all these methods are applicable largely to sample in natural moisture conditions. The mercury displacement method and use of resins recommended in literature seems to be hazardous to health. The direct methods also possess numerous inaccuracies in the volume measurements due to the likelihood of loss of sample during coating or immersions [14].

The non-contact measurement techniques includes the use of displacement transducers [15], laser sensors [16], digital imaging with high-resolution cameras [17, 18] particle image velocimetry (PIV) technique [19] and photogrammetric technique with pin-hole cameras [20, 21]. All these techniques appear to be more sophisticated and necessitate the knowledge of coding, 3D modeling, and simultaneous use of multiple softwares to process the 3D models. Though there exists very limited research that discusses the application of non-contact techniques, they have gained attention with respect to slurry and compacted samples prone to cracking by desiccation [22]. Among these non-contact volumetric strain measurement methods, digital imaging technique which uses hand-operated digital cameras and open-source softwares such as *'ImageJ', 'Scion image'* [21-23] provides reliable results and practicable for soils that are not highly prone to volume change placed under lightly loaded structures. The soil profiles in temperate zone can be more precisely using the high-end sophisticated photogrammetric technique whereas soils prevailing in tropic zone can be studied with digital imaging process.

This work focusses on quantifying the shrinkage behavior of low plasticity in the Warangal district of India is characterized by the pore volume change. The experimental procedure aims at determining the suction potential and shrinkage induced change in the volume of voids. The study utilizes a chilled mirror hygrometer (model WP4-T Dewpoint PotentioMeter) for suction measurement and digital image analysis process for capturing the diametrical change of the drying sample. The initially saturated state is found to be an ideal approach as low plasticity soil is devoid to lesser volume change in the partially saturated condition. This initial condition is expected to simulate the worst moisture variation. The vertical deformation is measured using the caliper and the combined dimensional change is used for computation of volume. The proposed approach used in this study is rather simple and efficient in contrast to the existing procedures that required expertized assistance. This paper does not discuss the comparison of the proposed practice with other routine fluid displacement methods or photogrammetric approaches. The mechanism of shrinkage is highlighted with the use of the DIP under the framework of unsaturated soil mechanics principles.

2. EXPERIMENTAL DETAILS

2. 1. Materials and Specimen Preparation The soil was mixed with distilled water and placed in airtight press bags to reach equilibrium for 24 hours. The mellowed soil was statically compacted to thickness of 20mm and diameter 70mm such that dry unit weight is 17.12 kN/m^3. The specimen for measuring suction was extracted for a of size 30 mm diameter and 10 mm height using a dedicated metal ring (see Figure 1).

Secondly, to measure shrinkage potential, the dry so passing through 0.075mm IS sieve was mixed with water content excess to its liquid limit (LL) to obtain a slurry. The slurry was placed in a grease coated aluminum cup of diameter 42 mm and depth 10 mm. It was placed in the laboratory to simulate the evaporation by air-drying.

2. 2. Measurement

2. 2. 1. Suction Potential Dewpoint PotentioMeter (model WP4-T, Decagon Devices, USA)

TABLE 1. Properties of soil sample

Soil Property	Unit	Value
Liquid Limit	%	42
Plastic Limit	%	31
Plasticity Index	%	11
Specific Gravity	--	2.61
Maximum dry unit weight	kN/m^3	17.12
Optimum moisture content	%	15.5
USCS		CL

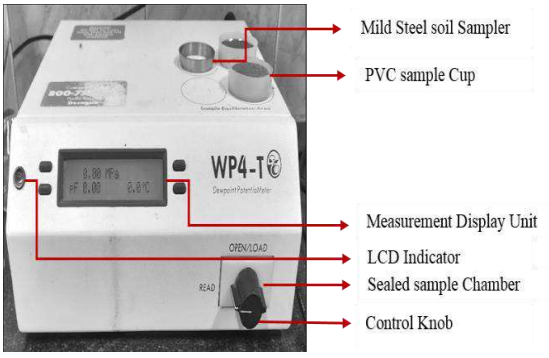

Figure 1. WP4-T Dewpoint PotentioMeter

(Figure 1) was used for the total suction measurement of the compacted specimen. The device measures the relative moisture of air above the soil sample in a sealed chamber and uses the principle of chilled mirror hygrometer. The accuracy is ±0.1 MPa for measurements from 0 to -10 MPa and ±1% for measurements from -10MPa to -300 MPa. The testing protocol followed as mentioned in ASTM D6836-16 [24]. The measurement takes time of about 5 -10 minutes and the instrument was operated at 20±2°C with their actual range of maximum 40°C. The SWCC is plotted by fitting the experimental data using the equation proposed by Fredlund and Xing [25] to obtain the complete curve.

$$W(\psi) = W_s \left[1 - \frac{ln\left(1+\frac{\psi}{h_r}\right)}{ln\left(1+\frac{10^6}{h_r}\right)}\right] \left\langle \left\{ ln\left[exp(1) + \left(\frac{\psi}{a_f}\right)^{n_f}\right]\right\}^{m_f} \right\rangle^{-1} \quad (1)$$

In Equation (1) W (ψ) is the moisture content corresponding to suction value ψ, a_f, n_f & m_f are fitting parameters and h_r is the residual suction in kilo-Pascal (kPa).

2. 2. 2. Shrinkage Characterization Shrinkage behavior was measured by allowing the slurry to dry placed open to the atmosphere exposed on its top surface. The research is limited to the examination of samples with sizes that are equivalent to those used in the mercury displacement method of shrinkage limit test. The other reason is that larger sizes may necessitate the use of high-resolution cameras fixed in varying positions to capture complete soil behaviour. The shrinkage of the soil was recorded by still image capture technique at regular time intervals (Figure 2). The captured image was analyzed and processed using the *'ImageJ'* software to quantify the radial shrinkage.

The mass of the specimen was measured to an accuracy of 0.01g and terminated when the difference in the mass was almost negligible. The specimen was subjected to a drying regime by containing it in constant temperature facility to achieve a gradual decrease in water content. The thickness change was measured using Vernier calipers such that loss of sample is minimal.

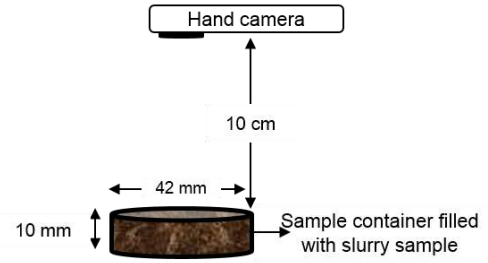

Figure 2. Experimental set-up for digital imaging capture process

The image capturing was done only to capture the radial deformation of the drying sample with a concentration on the open-top face of the shrinkage dish. The soil shrinkage curve was plotted with gravimetric water content variation agreeing to the void ratio of tested specimen assuming constant volume condition and the curve was categorized based on the shrinkage phases exhibited. The experimental data of the void ratio corresponding to water content variation is fitted with the hyperbolic equation proposed by Fredlund et al. [26]. A non-linear least square algorithm with the fit Equation (2) was be used to fit the experimental data.

$$e(w) = a_{sh}\left[\frac{w^{c_{sh}}}{b_{sh}^{c_{sh}}} + 1\right]^{\frac{1}{c_{sh}}} \quad (2)$$

$$\frac{a_{sh}}{b_{sh}} = \frac{G_s}{S} = \text{Constant} \quad (3)$$

where S represents the degree of saturation, G_s is the specific gravity of soil sample, a_{sh} is the minimum void ratio (e_{min}), b_{sh} is the slope of the tangent line and c_{sh} is the curvature of shrinkage curve. Equation (3) is a constant for a specific soil which shows that on determining the minimum void ratio of the soil sample, the slope of the tangent drawn to the shrinkage curve can be obtained. The shrinkage curve parameter c_{sh} was determined by the consistency observed in the experimental study conducted by Fredlund et al. [26] based on the initial condition of the test sample (i.e. compacted, slurry or undisturbed). The c_{sh} parameter for an initially slurry sample was determined as 25.31 with a standard deviation of ± 25.41. In this study, to perform the fit, the c_{sh} value suggested by Fredlund method had found to be satisfying. To observe and quantify the radial shrinkage of the saturated slurry sample at net zero stress condition, 12 Megapixel (MP) camera was mounted in position as shown in Figure 2. The images were captured every 3 hours in the day time between 930 h to 1800 h for 5 days represented according to the military time system. The average maximum daily temperature in the course of the testing which lasted for 5 days was found to be 32.3℃. At the end of 5th day, the sample was placed in the oven maintained at 60 ℃ for 24h to determine the dry weight of the soil sample. Final weight and volume observations were used along with the observations made during the entire test period of 5 days. The processing of images captured through standard arrangement was processed further to obtain the radial variation which is discussed in detail in the next section.

2. 2. 3. Digital Image Analysis The identification of the shrinkage response of saturated soil specimens subjected to desaturation is carried out by extracting the dimensional change information from the digital images captured. The captured images were processed further to acquire the required volumetric

change information of the shrinking soil sample. In this study, the qualitative, as well as quantitative characterization of the two-dimensional image, is done using the image processing software '*ImageJ 1.52a*' software developed at the University of Wisconsin. This software helps in spatial as well as grayscale calibration that makes it more reliable to measure distances and calculate area and pixel value by simulating real-time dimensional measurements. The threshold processing of the image will be followed up to segment it from 8-bit grayscale to an image of 2 colors, in general black and white based on the clustering concept.

3. RESULT AND DISCUSSIONS

The suction potential of soil in the desorption phase obtained from the Chilled mirror hygrometer was plotted against the corresponding gravimetric water content of the soil sample and represented as the SWCC as shown in Figure 3. The dataset obtained from the experiment was fit with Fredlund and Xing (F&X) model [25] which resulted in the air-entry value (AEV) of 220 kPa corresponding to a saturated water content of 18.82% and the residual water content value was obtained as 10.42 %.

The AEV represents the suction beyond which air starts receding into the pores of the sample and residual suction represents the region where further increase in suction will not result in reduction of water from the pores [27]. The F&X model was found to be the best fit for a comprehensive range of suction values and thus the model was chosen to fit the measured data to obtain the suction potential of soil specimen with varying water content. The volume change response of the specimen during testing was assumed to be nil as the dry density of the compacted specimen remained constant. The fit of the experimental data with Equation (1) was performed using the program "SWRC fit" which accomplishes nonlinear fitting [28]. As seen from the graph plotted in Figure 3, there is a negligible decrease of water content up to a suction increase of about 220 kPa and this was an indication that constant water content was observed in the range of low suction. The results adhere to the understandings that there is restricted water flow from the intra-aggregate pore spaces which are typically a property of the adsorption water layer [29]. There was a gradual decrease in the water content retention behavior of soil with suction increase beyond the air entry value. The residual water content from the graph indicated that with a further increase in the suction potential, there was no variation in the retention water. This gave an indirect assessment of the pore size distribution of the compacted specimen thus the interrelation between the retention water and the pore size characterization became an important facet to be concerned. The inter-aggregate pore water held under capillary pressure was removed with a suction increase up to the residual value and beyond this, there was no water-volume loss.

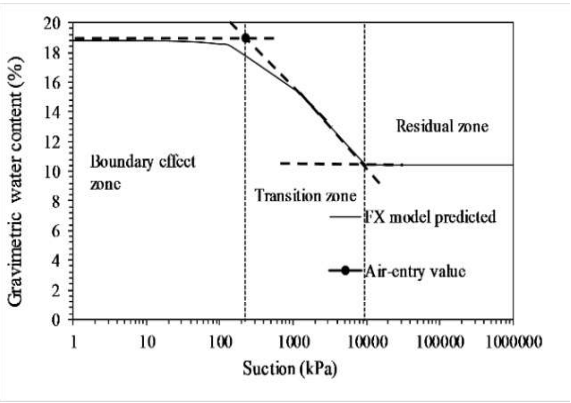

Figure 3. Soil water characteristic curve of test specimen

The radial shrinkage of the saturated sample was studied by allowing the sample to air-drying in the laboratory ambiance. The mass of the sample experienced changes as the temperature was varying. The sample was initially placed open to the atmosphere subjected to an average maximum daily temperature of 33°C. When it was confirmed that sample mass reduction is in a lower range based on observations, as they were placed in a temperature controlled set-up under 60°C for about 24 h . The sample imaging began and continued till it was transferred to the oven for complete desaturation. After removal of the sample from the oven, the final imaging to confirm the radial deformation was captured. As the sample was placed in a confined container, the vertical variation of the sample dimension was obtained using the Vernier caliper, and owing to the small size of the sample, handling was relatively easier. The captured images were analyzed and processed as the threshold images using the *'ImageJ'* software as shown in Figures 4 and 5. The image processing was done by the cluster method of thresholding the grayscale image at an initial threshold value of 8-bit. It was ensured to provide adequate lighting and negligible glaring to capture digital still images such that good contrast existed between background and foreground. This condition helped in assuring the best effect of an 8-bit threshold limit to perform better for all the captured images. This method backed an inaccurate measurement of the dimensional variation observed in the sample due to shrinkage. This imaging technique was found to be more reliable when the sample is experiencing shrinkage without being accompanied by cracking. Thus for soils with less expansive mineralogical composition, this approach is highly recommended. There exist limited studies that have used this *'ImageJ'* software for volume determination of expansive soils subjected to wet-dry cycles of moisture variation and that needs further explicit research to confirm the reliability of this imaging

Figure 4. Sequence of image processing

technique [22]. The variation of radial shrinkage observed in the specimen was quantified to be 15% of the initial sample size.

The processed threshold image of the slurry sample subjected to drying regime as shown in Figure 5.

The average vertical shrinkage of the sample subjected to gradual evaporation was about 17%. Proportional or primary shrinkage of compacted soil specimens was calculated using Equation (4). The dominant proportional shrinkage phase of this soil sample as shown in Figure 6 was quantified to be about 13%. This shrinkage refers to the phase where the volume of water loss is equal to the volume of void change which is predominantly due to the loss of moisture from the soil macropore and this phase is generally linear.

$$\text{Primary Shrinkage}, PS = \frac{(e_{is}-e_{ps})}{1+e_{is}}\ x\ 100 \qquad (4)$$

where e_{is} and e_{ps} represent the void ratio at the initiation and end of primary shrinkage, respectively (see Figure 6). The plot was made using the variation of the water content measured from the mass variation of sample and the void ratio was calculated corresponding to the varying water content. The shrinkage curve was identified to be with no inflection point and the wetting and drying side maximum curvature. This indicates the absence of intra-aggregate pores thus there exists no adsorption suction phase in this soil. The lack of residual shrinkage phase which possesses the character of reduced void volume compared to the water volume loss is also observed. The fitting parameters used in Equation (3) were determined as a_{sh} =0.91, b_{sh} = 0.35 and c_{sh}= 25.31 using the graphical plot made for the experimental data. The fitted curve is a linear proportional shrinkage phase and it can be categorized as Type D (SSC with phase II shrinkage) and the results are similar reported by Peng and Horn [6]. The presence of negligible inter-aggregate pores was attributed as the reason for the absence of a structural shrinkage phase. The existence of organic matter and the absence of clay minerals is supposed to depict this behavior and this also indicated the variation of inter aggregate pores with the variation of suction and water content. The existence of zero shrinkage phase is observed to be due to the non-existence of hydration by solid particle surfaces or the exchangeable cations [4].

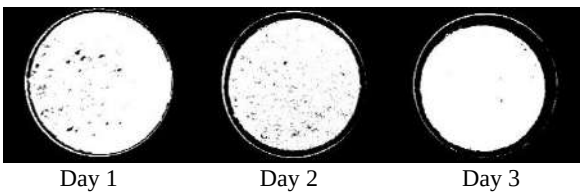

Figure 5. Threshold image of shrinkage from initial slurry state (White= soil solid)

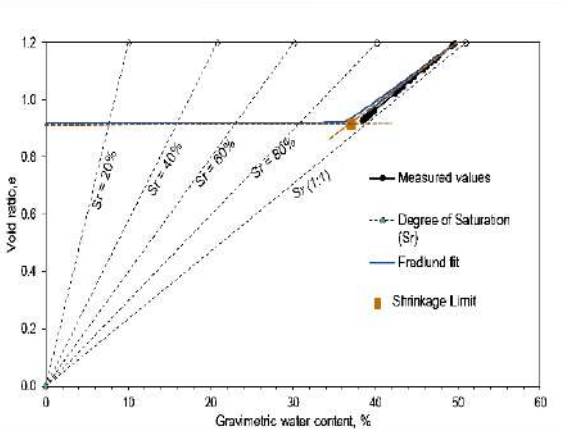

Figure 6. Soil shrinkage curve (SSC) of the sample

The test approach can also be utilised to analyse the shrinkage behaviour of samples prepared at various initial degrees of saturation, as confirmed with Figure 6. The results of this study are limited to samples that were air dried from saturated to dry state, and more research into the effect of drying-wetting cycles and varying temperatures on shrinkage behaviour is needed to gain a better understanding of the shrinkage mechanism.

4. CONCLUSIONS

This study emphasizes the use of principles of unsaturated soil mechanics to study the drying shrinkage behavior of low plasticity soil using advanced digital imaging processes. The following conclusions are observed from the study.

a. The volume change study based on total suction is identified as an ideal approach such that the suction

pressure existing in both inter and intra aggregate pore space will be considered. The silty soil considered for study undergoes the desaturation from the capillary phase (dominated in the completely water-saturated scenario) to the zero shrinkage phase where there is the nonexistence of hydrate water on the particle surface as well as lack of hydration water via the exchangeable cations.

b. The soil sample owing to its low plasticity, shows a proportional void volume change with respect to volume of water lost. This implies the absence of adsorption moisture range in the soil particle, but still an elaborate study on the wet-dry phase of moisture variation under a constant stress condition should be carried out to understand the volumetric changes. The crack initiation is restricted due to the confined small sample size used in this study and the effect of variation in area ratio of the sample should be considered for further study.

c. The *'ImageJ'* software was used to carry out the digital image analysis process and the method is observed to be easier and reliable. The analysis of small-sized sample is encouraged for image analysis technique so as to avoid optical distortions. In case of large sample sizes and for the generation of 3D volume model, photogrammetric technique which uses the pin-hole cameras will be advantageous.

5. REFERENCES

1. Yue, E., and Veenstra, J. N. "Prediction of active zone depth in Oklahoma using soil matric suction" ***Journal of GeoEngineering***, Vol. 13, No. 1, (2018), 29-38. DOI: 10.6310/jog.201803_13(1).3
2. Bore, T., Mishra, P. N., Schwing, M., Ribeiro, M., Wagner, N., and Scheuermann, A. "On Reconstructing the Soil Shrinkage Characteristic Curve by Dielectric Spectroscopy." ***International Geoscience and Remote Sensing Symposium***, Institute of Electrical and Electronics Engineers Inc., (2019), 6205-6208. https://doi.org/10.1109/IGARSS.2019.8899153.
3. Chen, P., and Lu, N. "Generalized equation for soil shrinkage curve." ***Journal of Geotechnical and Geoenvironmental Engineering***, Vol. 144, No. 8, (2018), 1-10. DOI: 10.1061/(ASCE)GT.1943-5606.0001889
4. Lu, N., and Dong, Y., "Correlation between soil-shrinkage curve and water-retention characteristics." ***Journal of Geotechnical and Geoenvironmental Engineering***, Vol. 143, No. 9, (2017), 1-11. DOI: 10.1061/(ASCE)GT.1943-5606.0001741
5. Sadrnezhad. S. A., "Numerical solution for heave of expansive soil." ***International Journal of Engineering***, Vol. 12, No. 1, (1999), 13-20.
6. Peng, Xinhua, and Horn, R. "Identifying six types of soil shrinkage curves from a large set of experimental data soil physics." ***Soil Science Society of America Journal***, Vol. 77, No. 2, (2013), 372-381. DOI: 10.2136/sssaj2011.0422
7. Ahmed, A., Hossain, M. S., Khan, M. S., and Shishani, A. "Data Based Real Time Moisture Modeling in Unsaturated Expansive Subgrade" ***Geotechnical Special Publication,*** 2017-Novem (GSP 303), (2018), 158-167. DOI: 10.1061/9780784481707.017
8. Manimaran, A., Seenu, S., Ravichandran, P. "Stimulation Behaviour Study on Clay Treated with Ground Granulated Blast Slag and Groundnutshell Ash", International Journal of Engineering, Vol. 32, No. 5, (2019), 673-678.
9. Janssen, D. J., and Dempsey, B. J. "Soil-moisture properties of subgrade soils", ***Transportation Research Record***, (1981), 61-67. DOI: 10.1016/0148-9062(82)91655-2
10. Fredlund, D. G., and Zhang, F. "Combination of shrinkage curve and soil-water characteristic curves for soils that undergo volume change as soil suction is increased" in 18th International Conference on Soil Mechanics and Geotechnical Engineering: Challenges and Innovations in Geotechnics, ICSMGE 2013, 2, (2013), 1109-1112.
11. Bensallam, S., Bahi, L., Ejjaaouani, H., and Shakhirev, V. "Shrinkage curve: Experimental study and modelling" ***International Journal of Engineering, Transactions A: Basics***, Vol. 25, No. 3, (2012), 203-210.
12. Cornelis, W. M., Corluy, J., Medina, H., Díaz, J., Hartmann, R., Van Meirvenne, M., & Ruiz, M. E., "Measuring and modelling the soil shrinkage characteristic curve" ***Geoderma***, Vol. 137, No. (1-2), (2006), 179-191. DOI: 10.1016/j.geoderma.2006.08.022
13. Pellissier, J. P., "Toluene and wax-freezing method of determining volumetric free swell" ***Geotechnical Testing Journal***, Vol. 14, No. 3, (1991), 309-314. DOI: 10.1520/gtj10575j
14. Tunny, J., "The influence of Saran Resin coatings on swelling of natural soil clods" ***Soil Science***, Vol. 109, No. 4, (1970), 254-256. DOI: 10.1097/00010694-197004000-00010
15. Crescimanno, G., and Provenzano, G., "Soil shrinkage characteristic curve in clay soils: Measurement and prediction" ***Soil Science Society of America Journal***, Vol. 63, No. 1, (1999), 25-32. DOI: 10.2136/sssaj1999.03615995006300010005x
16. Wong, J. M., Elwood, D., and Fredlund, D. G. "Use of a three-dimensional scanner for shrinkage curve tests" ***Canadian Geotechnical Journal***, Vol. 56, No. 4, (2019), 526-535. DOI: 10.1139/cgj-2017-0700
17. Bhadriraju, V., Puppala, A. J., Enayatpour, S., and Pathivada, S., "Digital Imaging Technique to Evaluate Shrinkage Strain Potentials of Fiber Reinforced Expansive Soils ", (2005), 1-12. ***American Society of Civil Engineers*** DOI: 10.1061/40785(164)22
18. Peng, X., Horn, R., Peth, S., and Smucker, A. "Quantification of soil shrinkage in 2D by digital image processing of soil surface", ***Soil and Tillage Research***, Vol. 91, No. (1-2), (2006), 173-180. DOI: 10.1016/j.still.2005.12.012
19. White, D. J., Take, W. A., and Bolton, M. D., "Soil deformation measurement using particle image velocimetry (PIV) and photogrammetry", ***Geotechnique***, Vol. 53, No. 7, (2003), 619-631. DOI: 10.1680/geot.2003.53.7.619
20. Li, L., Zhang, X., and Li, P., "Evaluating a new method for simultaneous measurement of soil water retention and shrinkage curves", ***Acta Geotechnica***, Vol. 14, No. 4, (2019), 1021-1035. DOI: 10.1007/s11440-018-0713-y
21. Upreti, K., and Leong, E. C., "Measurement of Soil Shrinkage Curve Using Photogrammetry", ***Geotechnical Special Publication***, *2017-Novem* (GSP 303), (2018), 71-80. DOI: 10.1061/9780784481707.008
22. Julina, M., and Thyagaraj, T., "Determination of volumetric shrinkage of an expansive soil using digital camera images", ***International Journal of Geotechnical Engineering***, 6362, (2018), 1-9. DOI: 10.1080/19386362.2018.1460961
23. Basson, M. S., and Ayothiraman, R., "Effect of human hair fiber reinforcement on shrinkage cracking potential of expansive clay", ***Bulletin of Engineering Geology and the Environment***, Vol. 79, No. 4, (2020), 2159-2168. DOI: 10.1007/s10064-019-01685-x

24. ASTM D6836 − 16. "Standard Test Methods for Determination of the Soil Water Characteristic Curve for Desorption Using Hanging Column, Pressure Extractor, Chilled Mirror Hygrometer, or Centrifuge", ***ASTM International***, (2016), 1-22. DOI: 10.1520/D6836-16.1.3

25. DG Fredlund and Xing, A., "Equations for the soil-water characteristic curve", Canadian ***Geotechnical Journal,*** Vol. 31, No. 4, (1994), 521-532. DOI: 10.1139/t94-061

26. Fredlund, M. D., Wilson, G. W., and Fredlund, D. G., "Representation and estimation of the shrinkage curve",in 3rd International Conference on *Unsatuarted Soils*, UNSAT-2002, Recife, Brazil, (2002), 145-149.

27. Leong, E. C., Tripathy, S., and Rahardjo, H., "Total suction measurement of unsaturated soils with a device using the chilled-mirror dew-point technique", ***Geotechnique***, Vol. 53, No. 2, (2003), 173-182. DOI: 10.1680/geot.2003.53.2.173

28. Seki, K., "SWRC fit – a nonlinear fitting program with a water retention curve for soils having unimodal and bimodal pore structure", ***Hydrology and Earth System Sciences Discussions***, Vol. 4, (2007), 407-437, DOI: 10.5194/hessd-4-407-2007.

29. Zhang, C., and Lu, N., "Soil Sorptive Potential: Its Determination and Predicting Soil Water Density", ***Journal of Geotechnical and Geoenvironmental Engineering***, Vol. 146, No. 1, (2020), 1-10. DOI: 10.1061/(ASCE)GT.1943-5606.0002188

Persian Abstract

چکیده

هدف از این مقاله درک بهتر رفتار چروکیدگی خاک با خاصیت انعطاف پذیری کم است که در وارانگال هند رواج دارد. در این مطالعه ، سازوکار و رفتار چروکیدگی با تغییرات مکش با استفاده از رویکردهای آزمایشی ساده و قابل اعتماد توصیف می شود. یافته ها مربوط به تغییر مکش ، مقدار آب و نسبت درجه حرارت خاکی است که از اشباع کامل به خشکیدن در هوا خشک شده است. چارچوب پیشنهادی از دو فرایند ساده استفاده می کند: یکی برای محاسبه پتانسیل مکش و دیگری برای توصیف مکانیزم انقباض. این مطالعه همچنین استفاده از نرم افزار ImageJ را برای جمع آوری نمونه با استفاده از پردازش تصویر دیجیتال (DIP) برجسته می کند. این یافته ها عدم وجود ماکروپورها را تأیید می کند و اثرات مکش مویرگی بر پاسخ انقباض در مطالعات تغییر حجم با استفاده از مکش به عنوان یک متغیر حالت تنش تکرار می شود.

International Journal of Engineering

Journal Homepage: www.ije.ir

Finite Element Analysis of Single-lap Adhesive Joints with Tapered Adherends

F. Marchione

Dipartimento di Ingegneria Civile, Edile e Architettura (DICEA), Università Politecnica delle Marche, via B. Bianche, Ancona, Italy

P A P E R I N F O

Paper history:
Received 21 May 2021
Received in revised form 02 July 2021
Accepted 04 July 2021

Keywords:
Tensile load
Single-lap adhesive joint
Adhesively bonded joints
Stress distribution
Finite Element analysis

A B S T R A C T

Adhesive joints are becoming increasingly popular in various industrial sectors. However, in spite of numerous recent studies in literature, the design phase of the adhesive joint is still challenging. The main issue in the design phase is the determination of the stress distribution in the adhesive layer under external mechanical loads. In the present study, a classical adhesive joint is analysed in comparison to its modified geometric configuration (i.e. tapered) aimed at reducing the magnitude of stress peaks. In particular, a single-lap joint with steel adherends bonded with a commercial epoxy adhesive is analyzed. A 3D finite element (FE) analysis is conducted to determine the distribution of normal and shear stresses in the mid-plane of the adhesive layer. The results obtained from the present study show that the inclusion of a small taper angle (i.e. 5°) leads to a remarkable reduction of normal stresses (up to 30%) compared to the classical configuration. It is observed that the further increase of the taper angle (up to 15°) does not lead to significant reductions of the stress peaks. The trend in shear stresses, on the other hand, is in contrast: an increase in the taper angle leads to an increase in the shear peaks. The method of tapering the adherends is effective in reducing the normal stresses, which are responsible for triggering the failure in the adhesive joint.

***doi**: 10.5829/ije.2021.34.10a.03*

NOMENCLATURE

EPX1	Epoxy adhesive		
α	Taper angles	ν	Poisson ratio (-)
ρ	Density (kg/m^3)	E	Young Modulus (GPa)

1. INTRODUCTION

Adhesive technology is experiencing numerous applications in various industrial sectors [1-3]. The widespread use of adhesive joints is due to a number of factors, including lower stress concentration, better fatigue behaviour and the possibility of joining different materials [4].

Although there are numerous studies in the literature [5-7], the design process of the adhesive joint is particularly difficult; both because of the non-linear mechanical properties of the adhesives [8, 9], and their behaviour after exposure to severe environmental conditions.

The adhesive joint known as single-lap joint (SLJ) presents a simple geometry for testing the joint's behaviour in tension. However, this type of joint, due to its geometric conformation, presents bending moments at the end of the adhesive region [10], which often represent the cause of the joint failure.

Several studies have been carried out with the aim of reducing the magnitude of the stress peaks at the ends of the adhesive joint, by making modifications on both the geometry of the adhesives-as demonstrated by Bouchikhi et al. [11], Marchione [12] – and on the geometry of the adhesives (e.g. spew fillet) - as shown by Crocombe et al. [13]. Sancaktar et al. [14] argue that adhesive failure depends on the tension peaks recorded at the ends of the joint. Therefore, by adopting techniques to contain the stress peaks - e.g. modifications in terms of geometry and materials - the value of the ultimate load can be reduced.

To date, there are numerous studies in the literature that illustrate valid methods for achieving this result, leading to a significant improvement in not only

*Corresponding Author Institutional Email: f.marchione@pm.univpm.it (F. Marchione)

Please cite this article as: F. Marchione, Finite Element Analysis of Single-lap Adhesive Joints with Tapered Adherends, International Journal of Engineering, Transactions A: Basics Vol. 34, No. 10, (2021) 2213-2218

mechanical [15], but also thermal [16] and durability [17] of the adhesive joint. The major limitation of the current state of the art is the absence of a parametric FE study with adhesives and adhesion configurations such as those proposed here. The study presented below illustrates how slight geometric variations of the adhesives result in changes of the stress state in the adhesive. This study is the result of an application of the adhesive joint in civil engineering for the construction of new building components (e.g. windows and curtain walls).

In fact, in the context of engineering design, a fundamental role is played by FE analysis. In fact, the accurate and rapid knowledge of the stress state represents the starting point for a correct design. The objective of the present work is to perform a parametric study on the trend of the stress state in a single-lap adhesive joint (SLJ). In particular, the trend of normal and shear stresses in a classical SLJ joint is compared to that of the same joint modified in its geometry through different taper angles of the adhesives (i.e. 5°-15°). A parametric study on the influence of the taper angle on the distribution of stress peaks in the mid-plane of the adhesive layer is therefore carried out.

2. FE ANALYSIS

The adhesive joint used for the FE analysis is graphically shown in Figure 1. This figure shows the geometry configuration of the adhesives in the modified configurations. The angle $\boldsymbol{\alpha}$ represents the inclination of the external surface of the adherends.

The adherends are 140 mm × 30 mm × 5 mm, in length, width and thickness, respectively. The bonding area is 30 mm × 50 mm; the thickness of the adhesive is set equal to 1.0 mm.

The same boundary conditions have been applied to all the configurations considered. Tables 1 and 2 show the mechanical properties of the materials considered.

Eight noded three-dimensional structural volume element (SOLID185 element) is employed for modelling the adhesive joints, with a maximum mesh dimension of 0.50 mm. The numerical modeling is carried out using the software ANSYS©19 with its solutor "Static Structural". Figure 2 shows the FE model. The analyzed joints are made of S235JR steel adherends and one commercial epoxy adhesive.

The analysis presented is of the static elastic-linear type, since it is intended to investigate the behaviour of

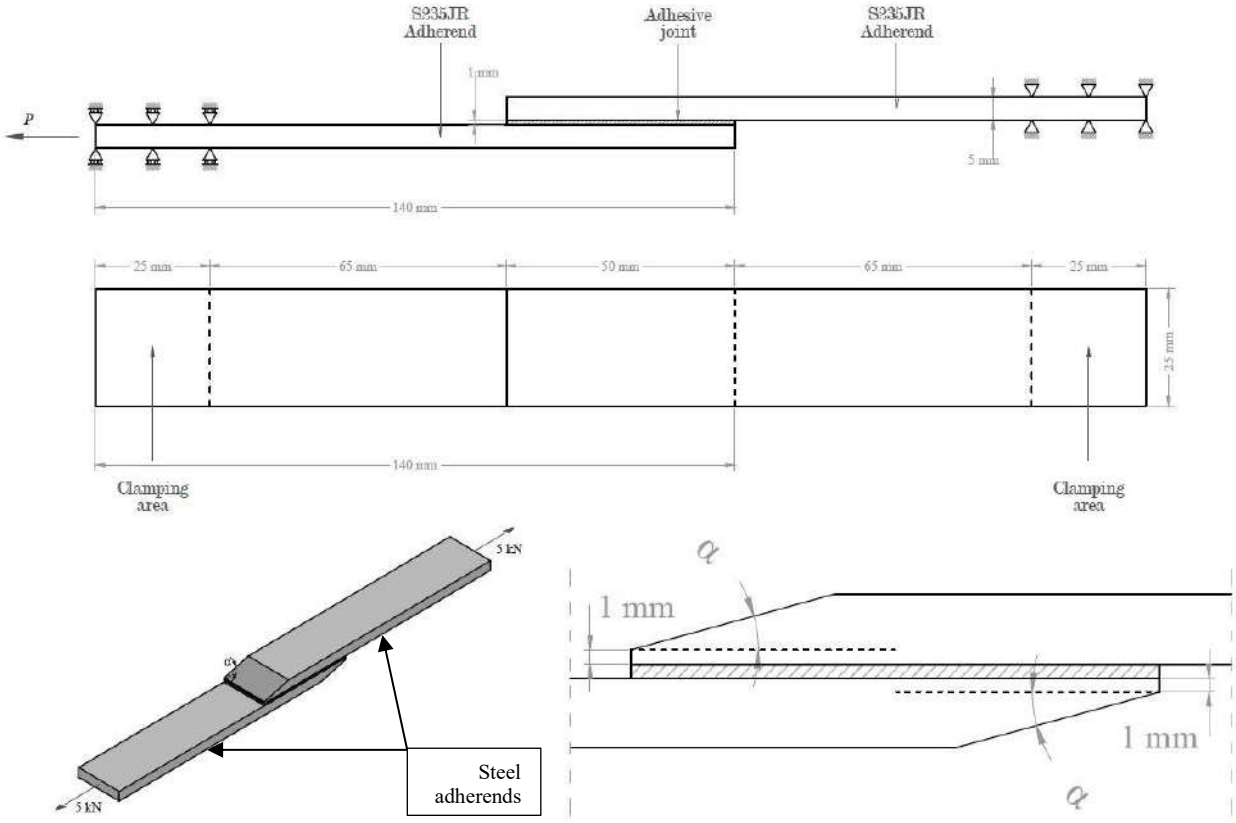

Figure 1. Geometry of Single lap adhesive joint: lateral and top view; 3D model and detail of the modified adherends' geometry in the bonding region

TABLE 1. Materials' characteristics for the FEA model

STEEL S235JR		
E_t [GPa]	**ρ [N/m^3]**	**ν [-]**
69	78000	0.30

TABLE 2. Adhesive's characteristics for the FEA model

EPX 1	
E [GPa]	**ν** [-]
3.00	0.40

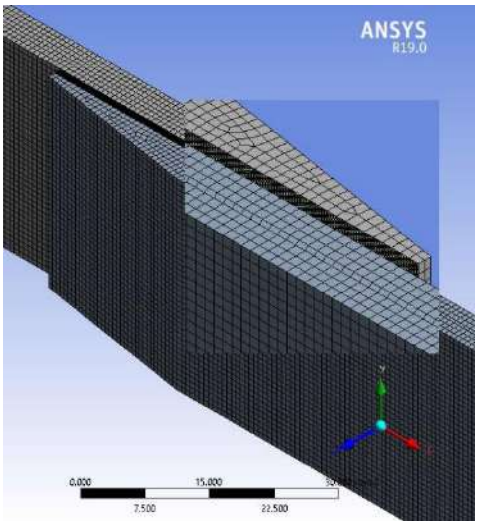

Figure 2. Meshed model for FE analysis

the joint in the service phase, in which it is assumed to be in the elastic phase for all the materials constituting the joint. The load to which one of the two adherends is subjected is 5 kN, which is purely representative of the service phase for joints between steel adherends, as demonstrated in the study conducted by Machalicka et al. [18].

The load path used is ramped, with a total duration of 60 seconds and a linear trend from 0 to 5 kN.

After solving the mathematical model in ANSYS, the mapping of the normal and shear stresses is extracted and plotted using the software MATLAB©.

3. RESULTS AND DISCUSSION

This section reports the results derived from the FE analysis of the joint, according to different gemetric combinations.

In particular, as illustrated above, the results are compared for joints with a taper angle of 90° (classical joint) with joints characterised by taper angles of 5° and 10°, respectively. The results are graphically shown in Figures 3 to 5. Figures 3(a) and 3(b) show the stress curve for the unmodified adhesive joint.

Figures 4(a) and 4(b) show the stress distribution for the adhesive joint with 5° tapered adherends.

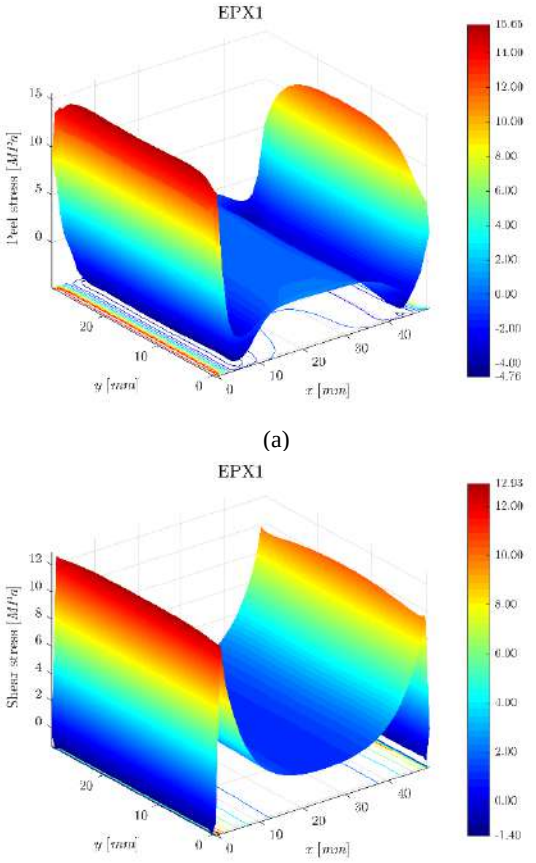

(a)

(b)

Figure 3. Peel and shear stress distribution for classical single-lap joint configurations

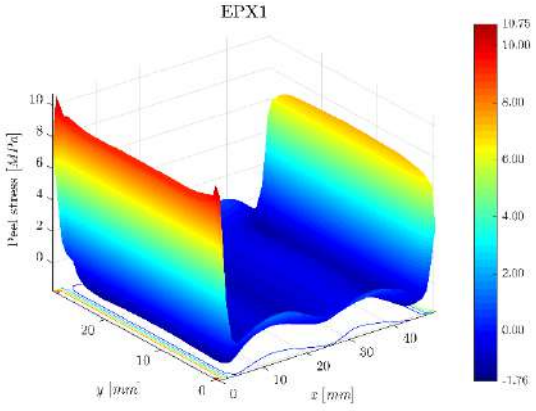

(a)

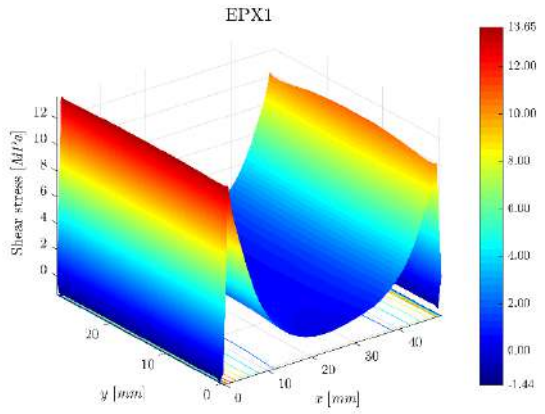

(b)

Figure 4. Peel and shear stress distribution for 5° taper adherends angle onfigurations

Figures5(a) and 5(b) show the stress distribution for the adhesive joint with 10° tapered adherends.

As previously stated, and as could be observed in Figures3 to 5, the stress distribution presents stress peaks

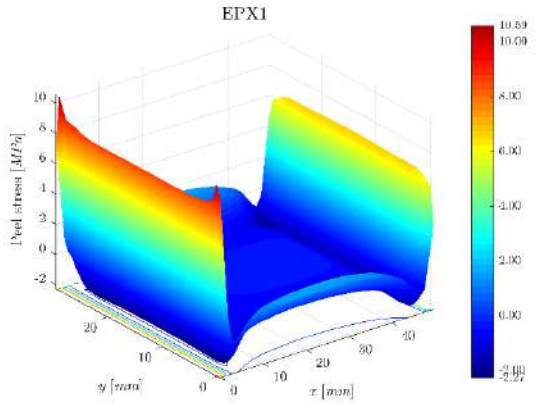

(a)

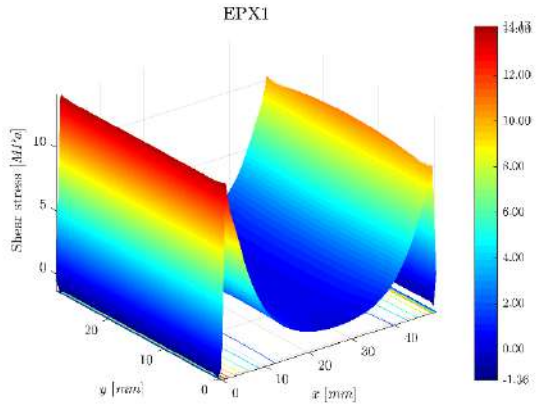

(b)

Figure 5. Peel and shear stress distribution for 10° tapering adherends angle onfigurations

at the ends of the adhesive joint, both in the case of shear and normal stresses.

The presence of such peaks (especially for normal stress) represents a negative factor for the mechanical behaviour of the joint, since they can be identified as the cause of the initiation of damage in the adhesive region. Therefore, by reducing the magnitude of these peaks at the same load, it is possible to develop greater joint resistance, postponing the occurrence of the critical stress peaks for the joint to higher loads.

This type of distribution remains qualitatively identical for all the configurations considered. It is also observed that the stress distribution does not vary significantly in the width of the adhesive joint; this aspect enhances 2D or algebraic analyses, which are able to estimate the stress distribution in a simplified manor.

The maximum values of the stresses are obtained at the lateral edge of the adhesive area, as is known.

The introduction of the taper adherens involves - in any case - a decrease in the normal stresses.

Table 3 shows the values of the stress peaks measured.

It can be observed that by inserting a taper angle of 5° in both adhesives, it is possible to obtain a reduction of the stress peaks of about -30% with respect to the classical configuration. In fact, compared to a normal stress peak of 15.65 MPa, it is possible to obtain a maximum value of 10.75 MPa.

Figure 6 summarizes the stress peaks observed.

TABLE 3. Stress peaks values

EPX 1		
Taper angle [°]	**Peel stress peak [MPa]**	**Shear Stress peak [MPa]**
-	15.65	12.93
5	10.75	13.65
10	10.59	14.17

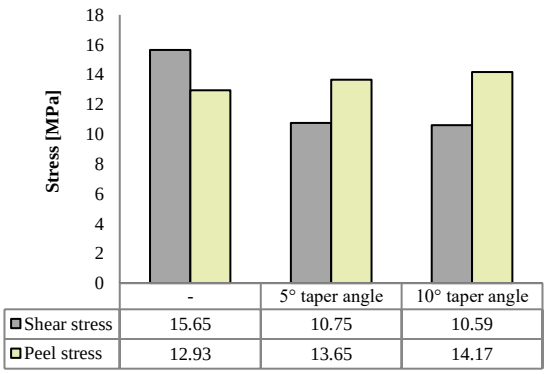

Figure 6. Peel and shear stress peaks observed for each geometric configuration

By increasing the taper angle of the adherends (10°), a decrease in the normal stress peaks is observed, although negligible compared to the previous configuration. On the contrary, for the shear stresses, an increase in the magnitude of the detected stress peaks is observed. In fact, an increasein the taper angle leads to an increase in the shear stresses, even if for low increments. This phenomenon is due to the decrease in stiffness of the adhesive joint, obtained by thinning the adhesives. This procedure leads to a reduction in the bending moments, bringing the behaviour of the joint closer to that of pure shear. Therefore, there is a considerable decrease in normal stress - often considered as the cause of the joint failure - accompanied by a slight increase in shear stresses.

4. CONCLUSIONS

To date, adhesive technology is very important for many production sectors. Therefore, the study and design of the joint is a fundamental element. The correct knowledge of the tensional state is the basis of this engineering process.

In literature there are numerous studies aimed at improving the mechanical behaviour of the joint, through geometric, chemical, mechanical modifications of the materials that compose it.

The aim of the present study is to numerically analyze the mechanical behaviour of a SLJ adhesive joint. In particular, the effects of the insertion of taper in the adhesives on the distribution of stress peaks in the adhesive region are analyzed. In particular, a S235JR steel-steel single-lap joint is considered.

The main outcomes are:

- The stress distribution is almost constant across the width of the adhesive region; therefore shear-lag and 2D analyses prove to be valid design tools;
- The stress distribution always maintains stress peaks at the edges of the adhesive region; in particular, it is the highest at the lateral edge of the overlap region;
- The insertion of tapered adherends results in a decrease in normal stresses, while at the same time resulting in a slight increase in shear stresses;
- The inclusion of tapered adherends has a positive effect on the mechanical behaviour of the joint, which shows behaviour closer to pure shear.

5. REFERENCES

1. F. Rubino, A. Nisticò, F. Tucci, and P. Carlone, "Marine Application of Fiber Reinforced Composites: A Review," ***Journal of Marine Science and Engineering***, Vol. 8, No. 1 (2020), 26, doi:10.3390/jmse8010026.
2. B. Hayman, J. Wedel-Heinen, and P. Brøndsted, "Materials Challenges in Present and Future Wind Energy," ***MRS Bulletin***, Vol. 33, No. 4, (2008), 343-353, doi:10.1557/mrs2008.70.
3. Y. Ciupack, H. Pasternak, C. Mette, E. Stammen, and K. Dilger, "Adhesive Bonding in Steel Construction-Challenge and Innovation," ***Procedia Engineering***, Vol. 172, (2017), 186-193, doi:10.1016/j.proeng.2017.02.048.

A. M. Amaro, M. A. Neto, A. Loureiro, and P. N. B. Reis, "Taper's angle influence on the structural integrity of single-lap bonded joints," ***Theoretical and Applied Fracture Mechanics,*** Vol. 96, (2018), 231-246, doi:10.1016/j.tafmec.2018.05.006.

4. T. Vallée, Y. Weinand, B. Hahn, and B. Stamm, "Numerical modelling and strength prediction of welded double lap joints made of timber," ***Procedia Engineering,*** Vol. 10, (2011), 1309-1314, doi:10.1016/j.proeng.2011.04.218.
5. W. A. Lees, "Adhesives in engineering design.," Vol. 211, ***Design,*** (1984), 307-335,
6. M. N. Saleh, M. Saeedifar, D. Zarouchas, and S. T. De Freitas, "Stress analysis of double-lap bi-material joints bonded with thick adhesive," ***International Journal of Adhesion and Adhesives,*** Vol. 97, (2020), 102480, doi:10.1016/j.ijadhadh.2019.102480.
7. F. Marchione, "Investigation of Vibration Modes of Double-lap Adhesive Joints: Effect of Slot", ***International Journal of Engineering, Transactions A: Basics,*** Vol. 33, No. 10, (2020), 1917-1923, doi:10.5829/ije.2020.33.10a.10.
8. F. Marchione, "Analytical Stress Analysis in Single-lap Adhesive Joints under Buckling," ***International Journal of Engineering, Transactions B: Applications,*** Vol. 34, No. 2, 313-318, (2021), doi:10.5829/ije.2021.34.02b.02.
9. E. Selahi, M. Tahani, and S. A. Yousefsani, "Analytical Solution of Stress Field in Adhesively Bonded Composite Single-Lap Joints Under Mechanical Loadings," ***International Journal of Engineering, Transactions C: Aspects,***, Vol. 27, No. 3 (C), 475-486, Mar. 2014,. doi:10.5829/idosi.ije.2014.27.03c.16.

A. S. Bouchikhi, A. Megueni, S. Gouasmi, and F. B. Boukoulda, "Effect of mixed adhesive joints and tapered plate on stresses in retrofitted beams bonded with a fiber-reinforced polymer plate," ***Materials & Design***, Vol. 50, (2013), 893-904, doi:10.1016/j.matdes.2013.03.052.

10. F. Marchione, "Stress distribution in double-lap adhesive joints: Effect of adherend reinforcement layer," ***International Journal of Adhesion and Adhesives,*** Vol. 105, (2021), doi:10.1016/j.ijadhadh.2020.102780.

A. D. Crocombe and R. D. Adams, "Influence of the Spew Fillet and other Parameters on the Stress Distribution in the Single Lap Joint," ***Journal of Adhesives***, Vol. 13, No. 2, (1981), 141-155, doi:10.1080/00218468108073182.

11. E. Sancaktar and P. Nirantar, "Increasing strength of single lap joints of metal adherends by taper minimization," ***Journal of Adhesion Science and Technology,*** Vol. 17, No. 5, (2003), 655-675, doi:10.1163/156856103321340796.
12. X. B. Zhu, X. Yang, Y. B. Li, and B. E. Carlson, "Reinforcing cross-tension strength of adhesively bonded joints using metallic solder balls," ***International Journal of Adhesion and Adhesives,*** Vol. 68, (2016), 263-272, doi:10.1016/j.ijadhadh.2016.04.009.
13. M. D. Banea, L. F. M. Da Silva, R. D. S. G. Campilho, and C. Sato, "Smart adhesive joints: An overview of recent developments," ***Journal of Adhesives***., Vol. 90, No. 1, (2014), 16-40, doi:10.1080/00218464.2013.785916.
14. C. Wu, Y. Bai, and X.-L. Zhao, "Improved bearing capacities of pultruded glass fibre reinforced polymer square hollow sections strengthened by thin-walled steel or CFRP," ***Thin-Walled Structures,*** Vol. 89, (2015), 67-75. doi:10.1016/J.TWS.2014.12.006.
15. K. Machalická, M. Vokáč, and M. Eliášová, "Influence of artificial aging on structural adhesive connections for façade applications," ***International Journal of Adhesion and Adhesives***, Vol. 83, (2018), 168-177, doi:10.1016/j.ijadhadh.2018.02.022

Persian Abstract

چکیده

اتصالات چسبنده در بخشهای مختلف صنعتی به طور فزاینده ای محبوب می باشند. با این وجود ، علی رغم مطالعات متعدد اخیر در زمینه ادبیات ، مرحله طراحی اتصال چسب هنوز هم چالش برانگیز است. مسئله اصلی در مرحله طراحی ، تعیین توزیع تنش در لایه چسب تحت بارهای مکانیکی خارجی است. در مطالعه حاضر ، یک اتصال چسب کلاسیک در مقایسه با پیکربندی هندسی اصلاح شده آن (یعنی مخروطی) با هدف کاهش میزان قله های تنش ، مورد تجزیه و تحلیل قرار گرفته است. به طور خاص ، یک اتصال تک دور با اتصالات فولادی که با یک چسب اپوکسی تجاری پیوند خورده است ، تجزیه و تحلیل می شود. برای تعیین توزیع تنش های طبیعی و برشی در وسط صفحه لایه چسب ، یک تحلیل اجزای محدود D3 (FEA) انجام شده است. نتایج به دست آمده از مطالعه حاضر نشان می دهد که درج زاویه کوچک مخروطی (یعنی ۵ درجه) منجر به کاهش چشمگیر تنش های طبیعی (تا ۳۰٪) در مقایسه با پیکربندی کلاسیک می شود. مشاهده شده است که افزایش بیشتر زاویه مخروطی (تا ۱۵ درجه) منجر به کاهش قابل توجه قله های تنش نمی شود. از طرف دیگر روند تنش های برشی در تقابل است: افزایش زاویه مخروطی منجر به افزایش قله های برشی می شود. روش مخروطی کردن چسبنده ها در کاهش تنش های طبیعی که مسئول تحریک شکست در اتصال چسب هستند ، موثر است.

IJE TRANSACTIONS A: Basics Vol. 34, No. 10, (October 2021) 2219-2237

International Journal of Engineering

Journal Homepage: www.ije.ir

Effect of Intensity Measure on the Response of a 3D-Structure under Different Ground Motion Duration

H. Rajabnejad, H. Hamidi*, S. A. Naseri, M. A. Abbaszadeh

Faculty of Civil Engineering, Babol Noshirvani University of Technology, Babol, Iran

PAPER INFO

Paper history:
Received 16 May 2021
Received in revised form 03 July 2021
Accepted 04 July 2021

Keywords:
Intensity Measure
Ground Motion Duration
Seismic Parameters
Residual Inter-story Drift
Correlation Coefficient

ABSTRACT

In seismic performance assessment of structures, the features of ground motion (GM) duration on the response of building structures remain vague and have inconclusive results. Also, intensity measures (IMs) link the ground motion hazard with the structural response; hence, using a suitable IM plays a significant role in the prediction of structural response. In this research, the effect of strong ground motion duration and the correlation coefficient of different intensity measures on the residual inter-story drift (RIDR) of a three-dimensional steel structure were investigated. Using nonlinear dynamic analyses and a total number of 34 earthquake records, the relationship between short- and long-duration seismic parameters including amplitude, energy, and frequency content parameters were investigated. The correlation between the 14 selected scalar intensity measures and the RIDR of the structure was also investigated. The results showed the highest correlation between the seismic parameters, such as Peak ground acceleration (PGA), Housner Intensity (HI), and Velocity spectrum intensity (VSI), with other seismic parameters in both short- and long-duration strong ground motions. Based on the maximum residual inter-story drift index, Mehanny and Cordova index (IM_C), Bojórquez and Iervolino index (I_{NP}), and the geometric mean of Sa (Sa_{ave}) intensity measures represented the least dispersion versus long-duration records. On the other hand, I_{NP}, Spectra acceleration at the period of T_1 Sa(T_1), and Sa_{ave} intensity measures showed the least dispersion versus short-duration records.

***doi**: 10.5829/ije.2021.34.10a.04*

1. INTRODUCTION

Two recent earthquakes in Chile, Maule (2010, Mw = 8.8), and Tohoku, Japan (2011, Mw = 9) have caused major structural failures. The earthquake records had some unique features (long duration) compared to other similar records happening in different parts of the world. The effect of earthquake duration on structures has attracted significant attention in recent decades. Considering how much and how long duration can directly affect the seismic response of structures, this study might be of high importance [1].

In general, since severe earthquakes tend to be recorded at many stations, each with different site conditions, every earthquake may be recorded with different characteristics. One of the most important properties, which is different in each station, is the strong ground motion duration. Due to the possibility of occurring earthquakes with similar severity in the coming years, a precise and comprehensive study on such earthquakes and their effects on different areas seems to be valuable [2–5].

Raghunandan et al. [2] evaluated the risk of the collapse of structures in a subduction region. Chandramohan et al. [6] found that the probability of collapse of the structure would rise by the increases in the strong ground motion duration. Barbosa et al. [7] studied the effect of duration of strong ground motion on the damage of steel structures using two damage indices. The results indicated more extensive damage to the structure under long-duration earthquakes. As a result, energy dissipation would become unavoidable. So as to reduce resistance and stiffness, using nonlinear quantitative finite element components; Chandrmohan et al. [6] and Barbosa et al. [7] obtained a coefficient. The coefficient

*Corresponding Author Institutional Email: h.hamidi@nit.ac.ir (H. Hamidi)

Please cite this article as: H. Rajabnejad, H. Hamidi, S. A. Naseri, M. A. Abbaszadeh, Effect of Intensity Measure on the Response of a 3D-Structure under Different Ground Motion Duration, International Journal of Engineering, Transactions A: Basics Vol. 34, No. 10, (2021) 2219-2237

was applied to investigate the impact of strong ground motion duration. In other research studies, where the cumulative increase of power is taken into account, it was seen that the rise in duration of strong ground motion led to a rise in the accumulation of damage to the structure [6,7]. Ruiz-Garcia [8] analyzed residual displacements caused by earthquakes with long strong ground motion duration and the results showed that ground motion duration did not have an important impact on the amplitude of peak residual drift demands in MDOF systems; but, records having a long duration tended to grow residual drift demands in the upper stories of long-period generic frames [8]. In studies conducted by Song et al. [9], Foschaar et al. [10], Raghunandan and Liel [11], Hancock and Bommer [12] and Zhang et al. [13], the probability of building collapse under both short- and long-duration ground motions were surveyed. The collapse probability of buildings was compared over the long and short duration of ground motion [9–13]. In a study by Bommer et al. [14], Iervolino et al. [15], and Bojorquez et al. [16] on the effect of strong ground motion on seismic response of structures, the direct effect of strong ground motion duration on maximum IDR was pointed out. Nassar and Krawinkler [17], Shome et al. [18], Tremblay, and Atkinson [19], and Chai [20] worked on the small effect of the duration of strong ground motion on the seismic response of structures. Bhargavi et al. [21] introduced a coefficient that can be utilized to rate the damage potential of any strong ground motion record regardless of the extent and region of the earthquake.

Bradley [22] evaluated the correlation between the mean time of strong ground motion and the range of cumulative intensities in order to select records. The results showed that ignoring the duration of strong ground motion in selecting accelerations may contribute to the scattered seismic response of the analysis. Zhou et al. [23] studied the effect of strong ground motion duration on reducing the damping factor and proposed a coefficient to modify the reduction damping coefficient. Nevertheless, in most of the studies on the duration of strong ground motion, both in the cases mentioned and in cases not mentioned here, modeling was either one or two-dimensional using the linear and nonlinear approaches. In a few studies, the structural responses were evaluated using three-dimensional models [24]. Some studies have pointed out the direction of using vector-valued intensity measures as a way to overcome this issue [6,25–27]. Yakhchalian et al. [28] with investigating the capability of different intensity measures (IMs), including Sa (T_1), as a common scalar IM and twelve vector-valued IMs for seismic collapse assessment of structures showed that using the new vector-valued IM leads to a more trustworthy seismic collapse assessment of structures. Kassem et al. [29] studied the efficiency of an improved seismic vulnerability index and concluded that variation in estimating the intensity measure might lead to uncertainties associated with a vulnerability assessment. Kassem et al. [30] in a study investigated on the quantification of collapse margin of a retrofitted university building in Beirut using three different strong ground motion duration. Farsangi et al. [31] considered the effect of coinciding horizontal and vertical ground excitations on the collapse margins of non-ductile structure using a general array of ground motions was chosen from the PEER NGA-WEST2 and Iran Strong Motions Network database. Nazri et al. [32] in investigating *Probabilistic of Structural Pounding Between Adjacent Buildings* obtained that structural damage is directly proportional to ground motion intensity.

In previous studies, the correlation of the response of structures with different intensities was examined, and in these studies, the frequency content, record duration, and other seismic parameters were different from each other. In this study, firstly, the records were examined which were very similar in terms of frequency content due to the similarity of the shape of the first mode spectrum, and secondly, the effect of strong ground motion duration on the *residual drift* values was investigated, which has not been studied in the past. Therefore, the simultaneous effect of the *uniformity of frequency contents*, and the study of *residual drift* values at different *intensities* were investigated in an experimentally verified real-scale structure for the first time in this study.

Accordingly, the effect of strong ground motion duration on the response of a real scale verified three-dimensional steel structure was investigated regarding

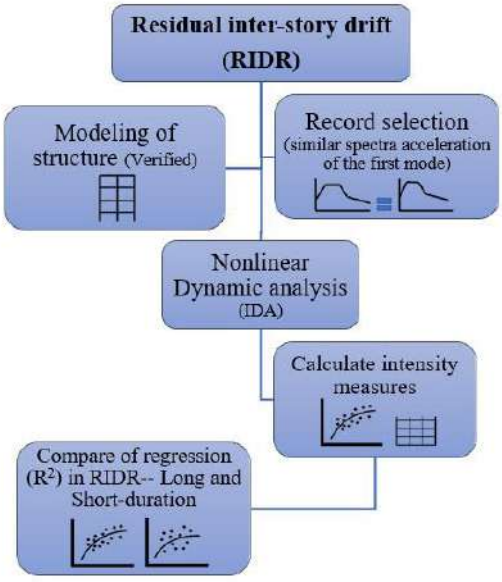

Figure 1. The process of determining and comparing the residual inter-story drift at long- and short- duration

different types of intensity measures. Two sets of long- and short-duration natural earthquake records were used to find out the effect of strong ground motion duration on seismic response of the abovementioned structure. Then, the effect of different intensity measures on the response of the structure was evaluated and the adequacy of the intensity measures was calculated. Using correlation coefficients, the dependency of seismic parameters was also studied. A summarized process for determination and comparison the residual inter-story drift at long- and short- duration is shown in Figure 1.

2. INTENSITY MEASURES

Parameters that quantify earthquake strengths are called "Intensity Measure". Selecting an appropriate intensity measure is important since the seismic performance of structures can be predicted more realistically in different engineering aspects such as nonlinear assessment and probabilistic seismic hazard analysis [33]. The importance of Intensity Measure (IM) results from associating seismic hazard analysis with seismic analysis of structures. Choosing an appropriate intensity measure can make a seismic evaluation of the structure more realistic. IM, a parameter that quantifies the strength of an earthquake, is a measure of the severity of probabilistic risk analysis used in seismic analysis of structures.

In other words, the IM is responsible for establishing a link between seismic hazard analysis and seismic analysis of structures. An appropriate IM tends to contain some characteristics, the most important of which are efficiency and severity of the measure [34]. Efficient Intensity measure is an intensity measure that is capable of predicting the response of structures at low dispersion. Many studies have been conducted on new intensity measures and comparison of the existing ones. One of the most commonly used intensity measures used to design and evaluate the seismic performance of structures is the pseudo-acceleration spectrum at first mode; Sa (T_1). Due to its convenient usage, many researchers have used it to evaluate the structures seismically. Another common intensity measure is the peak ground acceleration (PGA), which highly correlates with spectral acceleration components at low-frequency times. Lee et al. [35] developed fragility curves in masonry and concrete structures with high frequency using PGA. In 1998, Shome et al. [18] showed that using Sa (T_1) instead of PGA would improve the reliability of results.

Peak Ground Velocity (PGV) and Peak Ground Displacement (PGD) are other commonly used intensity measures. Although Sa (T_1) is most widely used, it is less reliable when used in the nonlinear behavior range of a structure than in the linear behavior of structure. An increase in the period due to nonlinear behavior causes the structure to be influenced by a different response spectrum from the one in the first mode (T_1). That is why researchers have proposed intensity measures that can accommodate parts of the response spectrum that would affect the response of the nonlinear behavior of structure. In 2004, Cordova et al. [36] proposed an intensity measure that, in addition to the spectral acceleration component during the first mode of a structure, would consider a component of spectral acceleration when the period was more than the first period of the first mode of structure. Bojórquez and Iervolino [37] suggested the I_{NP} intensity measure to evaluate the seismic performance of structures. Soleymani [38] investigated effects between intensity measures and three structural damage indicators containing the Bracci index, the modified flexural damage ratio index and the drift index for different ground motion. In this intensity measure, a part of the response spectrum that can have a significant effect on the nonlinear behavior of the structure is considered to be the part of the intensity measure. In this study, as shown in Table 1, the intensity measures were investigated.

3. LONG- AND SHORT- DURATION GROUND MOTIONS SET

The definitions of strong ground motion based on acceleration are divided into three broad categories, which are briefly presented in the following, with the other parts of definitions being based on the response to earthquake forces.

The first group is called Bracket Duration. The total time elapsed between the first and last passage of a certain level of acceleration is known as the duration of the bracket [39]. One of the disadvantages of this definition is that it only considers the first and the last level while ignoring the characteristics of the strong shake section. As a result, it is possible to calculate long, strong ground motion duration in earthquakes with both pre and post-shocks [40]. The second group is called Uniform Duration. In this definition, instead of the time between the first and last passage of a specific acceleration level, the total sum of the times in which the acceleration value exceeds this threshold is considered. Although this definition is less sensitive to the desired level in terms of bracket duration, it does not provide a sustained duration of the strong ground motion. The last group that is based on acceleration is called “significant duration”. It is based on the accumulation of energy in acceleration and is expressed as the square integral of acceleration, velocity, or displacement of the earth. If ground speed is used to calculate the integral, the calculated value can depend on energy density [41]; and if acceleration is used in the integration, the value obtained is the Arias intensity, which is the most common definition for strong motion duration [42]. The content of

the significant duration has the advantage of taking into account the characteristics of the entire acceleration and calculating the continuum time, which might be strong ground motion. The definitions are generally based on the duration of earthquakes, and the acceleration applied to the structures is not considered. Therefore, a method that considers the amounts of acceleration applied to the structures would improve the results.

Chandramohan et al. [6] used long and short duration records categories to classify records. The $D_{5\text{-}75\%}$ index was used to describe the time of strong ground motion, which at first was shown by Foschaar et al. [10]. This might be a good definition of distinct short and long-term ground motions. Chandramohan et al. [6] collected 2000 paired accelerations of some of the world's strong earthquakes in order to select long and short records. The accelerations were filtered using Boore and Bommer methods [43, 44]. In each acceleration, the spectral acceleration was plotted between 0.05 and 6 seconds. At intervals of every 0.05 seconds, a total of 120 points of spectral acceleration was selected to calculate points L_1, L_2, L_3 … and L_{120}, with the mean value of $\overline{L}$ for the long duration acceleration and points S_1, S_2, S_3 … and S_{120}

TABLE 1. The definition of the applied Intensity Measures (IMs)

Category	Name	Definition
Frequency response based IMs	$Sa(T_i)$	Sa at period of T_i T_1, T_2, and T_3 are the first, second, and third modes of vibration, respectively. $1.5T_1$, $2T_1$, $3T_1$ are the lengthened periods considering the effect of nonlinearity.
	$Sa_{avg\,(Ti,\,Tj)}$	The geometric mean of Sa between periods of T_i and T_j
	IM_c	Mehanny and Cordova, $IM_c = Sa(T_1).\left(\frac{Sa(T_2)}{Sa(T_1)}\right)^{0.5}; T_2 = 2T_1$
	I_{NP}	Bojórquez and Iervolino, $I_{Np} = Sa(T_1).Np^{0.4}; Np = \frac{Sa_{avg}(T_1..T_N)}{Sa(T_1)}; T_N = 2T_1$
	ASI	Acceleration spectrum intensity, $ASI = \int_{0.1}^{0.5} Sa(t)dT$
	VSI	Velocity spectrum intensity, $VSI = \int_{0.1}^{0.5} Sv(t)dT$
	HI	Housner Intensity, $HI = \int_{0.1}^{2.5} PSV(T)\,\mathrm{d}T$
Peak-based IMs	PGA	
	PGV	Peak ground velocity
	PGD	Peak ground displacement
Cumulative and duration-based IMs	AI	Arias intensity, $AI = \frac{\pi}{2g}\int_0^{t_{max}} a(t)^2 dt$
	$D_{s5\text{-}75}$	5-75% significant duration: The interval between the times at which 5% and 75% of Arias intensity are reached
	I_D	Cosenza and manfredi index (a dimension less metric of duration) $I_D = \frac{\int_0^{t_{max}} a(t)^2 dt}{PGA \times PGV}$ Where a(t) and t_{max} are acceleration time history and the length of ground motion record, respectively
	CAV	Cumulative absolute energy, $CAV = \int_0^{t_{max}} \lvert a(t)\rvert dt$
	SED	Specific Energy Intensity (I_c)

with the mean value of $\bar{S}$ for the short duration acceleration. The coefficient $k = \bar{L}/\bar{S}$ was applied to short-duration acceleration. Among spectral equivalent candidates, acceleration with a lower total of squared differences (Equation (1)) was chosen as a spectral equivalent [6]:

$$SSE = \sum_{i=1}^{120} \left(L_i - kS_i \right)^2 \quad (1)$$

where L_i and S_i represent the acceleration of long and short ground motion duration, respectively.

In this research, a collection of acceleration, prepared by Chandrmohan et al. [6] was used. The

TABLE 2. Long- and short- duration ground motions characteristics (some parts of the table were adopted from [6])

	Earthquake	Station name	$Ds_{5\text{-}75}$ (s)	PGA (g)	Sa (T_1=0.74) (g)	PGV (cm/s)	Specific Energy Density (cm^2/sec)	Housner Intensity (cm)	Acceleration Spectrum Intensity (g*sec)	Velocity Spectrum Intensity (cm)	Epicentral distance Rjb (km)
L1	1999 Kocaeli, Turkey	Bursa Tofas	26	0.101	0.276	17.236	1491.196	58.842	0.081	59.777	60.430
S1	1999 Chi-Chi, Taiwan-04	KAU085	20	0.087	0.254	17.949	1227.339	57.281	0.075	58.852	85.950
L2	2010 Maule, Chile	Constitucion	32	0.538	1.084	43.347	9077.681	222.043	0.750	254.645	37.230
S2	1981 Taiwan SMART1(5)	SMART1 O12	1	0.579	0.818	62.441	1547.465	162.453	0.592	198.262	58.000
L3	2011 Tohoku, Japan	Inawashiro	80	0.280	0.525	46.649	14367.241	211.890	0.235	218.919	173.000
S3	1992 Erzican, Turkey	Erzincan	2	0.282	0.577	78.149	3672.229	235.514	0.208	215.809	0.000
L4	2011 Tohoku, Japan	Naruko	71	0.208	0.263	32.982	17173.483	157.455	0.156	153.801	163.000
S4	1999 Chi-Chi, Taiwan-06	TCU118	24	0.240	0.279	48.926	8161.988	166.889	0.200	160.738	26.820
L5	2011 Tohoku, Japan	Shiroishi	77	0.364	0.511	30.557	5421.761	175.801	0.354	186.388	161.000
S5	1979 Imperial Valley-06	El Centro Array #4	3	0.450	0.600	36.828	2491.399	165.401	0.337	175.011	4.900
L6	2011 Tohoku, Japan	Kakuda	69	0.360	0.874	46.056	9020.616	214.282	0.284	228.848	147.000
S6	1995 Kobe, Japan	Takarazuka	2	0.445	0.864	43.659	2044.341	201.162	0.326	202.496	0.000
L7	2011 Tohoku, Japan	Yonezawa	78	0.206	0.429	24.497	4397.940	123.421	0.228	128.399	153.000
S7	1999 Chi-Chi, Taiwan-05	CHY063	13	0.213	0.445	26.512	1848.469	125.239	0.199	134.586	71.940
L8	2010 Maule, Chile	Concepcion San Pedro	32	0.607	1.478	41.449	9038.662	219.742	0.460	246.305	43.340
S8	1994 Northridge-01	Sun Valley - Roscoe Blvd	6	0.612	1.173	58.484	4086.042	227.189	0.417	236.493	5.590
L9	2011 Tohoku, Japan	Inawashiro	80	0.280	0.525	46.649	14367.241	211.890	0.235	218.919	173.000

S9	1994 Northridge-01	Jensen Filter Plant	4	0.275	0.720	74.777	5145.300	202.983	0.196	189.680	0.000
L10	1985 Valparaiso, Chile	Llolleo	28	0.712	0.985	40.307	5393.310	196.723	0.603	223.045	N. A
S10	1994 Northridge-01	Sun Valley - Roscoe Blvd	6	0.504	0.829	46.293	3967.398	192.404	0.568	221.410	5.590
L11	2011 Tohoku, Japan	Iwanuma	80	0.366	0.808	48.983	14259.192	246.579	0.437	256.265	137.500
S11	1999 Chi-Chi, Taiwan-03	TCU138	5	0.470	0.827	53.360	4854.271	242.445	0.437	253.626	9.780
L12	2011 Tohoku, Japan	Sakunami	75	0.423	0.484	26.038	3093.641	98.835	0.447	114.983	155.000
S12	1999 Chi-Chi, Taiwan-02	TCU067	5	0.502	0.533	39.897	514.903	84.486	0.470	109.310	0.620
L13	2008 Wenchuan, China	Deyangbaima	36	0.139	0.184	35.632	4833.612	62.772	0.118	61.748	49.700
S13	1999 Chi-Chi, Taiwan-04	CHY016	23	0.131	0.188	21.757	2815.592	65.523	0.140	66.198	66.640
L14	2008 Wenchuan, China	Dayiyinping	60	0.138	0.201	32.839	2435.809	64.483	0.145	65.947	51.850
S14	1999 Chi-Chi, Taiwan	TTN051	24	0.128	0.187	24.500	2903.311	64.401	0.140	65.229	30.770
L15	2010 Maule, Chile	Curico	37	0.475	0.464	27.694	4299.173	144.484	0.463	159.697	61.700
S15	1983 Coalinga-01	Parkfield - Stone Co	5	0.527	0.559	41.247	1515.489	141.656	0.435	169.733	32.810
L16	2008 Wenchuan, China	Dayiyinping	47	0.129	0.262	19.960	1412.653	54.957	0.153	59.763	51.850
S16	2010 El Mayor-Cucapah	Sam W. Stewart	10	0.204	0.217	22.907	2758.602	51.907	0.166	56.156	31.790
L17	2011 Tohoku, Japan	Kaminoyama	86	0.125	0.301	15.716	2031.403	85.045	0.121	91.690	185.000
S17	1989 Loma Prieta	Los Gatos - Lexington Dam	2	0.149	0.337	28.931	355.682	84.341	0.108	92.256	3.600

selected acceleration is mentioned in Table 2. As an example, the characteristics of the two categories of accelerations were compared and their spectral acceleration adaptation is shown in Figures 2 and 3.

Although the selected pair records contained different strong ground motion durations, they were similar in terms of spectral response. The dependency of accelerations to various time intervals, with a distinction between long and short ground motion durations, is shown in Figure 4.

These records, in addition to being scaled and categorized based on strong ground motion duration, had other characteristics. Consequently, to better realize the dispersion of these intensity measures, the relationship between PGA, PGV, M_w, and S_a ($T_1 = 0.74$) based on strong ground motion duration (D_{5-75}) is shown in Figure 5. In Figure 6, the relationship between three important duration parameters, i.e. D_{5-75}, M_w, and Sa ($T_1 = 0.74$) is shown in all records.

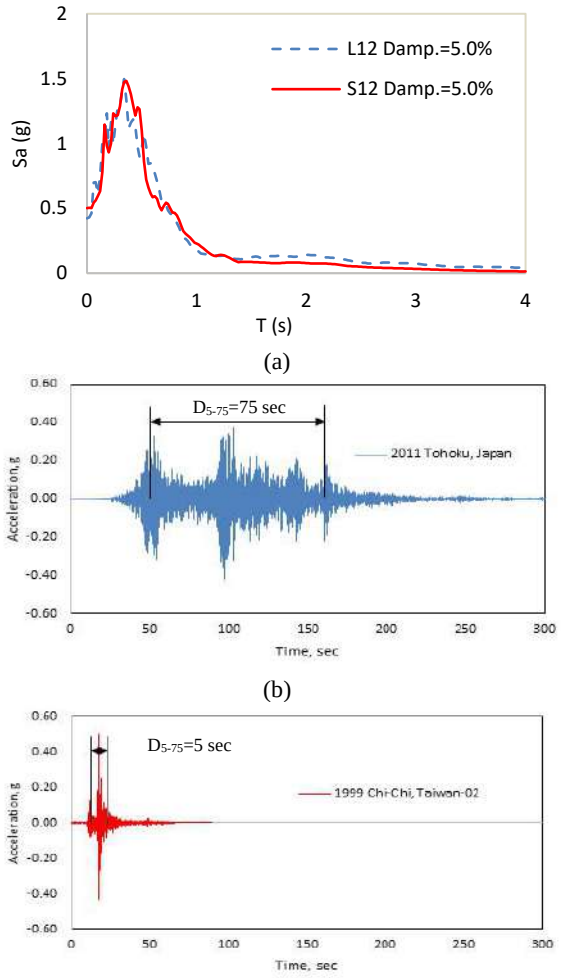

Figure 2. (a) Response spectra for earthquake record pair 12 b) Acceleration time-series for earthquake record pair 12 (Long duration) c) Acceleration time-series for earthquake record pair 12 (Short duration)

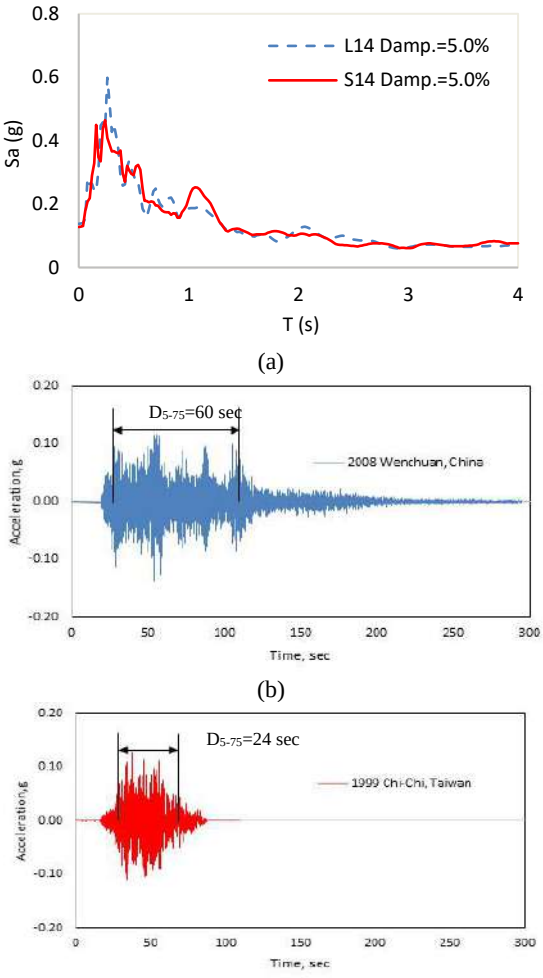

Figure 3. (a) Response spectra for earthquake record pair 14 b) Acceleration time-series for earthquake record pair 14 (Long duration) c) Acceleration time-series for earthquake record pair 14 (Short duration)

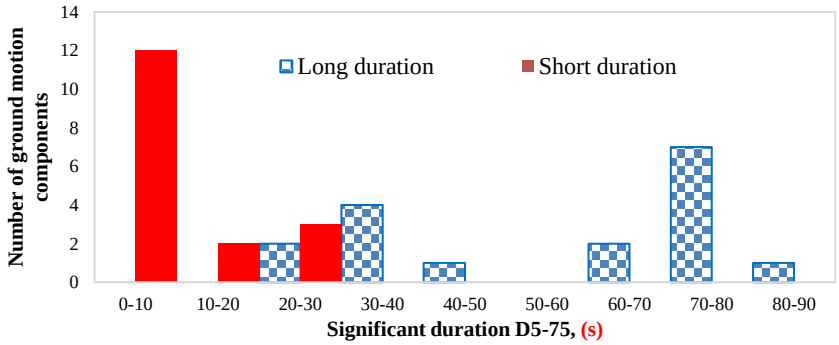

Figure 4. Histogram for all earthquake records used in this study (significant duration D_{5-75})

An optimal dispersion between the acceleration spectrum and duration of the strong ground motion could improve the results. In this regard, the correlation coefficient between the strong ground motion duration

and natural logarithm response spectrum at different periods was less than 0.2, as shown in Figure 7, indicating the optimal distribution between spectral accelerations at different periods and the strong ground motion duration. The purpose of correlation models is to examine the relationship between two or more variables, while regression seeks to predict one or more variables based on one or more other variables. Extensive use of the quantitative value of each of the seismic intensity measure criteria can be considered as its efficiency. The demand for each seismic intensity measure is obtained from Equation (2).

$$EDP=a\ (IM)^{b} \quad (2)$$

Equation (2) can be converted logarithmically with respect to the normal distribution. In this case, constant values can be obtained from the linear regression of the logarithmic equation. The efficiency of each intensity measure based on the residual dispersion (R^2) is obtained from Equation (3).

$$Log^{(EDP)}=Log^{(a)} + b\ Log^{(IM)} \quad (3)$$

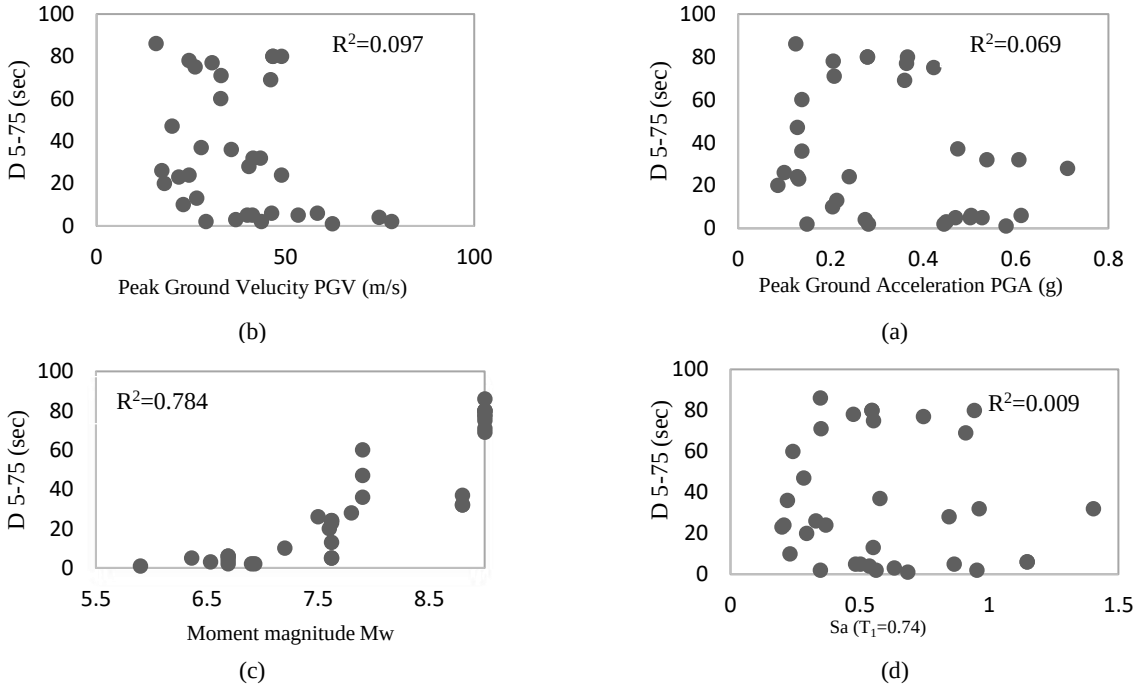

Figure 5. The relationship between intensity measures of: a) PGA to $D_{5–75}$ b) PGV to $D_{5–75}$ c) M_w to $D_{5–75}$ d) $D_{5–75}$

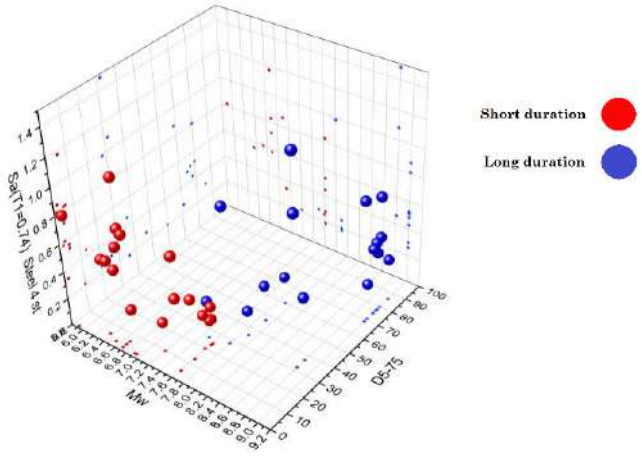

Figure 6. The relationship between intensity measures of Mw, $D_{5–75}$ and Sa(T_1= 0.74)

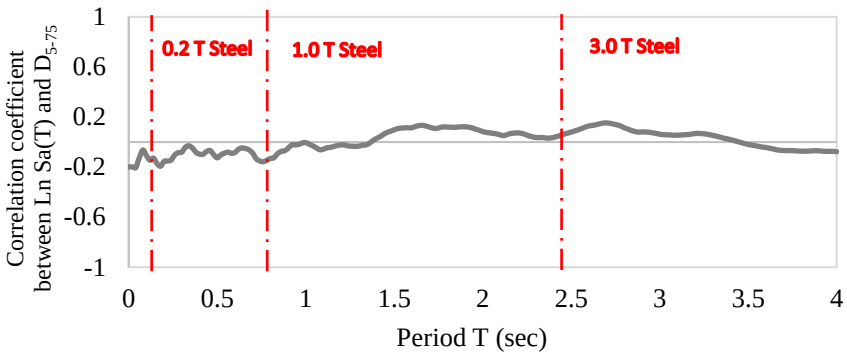

Figure 7. Correlation coefficient between significant duration, D_{5-75}, and natural logarithm of the spectral acceleration (S_a) vs. period (T) of vibration

4. STUDIED MODEL

4. 1. General Descriptions The steel structure used in this research consisted of four floors and was a regular, three-dimensional structure, made in the laboratory based on a real scale. It comprised two steel frames joined by beams with a 5-meter span. The height of the first floors was 3.2 meters and the other floors were 3.5 meters high. Figure 8 shows the laboratory sample of this structure. The design details and laboratory models are available in the reports Seismosoft [45]. Also, the details of the design, modeling, and constructing this laboratory model are achievable in reports [46]. In this study, verification of the result gained from maximum relative displacements at each level was carried out using laboratory observations of Pavan et al. [46], which is shown in Figure 8b.

The results of the modal analysis of the structures used in this study are summarized in Table 3.

4. 2. Modeling and Analysis Nonlinear analyses, especially dynamic analysis, are considered to be reliable and powerful tools in civil engineering practices [47–51]. In nonlinear modeling, beam and column elements were modeled using displacement-based fiber-section as shown in Figure 9. For steel materials, the initial stiffness and strength were assumed to decrease when hysteresis cycles continued. Steel sections were divided into approximately 100 fibers, following the Menegotto-pinto behavioral diagram. Also, columns and beams have been modeled through 3D displacement-based inelastic frame elements [46]. The modeled sections would automatically consider the two-way axial and flexural force coexistence. Shear and torsion in a cross-section were assumed to be uncoupled linear elastic. As a result, in the analysis of beam and column elements, the decay in stiffness and strength was ignored while the behavior was derived from shear and torsion. Floors were considered to be rigid diaphragms. Gravity loads and seismic masses at the joints of beams and columns were applied based on the dependent tributary area of each node. The damping ratio of 5% for the first and higher-mode, and Rayleigh-type damping according to mass and tangent stiffness properties was taken into account. Hilber-Hughes-Taylor Integration scheme was used to analyze time history.

Figure 8. (a) Four storey 3D steel moment resisting frame [46]

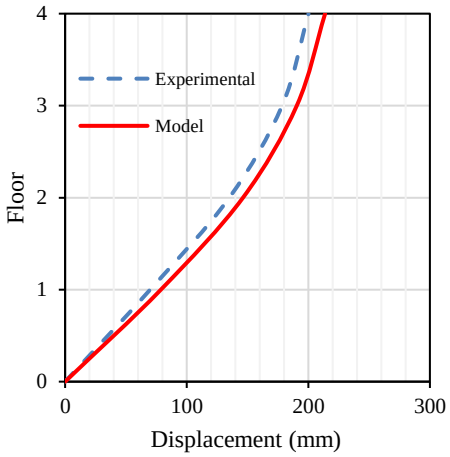

Figure 8. (b) Validation results of the experimental model and the model made in the software

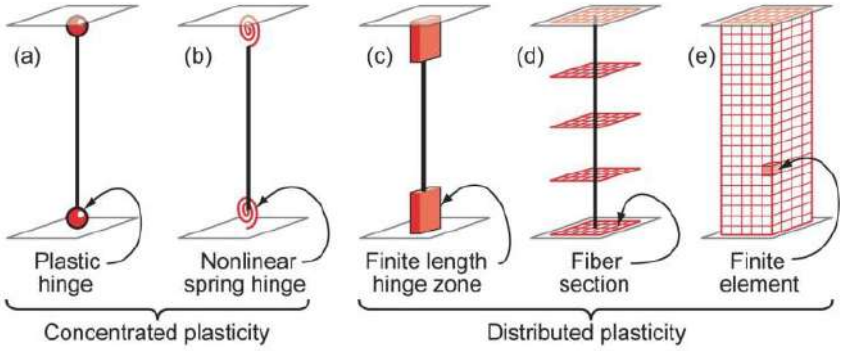

(a) Idealized modeling of nonlinear behavior of deformation control members [47]

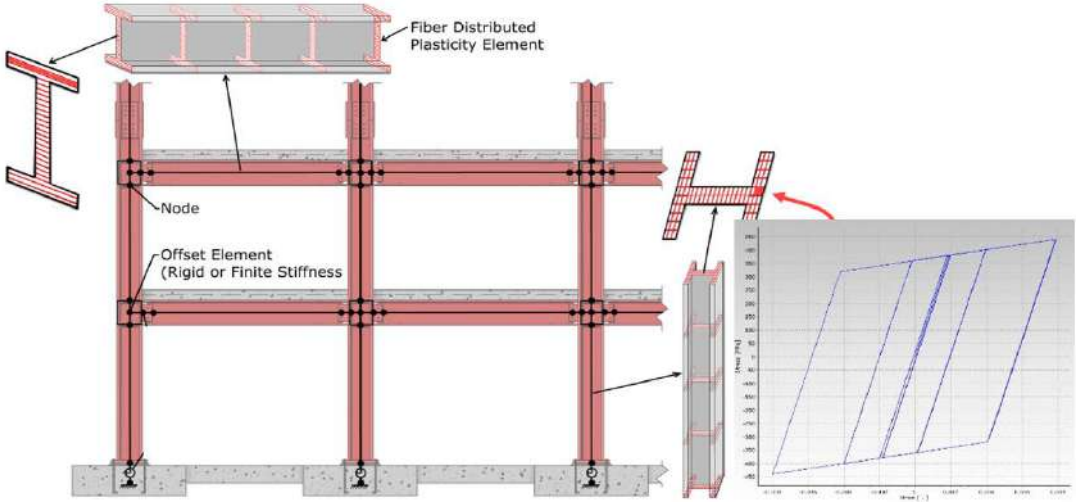

(b) Typical force-displacement diagram for bilinear steel model and hierarchical levels of distributed plasticity FE models [54]

Figure 9. Structural Modeling

TABLE 3. Numerical model and experiment specimen modal properties of the four-storey steel building

Mode	Periods of vibration (T)	Effective modal mass		
		UX (%)	UY (%)	RZ (%)
1	0.741	84.6	0.0	0.0
2	0.731	0.0	85.1	0.0
3	0.668	0.0	0.0	85.2
4	0.1379	0.0	3.3	0.0
5	0.1375	3.2	0.0	0.0

The nonlinear time history analysis as the most accurate numerical structural analysis [47,52] was performed using SeismoStruct 2016 software [53]. Since there were two record categories, each containing 17 records, to optimize the process of analyzing and evaluating the performance of the structure in nonlinear ranges, the 34 records were scaled so that the structure would reach its collapse threshold in each record. This considerably increased both the number of analysis operations and the accuracy of the results.

5. RESULTS AND DISCUSSION

5. 1. The Correlation between Seismic Parameters of Earthquakes After extracting the seismic parameters of the records whose corresponding values are shown in Table 3, the correlation between each seismic parameters was investigated. Then, the correlation was represented quantitatively for seismic parameters of the observed records, using the correlation concept previously discussed. The matrices derived from the

relationships between various seismic parameters in two categories of accelerations with long (Li) and short (Si) duration of motion are summarized in Tables 4 and 5. As shown in Tables 4 and 5, the highest PGA (Peak ground acceleration) correlation was related to AI (Arias intensity) and ASI (Acceleration spectrum intensity), which was the same in both long duration and short duration categories of records. The correlation coefficient in both short and long term categories showed a weak correlation between PGA and PGV/ PGA ratio, and SED (Specific Energy Density). PGV (Peak ground velocity) showed a strong correlation with most of the seismic parameters, the weakest correlation with PGV/PGA ratio, and the strongest correlation in both cases with HI (Housner Intensity). In general, PGV has a desirable correlation with energy-dependent seismic parameters. The results of the correlation of PGD (Peak ground displacement) seismic parameter showed that the dispersion was relatively high in the correlation of this parameter and the other seismic parameters. The least dispersion in both short and long term durations was related to energy-dependent parameters.

In examining seismic parameter PGV/PGA, although there was a weak correlation between this parameter and other seismic parameters, the dispersion of correlation in both short and long durations was very low, and the results were close to each other. A relatively strong correlation between AI and most of the seismic parameters was observed. The best parameters indicating the status of this parameter were PGA and ASI, which were similar in the results of both short and long term analyses. The results obtained from the seismic parameter analysis of SED showed a weak correlation between this parameter and other seismic parameters. The correlations were lower in short-term analysis than in the long-term one. Meanwhile, this parameter showed a relatively good correlation with PGV and HI. Due to the definition of the duration of Arias affecting ASI, the strong correlation of this parameter with PGA and AI could be predicted. This parameter would show a good correlation with energy-related parameters VSI and HI. The correlation of VSI with all of the seismic parameters, except PGV/PGA, was high, but data dispersion in both short and long term durations was not high. The strongest correlation between the studied parameters was related to VSI and HI, being very similar to each other. The results of analyzing this seismic parameter were slightly more in the long-duration than the short one.

TABLE 4. Correlation between seismic parameters of earthquake for Long ground-motion duration

	PGA	**PGV**	**PGD**	**PGV/PGA**	**Arias Intensity**	**SED**	**ASI**	**VSI**	**HI**
PGA	1								
PGV	0.50	1							
PGD	0.35	0.18	1						
PGV/PGA	-0.78	-0.01	-0.20	1					
Arias Intensity	0.90	0.56	0.23	-0.71	1				
SED	0.20	0.75	0.07	0.04	0.31	1			
ASI	0.91	0.45	0.15	-0.76	0.96	0.15	1		
VSI	0.74	0.82	0.25	-0.52	0.79	0.69	0.70	1	
HI	0.68	0.83	0.22	-0.45	0.73	0.75	0.63	0.99	1

TABLE 5. Correlation between seismic parameters of earthquake for Short ground-motion duration

	PGA	**PGV**	**PGD**	**PGV/PGA**	**Arias Intensity**	**SED**	**ASI**	**VSI**	**HI**
PGA	1								
PGV	0.52	1							
PGD	-0.25	0.25	1						
PGV/PGA	-0.66	0.27	0.42	1					
Arias Intensity	0.75	0.38	-0.14	-0.51	1				
SED	0.00	0.45	0.64	0.33	0.24	1			
ASI	0.94	0.43	-0.28	-0.68	0.85	-0.03	1		
VSI	0.75	0.80	0.12	-0.17	0.67	0.41	0.66	1	
HI	0.61	0.84	0.25	0.00	0.53	0.51	0.50	0.98	1

5. 2. Comparison of the Residual Inter-story Drift (RIDR) Since the records were matched for both short- and long-duration ones in terms of the response spectra, the acceleration applied to the structure was expected to be similar in both short and long durations. Therefore, by comparing the effect of the two accelerations with the same response spectra but different durations, we could ascertain the effect of duration on the response of the structures. Figure 10 shows how the residual inter-story drift ratio (RIDR) could change in the twenty pairs of records (L14, S14).

As shown in Figure10 (b), RIDR was larger in the long time mode (L14) than the short mode (S14). As shown in Figure 10 (a), Sa (T_1) was greater in L14 than S14 at the period of 0.74 seconds, which was related to the structure under analysis. This could be due to larger Sa (T_1) at the period of 0.74 second (the period of structure analysis), long duration of strong ground motion, and the reduction in the stiffness and strength of structural members in acceleration cycles.

5. 3. Comparison of Different Intensity Measures As mentioned previously, an efficient IM can predict the seismic response of structures with low dispersion. In this research, different intensity measures were compared according to RIDR, in long and short duration of strong motion. Figures 11-21 show the severity of the intensity measures based on RIDR in different duration modes in addition to the correlation coefficient (ρ) and regression (R^2) of these intensity measures.

Although the Sa (T1) intensity measure (IM) is the most useful parameter, the use of this intensity measure is less reliable in the range of nonlinear behavior where the stiffness of the structure decreases and the period of the structure increases compared to the linear behavior.

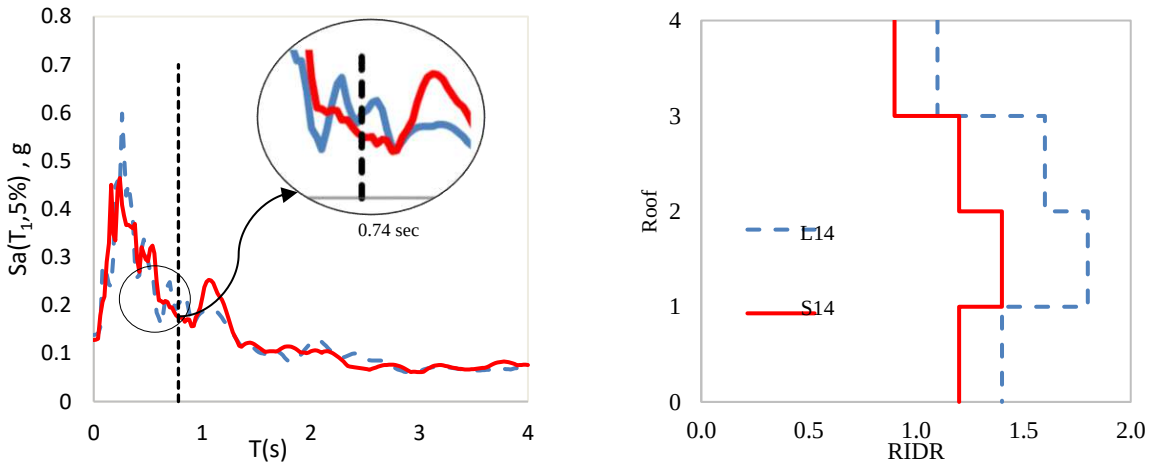

Figure 10. a) Sa(T_1,5%) curve for L14 and S14 records b) the comparison of RIDR for L14 and S14 records

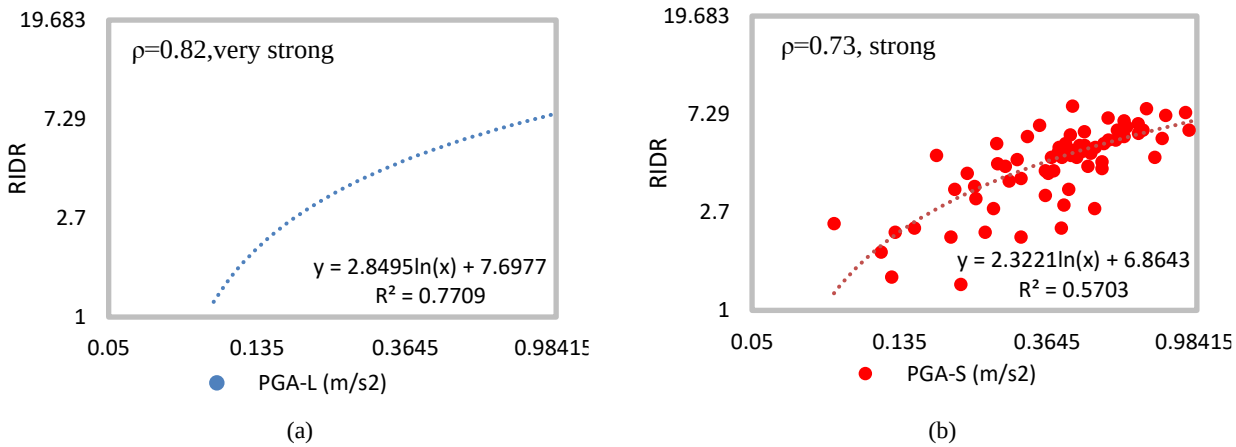

Figure 11. RIDR to Intensity measure of PGA curve for: a)Long ground-motion duration and b)Short ground-motion duration

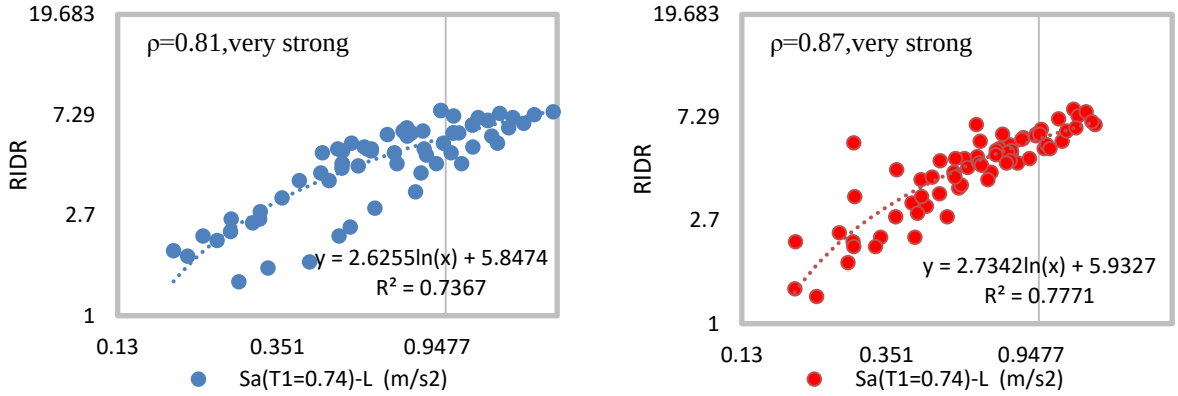

(a) (b)

Figure 12. RIDR to Intensity measure of Sa(T_1=0.74) curve for: a) Long ground-motion duration and b) Short ground-motion duration

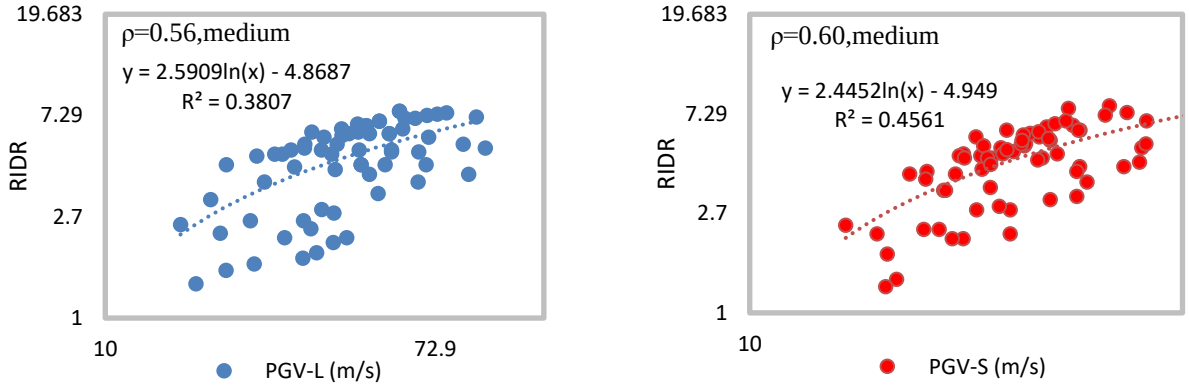

(a) (b)

Figure 13. RIDR to Intensity measure of PGV curve for: a) Long ground-motion duration b) Short ground-motion duration

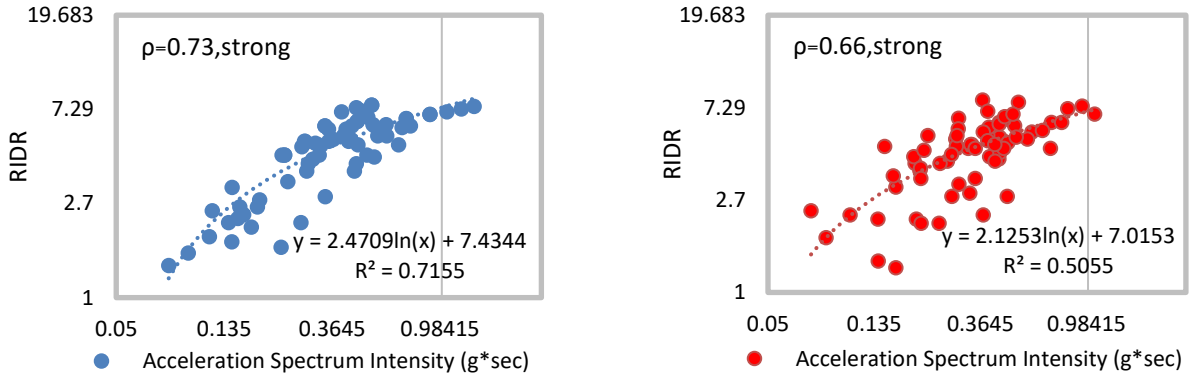

(a) (b)

Figure 14. RIDR to Intensity measure of ASI (Acceleration Spectrum Intensity) curve for: a) Long ground-motion duration b) Short ground-motion duration

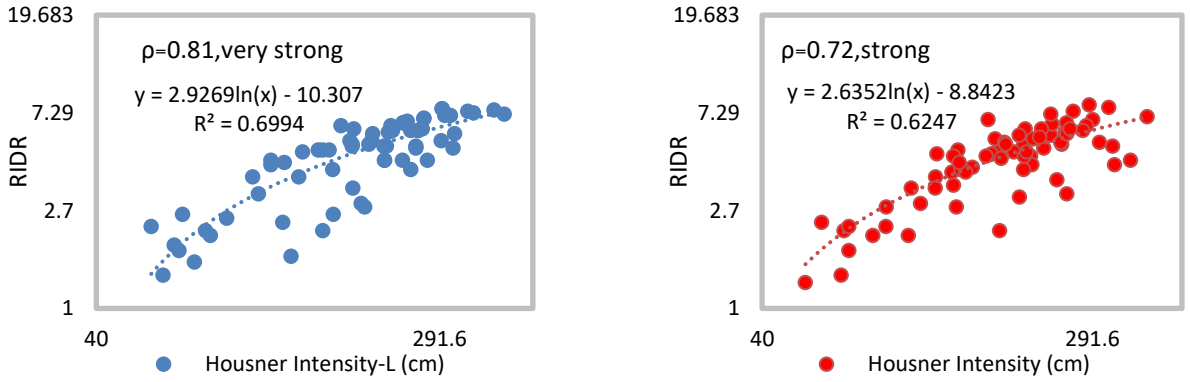

Figure 15. RIDR to Intensity measure of HI (Housner Intensity) curve for: a) Long ground-motion duration b) Short ground-motion duration

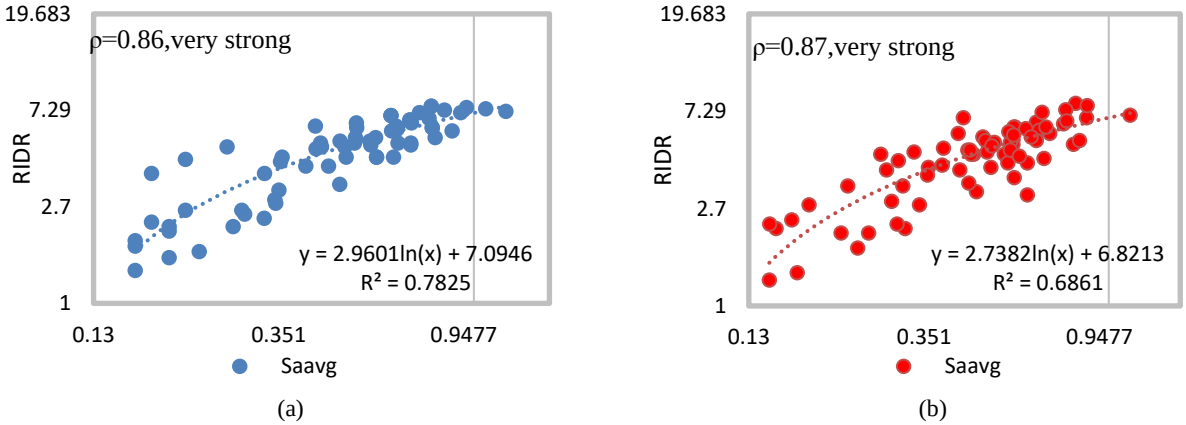

Figure 16. RIDR to Intensity measure of Sa_{avg} curve for: a) Long ground-motion duration b) Short ground-motion duration

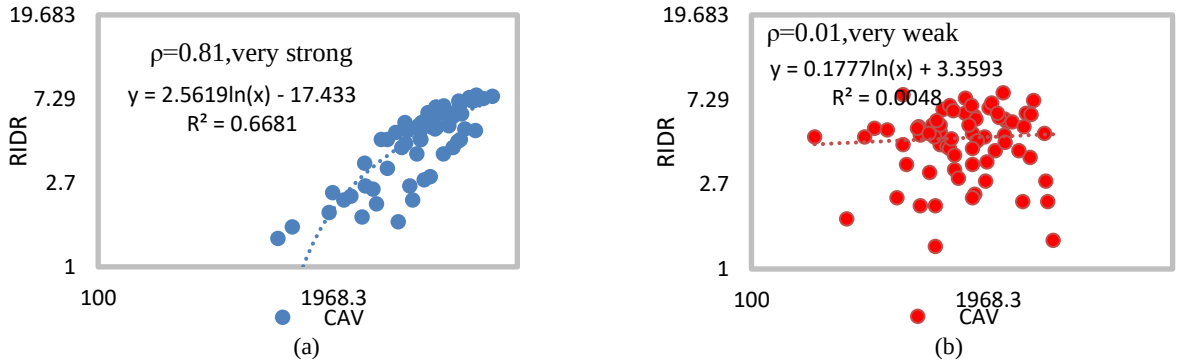

Figure 17. RIDR to Intensity measure of CAV (Cumulative absolute energy) curve for: a) Long ground-motion duration b) Short ground-motion duration

Increasing the period due to nonlinear behavior causes the structure to be affected by a range of response spectra different from values corresponding to the first mode period of the structure. Therefore, the appropriate intensity measure is a parameter that in addition to the spectral acceleration component at the time of the first mode of the structure, considers a component of the spectral acceleration at the time of period greater than the

time of the first mode of the structure. Accordingly, the use of INP intensity measure is recommended to evaluate the seismic performance of structures in nonlinear problems. In this intensity measure, a part of the response spectrum that has a great effect on the nonlinear behavior of the structure is considered as a part of the intensity measure. Therefore, this IM was considered to evaluate the residual drift of the stories due to the ground motion duration. Finally, a comparison was made between the efficiency of intensity measure in predicting nonlinear behavior and residual drift.

Figures 11-21 show the RIDR variations in different values of intensity measures in long and short durations of ground motion in detail. In each figure, the regression (R^2) shows the amount of RIDR dispersion for each variation in different intensity measures. The correlation coefficient (ρ) also specifies the degree of correlation of the data in each intensity measure. For example, in Figure 11, which illustrates the extent of RIDR variations in different PGA values, it is clear that as PGA increased, RIDR rose, too; however, the increase was more in the long term duration record mode than the short term one. The strong correlation coefficient in both forms would enhance the reliability of the results.

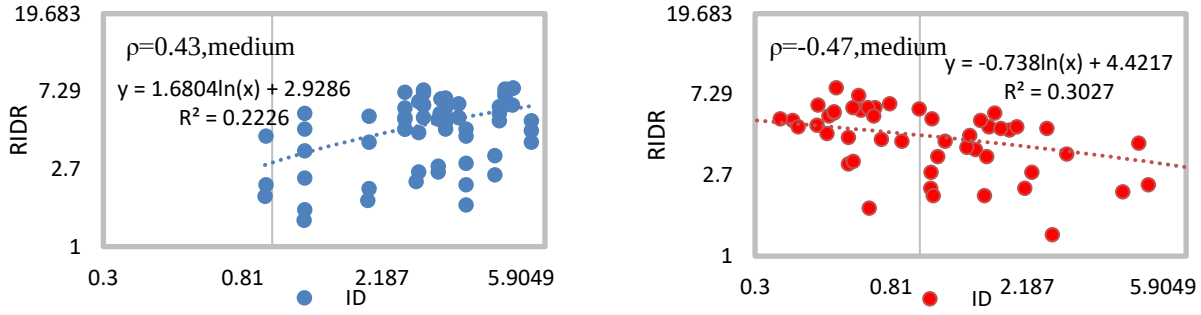

Figure 18. RIDR to Intensity measure of I_D curve for: a) Long ground-motion duration b) Short ground-motion duration

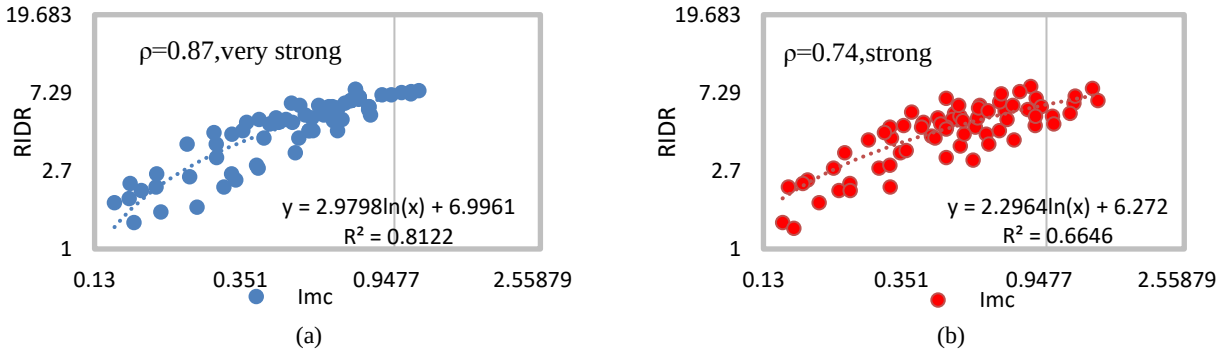

Figure 19. RIDR to Intensity measure of IMc curve for: a) Long ground-motion duration b) Short ground-motion duration

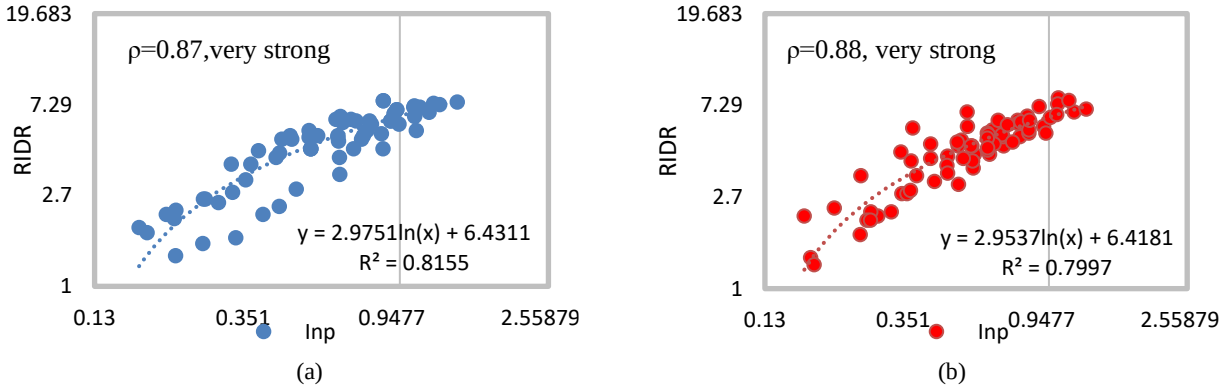

Figure 20. RIDR to Intensity measure of I_{NP} curve for: a) Long ground-motion duration b) Short ground-motion duration

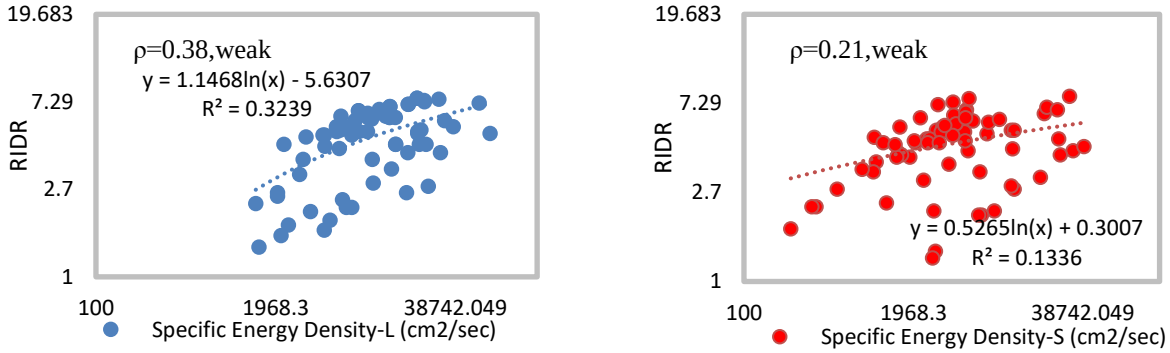

Figure 21. RIDR to Intensity measure of SED curve for: a) Long ground-motion duration b) Short ground-motion duration

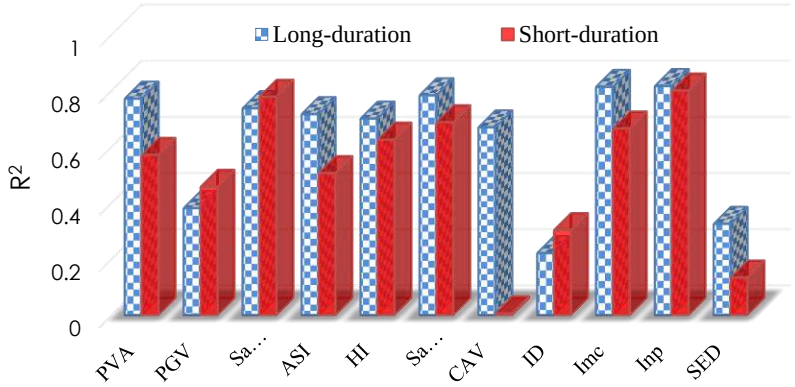

Figure 22. The comparison of regressions of intensity measures for the Long- and short-duration ground motion

In general, among eleven intensity measures in ten cases with an increase in various intensity measures, the RIDR ascended in both long- and short-durations strong ground motion. Only in I_D, and in the short term, a declining trend was observed. This could be due to the direct relationship between this intensity measure and the Arias duration which is one of the bases in sorting the records. In Figure 22, the comparison of intensity measures for the Long- and short- ground motion duration is shown. How various intensity measures affected RIDR in the long-duration motion mode could be as follows:

$$I_{NP} > IM_c > S_{a_{ave}} > PGA > S_a(T_1) > ASI > HI > CAV > PGV > SED > I_D$$

And in the short-duration motion mode as:

$$I_{NP} > S_a(T_1) > S_{a_{ave}} > IM_c > HI > PGA > ASI > PGV > I_D > SED > CAV$$

6. CONCLUSION

In this study, the impact of strong ground motion duration on the seismic response of a three dimensional model was investigated with respect to different types of intensity measures. Two sets of long- and short-duration natural earthquake records were utilized to discover the impact of strong ground motion duration on the seismic response of the abovementioned structure. In addition, the effect of different intensity measures on the response of the structure was assessed and the adequacy of the intensity measures was calculated. Utilizing correlation coefficients, the dependency of seismic parameters was surveyed. Indeed, in this research, the correlation between seismic parameters of earthquakes, quantitative comparison of RIDR and the effect of different intensity measures on the 4-floor steel structure of the RIDR were investigated under two acceleration categories with long and short ground motion duration. The following results can be highlighted:

1. The results showed that domain-based seismic parameters, such as PGA, PGV and, PGD could have a direct relationship with energy-based seismic parameters, e.g. AI, SED, ASI, VSI, and HI. This direct relationship is associated with relatively strong correlations, being higher in PGA relationships with more energy-based seismic parameters than PGV and PGD. The quantitative results indicated that PGV / PGA showed a direct relationship with other seismic

parameters, but a weak correlation was observed, which was more important in long-duration. Generally, PGA, HI, and VSI, in addition to a direct relationship with other seismic parameters (except PGV / PGA), represented the strongest correlation with other seismic parameters of both short- and long-duration ground motions.

2. Comparing RIDR in long and short strong ground motion duration modes indicated that with an increase in the duration, the RIDR would rise.
3. 11 intensity measures were compared in terms of long and short strong ground motion duration with regard to RIDR. The quantitative results, mentioned in section 5-3, showed that most of the intensity measures were directly related to RIDR (except I_D). In other words, with an increase in intensity measure, RIDR would rise. In general, in long-duration strong ground motions, I_{NP}, IMc, and $S_{a_{ave}}$intensity measures showed the least dispersion (highest regression) with RIDR, indicating that RIDR tended to increase with a steep rise in this magnitude. However, for the short-duration strong ground motions, I_{NP}, $S_a(T_1)$and $S_{a_{ave}}$intensity measures caused the least dispersion. The results of the mentioned intensity measures indicated the strongest correlation among intensity measures of the surveyed, which could predict the response of structures at low dispersion.

7. REFERENCES

1. Hancock J, Bommer JJ, Eeri M. "Earthquake Engineering Practice A State-of-Knowledge Review of the Influence of Strong-Motion Duration on Structural Damage", ***Earthquake Spectra,*** 2006;22:827-845. doi:10.1193/1.22205 76.
2. Raghunandan M, Liel AB, Luco N. "Collapse risk of buildings in the Pacific northwest region due to subduction earthquakes" ***Earthq Spectra***, (2015), Vol. 31, 2087-2115.
3. Chester D.K. "The 1755 Lisbon earthquake." ***Progress in Physical Geography***, Vol. 25, No. 3 (2001), 363-383. doi:10.1177/030913330102500304.
4. Bradley BA. Strong ground motion characteristics observed in the 4 September 2010 Darfield, New Zealand earthquake. ***Soil Dynamics and Earthquake Engineering***, Vol. 42, (2012), 32-46. doi:10.1016/j.soildyn.2012.06.004.
5. Hamidi H, Jamnani, Amiri JV, Rajabnejad H. Energy distribution in RC shear wall-frame structures subject to repeated earthquakes, ***Soil Dynamics and Earthquake Engineering***, Vol. 107, (2018), 116-128. doi:10.1016/j.soildyn.2018.01.010.
6. Chandramohan R, Baker JW, Deierlein GG. Quantifying the influence of ground motion duration on structural collapse capacity using spectrally equivalent records, ***Earthquake Spectra,*** Vol. 32, No. 2, (2016). doi:10.1193/122813EQS298MR2.
7. Barbosa AR, Ribeiro FLA, Neves LAC. Influence of earthquake ground-motion duration on damage estimation: application to steel moment resisting frames", ***Earthquake Engineering & Structural Dynamics***, Vol. 46, No. 1 (2017), 27-49. doi.org/10.1002/eqe.2769.
8. Ruiz-García J. "On the influence of strong-ground motion duration on residual displacement demands", ***Earthquake and Structures***, Vol. 1, No. 4, (2010), 327-344. doi:10.12989/eas.2010.1.4.327.
9. Song R, Li Y, van de Lindt J.W. "Impact of earthquake ground motion characteristics on collapse risk of post-mainshock buildings considering aftershocks", ***Engineering*** *Structures*, Vol. 81, (2014), 349-361. https://doi.org/10.1016/j.engstruct.2014.09.047.
10. Foschaar JC, Baker JW, Deierlein GG. "Preliminary assessment of ground motion duration effects on structural collapse" Proc. 15th World Confernce. Earthquake Engineering, 2012.
11. Raghunandan M, Liel AB. "Effect of ground motion duration on earthquake-induced structural collapse" ***Structural Safety***, Vol. 41, (2013), 119-133. https://doi.org/10.1016/j.strusafe.2012.12.002.
12. Hancock J, Bommer JJ. "Using spectral matched records to explore the influence of strong-motion duration on inelastic structural response. Soil", ***Dynamics and Earthquake Engineering,*** Vol. 27, (2007), 291-299. doi:https://doi.org/10.1016/j.soildyn.2006.09.004.
13. Zhang S, Wang G, Pang B, Du C. "The effects of strong motion duration on the dynamic response and accumulated damage of concrete gravity dams. Soil", ***Dynamics and Earthquake Engineering,*** Vol. 45, (2013), 112-124. doi:10.1016/j.soildyn.2012.11.011.
14. Bommer JJ, Magenes G, Hancock J, Penazzo P. "The influence of strong-motion duration on the seismic response of masonry structures" ***Bulletin of Earthquake Engineering***, Vol. 2, No. 1, (2004), 1-26. https://doi.org/10.1023/B:BEEE.0000038948.95616.bf.
15. Iervolino I, Manfredi G, Cosenza E. Ground motion duration effects on nonlinear seismic response. ***Earthquake Engineering & Structural Dynamics***, Vol. 35, No. 1, (2006), 21-38. doi:10.1002/eqe.529.
16. Bojorquez E, Iervolino I, Manfredi G, Cosenza E. Influence of ground motion duration on degrading SDOF systems. In First European Conference on Earthquake Engineering and Seismology (2006), 3-8.
17. Nassar AA, Krawinkler H. Seismic demands for SDOF and MDOF systems, John A. Blume Earthquake Engineering Center, Republished 1991;95. (Doctoral dissertation, Stanford University, 1991).
18. Shome N, Cornell CA, Bazzurro P, "Carballo JE. Earthquakes, records, and nonlinear responses", ***Earthquake Spectra*** 1998;14:469–500. doi:https://doi.org/10.1193/1.1586011.
19. Tremblay R, Atkinson GM. "Comparative Study of the Inelastic Seismic Demand of Eastern and Western Canadian Sites" ***Earthquake Spectra***, (2001), Vol. 17, 333-358. doi:10.1193/1.1586178.
20. Chai YH. "Incorporating low-cycle fatigue model into duration-dependent inelastic design spectra", ***Earthquake Engineering & Structural Dynamics***, Vol. 34, No. 1, (2005), 83-96. doi:10.1002/eqe.422.
21. Bhargavi P, Raghukanth STG. "Rating damage potential of ground motion records", ***Earthquake Engineering & Engineering Vibration***, Vol. 18, No. 2, (2019), 233-254. doi:10.1007/s11803-019-0501-1.
22. Bradley BA. Correlation of significant duration with amplitude and cumulative intensity measures and its use in ground motion selection. ***Journal of Earthquake Engineering***, Vol. 15, No. 6, (2011), 809-832. doi:10.1080/13632469.2011.557140.
23. Zhou J, Tang K, Wang H, Fang X. Influence of ground motion duration on damping reduction factor. ***Journal of Earthquake***

Engineering, Vol. 18, No. 5, (2014), 816-830. doi:10.1080/13632469.2014.908152.

24. Belejo A, Barbosa AR, Bento R. "Influence of ground motion duration on damage index-based fragility assessment of a plan-asymmetric non-ductile reinforced concrete building", ***Engineering Structures***, Vol. 151, (2017), 682-703. https://doi.org/10.1016/j.engstruct.2017.08.042.
25. Baker JW, Cornell CA. "Vector-valued ground motion intensity measures for probabilistic seismic demand analysis", Pacific Earthquake Engineering Research Center, College of Engineering, Stanford University; 2006.
26. Mazza F, Labernarda R. "Structural and non-structural intensity measures for the assessment of base-isolated structures subjected to pulse-like near-fault earthquakes. Soil", ***Dynamics and Earthquake Engineering***, Vol. 96, (2017), 115-127. doi:10.1016/j.soildyn.2017.02.013.
27. Zhou Y, Ge P, Han J, Lu Z. "Vector-valued intensity measures for incremental dynamic analysis. Soil", ***Dynamics and Earthquake Engineering,*** Vol. 100, (2017), 380-388. doi:10.1016/j.soildyn.2017.06.014.
28. Yakhchalian M, Nicknam A, Amiri GG. "Optimal vector-valued intensity measure for seismic collapse assessment of structures", ***Earthquake Engineering & Engineering Vibration,*** Vol. 14, No. 1, (2015), 37-54. doi:10.1007/s11803-015-0005-6.
29. Kassem MM, Nazri FM, Farsangi EN. "The efficiency of an improved seismic vulnerability index under strong ground motions", ***Structures***, Vol. 23, Elsevier; (2020), 366-382. doi:https://doi.org/10.1016/j.istruc.2019.10.016.
30. Kassem MM, Nazri FM, Farsangi EN. "On the quantification of collapse margin of a retrofitted university building in Beirut using a probabilistic approach", ***Engineering Science and Technology, an International Journal***, Vol. 23, No. 2, (2020), 373-381. doi:https://doi.org/10.1016/j.jestch.2019.05.003.
31. Farsangi EN, Yang TY, Tasnimi AA. "Influence of concurrent horizontal and vertical ground excitations on the collapse margins of non-ductile RC frame buildings", ***Structural Engineering and Mechanics***, Vol. 59, No. 4, (2016), 653-669. doi:http://dx.doi.org/10.12989/sem.2016.59.4.653.
32. Nazri FM, Miari MA, Kassem MM, Tan C-G, Farsangi EN. "Probabilistic evaluation of structural pounding between adjacent buildings subjected to repeated seismic excitations", ***Arabian Journal for Science and Engineering***, Vol. 44, No. 5 (2019): 4931-4945. doi:https://doi.org/10.1007/s13369-018-3666-4.
33. Yakhchalian M, Ghodrati Amiri G. "A vector intensity measure to reliably predict maximum drift in low-to mid-rise buildings", ***Proceedings of the Institution of Civil Engineers-Structures and Buildings***, Vol. 172, No. 1 (2019), 42-54. doi:https://doi.org/10.1680/jstbu.17.00040.
34. Luco N, Cornell CA. "Structure-specific scalar intensity measures for near-source and ordinary earthquake ground motions", ***Earthquake Spectra,*** (2007), Vol. 23, 357-392. doi:10.1193/1.2723158.
35. Lee BJ, Chou TY, Hsiao CP, Chung LK, Huang PH, Wu YB. "The statistics and analysis of building damage on Chi-Chi earthquake" International Train Programs Seismic Design Building Structure Taipei, Taiwan National Center Research Earthquake Engineering, 2002.
36. Mehanny SS, Cordova PP. "Development of a two-parameter seismic intensity measure and probabilistic design procedure" ***Journal of Engineering Applied Science***, Vol. 51, (2004), 233-252.
37. Bojórquez E, Iervolino I. "Spectral shape proxies and nonlinear structural response. Soil", ***Dynamics and Earthquake Engineering,*** Vol. 31, (2011), 996-1008. doi:10.1016/j.soildyn.2011.03.006.
38. Soleymani Abed. Investigation of Correlations between Seismic Parameters and Damage Indices for Earthquakes of Iran Region (TECHNICAL NOTE). ***International Journal of Engineering, Transactions B: Applications,*** Vol. 27, (2014), 283-292, doi: 10.5829/idosi.ije.2014.27.02b.12
39. Bommer JJ, Martinez-Pereira A. "The effective duration of earthquake strongmotion", ***Journal of Earthquake Engineering***, (1999), Vol. 3, 127-172. doi:https://www.worldscientific.com/doi/abs/10.1142/S1363246999000077.
40. Pagratis D. Prediction of earthquake strong ground-motion for engineering use. M Sc Diss 1995.
41. Sarma SK. "Energy flux of strong earthquakes", ***Tectonophysics*** Vol. 11, No. 3 (1971), 159-173. doi:https://doi.org/10.1016/0040-1951(71)90028-X.
42. Ghodrati AG, Mahmoudi H, Razavian ASA. "Probabilistic seismic hazard assessment of Tehran based on Arias intensity", ***International Journal of Engineering, Transactions B: Applications*** Vol. 23, No. 1, February 2010: Pp 1-20. doi:https://www.sid.ir/en/journal/ViewPaper.aspx?id=177545.
43. Boore DM. On pads and filters: Processing strong-motion data. *Bulletin of the Seismological Society of America*, Vol. 95, No. 2 (2005), 745-750. doi:https://doi.org/10.1785/0120040160.
44. Boore DM, Bommer JJ. "Processing of strong-motion accelerograms: needs, options and consequences", ***Soil Dyn Earthquake Engineering***, (2005), Vol. 25, 93-115. doi:https://doi.org/10.1016/j.soildyn.2004.10.007.
45. SeismoSoft, SeismoStruct. "A computer program for static and dynamic nonlinear analysis of framed structures." *Disponível online em: http://www. seismosoft.com* (2006).
46. Pavan A, Pinho R, Antoniou S. "Blind prediction of a full scale 3D steel frame tested under dynamic conditions" 14th World Conf. Earthquake Engineering, Beijing, China, Oct., 2008.
47. Deierlein GG, Reinhorn AM, Willford MR. Nonlinear structural analysis for seismic design. NEHRP Seismic Design Technical Brief, No. 4, 2010;1–36.
48. Ghodrati Amiri G, Hamidi Jamnani H, Ahmadi HR. "The Effect of Analysis Methods on the Response of Steel Dual-System Frame Buildings for Seismic Retrofitting", ***International Journal of Engineering, Transactions B: Applications,*** Vol. 22, No. 4 (2009), 317-331. https://www.sid.ir/en/journal/ViewPaper.aspx?ID=165187.
49. Nicknam A, Mosleh A, Hamidi Jamnani H. "Seismic performance evaluation of urban bridge using static nonlinear procedure, case study: Hafez bridge" ***Procedia Engineering***, Vol. 14, 2011. doi:10.1016/j.proeng.2011.07.296.
50. Jalilkhani M, Manafpour AR. "A simplified modal pushover analysis-based method for incremental dynamic analysis of regular rc moment-resisting frames", ***International Journal of Engineering, Transactions B: Applications,*** Vol. 31, No. 2, (2018), 196-203. doi:10.5829/idosi.ije.2015.28.02b.04.
51. Baharmast H, Razmyan S, Yazdani A. "Approximate incremental dynamic analysis using reduction of ground motion records", ***International Journal of Engineering, Transactions B: Applications,*** Vol. 28, No. 2, (2015), 190-197. doi:10.5829/idosi.ije.2015.28.02b.04.
52. Hamidi H, Khosravi H, Soleimani R. "Fling-step ground motions simulation using theoretical-based Green's function technique for structural analysis. Soil", ***Dynamics and Earthquake Engineering,*** Vol. 115, (2018), 232-245. https://doi.org/10.1016/j.soildyn.2018.08.023.
53. Sadeghi A, Abdollahzadeh G, Rajabnejad H, Naseri SA. "Numerical analysis method for evaluating response modification factor for steel structures equipped with friction dampers", ***Asian Journal of Civil Engineering***, Vol. 22, No. 2, (2021), 313-330. doi:https://doi.org/10.1007/s42107-020-

00315-2.

54. NIST (National Institute of Standards and Technology). "Guidelines for Nonlinear Structural Analysis for Design of Buildings Part IIa–Steel Moment Frames." (2017). (NIST GCR 17-917-46v2).

Persian Abstract

چکیده

در ارزیابی عملکرد سازه ها در هنگام زلزله، ویژگی های مدت زمان موثر حرکت قوی زمین برروی پاسخ سازه ها تا حدی مبهم باقی مانده و دارای نتایج غیر قطعی می باشند. سنجه شدت (IM) رابطه ای بین خطر حرکت زمین با پاسخ سازه ایجاد می کند. از این رو، استفاده از IM مناسب نقش مهمی در پیش بینی پاسخ سازه دارد. در این تحقیق، تأثیر مدت زمان حرکت قوی زمین و ضریب همبستگی سنجه شدت های مختلف، برروی جابجایی نسبی باقیمانده بین طبقات (RIDR) یک سازه فولادی سه بعدی مورد بررسی قرار گرفته است. با استفاده از تحلیل دینامیکی غیرخطی و ۳۴ رکورد زلزله، رابطه بین پارامترهای لرزه ای مدت زمان حرکت قوی زمین در دو حالت کوتاه و بلند شامل *دامنه*، *انرژی* و *پارامترهای محتوای فرکانسی* مورد ارزیابی قرارگرفت. همچنین، همبستگی بین ۱۴ سنجه شدت اسکالر وجابجایی نسبی باقیمانده بین طبقات RIDR سازه نیز بررسی شده است. نتایج نشان داده است که بیشترین همبستگی بین پارامترهای لرزه‌ای همچون PGA، HI و VSI با دیگر پارامترها در هر دو حرکت قوی زمین با مدت زمان کوتاه و بلند وجود دارد. براساس شاخص حداکثر دریفت باقیمانده بین طبقات، سنجه شدت های IM_C، I_{NP} و Sa_{ave} کمترین پراکندگی در برابر رکوردهای مدت زمان بلند را دارا بوده‌اند. از سوی دیگر، معیارهای شدت I_N، $Sa(T_1)$ و Sa_{ave} کمترین پراکندگی را در برابر رکوردهای مدت زمان کوتاه نشان داده است.

IJE TRANSACTIONS A: Basics Vol. 34, No. 10, (October 2021) 2238-2247

International Journal of Engineering
Journal Homepage: www.ije.ir

Robust Design of Reinforced Concrete Moment-resisting Frames

A. Sepas Hokamabadi*, S. Gholizadeh, S. Tariverdilo

Department of Civil Engineering, Faculty of Engineering, Urmia University, Iran

PAPER INFO

Paper history:
Received 08 June 2021
Received in revised form 06 July 2021
Accepted 06 July 2021

Keywords:
Reinforced Concrete
Moment-resisting Frames
Optimization, Robust Design
Time History Analysis
Non-linear Analysis

ABSTRACT

Reinforced concrete moment resisting frame (RCMRF) is one of the most popular structural systems. Conventionally, buildings with RCMRF systems are designed to satisfy the relative displacement, resistance, and flexibility requirements defined by the design codes. Structural design codes have given different ranges of design parameters that the designers and engineers must consider in the design process of structures and the values selected for these parameters affect the seismic behaviour of the structures. However, performance assessment of the RCMRF under the earthquake loading to limit the probable levels of damage has a complicated and difficult procedure that is time-consuming for designing of ordinary buildings. In this study, to prevent this time-consuming process, tighter ranges for design parameters have been attempted to improve the seismic performance of the RCMRFs. In this regard, databases of RCMFs were created for different ranges of design parameters. The Particle Swarm Optimization (PSO) algorithm is used to create these databases and RCMRFs are optimally designed according to ACI 318-14 code. Then, nonlinear time history analysis according to ASCE/SEI 7-16 code was performed on the RCMRFs in each one of the databases and the statistical analysis of local and global results acquired from the nonlinear time history analysis is carried out. Finally, tighter ranges of design parameters have been determined to achieve more robust structures without involvement in time-consuming processes.

doi: *10.5829/ije.2021.34.10a.05*

1. INTRODUCTION

Recent developments in construction technologies have made the design of more complex structures easier which are susceptible to undesirable effects of severe events such as an earthquake. It is difficult to prevent the collapse of structures under such events; nevertheless, the consequences of failure can be reduced significantly in the structures with adequate robustness. It seems that structural robustness can be suggested as a novel key concept in the design of concrete structures; however, quantification and methods of robustness assessment have not been sufficiently integrated yet. This study attempts to facilitate the design of robust structures in the medium-rise reinforced concrete (RC) buildings, which make up a large part of buildings, by providing simple approaches that are applicable and known to the structural engineers.

Structural designers have different strategies in selecting design parameters for RC frames. This issue drastically affects the performance of structures under earthquake and changes the robustness of the structures. This study uses Particle Swarm Optimization (PSO) algorithm as a well-known algorithm for structural design to avoid such issues and evaluate the impact of the selected parameters on robustness of the structures.

In specified ranges for various parameters, the structures designed by this algorithm are analyzed under the selected earthquakes using Non-Linear Time-history Analysis (NLTHA). The impact of design parameters variation on the seismic performance of the structures were assessed by employing statistical methods. Therefore, suitable parameters range can be determined to increase the structural robustness subject to earthquake loading.

* Corresponding Author Institutional Email: ar.sepas@urmia.ac.ir
(A. Sepas Hokamabadi)

Please cite this article as: M. Mohammadizadeh, B. Pourabbas, K. Foroutani, M. Fallahian, Conductive polythiophene nanoparticles deposition on transparent PET substrates: effect of modification with hybrid organic-inorganic coating, International Journal of Engineering (IJE), TRANSACTIONS C: Aspects Vol. 28, No. 3, (March 2015) 2238-2247

2. DESIGN ALGORITHM

Based on the reasons mentioned above, the design optimization algorithm selected in the present study is PSO algorithm which is one of the best metaheuristics and has been widely used in the past years.

2. 1. Sections Database A variety of different reinforcement patterns and sections can be used for the beams and columns in the RC frames. In this section, two main databases are developed for the sections of beams and columns to reduce the complexity of the optimization process. To create these databases, the provisions of the design code and some practical requirements are followed. Most concrete columns and beams usually have square and rectangular sections, which their length to width ratios vary between 1.1 and 2. The increment of dimensions of the sections is usually 5 cm. The size of the steel reinforcement is F18, F20, and F22 for beams and F20, F22, and F25 for columns. The strength of concrete is considered 280 kg/cm^2, longitudinal steel reinforcements, 4200 kg/cm^2, and shear reinforcements, 3000 kg/cm^2.

ACI 318-14 [1] code applies certain requirements for sections. These requirements include the minimum and maximum steel reinforcement ratio, the minimum concrete cover thickness of 4 cm for the reinforced concrete members, minimum diameter of the shear steel reinforcements, and the minimum space between longitudinal reinforcements. Complying with these requirements, a large number of sections can be created for beams and columns.

It is worth to mention that the requirements specified in ACI 318-14 code related to the frames with special ductility, were taken into consideration when developing the database [1].

2. 1. 1. Beams According to the ACI 318-14 Code [1], the following requirements should be considered for the beam sections:

1. As Figure 1a shows, at least four bars should be positioned at the four corners of the section.
2. The minimum space between the longitudinal bars should be 4 cm.
3. The minimum thickness of the concrete cover should be 4 cm.
4. The diameter of the ties is F10.
5. The bar layers should be limited to two layers.
6. The upper-layer reinforcements should be located in the same position as the lower layer reinforcements, and as shown in Figure 1b, the minimum free space between two layers should be 2.5 cm.
7. If a beam section requires a larger number of bars, all these reinforcements will be added to the second layer, symmetrical to the vertical axis of the section, and exactly above the lower layer of reinforcements. If the mentioned symmetry cannot be obtained, then the symmetry is to be created by adding another reinforcing bar, as shown in Figure 1c [2]

The requirements of section 10 of ACI 318-14 Code are observed for the minimum and maximum ratio of the flexural reinforcing bars [2]. Considering the mentioned provisions, 35 different dimensions of sections are created as follows:

$35 \times 40 \sim 70, 40 \times 45 \sim 75, 45 \times 50 \sim 80, 50 \times 55 \sim 85, 55 \times 60 \sim 90\ cm$

A total number of 8548 different sections are created for beams and a sample of the details is presented in Figure 2. This beam sections used in the present study.

2. 1. 2. Columns According to ACI 318-14 Code [1], the following requirements should be observed for the column sections:

A. The minimum clear spacing between the longitudinal reinforcing bars should be considered s_c=40mm.
B. The least number of reinforcing bars is four, and as shown in Figure 3a, they should be positioned at the four corners of the section.
C. The minimum concrete cover should be t_c=40mm.
D. Considering the special ductility of the frame, the diameter of ties should be F10, and their clear spacing is set at 12.5 cm.
E. As Figure 3b shows the arrangement of the bars should be symmetrical in the two opposite sides of the section.

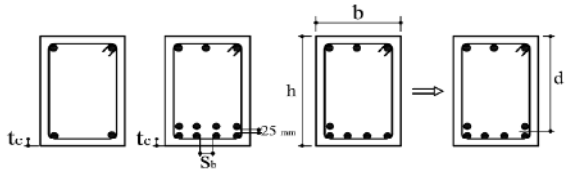

(a) (b) (c)

Figure 1. Restrictions for placement of reinforcements in the beams: (a) at least four reinforcing bars in the corners. (b) The minimum clear spacing between the longitudinal bars in two layers. (c) Reinforcing bar placement symmetry in relation to the vertical axis of the section. [2]

Beam Number	Width (cm)	Depth (cm)	Area (cm^2)	Moment of inertia (cm^4)	Number of bars		Bar size (mm)	Factord moment resistance (kg.cm)		Cost per unit length ($)
					Center	End		Center	End	
1	35	40	1400	186666.67	2	2	18	631328.03	631328.03	127.69
2	35	40	1400	186666.67	3	2	18	928479.89	631328.03	129.49
3	35	40	1400	186666.67	4	2	18	1213290.30	631328.03	131.29
4	35	40	1400	186666.67	2	2	20	769894.37	769894.37	129.38
5	35	40	1400	186666.67	3	2	20	1126626.09	769894.37	131.60
6	35	40	1400	186666.67	4	2	20	1464547.51	769894.37	133.82
7	35	40	1400	186666.67	2	2	22	919138.98	919138.98	131.24
8	35	40	1400	186666.67	3	2	22	1337398.22	919138.98	133.93
9	35	40	1400	186666.67	4	2	22	1728117.30	919138.98	136.61
10	35	40	1400	186666.67	2	3	18	631328.03	928479.89	129.49
11	35	40	1400	186666.67	3	3	18	928479.89	928479.89	131.29

Figure 2. Beams Database

F. The area of the longitudinal reinforcing bars should be between 1 and 3% of the total cross-section [2].
G. The maximum clear spacing between the longitudinal reinforcing bars should be considered S_c=150mm.

F20, F22 and F25 reinforcing bars are used in the column sections. A database containing 150 types of square sections with 40 cm to 90 cm dimensions and 5 cm steps, has been used for the columns. The strength of each column section under the applied loads (flexural and axial) is calculated using the P-M interaction curves. Eleven-point P-M interaction linear- diagram shown in Figure 4 has been used in this study.

2. 2. Frame Analysis All design conditions and requirements must be considered for the optimal design of a frame. To do so, internal forces such as axial forces, shear forces, and bending moments of each member are needed. These structural response values are calculated to design each of the frames using Finite Element Analysis. In the present study, only bending moments have been considered for the beams to simplify the calculations, while combined axial forces and bending moments have been considered for the columns. The analysis of columns also includes checking the column slenderness. If a column is determined to be slender, the slenderness coefficient is applied. According to ACI 318-14 Code, if a column is slender, the moment amplifies.

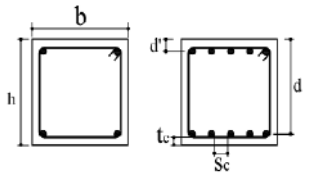

(a) (b)

Figure 3. Limitations of reinforcing bar placement in the Columns: (a) At least four longitudinal reinforcing bars in the four corners. (b) Symmetrical patterns of bars and the bar clear spacing and cover [2]

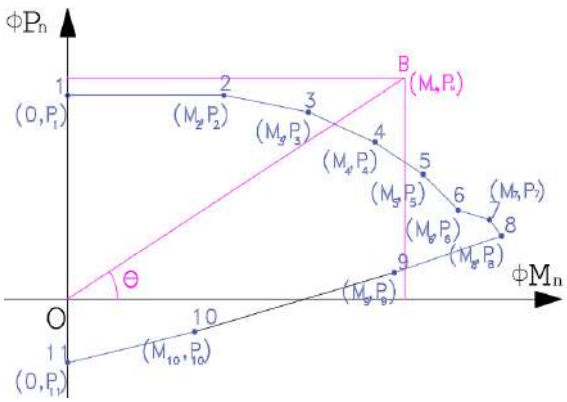

Figure 4. Eleven-point P-M interaction linear- diagram

2. 3. Geometric Constraints of the Problem In this constraint, the section dimensions and the number and size of the reinforcing bars of the upper floor column should be less than or equal to the lower floor column. The geometric structural members are shown in Figure 5.

Furthermore, in the beam-to-column connections, the beam width should be less than or equal to the width of the lower floor column, the dimensions of columns on each floor are also the same, but their reinforcing bars can be different, and the beams of lower floors have greater or equal dimensions to the beams of upper floors. These constraints are written as follows:

$$\begin{aligned} g_m^b &= \frac{b_b}{b_{cd}} - 1 \le 0, m = 1,2,\dots.nj \\ g_m^{bc} &= \frac{b_{cu}}{b_{cd}} - 1 \le 0, m = 1,2,\dots.nj \\ g_m^{bb} &= \frac{b_{bu}}{b_{bd}} - 1 \le 0, m = 1,2,\dots.nj \\ g_m^{bcie} &= \left|\frac{b_{ci}}{b_{ce}} - 1\right| \le 0, m = 1,2,\dots.nj \\ g_m^{dc} &= \frac{d_{cu}}{d_{cd}} - 1 \le 0, m = 1,2,\dots.nj \\ g_m^{bh} &= \frac{h_{bu}}{h_{bd}} - 1 \le 0, m = 1,2,\dots.nj \end{aligned} \quad (1)$$

2. 4. Design Constraints The constraints related to a force-based design should also be incorporated into the design and analysis process. For the beams, the corresponding moment demand in the middle (M_u^+) and at the ends of the member (M_{uR}^- andM_{uL}^-) should be less than the section capacity ($\emptyset M_n$). For the columns, the capacity of the column sections should also be larger than the corresponding demand. The interaction of axial force and bending moment are considered to assess the capacity of columns. Therefore, the pair of axial forces and bending moment (M_u, P_u) resulting from the imposed loads should not exceed the range of the column's interaction diagram. The section capacity and demand are calculated as follows to formulate this column constraint.

$$L_n = \sqrt{(\phi M_n)^2 + (\phi P_n)^2},\ L_u = \sqrt{(M_u)^2 + (P_u)^2} \quad (2)$$

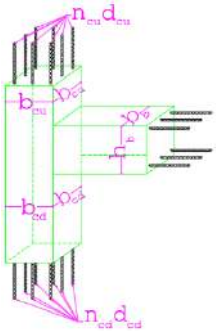

Figure 5. Geometries of structural members

Thus, if $L_u \leq L_n$, then the column section can be considered adequate. Finally, the formulation of constraints for the reinforced concrete frame can be expressed as follows:

$$g_1 = \frac{M_u^+}{\varphi M_n^+} - 1 \leq 0 \quad (3)$$

$$g_2 = |M_{uL}^-|/\varphi M_n^- - 1 \leq 0 \quad (4)$$

$$g_3 = |M_{uR}^-|/\varphi M_n^- - 1 \leq 0 \quad (5)$$

$$g_4 = \frac{L_u}{L_n} - 1 \leq 0 \quad (6)$$

2. 5. Constraints of Inter-story Drift According to 16.4.1.2 of ASCE 7-16 Code, the mean inter-story drift should not be larger than twice the values available in ASCE 7-16 Code (see Table 12.12-1). The inter-story drift should be computed as the difference of the deflections at the centres of mass at the top and bottom of the story under consideration [3].

$$\delta_x = \frac{C_d \delta_{xe}}{I_e} \quad (7)$$

C_d is the deflection amplification factor, calculated from ASCE 7-16 Code, Table 12.21, δ_{xe}, the deflection at the location required, determined by an elastic analysis, and I_e, the importance factor determined in accordance with ASCE 7-16 Code (section 11.5.1). The C_d coefficient for the reinforced concrete special moment frame is 5.5, which is extracted from ASCE 7-16 Code (Table 12.2-1) and I_e is obtained from ASCE 7-16 Code (section 11.5.1) equal to 1 [3], therefore:

$$\frac{C_d \delta_{xe}}{I_e} \leq \Delta_a \rightarrow \frac{C_d \delta_{xe}}{I_e} \leq 2 \times 0.02 \times h_{sx} \rightarrow \frac{\delta_{xe}}{h_{sx}} \leq 2 \times \frac{0.02}{5.5} = 0.00727 \quad (8)$$

h_{sx} is the story height below Level x. Ultimately, the formulation of the drift constraints for the inter-story drift of mentioned RC frames can be written as follows:

$$g_{di} = \frac{\delta_{xe}}{h_{sx} \times 0.00727} - 1 \leq 0 \quad , \quad i = 1,2, \ldots . n \quad (9)$$

2. 6. Strong Column Weak Beam (SCWB) Constraint ACI 318 adopts the strong-column/weak-beam principle by requiring that the sum of column moment strengths exceed the sum of beam moment strengths at each beam-column connection of a special moment frame. Studies conducted by Kuntz and Browning [3] and Maffei [4] have shown that the full structural mechanism can be achieved only when the column-to-beam strength ratio is relatively large (about four or more). Because this ratio is impractical in most cases, a lower strength ratio of 1.2 is adopted by ACI 318 [1]. The following inequality should be observed in all the structural joints to prevent the development of the mentioned state:

$$M_{n,top}^{col} + M_{n,bot}^{col} > \frac{6}{5}(M_n^+ + M_n^-) \quad (10)$$

In the expression above, the sides of the expression are the total plastic moment capacity for the members of the beams and columns at each structural joint.

2. 6. Optimization Formulation The formulation of optimal design in force-based design methods is as follows.

$$minimize: F(x)$$
$$subject\ to: g_i(x) < 0 \ , \ i = 1,2, \ldots ,n \ , x^L < x < x^U \quad (11)$$

In expression (7), x vector indicates the design variables, and F is the optimization objective function, which is a criterion for selecting the best designed structure. This part of the study aims to minimize the construction costs of the structure. Needless to mention, minimizing the objective function should not have an adverse impact on structural behaviour and efficiency. Therefore, the minimum point of the objective function should satisfy $g_i(x) < 0$ inequality, which is also termed as the problem constraints.

The main goal in the optimization of a RC frame is to minimize the construction cost, thus the objective function can be written as follows:

$$C = \sum_{i=1}^{nb} (C_C\, b_{b,i}\, h_{b,i} + C_S\, A_{S,b,i} + C_F\, (b_{b,i} + 2\, h_{b,i})\, L_i + \sum_{j=1}^{nc} \left(C_C\, b_{c,j}\, h_{c,j} + C_S\, A_{S,c,j} + 2C_F\, (b_{c,j} + h_{c,j})\right) H_j \quad (12)$$

In which C is the objective function, n_b the number of beams, $b_{b,i}$, $h_{b,i}$, L_i and $A_{s,b,i}$ are the width, height, length and the area of the bars in the i^{th} beam respectively, n_c is the number of columns, $b_{c,j}$,$h_{c,j}$,H_j and $A_{s,c,j}$ are the width, height, length, and the area of the bars in the j^{th} column respectively. C_C, C_S and C_F are the cost of each unit of volume of concrete, steel, and the cost of the unit of area of moulding according to American Society of Civil Engineers [5] respectively. Their values are $C_C = 105\ \$/\ m^3, C_S = 7065\ \$/\ m^3, C_F = 92\ \$/\ m^2$.

In this research, the constraints of the optimization problem have been applied using the concept of penalty function [6]. Thus, the penalty functions are written as below:

$$\Phi = F(1 + P_{beam} + P_{column}) \quad (13)$$

$$P_{beam} = r_p \sum_{i=1}^{nb} ((\max\{0, g_1\})^2 + (\max\{0, g_2\})^2 + (\max\{0, g_3\})^2)_i \quad (14)$$

$$P_{column} = r_p \sum_{j=1}^{nc} ((\max\{0, g_4\})^2 + (\max\{0, g_5\})^2 + (\max\{0, g_6\})^2 + (\max\{0, g_7\})^2)_j \quad (15)$$

In these equations, r_p is the positive parameters of the penalty function, P_{column} and P_{beam} are the penalty functions of the column and beam members [7].

3. PARTICLE SWARM OPTIMIZATION ALGORITHM

Recently a group of optimization algorithms has been created based on the simulation of the social interaction of a group of live creatures for achieving food resources. Particle Swarm Optimization (PSO) algorithm [8, 9] which was introduced by Eberhart and Kennedy [2], is an algorithm of that group. The PSO algorithm has had a very strong performance in comparison to similar algorithms and it can easily work with continuous and discrete variables and integers. In comparison to similar optimization methods, the PSO algorithm is much more effective and needs less function call to obtain better or similar results compared to other algorithms. It involves a very simple concept, and paradigms can be implemented in multiple lines of computer code, which conveniently accommodates the constraints and variables of a specific problem [10]. The formulation of this algorithm is described in literature [11-13].

4. DESIGN OF REINFORCED CONCRETE FRAMES

4. 1. Geometry of Frames For the force-based optimal design, two 6-story and 9-story, 3-bay frames were considered. In designing of these frames, the created databases for beam and column sections have been used. To create an efficient and limited search space of beams and columns, Lee's method [6] for optimization has been used. The capacity of sections obtained based on the ultimate capacity of the section by coding in MATLAB [14]. The frames being studied are the 3-bay frame from the middle axes of the 6-story and 9-story building plan, as shown in Figure 6.

4. 2. Loading the Frames In the models being studied, the lateral static loads of earthquake in the form of horizontal point load applied on the nodes of each story and the gravity loads for the dead load assumed as DL=500 kg/m^2 and LL=200 kg/m^2 for the live load.

The earthquake force was calculated according to ASCE 7-16 Code. The seismic coefficient for the 6-story building has been determined as 0.125, and 0.118 for the 9-story building, and earthquake base shear calculated and distributed along the height based on the expressions of the Code [3]. The loading combinations applied according to ACI 318-14 [1] for the assessment of demands in all the models.

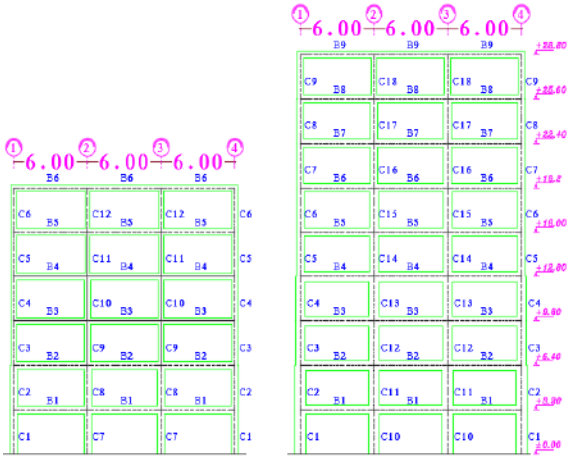

Figure 6. Typing of the selected frame for the 6-story and 9-story buildings (dimensions are in meters)

4. 3. Specifications of Materials The value of yield stress of the steel reinforcing bars and the compressive strength of the concrete in all the frames assumed as $f_c' = 280\ kg/cm^2, f_y = 4200\ kg/cm^2$.

5. ROBUSTNESS ASSESSMENT OF DESIGNS

In the real-world engineering, some uncertainties are considered during the design process. Considering the natural properties of the problem, the uncertainties would always exist, and depending on the source, the uncertainty can be reduced but cannot be avoided [15]. Uncertainty is not considered in definitive optimization. On the other hand, in the Robust Design Optimization (RDO), an additional objective function related to the random nature of problem parameters in the demand and capacity is considered. Therefore, for the optional structures in RDO, when the structural specifications or the seismic loading are considered as random variables, the aim is to minimize the initial cost and variation of the responses. A complete study of the available research papers about robust design optimization can be found in literature [16]. The RDO problem is stated as a multi- objective optimization problem as per the following description:

$$\begin{aligned} &\min_{s \in f} \quad [C_{in}(\boldsymbol{s}), COV_{EDP}(\boldsymbol{s}, \boldsymbol{x})] \\ &subject\ to: g_i(\boldsymbol{s}, \boldsymbol{x}) \geq 0\ i = 1, \dots, l \\ &s_j \in D^{n_d}\ j = 1, \dots, m \end{aligned} \tag{16}$$

where s and x represent the design and the random variables vectors, respectively. The objective functions considered are the initial construction cost, C_{in}, and the coefficient of variation of an EDP, COVEDP. The

conceptual difference between a DBO and an RDO optimisation problem, is explained schematically in Figure 7 [17].

5. 1. Assessment of the Design Fundamentals Affecting the Structure Robustness The input optimization database is reformed based on the variations of requirements in codes for different ranges of ρ of the columns (1%≤ρ<1.5%, 1.5%≤ρ<2%, 2%≤ρ<2.5% & 2.5%≤ρ≤3%) and beams (ρ_{min}<ρ≤1%, 1%<ρ≤ρ_{max}) and the best answers (optimized structures) obtained for each of these databases using the optimization algorithm. Figure 8 shows the created database for the 6-story structure with the values of ρ of columns.

5. 2. Selection of Answer Set It consists of N points from the end of the optimization convergence chart according to the initial costs, in which the points are the answers resulting from the optimization of a structure sorted by descending values of the objective function.

It is obvious that the required number of points must be selected according to the value of the acceptable error in the calculation of the standard deviation and mean, using the expressions in the statistical discussions. In this study, the Cochran formula has been used to determine sample size. This equation is as follows [18]:

$$n = ((z^2\, pq)/d^2) \,/\, ((1 + 1/N\,((z^2\, pq)/d^2 - 1))) \quad (17)$$

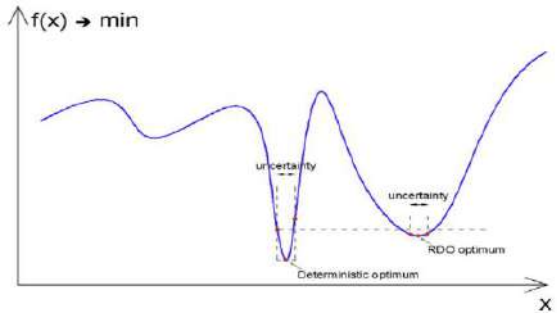

Figure 7. The concept of robust design optimisation [16]

In the equation above, n is the sample size, N, the statistical population size, z, the normal variable of the standard unit, which is equal to 1.96 at the confidence level of 95%. p is the proportion of the population that has the attribute in question and if not available, it will be considered 0.5. q is the proportion of the population that does not have the attribute in question and equals (1-p). d is the acceptable margin of error, which is usually considered 0.01 or 0.05 [18].

Based on the mentioned equation, the number of structures to be studied for the robustness is about 40, and to increase the accuracy of the results in this study, the tolerance of the objective function was limited to 5%. In each range, the most economic structures within this limit were selected and their number is larger than 40 structures. A sample of the created database is shown below.

5. 3. Non-Linear Time-History Analysis To investigate the effect of the variations in design parameters on the robustness of the structures, using the 12 accelerogram records of the surrounding area, nonlinear analysis of time history was performed for each of the selected statistical populations in section 5.2. The schematic chart of scaling the accelerograms is shown in Figure 9. These accelerograms were randomly extracted from the PEER databank and according to the method recommended in ASCE/SEI 7-16, each one was scaled to a 2% probability of exceedance in 50 years [19].

The expected yield stress of steel and strength of concrete was used in the non-linear time-history analyses according to ASCE/SEI 41-13 Code [20]; therefore, the expected yield stress of steel and strength of concrete is determined as f_y=5250 kg/cm^2, f_c'=420 kg/cm^2. Thus, the expected strength of unconfined concrete was fc'=420 kg/cm^2, the corresponding strain, 0.002, the ultimate strength, 224.0 kg/cm^2, and its corresponding strain, 0.004. The pattern suggested by Mander et al. [21] has been used in this study to define the non-linear stress-strain curve of the concrete materials in the compressive zone and in the confined

Structure #	Beams						Columns												Cost $
	B1	B2	B3	B4	B5	B6	C1	C2	C3	C4	C5	C6	C7	C8	C9	C10	C11	C12	
1	5540051018	5540051018	5540040720	5040040818	5040030620	5035020422	601222	551220	501020	501020	501020	451020	601420	551220	501020	501020	501020	451020	37884
2	5540061018	5540051018	5540051018	5040030622	5040030620	5035020422	601222	551220	501020	501020	501020	451020	601420	551220	501020	501020	501020	451020	37979
3	5540061118	5540051018	5540051018	5040030622	5040030620	5035020422	601222	551220	501020	501020	501020	451020	601420	551220	501020	501020	501020	451020	38041
4	5540071118	5540051018	5540051018	5040030622	5040030620	5035020422	601222	551220	501020	501020	501020	451020	601420	551220	501020	501020	501020	451020	38073
5	5540061118	5540061118	5540051018	5040030622	5040030620	5035020422	601222	551220	501020	501020	501020	451020	601420	551220	501020	501020	501020	451020	38106
6	5540071118	5540061118	5540051018	5040030622	5040030620	5035020422	601222	551220	501020	501020	501020	451020	601420	551220	501020	501020	501020	451020	38138
7	5540071118	5540071118	5540051018	5040030622	5040030620	5035020422	601222	551220	501020	501020	501020	451020	601420	551220	501020	501020	501020	451020	38170
8	5545051018	5545051018	5540050918	5040040818	5040030620	4540030620	601420	551420	551220	501020	501020	451020	601420	551420	551220	501020	501020	451020	38531
9	5545051018	5545051018	5540050918	5040050818	5040030620	4540030620	601420	551420	551220	501020	501020	451020	601420	551420	551220	501020	501020	451020	38588
10	5545051018	5545051018	5540050918	5040050918	5040030620	4540030620	601420	551420	551220	501020	501020	451020	601420	551420	551220	501020	501020	451020	38595

Figure 8. A part of the created database for the 6-story structure with the values of ρ of columns 2%≤ρ< 2.5%

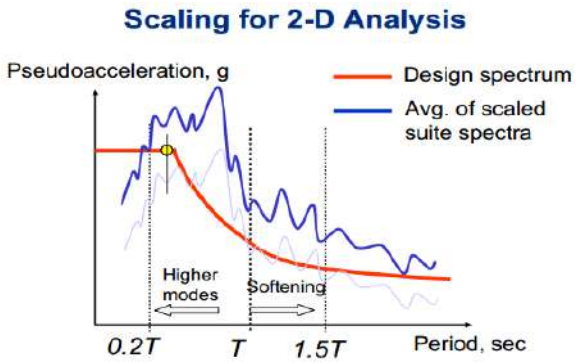

Figure 9. Schematic chart of scaling the accelerograms [22]

States [23-25], and it was computed by the program for each section of the columns, and then used in the non-linear time-history analyses [26].

5. 4. Selecting the Parameters for Sensitivity Analysis The parameters selected for sensitivity analysis consist of the story maximum plastic drift, and the maximum rotation of the plastic hinges in the beams and columns.

5. 5. Analysis of the Main Parameters Affecting the Structure Robustness Non-linear time-history analysis was conducted for the created databases of the structures, and the median of maximum values of parameters mentioned in the last section was extracted for each of the structural members based on the selected records. In order to obtain the dimensionless form of the data, these results were divided by their acceptance criteria values in the non-linear analyses according to ASCE/SEI 41-13 [20].

5. 6. Calculation of the Standard Deviation The standard deviation and mean was calculated for the median of maximum values of the selected parameters in each one of the statistical populations, and the chart for the average variations of the answers was drawn based on the input parameters variations together with the standard deviation of the outputs. The standard deviation equation is:

$$\sigma = \sqrt{\frac{1}{N}\sum_{i=1}^{N}(x_i - \mu)^2} \quad (18)$$

In which σ is the standard deviation, μ, mean of the data, N, number of the statistical population, and x is the data.

5. 7. Results from the Statistical Analyses of the Non-linear Time-history Analysis Output According to the discussions above, the output of non-linear time-history analysis is consisted of the maximum plastic inter-story drift, and maximum rotation of the plastic hinges in beams and columns of all stories. Here, at the first, the output of local data, i.e. maximum rotation ratio of plastic hinges in the beams and columns are presented according to the variations of the reinforcement ratio of columns. Next, the outputs related to the maximum rotation ratio of plastic hinges in the beams and columns according to the variations of the reinforcement ratio of beams are presented in Figure 10.

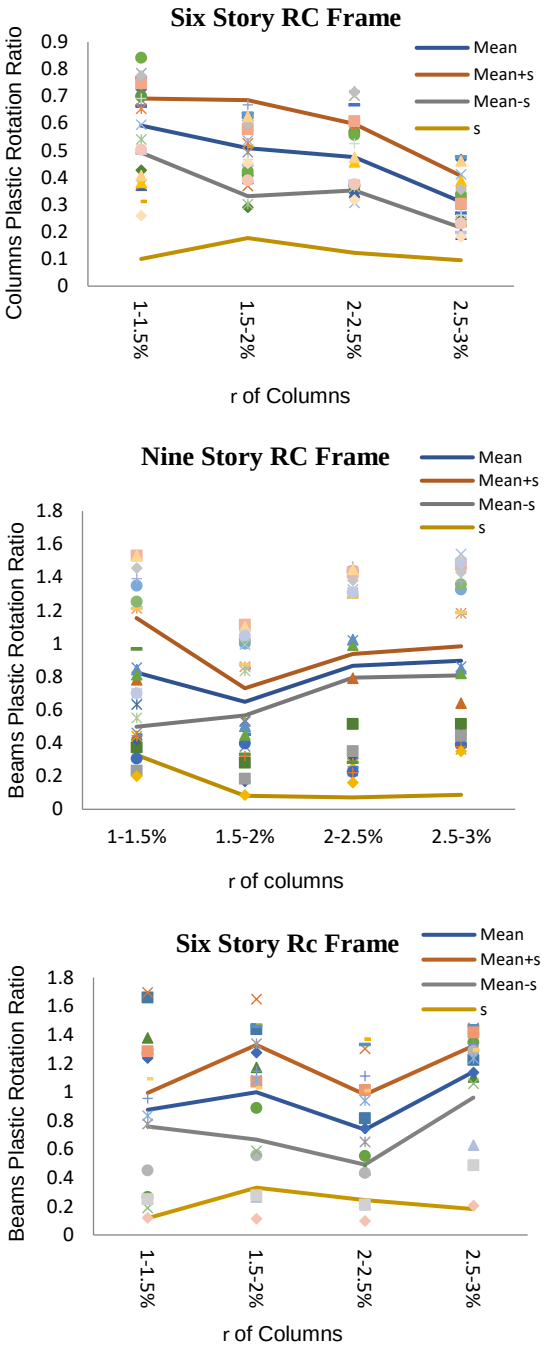

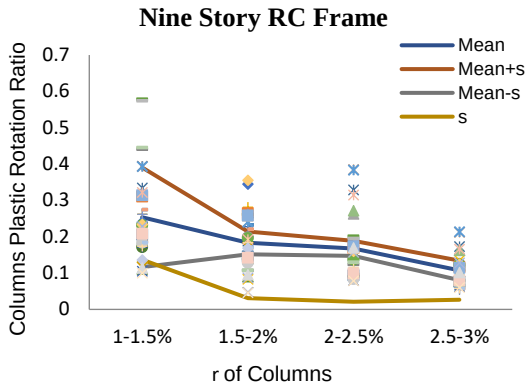

Figure 10. Charts of the average variations of the plastic hinges rotation ratio in beams and columns, and their variance according to the variations of the reinforcement ratio of columns in the 6-story & 9-story building

As understood from Figure 10, with an increase in the reinforcement ratio of the columns, the plastic hinges rotation in the columns decreases, and the plastic hinges rotation in the beams increases. This means that the failure mechanism moves towards the formation of the beam mechanism. In addition, the variance of plastic rotations also decreases with the increase in the reinforcement ratio of the columns. This results in an increase in the predictability of structural behaviour.

It can be seen in Figure 11 that with an increase in the reinforcement ratio of the beams, the plastic hinges rotation in the columns decreases, and the plastic hinges rotation in the beams increases. This shows that plastic hinges are first formed in beams. In addition, the variance of the plastic hinges rotations also decreases with an increase in the reinforcement ratio of the beams, and as a result, the predictability of structural behaviour increases.

As a global criterion in Figure 12, it can be seen that by increasing the ratio of steel in beams and columns, the behaviour of the structure improves.

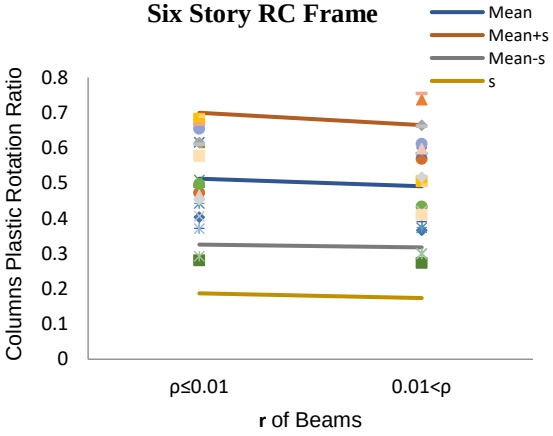

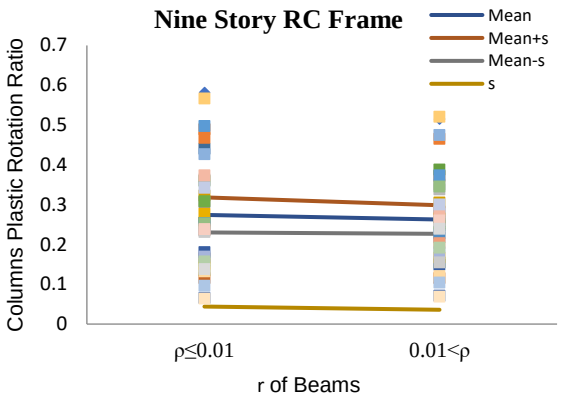

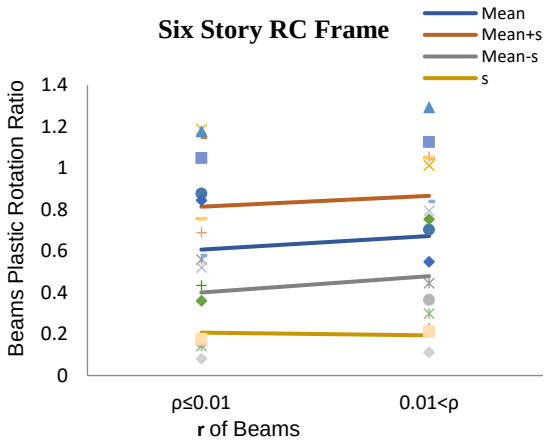

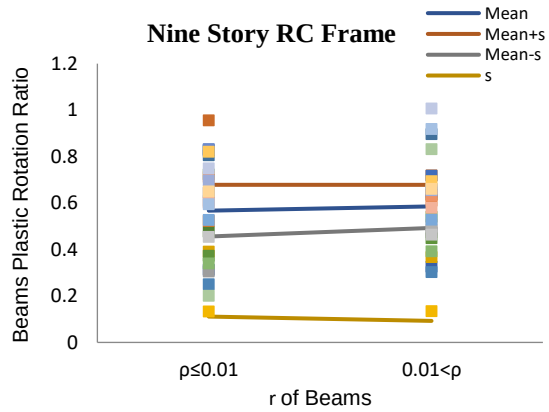

Figure 11. Charts of the average variations of the plastic hinges rotation ratio in beams and columns, and their variance according to the variations of the reinforcement ratio of beams in the 6-story & 9-story building

Therefore, with an increase in the ratio of reinforcing bars in the beams and columns, the probability of the formation and development of plastic hinges in the beams increases, while it decreases in the columns. As shown schematically in Figure 13.

The inter-stories drift of the structures resulted from non-linear time-history analysis, is presented above as a global criterion.

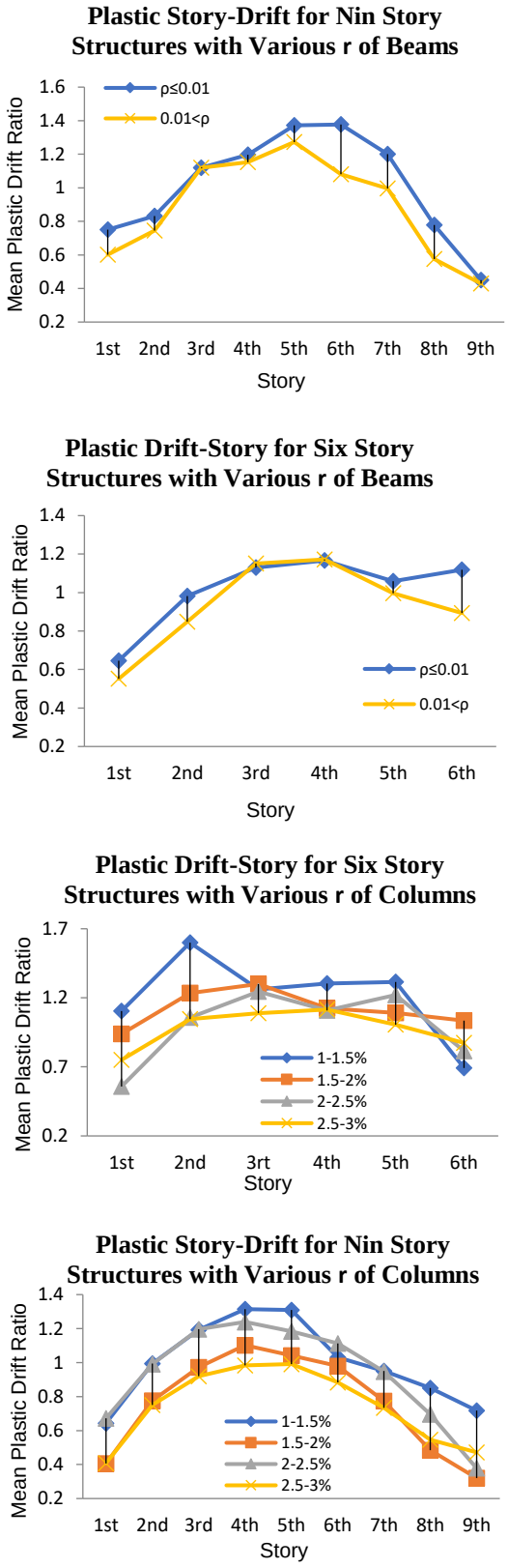

Figure 12. Chart of plastic drift ratio of the stories for the 6 & 9-story structures with various values of reinforcement ratio of beams & columns

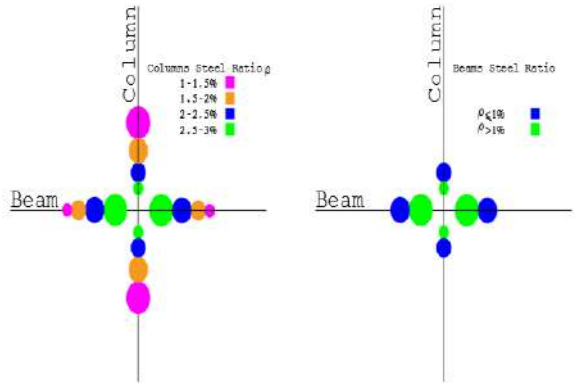

Figure 13. Variation of the probability of plastic hinges formation and development in the beams and columns, together with the variation of the reinforcement ratio in the beams and columns

6. CONCLUSION

The probability of failure can be significantly reduced for the structures which have adequate robustness. In fact, performance assessment of the designed structures by the practicing engineers under probable earthquakes has complicated steps to limit the possible damages.

In this study, an attempt is done to propose a methodology to design robust RC frames, which results in improving seismic performance of these structures. To do so, certain ranges are selected for the design parameters and several structures are designed using optimization algorithms within these ranges, and structural response evaluated by nonlinear time-history analysis are statistically analysed to assess the robustness of the optimal designs.

An increase in the probability of hinge formation in the beams leads to the increment of the probability of formation of beam mechanism, and the decrease in the variance of results also shows the increasing in the predictability of structural behaviour, both of which would lead to increased robustness of the structure.

According to the results of local and global criteria, it can be concluded that structural engineers, without engaging in complex calculations, can obtain structures with higher robustness by using sections sticking to the high steel ratio limits.

7. REFERENCES

1. Code, A., "Building code requirements for structural concrete, American Concrete Institute. (2014).
2. Kennedy, J. and Eberhart, R., "Ieee, particle swarm optimization", in 1995 Ieee International Conference on Neural Networks Proceedings, Vols 1-61995. (1948).
3. Kuntz, G.L. and Browning, J., "Reduction of column yielding during earthquakes for reinforced concrete frames, American Concrete Institute. (2003).

4. Maffei, J., Bonelli, P., Kelly, D., Lehman, D.E., Lowes, L., Moehle, J., Telleen, K., Wallace, J. and Willford, M., "Recommendations for seismic design of reinforced concrete wall buildings based on studies of the 2010 maule, chile earthquake", (2014).
5. Engineers, A.S.o.C., "Minimum design loads and associated criteria for buildings and other structures, American Society of Civil Engineers. (2017).
6. Lee, C. and Ahn, J., "Flexural design of reinforced concrete frames by genetic algorithm", ***Journal of Structural Engineering***, Vol. 129, No. 6, (2003), 762-774, doi: 10.1061/(ASCE)0733-9445(2003)129:6(762).
7. Vanderplaats, G.N., "Numerical optimization techniques for engineering design: With applications, McGraw-Hill New York, Vol. 1, (1984).
8. Eberhart, R. and Kennedy, J., "A new optimizer using particle swarm theory", in MHS'95. Proceedings of the Sixth International Symposium on Micro Machine and Human Science, Ieee. (1995), 39-43.
9. Kennedy, J. and Eberhart, R., "Particle swarm optimization", in Proceedings of ICNN'95-international conference on neural networks, IEEE. Vol. 4, (1995), 1942-1948.
10. Perez, R.l. and Behdinan, K., "Particle swarm approach for structural design optimization", ***Computers & Structures***, Vol. 85, No. 19-20, (2007), 1579-1588, doi: 10.1016/j.compstruc.2006.10.013.
11. Shi, Y. and Eberhart, R., "A modified particle swarm optimizer", in 1998 IEEE international conference on evolutionary computation proceedings. IEEE world congress on computational intelligence (Cat. No. 98TH8360), IEEE. (1998), 69-73.
12. Li, L.-J., Huang, Z., Liu, F. and Wu, Q., "A heuristic particle swarm optimizer for optimization of pin connected structures", ***Computers & Structures***, Vol. 85, No. 7-8, (2007), 340-349, doi: 10.1016/j.compstruc.2006.11.020.
13. Fourie, P. and Groenwold, A.A., "The particle swarm optimization algorithm in size and shape optimization", ***Structural and Multidisciplinary Optimization***, Vol. 23, No. 4, (2002), 259-267, doi: 10.1007/s00158-002-0188-0.
14. Gheyratmand, C., Gholizadeh, S. and Vababzadeh, B., "Optimization of rc frames by an improved artificial bee colony algorithm", ***Iran University of Science & Technology***, Vol. 5, No. 2, (2015), 189-203, doi.
15. Fadaee, M. and Grierson, D., "Design optimization of 3d reinforced concrete structures", ***Structural Optimization***, Vol. 12, No. 2, (1996), 127-134, doi.
16. Park, G.-J., Lee, T.-H., Lee, K.H. and Hwang, K.-H., "Robust design: An overview", ***AIAA Journal***, Vol. 44, No. 1, (2006), 181-191, doi: 10.2514/1.13639.
17. Fragiadakis, M. and Lagaros, N.D., "An overview to structural seismic design optimisation frameworks", ***Computers & Structures***, Vol. 89, No. 11-12, (2011), 1155-1165, doi: 10.1016/j.compstruc.2010.10.021.
18. Cochran, W.G., "Sampling techniques. 2nd edn john wiley & sons", New York, NY, (1963).
19. Moehle, J.P., Hooper, J.D. and Lubke, C.D., "Seismic design of reinforced concrete special moment frames", US Department of Commerce, (2008).
20. Pekelnicky, R., Engineers, S., Chris Poland, S. and Engineers, N., "Asce 41-13: Seismic evaluation and retrofit rehabilitation of existing buildings", Proceedings of the SEAOC, (2012).
21. Mander, J., Priestley, M. and Park, R., "Observed stress-strain behavior of confined concrete", ***Journal of Structural Engineering***, Vol. 114, No. 8, (1988), 1827-1849.
22. Menasri, Y., Nouaouria, M. and Brahimi, M., "Probabilistic approach to the seismic vulnerability of rc frame structures by the development of analytical fragility curves", ***International Journal of Engineering***, Vol. 30, No. 7, (2017), 945-954, doi: 10.5829/ije.2017.30.07a.03.
23. Council, A.T. and Agency, U.S.F.E.M., "Quantification of building seismic performance factors, US Department of Homeland Security, FEMA, (2009).
24. Goodwin, M.K., *Federal emergency management agency: An organization prepared*. 2008, Army Command And General Staff Coll Fort Leavenworth Ks.
25. Mander, J.B., Priestley, M.J. and Park, R., "Theoretical stress-strain model for confined concrete", ***Journal of Structural Engineering***, Vol. 114, No. 8, (1988), 1804-1826, doi.
26. Heidari, M., Behnamfar, F. and Zibasokhan, H., "A macro-model for nonlinear analysis of 3d reinforced concrete shear walls", ***International Journal of Engineering***, ***Transactions B: Applications,*** Vol. 31, No. 2, (2018), 220-227, doi: 10.5829/ije.2018.31.02b.05.

Persian Abstract

چکیده

قابهای خمشی بتن‌آرمه (RCMRF) از سیستمهای سازه‌ای هستند که کاربرد گسترده‌ای دارند. اصولاً ساختمان‌های با سیستم RCMRF به نحوی طراحی می‌شوند که نیازهای تغییر مکان نسبی، مقاومت و انعطاف پذیری، تعیین شده در آئین نامه‌های طراحی، را برآورده نمایند. در روند طراحی این سیستمها محدوده‌هایی برای پارامترهای طراحی در آئین نامه‌ها ارایه شده‌اند که مهندسین براساس آنها سازه‌ها را طراحی می‌کنند و مقادیر انتخابی برای این پارامترها بر روی رفتار لرزه ای سازه ها مؤثر است. ولی بررسی عملکرد سازه‌های طراحی شده توسط مهندسین، تحت زلزله‌های محتمل به منظور محدود نمودن خسارات احتمالی و کاهش ضعفهای موضعی و افزایش تحمل سازه در برابر زلزله دارای مراحلی بس دشوار و پیچیده است که طی این مراحل برای طراحی ساختمانهای معمولی زمان‌بر است. در این تحقیق محدوده‌هایی تنگ‌تر برای پارامترهای طراحی تعیین شده که در صورت رعایت این محدوده‌ها در زمان طراحی، مهندسین به طرحهایی دست خواهند یافت که عملکرد لرزه ای آنها بهتر باشد. در این راستا برای دامنه های مختلف پارامترهای طراحی، پایگاههای داده ای برای RCMRF ها ایجاد شد. در ایجاد این پایگاه داده ها از الگوریتم بهینه‌سازی دسته ذرات (PSO) استفاده شد و RCMRF ها بر اساس آئین نامه ACI318-14 بصورت بهینه طراحی شدند سپس سازه‌های بهینه طراحی شده براساس آئین نامه ASCE/SEI 7-16 تحت تحلیل غیر خطی تاریخچه–زمانی قرار گرفتند و تحلیلهای آماری برورودی نتایج محلی و کلی جامع حاصله از تحلیل غیر خطی انجام یافت. و نهایتاً براساس نتایج این تحلیلهای آماری، محدوده های تنگتری به منظور دستیابی به سازه های با استواری بالاتر بدون درگیر شدن در فرآیندهای زمان بر تعیین گردید.

International Journal of Engineering

Journal Homepage: www.ije.ir

Evaluating the Effect of Buckling-restrained Braces in Steel Buildings against Progressive Failure Using Different Simulation Strategies

B. Pordel Maragheh[a], A. Jalali*[a,b], S. Mohammad Mirhosseini[a]

[a] *Department of Civil Engineering, Arak Branch, Islamic Azad University, Arak, Iran*
[b] *Department of Civil Engineering, Faculty of Engineering, University of Kyrenia, Girne, Mersin 10, Turkey*

PAPER INFO

Paper history:
Received 18 April 2021
Received in revised form 06 July 2021
Accepted 06 July 2021

Keywords:
Alternative Load Path Method
Buckling-restrained Brace
Finite Element Method
Progressive Failure

ABSTRACT

Ignoring the primary damage to structural components due to blast load or fire is the alternate load path (APM) method's weakness in progressive failure analysis. The new technique used in this study examines the structure's more realistic responses by considering the initial cause of the failure. Also, buckling-restrained braces (BRBs) are applied to diminish the potential for progressive failure in braced steel buildings. Variables include the type of primary local loading (APM, blast loading, and heat caused by fire), the position of column removal in the plan (inner and outer frame), the type of brace (BRB and CB), and the number of stories (3, 5, and 8 stories). The buildings were simulated using ABAQUS. The results showed that BRBs in steel buildings under blast load, compared to conventional braces, reduce the potential of progressive failure. The use of BRBs provides much more energy absorption than conventional bracing systems due to brace buckling prevention.

***doi**: 10.5829/IJE.2021.34.10a.06*

1. INTRODUCTION

The utilization of buckling-restrained braces (BRBs) in braced steel building and its effect on improving structure behavior against progressive failure is the most important aim of this study.

Extensive studies have been conducted on progressive failure [1-6] and BRBs [7-10]. Each of them examines a part of this event. Palmer et al. [11] examined braced steel frames' performance and built two double story frames with a span in two different modes (with conventional braces (CBs) and BRBs). The results showed that BRBs compared to CBs showed more stable response against lateral loading. Akbarnia et al. [12] examined the effect of column removal on a three-story steel building equipped with BRBs and compared its performance with a three-story building with a flexural frame. The results showed that BRBs elements make steel structures well perform against external loadings such as earthquakes [12].

Yang et al. [13] investigated the role of composite slabs against progressive failure. They showed that the ratio of the dimensions of the composite slab is effective on the bending frame behavior. Mashhadi and Saffari [14] investigated the effect of members' secondary stiffness ratio on dynamic load coefficient in the nonlinear analysis of structures under column removal. They showed that the span length and number of floors in short and medium steel moment-resisting frames significantly affect the dynamic load coefficient.

Tavakoli and Hasani [15] investigated the effect of seismic parameter characteristics on the progressive failure potential in steel moment-resisting frames. The analysis results showed the dynamic response of the removed member under the seismic load is entirely dependent on the seismic characteristics such as the energy applied to the structure, the maximum ground acceleration, and the frequency content. Lin et al. [16] presented a new method for evaluating steel moment-resisting frames against blast loads. This method was compared with other common methods. They proved

* Corresponding Author E-mail: Abdolorahim_jalali_m@yahoo.com (A. Jalali)

Please cite this article as: B. Pordel Maragheh, A. Jalali, S. Mohammad Mirhosseini, Evaluating the Effect of Buckling-restrained Braces in Steel Buildings against Progressive Failure Using Different Simulation Strategies, International Journal of Engineering, Transactions A: Basics, Vol. 34, No. 10, (2021) 2248-2258

that the onset of damage in the first floors has a more practical effect on the failures' chain than the other floors. Naghavi and Tavakoli [17] investigated the effect of columns' response to progressive failure. For this purpose, a neural network method was used, and sensitivity analysis was performed. The results of this analysis can be used to estimate the response of steel structures to progressive failure. Ryu et al. [18] conducted finite element modeling for the progressive failure analysis of steel stiffened-plate structures in fires. They showed that fire consequences should be quantified accurately for the quantitative fire risk assessment. Zhou et al. [19] compared design methods for beam string structure based on reliability and progressive collapse analysis. The results showed that the representative beam string structure designed with fixed load partial factors and optimum resistance factor, which varies with cases, had high performance of anti-progressive collapse. Zheng et al. [20] studied the progressive collapse mechanism in braced and tied-back retaining systems under deep excavations. They showed that the progressive failure path extends from struts or anchors to piles and will lead to large-scale collapse. Musavi and Sheidaii [21] compared the seismic and gravity progressive collapse in dual systems with special steel moment-resisting frames and braces. The results showed that structures had better performance under seismic progressive failure than models under gravity loads because of more resistance, ductility, suitable load redistribution, and more structural elements in load redistribution.

In general, the studies mentioned above can be divided into three general categories. In the first group, researchers assessed the progressive failure of steel buildings with different load-bearing systems using the column removal method (alternate load path method or APM). In the second category, the method and type of analysis were evaluated. In the third category, new strategies for strengthening steel buildings against progressive failure were assessed. According to the above general classification in the present study, the type of progressive failure analysis method and the performance of buckling-restrained braces (BRBs) in reducing the progressive failure potential were evaluated. Three different methods were used to analyze the progressive failure. In the first method, APM, which is a common method, was used. In the second method, the progressive failure was evaluated by removing several columns and the heat caused by the fire. In the third method, progressive failure analysis was performed by direct simulation of blast waves. The overall purpose of presenting these three methods was that the primary cause of the progressive failure in the APM method is not very important. However, loads such as heat from fires and blast waves can create more critical states than the APM. On the other hand, BRBs, due to the combined performance of concrete and steel and buckling prevention, can help the load-bearing of columns in sudden and unusual loads. Therefore in this work, the performance of this type of braces against progressive failure was investigated.

2. PROCEDURE

Variables were the type of primary local loading (APM, blast loading, and heat caused by fire), the position of primary local failure in the plan (inner and outer frame), the type of brace (BRB and CB), and the number of stories (3, 5, and 8 stories). Table 1 presents the studied modes. Steel braced frame buildings with CBs and BRBs (3, 5, and 8-story) were first analyzed using Sap2000 [22] which is based on Iran national building regulations. The plan of the buildings was similar in all cases. The length of each span and the dimensions of the stairs were considered 6 and 4×6 meters. The building's lateral load resisting system was braced frame in both directions (CB and BRB). St37 building steel specifications were used to define steel. Box sections with a thickness of 10 mm were used to simulate the core and steel sheath of the BRBs. The compressive strength of concrete used in the BRBs was considered 24 MPa. Dead and live loads of the stories were 335 and 200 kg/m^2, respectively. Also, dead and live loads of the roof were 200 and 150 kg/m^2, respectively. ABAQUS [23] was used to simulate the buildings for progressive failure potential. Finally, the response of the structure to both blast and fire loadings was compared with the APM. Studies of progressive failure showed that removing columns at the lowest stories can create a more critical situation for the buildings [24-26]. Therefore, to evaluate the progressive failure in building frames, removing two columns in the lowest story was assessed. The results of the structural design were displayed in Table 2.

3. FINITE ELEMENTS SIMULATION

Finite element simulation was performed with ABAQUS software [23]. Structural elements include beam, column, brace, and roof, which are three-dimensional and deformable types. Materials include steel and concrete (the concrete core of BRBs and roof). BRBs consist of steel sheath (outer wall), concrete core, and central core. Shell, solid, and beam elements were used to simulate the box-shaped steel sheath, concrete core, and central core, respectively.

The explicit dynamic method in numerical solution was used for the analysis. Tie interaction constraint was utilized to define the interaction between members in all cases. The convergence examination method of the

TABLE 1. Introducing the modes in the present study

No.	Number of stories	Initial local loading type	Brace type	Frame	Name
1	3	No Remove	CB	----	3st-No R-CBr
2		Blast		Inner	3st-B-I-CBr
3				Outer	3st-B-O-CBr
4		Fire		Inner	3st-F-I-CBr
5				Outer	3st-F-O-CBr
6		APM		Inner	3st-APM-I-CBr
7				Outer	3st-APM-O-CBr
8		No Remove	BRB	----	3st-No R-BRB
9		Blast		Inner	3st-B-I-BRB
10				Outer	3st-B-O-BRB
11		Fire		Inner	3st-F-I-BRB
12				Outer	3st-F-O-BRB
13		APM		Inner	3st-APM-I-BRB
14				Outer	3st-APM-O-BRB
15	5	No Remove	CB	----	5st-No R-CBr
16		Blast		Inner	5st-B-I-CBr
17				Outer	5st-B-O-CBr
18		Fire		Inner	5st-F-I-CBr
19				Outer	5st-F-O-CBr
20		APM		Inner	5st-APM-I-CBr
21				Outer	5st-APM-O-CBr
22		No Remove	BRB	----	5st-No R-BRB
23		Blast		Inner	5st-B-I-BRB
24				Outer	5st-B-O-BRB
25		Fire		Inner	5st-F-I-BRB
26				Outer	5st-F-O-BRB
27		APM		Inner	5st-APM-I-BRB
28				Outer	5st-APM-O-BRB
29	8	No Remove	CB	----	8st-No R-CBr
30		Blast		Inner	8st-B-I-CBr
31				Outer	8st-B-O-CBr
32		Fire		Inner	8st-F-I-CBr
33				Outer	8st-F-O-CBr
34		APM		Inner	8st-APM-I-CBr
35				Outer	8st-APM-O-CBr
36		No Remove	BRB	----	8st-No R-BRB
37		Blast		Inner	8st-B-I-BRB
38				Outer	8st-B-O-BRB
39		Fire		Inner	8st-F-I-BRB
40				Outer	8st-F-O-BRB
41		APM		Inner	8st-APM-I-BRB
42				Outer	8st-APM-O-BRB

TABLE 2. Design results

Building	Storey	Beam	Column	Brace
3st	First	2IPE 300	Box 350× 350× 20	Box 200× 200× 20
	Second	2IPE 300	Box 350× 350× 20	Box 200× 200× 20
	Third	2IPE 270	Box 350× 350× 20	Box 200× 200× 20
	Fourth	2IPE 270	Box 350× 350× 20	Box 200× 200× 20
5st	First	2 IPE 300	Box 400× 400× 20	Box 200× 200× 20
	Second	2 IPE 300	Box 400× 400× 20	Box 200× 200× 20
	Third	2 IPE 270	Box 400× 400× 20	Box 200× 200× 20
	Fourth	2 IPE 270	Box 300× 300× 20	Box 200× 200× 20
	Fifth	2 IPE 270	Box 300× 300× 20	Box 150× 150× 20
	Sixth	2 IPE 270	Box 300× 300 × 20	Box 150× 150× 20
8st	First	2 IPE 300	Box 450× 450× 20	Box 200× 200× 20
	Second	2 IPE 300	Box 450× 450× 20	Box 200× 200× 20
	Third	2 IPE 300	Box 450× 450× 20	Box 200× 200× 20
	Fourth	2 IPE 300	Box 450× 450× 20	Box 150×150× 20
	Fifth	2 IPE 270	Box 450× 450× 20	Box 150× 150× 20
	Sixth	2 IPE 270	Box 350× 350× 20	Box 150× 150× 20
	Seventh	2 IPE 270	Box 350× 350× 20	Box 150× 150× 20
	Eighth	2 IPE 270	Box 350× 350× 20	Box 150× 150× 20
	Ninth	2 IPE 270	Box 350× 350× 20	Box 150× 150× 20

responses is used to specify the optimal mesh size in simulation. Also, concrete was simulated using concrete damage plasticity.

4. THE USED METHODS

Methods for investigating the progressive failure of the studied buildings include the APM, blast loading, and heat caused by fire, respectively. In this section, each of these methods is described.

4. 1. APM The general idea of APM is that the building should be designed so that if the normal load transfer paths are removed or damaged. There are other alternative paths for transferring the load to the ground. Therefore, structures are designed to remove columns or specific walls. The loads applied to the models under study are applied according to the Equations (1) and (2): [27]:

$$G_{LD} = \Omega_{LD}[(0.9 \text{ or } 1.2)\, D + (0.5L \text{ or } 0.2S)] \quad (1)$$

$$G = [(0.9 \text{ or } 1.2)\, D + (0.5L \text{ or } 0.2S)] \quad (2)$$

where, G_{LD} is increased gravity load for the upper floors of the column or removed wall, and G is gravity load for floors above a column or the wall, which is not

removed. This load combination must affect the span that is not loaded with a combination of G_{LD} load. In equations 1 and 2, D, L, and S are dead, live, and snow loads, respectively. Ω_{LD} is load increase coefficient for calculating deformation-controlled actions.

4. 2. Fire Load Application Method One of the issues that affect structures such as residential buildings, factories, offices, and industrial complexes is fire. This is especially important for steel structures because, in steel members, fire reduces strength and stiffness due to their high thermal conductivity and low thickness. After axial loading on the column, the fire was applied. Equation 3 was used to define fire heat. In this regard, T is the temperature change, and t is the duration of the fire. The mentioned equation is based on ISO834 [28, 29].

$$T = \text{Log}_{10}(8t + 1) + T_0 \quad (3)$$

4. 3. Blast Load Application Method CONWEP model [30] was used to apply blast loads. A possible blast can have different intensities. The blast loading intensity applied to the column will increase as the explosive increases and the distance from the blast center decreases. For this purpose, by defining the scaled distance (Z) of Equation (4), the overpressure produced by the blast (Ps), TNT material in kg (W) at R distance from the explosive center can be calculated from Equation (5).

$$Z = \frac{R}{W^{\frac{1}{3}}} \quad (4)$$

$$X = \text{Log}_{10}(Z) \quad (5)$$

$$\text{Log}_{10}(Z)[\text{Log}_{10}P_s] = -0.1319X^2 - 0.2331X + 0.4644 \quad (6)$$

The weight values of explosive (w), collision angle (α), and distance of the blast center ® were first determined. Then maximum pressure values and blast continuity time were determined for different modes. For this purpose, it was placed in the Friedlander blast load equation [31]:

$$P_{(t)} = P_{so}e^{-\frac{t}{t^*}}(1 - \frac{t}{t^*}) \quad (7)$$

In this Equation, P_{so} is the maximum pressure caused by the blast, $P_{(t)}$ is the pressure value in time t, and t* is the continuation time of the blast (when the pressure reaches to zero). To apply blast loads, an explosive weighing 500 kg TNT equivalent, for the external blast, is placed near the corner of the structure and at a distance of 5 meters from it, and in the case of internal blast, it is placed at a distance of 5 meters from the middle column.

5. VERIFICATION

5. 1. Verification of Progressive Failure Analysis Using APM The verification of progressive failure analysis with APM was performed using the method developed by Zhang et al. [32]. In the selected laboratory study, a one-story steel frame was constructed. This frame had one bay in one direction and two bays in the other direction. The beams and columns of the frame were made of H100×67×4.5×6 and H200×200×6×8, respectively. A 60 mm thick concrete slab was made on the beams. This slab was installed on the beams using shear studs. The length of the larger bay was 2.4 m, and the lengths of smaller bays were 1.8 m. According to Figure 1a, eight steel blocks with a total weight of 148 kN were placed in the middle of the span to simulate a gravitational load on the slab. One of the columns at the edge of the slab was suddenly removed using a knocking hammer, and its response was measured in the form of vertical displacement. More details about this experiment are provided in the literature [32]. The experimental frame, deformable shape, and displacement diagram of finite element and experimental specimen are shown in Figure 1. The experimental study's maximum displacement is about 10.7 mm. The maximum displacement in the finite element method is 10.9 mm. The difference between the two displacements is about 1.86 percent. Therefore, it can be stated that the hypotheses used to simulate the APM in the present study had good accuracy.

(a)

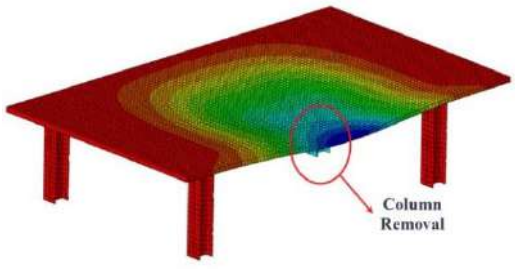

(b)

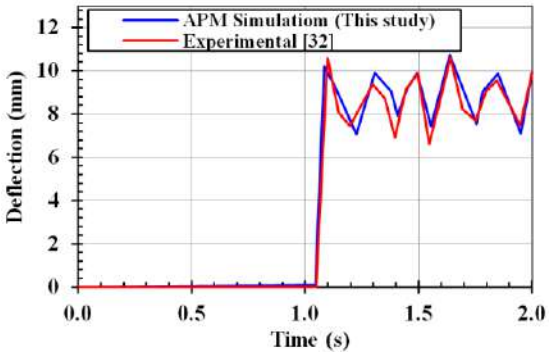

(c)

Figure 1. Verification of progressive failure analysis using APM a: Experimental specimen [32] b: FEM c: Comparison displacement diagrams

5. 2. The Verification of the Used Method in Simulation of Fire Loading The verification of the used method in simulation of fire loading was performed using method developed by Jiang et al. [33]. Three different frames were studied. The dimensions of the sections and the temperature applied to them were different in different modes.

The dimensions of hollow rectangular sections were 50×30×3 cm and 60×40×3.5 cm for columns and beams, respectively. The middle column of the first floor was warmed up using a furnace.

Figure 2 shows the plastic strain distribution, strength-time curves of the model, and the laboratory specimen. As can be seen, the highest and the lowest values of heat generated in the finite element modeling method in this study have a good precision compared to the experimental results. Therefore, this software has the appropriate and acceptable accuracy in modeling the heat load caused by fire.

5. 3. The Verification Used in Blast Load Simulation This validation, based on an experimental data reported by Lawver et al. [34], was performed by applying a blast load to a single column (Figure 3). Several steel columns were subjected to the blast load, and only the column with W360×122 specifications was selected for verification. Figure 3 shows the single column under blast load after analysis. Also, this figure compares the results of the study of Lawver et al. [34] and the simulated model. According to the obtained values, it is observed that the results are very close to each other. Therefore, the simulation method of the finite elements used to model the blast load has good accuracy.

6. INTERPRETING THE RESULTS

Although several studies on buildings' behavior against progressive failure are available, researchers still believe

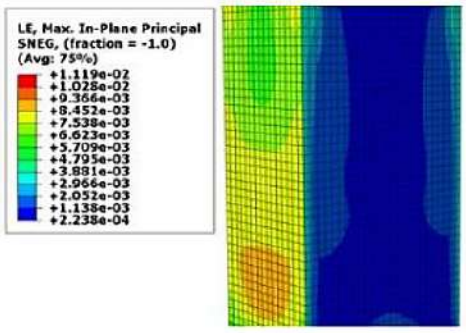

(a)

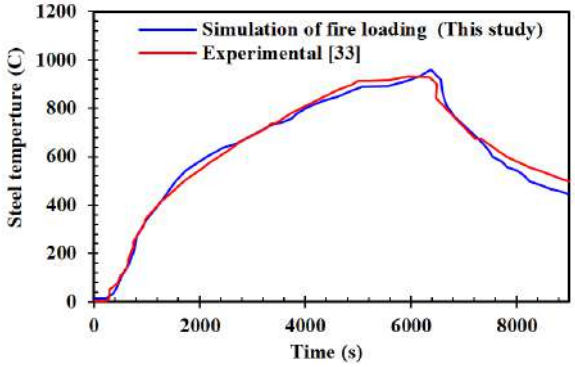

(b)

Figure 2. Verification used in progressive failure analysis using fire load application method a: Plastic strain b: Comparison of strength-time curves of finite element model and experimental specimen

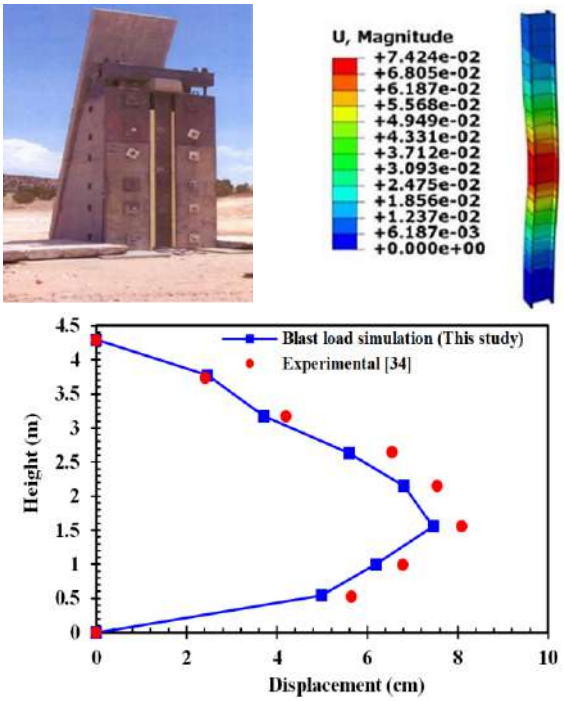

Figure 3. The verification used in the progressive failure analysis using the blast load application method a: Single column under blast load [34] b: Finite element model c: Comparison of column displacement (Numerical and Experimental)

that more research is needed to examine their behaviors against various parameters that may affect them. Experimental tests of these parameters' effect required considerable cost, time, and equipment, which in some cases is impossible or very difficult. Analytical models can be effective and have appropriate accuracy in predicting structural response. The simulation method introduced in the previous sections was used to perform sensitivity analysis of the desired variable parameters.

When various factors locally damage buildings, columns, as one of the most important members of the structure in preventing structural failure, have an important role in transferring and redistributing loads. Therefore, researchers' redistribution criterion of axial forces is one criterion that researchers have always considered in studies related to progressive failure [33-37].

The axial force changes of the columns of 3, 5, and 8-story simulated buildings will be examined. The values of the axial force changes of the columns around the local load application location (column removal location), compared to their values in the non-applied local load state according to the desired variables (BRB and ordinary brace), type of progressive failure analysis method (direct blast load application method, fire load application method and APM) and the position of the initial local load application (inner and outer frames) and the number of stories (3, 5 and 8 stories) have been calculated. The axial forces' values are the maximum axial force extracted from the diagrams related to the axial force of the columns. The resulting values are presented and analyzed separately in different graphs to understand better and compare the desired modes and examine the introduced variable parameters. After reviewing the maximum values of axial force in adjacent members to the local load application location, the effect of each of the studied parameters on the axial force changes of the columns is investigated in this section. Also, the deformable shape of several buildings under study is shown in Figure 4.

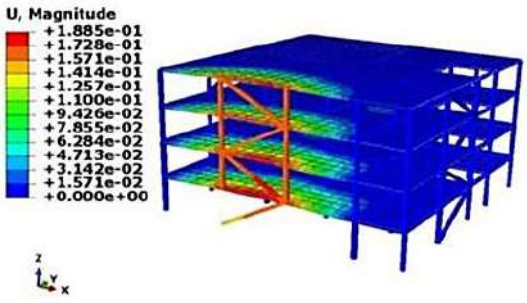

3st-APM-O-CBr

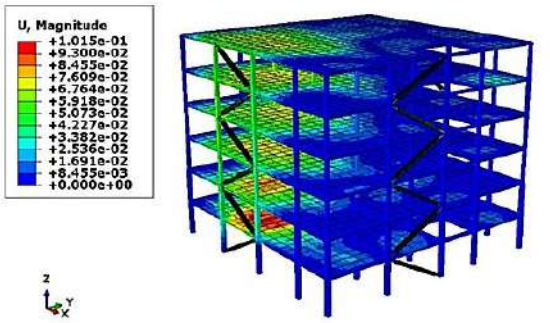

3st-B-I- BRB

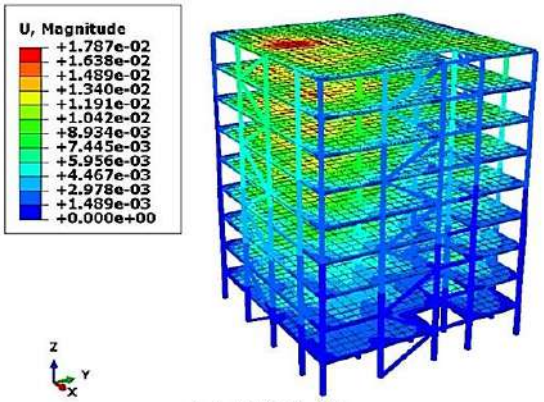

8st-APM-I-CBr

Figure 4. The deformable shape of several buildings under study

6. 1. Investigating the Type of Used Method

According to Figure 5**,** when the direct blast load method is used, an increase in axial forces is much more significant than in the APM modes. For example, in 3, 5, and 8-story steel buildings braced by CBs where the local load is applied as a blast load (inner frame), the maximum axial force of the adjacent columns to the load location is 3.6, 2.3, and 1.7 times more than their corresponding values in the column removal method (APM) (Figure 5a). On the other hand, in 3, 5, and 8 story steel buildings braced by CBs, local load, and column removal were applied on the outer frame, the maximum axial force of the adjacent columns to the load application location. In contrast, the direct blast load application method was used is 1.01, 2.19, and 1.88, times more than their corresponding values in the column removal method (APM) (Figure 5b). Also, according to Figure 5c, in 3, 5, and 8-story steel buildings braced by BRBs that the local load and column removal are applied on the inner frame, the maximum axial force of the adjacent columns to load application location, while the direct blast load application method was used, is 200, 59 and 49% more than their corresponding values in the column removal method (APM).

According to Figure 5d, in 3, 5, and 8-story steel

buildings braced by BRBs that the local load and column removal are applied on the outer frame, the maximum axial force of the adjacent columns to load application location, while the direct blast load application method was used, is 200, 67, and 64% more than their corresponding values in the column removal method (APM). Therefore, it can be concluded that when explosive is considered as the initial cause of the failure in the progressive failure analysis, the maximum force created in the adjacent columns to the impact area will be significantly higher than other methods. Because of the sudden pressure caused by blast applied to the columns and the stresses that are applied to the beams, the axial force of columns in the blast load application method is more than the APM. The APM in evaluating the axial load of the column has smaller values.

Although in the APM, several columns of the structure are completely removed and lose their function, the loads caused by the blast were applied in an impacting manner and create a more critical state in the structure. Therefore, it can be stated that the primary cause of the local failure and considering it during structure analysis against progressive failure can have much more accurate predictions of the actual behavior of the structure against the initial local failure.

6. 2. Position of Column Removal In this section, the position of column removal in the plan (outer and inner frame) on the redistribution of axial forces is examined. The maximum axial force is presented in Figure 6. As it can be seen, in buildings with fewer stories, the columns in the inner frame are in a much more critical position and bear more forces after applying the initial local load. However, as the height increases, the columns in the outer frame bear more forces. Therefore, the position of removing columns in the plan can depend on the number of stories. Changes in the columns' axial force in situations where the blast load was applied from the outside indicate that the columns, walls, and infills around the structure can play an imperative part within the structure reaction against impact waves. If the walls or infills are connected to the columns, a large amount of the pressure caused by the blast will reach the surrounding columns, which will cause them to be exposed to severe damage. However, suppose a solution can be found to separate the structural columns from the walls. In that case, the load transfer through the rigid diaphragm to the roof will be transferred to other columns and structural members. More members will bear the blast wave and the structure strength increases, and the potential for progressive failure decreases.

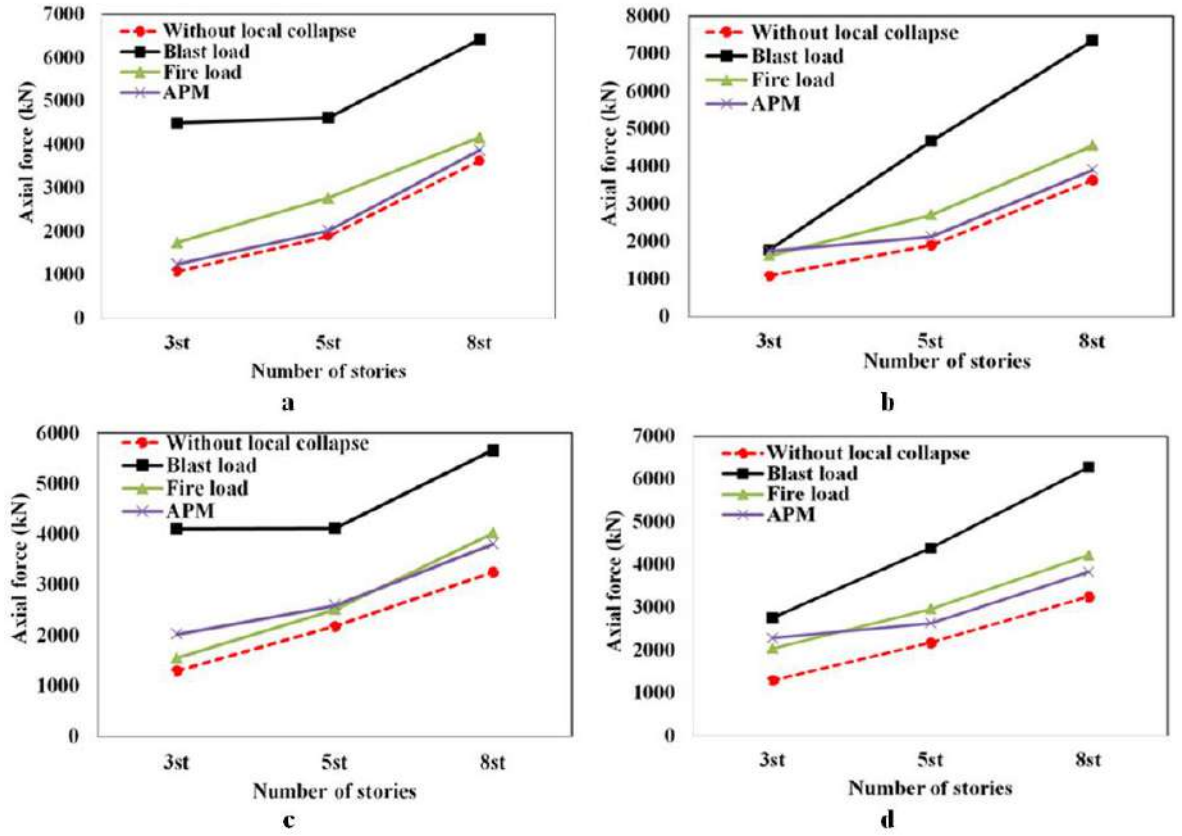

Figure 5. Comparison of methods used in progressive failure analysis a: Conventional brace - inner frame b: Conventional brace - outer frame c: BRB - inner framed: BRB - the outer frame

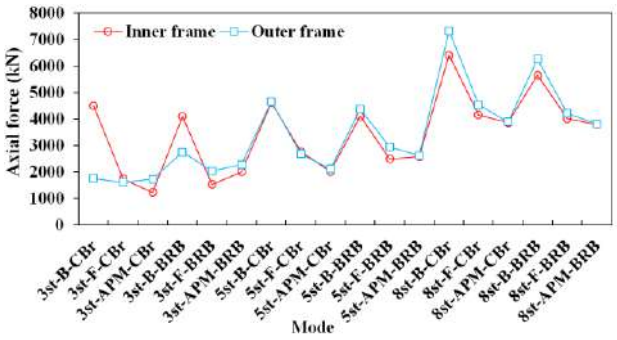

Figure 6. Examining the position of the column removal (outer and inner frame) in the stories on the changes of the maximum forces of the columns near to the initial local damage position

An interesting point that can be indicated in Figure 6 is that when the column is removed in the outer frame, the APM shows much more force is more conservative in this respect. The reason for this is that when the column is removed in the inner frame, more members of the structure participate in bearing additional loads and redistribution of forces. This creates fewer axial forces around the removal location. When the column is removed in the outer frame, fewer members contribute to the load distribution, creating more force in the columns around the removal location.

6. 3. Percentage of Changes in the Maximum Axial Forces Around the Local Failure Location

Figures 7a and 7b compare the percentage increase of the maximum axial forces around the local failure location to investigate the method used and the position of the position column removal in the stories. According to the desired variables, the values of the axial forces around the local failure location are calculated relative to their values in the non-removal mode. It should be noted that the axial forces' values are the maximum axial force when the blast load affects two columns of the inner frame and the elements around them. The columns' axial forces around the location of the local failure increased more than APM and fire loading methods. As shown in Figure 7b, explosion-induced loads on inner columns caused maximum axial forces around the local failure location to increase by 317% in the mode of blast load application. However, in the APM, removing the two columns in the inner frame caused maximum axial forces around the local failure location to increase by 15%. The analysis results showed that if explosives cause the primary local failure, considerable axial forces are created in the columns around the primary local failure location. These forces are not considered when APM is exerted. According to these results, the initial cause of failure should be considered. Because the force transfer by the residual structural members of the building under local failure can prevent the progressive failure, and if the initial failure is not predicted correctly, the structure response against the possible failures would not be appropriate. Therefore, it can be stated that the type of primary local failure is very influential, and ignoring it may activate to wrong divinations of building behavior. The heat application due to fire caused the axial forces created in the columns to be much higher than the APM.

6. 4. Investigating the Effect of BRBs

The performances of CBs and BRBs are compared in this section. Figures 8a and 8b compare the performance of CBs and BRBs on the structure response against progressive failure in modes affected by the blast load in the inner and outer frames. When the explosive was placed inside the structure, the BRBs showed much better performance in terms of axial force changes than CBs. The axial forces created in adjacent members to their blast location compared to the corresponding values in buildings with CBs are greatly reduced. This

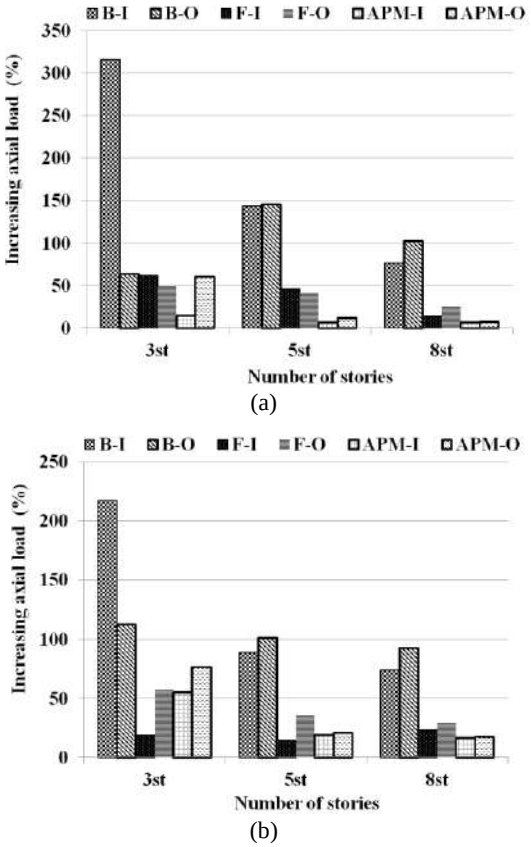

Figure 7. Increasing axial loads of the columns around the removal location compared to the non-removal mode a: buildings with CBs b: buildings with BRBs

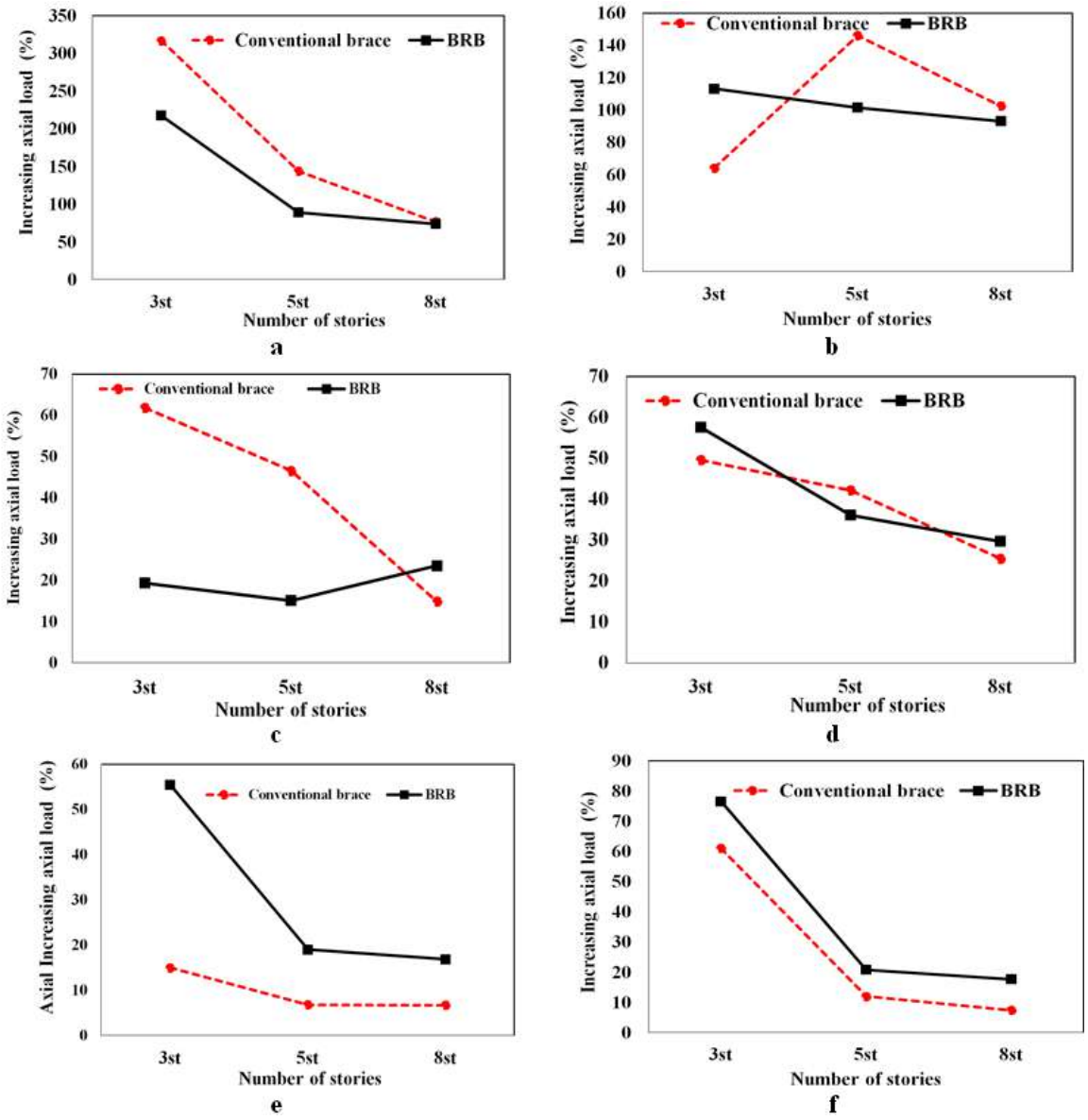

Figure 8. Comparison of the performance of CBs and BRBs on the structure response against progressive failure a: blast load-inner frame b: blast load-outer frame c: heat caused by fire-inner frame d: heat caused by fire-outer frame e: APM-inner frame f: APM-outer frame

is also true to some extent in buildings that were placed under an external blast. For example, the percentage increase in the axial force of a 5-story building braced with BRB is about 30 percent less than the corresponding value in buildings braced with CB.

The use of BRBs in steel buildings under blast load, compared to CBs, improves the structural performance and reduces the possibility of progressive failure. This is because CBs cannot buckle due to applied pressure and have similar behaviors in tension and pressure. However, BRBs can absorb higher energy by yielding brace in tension and pressure. Due to steel sheaths and the simultaneous effect of concrete and steel on tension and pressure, they have more energy loss capacity and more ductility than CBs. BRBs, with their compressive performance, can significantly contribute to bearing axial forces created by column removal to the adjacent columns of the blast location. Figures 8c to 8g show that the BRBs in some modes cause the difference between the axial force created in the removal and not removal methods to be reduced compared to CBs.

7. CONCLUSION

The results showed that APM is relatively easy without considering the loading type, but it is less accurate and unreliable for predicting progressive failure in the structures. The method that was used in this manuscript provides rather dependable prophecies of the failure caused by explosive and fire loads. The initial cause of the progressive failure and its application to the structure led to more realistic responses.

Also, due to the performance of BRBs in preventing the occurrence of buckling of the steel core (in order to allow the occurrence of compression yield phenomenon), absorbing more energy and covering the entire length of the steel core with concrete, it is expected that the potential for progressive failure in the structure is reduced.

8. REFERENCES

1. Aghakouchak, A. A., Garivani, S., Shahmari, A., and Heshmati, M. "Structural investigation of the collapse of the 16-story Plasco building due to fire." ***The Structural Design of Tall and Special Buildings***, Vol. 30, No. 1, (2021), e1815. DOI: org/10.1002/tal.1815.
2. Pordel Maragheh, B., Jalali, A., Mirhoseini Hezaveh, S. "Effect of Initial Local Failure Type on Steel Braced Frame Buildings against Progressive Collapse." ***International Journal of Engineering, Transactions A: Applications***, Vol. 33, No. 1, (2020), 34-46, DOI: 10.5829/ije.2020.33.01a.05
3. Bagheripourasil, M., Mohammadi, Y. (2015). "Comparison between Alternative Load Path Method and a Direct Applying Blast Loading Method in Assessment of the Progressive Collapse." ***Journal of Rehabilitation in Civil Engineering***, Vol. 3, No. 2, 1-15. doi: 10.22075/jrce.2015.367
4. Salimi, P., and Bondarabadi, H. R. "Progressive collapse in an eccentric braced frame through extended progressive collapse analysis algorithm." ***Asian Journal of Civil Engineering***, (2021), 1-8. DOI: org/10.1007/s42107-021-00358-z
5. Ryu, M. G., He, K., Lee, D. H., Park, S. I., Thomas, G., and Paik, J. K. "Finite element modeling for the progressive collapse analysis of steel stiffened-plate structures in fires." ***Thin-Walled Structures***, Vol. 159, (2021), 107262, DOI: org/10.1016/j.tws.2020.107262
6. Bagheripourasil, M., Mohammadi, Y., Gholizad, A. "Progressive collapse analysis methods due to blast loading in steel moment frames." ***Journal of Modeling in Engineering***, Vol. 15, No. 51, (2017), 51-65. DOI: 10.22075/jme.2017.2688
7. Mohammadi, Y., Bagheripourasil, M. (2021). "Investigation of steel buildings response equipped with buckling-restrained braces against progressive collapse." ***Journal of Structural and Construction Engineering***, Vol. 8, No. 2, (2021), DOI: 10.22065/jsce.2019.153064.1688
8. Ding, Y., and Zhao, C. "Cyclic tests for assembled X-shaped buckling restrained brace using two unconnected steel plate braces." ***Journal of Constructional Steel Research***, Vol. 182, (2021), 106680.
9. Mashhadiali, N., Saadati, S., Mohajerani, S. A. M., and Ebadi, P. " Hybrid braced frame with buckling-restrained and strong braces to mitigate soft story." ***Journal of Constructional Steel Research,*** Vol. 181, (2021), 106610, DOI: org/10.1016/j.jcsr.2021.106610
10. Hoveidae, N., and Radpour, S. "A novel all-steel buckling restrained brace for seismic drift mitigation of steel frames." ***Bulletin of Earthquake Engineering***, (2021), 1-31, DOI: org/10.1007/s10518-020-01038-0
11. Palmer, KD., Roeder, CW., Lehman, DE., Okazaki, T., and Shield, C., "Experimental performance of steel braced frames subjected to bidirectional loading." ***Journal of Structural Engineering***, Vol. 139, No. 8, (2012), 1274-1284. DOI: org/10.1061/(ASCE)ST.1943-541X.0000624.
12. Akbarinia, F., Adinehfar, Y., Davashi, H., Jalili, D., Bwiranvand, P., and Hosseini, M., "Investigating the effect of column removal on progressive collapse of building designed by buckling restrained braced and bending frames." ***Engineering Solid Mechanics***, Vol. 6, No. 1, (2018), 83-88. DOI: 10.5267/j.esm.2017.10.001.
13. Yang, B., Yang, Y., Zhou, X. H., Jiang, Q.F., and Kang, A. B.,"Component tests and numerical simulations of composite floor systems under progressive collaps." ***Journal of Constructional Steel Research***, Vol. 151, (2014), 25-40, DOI: org/10.1016/j.jcsr.2018.09.008.
14. Mashhadi, J., and Saffari, H. "Modification of dynamic increase factor to assess progressive collaps potential of structures." ***Journal of Constructional Steel Research***, Vol. 138, (2017), 72-78. DOI: org/10.1016/j.jcsr.2017.06.038.
15. Tavakoli, H., and Hasani, A., "Effect of Earthquake characteristics on seismic progressive collapse potential in steel moment resisting frame." ***Earthquackes and Structures***, Vol.12, No. 5, (2017), 529-541, DOI: org/10.12989/eas.2017.12.5.529.
16. Lin, S., Yang, B., Kang, S., and Xu, S., "A new method for progressive collapse analysis of steel frames." ***Journal of Constructional Steel Research***, Vol. 153, (2019), 71-84, DOI: org/10.1016/j.jcsr.2018.09.029.
17. Naghavi, F., and Tavakoli, H., "Probabilistic Prediction of Collapse in Columns of a Steel Structure Under Progressive Collapse Using Response Surface and Artificial Neural Network Methods." ***Iranian Journal of Science and Technology, Transactions of Civil Engineering***, (2021). DOI: org/10.1007/s40996-021-00593-z.
18. Ryu, M. G., He, K., Lee, D. H., Park, S. I., Thomas, G., & Paik, J. K. (2021). "Finite element modeling for the progressive collapse analysis of steel stiffened-plate structures in fires." ***Thin-Walled Structures***, Vol. 159, (2021), 107262. DOI: org/10.1016/j.tws.2020.107262.
19. Zhou, H., Jiang, Y., Adhikari, S., Yin, Q., & Cai, J. "Comparisons of design methods for beam string structure based on reliability and progressive collapse analysis." ***Structures***, Vol. 33, (2021), 2166-2176, DOI: org/10.1016/j.istruc.2021.05.085
20. Zheng, G., Lei, Y. W., Cheng, X. S., Li, X. Y., & Wang, R. Z. (2021). "Experimental study on progressive collapse mechanism in braced and tied-back retaining systems of deep excavations." ***Canadian Geotechnical Journal***, Vol. 58, No. 4, (2021), 540-564, DOI: org/10.1139/cgj-2019-0296.
21. Musavi-Z, M., Sheidaii, M. (2021). "Comparison of seismic and gravity progressive collapse in dual systems with special steel moment-resisting frames and braces." ***Journal of Civil and Environmental Engineering***, DOI: 10.22034/jcee.2021.38392.1914.
22. SAP 2000. Advanced structural analysis program. Version 12. Berkeley, CA, USA: ***Computers and Structures***, Inc. (CSI), (2009).
23. Abaqus theory manual. Version, Hibbitt. 2016. Pawtucket (RI): Karlsson and Sorensen, Inc.

24. Feng, F. "Response of a multi-storey steel composite building with concentric bracing under consecutive column removal scenarios." ***Journal of Constructional Steel Research***, Vol.70, (2012), 115126. DOI: org/10.1016/j.jcsr.2011.10.012.
25. Kaafi, P., & Ghodrati Amiri, G."Investigation of the progressive collapse potential in steel buildings with composite floor system." ***Journal of Structural Engineering and Geo-Techniques***, Vol. 10, No. 2, (2020), 1-8.
26. G. Amiri, G., Kaafi, P. "Investigation into the potential of progressive collapse in steel buildings with a composite roof." Sharif Journal of Civil Engineering, Vol. 32, No. 3.1, (2016), 87-96.
27. DOD. Design of Building to Resist Progressive collapse, Unified Facilities Criteria (UFC) 4-023-03, Department of Defense, Washigton, DC, (2013).
28. ISO-834 Fire resistance tests-elements—elements of building construction. International Standard ISO 834, Geneva, 1975.
29. Han, L., Yang, Y., Yang, H., Huo, J., "Residual strength of concrete-filled RHS columns after exposure to the IS0-834 standard fire." ***Thin-Walled Structures***, Vol. 40, No.12, 991-1012.
30. Kingery, C., and Bulmash, G., "Airblast parameters from TNT spherical air burst and hemispherical surface burst." US Army Armament and Development Center, Ballistic Research Experimental, (1984).
31. Catovic, A., "Review of the estimation methods for external blast loads on structures." ***Periodicals of Engineering and Natural Sciences (PEN)***, Vol. 9, No. 1, (2021), 104-126.
32. Zhang, J. Z., Li, G. Q., & Jiang, J. (2020). Dynamic effects on steel frames with concrete slabs under a sudden edge-column removal scenario. ***Journal of Structural Engineering***, Vol. 146, No. 9, (2020), 04020185, DOI: org/10.1061/(ASCE)ST.1943-541X.0002760
33. Jiang, B., Li, G. Q., Li, L., and Izzuddin, B. A. "Experimental studies on progressive collapse resistance of steel moment frames under localized furnace loading." ***Journal of Structural Engineering***, Vol. 144, No. 2, (2018), 04017190, DOI: org/10.1061/(ASCE)ST.1943-541X.0001947.
34. Lawver, D., Daddazio, R., Vaughan, D., Stanley, M., and Levine, H. "Response of AISC steel column sections to blast loading." In ASME 2003 Pressure Vessels and Piping Conference, American Society of Mechanical Engineers, (2003), 139-148.
35. Rahai, A., Asghshahr, M. S., Banazedeh, M., and Kazem, H. "Progressive collapse assessment of RC structures under instantaneous and gradual removal of columns." ***Advances in Structural Engineering***, Vol. 16, No. 10, (2013), 1671-1682, DOI: org/10.1260/1369-4332.16.10.1671.
36. Xie, F., Gu, B., and Qian, H. "Experimental study on the dynamic behavior of steel frames during progressive collapse." ***Journal of Constructional Steel Research***, Vol. 177, (2021), 106459, DOI: ORG/10.1016/j.jcsr.2020.106459.
37. Bagheripourasil, M., Mohammadi, Y., and Gholizad, A. "A proposed procedure for progressive collapse analysis of common steel building structures to blast loading." ***KSCE Journal of Civil Engineering***, Vol. 21, (2017), 2186-2194, DOI: org/10.1007/s12205-017-0559-0.

Persian Abstract

چکیده

ضعف روش مسیر بار جایگزین (APM) که یکی از روش‌های متداول تحلیل خرابی پیش رونده است، نادیده گرفتن خرابی اولیه یا آسیب اعضای سازه‌ای مجاور در اثر بار انفجار و یا آتش سوزی است. از این رو روش جدیدی که در این مطالعه مورد استفاده قرار گرفته است، با در نظر گرفتن عامل اولیه ایجاد خرابی پیش‌رونده و اعمال آنها به سازه، پاسخ های واقعی تری از سازه را مورد بررسی قرار می‌دهد. متغیرها شامل نوع بارگذاری موضعی اولیه (بدون در نظر گرفتن علت اولیه خرابی، بارگذاری انفجار و حرارت ناشی از آتش سوزی)، موقعیت حذف ستون در پلان (قاب بیرونی و داخلی)، نوع بادبند (معمولی و کمانش تاب) و تعداد طبقات (۳، ۵ و ۸ طبقه) می‌باشند. ساختمان‌ها با استفاده از ABAQUS به صورت سه بعدی شبیه سازی شدند. نتایج نشان داد که نوع بارگذاری اولیه نقش بسیار تاثیر گذاری بر پاسخ سازه دارد و عدم در نظر گرفتن خرابی اولیه می‌تواند منجر پیش‌بینی‌های نادرستی از پاسخ سازه شود. همچنین استفاده از مهاربندهای کمانش‌تاب در ساختمان‌های فولادی که تحت بار انفجار قرار گرفته‌اند، در مقایسه با مهاربندهای معمولی باعث بهبود عملکرد سازه می‌شود و احتمال وقوع خرابی پیشرونده را کاهش می‌دهد. دلیل این موضوع آن است که مهاربندهای معمولی قابلیت کمانش ناشی از فشار وارده را نداشته و دارای رفتار مشابه درکشش و فشار می‌باشند؛ این در حالیست که مهاربندهای کمانش تاب با تسلیم مهاربند درکشش و فشار توانایی جذب انرژی بالاتری دارند و به علت وجود غلاف فولادی و اثر همزمان بتن و فولاد درکشش و فشار ظرفیت اتلاف انرژی و شکل پذیری بیشتری نسبت به مهاربندهای معمولی دارند. در واقع مهاربندهای کمانش تاب با عملکرد فشاری خود می توانند در تحمل نیروهای محوری ایجاد شده ناشی از حذف ستون کمک قابل توجهی به ستون‌های مجاور محل انفجار داشته باشند.

IJE TRANSACTIONS A: Basics Vol. 34, No. 10, (October 2021) 2259-2265

International Journal of Engineering

Journal Homepage: www.ije.ir

Experimental and Finite Element Analysis of Single Stage Single Point Incremental Forming

D. Sureshkumar, N. Ethiraj*

Department of Mechanical Engineering, Dr.M.G.R Educational and Research Institute, Maduravoyal, Chennai, Tamilnadu, India

P A P E R I N F O

Paper history:
Received 10 May 2021
Received in revised form 12 June 2021
Accepted 18 July 2021

Keywords:
Finite Element Anlaysis
Single Stage Incremental Forming
Strain Measurement
Wall Angle

A B S T R A C T

Incremental forming is one of the non-traditional forming processes which is widely used in rapid prototyping and customized component manufacturing. One of the challenges encountered in single stage single point incremental forming (SSSPIF) is difficulty in achieving greater wall angle for a considerable depth. In this research work, the investigation is carried out by experimental and numerical simulation for reaching the maximum wall angle to a possible depth without any defects in SSSPIF. SSSPIF of truncated cone shaped component from 1mm thick AISI304 austenitic stainless steel are made at a different wall angles. Also, numerical simulation using LS-DYNA explicit solver is performed and the results are validated with the experimental values. Components with the wall angle of 64o is successfully made without any defects made in a single stage forming for a depth of 45 mm within the experimented process parameters. Major strain, minor strain and thickness distribution in the sheet material due to forming process are obtianed from experiments and finite element analysis (FEA). From the results of both experiment and FEA, it is observed that the major strain, minor strain and thinning effects are higher in the region below the major diameter of the truncated cone at all experimented wall angles. Also the FEA results have shown good agreement with the experimental values. Further it is seen that the strains are increasing with the increase of wall angle.

***doi**: 10.5829/ije.2021.34.10a.07*

1. INTRODUCTION

A newer non-conventional forming process known as incremental sheet metal forming is used recently for manufacturing customized components and medical implants. In this process, the desired shape and size of the part is imparted by rotating tool with hemispherical head, which moves in a specified generated path. Single point incremental forming (SPIF) is one of the types of incremental sheet forming (ISF) where single tool performs the operation by moving the tool in incremental step-down size. The required shape and size of the component may be obtained in a single stage or multi stage processes. Due to absence of die in this process, the initial investment is much lower when compared with the conventional forming process. AISI 304, an austenitic stainless steel, is very widely used material due to its strength, corrosion resistance and biocompatibility. Due to the characteristic of inactiveness with environment and non-toxic nature makes stainless steel a good candidature for food, chemical and medical industries.

In past, number of researchers have attempted to explore the incremental forming process due to the increase in need for customized components. The deformation mechanism was studied by Jackson and Allwood [1] in SPIF as well as in two point incremental forming (TPIF). It was presented from their study that the deformation is due to (i) shear and stretching in a plane perpendicular to the direction of tool movement and (ii) shear along the tool direction. Gupta and Jeswiet [2] have investigated the effect of tool-sheet interface temperature, which is generated due to the friction between them at high relative velocity of the tool, on formability and geometrical errors. They have suggested that, to certain extent, the higher rotational speed and feed rate of the tool are ideal process parameters for the

*Corresponding Author Institutional Email: ethiraj.mech@drmgrdu.ac.in (N. Ethiraj)

Please cite this article as: D. Sureshkumar, N. Ethiraj, Experimental and Finite Element Analysis of Single Stage Single Point Incremental Forming, International Journal of Engineering, Transactions A: Basics Vol. 34, No. 10, (2021) 2259-2265

better results. Wall angle of the formed component plays a crucial role in deciding the required forming force. The forming force increases with the increase of wall angle upto 60° and beyond which the force decreases due to the thinning effect of the formed part which may lead to a fracture [3]. The maximum wall angle that can be formed is depending on the type of material and its thickness. In case the part requires wall angle more than the maximum value, multi pass strategy is employed [4-6]. Safari [7] has experimented the two point incremental forming (TPIF) of 1mm thick AA3105 aluminium alloy sheet to form both internal and external cavities using different process parameters. It was concluded from his study that the component with 70° internal and internal cavity for the depth of 95 mm and 40 mm were fabricated by TPIF. Also, it was observed that the rotational speed of the tool and the pattern of forming influence greatly the formation of maximum height in external and internal surface cavitity [7]. Investigation on TPIF of the same complicate shaped component from the same material of 2 mm thickness was carried out by Safari and Joudaki [8]. It was concluded from their findings that the thinning of material was observed around 23.5 – 32.5% at different forming increment and moreover, the higher tool rotational speed and the pattern of forming reduced the thinning to 17.5% [8].

Also, to overcome the limitation in successful formation of the required wall angle, Duflou et. al. [9] have attempted heat assisted SPIF since the temperature helps in improving the formability of the material. In order to improve the precision and formability in SPIF, researchers employed different strategies like heating the sheet metal during forming process [10] and stretching forming in conjunction with conventional SPIF [11]. It was observed by Vahdani et al. [10] in their investigation that the maximum depth of formed component was not improved in hot SPIF eventhough there is an improvement in formability of the DC01steel material. Laser forming, one of the advanced forming processes, is used for making the different curved surfaces using the heat generated by the laser beam. Safari and Mostaan [12] have studied the formation of cylindrical surfaces with curvature of arbitary radius using laser forming. It was presented that the parallal lines of irradiation are necessary for producing the intended surfaces and the number of such lines is the important parameter for the success of forming [12]. The saddle shape with larger radius of curvature was successfully made by laser forming using spiral irradiating lines [13] and recommended the Out-to-In spiral pattern over In-to-Out spiral pattern for the better performance. But, in laser forming, more number of passes are required to produce larger angle and hence the cost of manufacturing may be high when compared with the IF process.

Apart from experimentations, researchers used FEA to simulate ISF and investigate the forming characteristic of the sheet metal [14-16]. Blaga and Oleksik [17] have tried 3 different forming paths to create a frustum of a cone using DC04 steel sheet and concluded that the spiral path is the best among used strategies due to the occurrence of homogenous distribution of strains. Similar spiral path was used in both experimentation and FEA to produce truncated cone in Stainless steel 304, DC06 and aluminum alloy AL5052 by Golabi and Khazaali [18], Li et al. [19] and Wang et al. [20]. Experiment and FEA was carried out by Neto et al. [21] using circular path and found that stress and strain FEA results are in good agreement with experimental results. Researchers used analysis software like ABAQUS [22-23], LS-DYNA [24] for predicting different output parameters efficiently. Shrivastava and Tandon [25] employed Radioss as a solver for explicit simulation and HyperView and Hypergraph for post processing. To measure the strains in the incrementally formed components, Centeno et al. [26] utilized ARGUS software for circle grid analysis. Nasulea and Oancea [27] has developed Tool Motion Points Generator (TMPG) software to input path for simulation in ANSYS. To improve the formability, Wang et al. [28] developed a newer spiral path strategy by interpolation and translation of a generated points from Unigraphics software. FEA was performed in double sided ISF and Multi stage ISF to find the strains and fracture limits by Moser et al. [29] and Wu et al. [30].

It is clear from the literature survey that the increase in the wall angle beyond certain value limits the height of the component formed in single stage of forming. Also, it is observed that most of the researchers investigated the components made with wall angle 30° to 60° for a part height of 25 to 60mm and increasing the wall angle above 60° produced the component height within the range of 10 to 35mm by single stage. So, it is obvious that producing a component with the wall angle more than 60° for a depth more than 35 mm in SSSPIF has imposed a challenge to the researchers. The main aim of this paper is to investigate the SSSPIF of 1 mm thick AISI 304 stainless steel component with wall angle more than 60° for a part depth of more than 35mm by experimental and FEA methods by selecting suitable process parameters. Also, the effect of wall angle formation on the various strains due to the deformation to understand the thinning and fracture of the component.

2. FINITE ELEMENT ANALYSIS

Simulation of single stage incremental forming was carried out in four different stages. In first stage, the individual parts like blank material, tool, clamping plate

and backing plates are 3D modeled and assembled. In second stage, this model was imported to finite element simulation software. Also, meshing, boundary condition, material properties and contact between parts are applied. In third stage, the CNC code for forming is converted into displacement curve and the final stage is solving and post processing.

LS-DYNA explicit solver is used for FEA of single point single stage incremental forming to determine the deformation characteristics of the material. In order to show the backing plate in the assembly, the full model is cut and shown in Figure 1. Total number of 62712 Belytschko-Tsay shell element with two integration points is considered for the forming simulation.

AISI 304 stainless steel sheet of 1mm thickness was considered as the blank material and necessary mechanical properties like Young's modulus of 2.1E5 MPa, Poisson's ratio of 0.3, density of 8000Kg/m^3 was applied. The hemispherical tool head is shown as spherical ball. The blank is considered as deformable and all other parts of the assembly are considered as rigid. Frictional coefficient of 0.1 and 0.4 are assumed for blank & tool and blank & supporting plates respectively using CONTACT ONEWAY SURFACE TO SURFACE keyword in LS DYNA. X, Y & Z coordinates of a path of a rotating tool from CNC code is converted into curve and stress strain curve of raw material was used as an input for simulation. Since the chosen tool path is spiral, partial or symmetrical model cannot be used and hence full model is used for simulation. The advantage of using spiral tool path over other is that no mark can be observed during step down tool movement. The approximate simulation time is around 140 hours for each full model. From the FEA results major, minor and thickness strain are measured and validated with the experimental work.

3. EXPERIMENTAL WORK

Truncated cone shaped components of austenitic stainless steel AISI304 are produced in a YCM make computerized numerically controlled (CNC) vertical machining center. The important specification of the machine such as maximum spindle speed and feed rate of 8000 rpm and 10000 mm/min, respectively. Purchased sheet is sheared into required dimension of 120x120x1mm and is laser etched with 5mm diameter circular grids. The blank is clamped firmly between the clamping and backing plate in a custom designed fixture. The tool diameter of 14mm with hemispherical end is made of High carbon high chromium (HCHCr) tool steel and heat treated to have the hardness in the range of 52–55 HRc. The setup of single point incremental forming process is presented in the Figure 2.

Initially the range of process parameters used are as follows: tool traversing speed 200 to 1250 mm/min; tool rotating speed 250 to 1000 rpm; and incremental depth 0.1 to 0.5mm. The process parameters are selected based on successful formation of the component without any defect and surface finish. For further experimentation the tool traversing speed of 1000 mm/min, tool rotating speed of 250 rpm and step down depth of 0.5mm are fixed and the wall angle is varied. In order to minimize the heat generated during forming process a continuous coolant of Blasco cut 4000 strong water soluble lubricant was used.

During forming process, the circular grids are deformed and to measure the size of the grids, the cup is cut into two halves (Figure 3) and measured using Arcs video measuring system (AVMS model- SVP 2010) at M/s Kosaka calibration lab, Chennai. Thinning effect is calculated by measuring the thickness before and after the forming process using MGW dial thickness gauge.

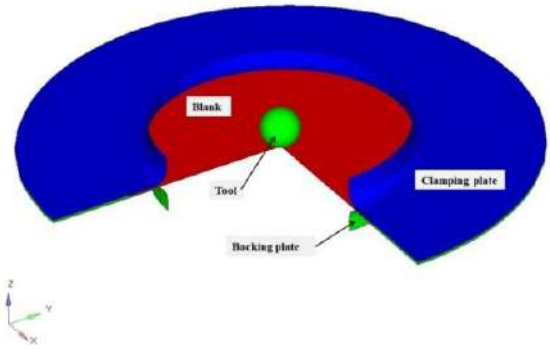

Figure 1. Assembly of SPIF for FEA

Figure 2. SPIF

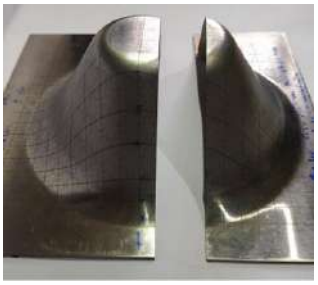

Figure 3. Half cut portion of the formed component

4. RESULTS AND DISCCUSSSION

The incrementally formed components by single stage SPIF experiments and FEA at various wall angles keeping the depth of 45mm as constant are shown in Figure 4 (a) and (b).

Increase in wall angle beyond 64º produced a fracture at a region close to the smaller diameter of the cone at a height of 21.2mm itself. This may be due to the reason that more bending and stretching causes higher deformation in early stages of forming and further movement of the tool cause fracture at a shorter height. The component with a fracture which is produced at a wall angle of 65º is shown in Figure 5.

4. 1. Effect of Wall Angle on Major and Minor Strain The results of the experimentation and FEA show that the strain in the major direction is increasing enormously with the increase of wall angle whereas it is marginal increase in case of minor direction. The comparison between major and minor strain observed in the experiment and FEA at different wall angles are presented in the Figures 6 and 7, respectively.

From Figure 6, it is observed that the FEA results are in good correlation with the experimental values. The maximum and minimum variation between the experiment and FEA is 10 and 0.2% at the deformed zones among all the experimented wall angles. Major strain increases with the increase of wall angle due to the reason that, the material undergoes more stretching and bending when the wall angle increases. At all wall angles, the major strain is noticed very close to the region below the blank clamp in both FEA and experiment. It may be attributed to the reason that the excessive strain at this region due to restriction on material flow imposed by the blank holder and the stretching and bending caused by the rotating tool. The same region was reported by Shrivastava and Tandon [25] during formation of truncated pyramid in SPIF.

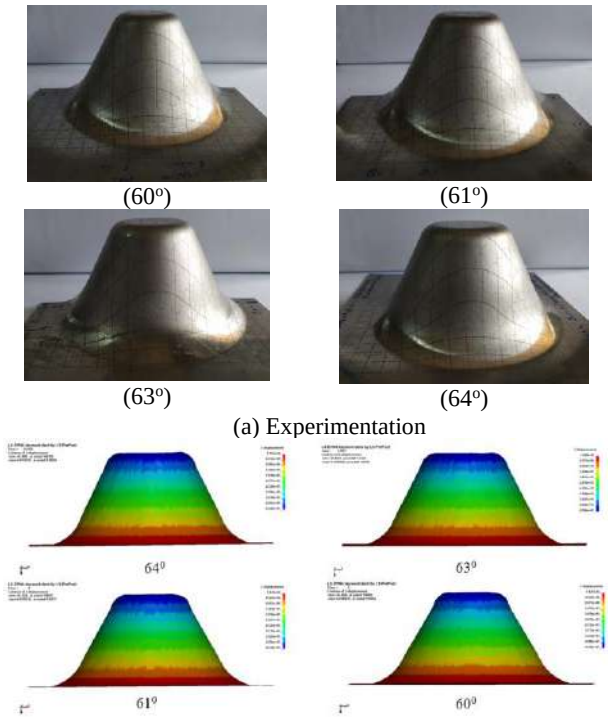

Figure 4. Component formed at different wall angles

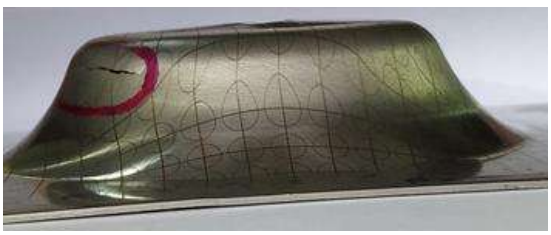

Figure 5. Component formed with 65º wall angle

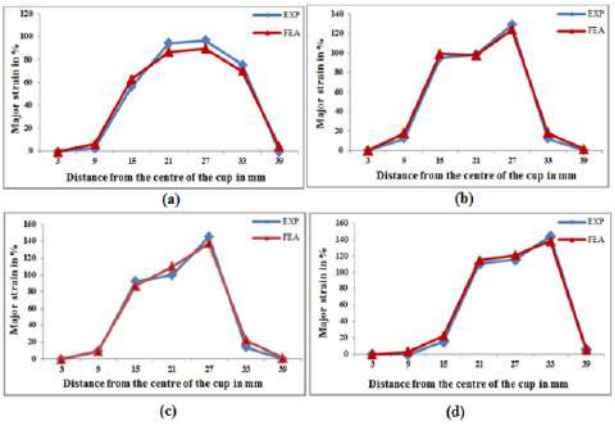

Figure 6. Comparison of Major strain at different wall angles (a): 60º; (b): 61º; (c): 63º and (d): 64º

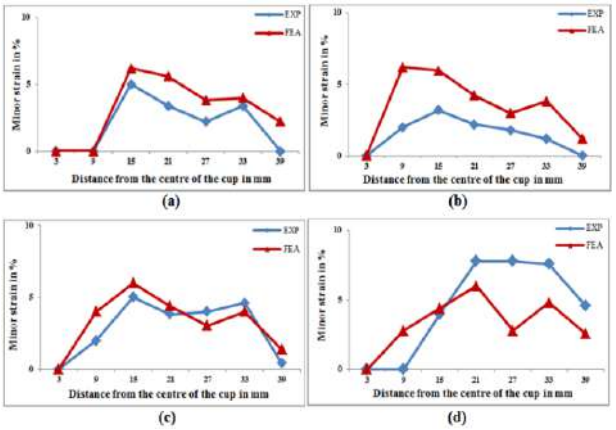

Figure 7. Comparison of Minor strain at different wall angles (a): 60º; (b): 61º; (c): 63º and (d): 64º

It is seen from the Figure 7 that the minor strain increases with the increase in wall angle and the results of FEA and experiments are in good agreement. Maximum of 7% and minimum of 0.4% minor strain variation are observed between FEA and experiment among all the experimented wall angles. In the forming zone, the diameter of the cone increases with increase in wall angle which deforms the material circumferentially and hence the minor strain is more. The minor strain increases from the major diameter region of the cone to the minor diameter region just before the bottom corner radius similar to the results obtained by Neto et al. [21].

In general, increase in the wall angle increases the axial force required to form. Also, biaxial straining and severe stretching caused by the downward spiral movement of the tool while forming the depth causes more strain. The above may be the reason for increase in major and minor strain when the wall angle is increased.

4. 2. Effect of Wall Angle on Thickness Strain Figure 8 shows the thickness strain comparison between experiment and FEA at various wall angles. Increase in wall angle, increases the thinning effect in the formed region in both experiment and FEA. The FEA result shows good association with the experimental values. The maximum thinning ranges from 0.49mm to 0.68mm in FEA and 0.45mm to 0.65mm in experiment with the increase of wall angle. As discussed earlier in section 4.1, both major and minor strain increases with increase in wall angle which leads to decrease in thickness below the blank clamping region near the major diameter of the cone component. Shrivastava and Tandon [25] observed that the maximum thickness reduction in the earlier stage of forming at a same region and also stated that the severity of reduction in the thickness is more when the wall angle increases. It is also observed that the corner region near the clamping plate causes more thinning due to changes in tool direction and twisting.

The reason for this severe thickness reduction was attributed to the bending of the material at the earlier stage of forming and is not disturbed throughout further forming process. Also more and more severe localized thinning occurs when the wall angle is increased to certain value. Beyond which the unexpected failure of the formed component is observed.

4. 3. Forming Limit Diagram The forming limit diagrams (FLD) showing the distribution of major and minor strain for different wall angles from LS DYNA post processing are presented in Figure 9.

It is observed from the figure that the number of points falling above both necking and failure limit curve are increasing when the wall angle is increased. Moreover, the maximum value of major strain is increasing more when compare to maximum value of

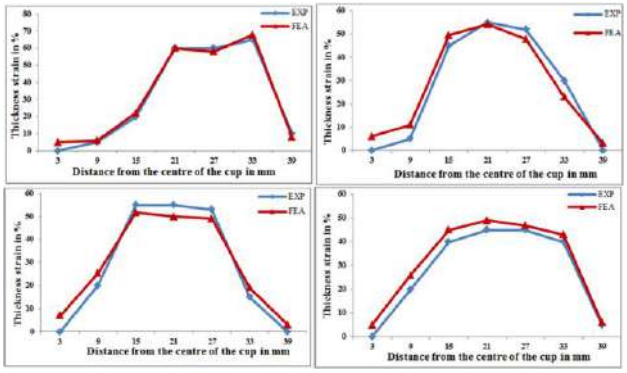

Figure 8. Comparison of thickness strain at different wall angles (a): 60º; (b): 61º; (c): 63º and (d): 64º

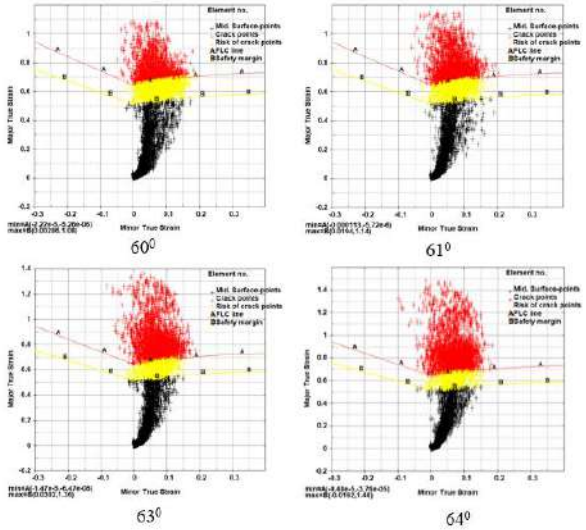

Figure 9. FLD for different wall angle

minor strain as the wall angle is increased. This may be attributed to the reason that severe strain caused by the biaxial straining and stretching due to depth of formation when the wall angle is increased.

5. CONCLUSION

The investigation on experiment and FEA of single stage single point incremental forming of truncated cone using AISI 304 austenitic stainless steel sheets are made to determine the maximum possible wall angle that may be achieved for the height of 45 mm. From the results of study, the following conclusions are drawn:

- Components to a depth of 45 mm are made successfully in single stage of forming up to the wall angle of 64º in the experimented process parameters.
- Good correlation exists between the experimental and FEA results.

- Maximum variations in the major and minor strain are 10 and 7%, respectively.
- Maximum thinning of 0.65mm and 0.68mm was observed at the region close to the larger diameter of the truncated cone at wall angle of 64° in both experiment and FEA, respectively.
- Severe major, minor and thickness strain is observed when the wall angle and depth of the component increased.
- FLDs also show more strain distribution above the limiting curves when the wall angle increases.
- Due to longer analysis running time, the success of FEA of incremental forming is a challenging one.

Further investigation of FEA of multi stage SPIF and reduction in analysis running time is under progress.

5. REFERENCES

1. Jackson, K., Allwood, J., "The mechanics of incremental sheet forming", ***Journal of Materials Processing Technology***. Vol. 209, No. 3, (2009), 1158-1174. https://doi.org/10.1016/j.jmatprotec.2008.03.025
2. Gupta, P., Jeswiet, J., "Effect of temperatures during forming in single point incremental forming", ***International Journal of Advanced Manufacturing Technology.*** Vol. 95, No. 9-12, (2018), 3693-3706. https://doi.org/10.1007/s00170-017-1400-0
3. Esmailian, M., Khalili, K., "Prediction of Tool Force in Two Point Incremental Forming by Slab Analysis", ***International Journal of Engineering, Transactions B: Applications.*** Vol. 33, No. 11, (2020), 2399-2407. https://doi.org/10.5829/ije.2020.33.11b.30
4. Adams D, Jeswiet J., "Design rules and applications of single-point incremental forming", ***Proceedings of the Institution of Mechanical Engineers Part B: Journal of Engineering Manufacture.*** Vol. 229, No. 5, (2015), 754-760. https://doi.org/10.1177/0954405414531426
5. Ndip-Agbor E, Cheng P, Moser N, Ehmann K, Cao J., "Prediction of rigid body motion in multi-pass single point incremental forming", ***Journal of Materials Processing Technology.*** Vol. 269, (2019), 117-127. https://doi.org/10.1016/j.jmatprotec.2019.02.007
6. Shigekazu T., "Incremental sheet metal formed square-cup obtained through multi stepped process", ***Procedia Manufacturing.*** Vol. 15, (2018), 1170-1176. https://doi.org/10.1016/j.promfg.2018.07.372
7. Safari, M., "Two-point incremental forming of a complicated shape with negative and positive dies", ***Iranian Journal of Materials Forming***. Vol. 4, No. 2, (2017), 51-61.
8. M. Safari, and J. Joudaki, "Fabrication of a complicated specimen with two-point incremental forming process", ***International Journal of Advanced Design and Manufacturing Technology***. Vol.12, No.4, (2019), 83-88.
9. Duflou JR, Habraken AM, Cao J, Malhotra R, Bambach M, Adams D, Vanhove H, Mohammadi A, Jeswiet J., "Single point incremental forming: state-of-the-art and prospects". ***International Journal of Material Forming.*** Vol. 11, No. 6, (2018), 743-773. https://doi.org/10.1007/s12289-017-1387-y
10. Vahdani M, Mirnia MJ, Bakhshi-Jooybari M, Gorji H., "Electric hot incremental sheet forming of Ti-6Al-4V titanium, AA6061aluminum, and DC01 steel sheets", ***The International Journal of Advanced Manufacturing Technology,*** Vol. 103, No.1-4, (2019), 1199-1209. https://doi.org/10.1007/s00170-019-03624-2
11. Choi H, Lee C., "A mathematical model to predict thickness distribution and formability of incremental forming combined with stretch forming", ***Robotics and Computer Integrated Manufacturing,*** Vol. 55, (2019), 164-172. https://doi.org/10.1016/j.rcim.2018.07.014
12. Safari M, Mostaan H., "Experimental and numerical investigation of laser forming of cylindrical surfaces with arbitrary radius of curvature", ***Alexandria Engineering Journal,*** Vol. 55, No. 3, (2016), 1941-1949. https://doi.org/10.1016/j.aej.2016.07.033
13. Safari M, Alves de Sousa R, Joudaki J., "Fabrication of saddle-shaped surfaces by a laser forming process: An experimental and statistical investigation", ***Metals,*** Vol. 10, No. 7, (2020), 883-895. https://doi.org/10.3390/met10070883
14. Nguyen DT, Kim YS., "A numerical study on establishing the forming limit curve and indicating the formability of complex shape in incremental sheet forming process", ***International Journal of Precision Engineering and Manufacturing,*** Vol. 14, No. 12, (2013), 2087-2093. https://doi.org/10.1007/s12541-013-0283-8
15. Memicoglu P, Music O, Karadogan C., "Simulation of incremental sheet forming using partial sheet models", ***Procedia Engineering,*** Vol. 207, (2017), 831-835.https://doi.org/10.1016/j.proeng.2017.10.837
16. Kim, H., Park, T., Esmaeilpour, R., andPourboghrat, F, "Numerical study of incremental sheet forming processes", ***IOP Conference Series: Journal of Physics.*** Vol. 1063, (2018), 012017. https://doi.org/10.1088/1742-6596/1063/1/012017
17. Blaga A., Oleksik V., "A study on the influence of the forming strategy on the main strains, thickness reduction, and forces in a single point incremental forming process", ***Advances in Material Science and Engineering,*** (2013), 1-10. http://dx.doi.org/10.1155/2013/382635
18. Golabi, S.I. Khazaali, H., "Determining frustum depth of 304 stainless steel plates with various diameters and thicknesses by incremental forming", ***Journal of Mechanical Science and Technology,*** Vol. 2 8, No. 8, (2014), 3273-3287.https://doi.org/10.1007/s12206-014-0738-6
19. Li, J., Li, S., Xie, Z., Wang, W., "Numerical simulation of incremental sheet forming based on GTN damage model", ***International Journal of Advanced Manufacturing Technology,*** Vol. 81, No.9-12, (2015), 2053-2065.https://doi.org/10.1007/s00170-015-7333-6
20. Wang, J., Nair, M., Zhang, Y., "An efficient force prediction strategy in single point incremental sheet forming", ***Procedia Manufacturing.*** Vol. 5, (2016), 761-771.https://doi.org/10.1016/j.promfg.2016.08.062
21. Neto, D. M., Martins, J. M. P., Oliveira, M. C., Menezes, L. F., Alves, J. L., "Evaluation of stress and strain states in the single point incremental forming process", ***International Journal of Advanced Manufacturing Technology,*** Vol. 85, No. 1-4, (2016), 521-534.https://doi.org/10.1007/s00170-015-7954-9
22. Panahi Leavoli, R., Gorji, H., Bakhshi-Jooybari, M., Mirnia, M. J., "Investigation on Formability of Tailor-Welded Blanks in Incremental Forming", ***International Journal of Engineering, Transactions B: Applications.*** Vol. 33, No. 5 (2020), 906-915.https://doi.org/10.5829/ije.2020.33.05b.23
23. Sajjad, M., Joy, J. A., Jung, D. W., "Finite element analysis of incremental sheet forming for metal sheet", ***Key Engineering Materials,*** Vol. 783, (2018), 148-153. https://doi.org/10.4028/www.scientific.net/KEM.783.148.
24. Maqbool, F., Bambach, M., "Dominant deformation mechanisms in single point incremental forming (SPIF) and their

effect on geometrical accuracy", ***International Journal of Mechanical Sciences,*** Vol. 136, (2018), 279-292. https://doi.org/10.1016/j.ijmecsci.2017.12.053

25. Shrivastava, P., Tandon, P., "Microstructure and texture based analysis of forming behavior and deformation mechanism of aa1050 sheet during single point incremental forming", ***Journal of Materials Processing Technology,*** Vol. 266, (2019), 292-310. https://doi.org/10.1016/j.jmatprotec.2018.11.012
26. Centeno, G., Bagudanch, I., Martínez-Donaire, A. J., Garcia-Romeu, M. L., Vallellano, C., "Critical analysis of necking and fracture limit strains and forming forces in single-point incremental forming", ***Materials and Design,*** Vol. 63, (2014), 20-29. https://dx.doi.org/10.1016/j.matdes.2014.05.066
27. Nasulea, D., Oancea, G., "Integrating a new software tool used for tool path generation in the numerical simulation of incremental forming processes", ***Strojniškivestnik-Journal of Mechanical Engineering,*** Vol. 64, No. 10 (2018), 643-651. https://doi.org/10.5545/sv-jme.2018.5475
28. Wang, J., Li, L., Zhou, P., Wang, X., Sun, S., "Improving formability of sheet metals in incremental forming by equal diameter spiral tool path", ***The International Journal of Advanced Manufacturing Technology,*** Vol. 101, No. 1-4, (2019), 225-234. https://doi.org/10.1007/s00170-018-2911-z
29. Moser, N., Pritchet, D., Ren, H., Ehmann, K. F., Cao, J., "An efficient and general finite element model for double-sided incremental forming", ***Journal of Manufacturing Science and Engineering,*** Vol. 138, No. 9, (2016), 091007 (1-10). https://doi.org/10.1115/1.4033483
30. Wu, M., Zha, G., Zirui, G., "FEA of vertical parts formed with multistage incremental sheet metal forming based on the forming limit stress diagram", ***International Journal of Advanced Manufacturing Technology,*** Vol. 93, No. 5-8, (2017), 2155-2160. https://doi.org/10.1007/s00170-017-0630-5

Persian Abstract

چکیده

شکل گیری افزایشی یکی از فرایندهای شکل گیری غیر سنتی است که به طور گسترده ای در نمونه سازی سریع و ساخت قطعات سفارشی استفاده می شود. یکی از چالش هایی که در شکل گیری افزایشی تک مرحله ای تک مرحله ای (SSSPIF)وجود دارد ، دشواری در دستیابی به زاویه دیواره بیشتر برای عمق قابل توجه است. در این کار تحقیقاتی ، تحقیق با شبیه سازی تجربی و عددی برای رسیدن به حداکثر زاویه دیواره تا عمق ممکن و بدون نقص در SSSPIF انجام شده است. SSSPIF از اجزای مخروطی شکل بریده شده از فولاد ضد زنگ آستنیتی AISI304 با ضخامت ۱ میلی متر در زاویه دیواره های مختلف ساخته شده است. همچنین ، شبیه سازی عددی با استفاده از حلگر صریح LS-DYNA انجام شده و نتایج با مقادیر آزمایشی تأیید می شوند. اجزای دارای زاویه دیواره ۶۴ درجه با موفقیت ساخته می شوند و هیچ نقصی در یک مرحله تشکیل نمی شود و برای عمق ۴۵ میلی متر در پارامترهای فرآیند آزمایش شده ایجاد می شود. کرنش عمده ، کرنش جزئی و توزیع ضخامت در ورق به دلیل فرآیند تشکیل از آزمایشات و تجزیه و تحلیل عناصر محدود (FEA)بدست می آید. از نتایج هر دو آزمایش و FEA ، مشاهده شده است که اثرات کرنش عمده ، کرنش جزئی و نازک شدن در منطقه زیر قطر اصلی مخروط کوتاه شده در تمام زوایای دیواره آزمایش شده بیشتر است. همچنین نتایج FEA توافق خوبی با مقادیر آزمایشی نشان داده است. بعلاوه مشاهده می شود که با افزایش زاویه دیواره ها کرنشها در حال افزایش هستند.

IJE TRANSACTIONS A: Basics Vol. 34, No. 10, (October 2021) 2266-2279

International Journal of Engineering

Journal Homepage: www.ije.ir

Physical Modelling of a Strip Footing on a Geosynthetic Reinforced Soil Wall Containing Tire Shred Subjected to Monotonic and Cyclic Loading

M. H. Hoseini, A. Noorzad*, M. Zamanian

Faculty of Civil, Water and Environmental Engineering, Shahid Beheshti University, Tehran, Iran

PAPER INFO

Paper history:
Received 5 May 2021
Received in revised form 9 July 2021
Accepted 22 July 2021

Keywords:
Geosynthetic Reinforced Wall
Physical Modeling
Strip Footing
Tire Shred
Bearing Capacity

ABSTRACT

In this study, the mechanical behavior of geosynthetic reinforced soil walls was investigated through physical modeling subjected to strip footing monotonic and cyclic loads at various stress paths. The influence of footing location, stress level, post-cyclic behavior and sand-tire shred admixture on the lateral deformations of the wall facing, bearing capacity and the settlement beneath the footing were assessed. To this aim, 12 physical model tests were conducted on a scale of 1: 4. Results indicated that the bearing capacity has increased with an increase in the offset distance of the strip footing to the wall facing and adding tire shred to the backfill material; but an increase is more prominent by adding tire shred to the backfill material. The location of the footing from the wall facing was a crucial parameter on the deformation of facing and the failure mode of the footing. Failure in the facing was the predominant mode of failure in the near facing footing. However, a rupture in the geosynthetic caused failure in the footing far from facing footing. Also, the results of cyclic loading tests showed both permanent displacement and residual settlement accumulated with load cycles and a majority of them occurred over the first fifteen cycles. Depending on where strip footing was located, it may or may not induce a magnifying effect on subsequent cyclic loading responses.

***doi**: 10.5829/ije.2021.34.10a.08*

1. INTRODUCTION

Using geosynthetic materials to increase the tensile load of the soil has been widely reported in recent decades [1-3]. Geosynthetic reinforced soil (GRS) walls are one of the traditional structures that are based on these types of materials. From the environmental point of view, GRS walls have been attracted due to higher flexibility, construction time, cost effectiveness and the possibility of using local materials.

Several experimental and numerical studies sought to investigate the monotonic and cyclic behavior of GRS walls. Among them, the effects of toe resistance [4, 5], backfill relative density [6, 7], facing inclination [8], the facing existence [9], the location and the value of the surcharge load on lateral deformations [10-14], backfill materials [15-17] and wall geometry on failure mode [18] are the most important parameters that have been reported in the literatures. The results of those works showed that by increasing the frictional resistance of the wall toe, the soil density, the surface angle to the vertical axis, and the load distance from the facing, the static bearing capacity of the wall increases, while the lateral deformations decrease. Another major finding is that the properties of the backfill soil and reinforcement layers have little influence on the geometry of the failure surface. However, parameters related to the geometry of the wall, such as the size and location of the bridge seating, and the height of the wall, have significant effects. In contrast to the extensive researches on GRS walls under static loading, very limited studies have been conducted on the behavior under cyclic loading conditions.

One of the most fundamental limitations of GRS walls is their limited bearing capacity, which has been estimated to be 192 kPa [19, 20]. Therefore, using materials like tire shred with high ductility properties

*Corresponding Author Institutional Email: a_noorzad@sbu.ac.ir (A. Noorzad)

Please cite this article as: M. H. Hoseini, A. Noorzad, M. Zamanian, Physical Modelling of a Strip Footing on a Geosynthetic Reinforced Soil Wall Containing Tire Shred Subjected to Monotonic and Cyclic Loading, International Journal of Engineering, Transactions A: Basics, Vol. 34, No. 10, (2021) 2266-2279

could enhance the bearing capacity of GRS walls. The performance of tire shreds when mixed with sand has been reported by many researchers [21, 22]. Despite the well-known performance of sand and tire shred mixtures, only a limited number of studies have employed such mixtures in the body of the reinforced soil walls. For instance, Xiao et al. [23] investigated the seismic behavior of a reinforced soil wall constructed by embedding tire shreds using a shaking table. They observed that under similar conditions, walls constructed with tire shreds, compared to the conventional type of reinforced soil walls, had experienced less lateral displacement, vertical settlement, acceleration, and stress.

Most of previous studies have been focused on the monotonic behavior of GRS walls. However, there are few studies directed to investigate the response of GRS walls subjected to cyclic loading. In this line, several uncertainties are associated with the influencial parameters on the failure mode of GRS walls under cyclic loading of a shallow foundation. In addition, few studies investigated the application of shredded tires for increasing the ductility of the GRS walls. Therefore, series of physical models with a scale of 1: 4 have been carried out. The monotonic behavior of these walls was studied and simulated under similar conditions to cyclic loading.

2. MATERIALS AND METHODS

2. 1. Experimental Setup The model test setup used in this study consist of a rigid soil chamber and a computer-controlled loading system. The length, width, and height of the cubic box are 1600, 400, and 800 mm, respectively. A polystyrene foam layer and a film of clay were placed in the beneath of the box to isolate it from the surrounding environment. A transparent Plexiglas wall (with a thickness of 10 mm) was placed on one side of the wall for visual observation. Figure 1(a) depicts an image of the setup. The stress and displacement of the wall facing and footing settlement was measured using a S-shaped load cell and three LVDTs. The positions of the reinforcement layers and the LVDTs are illustrated in Figure 1(b). For the tests on reduced-scale models in a 1-g gravitational field, similarity relationships must be considered to produce similar responses between model and prototype structures. The similitude relationships proposed by Iai [24] that have been widely used by other researchers [25, 26] have been used for this study. The length scaling factor was selected of 4 and it was referred to as the ratio of the prototype dimensions to the physical model dimensions. The geometry of the model, footing width, stiffness of geosynthetic, applied pressure, frequency and loading time were scaled. The theoretical scaling factors for the similitude relationships are summarized in Table 1.

2. 2. Soil Figure 2(a) presents the particle size distribution of the D11 Firuzkuh sand (according to the ASTM D-422-63 standard [27]) and the microscopic images of the grains are presented in Figure 2(b). Poorly-graded dry sand was used in the model tests. This sand was selected to simulate a reduced size and strength backfill. The mean particle size (D_{50}) was 1.45mm, while the uniformity coefficient (C_u) and the coefficient of curvature (C_c) were 1.6 and 1.2, respectively. As shown in Figure 2(b), the sand grains generally have semi-sharp corners (sub-angular to sub-rounded) with medium to low sphericity, as compared to the diagrams proposed by Maroof et al. [28].

(a)

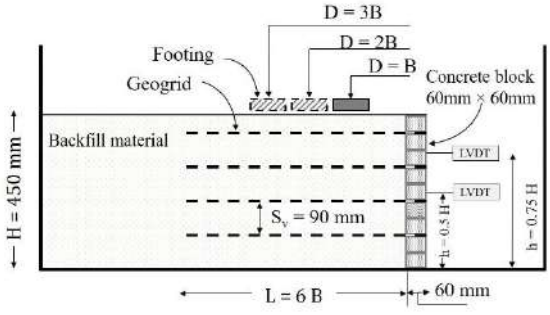

(b)

Figure 1. a) Photograph illustrating the Test setup, b) schematic view of apparatus and samples geometry

TABLE 1. Similitude relationships for 1-g tests [24]

Variable	Theoretical scaling factor	Scaling factor for λ=4
Length	λ	4
Material density	1	1
Strain	1	1
Mass	λ^3	64
Stress	λ	4
stiffness	λ^2	16
Time	$\lambda^{0.5}$	2
Frequency	$\lambda^{-0.5}$	0.50

According to the ASTM D4253 [29] standard, the maximum and minimum unit weights of the sand were 17.8 and 14.3 kN/m^3, respectively. In the direct shear test, the friction angle at the target relative density (RD) of 70% was 43 degrees. The obtained specific gravity (Gs) is 2.62. The properties of the soil are summarized in Table 2.

2. 3. Tire Shred Based on previous studies, the tire shred can significantly increase the modulus and shear strength of the granular layer [21, 22, 30]. The grain size distribution curve of the tire shred is depicted in Figure 2(a). The tire shred grains have a specific gravity, G_s, of 1.16, while the elastic modulus is 3.27 MPa. The tire shred particles were prepared from a truck tire after ensuring that they were free of any steel and cord. In the direct shear test (100 mm ×100 mm box), the friction angle was computed 31 degrees; while the friction angle from the tire shred-geosynthetic interaction became 30 degrees.

2.4. Reinforcement Layer According to ASTM [31], the typical tensile strength of the uniaxial geogrid ranges from 58 to 210 kN/m. Based on Table 1, the tensile strength reduces by the square of the scale value. Considering the scale value of 1:4 in this research, the tensile strengths reduced to the ranges of 3.5 to 13 kN/m. A geosynthetic with a 10 mm×10 mm aperture size and a failure tensile strength of 6.1 kN/m in each direction [31] was selected as a reinforcement layer to satisfy the required tensile strength. The aperture size is not highly important, except for the pull-out capacity. However, when the reinforcement length is 0.7 times the wall height, pull-out is often not an issue [19, 20]. In this study, the reinforcement layer length was 510 mm.

TABLE 2. Properties of the soil

Properties	Value
Specific gravity, G_s	2.62
Mean particle size, D_{50} (mm)	1.45
Effective particle size, D_{10} (mm)	0.91
Coefficient of uniformity, C_u	1.6
Coefficient of curvature, C_c	1.2
Maximum unit weights, γ_{max} (kN/m^3)	17.8
Minimum unit weights, γ_{min} (kN/m^3)	14.3
Optimum moisture content, (%)	2.5
Friction angle, φ(degree)	43
Friction angle from sand-geosynthetic interaction, (degree)	36
USCS soil clasification	SP

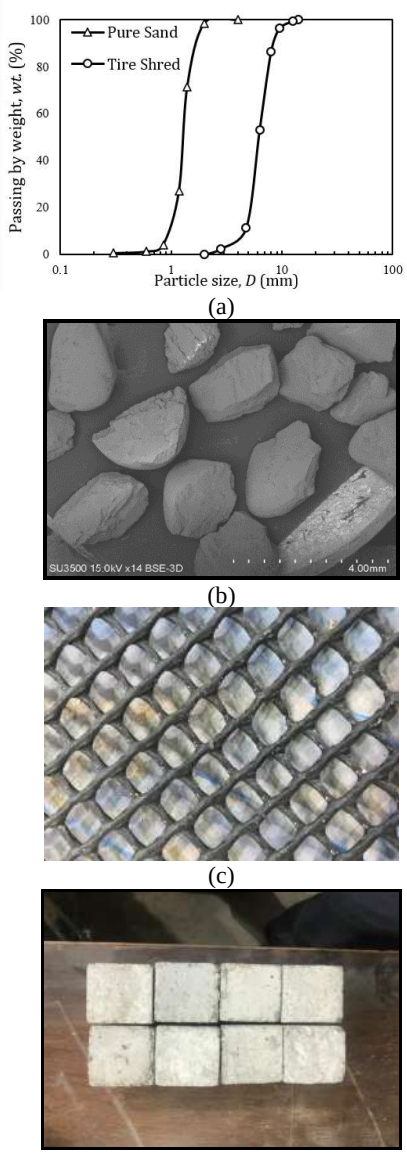

(a)

(b)

(c)

(d)

Figure 2. a) Grain size distribution of the sand, b) microscopic view of the grains, c) the geosynthetic, d) the facing block

The physical and mechanical properties of this type of geosynthetic, provided by the factory, are presented in Table 3, further Figure 2(c) shows a photograph of the geosynthetic.

2. 5. Facing Concrete blocks with a width of 60 mm, a length of 50 mm, and a height of 45 mm were used to build the facing panels. Figure 2(d) demonstrates the concrete blocks of the facing. According to FHWA [33], the joint between the facing blocks and the reinforcement layers in GRS walls is

TABLE 3. Physical and mechanical properties of the geosynthetic

Physical property		Mechanical property	
Aperture size (mm)	10×10	Ultimate tensile strength (kN/m)	6.1
Rib thickness (mm)	3.3	Maximum strain at maximum strength (%)	51.7
Weight of unit area (g/m^2)	700	Tensile strength at 10% strain (kN/m)	2.9
Polymer material	HDPE		

extremely weak. The lateral blocks of the wall facing were greased in order to eliminate the effects of the sidewalls on the sample. There is no connection between the facing and the reinforcement layers, except for the friction between the geosynthetic layers and the facing blocks.

2. 6. Strip Footing A metal sheet with a thickness of 25 mm, a width of 75 mm, and a length equal to the width of the box (i.e., 400 mm) was used to carry out the two-dimensional simulation (plane strain) of the strip footing on the wall.

2. 7. Sample Preparation The overall height of the wall in the model test was 450 mm that represents a wall with 1.8 m height in real scale. This height is acceptable for GRS bridge abutment as used by Adams and Saunder [34]. The reinforcement layers spacing and the soil friction angle has the greatest effect on the geosynthetic tensile forces [35]. In order to obtain higher ultimate passive force in GRS abutment, Ramalakshmi and Dodagoudar [36] found that the reinforcement layers spacing should be closer. However, in most cases, the spacing is chosen by the requirement of the project.

In this study, four geosynthetic layers were used at a spacing of 90 mm. To avoid pull-out effects, length of 510 mm was adopted for the reinforcement layers. The backfill was compacted in 2-cm layers with an optimum moisture content of 2.5% and a relative density about 70%. In all the tests containing the sand-tire shred mixture, the tire shred was used at a mass replacement rate of 7.5% with a rate in the range of 6% to 10%, as recommended by previous work [37, 38]. Moreover, a greased transparent polyethylene plastic sheet was placed on both of the inner sides of the box to eliminate the effects of the sidewalls on the sample.

3. EXPRIMENTAL PROGRAM

3. 1. Loading Pattern Overall, two series of tests were performed under different loading conditions. In the first series, the samples were subjected to monotonic loading, and the loading continued until failure has reached. Four monotonic tests were performed, i.e., three tests on sand backfill, and one on a mixture of sand and tire shreds. In those three tests, the samples were quite similar, and only the location of the strip footing was different. In the second series of experiments, the samples were first subjected to vertical cyclic loading, and then, after some delay and then unloading, they were subjected to monotonic loading until failure. The amplitude of the cyclic loading was selected as a percentage of the monotonic bearing capacity; a method that was used by previous studies [39-41]. Cyclic tests were initially loaded monotonically at 20% of q_u (q_u is the ultimate bearing capacity of the monotonic sand test when D=1B), and then, they were loaded with three different stress levels (i.e., 0.2 q_u, 0.4 q_u, and 0.6 q_u). Accordingly, 200 cycles were applied to each sample at the frequency of 0.1 Hz at every stress level (i.e., a total of 600 cycles for each sample). Islam and Gnanendran [42] reported that for a particular loading amplitude, the footing settlement slightly changed (by about 10 to 15%) with an increase in loading frequency from 0.2 to 5 Hz, and the effects became more evident at a higher loading frequency. Therefore, having a loading frequency of 0.1 Hz for the model has a negligible effect on the results. Three cyclic loading tests were conducted on GRS without tire shred, while one was performed on a backfill made of the sand-tire shred mixture. Figure 3 displays the loading pattern. Table 4 presents the testing program examined in this work.

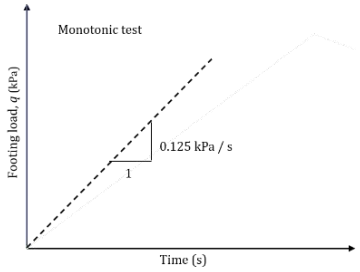

(a)

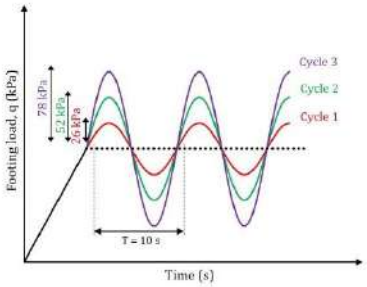

(b)

Figure 3. Loading pattern, a) monotonic loading, b) vertical cyclic loading

TABLE 4. Model test program

Type	Backfill material	Footing distance from facing	q_s/q_u (%)	q_c/q_u (%)
Monotonic	sand	1B, 2B, 3B	-	-
Monotonic	sand-tire shred	2B	-	-
yclic	Sand	1B, 2B, 3B	20	20, 40, 60
Cyclic	sand-tire shred	1B, 2B, 3B	20	20, 40, 60
Monotonic (post-cyclic)	sand	1B, 2B, 3B	-	-
Monotonic (post-cyclic)	sand-tire shred	2B	-	-

q_u=The ultimate bearing capacity of the monotonic sand test when D=1B
q_s=The initial monotonic loading
q_c=The cyclic loading amplitude

3. 2. Repeatability Test To check the repeatability of the results, the footing was placed at a distance of 2B from the facing, and then, two tests were carried out. The results for the bearing capacity against the footing settlement both showed the same behavior when repeated (Figure 4).

4. TEST RESULTS AND DISCUSSION

The results of the tests are presented in three categories, regardless of the backfill material, i.e., monotonic loading, cyclic loading, and post-cyclic loading behavior. In each section, the behaviors of the models with the sand backfill are discussed. Then, the results for the sand-tire shred mixture are given and discussed.

4. 1. Monotonic Loading Figure 5 displays the results of model test with pure sand backfill under failure conditions. Based on the results, the dominant failure mode for short distances between the footing and the wall facing (D=B) was related mainly to the failure of the wall facing (see Figure 12(a)). Moreover, with an increase in the distance from the facing, the role of the geosynthetic layers in the footing bearing capacity becomes more significant. At a long distance (D=3B) from the facing, the wall continued to carry until the geosynthetic ruptured, and then the sample has been failed. At D=2B and 3B, the failure first initiated at the corners of the strip footing, and it progressively mobilized toward the center of the wall. Khosrojerdi et al. [43] also have reported this observation for the sliding between the soil and the geotextile layers in GRS walls.

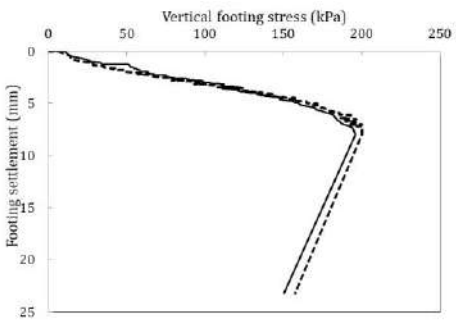

Figure 4. Result for two samples with the same properties

The variations in the footing settlement versus the vertical stress on the footing at different footing placement distances are displayed in Figure 5(a). As shown in this figure, with an increase in the distance between the footing and the facing, the maximum bearing capacity of the footing increases. Under different footing placement conditions, i.e., distances of B, 2B, and 3B, the maximum ultimate bearing capacity of the footing (regardless of the footing settlement) is 130, 210, and 230 kPa, respectively. Xiao et al. [32] stated that at distances of more than 0.4 of the wall height (D/H > 0.4), the bearing capacity of the footing remained constant. In the present study, the value of D/H for various locations of the footing (i.e., distances of 1B, 2B, and 3B) is 0.16, 0.34, and 0.5, respectively. The results indicate that by increasing the D/H to 0.5, the bearing capacity continues to be increased. However, an increase in bearing capacity from 2B to 3B is very small. It is worth noting that the load increases with a slope pertinent to the deformations. The slope of the load-deformation curve decreases with an increase in the distance between the footing and the wall facing. This means that the behavior of the reinforced soil approaches the ductile behavior with an increase in the distance from the wall facing, which can be attributed to the type of failure governing the model. When the footing is located at a distance of B from the facing, the local failure in the wall leads to a decrease in bearing capacity and extensive deformations in the footing. At this distance, heavy sliding occurs between the soil and the geosynthetic layer, and the load cannot be transferred to the lower layers of the wall. At this distance, the softening regime governing the GRS is mainly caused by the decrease in the sand shear strength, which leads to in the sliding of the upper layers of the facing blocks, and ultimately causes them to fall (see Figures 6(a) and 12(a)). Xie et al. [44] called this mechanism a log-spiral wedge and occurred when the footing is located closer to the facing or the GRS wall is tall. However, when the footing is at the distance of 3B from the facing, the footing bearing capacity is independent of the wall facing deformations, and the footing experiences collapsibility due to the geosynthetic rapture (see Figures 6(c) and 12(c)) and two-sided general shear mechanism is governing [44]. As a result, the flexible behavior of the geosynthetic

dominates the reinforced soil system. The failure in the soil beneath the footing is affected by the geosynthetic flexibility behavior with an increase in the load. However, regardless of the position of the footing, the GRS (without any connection between the reinforcement layers and the blocks) experiences the internal sliding type of failure at the end of the loading process (see Figure 12). This failure mode was discussed in literature [44, 45].

Since the lateral deformation is an important parameter in the stability assessment and construction of GRS walls, the changes in the horizontal displacement in the facing in relation to the footing settlement were recorded for two locations in the wall, i.e., the middle and the upper quarter parts of the wall, as depicted in Figures 1(b), 5(b) and 5(c). The horizontal displacement in the upper quarter of the wall in all the models is almost two times that of the middle of the wall. As noted by Mirmoradi and Ehrlich [10] the locations of the surcharge and footing change the deformation profile of the wall facing. The results show that the location of the surcharge has a significant impact on the lateral displacement of the facing. The lateral displacement in the samples placed at the distances of B and 2B has been increased linearly with an increase in the footing settlement to 0.7% and 1.8% of the wall height, respectively. Thereafter, the lateral deformation in the wall facing remained unchanged up to a settlement of approximately 4-5% of the wall height. This outcome can be attributed to the interlocking of the soil and the geosynthetic layers. In the initial deformations in the reinforced soil, the reinforcement layers did not start functioning yet, and the initial settlement was caused by the soil deformations. Immediately, the interaction between the soil and the geosynthetic has been commenced. With an increase in the footing settlement from 0.7% (for the distance of 1B) and 1.8% (for distances of 2B and 3B) to approximately 4-5%, a large fraction of the footing stresses and deformations have been transferred to the reinforced soil, and the wall facing did not deform. Then, as the settlement exceeded the wall bearing capacity threshold, the lateral deformations become larger, indicating the onset of the failure of the reinforced soil. This trend was observed in the upper quarter of the wall due to the size of the shallow foundation, and considerable deformations did not occur in the middle of the walls as stated by Ahmadi and, Hajialilue-Bonab [46] and Li et al. [47]. Interestingly, an increase in the deformations in the middle of the wall has occurred in the farthest footing (3B distance), as compared to the adjacent footings. Since the failure mode in this footing resulted in from a decrease in the strength of the soil beneath the footing (the effect of the facing failure on the bearing capacity is smaller), a large part of the stress was transferred to the depth of the soil until the geosynthetic has been raptured (see Figure 6(c)) and the deformations in the middle of the wall facing grew.

Another test was performed to improve the behavior of the reinforced soil at the distance of 2B from the facing inner edge by adding tire shred to the backfill. In

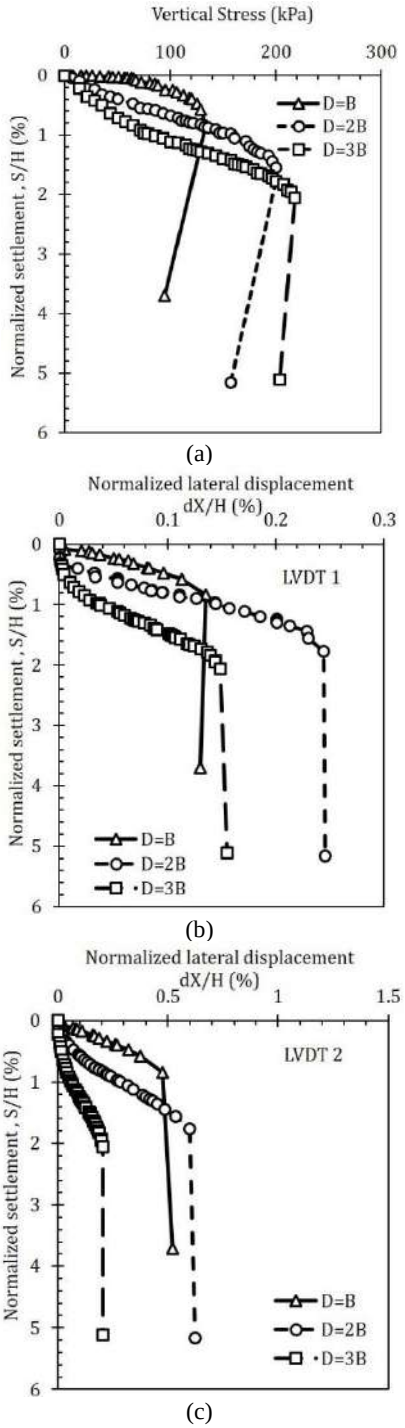

Figure 5. Results of monotonic loading tests on sand backfill, a) vertical stress vs. normalized vertical settlement, b, c) normalized lateral displacement vs. normalized vertical settlement at 0.5H and 0.75H, respectively

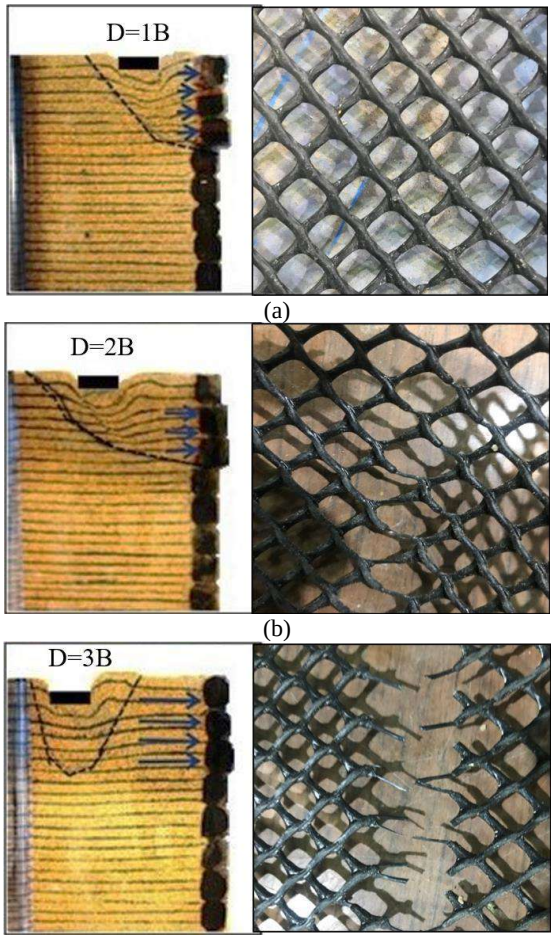

Figure 6. Deformation at the top layer of the geosynthetic after monotonic loading at a) D=1B, b) D=2B, and c) D=3B

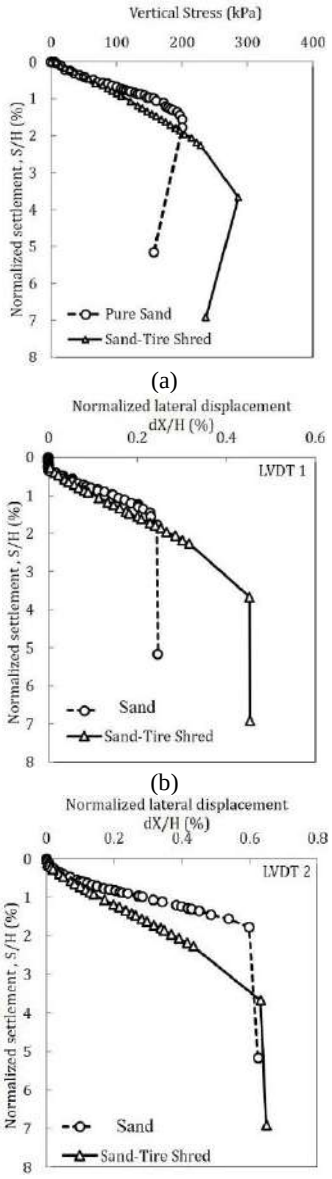

Figure 7. Results of monotonic loading tests on sand and sand-tire shred mixture, a) vertical stress vs. normalized vertical settlement, b, c) normalized lateral displacement vs. normalized vertical settlement at 0.5H and 0.75H, respectively

Figures 12(b) and 12(d), the failure mode of the wall is displayed for two states, i.e., first without tire shred, and second with sand-tire shred mixture. When the sand-tire shred mixture is used, the pressure is reduced, as noted by previous works [23,48]. The sample is exposed to more pressure, and the bearing capacity increases to approximately 290 kPa, which is almost 38% higher than the behavior of the pure sand sample (Figure 7(a)). Figures 7(b) and 7(c) demonstrate that the lateral deformations in both samples are similar before reaching a settlement of 1.7%. Afterward, the tire shred contributes to the bearing process, increasing the ductility of the lower middle part of the wall. In the upper-middle part of the wall, the deformation behavior of the sample has a milder slope, indicating that the tire shred grains take part in the bearing mechanism, and a larger load is transferred to the lower layers of the reinforced soil, which is visible in the form of distortions in the lower layer. Using 3D numerical modeling; Mahgoub and El Naggar [49] reported that tire shreds resulted in an improvement in transferring the stresses, reducing the stress influence zone underneath the footing.

4. 2. Cyclic Loading After the monotonic loading tests series, the new samples were tested under cyclic loading at three different stress levels. First, 20% of q_u (q_u is the ultimate bearing capacity of the monotonic test when D=1B) was considered as the dead load. Then, at each footing position, three different stress levels, i.e., 0.2, 0.4, and 0.6 of q_u, were applied to simulate the cyclic loadings. To this end, 200 cycles were applied to

the samples at each stress level. Figure 8 presents the values of the lateral displacement and the settlement of the footing in the GRS wall samples for three locations of the footing. In the GRS with pure sand backfill (Figures 8(a), 8(b) and 8(c)), it is observed that from cycles up to 15, the rate of the lateral deformation is almost sharp. However, as the number of cycles increases, this rate decreases. While from cycle 100 to the end, it grows slowly or remains constant. Alam et al. [50] state that the majority of the footing displacements and soil stresses occur within the primary loading cycles. In sand-tire shred mixture samples (Figures 8(d), 8e, and 8f) at a high-stress level (0.6 qu), the lateral deformations of the samples continue to increase, and reach a constant value after more cycles. It is also observed that at the same stress level, the lateral deformation decreases in all GRS walls by increasing the footing distance from the facing. In the GRS with pure sand backfill at small (0.2 q_u) and medium (0.4 q_u) stress levels, the value of the lateral deformation has increased to 1.5 to 3 times that of the case where the sand-tire shred mixture is used. In the sand-tire shred mixture samples at a high-stress level (0.6 q_u) for the location of footing at D=1B, the value of lateral displacements increases to 1.5 to 2 times that of the pure sand samples. The residual settlement at small and medium stress levels for the pure sand samples is

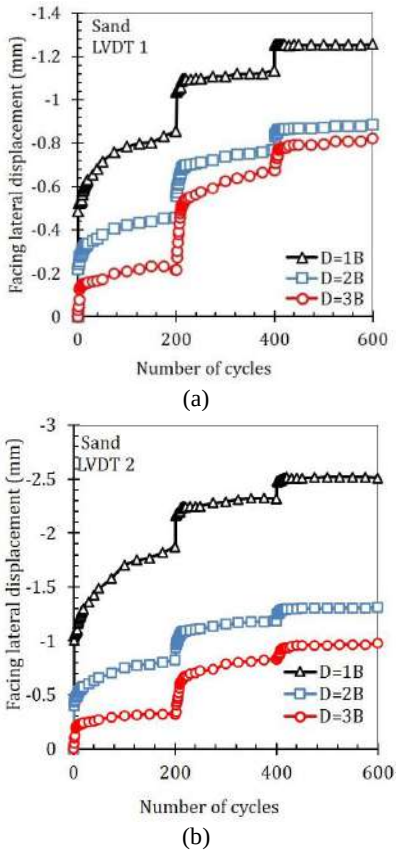

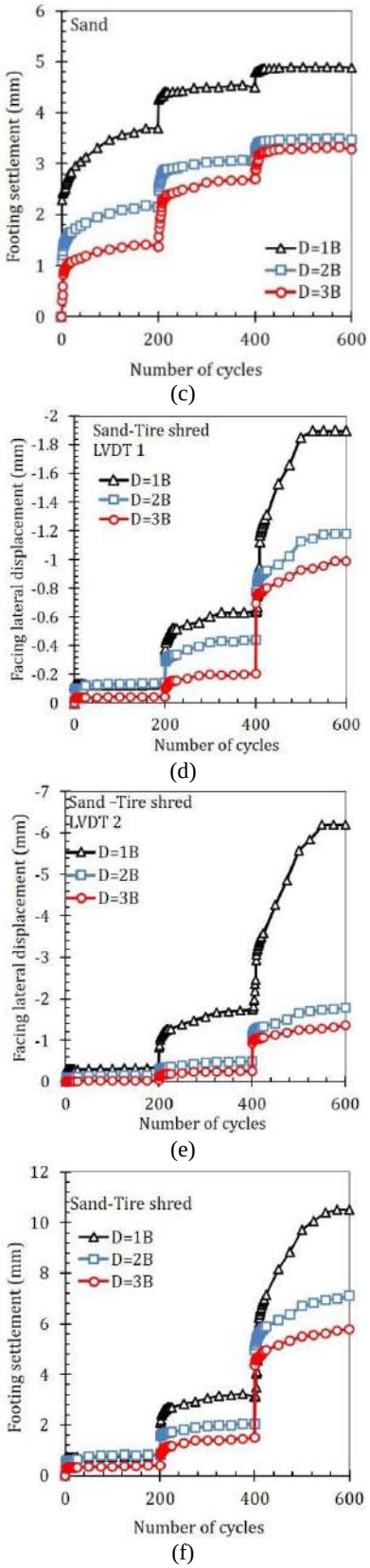

Figure 8. Results of cyclic loading: (a, b and c) on backfill without tire shred, (d, e and f) on sand-tire shred mixture backfill

higher; however, at a large stress level, this value for the sand-tire shred mixture is almost two times that of the pure sand samples.

Figure 9 shows the lateral deformation profile of the facing for all locations of footing at different stress levels. Regardless of the backfill material, with an increase in distance from the facing, the lateral deformation of the facing decreases. Also, with an increase in stress level in the cyclic loading without considering the location of the footing, the lateral deformation of the wall facing increases. Interestingly, the lateral deformation of sand-tire shred mixture GRS at low and medium stress levels is less than sand GRS wall, but at high-stress levels, it causes inverse behavior irrespective of the location of the footing.

4. 3. Post-Ccyclic Loading Following the cyclic loading, the monotonic loading of the samples was carried out at each position in the strip footing. Figure 12 presents the wall failure modes. According to these results, the wall deformations have increased at the end of the test. The bearing capacity of the specimens located at the distances of 2B and 3B has increased by approximately 23 and 26%, as compared to the pre-cyclic loading state, respectively (Figure 10(a)). However, in the sample at the least distance (B), the bearing capacity remained almost unchanged because of the very large effect of the wall facing on the sample under cyclic loading. As shown in Figures 10(b) and 10(c), the lateral deformations in the upper-middle part have increased, while they have decreased in the lower-middle part, except for the samples located at very short distances. In the upper half of the wall, lateral deformations have occurred in samples placed at the distances of B and 2B with an increase in stress. Consequently, the sliding mode and the internal instability of the wall are observed.

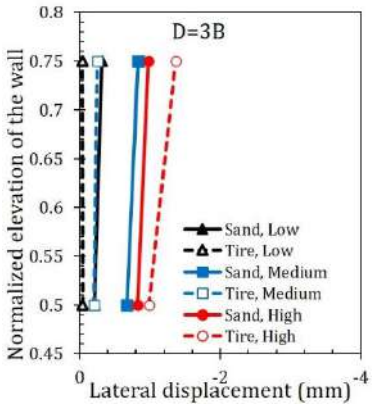

(c)

Figure 9. Lateral displacement profile of the facing in three stress levels (low, medium and high) different location of the footing a) D=1B, b) D=2B and c) D=3B

There are continued settlements in the footing with an increase in stress in the GRS containing tire shred (Figure 11). The sample experiences settlement from the onset of the loading due to the ductility of the tire shreds. However, this settlement is accompanied by little lateral deformation in the upper part of the wall up to a settlement of approximately 1.3%. Therefore, the footing settlements are reversible, and the lateral deformations in the wall are postponed until the sample

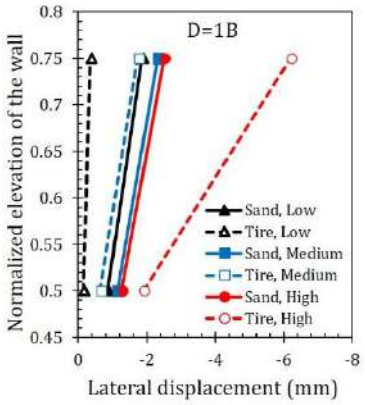

(a)

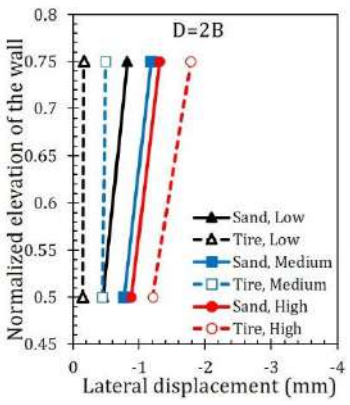

(b)

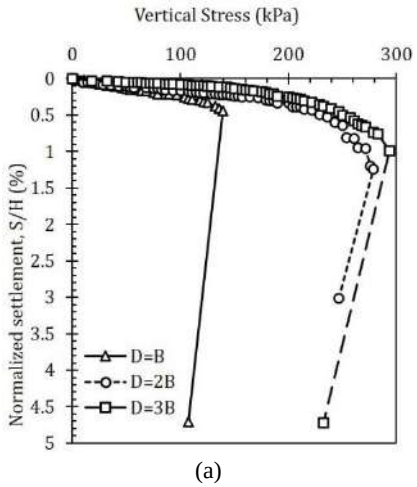

(a)

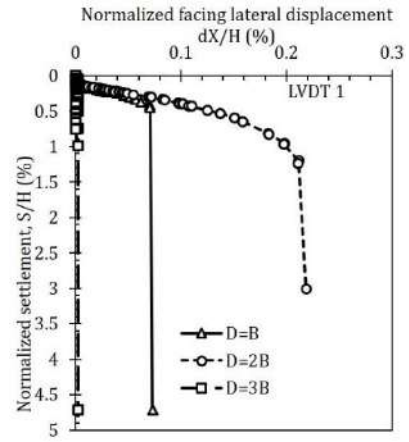

(b)

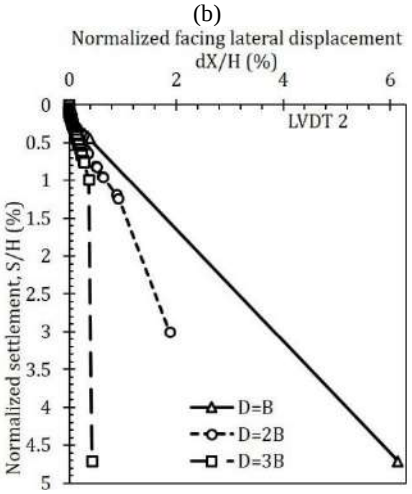

(c)

Figure 10. Results of post- cyclic loading on sand backfill, a) vertical stress vs. normalized vertical settlement, b, c) normalized lateral displacement vs. normalized vertical settlement at 0.5H and 0.75H, respectively

exceeds 90% of the peak strength. However, dX/H in the sand samples at the peak strength is approximately 1%, and it continues with the same rate until failure.

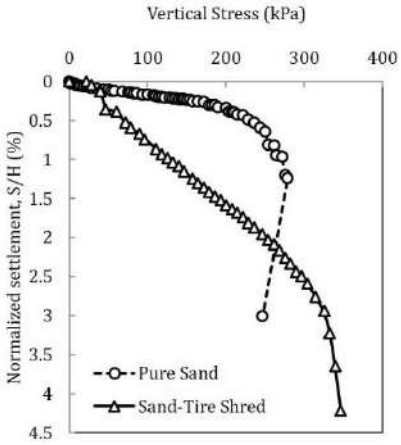

(a)

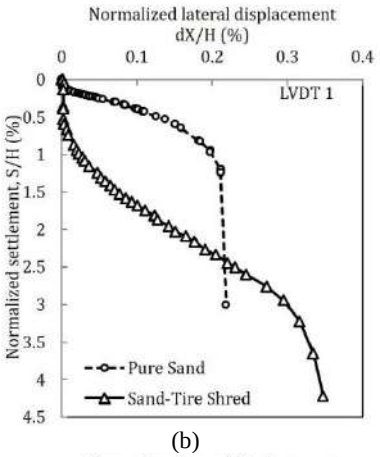

(b)

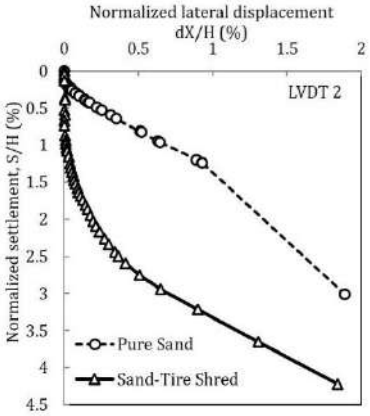

(c)

Figure 11. Results of post-cyclic loading tests on sand and sand-tire shred mixture, a) vertical pressure vs. normalized vertical settlement, b, c) normalized lateral displacement vs. normalized vertical settlement at 0.5H and 0.75H, respectively

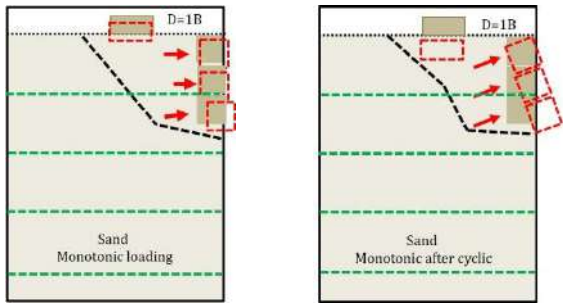

(a) (e)

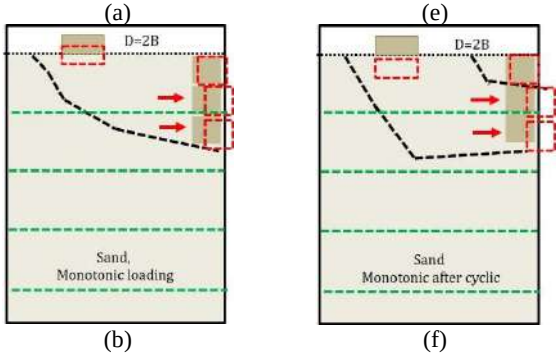

(b) (f)

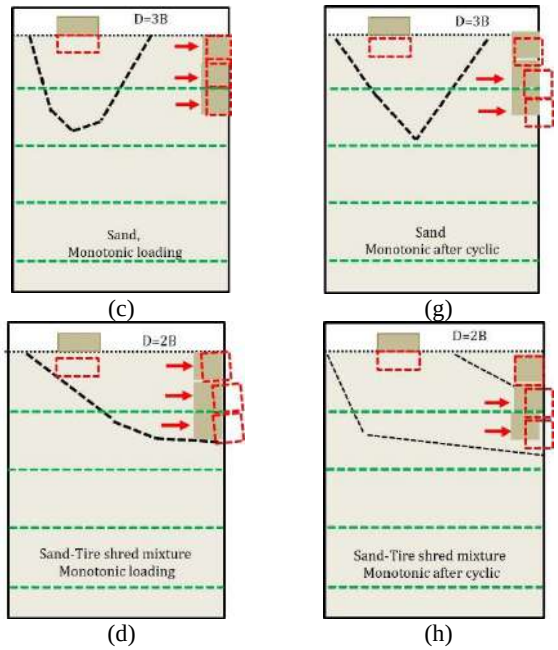

Figure 12. Failure modes for the strip footing on the GRS wall under monotonic loading before (a, b, c, d) and after cyclic loading (e, f, g, h), (drawn based on Figure 6)

The behavior of walls in monotonic and monotonic post-cyclic loading at different levels of vertical strain is illustrated in Figure 13. Figure 13(a) shows the vertical stress-vertical strain curve for the footing located on the wall. As it is observed, at the same strain levels, sand GRS presents more strength, but sand-tire shred GRS have displayed more strain due to their high ductility and increasing more resistance. Also, the monotonic post-cyclic behavior of the sand GRS, despite its higher strength, had less ductility, but in the GRS including the tire shred, the value of the change in strength and decrease in ductility is negligible.

The behavior of the lateral wall strain profiles for different percentages of vertical strain for monotonic and monotonic post-cyclic loading are demonstrated in Figures 13(b) and 13(c), respectively. At the same

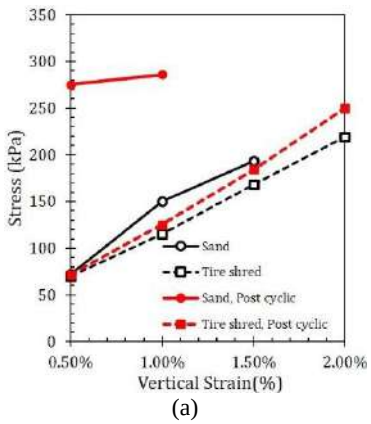

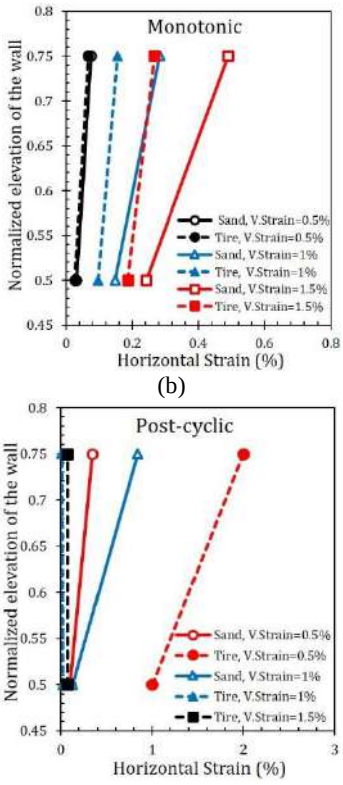

Figure 13. The behavior of walls in monotonic and monotonic post-cyclic loading at different levels of vertical strain a) the vertical stress-vertical strain curve, b and c) the behavior of the lateral wall strain profiles for different percentages of vertical strain in monotonic and post cyclic loading

vertical strain levels, the sample with the tire shred indicates less horizontal strain. The sand GRS has been failed at lower strain levels. Table 5 presents a summary to compare sand and sand-tire shred mixture parameters.

5. CONCLUSIONS

Experimental physical models were constructed to investigate the performance of the GRS walls subjected to monotonic and cyclic loadings. The wall facing was made of concrete blocks, and four layers of geosynthetic

TABLE 5. comparison of sand and sand-tire shred mixture

Test result	Pure sand	Sand-tire shred mixture
Ultimate bearing capacity, kPa	210	290
Maximum lateral deformation, mm	2.7	2.9
Bearing capacity at 0.5% vertical strain, kPa	68	68
Bearing capacity at 1% vertical strain, kPa	155	117
Bearing capacity at 1.5% vertical strain, kPa	192	171

were used in the reinforced soil wall. The effects of the position of the strip footing, stress level and sand-tire shred admixture on the lateral deformations of the wall facing, bearing capacity and the settlement beneath the footing were studied. The following conclusions can be made based on the findings from this study; however, they are limited to cases similar to those physical models considered in this study:

- The stress level significantly influenced the lateral wall deformations at the near facing footing. However, the effects of the stress level on the lateral deformations decrease drastically at far footings. The local failure of the wall was the dominant failure mode in the near facing footing. However, with an increase in the distance from the wall facing, the failure mode is shifted to internal sliding.
- Using the sand-tire shred admixture, the bearing capacity of the footing on the GRS wall was increased. Moreover, at small stress levels, the deformation behaviour of the tire shred GRS wall is more appropriate than the sand GRS wall; but at high stress levels, the deformation behaviour of the shred tire GRS is higher than that of the sand GRS.
- At post cyclic loading the bearing capacity of the samples placed at the longer distances from the facing has increased in comparison to the monotonic loading samples. However, at the short distance, the bearing capacity remains almost unchanged.

It is worthy to note that, the frequency effect and the connection between the facing blocks and geosynthetic layers are not considered. Besides, the findings are based on 12 small-scale model tests. The applicability of the results to other situations required further investigation.

6. ACKNOWLEDGMENTS

Funding received from Shahid Beheshti University (SBU) grant and the Sad Afzar company, is gratefully acknowledged.

7. REFERENCES

1. Aggarwal, P., Sharma, K. G., Gupta K. K., "Modeling of unreinforced and reinforced pavement composite material using HISS model", ***International Journal of Engineering***, Vol. 20, No. 1, (2007), 13-22.
2. Abbaszadeh, R., Vafaeian, M., "Laboratory model tests to study the behavior of soil wall reinforced by weak reinforcing layers", ***International Journal of Engineering***, Vol. 21, No. 4, (2008), 361-374.
3. Bahrami, M., Marandi S. M., "Large-scale experimental study on collapsible soil improvement using encased stone columns", ***International Journal of Engineering***, Vol. 34, No. 5, (2021), 1145-1155, DOI: 10.5829/ije.2021.34.05b.08.
4. Ehrlich, M., Mirmoradi SH. "Evaluation of the effects of facing stiffness and toe resistance on the behavior of GRS walls", ***Geotextile and Geomembranes*** Vol. 40, (2013), 28-36, DOI: 10.1016/j.geotexmem.2013.07.012.
5. Mirmoradi, SH., Ehrlich, M. "Evaluation of the effect of toe restraint on GRS walls", ***Transportation Geotechnics***, Vol. 8, (2016), 35-44, DOI: 10.1016/j.trgeo.2016.03.002.
6. Ehrlich, M., Mirmoradi, SH., Saramago, RP. "Evaluation of the effect of compaction on the behavior of geosynthetic-reinforced soil walls", ***Geotextile and Geomembranes,*** Vol. 34, (2012), 108-115, DOI: 10.1016/j.geotexmem.2012.05.005.
7. Zheng, Y., Fox, PJ., McCartney, JS. "Numerical study of the compaction effect on the static behavior of a geosynthetic reinforced soil-integrated bridge system", ***Geotechnical Speccial Publications***, (2017), 33-43, DOI: 10.1061/9780784480458.004.
8. Mirmoradi, SH., Ehrlich, M., Chinchay, P., Dieguez, C. "Evaluation of the combined effect of facing inclination and uniform surcharge on GRS walls", ***Geotextile and Geomembranes***, Vol. 47, No. 5, (2019), 685-691, DOI: 10.1016/j.geotexmem.2019.103485.
9. Doger, R., Hatami, K. "Influence of facing on the performance of GRS bridge abutments", ***International Journal of Geosynthetics and Ground Engineering***, Vol. 6, No. 4, (2020), DOI: 10.1007/s40891-020-00225-y.
10. Helwany, SMB., Wu, JTH., Kitsabunnarat, A. "Simulating the behavior of GRS bridge abutments", ***journal of Geotechnical and Environmental Engineering***, Vol. 33, (2007), 1229-1240, DOI: 10.1061/(ASCE)1090-0241(2007)133:10(1229).
11. Zheng, Y., Fox, PJ. "Numerical investigation of geosynthetic-reinforced soil bridge abutments under static loading", ***Journal of Geotechnical and Environmental Engineering***, Vol. 142, (2016), 1-13, DOI: 10.1061/(ASCE)GT.1943-5606.0001452.
12. Ardah, A., Abu-farsakh, M., Voyiadjis, G. "Numerical evaluation of the performance of a geosynthetic reinforced soil-integrated bridge system (GRS-IBS) under different loading conditions", ***Geotextile and Geomembranes***, Vol. 45, No. 6, (2017), 558-569, DOI: 10.1016/j.geotexmem.2017.07.005
13. Abu-Farsakh, M., Ardah, A., Voyiadjis, G. "Numerical investigation of the performance of a geosynthetic reinforced soil-integrated bridge system (GRS-IBS) under working stress conditions", ***Geotechnical Special Publications***, (2018), 76-87, DOI: 10.1061/9780784481608.008.
14. Mirmoradi, SH., Ehrlich, M. "Experimental evaluation of the effects of surcharge width and location on geosynthetic-reinforced soil walls", ***International Journal of Physical Modelling in Geotechnics***, Vol. 19, (2019), 27-36, DOI: 10.1680/jphmg.16.00074.
15. Helwany, SMB., Reardon, G., Wu, JTH. "Effects of backfill on the performance of GRS retaining walls", ***Geotextile and Geomembranes***, Vol. 17, (1999), 1-16, DOI: 10.1016/S0266-1144(98)00021-1.
16. Hatami, K. "Parametric analysis of reinforced soil walls with different backfill material properties", Geo engineering centre at queen's-RMC royal military college of Canada, (2005).
17. Hatami, K., Witthoeft, AF. "A numerical study on the use of geofoam to increase the external stability of reinforced soil walls", ***Geosynthetic International***, Vol. 15, (2008), 452-470, DOI: 10.1680/gein.2008.15.6.452.
18. Zheng, Y., Fox, PJ., McCartney, JS. "Numerical simulation of deformation and failure behaviour of geosynthetic reinforced soil bridge abutments", ***Journal of Geotechnical and Environmental Engineering***, Vol. 144, No. 7, (2018), DOI: 10.1061/(ASCE)GT.1943-5606.0001893.
19. Wu, JTH., Ooi, PSK. "Synthesis of geosynthetic reinforced soil (GRS) design topics", HWA-HRT-14-094, Federal Highway Administration, Washington, D.C., USA., (2015),

20. Xiao, C., Han, J., Zhang, Z. "Experimental study on performance of geosynthetic-reinforced soil model walls on rigid foundations subjected to static footing loading", ***Geotextile and Geomembranes***, Vol. 44, (2016), 81-94, DOI: 10.1016/j.geotexmem.2015.06.001.
21. Masad, E., Taha, R., Ho, C., Papagiannakis, T. "Engineering properties of tire/soil mixtures as a lightweight fill material", ***Geotechnical Testing Journal***, Vol. 19, (1996), 297-304, DOI: 10.1520/GTJ10355J.
22. Chaney, R., Demars, K., Feng, Z-Y. Sutter K. "Dynamic properties of granulated rubber/sand mixtures", ***Geotechnical Testing Journal***, Vol. 23 No. 3, (2000), 338-344, DOI: 10.1520/GTJ11055J.
23. Xiao, M., Bowen, J., Graham, M., Larralde, J. "Comparison of seismic responses of geosynthetically reinforced walls with tire-derived aggregates and granular backfills", ***Journal of Materials in Civil Engineering***, Vol. 24, (2012), 1368-1377, DOI: 10.1061/(ASCE)MT.1943-5533.0000514.
24. Iai, S. "Similitude for shaking table tests on soil-structure-fluid model in 1g gravitational field", ***Soils and Foundations***, Vol. 29, (1989), 105-118, DOI: 10.3208/sandf1972.29.105.
25. Komak Panah, A., Yazdi, M., Ghalandarzadeh, A. "Shaking table tests on soil retaining walls reinforced by polymeric strips", ***Geotextile and Geomembranes***, Vol. 43, (2015), 148-161, DOI: 10.1016/j.geotexmem.2015.01.001.
26. Latha, GM., Santhanakumar, P. "Seismic response of reduced-scale modular block and rigid faced reinforced walls through shaking table tests", ***Geotextile and Geomembranes***, Vol. 43, (2015), 307-316, DOI: 10.1016/j.geotexmem.2015.04.008.
27. ASTM D422-63. "Standard test method for particle-size analysis of soils", ASTM International, West Conshohocken, PA, USA., (2007).
28. Maroof, MA., Mahboubi, A., Noorzad, A., Safi, Y. "A new approach to particle shape classification of granular materials", ***Transportation Geotechnics***, Vol. 22, (2020), DOI: 10.1016/j.trgeo.2019.100296.
29. ASTM D4253. Standard test methods for maximum index density and unit weight of soils using a. ASTM International, West Conshohocken, PA, USA., (2006).
30. Indraratna, B., Sun, Q., Grant, J. "Behaviour of subballast reinforced with used tyre and potential application in rail tracks", ***Transportation Geotechnics***, Vol. 12, (2017), 26-36, DOI: 10.1016/j.trgeo.2017.08.006.
31. ASTM D6637. "Standard Test method for determining tensile properties of geogrids by the single or multi rib tensile method", ASTM International, West Conshohocken, PA, USA. (2010).
32. Xiao, C., Han, J., Zhang, Z. "Experimental study on performance of geosynthetic-reinforced soil model walls on rigid foundations subjected to static footing loading", ***Geotextile and Geomembranes***, Vol. 44 No. 1, (2015), 81-94, DOI: 10.1016/j.geotexmem.2015.06.001.
33. Adams, M., Nicks, J., Stabile, T., Wu, J., Schlatter, W., Hartmann, J. "Geosynthetic reinforced soil integrated bridge system, Synthesis report", 64., (2011).
34. Adams M.T., Saunders S.A. "Upper ouachita national wildlife refuge GRS abutments for replacement bridges", Presentation by Adams, M., and Saunders, S.A., FHWA., (2007).
35. Zheng, Y., Fox, PJ., Mccartney, JS. "Numerical study on maximum reinforcement tensile forces in geosynthetic reinforced soil bridge abutments", ***Geotextile and Geomembranes***, Vol. 46, (2018), 634-645, DOI: 10.1016/j.geotexmem.2018.04.007.
36. Ramalakshmi, M., Dodagoudar, GR. "Passive force–displacement behaviour of GRS bridge abutments", ***International Journal of Geosynthetics and Ground Engineering***, Vol. 4, (2018), DOI: 10.1007/s40891-018-0145-7.
37. Prasad, DSV., Raju, GVRP. "Performance of waste tyre rubber on model flexible pavement", ***Journal of Engineering and Applied Science***, Vol. 4, (2009), 89-92.
38. Munnoli, PM., Sheikh, S., Mir, T., Kesavan V, Jha R. "Utilization of rubber tyre waste in subgrade soil", ***IEEE Glob. Humanit. Technol. Conf***. South Asia Satell., IEEE, (2013), 330-333, DOI: 10.1109/GHTC-SAS.2013.6629940.
39. Yeo, B., Yen, SC., Puri, VK., Das, BM., Wright, MA. "A laboratory investigation into the settlement of a foundation on geogrid-reinforced sand due to cyclic load", ***Geotechnical and Geological Engineering***, Vol. 11, (1993), 1-14, DOI: 10.1007/BF00452917.
40. El-Sawwaf, M., Nazir, AK. "Behaviour of repeatedly loaded rectangular footings resting on reinforced sand", ***Alexandria Engineering Journal***, Vol. 49, (2010), 349-356, DOI: 10.1016/j.aej.2010.07.002.
41. Moghaddas Tafreshi, SN., Dawson, AR. "Behaviour of footings on reinforced sand subjected to repeated loading- Comparing use of 3D and planar geotextile", ***Geotextile and Geomembranes***, Vol. 28, (2010), 434-447, DOI: 10.1016/j.geotexmem.2009.12.007.
42. Islam, MA., Gnanendran, CT. "Slope stability under cyclic foundation loading - Effect of loading frequency", ***Geo-Congress Reston***, VA: American Society of Civil Engineers, (2013), 750-761, DOI: 10.1061/9780784412787.075.
43. Khosrojerdi, M., Qiu, T., Xiao, M., Nicks, J. "Effects of backfill constitutive behaviour and soil–geotextile interface properties on deformations of geosynthetic-reinforced soil piers under static axial loading", ***Journal of Geotechnical and Environmental Engineering***, Vol. 146, (2020), DOI: 10.1061/(ASCE)GT.1943-5606.0002313.
44. Xie, Y., Leshchinsky, B., Han, J. "Evaluation of bearing capacity on geosynthetic-reinforced soil structures considering multiple failure mechanisms", ***Journal of Geotechnical and Environmental Engineering***, Vol. 145, (2019), DOI: 10.1061/(ASCE)GT.1943-5606.0002072.
45. Bathurst, RJ. "Challenges and recent progress in the analysis, design and modelling of geosynthetic reinforced soil walls", ***10th International Conference of Geosynthetic*** *ICG* (2014).
46. Ahmadi, H., Hajialilue-Bonab, M., "Experimental and analytical investigations on bearing capacity of strip footing in reinforced sand backfills and flexible retaining wall", ***Acta Geotechinca***, Vol. 7, (2012), 357-373, DOI: 10.1007/s11440-012-0165-8.
47. Li, L-H., Yu, C-D., Xiao, H-L., Feng, W-Q., Ma, Q., Yin, J-H. "Experimental study on the reinforced fly ash and sand retaining wall under static load", ***Construction and Building Materials***, Vol. 248, (2020), DOI: 10.1016/j.conbuildmat.2020.118678.
48. Mahgoub, A., El Naggar, H. "Innovative application of tire-derived aggregate around corrugated steel plate culverts", ***Journal of Pipeline Systems and Engineering Practices***, Vol. 11, (2020), Article 04020025, DOI: 10.1061/(ASCE)PS.1949-1204.0000466.
49. Mahgoub, A., El Naggar, H. "Shallow foundations on lightweight TDA backfill: Field tests and 3D numerical modelling", ***Computers and Geotechnics***, Vol. 126, (2020), DOI: 10.1016/j.compgeo.2020.103761.
50. Alam, MJI., Gnanendran, CT., Lo, SR. "Modelling the settlement behaviour of a strip footing on sloping sandy fill under cyclic loading conditions", ***Computers and Geotechnics***, Vol. 86, (2017), 181-92, DOI: 10.1016/j.compgeo.2017.01.010.

Persian Abstract

چکیده

در این مقاله، رفتار مکانیکی دیواره های خاک مسلح ژئوسنتتیکی (GRS) با استفاده از مدل سازی فیزیکی تحت بارهای مونوتونیک و سیکلی ناشی از پی نواری در مسیرهای مختلف تنش بررسی شده است. تأثیر محل قرارگیری پی، سطح تنش، رفتار مونوتونیک نمونه ها پس از بارگذاری سیکلی و استفاده از مخلوط ماسه–خرده تایر بر روی تغییر شکل های جانبی رویه دیوار، ظرفیت باربری و نشست پی نواری مورد بررسی قرار گرفت. برای این منظور، ۱۲ آزمایش مدل فیزیکی با مقیاس ۱:۴ انجام شد. نتایج نشان داد که با افزایش فاصله پی نواری از رویه دیوار و افزودن خرده تایر به مصالح دیوار، ظرفیت باربری افزایش می یابد، اما افزایش ظرفیت باربری ناشی از افزودن خرده تایر به مصالح خاکریز به مراتب بیشتر است. همچنین محل قرارگیری پایه از رویه دیوار پارامتر مهمی در تغییر شکل رویه دیوار و حالت خرابی پی بود. مد غالب گسیختگی برای زمانی که پی در نزدیکی رویه دیوار قرار داشت، به صورت خراب شدن کلی رویه بود اما در حالت قرارگیری پی نواری با فاصله دور از رویه دیوار، پارگی ژئوسنتتیک عامل خرابی مجموعه دیوار و پی نواری بود. همچنین نتیجه آزمایشات بارگذاری سیکلی نشان داد که جابجایی دائمی رویه و نشست باقیمانده پی نواری با سیکل های بار به طور تجمعی افزایش می یابند و اکثر آنها در پانزده سیکل اول رخ می دهند.

IJE TRANSACTIONS A: Basics Vol. 34, No. 10, (October 2021) 2280-2293

International Journal of Engineering
Journal Homepage: www.ije.ir

Comparative Study on Structural Behavior of Reinforced Concrete Straight Beam and Beams with out Plane Parts

M. S. Mohsin, N. A. Alwash, M. M. Kadhum*

Civil Engineering Department, College of Engineering, Babylon University, Iraq

P A P E R I N F O

Paper history:
Received 21 May 2021
Received in revised form 25 June 2021
Accepted 02 July 2021

Keywords:
Concrete Beams
Out of Plane Part
Normal Strength Concrete
Angle of Twist

A B S T R A C T

This paper aims to experimentally investigate and compare the structural behavior of reinforced concrete straight beam and other beams there made with one, two, and three out of plane parts. The study focused on the effect of the number and location of the out plane parts on the beams mid span deflection, and rotation, as well as the ductility index, cracking loads, and failure modes. Four beams were fabricated with a cross-sectional width of 150 mm and a depth of 200 mm, and 2000 mm in length. All the beams were made with normal strength concrete and constant longitudinal reinforcement ratio 0.011 for negative and positive moments. All the beam specimens were clamped by a special steel fixed ends and subjected to the two-point load up to their failure. The obtained results presented that the load bearing capacity of straight beam was higher than the beams with out of plane parts. Furthermore, the beam with two out of plane parts has capacity higher than the beams with one and three out of plane part by 5.86 and 55.07%, respectively. In addition, the results showed that the ductility increased with increasing number of out of plane parts by 5.52%, and 32.71% as copared with the beam with one out of plane part.

***doi**: 10.5829/ije.2021.34.10a.09*

1. INTRODUCTION

A reinforced concrete structures can be cast to take the shape required, making it widely used to mix the architectural and structural requirements. It is also maintain the aesthetic of the buildings, because it is yields as rigid members with minimum apparent deflection. In some special cases in low-rise and high-rise buildings inside and outside them, the designer need to change the straight path of the beams to a non-straight path, whether for architectural purposes or to reduce the number of columns to provide a wider utilization of space, like corner beams, balcony beams, grid beams system, zigzag concrete beams, and other architectural application requirements. Examples of this type of members as in Sky House Tokyo in Japan, Complex structural layout in China, Cross-bracing concrete beam in Budapest metro stations, Concrete Balconies in National Theatre, London and Modern concrete buildings with cantilever corner balcony beams as shown in Figure 1. This variation within the axis of the beam led to a change in its structural behavior in terms of its strength including bending, shear, torsion and lateral torsional buckling as compared with the straight members. Therefore, there are researchers studied the structural behavior of the reinforced concrete beams under combined loading of torsion, bending, and shear to evaluate the effect of load application method on the beam .

Owainati [1] studied the effects of using different combinations loadings of torsion, bending and shear with the different torsion to shear ratio, and different ratios of transverse and longitudinal reinforcement on the structural behavior of rectangular reinforced concrete beams that made with a wing loading arms at the front and back sides of the beam to apply the torsional loads. The study concluded that the cracks' shapes and failure mode was affected by the loading type. Moreover, an increase in the ratio of longitudinal and transverse reinforcement enhanced each of the

*Corresponding Author Institutional Email: eng.mohammed.mansour@uobabylon.edu.iq (M. M. Kadhum)

Please cite this article as: M. S. Mohsin, N. A. Alwash, M. M. Kadhum, Comparative Study on Structural Behavior of Reinforced Concrete Straight Beam and Beams with out Plane Parts, International Journal of Engineering, Transactions A: Basics, Vol. 34, No. 10, (2021) 2280-2293


(a) Sky House Tokyo, Japan


(b) Complex structural layout, China


(c) Cross-bracing in Budapest metro stations


(d) Balconies in National Theatre, London


(e) Modern concrete buildings with cantilever corner balcony beams

Figure 1. Beam with out of plane parts applications

cracking and ultimate load, but the transverse reinforcement is more effective in increasing the cracking torsional moment. Ali and Anis [2] analyzed the reinforced concrete floor to spandrel beam assembly by experimental work and analytical solution to study the effects of loading arrangement on the structural behavior like flexural strength, torsional capacity and deformations. The structural model loaded by two types of loading, first one by applied concentrated load at mid-span of the floor beam and made the spandrel beam exposed to pure torsional moment, while the second one by applied concentrated load at the joint of floor beam to spandrel beam in addition to first loading and made it exposed to combined loading. According to the load-deflection relationship, the study results showed that the ductility decreased and the angle of twist at the ultimate load increased when the model exposed to the combined loading type two. Kamiński and Pawlak [3] adopted the experimental work and numerical analyses to investigate the load capacity and stiffness of angular and rectangular beams under two types of loading. The first type of loading was a pure torsional moment and the second type was a combined load of a torsional moment plus a shearing force and a bending moment. The analyses results conclude that the load capacity and stiffness of the beams decreased when their exposed to combined loading of both a torsional moment and bending moment as compared with the beams that just loaded with a torsional moment.

ACI 445.1R-12 [4] based on the theoretical and experimental results of many previous researches for the reinforced rectangular concrete beams under three types of loading pure torsion, bending plus torsion, and shear plus torsion and explained that the presence of a bending moment reduced the torsional ductility of the beams and the torsion to bending moment ratio affected on the diagonal compression angle and the pattern of the cracks, the cracks were diagonal on the bottom face under pure torsion, but the cracks angle became normal to the longitudinal axis of the beam under pure bending. Elsayed et al. [5] investigated the effect of increasing the angle of cantilever's inclination and reinforcement ratio on the behavior of rectangular cross-section reinforced concrete beams. The result of the investigation summarized that increasing the angle of cantilever inclination has a little effect on the cracking and ultimate loads, but the overall stiffness of beams which depend on the maximum deflection and maximum strain and highly affected. An increase in the main longitudinal reinforcement ratio led to an increase in the diagonal cracking load, ultimate load, and flexural cracking load, respectively. Kai and Li [6] tested reinforced concrete frames subjected to the loss of the ground corner which represents corner panels. The experimental and analytical study results showed that the loss of the corner column caused the progressive collapse of the frame and plastic hinge developed at the beam end near to the corner joint when using a moderate ratio of transverse reinforcement in the corner joint region .

Rafeeq [7] studied by experimental work the behavior of fixed ends rectangular reinforced concrete beams subjected to the two different types of loading, first one was bending plus shear and the second one was bending and shear plus torsion. The study concluded that the torsional load is substantially reduced the beam load bearing capacity. Thus, if torsional loading is not considered in beam design or the beam has a deficiency

in torsional reinforcement, it is necessary to strengthen the beam. Talaeitaba and Mostofinejad [8] investigated the behavior of fixed supports RC beams under combined shear and torsion. The first case by applying pure shear force, and the other cases was shear plus different value of torsion and the last case was pure torsion. The experimental test results showed that the beam under pure shear has the highest ultimate load of all tested beams and the beam under combined of shear plus high torsion value is the lowest bearing capacity, but the beam under pure torsion has the middle bearing capacity value of them.

Amulu and Ezeagu [9] studied the effect of the combined loadings of torsional moments, bending moments, and shear forces on the behavior of normal strength reinforced concrete beams by using standard design codes and experimental work. This study concluded that the beams failures were due to the combined actions of torsion, shear, and bending moment effects. Therefore, an increase in the capacity of the beams to resist the applied combined loads, were as a result of the increased longitudinal and transverse reinforcements ratio. Also proved that the capacity of the beams can be increased to resist the effects of combined loads by using the amount of reinforcement obtained from torsional design calculations and should be provided in addition to the total amount of bending and shear reinforcement at ultimate loads. Nagendra and Kumar [10] analyzed rectangular reinforced concrete beams with a cantilever L-span under torsional loading by experimental work and numerical analysis to study the effects the reductions of longitudinal and transverse reinforcement on the beams behavior. The beams were provided with reinforcement to resist bending moment and without torsional moment resisting reinforcement. The torsional test is based on the strength of membrane elements subjected to pure shear that was also applied to beams subjected to combined shearing forces, bending moments. The experimental and numerical analysis results showed that the decreasing of longitudinal and transvers reinforcement caused a reducing of beams torsional capacity, but the reducing of longitudinal reinforcement caused the beam failed earlier than beam with reducing of transvers reinforcement.

Most of the researches currently available have been focused on the structural behavior of the beams under the effect of combined loads that loaded by side arms in pure torsion or combined of shear force, bending moment, and torsion moment, but it is too limited or in the otherwise is not available researches about reinforced concrete beam with out of plane parts. As indicated by the best of the authors' knowedge, this study is the first experiment to investigate the structural behavior of beams with the out of plane parts as compared with the straight beam. The main objective of this research is to discover the difference in behavior between the straight beam and the beam containing out of plane parts in its longitudinal path, as well as the effect of the locations and number of these out of plane parts on the structural behavior. Therefore, a laboratory result was obtained proved that the classical method of design of straight beam needs to be modified including the torsional effect resulting from existing out of plane parts, and their failure mode was different and their load bearing capacity was also less than the straight beam.

2. EXPERIMENTAL PROGRAM

2. 1. Specimens Preparation In this paper, all reinforced normal strength concrete beams with one, two, and three out of plane parts and straight control beam were fabricated and loaded with a constant a/d ratio of 2.647. All tested specimens had a total span 2000 mm and effective span 1500 mm with rectangular cross-section of 150 mm width, 200 mm depth. The beams description and their material hardened properties are summarized in Table 1. All specimens were designed according to ACI Code [11], the reinforcement cage include six deformed longitudinal bars of a 12mm diameter, and 8mm diameter bars as square ties with 135^0 minimum inside bend standard hook with a uniformly spaced 81mm center to center along the beams length, as shown in Figure 2. The

TABLE 1. The beams label and their material hardened properties

Symbols	Refer to	Splitting tensile strength (MPa)	Flexural Tensile Strength (Modulus of Rupture) (MPa)	Average concrete compressive strength at 28 days (MPa)
NSC-S	Normal Strength Concrete Straight Beam	2.56	7.37	35
NSC-1OP	Normal Strength Concrete Beam with One Out of Plane Part	2.56	7.37	35
NSC-2OP	Normal Strength Concrete Beam with Two Out of Plane Part	2.56	7.37	35
NSC-3OP	Normal Strength Concrete Beam with Three Out of Plane Parts	2.56	7.37	35

*Standard cylinders (150mm×300 mm) were used to evaluate the compressive strength of concrete.

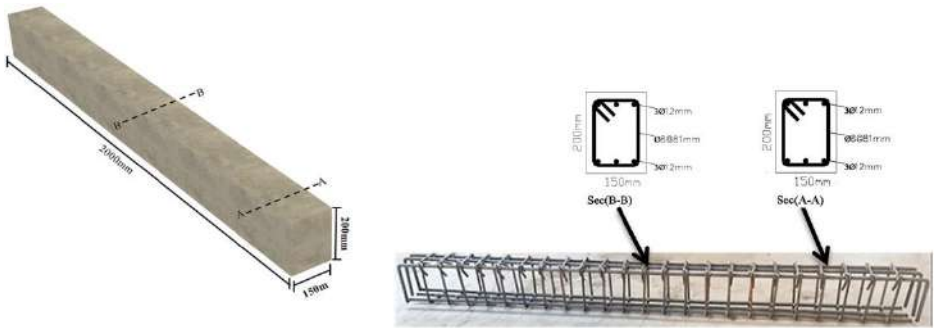

(a) Geometry and reinforcement of NSC-S beam

(b) Geometry and reinforcement of NSC-1OP beam

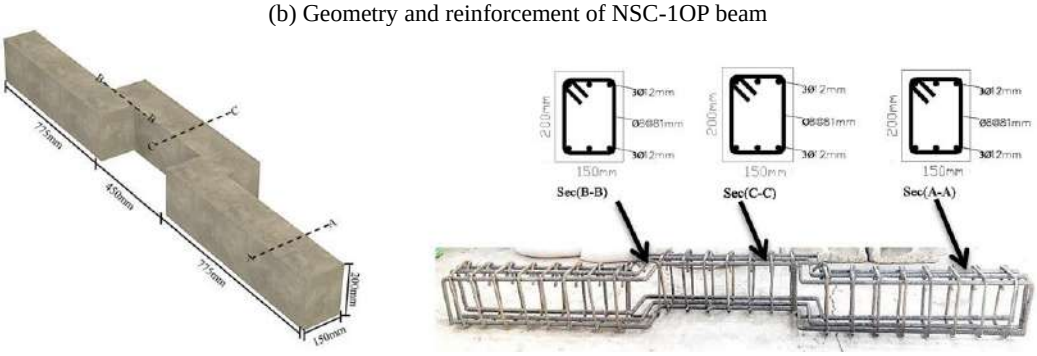

(c) Geometry and reinforcement of NSC-2OP beam

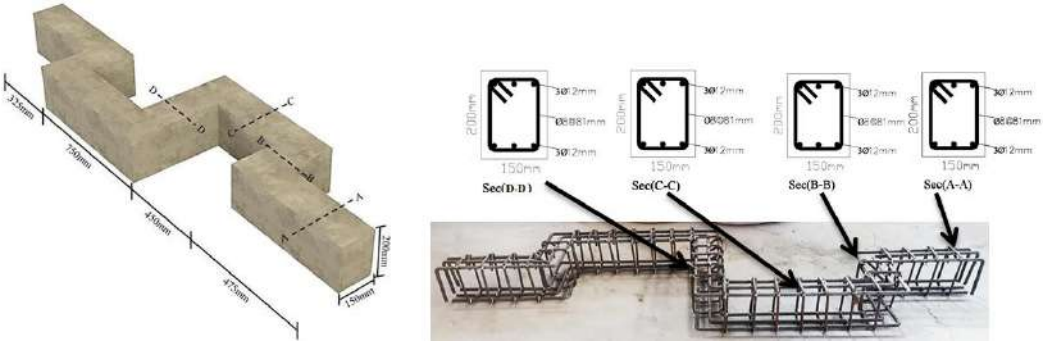

(d) Geometry and reinforcement of NSC-3OP beam

Figure 3. Geometry and reinforcement details of tested beams

reinforcement cage was incorporated into plywood molds and using 160 mm concrete spacers as a concrete cover from all sides. The tensile yield strengths for 8 mm and 12 mm bars were 559 and 413 MPa, respectively. The flexural tensile strength was estimated for the prisms of dimensions (100×100×400) mm according to ASTM C78-02 [12]. The tensile strength also measured by splitting tensile strength for concrete cylinders of (100 mm diameter ×200 mm length) according to ASTM C496/C 496M-04 [13].

The longitudinal and transverse reinforcement that used in the beams with out of plane part was the same that used in the control straight beam. The control beam designed according to ACI Code [11] based on its own of bending moment and shear force. The longitudinal reinforcement of flexural behavior was used as a

constant ratio of 0.011 for a negative and positive moment and then the required transverse tie reinforcement was calculated and the ultimate load that was expected to applied in the experimental work. The analytical equations based on the case that shown in Figure 3 and used to calculate the required applied load and the required transverse reinforcement as below:

$$R_A = V_A = R_B = V_B = P \quad (1)$$

$$M_A = M_B = \frac{P.a(L-a)}{L} \quad (2)$$

$$M_C = M_D = \frac{P.a^2}{L} \quad (3)$$

where; P is the applied load, R_A and R_B is the reactin at suupports, V_A and V_B is the shear force at suupports, and L is the effctive span of beam.

Then substitute these equations into the ACI Code [11] design equations to calculate the applicable ultimate load (P) at supports and mid span as below:
(a) Calculate nominal strength bending moment as:

$$M_n = A_s.f_y\ (d - \frac{a}{2}) \quad (4)$$

(b) Calculations of ultimate load at supports by equating the nominal bending moment strength to the applied load bending moment at point A or B as:

$$M_n = M_A + M_{D.L} = \frac{P.a(L-a)}{L} + \frac{W_{Self}.L^2}{12}$$
$$P_{Max} = \frac{M_n.L}{a(L-a)} - \frac{W_{Self}.L^3}{12a(L-a)} \quad (5)$$

(c) Calculations of ultimate load at mid span by equating the nominal strength bending moment to the applied load bending moment at point C or D as:

$$M_n = M_C + M_{D.L} = \frac{P.a^2}{L} + \frac{W_{Self}.L^2}{24}$$
$$P_{Max} = \frac{M_n.L}{a^2} - \frac{W_{Self}.L^3}{24\,a^2} \quad (6)$$

where; M_n is the nominal bending moment, M_C is the live load bending moment at loading point, $M_{D.L}$ is the dead load bending moment, W_{self} is the beam self-weight, A_s is the area of reinforcement, f_y is the yield strength of reinforcement, d is the effective depth of beam, ɑ is the shear span, and a= compression stress block depth = $\frac{A_s f_y}{0.85 f c' b}$.

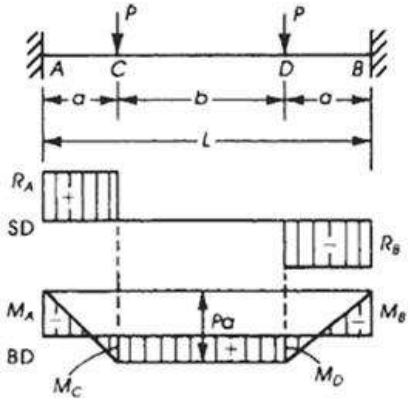

Figure 3. Fixed ends beam aid

The shear reinforcement required and their spacing was calculated as follows:

$$ØV_C = 0.75 b_w d \frac{\sqrt{f_c'}}{6} \quad (7)$$

$$V_S = \frac{1}{Ø}(V_U - ØV_C) \quad (8)$$

$$S = \frac{A_v f_y d}{V_S} \quad (9)$$

Check for maximum spacing to provide Av as:

$$S = \begin{cases} \frac{16\,A_v f_y}{b_w d\sqrt{f_c'}} \\ \frac{3A_v f_y}{b_w} \\ \frac{d}{2} \\ 600 \end{cases} \quad (10)$$

where; V_C is the Shear strength of concrete, V_U is the shear force due to applied loads, b_w is beam width, A_v is the total area of shear reinforcement within a spacing S, V_S is the shear reinforcement strength, S is the spacing between stirrups or ties.

All the beams without of plane parts reinforced with the same reinforcement of the control straight beam in flexural and shear.

The beams in this study were fabricated by using normal strength concrete (NSC) that designed according to ACI Committee 211.1-01[14] by using an ordinary Portland cement, natural clean sand, partial crashed coarse aggregate with maximum size 12mm, and water, as shown in Table 2.

The properties of fresh concrete were found by workability slump flow test and fresh density and shown in Table 3; while the hardened properties evaluated by compressive strength, splitting tensile strength, and flexural tensile strength test as mentioned in Table 1.

TABLE 2. Mix design to produce 1m^3 of normal strength concrete.

Cement (kg)	Fine aggregate (kg)	Coarse aggregate (kg)	Water (kg)
400	818.16	946	214.6

TABLE 3. The properties of fresh concrete test results

Concrete Type	Slump flow (mm)	Fresh density (Kg/m^3)
NSC	60	2422

The models were prepared to compare the structural behavior of NSC beams with out of plane part with a control NSC-S beam to evaluate the effect of the number and location of these out of plane parts on their structural behavior as compared with the straight beam.

2. 2. Test Setup and Instrumentation The tested beams were supported by using a special clamping steel frame of HP section which clamped to ends of the beams as shown in the schematic drawn in Figure 4 and experimental test set up in Figure 5. A

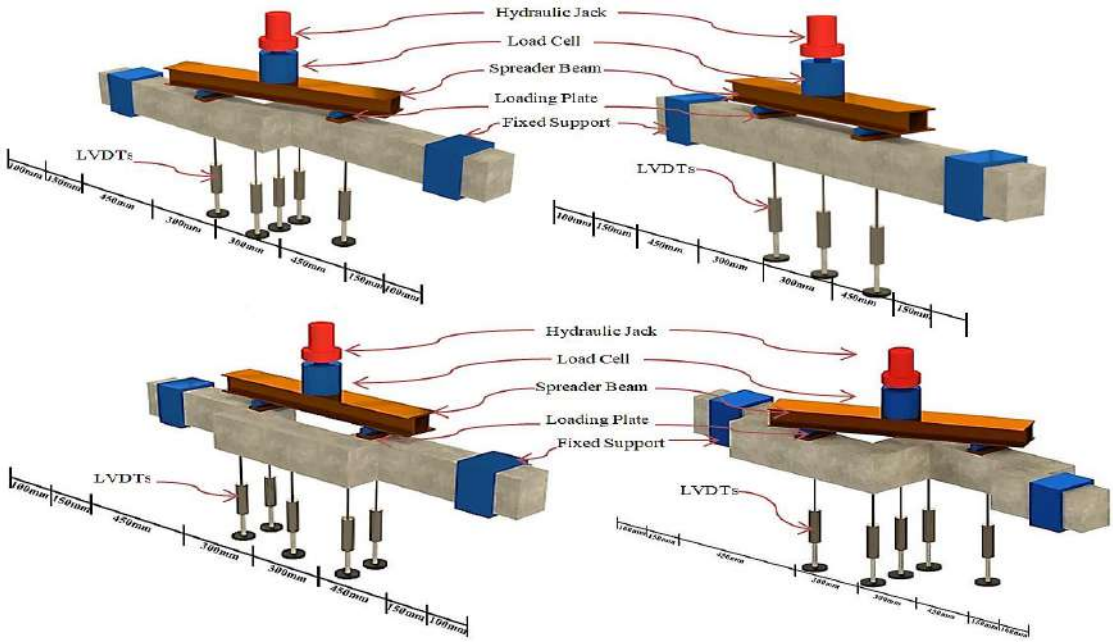

Figure 4. Schematic of Test set up

Figure 5. Experimental Test set up

clear span of 1500 mm between the supports was loaded with a two-point load to evaluate the structural performance of the beams. The shear span to effective depth (a/d) ratio was fixed value by using a distance of 450mm from the loading point to the interior face of support. The length of the flexural span between the loading points is equal to 600 mm. The universal test machine with a hydraulic jack of 1000 KN capacity were used to applied the load with gradually increments of 5 KN up to failure. The load was monitored by installing the load cell between the jack and a spreader stiff beam. The deflection at mid span and under the loading points was monitored by using electrical LVDTs were positioned vertically under the beams. The angle of twist at the mid span of beams was measured by taking the difference between readings of back and front LVDTs and divided by the distance between them and using trigonometric functions.

All the test devices described above were connected to an electrical data logger that was computerized to readings and saving the data per second n the course of experimental run.

3. EXPERIMENTAL RESULTS

3. 1. General Behavior and Crack Patterns

The development of cracks at each stage of loading was measured and marked on the beams to observe the growth, sequence, and pattern of cracking during the test up to the specimen's failure. The beams' cracks patterns at the failure load after rleas load are shown in Figure 6 and their failures before release the load are shown in Figure 7. The specimens with one and two out of plane part were failed in the torsion at out of plane part then followed by flexure mode at the fixed supports. The specimen with three out of plane parts was failed in the torsion at out of plane parts. In general, the torsional cracks of beams were started at the interior corners of out of plane parts and continued from bottom to the top then distributed at the top face of beam in the mid span region and at the side faces of the out of plane parts, while the flexural and other torsional cracks observed bellow the point load and at the shear span (a), and flexural cracks at the supports.

The torsional and flexural cracks increased, widened, and traveled with increasing the applied load. In NSC-1OP the torsional cracks started at the out of plane part then followed by vertical flexural and inclined torsional cracks below the point load and inclined torsional cracks at the shear span (a), then finally flexural cracks at the support. In NSC-2OP the first cracks appear at the interior corner of out of plane parts then flowed be vertical flexural cracks at mid span and at last, the negative moment cracks started at the supports. NSC-3OP torsional cracks were started at the out of plane parts and below the point load, and then followed by the combined torsional and flexural cracks at the supports. The cracks propagated from the corners to the faces of out of plane parts in diagonal shape and increase in their width at the same time increasing number of support cracks up to the beam failure. In NSC-S the first vertical flexural cracks appeared at the mid span and at the fixed supports then followed by the vertical flexural cracks under the loading points and at last, the inclined shear cracks appeared at the shear span (a).

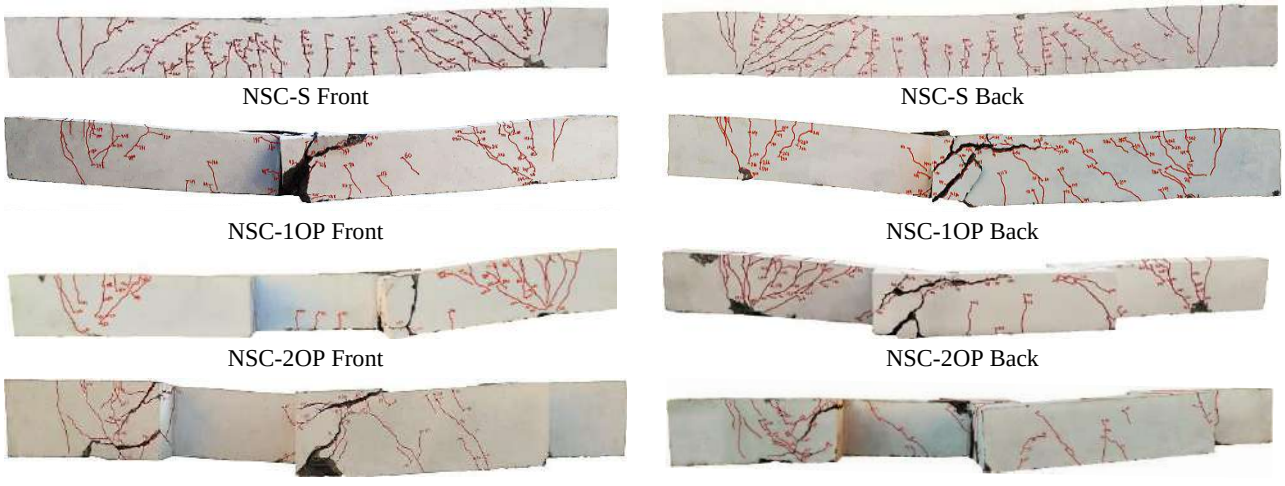

Figure 6. Experimental crack patterns of specimens at the failure load

Figure 7. Specimens behavior at the failure load

Finally, at the failure load, the flexural cracks at the fixed support rapidly expanded and almost reached to the bottom face of the beam, followed by the concrete crushing at the mid span region. It is worth mentioning that the cracking load of NSC-S was highest among them and NSC-3OP was lowest, but NSC-1OP and NSC-2OP were of approximation the same value. The cracking and ultimate loads for beams are plotted in Figure 8 and the maximum cracks width at the ultimate load are plotted in Figure 9. The cracks under different loading characteristics are shown in Figure 10.

3. 2. Load-deflection Characteristics

3. 2. 1. General Behavior The load-deflection response of all the tested beams for measured deflection at mid span is shown in Figure 11. This response is the main result to evaluate each of the ductility, energy absorption, and stiffness. From the curves it can be revealed that the NSC-S beam has the highest ultimate load of all the beams without of plane parts and less central deflection. It is worth to mention that the NSC-2OP beam has ultimate load higher than the NSC-1OP and NSC-3OP beams. This behavior due to the axis of the mid span part of NSC-2OP beam is parallel to the beam axis and decreased the applied torsional moment at this part which led to increase the load-carrying capacity, while the NSC-1OP and NSC-3OP have mid span part perpendicular to the beam axis and increase torsional moment at these parts which led to decrease the load-carrying capacity.

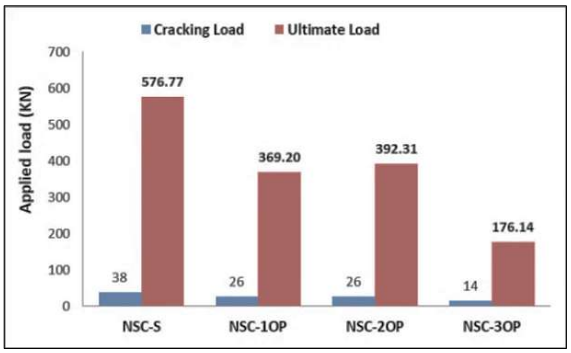

Figure 8. Cracking and ultimate loads of beams

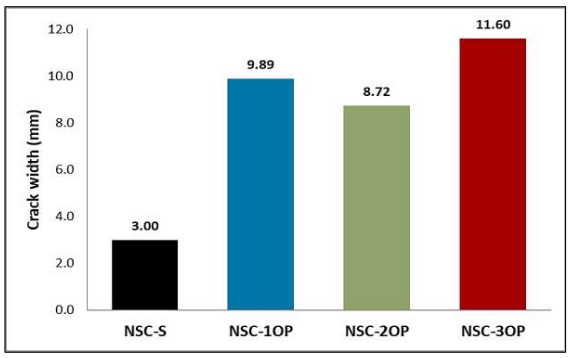

Figure 9. Maximum cracks width at the ultimate load

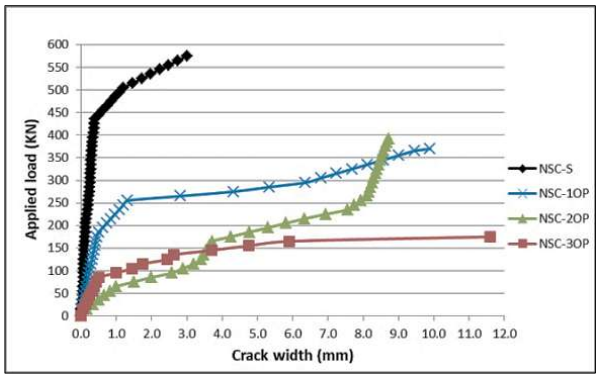

Figure 10. Load and crack with response of specimens

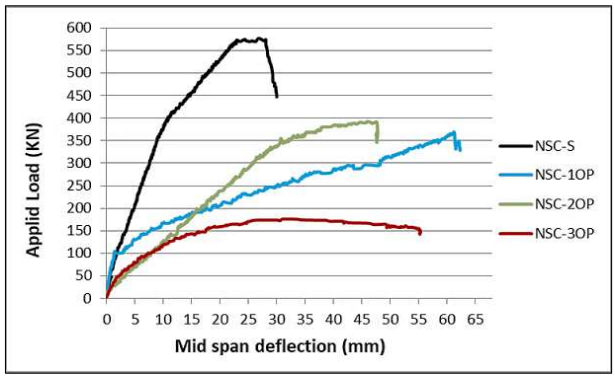

Figure 11. Load and mid span deflection response of specimens

The relations between the loads and deflections also can be described by the beam deflection shapes along the span between the supports as shown in Figure 12. The deflection shape at the ultimate load was carried out in the experimental work by taking the readings of LVDTs that installed under the mid span point and under the loading points.

From the load-mid span deflection and deflection shape responses it can be summarized that the NSC-S beam has an ultimate load 35.96%, 33.33%, and 69.46% higher than NSC-1OP, NSC-2OP, and NSC-3OP beam, respectively. The mid span deflection of NSC-1OP, NSC-2OP, and NSC-3OP beam was higher than NSC-S beam by 56.23%, 47.68%, and 45.99%, respectively. These results gave indicate that the increase number of out of plane parts reduced the deflection at the ultimate load and made the deflection shape is close to the shape of the NSC-S beam. The ultimate load capacities, related deflection, and failure mode of all the tested beams are summarized in Table 4.

3. 2. 2. Displacement Ductility Index

Among many aspects required in reinforced concrete structural members design, ductility has become involuntary by the standard codes ACI 318, EUROCODE 8, and ABNT NBR 6118 [15-17]. In this context, Shadmand et al. [18] mentioned that the ductility represents the one of the materials properties which can be defined as the ability of material or a

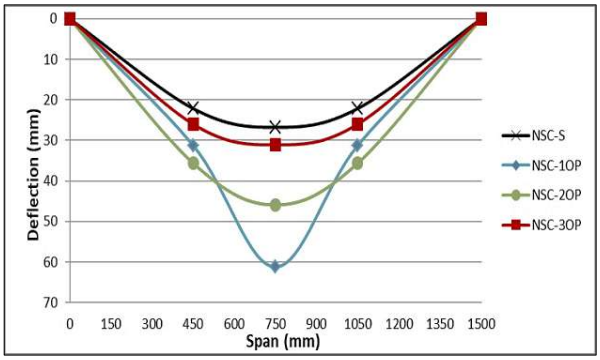

Figure 12. Deflection shape response of specimens

TABLE 4. The experimental results output of all the tested beams

Beams	Failure load P_U [kN]	Mid span deflection Δ_U (mm)	Yield load P_y [kN]	Mid span deflection Δ_y (mm)	Ductility index	Energy absorption (KN.mm)	Energy ductility index	Failure mode
NSC-S	576.76	26.79	432.57	13.45	2.05	11924.52	2.19	Flexure at support and mid span
NSC-1OP	369.36	61.21	277.02	36.00	1.71	15283.11	1.14	Torsion at out of plane part
NSC-2OP	392.30	45.92	294.22	25.39	1.81	12147.94	1.90	Torsion at out of plane part and flexure at support
NSC-3OP	176.14	31.09	132.10	11.57	2.69	7929.77	3.43	Torsion at all the out of plane parts

member to undergo large deformations without significant resistance loss or rupture before collapse. In concrete structural members, it is can be obtained by the ratio of steel reinforcement within it; because mild steel is a ductile material that can be bent and twisted without rupture [19,20]. Ductility of structural member in experimental work can be estimated in terms of ductility index.

According to Kim et al, [21], Maghsoudi and Bengar [22] and Faez et al. [23] ductility index is defined as follows:

$$\mu = \frac{\Delta_U}{\Delta_y} \quad (11)$$

where; μ is the ductility index, Δ_U is the defection of the beam at the ultimate load, and Δ_y is the defection of the beam at the yield load.

Researchers proposed several approaches to evaluate this term; while Park [24-25] depended on the equivalent elasto-plastic yield point that depends on the equivalent elasto-plastic energy absorption;, otherwise used the ultimate load deflection at the first fracture of any element that occurs at the end of the elastic zone and causes reduction in stiffness as shown in Figure 13. In this strategy, the yield point deflection (Δy) is represent the intersection point of two lines; the first line is a horizontal tangent to the load-deflection curve at the ultimate load, whilst the second one is a line passing through the origin point to the point that represents 75% of the ultimate load.

The deflections at the yield and ultimate loads as well as the ductility indexes of all beams are listed in Table 4 and plotted in Figure 14. As can be seen from this table and figure that the ductility of NSC-1OP and NSC-2OP was less than NSC-S by 16.58% and 11.70%, respectively, while NSC-3OP is 23.79% higher than NSC-S. Furthermore, it can be seen that increasing number of out of plane parts improved the ductility and reduced the difference with NSC-S. Moreover, these indications explained by relative ductility indexes that evaluated for the beams with out of plane parts relative to the control straight beam as plotted in Figure 15.

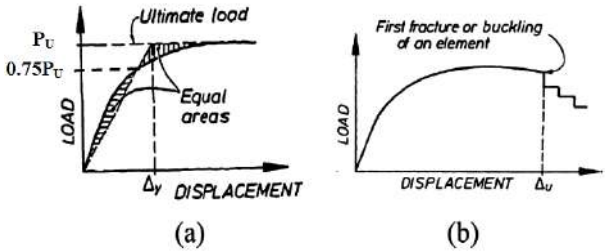

Figure 13. Park definition for displacements [19, 20]: (a) yield displacement by equivalent elasto-plastic energy absorption. (b) The ultimate deflection is based on the first fracture of an element

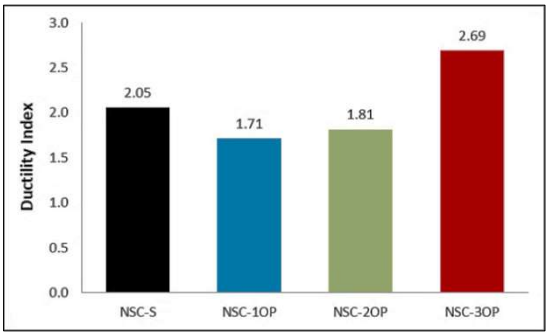

Figure 14. Beams ductility index

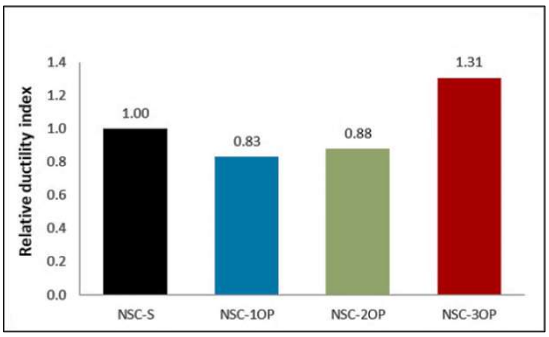

Figure 15. Beams relative ductility index

3. 2. 2. Energy Ductility Index The energy absorption capacity of the concrete beam can be approximated as the area under the load-deflection curve up to its ultimate load, which represents the energy absorption that could sustain before displaying a significant drop in load carrying capacity [26-28]. Absorbed energy can be obtained by integrating the area at each loading step in load-displacement relationship [29-32]. Figure 16 represent the load-deflection curve where; the total energy *E* done by integrate the product the magnitude of the load *P* and of the small deflection *dx* and which is equal to the area under the load-deformation diagram between x = 0 and x = x_1 and can be written as:

$$E = \int_0^{x_1} P\, dx \quad (12)$$

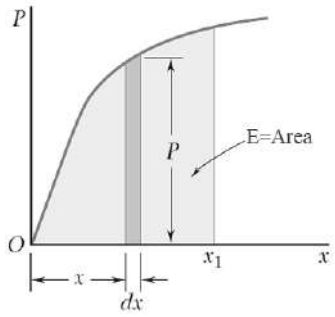

Figure 16. Determination of energy based ductility capacity

The calculations of the area under the load-deflection curves for all tested beams are illustrated in Figure 17 and summarized in Table 4. The results showed that the NSC-1OP beam has the highest value of energy absorption and this value decreased when the number of out of plane parts increased as compared with the straight beam.

Thomsen et al. [32], Maghsoudi and Bengr [33] defined the energy ductiliy index as (μ_E) which is the ratio between the energy of the system at failure (E_u) and the energy of the system at yielding load of tensile steel reinforcement at the central support (E_y):

$$\mu_E = \frac{E_u}{E_y} \quad (13)$$

where E_u is the failure energy of the beam at ultimate load, E_y is the elastic energy at first steel yield load as shown in Figure 18, and μ_E is the energy ductility index.

The energy ductility index that estimated according to Equation (13) for the tested beams are plotted in Figure 19.

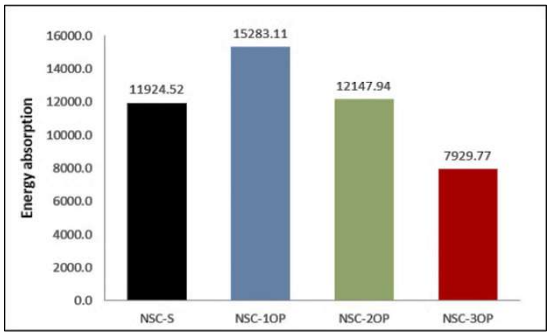

Figure 17. Beams total energy absorption

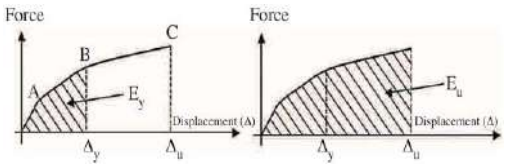

Figure 18. Determination of energy based ductility capacity

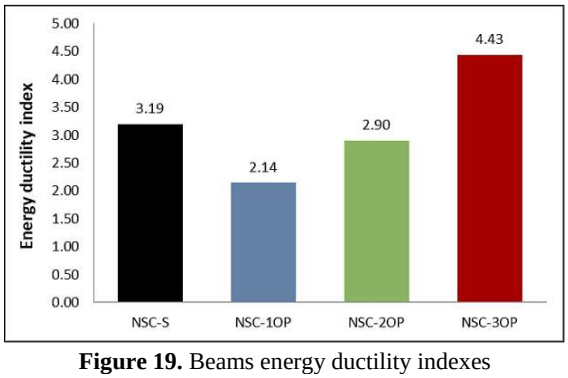

Figure 19. Beams energy ductility indexes

Abdulraheem [34] proposed approach to evaluate the ability of RC beams to absorb the energy in terms of energy ductility index μ_{en} by classified the total energy absorption into two regions, elastic energy zone E_{el} and plastic energy zone E_{PL} and can be estimated as the ratio of the plastic energy to the elastic energy as shown in Figure 20, and calculated using the following equation:

$$\mu_{en} = \frac{E_{Pl}}{E_{el}} = \frac{E_{total} - E_{el}}{E_{el}} \quad (14)$$

where E_{pl} is the plastic energy that represents the area under the load-deflection curve from the yielding point up to the ultimate load, and E_{el} is the elastic energy that represents the area under the linear part of the load-deflection curve up to the yielding point as shown in Figure 20.

In this study, Equation (14) used to estimate the energy absorption index for the tested beams, becase it gave results more acceptable as copare with the displacemnt ductility index. The estimated results are summarized in Table 4 and plotted in Figure 21.

3. 2. 3. Twisting Angle The angle of twist for the cross-sections at the mid span was calculated at each stage of load increase in the experiment up to the beam rupture. The angle was measured by taking the maximum absolute different readings between the LVDTs that installed at the at front and back points and the LVDT at centerline of the beam which installed as

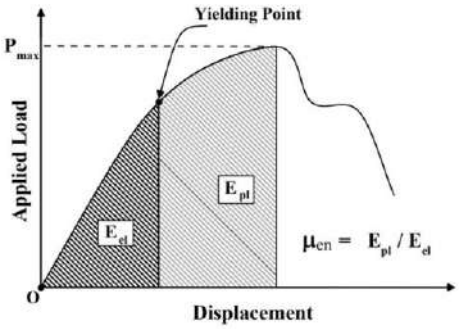

Figure 20. Procedure of energy absorption index Evaluation

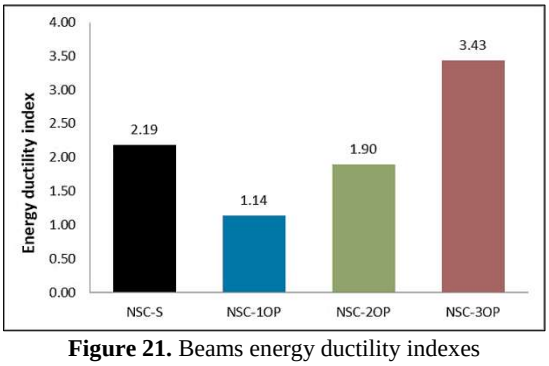

Figure 21. Beams energy ductility indexes

shown in Figure 4, then divided on the distance between them and took the average of front and back angles. The load and mid span twisting response is explained in Figure 22.

The load-mid span rotation response used to study the effect of increase number of out of plane parts and their locations on the beams rotational behavior. It can be observed that the NSC-2OP beam has the angle of twist at the ultimate load higher than NSC-1OP and NSC-3OP beams by 27.32% and 38.59%. That means the perpendicular direction of mid span part to the beam axis has a greatly effect on the decreasing of the angle of twist, especially when increase the number of out of plane parts. The beams twisting angle at service and ultimate load are addressed in Table 5 and plotted in Figure 23.

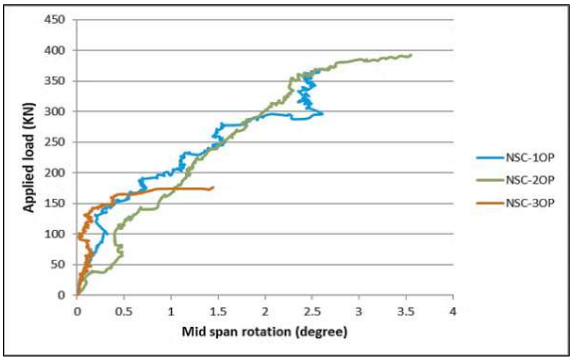

Figure 22. Applied load versus twisting angle of the beams

TABLE 5. The mid-span twisting angle of all the tested beams

Beams	* Twisting angle at service load (degree)	Twisting angle at ultimate load (degree)
NSC-1OP	1.56^0	2.58^0
NSC-2OP	1.80^0	3.55^0
NSC-3OP	1.10^0	2.18^0

*Service load = 65% ultimate load

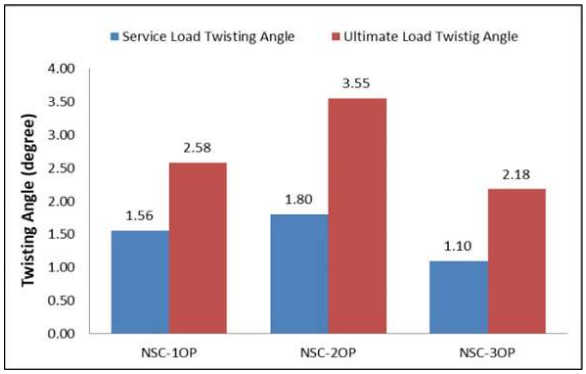

Figure 23. Twisting angle of beams at service and ultimate load

4. CONCLUSIONS

Based on the experimental investigations, the effect of the out plane part on the structural behavior of straight and with out of plane part RC beams subjected to static loads are examined. The following are the most important notices for observed and recorded results:

1. The presence of out of plane part decreased the load-bearing capacity of all the beams with out of plane part beam as compared with the straight beam by 35.96%, 33.33%, and 69.46%.
2. The ductility of the beams that estimated by displacement ductility index and energy ductility index methods gave indication that the ductility of the beams with out of plane parts increased when increasing the number of these out of plane parts until to reach and pass the ductility of the straight beam when using beam with three out of plane parts.
3. The cracks width- load characteristics were affected by the number and loaction of out of plane parts and the maximum crack width of the straight beam is the smallest one and the crack of the beams was affected by the location and direction of the out of plane part relative to the axis of beam at mid span, because the maximum crack width of the beam with two out of plane parts is smaller than of the beams with one and three out of plane parts.
4. The angle of twist of the beams was also affected by the location and direction of the out of plane part relative to the axis of the beam at mid span, because the twisting angle of the beam with two out of plane parts is higher than of the beams with one and three out of plane parts at the service and ultimate load.
5. The failure mode of beams with one and two out of plane parts was occurred by torsional cracking propagation at the out of plane part and torsional and flexural cracks at the other spans and at the supports faces, and the beam with one and three out of plane parts was failed by torsional cracks propagation at the out of plane parts, while the straight beam was failed by flexural cracks at the mid span and at the supports.

From the study conclusions above, it can be seen that the load bearing capacity and the structural behavior of beams with out of plane parts was affected by the number and locations of the out of plane parts.

5. REFERENCES

1. Owainati, S. A. R. "Behaviour of reinforced concrete beams under torsion, bending and shear." (1973). https://spiral.imperial.ac.uk/handle/10044/1/20540
2. Ali, Mohamad, and A. Anis. "Strength and behaviour of reinforced concrete spandrel beams." KB thesis scanning project 2015 (1983). http://hdl.handle.net/1842/12664

3. Kamiński, M., and W. Pawlak. "Load capacity and stiffness of angular cross section reinforced concrete beams under torsion." ***Archives of civil and Mechanical Engineering***, Vol. 11, No. 4 (2011): 885-903. doi: 10.1016/S1644-9665(12)60085-5.
4. ACI-ASCE Committee 445. ***" Report on Torsion in Structural Concrete"*** American Concrete Institute of the Advancing concrete knowledge, No IR12 (2013). https://www.amazon.com/ACI-445-1R-12-Torsion-Structural-Concrete-ebook/dp/B00E4VDIV4
5. Elsayed. A. A., Noaman. M., Abdallah. M. A. M., Abdelrahim. M. A. A. "Behavior of R.C. Beams with Inclined Cantilever." IOSR Journal of Mechanical and Civil Engineering, Vol. 12, No. 4, (2015), 74-96. doi: 10.9790/1684-12427496
6. Qian, Kai, and Bing Li. "Performance of three-dimensional reinforced concrete beam-column substructures under loss of a corner column scenario." ***Journal of Structural Engineering,*** Vol. 139, No. 4, (2013), 584-594. doi:10.1061/(asce)st.1943-541x.0000630.
7. Rafeeq, Ranj. "Torsional Strengthening of Reinforced Concrete Beams Using CFRP Composites." (2016). doi:10.15760/etd.3121.
8. Talaeitaba, Sayed Behzad, and Davood Mostofinejad. "Fixed supports in assessment of RC beams' behavior under combined shear and torsion." ***International Journal of Applied***, Vol. 1, No. 5, (2011), http://www.ijastnet.com/journals/Vol_1_No_5_September_2011/15.pdf
9. Amulu, C. P., and C. A. Ezeagu. "Experimental and analytical comparison of torsion, bending moment and shear forces in reinforced concrete beams using BS 8110, euro code 2 and ACI 318 provisions." ***Nigerian Journal of Technology***, Vol. 36, No. 3, (2017), 705-711. doi: 10.4314/njt.v36i3.7.
10. Nagendra Prasad. N and Naresh Kumar. Y, "Torsional behavior of reinforced concrete 'L' beam, International journal of advanced research in basic engineering science and technology, ISSN: 2456-5717, Vol. 3, Special issue 35, (2017).
11. American Concrete Institute (ACI), ACI 318-319: building code requirements for structural concrete, Farmington Hills, (2019). doi: 10.2307/3466335.
12. Standard, A. S. T. M. "C78. 2002. Standard test method for flexural strength of concrete (using simple beam with third point loading)." Annual Book of ASTM Standards, Vol. 4, No. 2, (2002). doi: 10.1520/c0078-02
13. Astm, C. "496/C 496M-04." Standard test method for splitting tensile strength of cylindrical concrete specimens, Vol. 4 (2004), 5. doi: 10.1520/c0496_c0496m-04
14. Dixon, Donald E., Jack R. Prestrera, George RU Burg, Subcommittee A. Chairman, Edward A. Abdun-Nur, Stanley G. Barton, Leonard W. Bell et al. "Standard Practice for Selecting Proportions for Normal, Heavyweight, and Mass Concrete (ACI 211.1-91)." (1991), 1-38. https://kashanu.ac.ir/Files/aci%20211_1_91.pdf.
15. Brazilian Association of Technical Standards NBR 6118 2014 - Design of Concrete Structures - Procedure. Rio de Janeiro, ABNT. 2014. doi: 10.1590/s1983-41952015000400008
16. ACI Committee. "Building code requirements for structural concrete:(ACI 318-02) and commentary (ACI 318R-02)." American Concrete Institute, 2002. https://hoseinzadeh.net/ACI-318-02.pdf
17. Code, Price. "Eurocode 8: Design of structures for earthquake resistance-part 1: general rules, seismic actions and rules for buildings." Brussels: European Committee for Standardization (2005). https://www.phd.eng.br/wp-content/uploads/2015/02/en.1998.1.2004.pdf
18. Shadmand, M., A. Hedayatnasab, and O. Kohnehpooshi. "Retrofitting of Reinforced Concrete Beams with Steel Fiber Reinforced Composite Jackets." ***International Journal of Engineering, Transactions B: Applications,*** Vol. 33, No. 5 (2020), 770-783. doi: 10.5829/ije.2020.33.05b.08.
19. Punmia, B. C. *Reinforced Concrete Structures* Vol. I. Vol. 1. Firewall Media, 1992. https://books.google.ps/books?id=6g1fu4pRDCkC
20. Khamees, Shahad S., Mohammed M. Kadhum, and Nameer A. Alwash. "Effect of hollow ratio and cross-section shape on the behavior of hollow SIFCON columns." ***Journal of King Saud University-Engineering Sciences***, Vol. 33, No. 3 (2021): 166-175. doi: 10.1016/j.jksues.2020.04.001 .
21. Kim, Sung Bae, Na Hyun Yi, Hyun Young Kim, Jang-Ho Jay Kim, and Young-Chul Song. "Material and structural performance evaluation of recycled PET fiber reinforced concrete." ***Cement and Concrete Composites***, Vol. 32, No. 3, (2010), 232-240. doi:10.1016/j.cemconcomp.2009.11.002 .
22. Maghsoudi, A. A., and H. Akbarzadeh Bengar. "Acceptable lower bound of the ductility index and serviceability state of RC continuous beams strengthened with CFRP sheets." ***Scientia Iranica***, Vol. 18, No. 1, (2011), 36-44. doi: 10.1016/j.scient.2011.03.005 .
23. Faez, A., A. Sayari, and S. Manei. "Retrofitting of RC Beams using Reinforced Self-compacting Concrete Jackets Containing Aluminum Oxide Nanoparticles." ***International Journal of Engineering, Transactions B: Applications,*** Vol. 34, No. 5, (2021), 1195-1212. **doi**: 10.5829/ije.2021.34.05b.13.
24. Park, R. "Ductility evaluation from laboratory and analytical testing." In Proceedings of the 9th world conference on earthquake engineering, Tokyo-Kyoto, Japan, Vol. 8, 605-616.1988. https://www.iitk.ac.in/nicee/wcee/article/9_vol8_605.pdf.
25. Park, Robert. "Evaluation of ductility of structures and structural assemblages from laboratory testing." ***Bulletin of the New Zealand Society for Earthquake Engineering***, Vol. 22, No. 3, (1989), 155-166. doi: 10.5459/bnzsee.22.3.155-166.
26. Jaafer, Abdulkhaliq Abdulyimah. "Experimental investigation on the ferrocement slabs with a sifcon matrix." Wasit Journal of Engineering Sciences 3, No. 1, (2015), 40-54. doi: 10.31185/ejuow.vol3.iss1.34.
27. Goldston, Matthew, A. Remennikov, and M. Neaz Sheikh. "Experimental investigation of the behaviour of concrete beams reinforced with GFRP bars under static and impact loading." ***Engineering Structures***, Vol. 113, (2016), 220-232. doi: 10.1016/j.engstruct.2016.01.044.
28. Jomaah, Muyasser M., and Diyaree J. Ghaidan. "Energy Absorption Capacity of Layered Lightweight Reinforced Concrete Beams with Openings In Web." ***Civil Engineering Journal***, Vol. 5, No. 3, (2019), 690-701. doi: 10.28991/cej-2019-03091279
29. Ohno, Tomonori, and Takashi Nishioka. "An experimental study on energy absorption capacity of columns in reinforced concrete structures." ***Doboku Gakkai Ronbunshu***, No. 350, (1984), 23-33. doi: 10.2208/jscej.1984.350_23.
30. Beer, Ferdinand P., Elwood Russell Johnston, John T. DeWolf, and David F. Mazurek. ***Mecânica dos materiais***. Amgh, 2011.
31. Yu, R., P. Spiesz, and H. J. H. Brouwers. "Energy absorption capacity of a sustainable Ultra-High Performance Fibre Reinforced Concrete (UHPFRC) in quasi-static mode and under high velocity projectile impact." ***Cement and Concrete Composites***, Vol. 68, (2016), 109-122. doi: 10.1016/j.cemconcomp.2016.02.012
32. Thomsen, Henrik, Enrico Spacone, Suchart Limkatanyu, and Guido Camata. "Failure mode analyses of reinforced concrete beams strengthened in flexure with externally bonded fiber-

reinforced polymers.", ***Journal of Composites for Construction,*** Vol. 8, No. 2, (2004), 123-131. doi: 10.1061/(asce)1090-0268(2004)8:2(123).

33. Maghsoudi, A. A., and H. Akbarzadeh Bengar. "Moment redistribution and ductility of RHSC continuous beams strengthened with CFRP." ***Turkish Journal of Engineering and Environmental Sciences***, Vol. 33, No. 1, (2009), 45-59. doi: 10.3906/muh-0901-6.

34. Abdulraheem, Mustafa S. "Experimental investigation of fire effects on ductility and stiffness of reinforced reactive powder concrete columns under axial compression." ***Journal of Building Engineering,*** Vol. 20, (2018), 750-761. doi: 10.1016/j.jobe.2018.07.028

Persian Abstract

چکیده

هدف از این مقاله بررسی و مقایسه رفتار ساختاری تیر مستقیم بتن آرمه و سایر تیرهای ساخته شده در آنجا با یک ، دو و سه قسمت خارج صفحه است. این مطالعه بر روی تأثیر تعداد و محل قطعات صفحه خارج بر روی انحراف و بازتاب دهانه میانه تیرها ، و همچنین شاخص شکل پذیری ، بارهای ترک خوردگی و حالت های خرابی متمرکز شده است. چهار تیر با عرض مقطع ۱۵۰ میلی متر و عمق ۲۰۰ میلی متر و طول ۲ متر ساخته شده است. تمام تیرها با بتن با مقاومت نرمال و نسبت تقویت طولی ثابت ۰.۰۱۱ برای گشتاورهای منفی و مثبت ساخته شده اند. تمام نمونه های پرتو توسط انتهای ثابت فولادی گیر شده و تحت شکست دو نقطه ای قرار گرفتند. نتایج به دست آمده نشان داد که ظرفیت تحمل بار تیر مستقیم بیشتر از تیرهای خارج از قطعات صفحه است. بعلاوه ، پرتوی دارای دو قسمت از صفحه دارای ظرفیت بالاتر از پرتوهای دارای یک و سه قسمت از صفحه به ترتیب ۵.۸۶ و ۵۵.۰۷٪ است. علاوه بر این ، نتایج نشان داد که انعطاف پذیری با افزایش تعداد قطعات خارج صفحه ۵.۵۲٪ و ۳۲.۷۱٪ در مقایسه با پرتو با قسمت خارج صفحه افزایش می یابد.

IJE TRANSACTIONS A: Basics Vol. 34, No. 10, (October 2021) 2294-2301

International Journal of Engineering

Journal Homepage: www.ije.ir

Modified Damage Index Calculation Method for Frame-Shear Wall Building Considering Multiple Demand Parameters

D. Mibang*, S. Choudhury

Depatment. of Civil Engineering, National Institute of Technology Silchar, India

P A P E R I N F O

Paper history:
Received 23 July 2021
Received in revised form 13 August 2021
Accepted 15 August

Keywords:
Reinforced Concrete Frame Shear Wall Building
Correlation Matrix
Engineering Demand Parameters
Damage Evaluation
Non Linear Time History Analysis
Global Damage Index

A B S T R A C T

In this study, multiple objectives on earthquake damage assessment procedures have been investigated. The Unified performance-based design (UPBD) method has been used to design the Reinforced Concrete (RC) frame shear wall building. First, the Damage index (DI) of the building has been estimated by using Park and Ang method. It has been found that this method is highly time-consuming. Hence, it is not found suitable for large scale investigation. Therefore, a new approach has been suggested to reduce the computational time and efforts in the case of complex structures in evaluating the global damage index (GDI). In this present study, the most three influencing parameters of the building have been considered to find the GDI. It has also been observed that the most damage occurs on the ground storey of the building. The suggested method efficiently calculates a reliable GDI that can assess building damage from small to large scale buildings.

***doi**: 10.5829/ije.2021.34.10a.10*

NOMENCLATURE

DI	Damage Index	GM	Ground Motion
MDOF	Multi-degree of freedom	h_b	Beam depth
SDOF	Single degree of freedom	θ_{pb}	Allowable plastic rotation of the beam
UPBD	Unified performance-based design	Δ_d	Design displacement
SCGM	Spectrum compatible ground motions	m_e	Effective mass
GDI	Global damage index	h_e	Equivalent heigh
EDPs	Engineering Demand Parameters	m_i	Mass of *i-th* storey
LDI or SDI	Local or storey wise damage index	Δ_{iyw}	Yield displacements of the wall in *i*-th storey
DDBD	Direct displacement-based design	Δ_i	Profile displacement
ESDOF	Equivalent single degree of freedom	N	Number of the storey
SCGM	Spectrum compatible ground motions	μ_w	Displacement ductility of the wall
LSPL	Life safety performance level	$\Delta_{he,y}$,	Yield displacement of the wall
θ_{yw}	Yield rotation of the wall	M_w	Wall moment
θ_{pw}	Plastic rotation of the wall	ξ_w	Wall damping moment
θ_{yw}	Yield rotation of the wall	$M_{ot,f}$,	Frame overturning moment
ϕ_{yw}	Yield curvature	ξ_f	Frame damping
$h_{\inf}$	Inflection height	$T_{e,trial}$	Trial effective time period
ε_y	Yield strain of rebar	r	Post-yield stiffness ratio
L_w	The horizontal length of the wall	K_e	Effective stiffness
t_w	The thickness of the wall	V_b	Base shear
τ_c	Permissible shear stress of concrete	δ_M	Optimum deformation under earthquake loading
DL, LL, F_x, F_y	Dead load, live load, seismic load in the *x*-Direction and y-direction	δ_u	Optimum deformation monotonic loading
β	Non-negative parameter	Q_y	Yield strength,

*Corresponding Author Institutional Email: durga_rs@civil.nits.ac.in (D. Mibang)

Please cite this article as: D. Mibang, S. Choudhury, Modified Damage Index Calculation Method for Frame-Shear Wall Building Considering Multiple Demand Parameters, International Journal of Engineering, Transactions A: Basics, Vol. 34, No. 10, (2021) 2294-2301

θ_d	Design drift	dE	Hysteresis energy
η	Reduction factor corresponding to the damping	$d_{\max}$	Optimum roof displacement
θ_{yw}	Yield rotation of the wall	ϕ_{yw}	Yield curvature of wall
V_{Wall}	Shear carried by the walls	F_i	Force applied in the *i-th* floor level
D_{Story}	Storey wise damage index	C	Regression constant
$E_{storey,i}$	Hysteretic energy dissipated of i^{th} storey	E_i	Hysteretic energy dissipated of i^{th} member
D_i	*DI* of i^{th} member	n	Number of members in a particular storey
D_{global}	*DI* of the entire structure	t_w	Thickness of the wall

1. INTRODUCTION

Structures get damaged and often collapse under high intensity of earthquakes. The Damage Index (DI) is a parameter that can be used to quantify the amount of damage suffered by the structure. Damage is the process of deterioration of a structure's strength, ductility and stiffness, and that is why estimation of damage index is very important. Structural design should be done to minimize the damage. Reinforced concrete (RC) frame shear wall buildings are mainly used for residential, commercial and office buildings. This type of buildings is efficient in resisting earthquake loads. But still, there can be damage to such buildings leading to severe economic losses [1-3]. Several approaches are available for evaluating DI and have been proposed by numerous researchers [4-8]. Park and Ang [9] considered only two parameters to determine the DI of the structures, namely, maximum deformation and hysteretic energy. The limitations have been highlighted in determining DI of the buildings considering the displacement mode shapes, have been identified experimentally. Yazdannejad and Yazdani [10] have improved the Park and Ang damage model by adding stiffness using Bayesian framework. Hait et. al [11] have considered U-, L- and rectangular-shaped RC frame buildings and found rectangular-shaped buildings are least vulnerable to damage. From Several studies based on DI, it has been observed that, there are many approaches available for evaluating DI, but those are either incomplete or tedious to use. Likewise, Park and Ang's approach is tedious and time-consuming. Estimation of the DI by adding multiple parameters that define the buildings real damage state under seismic excitation may lead to more accurate results.

In the present study, an 8-storey RC frame-shear wall building of Life Safety performance level has been considered for the assessment of DI. The unified performance-based design (UPBD) method has been employed for designing the RC frame shear wall building. Nonlinear time history analysis (NLTHA) is performed under spectrum compatible ground motions (SCGM) as per EC-8 demand spectrum at 0.45g level and type B soil. In this study, the 3 most influential parameters have been considered to determine the building's global damage index (GDI). Here, a relationship between Park and Ang DI and Engineering Demand Parameters (EDPs) has been developed to increase the ease of finding the DI of the buildings.

2. DAMAGE INDEX

The damage index (DI) is a criterion that measures the amount of damage in a structure for a specified hazard level. These damage indices of the structures are expressed by different response parameters obtained from analytical assessment. Researchers have proposed several methods on DI, but most of them have considered limited EDPs; therefore, it could not give accurate results of the DI of the structures. To compute the DI of the structure, there is a need to assume more EDPs to get accurate results. DI is classified into two ways: local or storey wise damage index (LDI or SDI) and GDI, and the brief description reported in literature [12].

3. DESIGN PHILOSOPHY USED

Sullivan et al. [13] established the direct displacement-based design (DDBD) method for dual frame buildings. In this method, interstorey drift was the only target design parameter considered as well as the member sizes are also decided by trial and error process. In contrast, in the UPBD method, two target design criteria, namely, drift and performance level (in terms of plastic rotation) can be satisfied. This method also gives member size at the beginning of design process which avoids iteration. Choudhury and Singh [14] introduced the UPBD method for RC Frame buildings and UPBD method for frame-shear wall building has been reported by Mibang and Choudhury [15]. In the design process the multiple degrees of freedom (MDOF) structure is represented by an equivalent single degree of freedom (ESDOF) system as shown in Figure 1. For the benefit of readers, the basics of UPBD method for frame-shear wall building are discussed here in brief. The drift rotation of the building consists of yield rotation and plastic rotation of the wall. As per Figure 1, Equation (1) is obtained.

$$\theta_d = \theta_{yw} + \theta_{pw} \quad (1)$$

The yield rotation of the wall and yield curvature of the wall can be determined by Equations (2) and (3), respectively.

$$\theta_{yw} = \phi_{yw} \frac{h_{inf}}{2} \quad (2)$$

$$\phi_{yw} = \frac{2\varepsilon_y}{L_w} \quad (3)$$

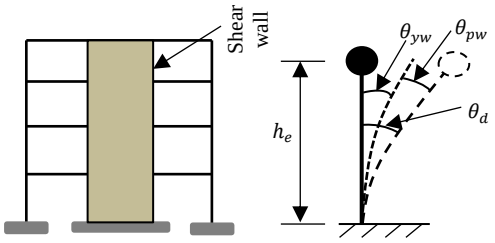

(a) MDOF system (b) ESDOF system

Figure 1. MDOF and ESDOF systems

Using Equations (1), (2) and (3), Equation (4) is obtained.

$$L_w = \frac{\varepsilon_y h_{inf}}{\theta_d - \theta_{pw}} \tag{4}$$

The thickness of the wall (t_w) is obtained from Equation (5).

$$t_w = \frac{V_{Wall}}{0.8 \times L_w \times \tau_c \times N_w} \tag{5}$$

Factor 0.8 is used to reflect the fact that 80% of the wall length is considered effective in taking shear (IS 456 2000). The beam depth can be determined by Equation (6).

$$h_b = \frac{0.5 \varepsilon_y l_b}{\theta_d - \theta_{pb}} \tag{6}$$

The width of the beam is taken as 1/4th to 1/3th of beam depth as per common practice. The h_{inf} is a parameter of dual system design, and it can be found out by determining the moments that are borne by frame and shear wall.

The yield displacement profile of the wall is obtained using Equations (7).

$$\Delta_{iyw} = \frac{\emptyset_{yw} h_i h_{inf}}{2} - \frac{\emptyset_{yw} h_{inf}^2}{6}, \text{ when} h_i \geq h_{inf} \tag{7a}$$

$$\Delta_{iyw} = \frac{\emptyset_{yw} h_i^2}{2} - \frac{\emptyset_{yw} h_i^3}{6 h_{inf}}, \text{ when } h_i \leq h_{inf} \tag{7b}$$

$$\emptyset_{yw} = \frac{2\varepsilon_y}{L_w} \tag{7c}$$

Design displacement profile is obtained from Equation (8)

$$\Delta_i = \Delta_{iyw} + \left(\theta_d - \phi_{yw} h_{inf}/2\right) h_i \tag{8}$$

The MDOF building is converted to an ESDOF and the properties of ESDOF system are determined by using Equations (9) to (11).

$$\Delta_d = \frac{\sum_{i=1}^{n} m_i \Delta_i^2}{\sum_{i=1}^{n} m_i \Delta_i} \tag{9}$$

$$m_e = \frac{\sum_{i=1}^{n} m_i \Delta_i}{\Delta_d} \tag{10}$$

$$h_e = \frac{\sum_{i=1}^{n} m_i \Delta_i h_i}{\sum_{i=1}^{n} m_i \Delta_i} \tag{11}$$

Wall ductility demand is determined by Equation (12).

$$\mu_w = \frac{\Delta d}{\Delta_{he,y}} \tag{12}$$

Frame ductility is determined by Equations (13) and (14).

$$\mu_f = \left(\frac{\Delta_i - \Delta_{i-1}}{h_i - h_{i-1}}\right) \frac{1}{\theta_{yf}} \tag{13}$$

$$\theta_{yf} = \frac{0.5 l_b \varepsilon_y}{h_b} \tag{14}$$

The trial value of the effective period is obtained from Equations (15) and (16).

$$T_{e,trial} = \frac{N}{6} \sqrt{\mu_{sys}} \tag{15}$$

$$\mu_{sys} = \frac{M_w \mu_w + M_{ot,f} \times \mu_f}{M_w + M_{ot,f}} \tag{16}$$

The frame equivalent viscous damping and the wall equivalent viscous damping components are calculated using Equations (17) to (19).

$$\xi_w = \frac{95}{1.3\pi}\left(1 - \mu_w^{-0.5} - 0.1 \times r \times \mu_w\right)\left(\frac{1}{\left(T_{e,trial}+0.85\right)^4}\right) \tag{17}$$

$$\xi_f = \frac{120}{1.3\pi}\left(1 - \mu_w^{-0.5} - 0.1 \times r \times \mu_f\right)\left(1 + \frac{1}{\left(T_{e,trial}+0.85\right)^4}\right) \tag{18}$$

$$\xi_{SDoF} = \frac{M_w \xi_w + M_{ot,f}\, \xi_f}{M_w + M_{ot,f}} \tag{19}$$

Displacement spectra corresponding to design spectra are drawn for various dampings. For this purpose, Equation (20) is utilized. Displacement spectra corresponding to EC-8 design spectra for soil type B and at 0.45g level have been used in the present study and are shown in Figure 2.

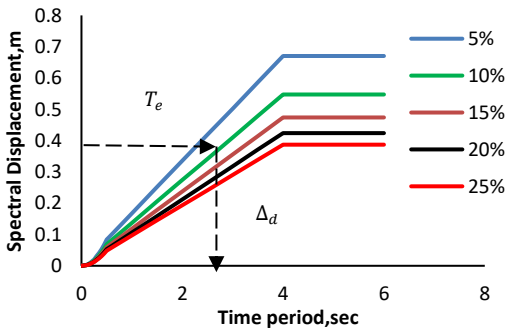

Figure 2. Displacement Spectra corresponding to EC-8 design spectra for soil type B at 0.45g level

$$\eta = \sqrt{\frac{10}{(5+\xi_{ESDOF})}} \geq 0.55 \quad (20)$$

Effective stiffness (K_e) is give by Equation (21).

$$K_e = \frac{4\pi^2 m_e}{T_e^2} \quad (21)$$

Base shear (V_b) is given by Equation (22).

$$V_b = k_e \Delta_d \quad (22)$$

The computed base shear is distributed to different floors as per Equation (23).

$$F_i = V_b \frac{m_i \Delta_i}{\sum_{i=1}^{n} m_i \Delta_i} \quad (23)$$

Where, F_i is the force applied in the *i*-th floor level of the building.

The combinations of load used for design are:

$DL + LL$

$DL + LL \pm F_x$

$DL + LL \pm F_y$

Design is done using the expected strength of materials [16]. The capacity design has to be done so that the column to beam capacity ratio is more than 1.4 according to 13920:2016.

3. DESIGN OF REPRESENTATIVE BUILDING

3. 1. Model Selection In the present study, an 8-storey frame-shear wall building has been considered. The plan and elevation of the building are shown in Figure 3. The building has been designed using the UPBD method for target performance objective of LS performance level and 2% drift. The sizes of beams and columns are given in Table 1. The material specifications are given in Table 2. NLTHA is performed under five spectrum compatible ground motions (SCGM) as per EC-8 [17] demand spectrum at 0.45g level and type B soil condition. The SCGMs are generated using software of Kumar [18]. The details regarding SCGMs have been given in Table 3. The match of response spectra out of SCGMs with the EC-8 demand spectrum is shown in Figure 4. Finite element software SAP2000 v. 21 [19] has been used to model, design, and analyze the building. The storey height is kept constant to 3.1 m.

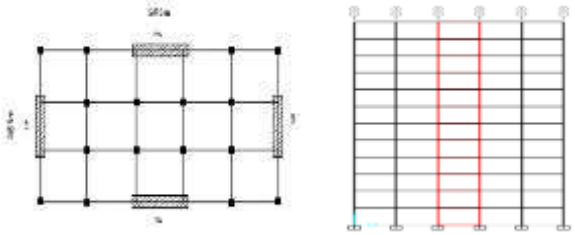

(a) Plan (b) Frame elevation

Figure 3. Building model considered in the study (a) Plan (b) elevation [SW indicates shear wall]

TABLE 1. Sizes of members in the building considered (mm)

Building name	Inner Column (mm)	Outer column storey-wise (mm)	Beam size (mm)	Shear wall thickness (mm)	Length of wall (mm)
B-8-LS	700×700	800×800 (1-4) 750×750 (5-6) 700×700 (7-8)	700× 450	150	5000

TABLE 2. Material properties related to concrete and rebar

Materials properties	Unit	Values
concrete compressive strength (*fck*)	MPa	30
steel yield strength (*fy*)	MPa	500
Modulus of elasticity of concrete (*Ec*)	MPa	$5000\sqrt{fck}$
Modulus of elasticity of steel (*Es*)	MPa	200000
Poisson's ratio (steel)	-	0.3
Poisson's ratio (concrete)	-	0.15

TABLE 3. Details of SCGMs used

Sl.No.	Name	Background Equation (India)	Year of occurrence	Durations in sec
1	GM1	Baithalangso	1988	78.05
2	GM2	Nonghklaw	1986	29.54
3	GM3	Silchar	1988	46.81
4	GM4	Umsning	1981	70.52
5	GM5	Barkot	1991	31.61

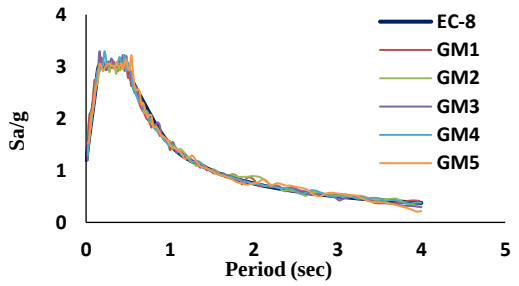

Figure 4. Match of response spectra of SCGMs with EC-8 design spectrum

4. DI OF STRUCTURE

In recent years, several DI models have been introduced by many researchers to predict the structural damage. Among all the methods, Park and Ang is the most common and popular approach (Equation (24)) used by other researchers. It also gave the expression for the local damage index (LDI) (Equation (25)) as well as global damage index (GDI) (Equation (26)). Nevertheless, this method is very time-taking in calculating the GDI.

Therefore, there is a need for some method which can provide ease in finding the GDI of structure.

$$DI = \frac{\delta_M}{\delta_u} + \frac{\beta}{Q_y \delta_u} \int dE \quad (24)$$

Storey DI and Entire storey DI are evaluated using Equations (24) and (25).

$$SDI = \frac{\sum_{i=1}^{n} D_i E_i}{\sum_{i=1}^{n} E_i} \quad (25)$$

$$GDI = \frac{\sum_{storey,i=1}^{n} D_{storey,i} E_{storey,i}}{\sum_{storey,i=1}^{n} E_{storey,i}} \quad (26)$$

5. 1. Procedure Followed for the Proposed DI Assessment In the literature review, it has been found that limited work had been carried out considering multiple EDPs for calculating the DI of the buildings. In this study, multiple EDPs have been considered for calculating the DI, and these parameters have been combined in a mathematical expression to find the DI of the building. Out of four engineering demand parameters, 3 parameters have been found to be the most influential EDPs for the building. To determine the most significant parameters among the four EDPs, a correlation matrix has been prepared. The top three influencing EDPs are selected from the correlation matrix, as shown in Table 4. The corresponding $R^2 > 90\%$ is maximum, and hence it can be considered the most influencing parameter variable on DI.

By combining the 3 most influential parameters, a new expression can be proposed for finding the DI of the building, and a correlation has been established by linear regression analysis (LRA) between Park and Ang global DI and EDPs. The proposed DI expression is shown in Equation (27).

$$GDI = 0.083 \times \text{IDR} + 0.088 \times \theta + 0.682 \times d_{max} + 0.242 \quad (27)$$

Equation (27) has been generated from the considered EDPs, which were evaluated by considering 10 data points from the simulated model. The flow chart of the proposed method is shown in Figure 5.

TABLE 4. Correlation matrix for selected EDPs to categorize the most suitable variables

	GDI	IDR	Joint Rotation	Roof Displacement	Hysteresis Energy
GDI	1.0	0.962	0.959	0.954	0.500
IDR	0.962	1.0	**0.969**	**0.950**	0.479
Joint Rotation	0.959	0.969	1.0	**0.943**	0.443
Roof Displacement	0.954	0.950	0.943	1.0	0.572
Hysteresis Energy	0.500	0.479	0.443	0.572	1.0

In this study, ground storey experiences the maximum damage; therefore, the contribution of the ground storey is maximum in GDI. Comparing the GDI and the ground storey damage, it has been found that 0.819 times of ground storey DI displays equivalent GDI with an accuracy level of 92% (R^2=0.92). The expression is given by Equation (28). This method can be used only when the ground storey damage is known.

$$\text{GDI} = 0.819 \times \text{DI of the ground storey} \quad (28)$$

The damage index (DI) by using 3 individual response parameters is expressed by Equation (29).

$$\begin{aligned} \text{DI} &= 0.1539 \times \text{IDR} + 0.243 \text{ for IDR} \\ \text{DI} &= 4.6703 \times \theta + 0.4367 \text{ for } \theta \\ \text{DI} &= 1.3729 \times d_{max} - 0.2556 \text{ for } d_{max} \end{aligned} \quad (29)$$

5. RESULTS AND DISCUSSIONS

In this study, an NLTHA has been performed to determine the actual response in each step of the building. Park and Ang DI approach is very time-taking as well as consuming lots of time with the increase of the height of the building. Thus, the author attempted to establish a connection between Park and Ang method and calculated EDPs GDI of structure. Finally, the proposed method, i.e. calculated EDPs GDI, is compared with Park and Ang GDI method and shown in Figure 7. To validates the proposed method, another building with a different storey height (H=3.3m) has been analyzed, and GDI has been evaluated. It has been found that after changing the height of the floor of the building, the proposed approach is also capable of assessing the DI same way like Park and Ang GDI shown in Figure 6, and it proves that the proposed method gives approximate same results as the park and Ang GDI method.

The proposed method calculates GDI almost same as park and Ang method (R^2 =0.95) as shown in Figure 7. The estimated slope of the proposed method (eqution 27) is 0.945 which shows good correlation between these two methods.

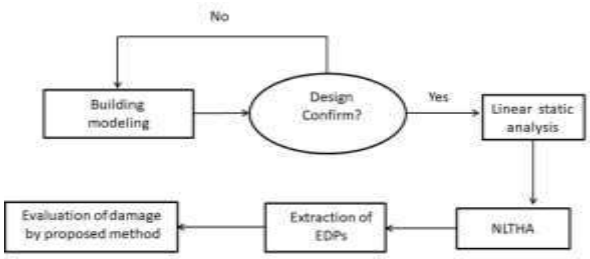

Figure 5. Flow chart followed by the proposed method

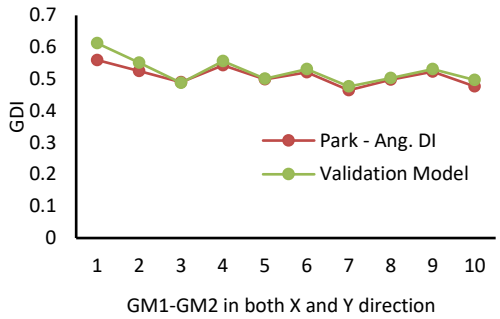

Figure 6. Comparison between Park and Ang. and proposed (Equation (27)) GDI

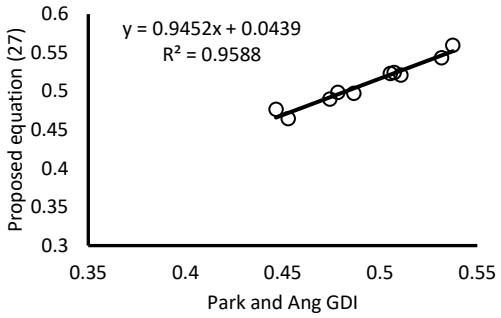

Figure 7. The fit of the Park-Ang GDI with the proposed GDI (Equation 27)

Figure 8 shows a connection between Park and Ang DI and individual EDPs. This method decreases the computational time and would fit the investigation of large-scale damage index (DI).

It is observed from Figures 9 and 10 that the calculated values of DI are highest at the ground storey level. Therefore, the contribution of the ground storey is maximum to GDI. A suitable correlation between ground Storey damage and GDI, has been found from the current study (Equation (28)). Therefore, GDI to ground storey DI ratio is 0.819. Likewise, the ratios for other floors can be obtained. Actual GDI versus empirical GDI (Equation (28)) is plotted in Figure 11 and it shows that there is a high accuracy rate of the empirical formula, which is greater than 92%.

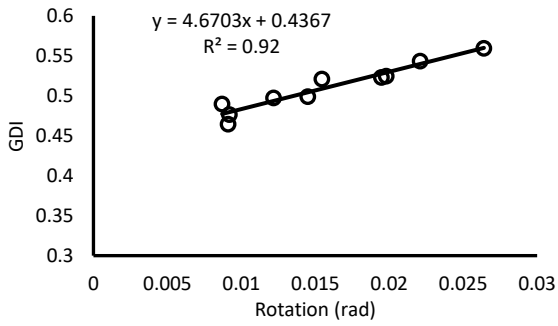

(a)

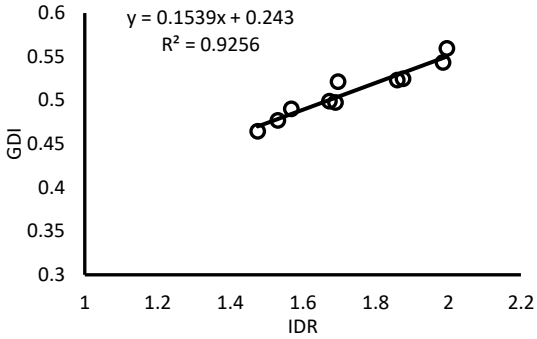

(b)

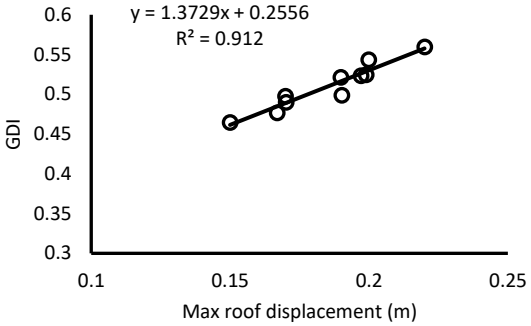

(c)

Figure 8. The comparison presented between individual EDPs and Park-Ang. DI a) Rotation versus GDI, b) IDR versus GDI, c) Max roof disp. versus GDI

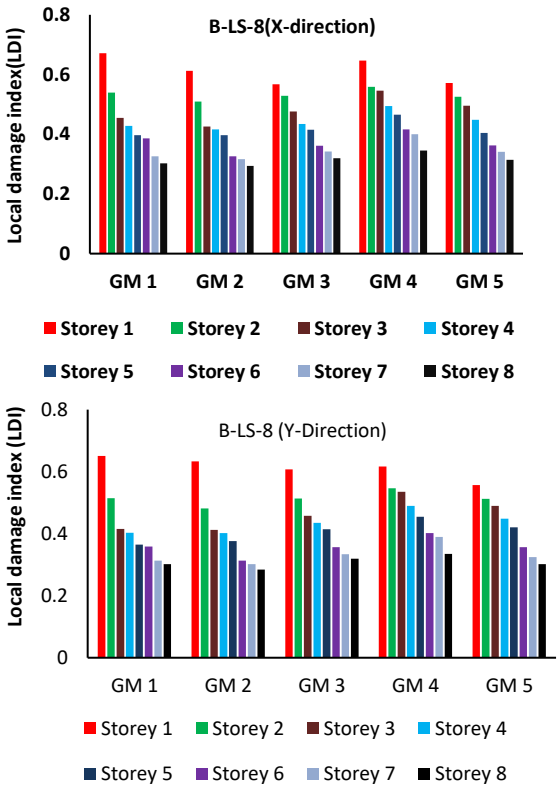

Figure 9. Storey-wise damage index (LDI) is shown for five ground motions in both X and Y directions

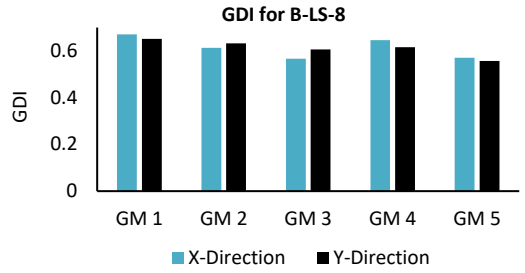

Figure 10. Park and Ang. Global damage index of an 8-storey building in both the X-Y directions

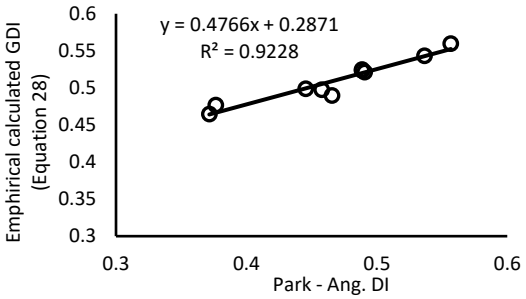

Figure 11. Empirically calculated GDI (from Equation 28) versus Park and Ang DI

5. CONCLUSION

In this study, 3 different expressions are proposed for the assessment of the DI of RC frame-shear wall building. The proposed approach considers maximum roof displacement, IDR, and joint rotation as EDPs. The reason behind proposing a new approach is to reduce the computational time as well as effort. The new proposed equation is simple, accurate, and easy to apply. The outcome of the current research shows that the proposed equation (Equation 27) simplifies the Park and Ang approach. Therefore, this proposed approach is suitable for evaluating the DI of the building from a small to large scale. Also, Equation (28) can be used for evaluating the DI of buildings but this equation can be used only after finding storey wise DI. Equation (29) can also be used for finding the GDI of the building, but the level of accuracy is lesser than both the proposed equation (Equations. 27 and 28). According to the correlation matrix shown in Table 1, where 4 engineering demand parameters has been chosen, and it has been found that 3 parameters (i.e. joint rotation, optimum roof displacement, and Inter storey drift ratio) are found as the most influential parameters with the accuracy rate of 95% ($R^2 = 0.95$ with GDI). As a result, this proposed approach can be used to find the GDI of a structure to achieve a high degree of accuracy. It has been found that the maximum damage occurs at the lower storey of the building; therefore, the ground storey should be designed with special care.

6. REFERENCES

1. Abdollahzadeh, Gh. and Niknafsb, S., "Evaluation of Damage Distribution in Elements of Dual Frames", ***International Journal of Engineering, Transactions B: Applications,*** Vol. 25, No. 4, (2012), 279-288. doi:10.5829/idosi.ije.2012.25.04b.04.
2. Lu, X., Lu. XZ, Guan., H. and Ye, LP., "Collapse simulation of reinforced concrete high-rise building induced by extreme earthquakes", ***Earthquake Engineering and Structural Dynamics*** Vol. 42, No. 5, (2013) 705-23. doi:10.1002/eqe.2240
3. Lu, X., Huang, Z. and Zhou, Y., "Global seismic damage assessment of high-rise hybrid structures. ***Computational Concrete***, Vol. 8 No. 3, (2011), 311-325. doi: http://dx.doi.org/10.12989/cac.2011.8.3.311
4. Kassem, M M., Nazri, F M., Farsangi, E N. and Ozturk, B., "Improved Vulnerability Index Methodology to Quantify Seismic Risk and Loss Assessment in Reinforced Concrete Buildings", ***Journal of Earthquake Engineering,*** (2021), 1-36. https://doi.org/10.1080/13632469.2021.1911888.
5. Ghasemi, S., Amiri, GG. and Dehcheshmeh, MM., "Structural Damage Assessment via Model Updating Using Augmented Grey Wolf Optimization Algorithm" ***International Journal of Engineering, Transactions A: Basics,*** Vol. 33, No 7, (2020), 1173-1182. doi:10.5829/ije.2020.33.07a.02
6. Mergos, PE. and Kappos, AJ., "Seismic damage analysis including inelastic shear flexure interaction", ***Bulletin of Earthquake Engineering***, Vol. 8, (2010), 27-46. doi: 10.1007/s10518-009-9161-2
7. Huang, W., Qian, J. and Zhou, Z., "Seismic damage assessment of steel-reinforced concrete members by a modified Park-Ang Model", ***Journal of Asian Architectural Building Engineering***, Vol. 15, No. 3, (2016), 605-611. doi:10.3130/jaabe.15.605
8. Parsaeifard, N. and Nateghi A, F., "The Effect of Local Damage on Energy Absorption of Steel Frame Buildings During Earthquake", ***International Journal of Engineering, Transactions B: Applications,*** Vol. 26, No. 2, (2013), 143-152. doi: 10.5829/idosi.ije.2013.26.02b.05
9. Park, Y-J., Ang, H-S. and Wen, YK., "Seismic damage analysis of reinforced concrete buildings", ***Journal of Structural Engineering*** Vol. 111, No. 4, (1985), 740-757. https://doi.org/10.1061/(ASCE)0733-9445
10. Yazdannejad, K. and Yazdani, A., "Bayesian updating of the Park and Ang damage index for RC frame buildings under near-fault ground motions", ***Science Iranica,*** Vol. 25, No. 2, (2018), 606-616. doi: 10.24200/SCI.2017.4188
11. Hait, P., Sil, A. and Choudhury, S., "Damage Assessment of Reinforced Concrete Buildings Considering Irregularities", ***International Journal of Engineering, Transactions A: Basics,*** Vol. 32, No. 10, (2019), 1388-1394. doi:10.5829/ije.2019.32.10a.08
12. Massumi, A. and Monavari, B., "Energy based procedure to obtain target displacement of reinforced concrete structures", ***Structure of Engineering Mechanics,*** Vol. 48, No. 5, (2013), 681-695. doi:10.12989/sem.2013.48.5.681
13. Sullivan, T.J., Priestley, M.J.N. and Calvi, G.M., "Direct Displacement-Based Design of Frame-Wall Structures", ***Journal of Earthquake Engineering,*** Vol. 10, (Special Issue 1), (2006), 91-124. https://doi.org/10.1080/13632460609350630
14. Choudhury, S. and Singh, S.M., "A Unified Approach to Performance-Based Design of RC Frame Buildings", ***Journal of the Institution of Engineers (India) Series A***, Vol. 94, No. 2, (2013), 73-82. doi:10.1007/s40030-013-0037-8
15. Mibang, D. and Choudhury, S., "Unified Performance-Based Design of RC Dual system", ***Research Square Preprint,*** (2021), doi: 10.21203.

16. ASCE/SEI 41-13., American Society of Civil Engineers Seismic Evaluation and Retrofit of Existing Buildings (2014).
17. Euro code-8., "Design of Structures for Earthquake Resistance. Part 1: General Rules, Seismic Actions, and Rules for Buildings", ***Comite European de Normalization***, Brussels (2004).
18. Kumar., "A Generation of spectrum compatible ground motion", 13th World Conference of Earthquake Engineering, Canada (2004).
19. SAP2000-v21., "Structural analysis programme", Berkley, CA, USA: Computer and Structures Inc.

Persian Abstract

چکیده

در این مطالعه ، اهداف متعددی در مورد روش های ارزیابی خسارت زلزله مورد بررسی قرار گرفته است. روش طراحی متحرک مبتنی بر عملکرد (UPBD)برای طراحی ساختمان دیوار برشی قاب بتنی مسلح (RC)استفاده شده است. ابتدا ، شاخص آسیب (DI)ساختمان با استفاده از روش پارک و انگ برآورد شده است. مشخص شده است که این روش بسیار وقت گیر است. بنابراین ، برای تحقیقات در مقیاس بزرگ مناسب نیست. بنابراین ، یک روش جدید برای کاهش زمان محاسبه و تلاش در مورد ساختارهای پیچیده در ارزیابی شاخص خسارت جهانی (GDI)پیشنهاد شده است. در این مطالعه حاضر ، سه پارامتر تأثیرگذار ساختمان برای یافتن GDI در نظر گرفته شده است. همچنین مشاهده شده است که بیشترین آسیب در طبقه همکف ساختمان رخ می دهد. روش پیشنهادی یک GDI قابل اعتماد را محاسبه می کند که می تواند آسیب ساختمان را از ساختمانهای کوچک تا بزرگ ارزیابی کند.

IJE TRANSACTIONS A: Basics Vol. 34, No. 10, (October 2021) 2302-2312

International Journal of Engineering

Journal Homepage: www.ije.ir

Sensitivity Analysis of Behavior of Simple Trapezoidal Steel Plates to Introduce a New Yielding Damper

H. Labibi[a], M. Gerami*[a], M. Hosseini[b]

[a] *Earthquake Engineering Department of Civil Engineering Faculty, University of Semnan, Semnan, Iran*
[b] *Structural Engineering Research Center, International Institute of Earthquake Engineering and Seismology (IIEES), Tehran, Iran*

PAPER INFO

Paper history:
Received 05 May 2021
Received in revised from 10 August 2021
Accepted 15 August 2021

Keywords:
Seismic Behavior
Nonlinear Analysis
Yielding Damper
Energy Dissipation

ABSTRACT

Over years, the energy absorption process against different kinds of loading has always been one of the most important issues in the engineering science. To address this, many kinds of dampers such as viscoelastic, friction, yielding, mass, and liquid dampers have been invented. Among all these dampers, steel yielding dampers are one of the most economic, available, suitable, and best choices for the long return period of seismic cyclic loading on structures. However, it seems that there are not sufficient studies on these dampers to convince the designers to use them widely. This research tries to show the effects of geometrical parameters on the energy absorption and cyclic behavior on a specific simple trapezoidal steel yielding damper using the finite element method, then the effect of using a new steel damper on base shear and roof acceleration responses of a three storey building studied by nonlinear time history analysis. According to the results, there are some effective and less effective parameters whose variation such as geometrical parameters can seriously change the total energy absorption level and improve the damper hysteresis loops as well as ductility under specific cyclic loading and showed that using a new steel damper will result in the significant decreasing in base shear and roof acceleration of the building.

***doi**: 10.5829/ije.2021.34.10a.11*

NOMENCLATURE

E	Steel module of elasticity (kN/mm^2)	PGA	Peak ground acceleration of ground motion (m/S^2)
F_y	Steel yielding strength (kN/mm^2)	PGV	Peak ground velocity of ground motion (m/S^2)
P_n	Yielding plate nominal yielding load (kN)	α	Trapezoidal plates angle (deg)
K_{eff}	Yielding plate elastic stiffness (kN/mm)	θ	Brace angle (deg)
V_s	Soil shear wave velocity (m/s)	β	Effective damping
b	Yielding plate width (mm)	t_0	Yielding plate thickness (mm)
t_1, t_2	Moving & fixed support plates thickness (mm)	A	Hysteresis loop area (kN.mm)

1. INTRODUCTION

Controlling and damping the structural seismic energy at the time of an earthquake has always been an important issue for structural earthquake researchers. Nowadays, codes allow designers to take account of plastic hinges in some parts of structures. In addition, they offer some sections and connections to concentrate on the damaged area such as reduced beam sections. However, it is a fact that some parts of the structure will get damaged and should be replaced after a major shock. Thus, researchers are trying to find damage control approaches to reduce the damaged area and increase the energy dissipation of structures. The use of dampers is one of the most considerable ways to achieve this goal. Dampers can dissipate the input earthquake energy without any significant damage to the main parts of the structure. Among all dampers, steel yielding dampers are the most available, economic, and easy to construct. Concerning the energy absorption process of steel, it should yield due to shear force and bending moment, so steel yielding dampers should be embedded such that they deform due

*Corresponding Author Institutional Email: mgerami@semnan.ac.ir
(M. Gerami)

Please cite this article as: H. Labibi, M. Gerami, M. Hosseini, Sensitivity Analysis of Behavior of Simple Trapezoidal Steel Plates to Introduce a New Yielding Damper, International Journal of Engineering, Transactions A: Basics, Vol. 34, No. 10, (2021), 2302-2312

to the lateral force of structures during an earthquake. ADAS dampers are one of these useful dampers. They are made of many yielding plates, placed above a chevron brace and yield together; meanwhile, it seems they can also be used in many other places of structure such as base plates, beam-to-column connections, and diagonal braces. The related history and evolution of these kinds of dampers are expressed further. Since 1976, many researchers have been trying to find a way to use steel yielding dampers in structures. In 1976, Kimura et al.[1] and in 1980 Mochizuki et al. [2] began their studies on dampers by researching non-buckling braces. The first type of this type of brace was introduced by Wanatabe et al. [3] in 1988. In 1990, Fujimoto et al. [4] installed them on 10- to 15-storey office buildings in Japan after conducting several experiments on non-buckling braces and preparing a numerical model. Extensive research has been conducted on various types of dampers since then. In 2019, Daniel et al. [5] studied seismic mitigation of Magnetorheological dampers. In 2019, Del Gobbo and Marcantonio [6] also evaluated the seismic performance of three types of four-, eight- and sixteen-story buildings by installing viscous dampers. He concluded that the use of dampers could significantly reduce the cost of repairing a structure once it occurred if any of the methods of placing the dampers were considered and an optimal design was achieved. Elsewhere, dealing with friction dampers, Taiyari et al. [7] in 2019 evaluated the seismic performance of two real four- and ten-storey structures using friction dampers. They concluded that the use of this type of damper plays an effective role in reducing the seismic parameters of the structure. Various yielding dampers have always been considered by researchers due to their optimal performance and energy absorption, stable cycle diagram, and ease of construction, as well as the flexibility of their shape and design. In 2018, Gerami and Kafi [8] conducted studies on the effect of the presence of yielding dampers at predetermined points on the seismic performance of convergent bracing frames. They proved that by using theoretical foundations and numerical modeling if the sections of the bracing members are properly reduced at certain points, the seismic behavior of the braced frame will be significantly improved. The use of a variety of ring and U-shaped elements has also been one of the favorite fields of damping researchers due to the high energy absorption process; among them, we can mention in 2014 Kafi et al. [9] and Zahraei and Cheraghi [10] in 2016. Yielding slit dampers are also a type of yielding damper that has recently been researched for use. In 2008, Chan and Albermani [11] examined the use of slit dampers in braced frames and performed several laboratory tests. They concluded that due to yielding of this type of damper in small rotations, it quickly enters the process of energy absorption during an earthquake. Also, considering the re-hardening after yielding, the ultimate strength of the fuse increases to twice its yielding rate. The use of parallel yielding plates in the design of yield dampers is a method considered in recent years due to its many advantages. In 2020, Maleki et al. [12] studied the effect of Curved-TADAS dampers on seismic response of moment resisting steel frames. The parallel triangular and trapezoidal plates used in XADAS[2] and TADAS[3] dampers have also been considered by researchers due to the high uncertainty of the part and the wide energy absorption in the entire yielding surface. In 1995, Soong et al. [13] considered a yielding damper using triangular parallel plates for the use on the upper part of Chevron braces. In 2009, Chan et al. [14] used shear steel plates to absorb energy in Chevron braces. After nineteen monotonic and cyclic laboratory tests, they concluded that the system had a completely stable behavior and that a large amount of energy was absorbed. In 2011, Krawinker et al. [15] performed experiments on the rhombic slit dampers. Indeed, the geometry of this damper was designed to better distribute the yielding and energy absorption process of the steel on its surface. In 2011, Akula [16] tested a type of yielding damper using U-shaped components. By designing a kind of connecting piece, he was able to arrange the U-shaped pieces in such a way that it would deform suitably by absorbing axial force and absorbing energy. In 2012, Hosseini and Noroozinejad [17] along with Hosseini and Alavi [18] in 2014 proposed the idea of telescopic columns when the rocking motion of the structure by using parallel yielding plates in the side columns. After experimental studies and nonlinear analysis, they proved that the use of parallel steel plates as interchangeable yielding dampers can provide desirable results in the behavior of the structure during an earthquake. In 2013, Li et al. [19] investigated the use of parallel yielding plates in series in the upper part of Chevron braces in reinforced concrete frames. They also installed and tested a prototype of this type of system in a reinforced concrete building. Finally, they concluded that the stiffness of this system subjected to small earthquakes and the possibility of yielding in large earthquakes provided a good opportunity for the seismic resistance and energy absorption. After several numerical analyses, they concluded that the use of this system in a reinforced concrete structure understudy will reduce seismic responses. In 2016, Aghakouchak et al. [20] investigated the effect of using a new type of damper called a sawtooth steel yielding damper to improve the cyclic behavior of steel frames. The results of finite element modeling as well as the conducted experiments showed that the designed damper produced responses by the design objectives. The tested specimens also revealed

[2] X-Shaped Plate Added Damping and Stiffness

[3] Triangular-Shaped Plate Added Damping and Stiffness

a completely stable hysteresis loop curve before tooth fracture while tolerating significant cumulative displacement. Gray et al. [21-24] introduced a yielding damper using parallel triangular pieces from 2012 to 2017. During several years of research, he built his damper by casting. Finally, after doing a few tests on the damper, he tested it by installing on a real-size frame. The experimental results indicated the optimal behavior of the bracing frame equipped with dampers. Also in 2019, Zibasokhan et al. [25] introduced a new type of yielding damper with parallel plates to improve the seismic performance of braced structures. After conducting several experimental studies, they concluded that the frame containing the proposed damper had a stable and desirable cyclic behavior. As mentioned in the literature, the constituent component of the damper, the trapezoidal plate, can be used as a part of new dampers. However, there is no perfect research on this field and it seems that a sensitivity analysis is required on the effective parameters of this important component. This research tries to show the sensitivity of the steel trapezoidal fuse due to changing geometrical specifications then a nonlinear time history analyses done on a three-story building which has been equipped by the new steel yielding damper made by trapezoidal plates and the base shear and roof acceleration responses were comprised using OpenSees. The model is made of two parallel and one simple trapezoidal fuse (Figure 1). Considering the function of the damper, two parallel plates move across each other so the fuse part yields and energy absorption process begins. The small sideway of the fuse part can be easily moved into the embedded gap where the large one is welded into another plate. The gap seize is so that pieces can be easily made but the extra gap can have some negative effects on the function of the damper and hysteresis loops. Eventually, this small simple model can act as a small part of a large damper.

2. MODELING VERIFICATION

To ensure that the analytical results are reliable, the finite element modeling procedure and results should be controlled with a similar experimental model. Hosseini and Alavi [18] tested a kind of energy dissipation device, whose hysteresis loops could be the modeling reference. Figure 2 shows the hysteresis loops verification.

3. ANALYSIS

The model behavior was measured by 28 finite element analyses by ABAQUS software. For this purpose, the three main effective parameters were selected. The first is material properties including yielding and ultimate strength, the module of elasticity and ductility effect on

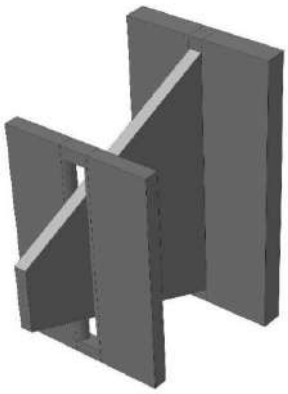

Figure 1. General shape of the damper element

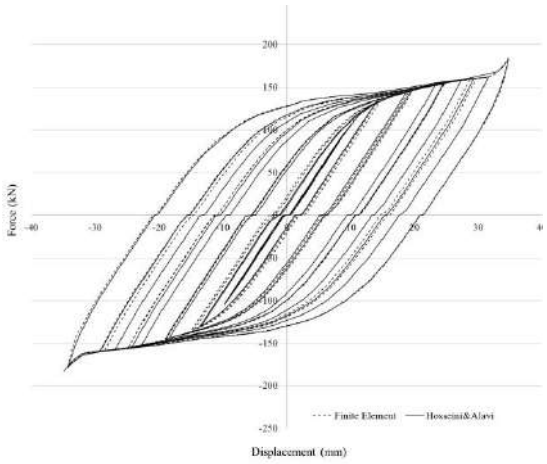

Figure 2. Modeling Verification

the damper behavior. since yielding dampers are usually made of structural steel (ST37), so the related effective parameters obtained from the laboratory test of structural steel by Hosseini and Alavi [18], which is shown in Figure 3. The friction coefficient is considered 0.3.

The second analysis setting is related to the software which involves loading speed, size of meshing, and the solution method affecting the results. For the second category of the parameters, the model hysteresis loops

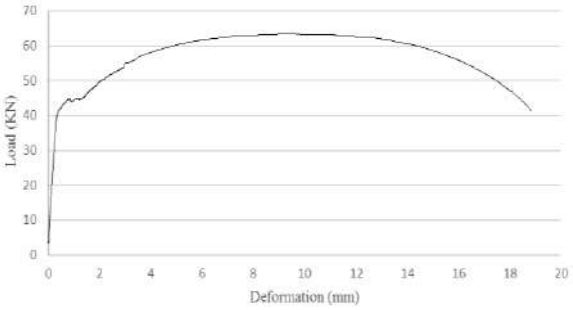

Figure 3. The Hosseini & Alavi Stress-Strain Diagram [18]

are verified against experimental test results. loading protocol (Figure 4) and loading speed, analysis method, the element type of meshing, and size of meshing fall in this category. The static nonlinear method was used to calculate the results. For this purpose, the maximum 45 mm displacement at 1.8 s was applied to the model according to Figure 4 loading diagram. The first step of the analysis was supposed to be 5e-5 and the maximum step time was described as 0.01 s. It should say that according to the model verification, the chosen analytical parameters are correct and can be fixed.

Due to sensitivity and excessive distortion of the fuse part, the element C3D10 was selected for this part and the element C3D8R was selected for the other parts of the damper. Figure 5 reveals the shape of these elements.

Figure 6 indicates the meshing size and element assignment and arrangement of the parts. As stated earlier, the fuse part meshing assignment is different from the other parts due to its excessive distortion. Due to the support condition of the fuse part, the bending moment will decrease from the large sideway of the plate to the small sideway, but the shear force of the fuse will not change along with the plate. This, for obtaining a good yielding distribution and maximum energy absorption, the trapezoidal shape of the plate was chosen. The small sideway of the fuse support is prepared in a way that the fuse plate can slide inside the gap. This feature will not cause any tension to the fuse plate as well as connections welding. Also, the total displacement domain of the damper will increase.

3. 1. Geometrical Effective Parameters Distance of two parallel plates, fuse plate thickness, fuse thickness

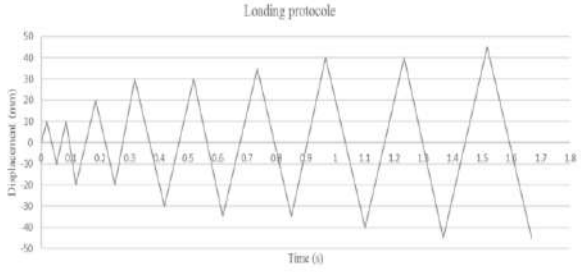

Figure 4. Loading protocol

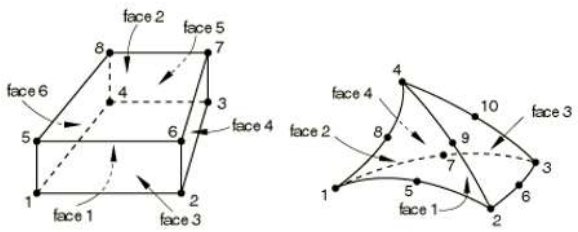

Figure 5. The shape of elements C3D8R (Left) & C3D10 (Right)

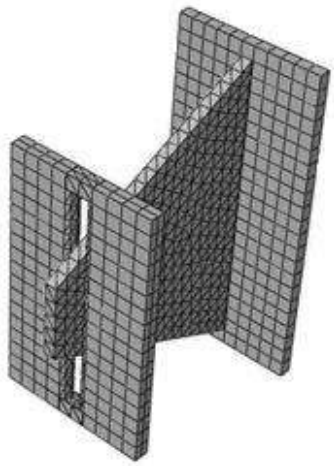

Figure 6. Meshing assignment of the damper model

to parallel plates ratio, fuse shape angle, and the gap between fuse plate and the support plate fall in this category with each being disused individually further. The response of the fuse plate can be predicted using simple equations [7]; Equations (1) and (2) predict the fuse nominal yield load, P_n, and fuse elastic stiffness, $K_{eff.}$

$$P_n = \frac{bt^2}{4L} F_y \quad (1)$$

$$K_{eff} = \frac{bt^3}{6L^3} E \quad (2)$$

where, b is the width of the fuse plate at its base, t represents the effective thickness, L is the length of the fuse plate, F_y denotes the yielding strength of the selected construction steel, and E is the module of its elasticity.

3. 1. 1. Two Parallel Plates' Distance One of the most important effective parameters on the damper behavior is the distance of two parallel plates. According to the analyses, as the distance increases, so does the displacement domain of the damper and hence the fuse yielding distribution. On the other hand, upon reduction of the distance of the two parallel plates, more stiffness will result. On the other hand, the ultimate strength of the damper will increase. Figure 7 shows the hysteresis loops of 7 to 13 centimeters, distances of two parallel plates, which prove the above points. Note that there are two yielding mechanisms in this situation: first, the bending mechanism, which occurs in large distances and second the shear mechanism, which occurs in small distances. In the first mode, the energy dissipation of the fuse is not considerable and as the distance increases, the shear yielding mechanism will be associated with the bending mode where the absorbing energy will grow. On the other hand, in small distances, the energy dissipation will decline again because of the small yielding area. Thus, there is an optimum distance between two parallel plates where both the bending and shearing yielding

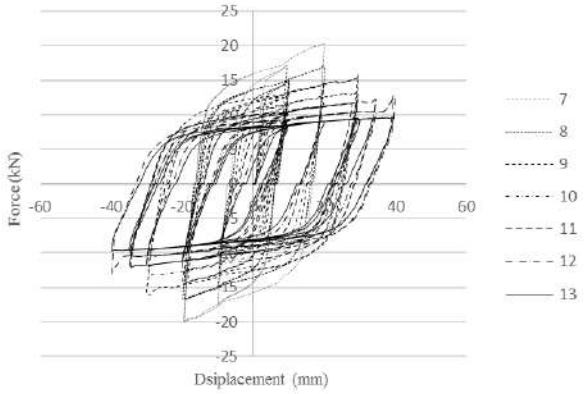

Figure 7. 7 to 13 centimeters analyses result of the two parallel plates distance

mechanisms maximize the energy absorption on the fuse plate. In addition, because of major rotations in the fixed end of the plate, the connection should withstand the cyclic moments and yielding rotations.

3. 1. 2. Yielding Plate to Parallel Plate's Thickness Ratio One of the other effective geometrical parameters in the damper behavior is the ratio of the fuse plate thickness to any of the parallel plate's thickness. To examine it, by changing the large plate thickness and fixing the other parameters, six analyses were performed as shown in Table 1. Further, for the second condition, these analyses were conducted for the small plate as detailed in Table 2. The ratio was supposed to be between zero and two and then this domain was divided into six conditions, which can show a good index in the analysis results.

Figure 8 reveals the hysteresis loops obtained from the first condition analyses. According to the results and obtained hysteresis loops, as the ratio decreased, so did the energy absorption and the damper displacement domain while the stiffness of the device increased. No change was observed in the ultimate strength and it seems that the total shape of the loops was acceptable and stable. Note that although at large thickness ratios, the dissipated energy increases, but as the large plate thickness drops,

TABLE 1. Geometrical specification of models for the first situation sensitivity analyses

Analysis	t_0	α	Distance	Gap	t_2	t_1	t_0/t_1
S1A1	8	65	130	0.5	10	24	0.33
S1A2	8	65	130	0.5	10	12	0.67
S1A3	8	65	130	0.5	10	8	1.00
S1A4	8	65	130	0.5	10	6	1.33
S1A5	8	65	130	0.5	10	4.8	1.67
S1A6	8	65	130	0.5	10	4	2.00

TABLE 2. Geometrical specification of models for the first situation sensitivity analyses

Analysis	t_0	α	Distance	Gap	t_1	t_2	t_0/t_2
S1A7	8	65	130	0.5	15	24	0.33
S1A8	8	65	130	0.5	15	12	0.67
S1A9	8	65	130	0.5	15	8	1.00
S1A10	8	65	130	0.5	15	6	1.33
S1A11	8	65	130	0.5	15	4.8	1.67
S1A12	8	65	130	0.5	15	4	2.00

the welding will be more sensitive and less reliable in cyclic loading. On the other hand, the thick plate will increase the weight of the device, so the aftershock replacement will be hard. Thus, it seems the designer should choose an economic functional ratio for his design goals. The results of the second analysis conditions show that as the ratio decreased, the displacement domain of the damper would increase, but the energy absorption of the damper would not change significantly. It seems that because of the small contact between the fuse plate and the small plate due to the inner curvature of the support gap, the small plate thickness will not affect the results considerably. Figure 9 displays the hysteresis loop of these analyses. Note that the S1A11 and S2A12 analyses could not be completed because of excessive distortion and fracture of the small support plate.

3. 1. 3. The Angle of Yielding Plate The other effective geometrical parameter is the fuse angle (Figure 10).

The condition of the fuse plate is such that it should withstand the bending moment and shear force on the large side fixed end and only the shear force on the free small side. Thus, for better uniform yielding in the fuse plate area, its geometry should be trapezoidal. The extent of dissipated energy is dependent on the plate angle; as

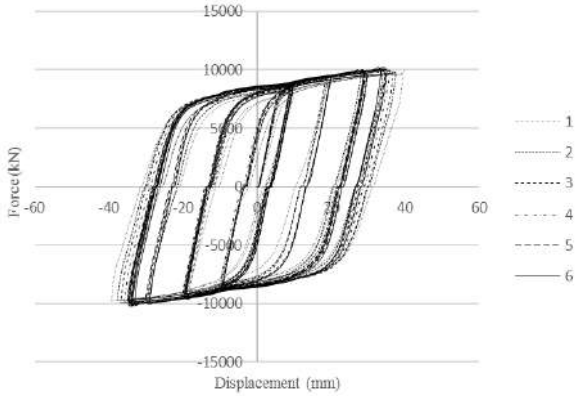

Figure 8. Hysteresis loops obtained from S1A1 to S1A6 analyses

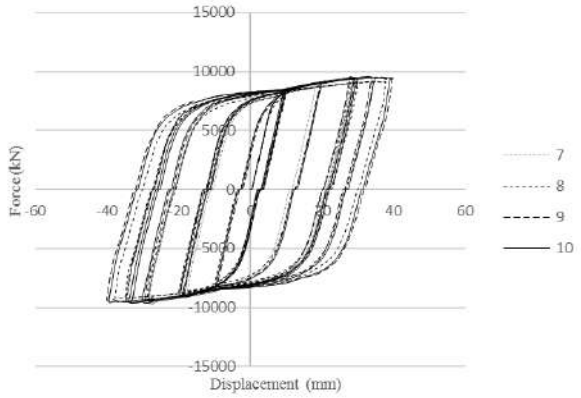

Figure 9. Hysteresis loops obtained from S1A7 to S1A10 analyses

the fuse angle rises, the distance between the two parallel plates can be enlarged and then the steel yielding surface and energy absorption increases. Also, when the distance between two parallel plates increases, the displacement domain of the damper will grow. On the other hand, as the fuse angle diminishes, the steel yielding uniform extension will improve. Also, the distance between two parallel plates will decline and so will its displacement domain. The condition of the fuse plate is such that it should withstand the bending moment and shear force on the large side fixed end and only the shear force on the free small side. Thus, for better uniform yielding in the fuse plate area, its geometry should be trapezoidal. The extent of dissipated energy is dependent on the plate angle; as the fuse angle rises, the distance between the two parallel plates can be enlarged and then the steel yielding surface and energy absorption increases.

When the distance between two parallel plates increases, the displacement domain of the damper will grow. On the other hand, as the fuse angle diminishes, the steel yielding uniform extension will improve. Also, the distance between two parallel plates will decline and so will its displacement domain. Table 3 shows the considered analyses to capture the effects of this parameter. For this purpose, four angles between 60 to 75 degrees were considered according to previous studies.

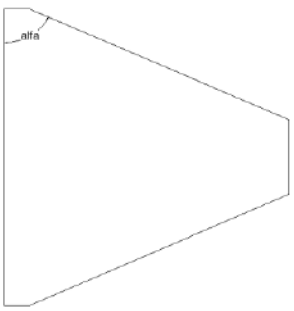

Figure 10. Yielding element angle (α)

Figure 11 displays the hysteresis loops obtained from these analyses. As shown in this figure, as the fuse angle rises, the stiffness of the damper will increase, but the displacement domain of the damper will drop and there is no significant change in its ultimate strength. It seems that the plates with smaller angles have better tolerance against the cyclic deformation and yielding.

3. 1. 3. The Gap Between the Yielding Plate and Support Plates The other effective parameter is the gap between the fuse plate and the support plates. If the fuse thickness is 8 mm, the gap between the fuse and the support should not be less than 0.5 mm for damper easy construction. On the other hand, selecting large gaps can affect the damper behavior and degree of energy absorption. Meanwhile, use of large gaps makes the device have small free movements to obtain the fuse stiffness. Therefore, this issue causes a kind of a shock to the damper in real loading, which is not optimal. Choosing the minimum size of the gap will enhance the stiffness of the damper and augment the end moment as well as rotation of the fuse plate. Table 4 reports the considered analyses to capture the effect of this geometrical parameter. Figure 12 shows the hysteresis loops of these analyses. As shown in this figure, the displacement domain and amount of energy absorption of the damper increased due to increasing gap distance, but the stiffness and ultimate strength of the device decreased in large displacements. It seems the total shape of the

TABLE 3. Considered analyses to discover the yielding element angle effects

Analysis	t_0	α	Distance	Gap	t_2	t_1
S2A1	8	60	80	0.5	10	15
S2A2	8	65	80	0.5	10	15
S2A3	8	70	80	0.5	10	15
S2A4	8	75	80	0.5	10	15

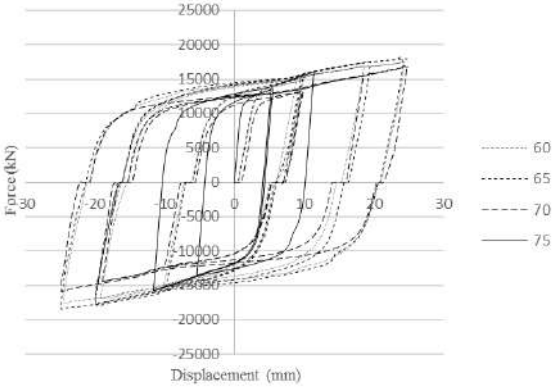

Figure 11. Hysteresis loops of changing yielding element angle

TABLE 4. The supports gap sensitivity analyses

Analysis	t_0	α	Distance	Gap	t_2	t_1
S3A1	8	65	80	0.5	10	15
S3A2	8	65	80	1.0	10	15
S3A3	8	65	80	2.0	10	15

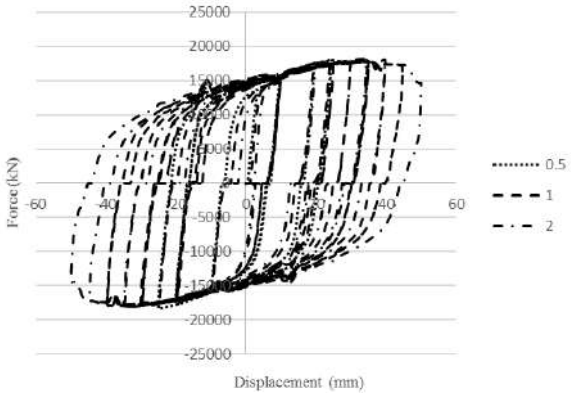

Figure 12. Hysteresis loops of changing fuse and support gap

hysteresis loops is stable and no significant change has occurred in the hysteresis shapes by altering the gap distance; however, the large gap models can dissipate more cyclic energy.

3. 1. 4. Yielding Plate Thickness The fuse plate thickness is another effective parameter on damper behavior; elevation of this value will increase the shearing rule in the energy absorption process. It will also boost the ultimate strength and stiffness of the damper. Table 5 provides the analyses considered for the sensitivity of this parameter.

As shown in Table 5, four analyses were considered to discover the damper sensitivity of the fuse thickness between 5 and 20 mm. According to the results and hysteresis loops are shown in Figure 13, Increasing the fuse thickness will cause augmented fuse end moment; so, the risk of damper fracture will increase. On the other hand, a reduction of this value will cause a reduction in the shearing and bending yielding extension and hence the energy absorption. In addition, as the fuse thickness

TABLE 5. Analyses considered for yielding plate thickness

Analysis	t_0	α	Distance	Gap	t_2	t_1
S4A1	**5**	65	130	0.5	10	15
S4A2	10	65	130	0.5	10	15
S4A3	15	65	130	0.5	10	15
S4A4	20	65	130	0.5	10	15

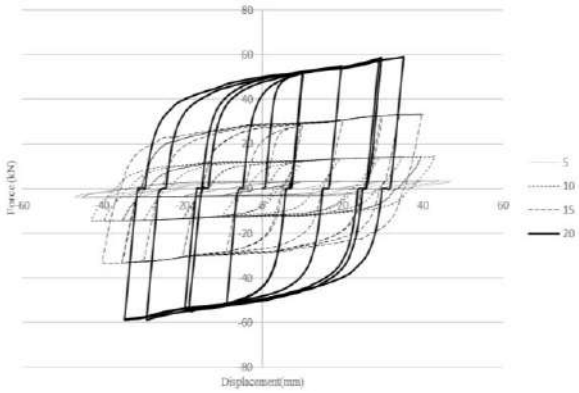

Figure 13. Hysteresis loops obtained from analyses S4A1 to S4A4

increases, so do the stiffness and the energy absorption of the damper, but the ultimate displacement domain of the damper decreases due to the fuse fixed end fracture risk.

4. TWO-LEVEL DAMPER

To assessment the application of the studied plates, a two-level performance damper was designed for use in the building's brace frames. The design of the damper is in such a way that in small displacements the two taller plates with smaller stiffness bear the force and absorb energy but as the displacement increases, the other (shorter) plates help the taller ones. The outer box restricts the damper displacement to exceeds a specific value. Figure 14 shows the damper dimension details and its placement in the frame. Figure 15 displays the hysteresis loops obtained from finite element analysis in terms of force capacity and damper deformation. As shown in the figure, the resulting diagram has stable cycles and two-level performance. The damper capacity for deformation of 60 mm was 870 kN in one direction and 550 kN in the other. The asymmetry in the diagram is due to the pyramidal geometry of the inner part, which though has little effect on the overall performance of the damper.

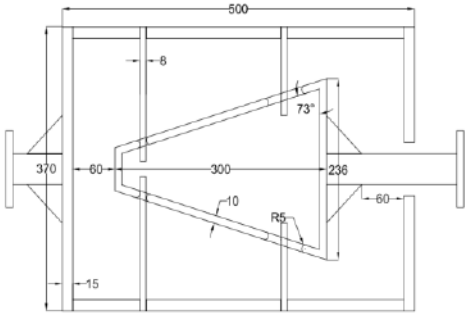

(a) Damper configuration

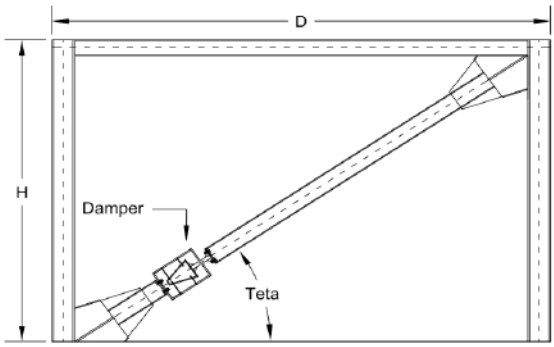

(b) Damper placement in the frame

Figure 14. The location of the new designed damper in the frame and its details

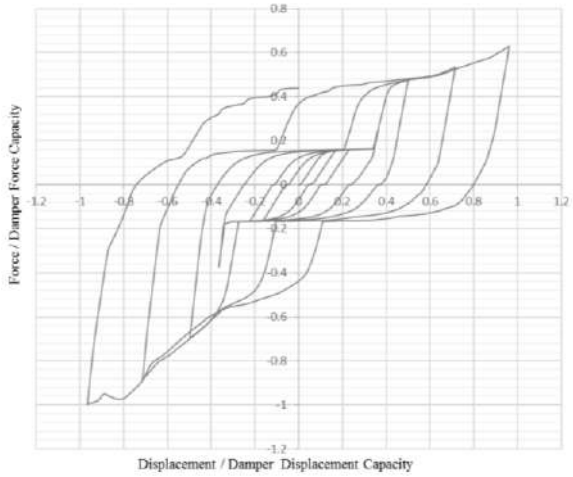

Figure 15. Hysteresis loops obtained from finite element analyses

In general, as the number of yielding plates increases, the angle of the pyramidal section decreases and the asymmetry in the graph diminishes due to the increase in the length of the pyramidal section. Table 6 also outlines the parameters of effective stiffness, effective damping, and confined area calculated in each loading cycle for the finite element model.

TABLE 6. Calculated parameters for each loading cycle

Cycles	Displacement Ratio	Force Ratio	K_{eff}	β	A
1, 2	0.17, 0.17	0.16, 0.15	1.40	0.182	154
3, 4	0.24, 0.24	0.17, 0.16	1.04	0.288	346
5, 6	0.38, 0.38	0.37, 0.26	1.26	0.206	780
7, 8	0.52, 0.52	0.7, 0.47	1.71	0.173	1663
9, 10	0.74, 0.74	0.89, 0.53	1.45	0.228	3800
11, 12	1, 1	1, 0.63	1.23	0.278	7162

In general, as the number of yielding plates increases, the angle of the pyramidal section decreases and the asymmetry in the graph diminishes due to the increase in the length of the pyramidal section. Table 6 also outlines the parameters of effective stiffness, effective damping, and confined area calculated in each loading cycle for the finite element model.

5. TIME HISTORY ANALYSIS

An OpenSees code was developed to comprise the nonlinear time history analyses responses of a three storey three span CBF frame. Figure 16 shows the frame configuration and sections. the frame was designed based on the AISC 360-10 [26] criteria. Seven far field earthquakes based on the soil and fault condition selected from the FEMA P-695 [27] suggested ground motions for the time history analyses. Table 7 shows the

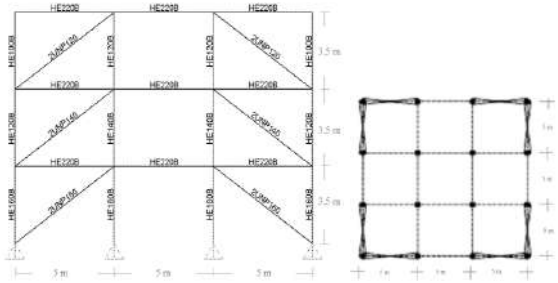

Figure 16. Frame configuration

TABLE 7. Ground motions characteristics [27]

ID No.	Record Seq. No.	Name	Magnitude	Site-Source Distance (km)	Vs	PGA	PGV
1	1602	Duzce	7.1	12.4	326	0.82	62
2	169	Imperial Valley	6.5	22.5	275	0.35	33
3	174	Imperial Valley	6.5	13.5	196	0.38	42
4	1116	Kobe	6.9	28.5	256	0.24	38
5	1158	Koceaeli	7.5	15.4	276	0.36	59
6	900	Landers	7.3	23.8	354	0.24	52
7	848	Landers	7.3	20	271	0.42	42

specifications of the selected ground motions. To prevent buckling of the brace members, dampers with the capacity of 90% of brace members capacity designed to use at any story and the maximum displacement capacity of dampers are adjusted to the maximum allowable drift of the building stories. to understand the effect of dampers on the building seismic behavior the base shear and roof acceleration responses were studied. Figure 17 and Figure 18 respectively show the base shear and roof acceleration comparative diagrams.

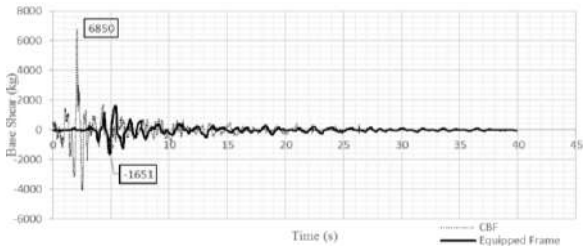

(a) Duzce (1602) comparative response diagram

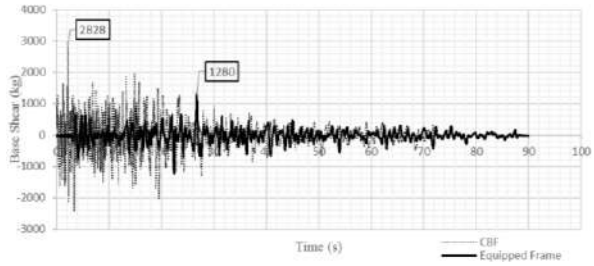

(b) Imperial Valley (169) comparative response diagram

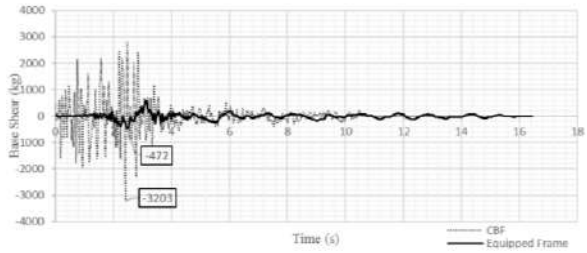

(c) Imperial Valley (174) comparative response diagram

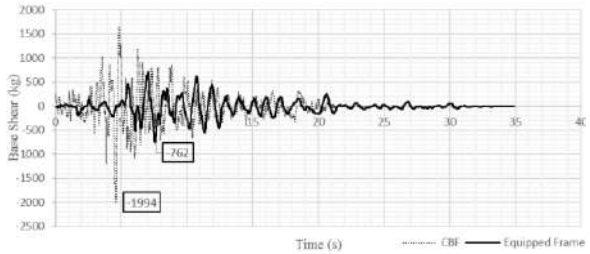

(d) Kobe (1116) comparative response diagram

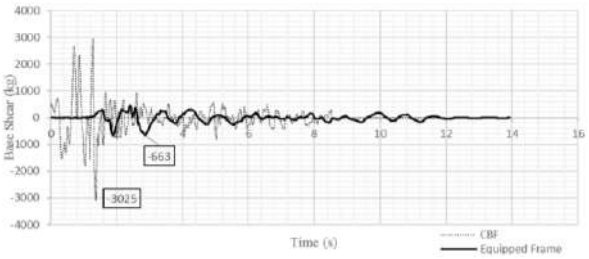

(e) Kocaeli (1158) comparative response diagram

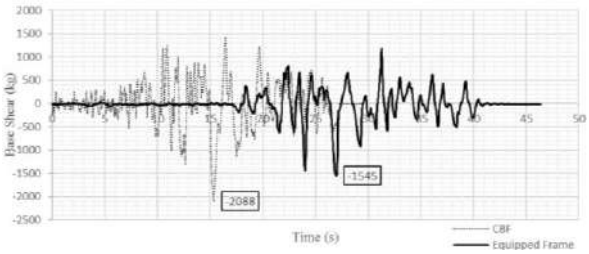

(f) Landers (900) comparative response diagram

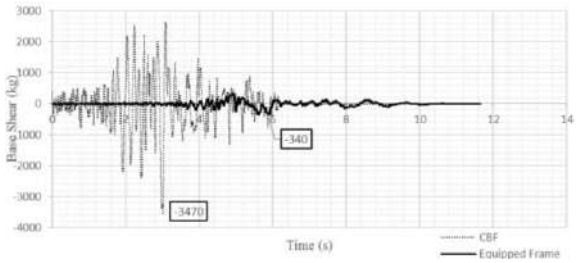

(g) Landers (848) comparative response diagram

Figure 17. Base shear comparative time history response diagrams

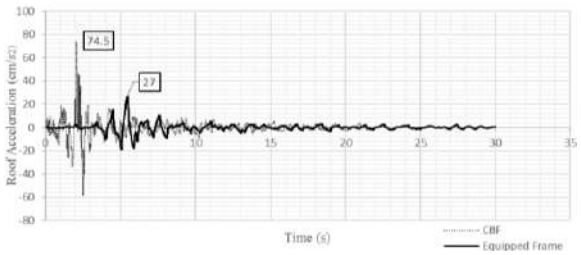

(a) Duzce (1602) comparative response diagram

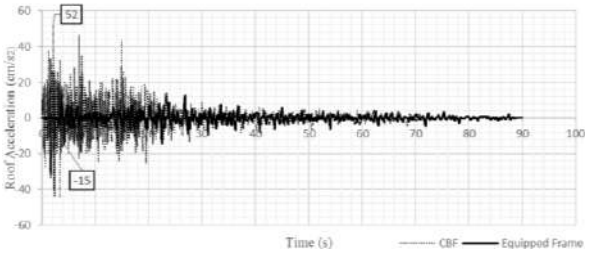

(b) Imperial Valley (169) comparative response diagram

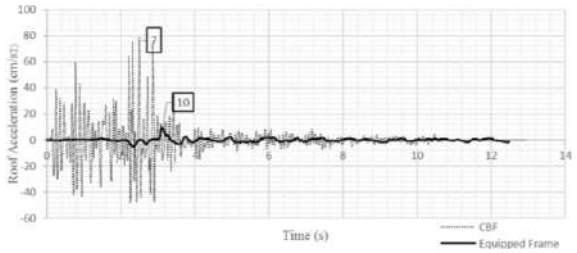

(c) Imperial Valley (174) comparative response diagram

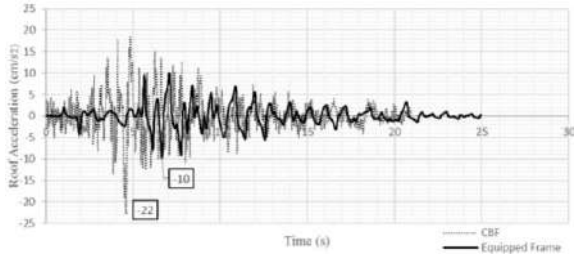

(d) Kobe (1116) comparative response diagram

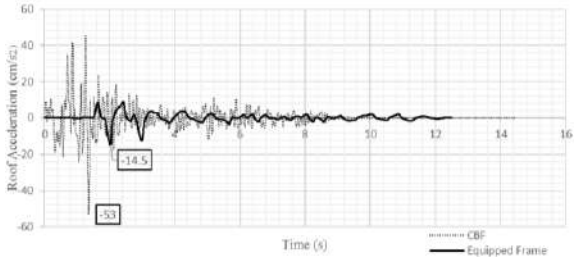

(e) Kocaeli (1158) comparative response diagram

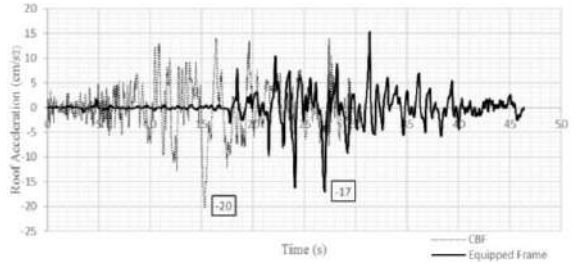

(f) Landers (900) comparative response diagram

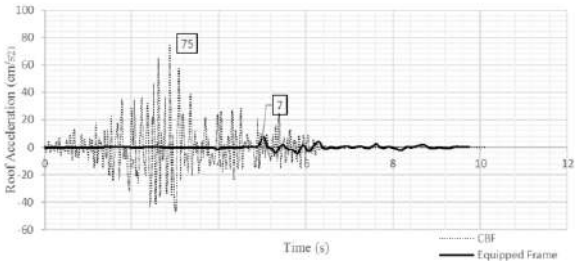

(g) Landers (848) comparative response diagram

Figure 18. Roof acceleration comparative time history response diagrams

6. CONCLUSION

According to the analyses performed for the damping device, the conclusions are presented as follows:

1. Trapezoidal plates as a fuse in steel yielding dampers can give steady reliable hysteresis loops and their shape will cause better yielding extension and energy absorption.
2. Among the sensitivity analyses performed for the geometrical parameters, the distance of two parallel plates and fuse plate thickness parameters had the most substantial effects on the damper analysis result. Elevation of the distance of two parallel plates will cause enhanced dissipated energy and damper cyclic moving domain, but adequate free length should be prepared for the fuse plate to withstand the shear force and not to exit the gap.
3. The rise of the fuse thickness might cause permanent shear deformation on the plate, which makes the fuse cyclic moving difficult.
4. Although small angles of the fuse plate can give a good uniform yielding, but the smaller the angle, the lower the length of the fuse and so the smaller the distance of the two parallel plates is. On the other hand, the large fixed side of the fuse plate can have an interaction with the architectural part of the structure.
5. As shown in the comparative diagrams, using the two-level performance damper had a significant decreasing effect on the base shear and roof acceleration response of the CBF frame under the seven time history far field ground motion analyses.

7. REFERENCES

1. Kimura, Kazuhiro, K. Yoshioka, T. Takeda, Z. Fukuya, and K. Takemoto. “Tests on braces encased by mortar in-filled steel tubes.” In Summaries of Technical Papers of Annual Meeting, Architectural Institute of Japan, Vol. 1041, (1976), 1-42.
2. Mochizuki, N., Y. Murata, N. Andou, and S. Takahashi. “An experimental study on buckling of unbonded braces under centrally applied loads.” In Annual Meeting of the Architectural Institute of Japan (in Japanese), (1988).
3. Watanabe, Atsushi, Yasuyoshi Hitomi, Eiichiro Saeki, Akira Wada, and Morihisa Fujimoto. "Properties of brace encased in buckling-restraining concrete and steel tube." In Proceedings of Ninth World Conference on Earthquake Engineering, Vol. 4, (1988), 719-724, https://www.iitk.ac.in/nicee/wcee/article/9_vol4_719.pdf
4. Fujimoto, Morihisa, Akira Wada, Eiichiro Saeki, Toru Takeuchi, and Atsushi Watanabe. “Development of unbonded brace.” ***Quarterly Column,*** Vol. 115, (1990), 191-96, http://www.arch.titech.ac.jp/Takeuti_Lab/img/Papers/002-Development%20of%20Unbonded%20Brace%201990.1.pdf.
5. Daniel, C., G. Hemalatha, L. Sarala, D. Tensing, and S. Sundar Manoharan. “Seismic mitigation of building frames using magnetorheological damper.” ***International Journal of Engineering, Transactions B: Applications,*** Vol. 32, No. 11 (2019), 1543-1547, DOI: https://dx.doi.org/10.5829/ije.2019.32.11b.05.
6. Del Gobbo, Giuseppe Marcantonio. “Placement of fluid viscous dampers to improve total-building seismic performance.” In Proceedings of the CSCE Annual Conference, Laval, Montreal, QC, Canada, (2019), 12-15,

https://www.csce.ca/elf/apps/CONFERENCEVIEWER/conferences/2019/pdfs/PaperPDFversion_175_0225040259.pdf.

7. Taiyari, Farshad, Federico M. Mazzolani, and Saman Bagheri. "Damage-based optimal design of friction dampers in multistory chevron braced steel frames." ***Soil Dynamics and Earthquake Engineering***, (2019), 11-20, DOI: https://doi.org/10.1016/j.soildyn.2019.01.004.
8. Kachooee, Ali, Mohammad Ali Kafi, and Mohsen Gerami. "The effect of local fuse on behavior of concentrically braced frame by a numerical study." ***Civil Engineering Journal,*** Vol. 4, No. 3, (2018), 655-67, DOI: http://dx.doi.org/10.28991/cej-0309123.
9. Andalib, Zahra, Mohammad Ali Kafi, Ali Kheyroddin, and Mohammad Bazzaz. "Experimental investigation of the ductility and performance of steel rings constructed from plates." ***Journal of Constructional Steel Research***, Vol. 103, (2014), 77-88, DOI: https://doi.org/10.1016/j.jcsr.2014.07.016.
10. Cheraghi, Abdullah, and Seyed Mehdi Zahrai. "Innovative multi-level control with concentric pipes along brace to reduce seismic response of steel frames." ***Journal of Constructional Steel Research***, Vol. 127, (2016), 120-135, DOI: https://doi.org/10.1016/j.jcsr.2016.07.024.
11. Chan, Ricky WK, and Faris Albermani. "Experimental study of steel slit damper for passive energy dissipation." ***Engineering Structures,*** Vol. 30, No. 4, (2008), 1058-1066, DOI: https://doi.org/10.1016/j.engstruct.2007.07.005.
12. Shojaeifar, Hamid, Ahamd Maleki, and Mohammad Ali Lotfollahi-Yaghin. "Performance evaluation of curved-TADAS damper on seismic response of moment resisting steel frame." ***International Journal of Engineering, Transactions A: Basics,*** Vol. 33, No. 1, (2020), 55-67, DOI: https://dx.doi.org/10.5829/ije.2020.33.01a.07.
13. Dargush, G. F., and T. T. Soong. "Behavior of metallic plate dampers in seismic passive energy dissipation systems." ***Earthquake Spectra,*** Vol. 11, No. 4, (1995), 545-568, DOI: https://doi.org/10.1193%2F1.1585827.
14. Chan, Ricky WK, Faris Albermani, and Martin S. Williams. "Evaluation of yielding shear panel device for passive energy dissipation." ***Journal of Constructional Steel Research,*** Vol. 65, No. 2, (2009), 260-268, DOI: https://doi.org/10.1016/j.jcsr.2008.03.017.
15. Ma, X., H. Krawinkler, and G. G. Deierlein. "Seismic design and behavior of self-centering braced frame with controlled rocking and energy dissipating fuses", ***Blume Earthquake Engineering,*** Vol. 174, Center TR, (2011), https://stacks.stanford.edu/file/druid:rw990bk7960/TR%20174_Ma.pdf
16. Akula, Srikanth. "A high displacement metallic yielding device for passive energy dissipation." State University of New York at Buffalo, (2011), https://www.proquest.com/openview/b346183ac7d166116532957be773cc16
17. Hosseini, Mahmood, and Ehsan Noroozinejad Farsangi. "Telescopic columns as a new base isolation system for vibration control of high-rise buildings." ***Earthquakes and Structures***, Vol. 3, No. 6, (2012), 853-867, DOI: http://dx.doi.org/10.12989/eas.2012.3.6.853.
18. Hosseini, Mahmood, and S. Alavi. "A kind of repairable steel buildings for seismic regions based on buildings' rocking motion and energy dissipation at base level." ***International Journal of Civil and Structural Engineering-IJCSE***, Vol. 1, No. 3, (2014), https://www.academia.edu/28041683.
19. Li, Gang, and Hong-Nan Li. "Experimental Study and Application of Metallic Yielding–Friction Damper." ***Journal of Earthquake and Tsunami,*** Vol. 7, No. 03, (2013), 1350012, DOI: http://dx.doi.org/10.1142/S1793431113500127.
20. Garivani, S., A. A. Aghakouchak, and S. Shahbeyk. "Numerical and experimental study of comb-teeth metallic yielding dampers." ***International Journal of Steel Structures,*** Vol. 16, No. 1 (2016), 177-196, DOI: http://dx.doi.org/10.1007/s13296-016-3014-z.
21. Gray, M. G., C. Christopoulos, and J. A. Packer. "Cast steel yielding fuse for concentrically braced frames." In Proceedings of the 9th US National and 10th Canadian Conference on Earthquake Engineering, Vol. 9. Earthquake Engineering Research Institute and the Canadian Association for Earthquake Engineering Oakland, CA, USA and Ottawa, ON, Canada, (2010), DOI: http://dx.doi.org/10.1061/(ASCE)ST.1943-541X.0000910.
22. Gray, M. G., C. Christopoulos, J. A. Packer, and D. G. Lignos. "Development, validation, and modeling of the new cast steel yielding brace system." In 20th Analysis and Computation Specialty Conference, (2012), 71-82, DOI: https://doi.org/10.1061/9780784412374.007.
23. Gray, Michael G., Constantin Christopoulos, and Jeffrey A. Packer. "Cast steel yielding brace system for concentrically braced frames: concept development and experimental validations." ***Journal of Structural Engineering,*** Vol. 140, No. 4, (2014), 04013095, DOI: https://doi.org/10.1061/(ASCE)ST.1943-541X.0000910.
24. Gray, Michael G., Constantin Christopoulos, and Jeffrey A. Packer. "Design and full-scale testing of a cast steel yielding brace system in a braced frame." ***Journal of Structural Engineering,*** Vol. 143, No. 4, (2017), 04016210, DOI: https://doi.org/10.1061/(ASCE)ST.1943-541X.0001692.
25. Zibasokhan, Hassan, Farhad Behnamfar, and Mojtaba Azhari. "Experimental study of a new pure bending yielding dissipater." ***Bulletin of Earthquake Engineering,*** Vol. 17, No. 7, (2019), 4389-4410, DOI: 10.1007/s10518-019-00616-1.
26. American Institute of Steel Construction. ANSI/AISC 360-10 "Specification for structural steel buildings", ***AISC***, (2010).
27. Federal Emergency Management Agency (FEMA) P695 "Recommended Methodology for Quantification of Building System Performance and Response Parameters." Project ATC-63, Prepared by the Applied Technology Council, Redwood City (2009).

Persian Abstract

چکیده

فرآیند جذب انرژی برای کاهش نیروهای وارده همواره یکی دغدغه‌های علم مهندسی سازه بوده است. بدین منظور انواع مختلفی از میراگرها همچون میراگرهای اصطکاکی، جرمی و تسلیمی ابداع شده اند؛ از این میان میراگرهای فلزی تسلیم شونده جزو میراگرهای اقتصادی و کاربردی بوده که عملکرد مناسبی را در عمل و در آزمایشات به نمایش گذاشته‌اند. لکن هنوز مطالعات کافی برای استفاده‌ی گسترده‌ی آنها در طراحی و مقاومسازی سازه‌ها صورت نگرفته است. در این تحقیق سعی شده است تا با استفاده از روش اجزای محدود، تحلیل‌های حساسیت ابعاد هندسی بر روی جز موثر میراگرهای فلزی با ورق موازی انجام شده و سپس با استفاده از نتایج به دست آمده یک نوع میراگر تسلیمی دو سطحی جدید طراحی و ارائه گردد. در نهایت عملکرد میراگر مذکور با استفاده از مقایسه نتایج تحلیل‌های تاریخچه زمانی غیر خطی، در یک قاب فرض شده مورد بررسی قرار گیرد. نتایج به دست آمده نشان داد، تغییر در برخی پارامترهای هندسی تاثیر زیادی بر روی عملکرد و میزان جذب انرژی میراگر داشته و برخی از پارامترهای دیگر تاثیرات اندکی بر روی این دو مولفه دارند. همچنین استفاده از میراگر جدید توانست کاهش موثری را در پاسخ‌های لرزه‌ای قاب مورد نظر ایجاد نماید.

International Journal of Engineering

Journal Homepage: www.ije.ir

Analysis on Effect of Fullerene Soot on the Chemical and Physical Properties of Cement Mixtures

E. Y. Tsigelnyuk[a], V. S. Kovalchuk*[a], V. I. Gerasimov[b], E. A. Efimova[c]

[a] *Department of Drilling Wells, Oil and Gas Faculty, St Petersburg Mining University, St Petersburg, Russian Federation*
[b] *Department of Experimental Physics, Higher school of applied physics and space technologies, Peter the Great St. Petersburg Polytechnic University (SPbPU), St Petersburg, Russian Federation*
[c] *ESTiUM, St Petersburg, Russian Federation*

PAPER INFO

Paper history:
Received 07 June 2021
Received in revised form 22 August 2021
Accepted 23 August 2021

Keywords:
Cement
Well Casing
Grouting Mixtures
Carbon Materials
Fullerene
Fullerene Soot

ABSTRACT

This article reports on the relevance and the necessity of the introduction of various additives in the composition of grouting mixtures. The analysis of cement compositions with various modifications of carbon is briefly outlined. A method for obtaining fullerene soot and an analysis of its effect on the chemical and physical properties of grouting compositions made of alumina cement is presented. The physical, mechanical and operational properties of the modified grouting mixture are considered. The optimal content of carbon nanoparticles in the binder is 0.1-0.5% by weight of cement (BWOC). The introduction of fullerene soot makes it possible to obtain high mechanical properties of cement stone (an increase in uniaxial compression strength by about 15% and a decrease in porosity by about 20%) in comparison with cement mix without additives. It has been determined that use of carbon materials is environmentally friendly. Addition of fullerene soot to cement system does not affect the cement hydration processes, which provides micro-reinforcement of the cement stone, and prevents the propagation of cracks in it at nanoscale.

***doi**: 10.5829/ije.2021.34.10a.12*

1. INTRODUCTION[1]

Nowadays, new approaches of solving the problem of technologically successful well cementing are being studied all over the world. During the construction of wells for various purposes (geological, oil and gas, hydrogeological, geotechnical, technical, etc.), special attention is paid to the quality of the walls of the mine operation. Lack of wellbore cementing leads to migration of formation fluids and gases through the annulus, that do not correspond requirements, standards and safety rules of facilities' operation.

To meet all the necessary technological requirements, various additives are introduced into the grouting mixtures that satisfy the drilling conditions [1-4]. The introduction of additives into plugging systems allows to increase the quality of reservoir isolation [5-6], to solve the problem of cracks [7-10] at various aggressive temperatures and pressure conditions [11-13], to increase the reliability and durability of rock separation [14-16]. In recent decades, a large number of scientists have tried to improve the properties of cement-based materials using various nanomaterials due to their excellent chemical, physical and mechanical properties [17-19]. The influence of a sufficiently small amount of 0.5% BWOC nanosynthetic graphite on grouting slurries was determined [20]. Another modification of graphite, graphite nanoplates, was used [21-22] in order to improve the physicomechanical characteristics and nanoscale reinforcement of cement stone. As reported by Alkhamis and Imqam [23], the presence of graphene nanoplates significantly improved the chemical and physical properties of the cement composition and the long-term reliability of oil wells. Al-Awami [24] carried out the

*Corresponding Author Institutional Email: vlada.1995@inbox.ru (V. S. Kovalchuk)

Please cite this article as: E. Y. Tsigelnyuk, V. S. Kovalchuk, V. I. Gerasimov, E. A. Efimova, Analysis on Effect of Fullerene Soot on the Chemical and Physical Properties of Cement Mixtures, IJE TRANSACTIONS A: Basics Vol. 34, No. 10, (October 2021) 2313-2318

effect of carbon nanotube on the rheological and physical properties of cement slurry under high pressure. Rahman et al. [25], Khan et al. [26] showed the properties of cement modified with multi-walled carbon nanotubes under HPHT conditions, and changed its mechanical and thixotropic properties. Mendoza et al. [27] studied the effect of multi-walled carbon nanotubes up to 0.50% BWOC on the hydration of cement paste at different temperatures. Smirnyagina et al. [28] presented the results of thermodynamic modeling in the cement-water-carbon nanomodifier system. Wang and Song [29] reported that ash-cement pastes have a higher adsorption capacity and the degree of adsorption increases with an increase in the degree of ash substitution. Termkhajornkit et al. [30] investigated the self-healing ability of ash cement stone. The influence of different amounts of fly ash replacing cement on the compressive strength of cement stone is presented in literature [31-33]. When replacing 15-50% BWOC with fly ash, the advantages and disadvantages of the resulting mixture were determined.

The analysis of the experimentally obtained results of world research on the introduction of carbon materials into the grouting mixtures showed the ambiguity of their influence on the quality of the cement stone. Despite the lack of research on this topic, it can be assumed that there is a possibility of the influence of carbon materials on the quality of grouting mixtures and cement stones for high-quality well casing.

2. MATERIALS

Fullerene soot (FS) is a product of the first stage in the production of carbon nanomaterials - fullerenes. In the process of erosion of graphite electrodes in an electric arc in an atmosphere of a protective gas, soot is formed with a large number of fulleroid-type clusters of different shapes. It should be especially noted that the graphite used for the production of electrodes has a high spectral purity with a minimum amount of impurities (<< 200 ppm). The total content of fullerenes in soot is 8±2 wt%, of which the ratio of the number of C60 to C70 molecules is 3:1 and less than 2% of higher fullerenes. The main structural units of FS are graphite-like nanocrystallites in the form of defective and distorted bundles of hexagonal carbon networks. FS has a large specific surface (tens and hundreds of m^2/g) and a normal particle size distribution in the range of 10 nm - 150 μm [34-35].

When carrying out experimental studies, alumina cement (AC) with an additive in the form of FS were used as a basis for grouting mortars. The characteristics of the chemical composition of the cement used according to the manufacturer's passport are presented in Table 1.

TABLE 1. The chemical composition of the used AC

Cement	Content of oxides of elements, %				
	Al_2O_3	MgO	SiO_2	Fe_2O_3	CaO
AC	38,10	7,40	2,10	2,80	23,40

3. METHODS

Experimental studies were carried out in St Petersburg Mining University. The structural and chemical parameters of the materials and grouting compositions as well as the physical and mechanical properties of the cement stone were studied in accordance with international standards ISO 10426-1, ISO 10810, ISO/TR 12389, ISO 1332, ISO 29581, BS EN 196, and Standard Operating Procedures of each device. The optimal percentages of the reagents with the mixing water volume and with each others were selected empirically used in the theory of experiment planning, taking into account their compatibility and the main parameters of the resulting grouting mixture and cement stone.

3. 1. Determination of the Phase Composition

Powder X-ray diffractometry was performed on a Shimadzu XRD-7000 X-ray diffractometer and was used to determine the phase analysis of carbon materials and crushed cement stones.

3. 2. Determination of the Change in Mass of a Sample Dependent on Temperature

Thermogravimetry has been used to measure heat flux and the change in material weight as a function of temperature in a controlled atmosphere. Thermal analyzer SDT Q600, manufactured by TA Instruments, USA, was used for thermal analysis of cement stones. The temperature range of the research was from 0 to 1000 °C.

3. 3. Determination of the Strength of Cement Stone

To determine the strength of the cement stone, after preparation and measurement of structural and rheological parameters grouting compounds were poured into special forms 40x40x40 mm in order to harden for 1, 3, 10 days. Compressive strength was calculated as the arithmetic mean of the two largest test results on three specimens. This testing was carried out using a Controls-Pilot 3 semi-automatic compression and flexural testing machine.

3. 4. Determination of Cement Stone Porosity

The complex system SkyScan 1173 (X-ray microtomograph) was used to determine the porosity of the hardened cement stone.

4. RESULTS AND DISCUSSION

4. 1. Determination of the Phase Composition

Diffraction curves reflecting the high amorphous phase are shown in Figure 1. It was determined that the FS contains crystalline carbon.

Next, a phase analysis of a cement stone made of AC and water without additives was carried out. The main phases of alumina cement are Al_2O_3 (28.21%) CaO (19.49%), TiO_2 (10.69%), SiO_2 (8.44%), Fe_2O_3 (4.74%), MgO (1.17%), presented in Table 2.

It can be noted that during cement hydration, the Al_2O_3 phase decreased by 35%, while the CaO phase decreased by 20%. The presence of the MgO compound also sharply decreased (by about 7 times), while Fe_2O and SiO_2 increased by about 1.7 and 4 times, respectively.

With the introduction of FS and the process of hydration, an increase in the content of the Al_2O_3 and CaO phases is observed on average by 10-15%, as well as an insignificant increase in the content of MgO, Fe_2O, SiO_2 compounds (by about 3-12%).

The main crystalline phases of alumina cement are $CaTiO_3$, $SiO_2.xH_2O$ and $KAlSi_2O_6$. It can be noted that the introduction of FS did not affect the elementary composition of the cement stone.

Diffraction curves reflecting the intensity of the peak (CaTiO3) - the phase composition of the studied cement powders - are shown in Figures 2 and 3. The low intensity of the peaks as a result of X-ray amorphous analysis indicates the amorphous state of the cement stone. Consequently, there is a large error in determining the composition of the cement stone.

4. 2. Determination of the Change in Mass of a Sample Depending on Temperature

DTG curves - the dependences of the change in the mass of grouting compositions on the temperature of two samples of cement stone without additives and composition with FS are shown in Figures 4 and 5.

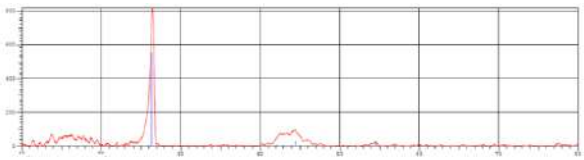

Figure 1. X-ray diffraction pattern of fullerene soot, where the peak is crystalline carbon C (graphite)

TABLE 2. Phase chemical composition of the studied samples of cement stone without and with the addition of FS

Chemical phase	Al_2O_3	CaO	TiO_2	SiO_2	Fe_2O_3	MgO
AC	28.21	19.49	10.69	8.44	4.74	1.17
AC + FS	31.35	22.35	5.11	9.39	4.92	1.28

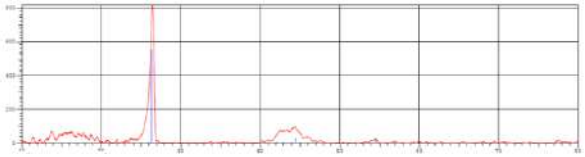

Figure 2. X-ray diffraction pattern of AC without additive, the peaks are $CaTiO_3$ phase

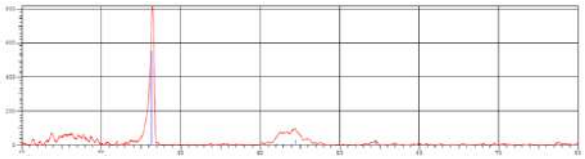

Figure 3. X-ray diffraction pattern of AC with the addition of FS, the peaks are $CaTiO_3$ phase

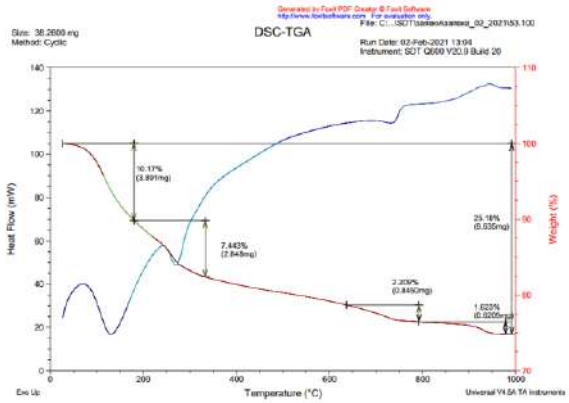

Figure 4. Thermograms of cement sample composition without additives

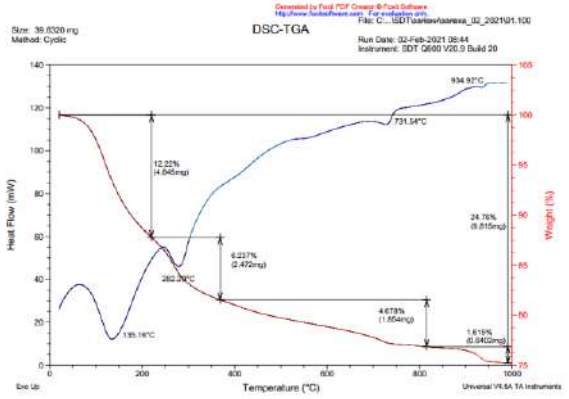

Figure 5. Thermograms of cement sample composition with FS content

Thermal analysis of AC without additives showed losses of H_2O - 5.99% and CO_2 - 19.03%. With the introduction of fullerene soot, a slight decrease in the mass of the cement stone sample is observed with the following values: H_2O - 5.04% and CO_2 - 19.70%. Thus,

it can be noted that the water content of the modified grouting mixture decreased, and the release of CO_2 increased.

Thermal analysis showed approximately the same curves. It was determined that FS does not affect the hydration process. Thus, there is a partial compaction of the cement structure and the porosity and permeability of the cement stone decreases. A gradual decrease in the mass of the sample is associated with the loss of water (at a temperature of 85-105 °C), and then hydrates, hydroxides, and after 750 °C - the decrystallization of the cement structure.

4. 3. Determination of the Strength of Cement Stone The obtained results for the modification of AC with FS in an amount of 0.1-0.5% of the cement mass showed an increase in uniaxial compressive strength by about 15-25% compared to a solution without additives. Moreover, the most rates of strength are in the initial period of hardening. The most optimal amount of FS was 0.1-0.5% BWOC. With a decrease in the FS content, a deterioration in the strength characteristics of the grouting compounds is observed in the first week of hardening.

According to the results of the uniaxial compression strength of the cement stone samples, the most durable is the composition number 3 - AC with the addition of 0.3% BWOC FS. This sample showed the maximum increase in uniaxial compressive strength, and it also meets all the technological conditions for industrial implementation. The results of the study of strength are presented in Table 3.

4. 4. Determination of Cement Stone Porosity The next step of examining of hard-set cement was a computer micro tomography analysis to evaluate the pore structure and permeability of the pure cement stone (1) and sample with the addition FS 0.1% (2), 0.3% (3), 0.5% (4). The introduction of FS decreases total porosity of up to 30% depending on the amount of modifier. These results make it possible to believe in the reduced permeability of the cement stone and durability during operation.

The results of main obtained porosity indicators are presented in Table 4, and graphs with an illustration of the computer models of the pore space (pores - green frames) of cement stone samples with different FS contents are presented in Figure 6.

TABLE 3. Results of uniaxial compressive strength of grouting mixtures specimens based on AC

Compression strength	1	2	3	4
After 1 day, MPa	4.86	5.53	6.01	5.88
After 3 days, MPa	7.45	9.62	11.69	10.97
After 10 days, MPa	18.97	18.05	20.64	20.05

TABLE 4. Results of a study of the porosity of grouting solutions samples based on AC

Number of sample	1	2	3	4
Additive	**-**	**0.1%**	**0.3%**	**0.5%**
Volume of closed pores, mm^3	9.13	9.65	10.50	10.82
Volume of open pore space, mm^3	8.20	6.95	4.39	2.19
Total volume of pore space, mm^3	17.33	16.60	14.90	13.01
Closed porosity, %	2.65	2.70	2.74	2.73
Open porosity, %	1.91	1.80	0.92	0.61
Total porosity, %	4.55	4.50	3.66	3.34

As a result of studies of cement stone on a computer microtomograph, the following data were obtained: with an increase in the FS content, a sharp decrease in the number of open pores occurs with a simultaneous increase in closed pores. In general, the pore volume decreases. There is also a decrease in porosity with an increase in the content of FS in the cement slurry. Moreover, the values of open porosity decrease much more strongly with a fairly stable and small increase in closed porosity.

The filtration resistance of cement stone is inversely proportional to its porosity. Thus, there are no channels for the penetration of filtrate and damage to the integrity and durability of the cement stone.

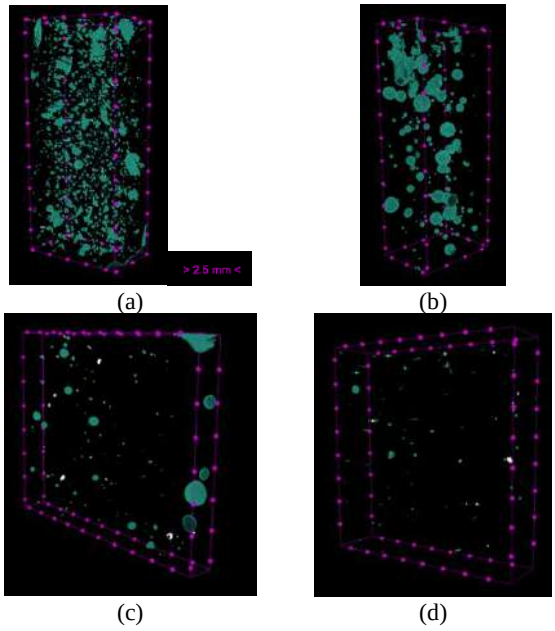

Figure 6. Computer model of the pore space of grouting compositions a) composition without additives, b) composition with FS 0.1%, c) composition with FS 0.3%, d) composition with FS 0.5%

Having analyzed all the test results obtained, it is possible to determine the boundaries for the preparation of a grouting slurry from alumina cement, which can be used for cementing the annulus in particularly difficult mining and geological conditions.

According to the results of laboratory tests of the modified grouting slurry, it was determined that the use of AC with tap water does not meet the set objectives of industrial implementation. Fast-setting AC has sufficient strength, but critically high mobility and fluid loss, especially in the early period of thickening of the cement slurry. There is an urgent need to use hardening and plasticizing additives.

5. CONCLUSION

The introduction of carbon materials into the cement mixtures contributes to an increase in strength, but it is necessary to regulate their concentration and consider the joint use of cements with FS. The grouting mixtures obtained according to the given technological parameters, containing FS, satisfy the task, each of them is easy to prepare, contains inexpensive and environmentally friendly additives.

The results obtained for the modification of AC with FS in an amount of 0.1-0.5% BWOC showed an increase in uniaxial compressive strength by about 15-25% compared to solutions without additives. With an insufficient content of FS, a deterioration in the strength characteristics of the cement compositions is observed in the first week of hardening. The increase in the strength of cement stone for uniaxial compression is associated with the mechanism of interaction of cement with FS, which at the molecular level stick cement particles together and create a dense structure during the hardening of cement slurry.

Carbon materials act as additives to increase the mobility of the cement slurry, which affects the successful achievement of the necessary technological requirements. Analysis of the results of computed tomography showed that at the molecular level, the bond between FS and cement improves the permeability characteristics, reducing the number and volume of pores in the cement stone. It was determined that FS does not affect the cement hydration processes. The introduction of carbon additives leads to a decrease in the porosity and permeability of the cement stone without losing its technological properties. The addition of FS provides micro-reinforcement of the cement stone and prevents the propagation of cracks in it at the nanoscale.

6. ACKNOWLEDGMENTS

This work was supported by the Russian Foundation of Basic Researches (15486ГУ/2020).

7. REFERENCES

1. Tabatabaee Moradi, S. S. and Nikolaev, N. I. “Considerations of Well Cementing Materials in High-pressure, High temperature Conditions”, International Journal of Engineering, Transactions C: Aspects, Vol. 29, No. 9, (2016) 1214-1218, DOI: 10.5829/idosi.ije.2016.29.09c.05.
2. Tabatabaee Moradi, S. S., Nikolaev, N. I. and Yasin, N., “Developing High Resistant Cement Systems for High-pressure, High temperature Applications”, Paper presented at the SPE Russian Petroleum Technology Conference, Moscow, Russia, (2015), DOI: 10.2118/176523-MS.
3. Tabatabaee Moradi, S. S., Nikolaev, N. I. and Leusheva, E. L., “Improvement of Cement Properties Using a Single Multifunctional Polymer”, International Journal of Engineering, Transactions A: Basics, Vol. 31, No. 1, (2018), 181-187, DOI: 10.5829/ije.2018.31.01a.24.
4. Tabatabaee Moradi, S. S. and Nikolaev N. I., “Sedimentation Stability of Oil Well Cements in Directional Wells”, International Journal of Engineering, Transactions A: Basics, Vol. 30, No. 7, (2017), 1105-1109, DOI: 10.5829/ije.2017.30.07a.21.
5. Saidova, Z., Yakovlev, G., Smirnova, O., Gordina, A. and Kuzmina, N. “Modification of Cement Matrix with Complex Additive Based on Chrysotyl Nanofibers and Carbon Black”, Applied Sciences, Vol. 11, (2021), 6943, DOI: 10.3390/app11156943.
6. Nutskova, M. V. and Rudyaeva, E. Yu., “The effect of water-swellable polymer on well drilling with mud loss”, Perm Journal of Petroleum and Mining Engineering, Vol. 17, No. 2, (2018), 104-114, DOI: https://doi.org/10.15593/2224-9923/2018.2.1.
7. Varghese, A., Anand, N. and Arulraj, P. G., “Influence of Fiber on Shear Behavior of Concrete Exposed to Elevated Temperature”, International Journal of Engineering, Transactions A: Basics, Vol. 33, No. 10, (2020), 1897-1903, DOI: 10.5829/ije.2020.33.10a.08.
8. Zimina, D. A. and Nutskova, M. V., “Research of technological properties of cement slurries based on cements with expanding additives, portland and magnesia cement”, IOP Conference Series: Materials Science and Engineering, Vol.666, (2019), 012066, DOI: 10.1088/1757-899X/666/1/012066.
9. Zimina, D. A., Zhapkhandaev, C. A. and Petrov, A. A. “Analysis of the effect of nanosilicates on the strength and porosity of cement stone”, Key Engineering Materials, Vol. 854, (2020), 175-181, DOI: 10.4028/www.scientific.net/KEM.854.175.
10. Dvoynikov, M.V., Kuchin, V.N., and Mintzaev, M.Sh. "Development of viscoelastic systems and technologies for isolating water-bearing horizons with abnormal formation pressures during oil and gas wells drilling", Journal of Mining Institute, Vol. 247, (2021), 57-65, DOI:10.31897/PMI.2021.1.7.
11. Reza Kashyzadeh, K., Ghorbani, S. and Forouzanmehr, M., “Effects of Drying Temperature and Aggregate Shape on the Concrete Compressive Strength: Experiments and Data Mining Techniques”, International Journal of Engineering, Transactions C: Aspects, Vol. 33, No. 9, (2020), 1780-1791, DOI: 10.5829/ije.2020.33.09c.12.
12. Borzouyi Kutenayi, S., Kiahosseini, S. R. and Talebpour, M. H., “The Effect of Caspian Sea Water on Corrosion Resistance and Compressive Strength of Reinforced Concrete Containing Different SiO2 Pozzolan”, International Journal of Engineering, Transactions A: Basics, Vol. 30, No. 10, (2017), 1464-1470, DOI: 10.5829/ije.2017.30.10a.06.
13. Tabatabaee Moradi, S. S., Nikolaev, N. I. and Nikolaeva, T. N. “Development of spacer fluids and cement slurries compositions for lining of wells at high temperatures”, Journal of Mining Institute, Vol. 242, (2020), 174-178, DOI: 10.31897/PMI.2020.2.174.
14. Delaram, F., Mohammadi, Y. and Adlparvar M. R. “Evaluation of the Combined Use of Waste Paper Sludge Ash and Nanomaterials on Mechanical Properties and Durability of High Strength

Concretes", International Journal of Engineering, Transactions A: Basics, Vol. 34, No. 7, (2021), 1653-1666, DOI: 10.5829/ije.2021.34.07a.10.
15. Wani S. B. "Influence of Bi-directional Fibreglass Grid Reinforcement on Drying Shrinkage and Mechanical Properties of Lightweight Foamed Concrete", International Journal of Engineering, Transactions A: Basics, Vol. 34, No. 1, (2021), 10-18, DOI: 10.5829/ije.2021.34.01a.02.
16. Nikolaev, N. I. and Leusheva, E. L., "Low-density cement compositions for well cementing under abnormally low reservoir pressure conditions", Journal of Mining Institute, Vol. 236, (2019), 194-200, DOI: 10.31897/pmi.2019.2.194.
17. Li, G. Y., Wang, P. M. and Zhao, X., "Mechanical behavior and microstructure of cement composites incorporating surface-treated multi-walled carbon nanotubes", Carbon, Vol. 43, (2005), 1239-1245, DOI: 10.1016/j.carbon.2004.12.017.
18. Zhao, Z., Qi, T., Zhou, W., Hui, D., Xiao, C., Qi, J., Zheng, Z. and Zhao, Z., "A review on the properties, reinforcing effects, and commercialization of nanomaterials for cement-based materials", Nanotechnology Reviews, Vol. 9, (2020), 349-368, DOI: 10.1515/ntrev-2020-0023.
19. Du, M., Jing, H., Gao, Y., Su, H. and Fang, H., "Carbon nanomaterials enhanced cement-based composites: advances and challenges", Nanotechnology Reviews, Vol. 9, (2020), 115-135, DOI: 10.1515/ntrev-2020-0011.
20. Shawgi, A., Chinedum, P. E. and Saeed, S., "Improvement in Cement Sealing Properties and Integrity Using Conductive Carbon Nano Materials: From Strength to Thickening Time", SPE Annual Technical Conference and Exhibition, 24-26 September, Dallas, Texas, USA, (2018), DOI: 10.2118/191709-MS.
21. Peyvandi, A., Taleghani, A. D., Soroushian, P. and Cammarata, R., "The Use of Low-Cost Graphite Nanomaterials to Enhance Zonal Isolation in Oil and Gas Wells", SPE Annual Technical Conference and Exhibition, 9-11 October, San Antonio, Texas, USA, (2017), DOI: 10.2118/187105-MS.
22. Tabatabaei, M., Taleghani, A. D. and Alem, N., "Economic Nano-Additive to Improve Cement Sealing Capability", SPE Western Regional Meeting, 23-26 April, San Jose, California, USA, (2019), DOI: 10.2118/195259-MS.
23. Alkhamis, M. and Imqam, A., "New Cement Formulations Utilizing Graphene Nano Platelets to Improve Cement Properties and Long-Term Reliability in Oil Wells", In SPE Kingdom of Saudi Arabia Annual Technical Symposium and Exhibition, Conference Paper, (2018), DOI: 10.2118/192342-MS.
24. Al-Awami, A. H., "Carbon Nanotube Under High Pressure", SPE Kingdom of Saudi Arabia Annual Technical Symposium and Exhibition, 23-26 April, Dammam, Saudi Arabia, (2018), DOI: 10.2118/192185-MS.
25. Rahman, M. K., Khan, W. A., Mahmoud, M. A. and Sarmah, P., "MWCNT for Enhancing Mechanical and Thixotropic Properties of Cement for HPHT", Applications Offshore Technology Conference Asia, 22-25 March, Kuala Lumpur, Malaysia, (2016), DOI: 10.4043/26465-MS.
26. Khan W. A., Rahman M. K., Mahmoud M. A. and Sarmah P., "MWCNT for Enhancing Mechanical Properties of Oil Well Cement for HPHT", Applications SPE/IADC Middle East Drilling Technology Conference and Exhibition, 26-28 January, Abu Dhabi, UAE, (2016), DOI: 10.2118/178175-MS.
27. Mendoza, O., Pearl Jr, W., Paiva, M., Miranda, C. and Toledo Filho, R., "Effect of a commercial dispersion of multi walled carbon nanotubes on the hydration of an oil well cementing paste", Frontiers of Structural and Civil Engineering, Vol. 10, (2016), 174-179, DOI: 10.1007/s11709-015-0324-8.
28. Smirnyagina, N., Tsyrenov, B. and Urkhanova, L, "Thermodynamic calculations on system «Portland cement - water - carbon nanomodifier»", IOP Conference Series: Materials Science and Engineering, Vol. 880, (2020), 012025, DOI: 10.1088/1757-899X/880/1/012025.
29. Wang, Z. and Song, Y., "Adsorption properties of CFBC ash-cement pastes as compared with PCC fly ash-cement pastes", International Journal of Coal Science & Technology, 3, (2016), DOI: 10.1007/s40789-016-0103-8.
30. Termkhajornkit, P., Nawa, T., Yamashiro, Y. and Saito, T., "Self-healing ability of fly ash-cement systems", Cement & Concrete Composites - Cement Concrete Composites, Vol. 31, (2009), 195-203, DOI: 10.1016/j.cemconcomp.2008.12.009.
31. Cho, Y. k., Jung, S. and Choi, Y., "Effects of chemical composition of fly ash on compressive strength of fly ash cement mortar", Construction and Building Materials, Vol. 204, (2019), 255-264, DOI: 10.1016/j.conbuildmat.2019.01.208.
32. Elmrabet, R., Harfi, A. and Youbi, M. S., "Study of properties of fly ash cements", Materials Today: Proceedings, Vol. 13, (2019), 850-856, DOI: 10.1016/j.matpr.2019.04.048.
33. Moses, P., Chockalingam, M. P., Venkatakrishnaiah, R. and Dayakar, P., "Strength aspects of fly ash in cement mortar", International journal of advanced research in engineering & technology, 11, (2020), DOI: 10.34218/ijaret.11.1.2020.006.
34. Kraetschmer, W., Lamb, L. D., Fostiropoulos, K. and Huffman, D., "Solid C60 A New Form of Carbon", Nature, Vol. 347, (1990), 354-358, doi:10.1038/347354a0.
35. Nimibofa, A., Ebelegi, A., Abasi, C. and Donbebe, W. "Fullerenes: Synthesis and Applications", Journal of Materials Science Research, Vol. 7, (2018), DOI: 10.5539/jmsr.v7n3p22.

Persian Abstract

چکیده

این مقاله ارتباط و ضرورت معرفی افزودنی های مختلف در ترکیب مخلوط های تزریق را گزارش می دهد. تجزیه و تحلیل ترکیبات سیمان با تغییرات مختلف کربن به طور خلاصه شرح داده شده است. روشی برای به دست آوردن دوده فولرن و تجزیه و تحلیل تأثیر آن بر خواص شیمیایی و فیزیکی ترکیبات تزریق از سیمان آلومینا ارائه شده است. خواص فیزیکی ، مکانیکی و عملیاتی مخلوط گروت اصلاح شده در نظر گرفته می شود. محتوای بهینه نانوذرات کربن در چسب ۱/۰ تا ۰/۵ درصد وزن سیمان (BWOC) است. معرفی دوده فولرن امکان دستیابی به خواص مکانیکی سنگ سیمان (افزایش مقاومت فشاری تک محوری حدود ۱۵ درصد و کاهش تخلخل در حدود ۲۰ درصد) در مقایسه با مخلوط سیمان بدون افزودنی را ممکن می سازد. مشخص شده است که استفاده از مواد کربن سازگار با محیط زیست است. افزودن دوده فولرن به سیستم سیمان بر فرآیندهای هیدراتاسیون سیمان که باعث تقویت ریز سنگ سیمان می شود ، تأثیر نمی گذارد و از انتشار ترک های موجود در آن در مقیاس نانو جلوگیری می کند.

IJE TRANSACTIONS A: Basics Vol. 34, No. 10, (October 2021) 2319-2331

International Journal of Engineering

Journal Homepage: www.ije.ir

Seismic Analysis of Double Deck Floating Roofs of Siraf Storage Tanks with Condensate, Light and Heavy Crude Oils

H. Ahmadi*[a], M. H. Kadivar[b]

[a] *International College, Shiraz University, Shiraz, Iran*
[b] *School of Mechanical Engineering, Shiraz University, Shiraz, Iran*

PAPER INFO

Paper history:
Received 2 July 2021
Received in revised form 17 August 2021
Accepted 23 August 2021

Keywords:
Hydroelasticiy
Slosh
Foam Seal
Fluid-Structure Interaction
Earthquake

ABSTRACT

Seismic vibration of the double deck floating roof of Siraf storage tanks located in southern Iran has been studied. Condensate of Nar and Kagan gas field in the south of Iran as a very light hydrocarbon, Lavan as light and Soroosh as heavy crude oil content have been chosen. In addition to fluid-structure interaction, intermediate stiffeners, foam seal with nonlinear radial compression behavior and contact friction between the seal and the inner side of the wall are also considered. Under the above conditions, modal and time history analysis have been performed. For time history analysis, Sarpol-e Zahab and Shonbeh earthquakes in Zagros seismotectonic province of Iran and Sakaria as an earthquake near Iran were selected. Dominant natural frequencies, mode shapes of the roof parts and damping ratios of the first and second natural frequencies in addition to overall and spectral behavior of the roof in each liquid case were obtained and discussed. Changing condensate to Soroosh oil made about 17% hydroelastic natural frequency decrement and about 10% damping ratio decrease for the first natural frequency. The results showed that dominant natural frequencies and the relevant damping ratios decrease with moving from light to heavy liquid. The vibration of the roof fundamentally depends on the frequency content of earthquakes to such natural frequencies. Also, a floating roof in heavier liquid is more vulnerable to vibration according to the scaling method and steady-state amplitude.

***doi**: 10.5829/ije.2021.34.10a.13*

NOMENCLATURE

$[C]$	Proportional damping matrix	u_i	The steady-state amplitude of the i^{th} mode (m)
$[F]$	Excitation coefficient matrix	$\{W\}$	Modal displacement of the roof
g	Gravity (m/s^2)	**Greek Symbols**	
i	Natural frequency number	φ	Interpolation function
$[M]$	Modal mass matrix	ς	Damping ratio
$[K]$	Modal stiffness matrix	ρ	Density (kg/m^3)
$[R]$	Excitation participation matrix	ω_i	i^{th} natural frequency
$[S]$	Inertial coefficient matrix	**Subscripts**	
$[U]$	Stiffness coefficient matrix	r	Roof
u_g	Tank base displacement excitation (m)	add	Added mass or stiffness

1. INTRODUCTION

A floating roof is one of the ways to prevent product evaporation loss from storage tanks and to eliminate the possibility of a flammable atmosphere. The floating roof rises and falls with the liquid level to help reduce evaporation and prevent the buildup of dangerous gases. There are two geometrical types of floating roof: Single Deck Floating Roof (SDFR) and Double Deck Floating Roof (DDFR). SDFR consists of a deck plate and an

*Corresponding Author Institutional Email: a*hmadihs1354@gmail.com* (H. Ahmadi)

Please cite this article as: H. Ahmadi, M. H. Kadivar, Seismic Analysis of Double Deck Floating Roofs of Siraf Storage Tanks with Condensate, Light and Heavy Crude Oils, International Journal of Engineering, Transactions A: Basics, Vol. 34, No. 10, (2021) 2319-2331

outer pontoon. DDFR is fundamentally made up of lower deck, upper deck and stiffening structures between them. Figure 1 shows the schematic configuration of a DDFR storage tank. SDFR is normally used for relatively small and DDFR for larger tank diameter [1]. Due to the wider application of DDFR, this type has been considered for analysis. However, general conclusions can be extended to SDFRs.

Due to the extensive use of floating roofs throughout the industry to store volatile and flammable products such as crude oil or condensate, safety-related attention must be considered seriously. The liquid surface of the storage tank can undergo long period oscillations during seismic excitation which is called the sloshing phenomenon [2]. As sloshing is a liquid-surface phenomenon, floating roofs are more exposed to such oscillations. In addition, buoyancy consideration of the roofs makes them more vulnerable to instability. Hence, Floating roof oscillations due to slosh may result in devastating consequences such as the sinking of the roof, vast destructive fires and/or release of flammable or toxic products from the tank. For example, during the 2003 Tokachi-oki earthquake in northern Japan, seven storage tanks experiencing large amplitude slosh suffered severe damages such as ring fires and sinking of floating roofs. In one tank with a ring fire, the flame was confined to the rim of the tank roof. The sinking of the roof in another tank leads to open-top fire. Some other tanks also suffered sinking of the floating roof, exposing the kerosene to the atmosphere [3]. During the 1999 Izmit earthquake in Kocaeli of Turkey, some tanks in Turpas refinery have suffered excessive sloshing and their roof rubbing with the walls and then created instantly sparks igniting the liquid. The fire then spread to other crude oil tanks damaging 30 to 45 tanks covered by a floating roof [4]. Hence, seismic analysis of floating roofs is important. The several attempts which were made toward vibration mitigation of floating roof vibration and risk assessment of petroleum storage tanks indicate the importance of this field [5-8].

Numerous efforts were made to improve the structural and analytical model of a floating roof in seismic analysis. As an early attempt, Amabili [9] studied vibrations of circular plates resting on a sloshing liquid free surface. Golzar et al. [10, 11] idealized floating roofs as an isotropic elastic plate with uniform stiffness and thickness. Matsui [12] modeled SDFR as an elastic curved beam connected to the pontoon. Salarieh et al. [13] modeled deck plate as a flexural element rather than a membrane. Yamauchi et al. [14] discussed the nonlinearity of the SDFR deformation pattern. Sakai et al. [15, 16] assumed some uniform circumferential web plates at equal radial distances of the deck to model a more actual floating roof. Yoshida et al. [17, 18] introduced an axis-symmetric finite element model for the roof to obtain natural periods and vibration modes of the floating roof due to sloshing. Utsumi et al. [19] investigated internal resonances in the vibration analysis of the SDFR. Goudarzi [20] considered a contribution of the second sloshing mode to the seismic behavior of the SDFR. He considered some detailed geometry of the floating roof including compartments and inside truss works in the numerical model [21]. Meera and Reshmi [22] investigated the dynamic stability of SDFR with and without deck stiffeners. In the latter study, only modal analysis was performed.

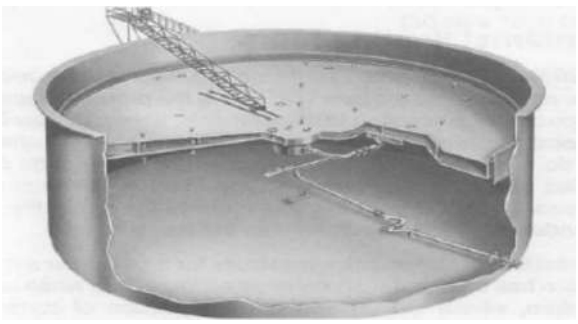

Figure 1. Schematic configuration of a DDFR storage tank [1]

To prevent product loss and atmospheric contamination, the gaps between the outer rim of the floating roof and the tank are closed up by flexible seals. There are scarce studies considering the outer rim seal in seismic analysis. Hosseini et al. [23] modeled the seal by introducing some radial pre-compressed only-compression springs for calculating the seismic response of the SDFR. Belostotsky et al. [24] addressed a non-linear radially located two-node element for the seal.

In our work, in addition to intermediate stiffeners, foam seal with nonlinear radial compression behavior and friction between the seal and the inner side of the wall are also considered.

Coupling of liquid slosh to the floating roof vibration is established through Fluid-Structure Interaction (FSI) [25]. Literature review about this phenomenon can help to find out the fundamental effects of liquid on floating roof vibration. In this regard, Sakai et al. [15] derived analytical relations for obtaining added mass and added stiffness matrix of liquid in the presence of a flexible floating roof. Shabani and Golzar [26] and also Sivy et al. [27] introduced the contribution of the fluid to the excitation value in addition to considering the added mass and added stiffness of the liquid. Shabani [28] introduced a complete contribution of the fluid by adding a damping matrix accounting for viscous liquid-wall interaction and friction between roof and wall. In the aforementioned works, each seismic analysis of floating roof was limited to a specified liquid content, and the vibration result cannot be demonstrated explicitly in terms of liquid properties. On the other hand, there are extensive types of petroleum products throughout oil industries having different densities and viscosities. In addition, ambient temperature variation can change these

properties. In the present study, numerical methods based on a finite element have been established for evaluating the effect of liquid variation on floating roof vibration. In this way, added mass, added stiffness and excitation effects are involved in the analysis. Rayleigh damping are also considered for structures and liquid. As a case study, seismic analysis of a DDFR including condensate, light and heavy Iranian crude oil has been performed. A storage tank located in Siraf port of Iran is selected for analysis, and is excited by significant earthquakes occurred in and near the country. Statistical analysis of Yazdani and Kowsari [29] predicted high probability density of earthquake occurrence for Zagros seismotectonic province. On the other hand, many of oil storage tanks of crude oil are situated in this seismotectonic province. Therefore, two earthquakes of this province are selected for analysis as domestic ground motion events.

2. FLOATING ROOF VIBRATION ANALYSIS

Assuming a simplified orthogonality condition, the hydroelastic behavior of the system is defined as [28]:

$$([M_r] + [M_{add}])\{\ddot{W}\} + [C]\{\dot{W}\} + ([K_r] + [K_{add}])\{W\} = -[R]\ddot{u}_g \quad (1)$$

In Equation (1), the contribution of the liquid to hydroelastic vibration of the roof is represented by added mass, added stiffness, proportional damping and excitation participation matrices. The uncoupled added mass matrix can be defined by:

$$[M_{add}] = \rho[S] \quad (2)$$

the added stiffness matrix by:

$$[K_{add}] = \rho g[U] \quad (3)$$

and excitation participation matrix by:

$$[R] = \rho[F] \quad (4)$$

Using Equation (1), the equation of motion for the i^{th} mode can be written as:

$$\ddot{w}_i(t) + 2\omega_i\varsigma_i\dot{w}_i(t) + \omega_i^2 w_i(t) = -\frac{\rho[F]}{[M_r]+\rho[S]}\ddot{u}_g(t) \quad (5)$$

Equation (5) summarizes the contribution of liquid in the form of natural frequency, light damping and excitation.

Application of u_g as a sinusoidal excitation and following the procedure represented by Chopra [30], the roof displacement at resonance varies with time as

$$w_i(t) = \frac{\rho[F]u_g}{[M_r]+\rho[S]}\frac{1}{2\varsigma}(1 - e^{-\varsigma\omega_n t})\cos\omega_n t \quad (6)$$

The seismic vulnerability of the system can be represented by steady-state vibration amplitude. The steady-state amplitude can be achieved by harmonic excitation of the base at natural frequency and computation of the amplitude after enough simulation time.

$$u_i = \frac{\rho[F]}{[M_r]+\rho[S]}\frac{u_g}{2\varsigma}\varphi \quad (7)$$

Equations (6) and (7) show that the effect of damping on the vibration response of the aforementioned system is also substantial.

3. ANALYSIS OF DOUBLE DECK STORAGE TANK

A cylindrical storage tank with DDFR that is under operation is considered for analysis. The General configuration of the main structural parts of the tank as illustrated in Figure 1. Modal and time history analysis have been performed to obtain the seismic behavior of the roof. In this regard, a finite element method using ANSYS Parametric Design Language (APDL) was employed, and a macro has been provided for hydroelastic analysis of the tank [31]. Figure 2 outlines the elemental model of the system. Cutaway views are used to permit the demonstration of all the essential parts in the figure.

The tank body and DDFR specifications are selected according to the Siraf storage tank located in the south of Iran. Specifications of the storage tank and shell are summarized in Table 1.

For liquid content, condensate of Nar and Kangan gas field in the south of Iran was selected as a very light hydrocarbon. In addition, Lavan was considered as light and Soroosh as heavy crude oil. Table 2 shows the density and viscosity of the three liquid types [32]. 8-node compressible fluid element has been selected for liquid analysis to calculate either the propagation properties of the waves in the environment and also Fluid-Structure Interaction (FSI). A pressure-based wave equation was utilized for numerical analysis of the fluid. In addition, for liquid-roof and liquid-shell interfaces, displacements DOF were also activated to establish FSI.

Another approach is the displacement-based wave equation. However, in this method, displacement Degrees Of Freedom (DOF) within the fluid may lead to zero pivots and divergence.

Floating roof dimensions are given in Table 3. Lower and upper decks of the roof are stiffened by bulkheads, trusses and rafters. In Figure 3, the overall configuration of the stiffeners has been demonstrated. Details of trusses and rafters are also shown in Figure 4. Bulkheads are dividing walls between separate compartments. 4-node shell elements with 6-DOF at each node were used for the lower deck, upper deck, bulkheads, and also for the shell body of the tank. Trusses have been modeled as 2-node beams to cover both translational and rotational DOF. 2-node beams were also used for rafter modeling.

There are various types of seals to fill the gap between the outer rim of the roof and shell such as pantograph, foam and tube seals. In this regard, foam seal as in Figure 5 has been selected. Floating roof seals are similar to gaskets as they fill the space between two mating surfaces for fluid leakage prevention. Thus, an 8-node gasket element with 3-DOF at each node has been chosen for seal modeling. The element is capable of both through-thickness and transverse shear deformation. Figure 6 shows a magnified picture in which the situation of the seal concerning the shell and stiffeners is depicted. Also, the nonlinear relation between radial stress and strain of the seal is shown in Figure 7. The governing stress-strain relationship has been estimated considering the reasonable stiffness of the foams provided by manufacturers [33]. This relation was entered into the macro via data tables. In ANSYS APDL, tabular data of material properties are activated using the TB command [31]. Elastic contributions of the seal accessories like seal envelopes are also considered in the stress-strain curve. In addition, an estimated value for the elastic behavior of the weather shield depicted in Figure 5 has been added to the peripheral constraint. The latter is sometimes referred to as a secondary seal with respect to the primary seal.

TABLE 1. Storage tank general and shell specifications

Parameter	Value
Tank height	14 m
Tank diameter	60 m
Rated wall thickness	0.02 m
Liquid height considering sufficient freeboard	12 m
Metal density	7850 kg/m3
Metal Young's modulus (Low carbon steel)	2e11 N/m2
Metal Poisson's ratio	0.3
Metal damping ratio	0.03

TABLE 2. Specifications of three liquid content cases

Liquid type	Density (kg/m^3)	Viscosity (10^{-3} Pa.s)
Natural gas condensate	648	0.89
Lavan (Light crude oil)	848	6.16
Soroosh (Heavy crude oil)	941	698.64

TABLE 3. Floating roof dimension

Parameter	Value (m)
Height	0.672
Upper deck thickness	0.00477
Lower deck thickness	0.00637
Height in contact with seal	0.40
Gap between roof rim and shell	0.20

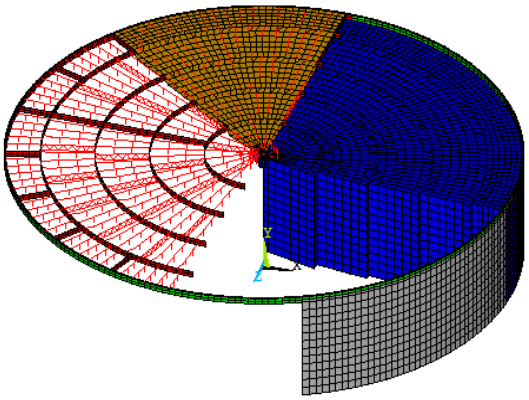

Figure 2. Cutaway views of the overall model (blue: liquid, brown: upper deck, red: roof stiffeners, green: seal, grey: shell)

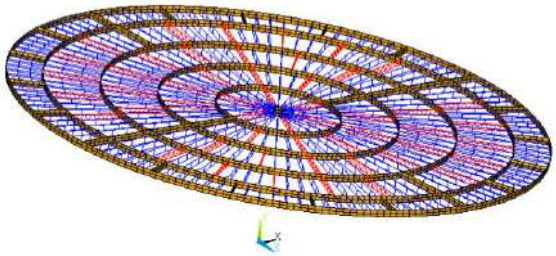

Figure 3. Eelemental configuration of the intermediate stiffeners of the roof (red: trusses, blue: rafters, brown: bulkheads)

Figure 4. Detail of trusses and rafters of the roof

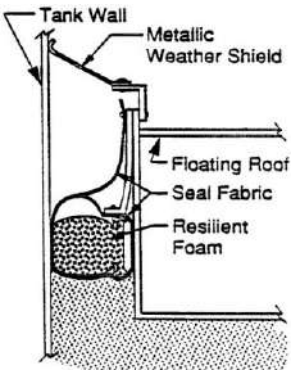

Figure 5. A typical foam seal

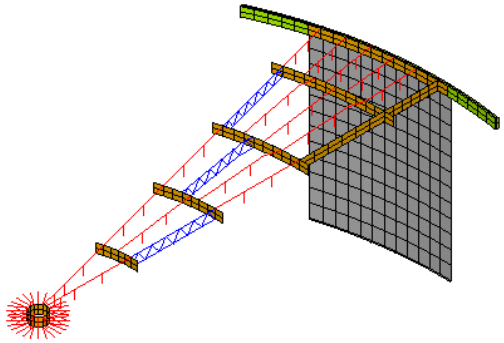

Figure 6. Magnified picture of shell(grey), seal(green), bulkheads(brown), rafters(red) and trusses(blue)

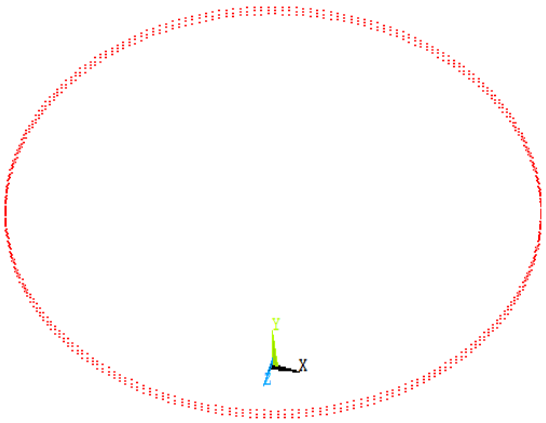

Figure 8. Distribution of contact elements around the seal

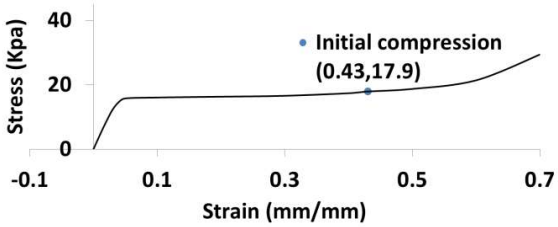

Figure 7. Stress-strain diagram of foam seal with Initial Stress and Strain

The roof seal is installed by an initial compression. The initial compressive stress of 17.9KPa has been considered for sealing. Having the stress value, the initial compressive strains can be obtained from Figure 7 as

$$\varepsilon_0 = 0.43 mm / mm. \quad (8)$$

The outer rim of the floating roof is in contact with the inner side of the shell. Thus, the boundary conditions of the roof are different from almost most studies performed in the literature. Seals are fixed to the outer rim of the floating roof to have vertical movement with it during liquid level variation. However, the seal and shell movements are different. Thus, friction forces between the seal cover and shell are considered in this work. Contact force transmission will be established only in the case of closed contact [31]. Several approaches are available for defining contact interaction between the inner side of the shell and seal. In this study, node-to-node contact elements have been chosen. The distribution of contact elements between the seal and shell has been shown in Figure 8. This type of element represents contact and sliding between any two nodes of the shell and seal. The element has two nodes with three translational DOF at each node. It is capable of supporting compression in the normal direction of contact and Coulomb friction in the tangential direction. Weak springs with 1e-6N/m stiffness have been taken into account to prevent open contact and to aid in convergence, but sliding is permitted throughout the analysis. Solution of contact force and displacement is performed by contact algorithm. Several contact algorithms are available for the solution of contact problems such as Lagrange multiplier and penalty method. By the penalty method, tangential stiffness can be obtained by multiplication of friction coefficient and radial stiffness, which is suitable for the current study. Therefore, the penalty method has been selected.

For damping consideration, light damping has been adopted for the overall system. For structural parts, the metal damping ratio as in Table 1 was used. For liquid, viscous dissipation of the surface waves according to Table 2 was considered as the primary source of liquid damping. Damping of the seal was estimated according to the usual hysteresis loops present in polyurethane (PU) foams [34]. The equivalent damping ratio due to contact friction was approximately calculated based on friction coefficient between nylon and steel (0.6), average radial stress (from Figure 7), contact area and average critical damping (computed from the result of modal analysis). For the equivalent damping ratio calculation method readers can refer to [35].

The tanks are assumed to be anchored to the rigid ground such that no sliding or uplift may occur. Therefore, all base nodes located on the floor are fully restrained in all directions. As a result of this perfect anchorage assumption, the tank floor may not be included in the FE modeling of such containers. Since only an anchored tank is considered in this study, the tank floor is not modeled in FE simulation [36].

Gravity acceleration (g) has been applied to the liquid as body acceleration. Initial hydrostatic stability was established by ignoring the gravity acceleration of the roof. Hence, pressure results on the roof-liquid interface will be dynamic pressure, i.e. pressure due to the roof oscillation in the fluid.

FSI was applied for both shell-liquid and roof-liquid interfaces by the selection of liquid and structure nodes

and elements at the interface. Then, the surface load at the selected nodes was labeled as FSI. Common nodes have been used for fluid and structure elements at the shell. However, for the roof lower deck and liquid surface, different nodes have been used but with the same vertical and radial position.

Modal and time history analysis have been performed considering the aforementioned models. Modal analysis was implemented by a solution to the eigenvalue problem. For time history solution with the FSI problem, simultaneous or partitioned coupling can be employed. In simultaneous strategy, the whole system is treated as a monolithic entity, and the components are advanced simultaneously in time. In partitioned treatment, the field models are treated computationally as isolated systems that are separately stepped in time. In this study, the simultaneous coupling method has been used for time history analysis [37]. For full transient Analysis, an optimized strategy has been taken considering time intervals, element sizes, the total number of elements and elements with contact algorithm. In this way, 0.03s time steps have been taken into account regarding 95071 elements and also so many node-to-node contact elements generated.

The linear solution assumes small deflection so that the resulting stiffness and mass distribution changes can be considered insignificant. In contrast, when a structure experiences large deflections, forces will change direction, and the elements will undergo large rotations and displacements. This effect is known as geometric nonlinearity which may substantially change the final results of a numerical analysis [21]. For such nonlinear analysis, Newmark's integration scheme solution was conducted in association with Newton-Raphson iterative algorithm [38]. After each time step, mass and stiffness matrices were updated to consider the geometric nonlinearity of the system.

4. RESULTS

Modal analysis was initially performed to obtain dominant frequencies. As stated before, FSI between fluid-Wall and Fluid-Roof has been considered. In Figure 2, the elemental configuration of the tank, liquid and roof was outlined. A total of 95071 elements have been generated in the system.

4. 1. Natural Frequencies The first dominant natural frequencies of the tank for different oil contents, i.e., Iranian condensate, Lavan and Soroosh crude oil are calculated and are shown in Table 4. The first two dominant natural frequencies are indexed as fn1 and fn2 for simplicity.

As it can be seen, the two fundamental natural frequencies for heavy crude oil i.e. Soroosh oil are about 17% less than for Iranian condensate, while this value for Lavan crude oil is about 5% less than for condensate.

4. 2. Mode Shapes The mode shape of the upper deck for the first two modes is shown in Figures 9 and 11. In addition, a sector of the deck has been selected and in this sector, the behavior of the upper, lower and intermediate structures including rafters, bulkheads and trusses are demonstrated (Figures 10 and 12).

As was shown in Figures 10 and 12, each element of the intermediate structure has its mode of vibration that affects and makes the final mode shape of the deck. Due to the continuity of the deck, in general, upper, lower and intermediate structures follow the same shape pattern. The bottom surface of the lower deck is in contact with the oil and its upper surface is connected to stiffeners. In addition, the lower deck is about 33% thicker than the upper deck. Hence, its amplitude is 2%~3% less than the upper deck. Maximum vibration will occur due to fn1 which is the most dominant natural frequency. Hereafter, the maximum absolute value of mode shapes will be referred to as the high spot that is the peak area of the upper deck as depicted in Figures 9 to 12.

As the main dynamic effect on the floating roof is due to the fluid sloshing, only vertical deformations (Y global direction) are shown. Inspection of the roof horizontal movements concerning the wall inside indicates relatively less value due to the nature of surface vertical waves.

As was expected, the modal shapes of the roof in all the three liquid contents, i.e. condensate, Lavan and Soroosh crude oils are almost the same as it is shown in Figures 10 and 12.

Detail of bulkheads, trusses and rafters for fn1 mode shape in and around high spot is depicted in Figure 13. This figure shows that rafters are more vulnerable to vibration than other stiffeners. This fact notifies the revision of the design regarding this structure.

As modal analysis is performed in the absence of excitation, and excitation is affected by liquid, the modal

TABLE 4. Natural frequencies of three liquid content cases

Liquid type	fn1 frequency (Hz)	fn2 frequency (Hz)
condensate	0.1813	0.7100
Lavan	0.1581	0.6236
Soroosh	0.1504	0.5920

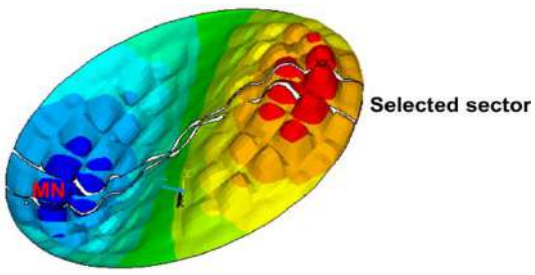

Figure 9. fn1 mode shape of the upper deck

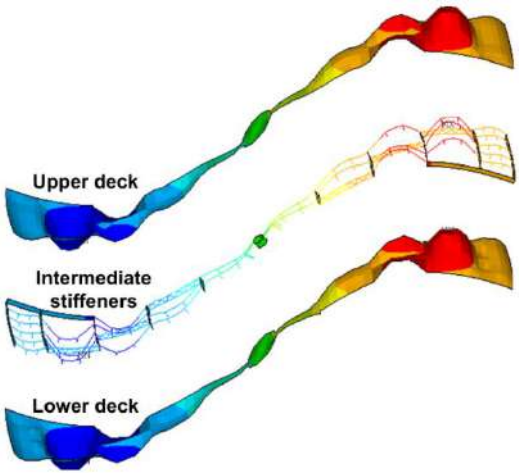

Figure 10. fn1 mode shape of the sector selected in Figure 8 including a lower deck, Intermediate structures and upper deck

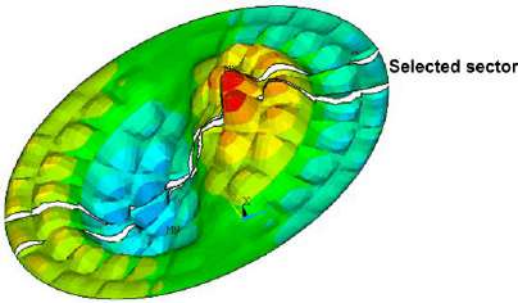

Figure 11. fn2 mode shape of the upper deck

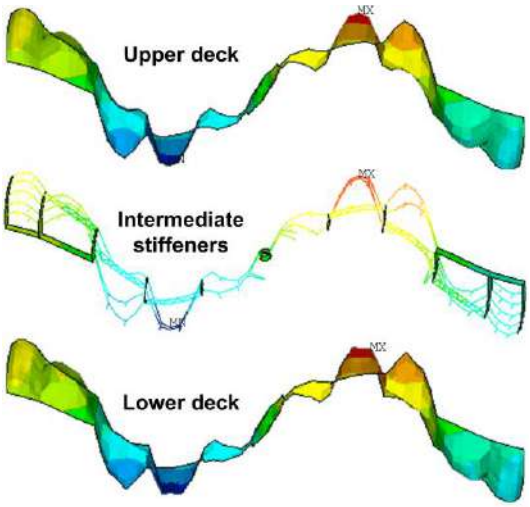

Figure 12. fn2 mode shape of the sector selected in Figure 10 including a lower deck, intermediate structures and upper deck

approach cannot represent the complete effects of the liquid on the vibration behavior of the roof according to Equation (1). Furthermore, vibration amplitude cannot be

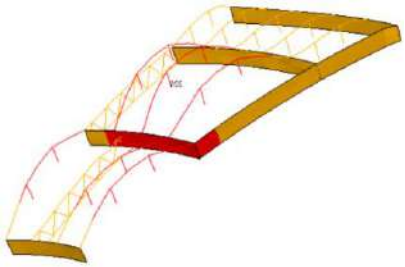

Figure 13. Mode shape detail of bulkheads, trusses and rafters for fn1

obtained by a modal approach. On the other hand, the vibration amplitude of the roof during an earthquake is the main concern in seismic analysis. One of the methods for amplitude evaluation of the vibrating systems is response spectrum modal analysis. This method was used so far for some structures [39] and open storage tanks [27]. However, this approach is based on linear theory, and accurate results cannot be achieved in this analysis. Hence, a more extensive effect of liquid properties variation on seismic behavior of the roof will be investigated in the next sections by performing time history analysis.

4. 3. Time History Analysis Time history analysis of the system has been performed during base acceleration excitation. The system specifications are as stated before and FSI is adopted as in the modal analysis. Nonlinear stress/strain relation of the seal and frictional contact were also used.

The base of the storage tank was excited horizontally by the 1999 Izmit earthquake in Sakaria of Turkey taken from SiesmoSignal software accelerograms [40], the 2017 Sarpol-e Zahab earthquake in the east of Iran [41] and the 2013 Shonbeh earthquake in the south of Iran [41]. The first two earthquakes have dominant amplitude at lower frequencies around fn1. Therefore, it has been employed for fn1 vibration evaluation. The two earthquakes have different properties at fn1 as will be shown in Figures 19 and 22. Excitation of Sarpol-e Zahab at fn1 increases from light to heavy oil. Sakaria acts in the reverse order; it decreases from light to heavy oil at fn1. More detail of the figures will be described in advance. The motivation of the choice is to see how much difference can affect DDFR response at fn1. Regarding the aforementioned characteristic, earthquakes such as El Centro which have critical point near fn1 in amplitude vs frequency function are not suitable for this purpose.

Shonbeh earthquake has dominant vibration at higher frequencies. Hence, it was used for fn2 excitation. However, some frequency modulations were applied to the strong portion of it to be more effective on fn2.

All the prescribed vibration modes were observed in the time history analysis. El Centro earthquake was employed as a rich frequency content earthquake for

producing a combination of several modes together. For instance, Figure 14a shows the simultaneous appearance of fn1 and fn2 modes of the upper deck for Soroosh oil content at t=8.67s excited by this earthquake. In Figure 14b, a mode shape obtained by Meera and Reshmi [22] for a DDFR with a fixed boundary has been illustrated. Comparison of the periphery displacement of the two mode shapes verifies the involvement of friction around the roof periphery in the present work.

In Figure 15, the vibration pattern of different parts of the tank due to the Sakaria earthquake was shown in cutaway views. In addition, dynamic pressure on the liquid surface at the same time was demonstrated in Figure 16. As can be observed, the pressure profile on the contact area satisfies the displacement profile of the roof, i.e. maximum liquid dynamic pressure on the roof coincides with maximum displacement, and minimum pressure coincides with minimum displacement. This phenomenon verifies FSI existence at the roof-oil interface. In each figure, maximum and minimum spots are denoted by 'MX' and 'MN' respectively.

Vibration amplitude has been investigated in time and frequency domains. In this way, the high spot vibration of the upper deck has been selected for time wave demonstration. This spot was indicated in Figure 9 as MN in red color.

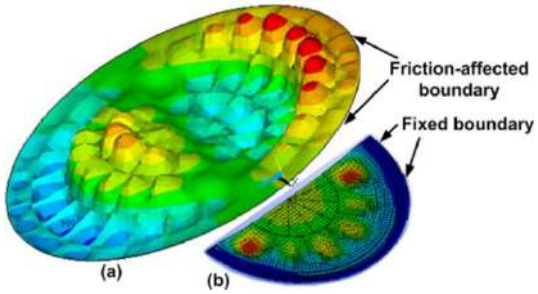

Figure 14. (a) Vibration pattern of the upper deck at t=8.67s for Soroosh crude oil content due to El Centro earthquake, (b) mode shape obtained by Meera and Reshmi [22]

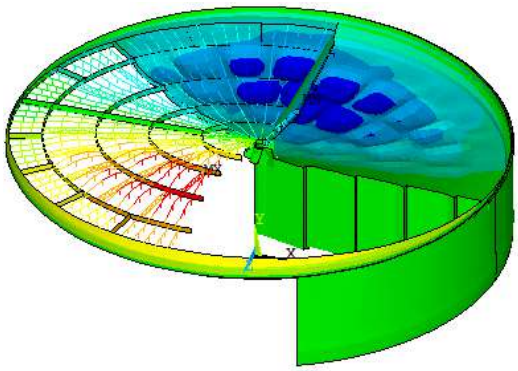

Figure 15. Vertical vibration pattern of the different parts of the tank in cutaway views due to Sakaria earthquake at t=7.29s

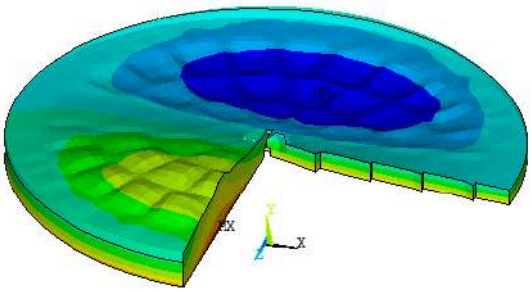

Figure 16. Pressure pattern of the oil surface due to Sakaria earthquake at t=7.29s (Minimum pressure is indicated by MN and maximum by MX)

In Figure 17, the time history of the Sarpol-e Zahab earthquakes has been demonstrated. In the current study, Peak Ground Acceleration (PGA) has been taken 0.3g as can be observed in the excitation time waves. Figure 18 gives vibration amplitudes of the roof for the three liquid content cases in the time domain due to this ground excitation. The earthquake duration was the 30s. However, time history analysis was extended up to the 40s to have forced and some free vibration. As it can be seen, DDFR vibration's amplitude increases from condensate to Soroosh crude oil during the Sarpol-e Zahab earthquake. Also, as is expected, the heavier oil's amplitudes occur later than lighter oil due to its long period of time.

Figure 19 shows the Power Spectrum (PS) of the Sarpol-e Zahab earthquake and the roof's highest spot vibration due to this earthquake. As shown in the figure, dominant PS frequencies deviate a little from natural frequencies (solid circles) towards higher excitation. This phenomenon implies the influence of forcing frequency on PS in addition to the natural frequency.

In Figure 19, excitation has been increased from condensate to Soroosh oil for fn1. This manner causes the roof Root Mean Square (RMS) of vibration to increase from condensate to Soroosh crude oil.

The same method was used for fn2 vibration amplitude analysis. In this regard, the Shonbeh earthquake was found to have high-frequency contents, and therefore it was used for producing fn2 mode. However, frequency characteristics of the earthquake have been modified in each liquid case to have sufficient excitation values at fn2. In this excitation case, excitation amplitude and PS, and the resulting vibration magnitude and PS at fn2 have been increased from condensate to Soroosh crude oil.

In Figure 18 and also Shonbeh earthquake, vibration magnitude has been represented as a function of time. However, the liquid cases must be compared irrespective of time. Time parameters can be canceled out by extending simulation duration to infinity. For this purpose, the Sakaria earthquake was employed. The time history of this earthquake was shown in Figure 20. Figure 21 shows time domain vibration of the roof's highest spot

due to the Sakaria earthquake for more than 40s. Excitation was the 20s. However, an investigation was extended to the 120s as relative infinite time. Figure 22 gives PS relating to infinite time waves. In this figure, excitation and vibration amplitude RMS at fn1 have been decreased from condensate to Soroosh.

As it was seen, excitation at the natural frequency plays the main role in the amplitude decrement or increment. Roof vibration increases with excitation rise and vice versa. Hence, evaluation has been performed so far according to the frequency content of the excitation.

To have excitation-independent in addition to time-independent evaluation, the excitation curve in Figure 22 was scaled up so that it passes through the maximum PS of the condensate case. As can be seen, the positions of PS peaks for Lavan and Soroosh are slightly higher than the scaled excitation curve. This circumstance shows that a floating roof is more vulnerable to vibration in heavier liquids i.e. Lavan and Soroosh.

In another point of view, in the time wave demonstrations, sharp edges of the vibration curves imply high-frequency existence. Therefore, Figures 18 and 21 indicate that high-frequency vibrations generally decay faster than low-frequency ones due to more damping as can be expected. However, the time of disappearance also depends on the excitation initiation time. Hence, high-frequency components may have low

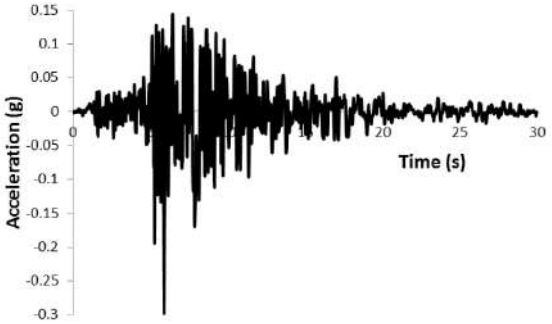

Figure 17. Time history of Sarpol-e Zahab earthquake

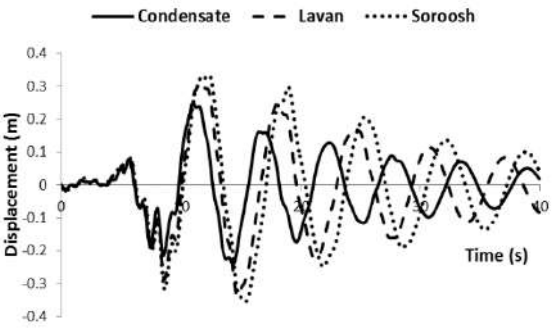

Figure 18. Time domain vibration of the roof highest spot for three liquid cases excited by Sarpol-e Zahab earthquake

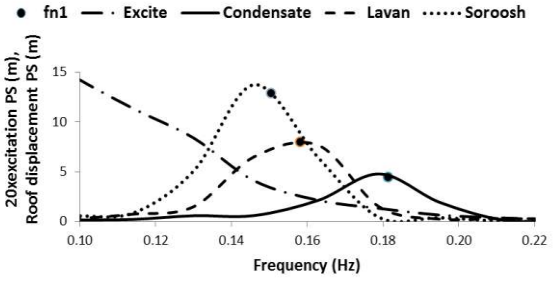

Figure 19. Vibration PS of Sarpol-e Zahab earthquake and the relevant roof highest spot for three liquid cases

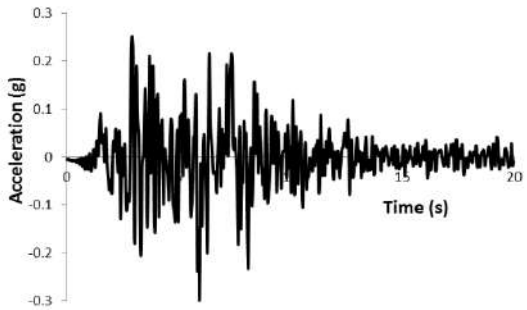

Figure 20. Time history of Sakaria earthquake

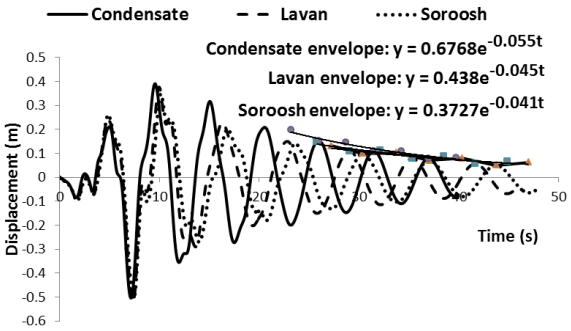

Figure 21. Time domain vibration of the roof highest spot for three liquid cases excited by Sakaria earthquake

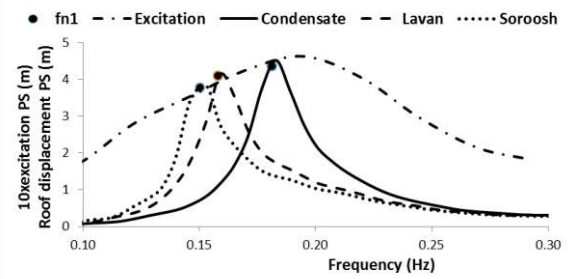

Figure 22. Vibration PS of Sakaria earthquake and the relevant roof highest spot for three liquid cases

or high contributions to the maximum vibration peak. For Sarpol-e Zahab earthquake as shown in Figure 18, maximum absolute displacement has been taken place after higher frequencies disappeared. On the other hand, in vibration due to the Sakaria earthquake, a trace of the second mode (fn2) exists in addition to the first mode (fn1). The influence of fn2 on the maximum peak can be recognized by comparing the high spot position of Figure 15 with Figure 9 corresponding to fn1 mode shape and Figure 11corresponding to fn2 mode shape. As can be seen, the high spot has moved slightly to the inside of the deck. After maximum peak elapses, fn2 will vanish earlier than fn1 so that the final cycles are approximately coincident with the fn1 time wave. This characteristic will be employed for the computation of the fn1 equivalent damping ratio.

The equivalent damping ratio is another factor that affects vibration response. In Figures 18 and 21, vibration decays more slowly in the last periods of free vibration expressing logarithmic decrement. Also, it was observed that natural periods obtained in the last periods of free vibrations conform to the natural periods determined by modal analysis. Hence, natural periods are approximately constant during simulation. Therefore, logarithmic decrement can be used for damping ratio determination during free vibration. Free vibration behavior after the Sakaria earthquake was employed for fn1 damping ratio computation. In this regard, the envelope curves and the relevant exponential relationships for the computation of fn1 equivalent damping ratios can be observed in Figure 21. For each liquid case, the exponent of the envelope curves in the free vibration part is '$-\varsigma\omega_1 t$'. Hence damping ratio can be computed for each case. The same method was employed for the calculation of the fn2 equivalent damping ratio. As stated before, the Shonbeh earthquake was used for producing vibration with fn2 dominant amplitude. Equivalent damping ratios of fn1 and fn2 obtained by this method have been summarized in Table 5. Tables 4 and 5 indicate that natural frequency values and damping ratios have been decreased from light to heavy liquid content. Damping decrement due to liquid variation is small for fn1. For instance, liquid change from condensate to Soroosh leads to a 10% decrement of damping ratio, while this value is 4% for Lavan to Soroosh. However, for fn2, natural frequencies and damping ratios are both affected substantially by liquid change. Hence, the system with heavier liquid has a smaller damping ratio. This phenomenon is because the heavier liquid has more participation in the roof vibration. As liquid has lower damping than that of structures, this phenomenon causes the damping ratio of the whole system to be decreased.

Stress evaluation of the floating roof has been performed by checking the stress of the upper and lower deck at the time of maximum displacement. This circumstance arose at 7.29s due to the Sakaria earthquake

TABLE 5. Equivalent damping ratios (ς) of the first and second natural frequencies for three liquid cases

Liquid type	ς for fn1	ς for fn2
condensate	0.0483	0.0646
Lavan	0.0453	0.0569
Soroosh	0.0434	0.0538

in the condensate case as can be observed in Figure 23. The upper deck undergoes more stress. Hence, the stress distribution of the upper deck in the earthquake direction was selected for demonstration and was shown in Figure 23. As can be seen, stress values are in the elastic limit of the roof material which is low carbon steel.

Von Mises stress of the upper and lower deck was also checked which exhibits safety of the structure according to maximum distortion energy criteria.

In this analysis, earthquakes were scaled to the peak ground acceleration of 0.3g to obtain convergent numerical conditions as possible. This scaling maintains main structural deformations in almost linear behavior. However, in hazardous conditions, excitation may exceed this value, and nonlinear behavior of the structure material is needed to be defined through data tables as described for foam seal material. On the other hand, large permanent deformations of the roof especially in the periphery may cause liquid splash or spill out which is a potential for roof instability or sinking. However, this process cannot be simulated by hydroelastic analysis which has been presented so far. Therefore, a low value of scaling is preferred.

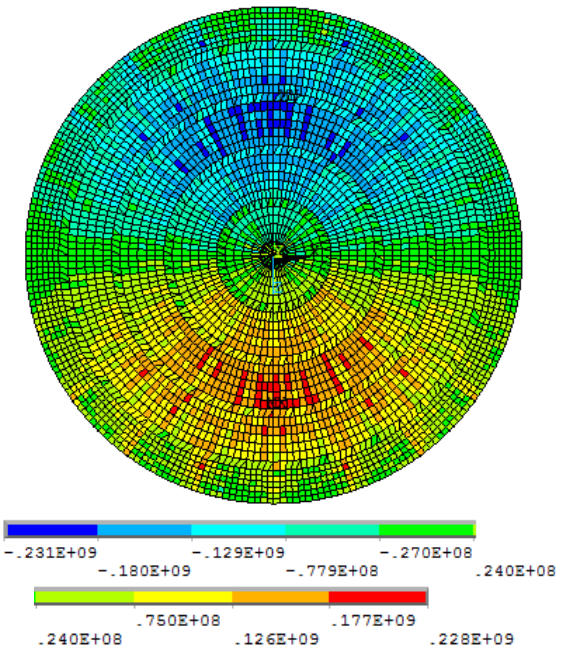

Figure 23. Stress distribution of the upper deck in the excitation direction at 7.29s during the Sakaria earthquake

The scaling method used in Figure 22 assumes a linear relationship between excitation and vibration amplitude. To add nonlinearity, the steady-state method has been proposed as an alternative. The basic concept of this procedure has been introduced in Equation (7). In this approach, the steady-state response of the roof in light and heavy crude oils is compared by applying equal harmonic amplitudes at their natural frequencies. Following this procedure, harmonic displacements at the first natural frequencies with equal amplitude were applied to the condensate tank as light and Soroosh as a heavy crude oil system as:

$$u_g = \begin{cases} 0.15\sin(1.1391t) & \text{(m) for condensate} \\ 0.15\sin(0.9450t) & \text{(m) for Soroosh} \end{cases} \quad (9)$$

Vibration responses were compared as shown in Figure 24. Simulation time was extended to steady-state condition to have time-independent evaluation. Refer to Equation (6) for more clarity. According to steady-state amplitude, a floating roof in heavy crude oil is more vulnerable to vibration than in lighter oil. It can be seen from Figure 24 that the heavier oil's steady-state amplitude occurs later than lighter oil due to its long period. These two phenomena conform to the results achieved in the previous analysis.

Figure 24 also shows that baseline of the oscillation is slightly lower than zero due to buoyancy problems.

5. VALIDATION OF NUMERICAL MODEL

The differences between the current numerical model with those available in the literature prevent us from achieving comparable models; Contact friction between seal and wall and the proposed complicated stiffeners haven't been presented so far. Also, the exact time wave and frequency characteristics of the excitation sources used in the literature are not accessible. Therefore, simplification of the proposed model is inevitable invalidation. In this regard, natural frequencies in the condition of the unroofed rigid tank were computed using the analytical technique recommended in European standard Eurocode 8 [42]. The considered tank was assumed to have fixed conditions at the base as in the present work. Characteristics of the model were then developed toward the current model in steps to investigate the result deviation. In the second step, the side shell was revised from rigid to flexible. This modification led to considerable change in a result that verifies FSI existence between shell and liquid. Afterward, a floating roof and seal were added to the model but without slipping permission for the roof along with the tank height. In this step, FSI between roof and liquid can be recognized from natural frequency change. Also, it can be verified further by investigation of Figures 15 and 16 as stated before. Finally, the model was completed by introducing a frictional slip between seal and shell. The contribution of slippage to the roof vibration has been verified in Figure 25. In this figure, the vibration time waveform of the same node at the roof periphery due to the Sakaria earthquake was compared for the two cases of no-slip and frictional slip. As can be seen, the maximum amplitude has been increased in frictional slipping cases. In addition, in Figures 14a and 14b, the frictional slipping boundary was compared with the fixed boundary. However, dominant natural frequencies have not been changed considerably by frictional slip addition in the actual range of friction coefficients. The result of the aforementioned gradual development of the model has been summarized in Table 6. The table also shows the substantial effect of the roof on fn2 frequency. Therefore, fn2 frequency is more structure-dependent than fn1.

So far, verification has been performed assuming zero dampings for the system. For further verification, the damping ratios provided in Table 5 were compared with Eurocode 8 recommendations that show acceptable agreement [42].

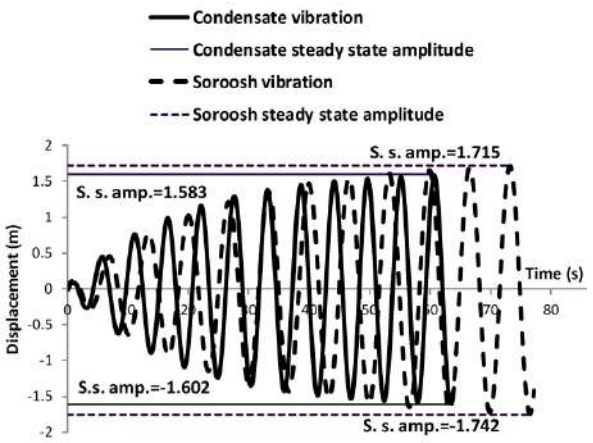

Figure 24. Vibration increment and steady-state amplitude of the roof for condensate and Soroosh crude oil in response to equal harmonic excitations

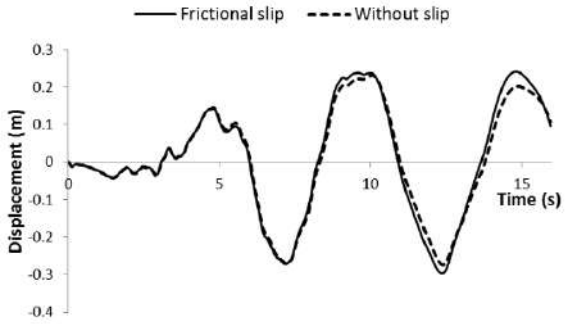

Figure 25. Maximum roof periphery vibration in no-slip and frictional slip cases of the seal-shell contact area

TABLE 6. The first and second natural frequencies for condensate liquid case with the gradual development of the model

Model type	fn1	fn2
Eurocode 8 for unroofed rigid tank	0.0978	0.2072
Current numerical model for unroofed rigid tank	0.0983	0.2081
Current numerical model for unroofed flexible tank	0.1345	0.2243
Current numerical model for a roofed flexible tank with seal and contact friction	0.1813	0.7100

6. CONCLUSION

The behavior of Siraf double deck floating roof, in the south of I.R.Iran, with foam seal and fluid-structure interaction were studied for condensate, light and heavy crude oils. It was seen that the upper, lower and intermediate structures have the same dominant mode shapes and it is important to keep this integrity in the design phase. The mode shape was almost independent of the oil's type. The natural frequency and damping ratio decrease as the oil becomes heavier. The first hydroelastic natural frequency of the roof in Soroosh oil, heavy oil, is about 17% less than for Iranian condensate, light oil while damping ratio decrease is about 10%.

The vibration of the roof mainly depends on the frequency content of the earthquake to the roof's hydroelastic natural frequencies. For Sarpol-e Zahab and Shonbeh earthquakes, the heavier oil had dominant amplitude while for the Sakari earthquake the lighter oil had dominant amplitude.

Floating roof in heavy crude oil is more vulnerable to vibration than in light oil according to scaling method and steady-state amplitude.

7. REFERENCES

1. Kuan, S.Y., "Design, construction and operation of the floating roof tank", University of Southern Queensland, Mechanical and Mechatronic Engineering, Australia, Bachelor of Engineering, (2009).
2. Trimulyono, A., Chrismianto, D., Samuel, S. and Aslami, M.H., "Single-phase and two-phase smoothed particle hydrodynamics for sloshing in the low filling ratio of the prismatic tank", ***International Journal of Engineering, Transactions B: Applications***, Vol. 34, No. 5, (2021), 1345-1351., DOI: 10.5829/IJE.2021.34.05B.30
3. Hatayama, K., "Lessons from the 2003 tokachi-oki, japan, earthquake for prediction of long-period strong ground motions and sloshing damage to oil storage tanks", ***Journal of Seismology***, Vol. 12, No. 2, (2008), 255-263., DOI: 10.1007/s10950-007-9066-y
4. Manser, W.S., Touati, M. and Barros, R.C., "The maximum sloshing wave height evaluation in cylindrical metallic tanks by numerical means", MATEC Web Conference., Vol. 95, (2017), 17005., https://doi.org/10.1051/matecconf/20179517005
5. Utsumi, M., "Vibration reduction of a floating roof by dynamic vibration absorbers", ***Journal of Pressure Vessel Technology***, Vol. 133, No. 4, (2011)., DOI: 10.1115/1.4002923
6. Kobayashi, N., Sato, T. and Torisaka, A., "Passive control of liquid sloshing in floating roof tank with multi dynamic absorber", in ASME 2013 Pressure Vessels and Piping Conference. Vol. Volume 8: Seismic Engineering, No. Issue, (2013)., DOI: 10.1115/pvp2013-97229
7. Hasheminejad, S.M. and Mohammadi, M.M., "Active sloshing control in a smart flexible cylindrical floating roof tank", ***Journal of Fluids and Structures***, Vol. 66, (2016), 350-381., https://doi.org/10.1016/j.jfluidstructs.2016.07.022
8. Esfandian, H., Goodarzian Urimi, M. and Shokoohi Rad, A., "Risk assessment of gasoline storage unit of national iranian oil product distribution company using phast software", ***International Journal of Engineering, Transactions A: Basics***, Vol. 34, No. 4, (2021), 763-768., DOI: 10.5829/IJE.2021.34.04A.02
9. Amabili, M., "Vibrations of circular plates resting on a sloshing liquid: Solution of the fully coupled problem", ***Journal of Sound and Vibration***, Vol. 245, No. 2, (2001), 261-283., https://doi.org/10.1006/jsvi.2000.3560
10. Golzar, F.G., Shabani, R., Tariverdilo, S. and Rezazadeh, G., "Sloshing response of floating roofed liquid storage tanks subjected to earthquakes of different types", ***Journal of Pressure Vessel Technology***, Vol. 134, No. 5, (2012)., DOI: 10.1115/1.4006858
11. Golzar, F.G., Shabani, R. and Tariverdilo, S., "Stress analyses in single deck and double deck floating roofs subjected to earthquake ground motions", ***Scientia Iranica***, Vol. 24, No. 2, (2017), 727-739., DOI: 10.24200/sci.2017.4057
12. Matsui, T., "Sloshing in a cylindrical liquid storage tank with a single-deck type floating roof under seismic excitation", ***Journal of Pressure Vessel Technology***, Vol. 131, No. 2, (2009)., DOI: 10.1115/1.3062939
13. Salarieh, H., shabani, r. and tariverdilo, s., "Effect of flexural and membrane stiffness on the analysis of floating roofs", ***International Journal of Engineering, Transactions A: Basics***, Vol. 23, No. 1, (2010), 57-64., http://www.ije.ir/article_71832_fcf49782751cad16e30f173312ef4676.pdf
14. Yamauchi, Y., Kamei, A., Zama, S. and Uchida, Y., "Seismic design of floating roof of oil storage tanks under liquid sloshing", in ASME 2006 Pressure Vessels and Piping/ICPVT-11 Conference. Vol. Volume 4: Fluid Structure Interaction, Parts A and B, (2006), 1407-1415., DOI: 10.1115/pvp2006-icpvt-11-93280
15. Sakai, F., Inoue, R. and Hayashi, S., "Fluid-elastic analysis and design of sloshing in floating-roof tanks subjected to earthquake motions", in ASME 2006 Pressure Vessels and Piping/ICPVT-11 Conference. Vol. Volume 4: Fluid Structure Interaction, Parts A and B, (2006), 1437-1446., DOI: 10.1115/pvp2006-icpvt-11-93622
16. Sakai F., I.R., "Some considerations on seismic design and controls of sloshing in floating-roofed oil tanks", in The 14th World Conference on Earthquake Engineering, Beijing, China. (2008).
17. Yoshida, S., Sekine, K. and Iwata, K., "Sloshing characteristics of single deck floating roofs in aboveground storage tanks: Natural periods and vibration modes", in ASME 2009 Pressure Vessels and Piping Conference. Vol. Volume 7: Operations, Applications and Components, (2009), 191-199., DOI: 10.1115/pvp2009-77187
18. Yoshida, S., Sekine, K. and Mitsuta, T., "Axisymmetric finite element analysis for sloshing response of floating roofs in cylindrical storage tanks", ***Journal of Environment and Engineering***, Vol. 5, No. 1, (2010), 27-38., DOI: 10.1299/jee.5.27

19. Utsumi, M., Ishida, K. and Hizume, M., "Internal resonance of a floating roof subjected to nonlinear sloshing", ***Journal of Applied Mechanics***, Vol. 77, No. 1, (2009)., DOI: 10.1115/1.3173768
20. Goudarzi, M.A., "Seismic behavior of a single deck floating roof due to second sloshing mode", ***Journal of Pressure Vessel Technology***, Vol. 135, No. 1, (2012)., DOI: 10.1115/1.4007291
21. Goudarzi, M.A., "Seismic design of a double deck floating roof type used for liquid storage tanks", ***Journal of Pressure Vessel Technology***, Vol. 137, No. 4, (2015)., DOI: 10.1115/1.4029111
22. Meera, U.S. and Reshmi, P.R., "Dynamic analysis of single deck floating roof with deck stiffeners", ***International Research Journal of Engineering and Technology***, Vol. 04, No. 04, (2017), 3522-3526., https://www.irjet.net/archives/V4/i4/IRJET-V4I4844.pdf
23. Hosseini, M., Soroor, A., Sardar, A. and Jafarieh, F., "A simplified method for seismic analysis of tanks with floating roof by using finite element method: Case study of kharg (southern iran) island tanks", ***Procedia Engineering***, Vol. 14, (2011), 2884-2890., https://doi.org/10.1016/j.proeng.2011.07.363
24. Belostotsky, A.M., Akimov, P.A. and Afansyeva, I.N., "Multilevel methodology of numerical seismic analysis of coupled systems "foundation – shell – pontoon (floating roof) – column(s) – fluid"", ***Procedia Engineering***, Vol. 153, (2016), 89-94., https://doi.org/10.1016/j.proeng.2016.08.085
25. Gnitko, V., Degtyariov, K., Naumenko, V. and Strelnikova, E., "Bem and fem analysis of the fluid-structure interaction in tanks with baffles", ***International Journal of Computational Methods and Experimental Measurements***, Vol. 5, No. 3, (2017), 317-328., DOI: 10.2495/CMEM-V5-N3-317-328
26. Shabani, R. and Golzar, F.G., "Large deflection analysis of floating roofs subjected to earthquake ground motions", ***Nonlinear Analysis: Real World Applications***, Vol. 13, No. 5, (2012), 2034-2048., https://doi.org/10.1016/j.nonrwa.2011.12.026
27. Sivy M., M.M., Chlebo O., Havelka R., "Sloshing effects in tanks containing liquid", in MATEC Web of Conferences, Bratislava, Slovakia. Vol. 107, (2017), 7., https://doi.org/10.1051/matecconf/201710700069
28. Shabani, R., "Stress patterns in single deck floating roofs subjected to ground motion accelerations", ***International Journal of Engineering, Transactions C: Aspects***, Vol. 26, No. 12, (2013), 1495-1504., DOI: 10.5829/idosi.ije.2013.26.12c.10
29. Yazdani, A.-. and Kowsari, M., "Statistical prediction of the sequence of large earthquakes in iran", ***International Journal of Engineering, Transactions B: Applications***, Vol. 24, No. 4, (2011), 325-336., DOI: 10.5829/idosi.ije.2011.24.04b.03
30. Chopra, A.K., "Dynamics of structures: Theory and applications to earthquake engineering", Fourth Edition ed, Berkeley, Prentice Hall, (2012)
31. ANSYS.Inc. *Customer support | ansys*. 26 August 2021]; Available from: https://www.ansys.com/support.,
32. NIOC, R.I.P.I. *Petroleum products specifications*. 26 August 2021]; Available from: https://www.nioc-intl.com/EN/PetroleumSpec.aspx
33. *Tank technology engineering service co. Ateco: External floating roof seals*. 26 August 2021]; Available from: https://www.atecotank.com/floating-roof-seal/external-floating-roof-seals/
34. Alzoubi, M., Al-Waked, R. and Tanbour, E., "Compression and hysteresis curves of nonlinear polyurethane foams under different densities, strain rates and different environmental conditions", ***Journal of Mechanical Engineering***, Vol. 9, (2011), 101-109., doi: 10.1115/IMECE2011-62290
35. Thomson, W.T. and Dahleh, M.D., "Theory of vibration with applications, India, Pearson, (1997), 544.
36. Moslemi, M. and Kianoush, M.R., "Parametric study on dynamic behavior of cylindrical ground-supported tanks", ***Engineering Structures***, Vol. 42, (2012), 214-230., https://doi.org/10.1016/j.engstruct.2012.04.026
37. Yenduri, A., Ghoshal, R. and Jaiman, R.K., "A new partitioned staggered scheme for flexible multibody interactions with strong inertial effects", ***Computer Methods in Applied Mechanics and Engineering***, Vol. 315, No., (2017), 316-347., https://doi.org/10.1016/j.cma.2016.10.044
38. Sivý, M. and Musil, M., "Seismic resistance of storage tanks containing liquid in accordance with principles of eurocode 8 standard", ***Strojnícky časopis - Journal of Mechanical Engineering***, Vol. 66, No. 2, (2016), 79-88., doi:10.1515/scjme-2016-0021
39. Norouzi, A.H., Gerami, M., Vahdani, R. and Sivandi-Pour, A., "Effects of multiple structure-soil-structure interactions considering the earthquake waveform and structures elevation effects", ***International Journal of Engineering, Transactions B: Applications***, Vol. 33, No. 5, (2020), 744-752., doi: 10.5829/ije.2020.33.05b.05
40. Seismosoft.Co. *Seismosignal support*. 26 August 2021]; Available from: https://seismosoft.com/support/seismosignal-support/
41. *Iran road, housing & urban development research center: Iran strong motion network*. 22 August 2021]; Available from: https://smd.bhrc.ac.ir/Portal/en/Search/BigQuakes
42. Standardization, E.C., *Eurocode 8- design of structures for earthquake resistance- part 4: Silos, tanks and pipelines*, in *Specific principles and application rules for tanks*. 2006, European Committee for Standardization: Brussels.81.

Persian Abstract

چکیده

ارتعاش لرزه‌ای سقف دوعرشه‌ای مخازن سیراف واقع در جنوب ایران بررسی گردیده است. میعانات گازی میدان نار و کنگان در جنوب ایران به عنوان هیدروکربن بسیارسبک، لاوان جهت نفت خام سبک و سروش برای نفت خام سنگین به عنوان محتویات مخزن در نظر گرفته شد. علاوه بر اندرکنش سیال–سازه، نقش آب‌بند فومی و اصطکاک تماسی بین آب‌بند و پوسته نیز مدنظر قرار گرفت. در شرایط ذکر شده فوق، تحلیل مودال و زمانی انجام شد. در تحلیل زمانی، زلزله‌های سرپل‌ذهاب و شنبه از استان زلزله‌ای زاگرس و ساکاریا از زلزله‌های مجاور ایران انتخاب گردید. فرکانس‌های طبیعی غالب، شکل‌مودهای اجزای سقف و ضریب میرایی فرکانس‌های طبیعی اول و دوم به همراه رفتار کلی زمانی و طیفی سقف برای هیدروکربن بسیار سبک تا سنگین ایران بدست آمده و ارزیابی شد. فرکانس طبیعی هیدروالاستیک سقف در نفت سروش حدود ۱۷٪ و ضریب میرایی حدود ۱۰٪ نسبت به حالت میعانات گازی کاهش داشت. محاسبات نشان داد فرکانس‌های طبیعی هیدروالاستیک غالب و ضرایب میرایی آنها با سنگین شدن مایع کاهش می‌یابد و ارتعاش سقف اساسا" به رابطه محتویات فرکانسی زلزله با این فرکانس‌های طبیعی بستگی دارد. همچنین نتیجه‌گیری شد بر اساس روش مقیاس و دامنه ارتعاش حالت پایدار، سقف شناور در حالت مایع سنگین‌تر لرزه‌پذیری بیشتری دارد.

International Journal of Engineering

Journal Homepage: www.ije.ir

Mass Production and Growth Mechanism of Carbon Nanotubes in Optimized Mechanothermal Method

S. O. Mirabootalebi*, G. H. Akbari, R. M. Babaheydari

Department of Materials & Metallurgy, Shahid Bahonar University of Kerman, Kerman, Iran

P A P E R I N F O

Paper history:
Received 8 May 2021
Received in revised form 8 August 2021
Accepted 24 August 2021

Keywords:
Carbon Nanotubes
Multi-walled Carbon Nanotubes
Synthesis of Carbon Nanotubes
Growth Mechanism of Carbon Nanotubes
Mechanothermal Method
Mass Production of Carbon Nanotubes

A B S T R A C T

There are a lot of major parameters in the mechanothermal approach such as milling time, ball-to-powder weight ratio (BPR), and cup speed which play a key role in the quality and quantity of the carbon nanotubes (CNTs). In this study, these essential factors in the mechanothermal method were optimized to maximize the efficiency of the process, and also the growth mechanism of CNTs was investigated. For these purposes, the milling of graphite was performed in a high alloy steel vial (Standard No. 1.2550 key-to-steel) for 330 h at the vial speed of 300 rpm in a planetary ball mill. The morphology and crystal structures of the graphite powder during the mechanical activation were studied by x-ray diffraction (XRD), Zeta-Sizer, and scanning electron microscope/energy-dispersive x-ray spectroscopy (SEM/EDX). After the heat treatment of amorphous carbon at 1400 ˚C, the CNTs were synthesized and their quality and quantity were analyzed by transmission electron microscopy (TEM), atomic force microscopy (AFM), XRD, Raman spectroscopy, and differential thermal analysis/thermogravimetric analysis (DTA/TGA). A special type of tip-growth mechanism based on the motion of the catalyst particles was proposed regarding the TEM images. According to this mechanism, the diameter, length, and shape of the CNT are completely dependent on a random motion of the catalyst particle at the tip of the nanotube. As a consequence, the growth mechanism in the mechanothermal process does not follow a certain pattern and this is the main reason for the spring-like and curved shape of the nanotubes. Furthermore, results of the differential thermal analysis revealed that the yield of fabricated multi-walled carbon nanotubes (MWCNTs) is more than 97% of the precursor.

***doi**: 10.5829/ije.2021.34.10a.14*

1. INTRODUCTION

The main methods for the production of carbon nanotubes are arc discharge [1], laser ablation [2], chemical vapor deposition (CVD) [3], electrolysis [4], and mechanothermal [5]. In the CVD and flame approaches, a high weight percentage of metal impurities is usually produced which required complex purification steps. Laser ablation, electrolysis, and arc discharge are suitable methods for the synthesis of high-quality CNTs, although they are not suitable for mass production and they need special equipment.

Mechanothermal is a simple and economic method for the large-scale generating of carbon nanotubes without producing a lot of metal impurities [6, 7]. Most of the generated CNTs in this way are bamboo and spring shape of MWCNTs with several millimeters in length [8, 9]. In the mechanothermal technique, graphite powder is milled and changed to amorphous carbon, and then in the annealing step, the carbon nanotubes are formed [10]. Indeed, the ball-milling and heat-treatment act as the nucleation and growth step, respectively [11]. The first mechanothermal method for synthesizing CNT was reported in 1999 by Chen et al. [12]. Then, Manafi et al. [9, 13] performed precise analyses to show the high capacity of this procedure for the fabrication of high-quality CNTs. Next, Guler et al. [14] generated carbon nanotubes in the shortest possible time and they developed the method.

Major parameters in the ball milling such as the time of milling by making the suitable precursor play an important role in the mechanothermal process for the

*Corresponding Author Institutional Email: oveis@eng.uk.ac.ir (S. O. Mirabootalebi)

Please cite this article as: S. O. Mirabootalebi, G. H. Akbari, R. M. Babaheydari, Mass Production and Growth Mechanism of Carbon Nanotubes in Optimized Mechanothermal Method, International Journal of Engineering, Transactions A: Basics Vol. 34, No. 10, (2021), 2332-2340

production of carbon nanotube [15]. On the one hand, structural defects and metal particles, which enter the powder during the milling, act as the catalysts for the formation of carbon nanotubes. Consequently, milling in an agate vial has a much lower efficiency for the production of CNTs than steel vial [16]. So, an increase in the volume of metal catalysts is equal to an increase in the yield of the process. On the other hand, the purification of the CNTs, in this case, becomes more difficult. In addition, high vial speed and milling time can lead to producing crumples of graphite sheets that are very stable and rarely converted to the tubular structure of CNT after the annealing step. Moreover, the temperature of the heat treatment is the other effective variable that should be in a certain range (1000-1800˚C) at the annealing step [10, 16]. This temperature is about half of the melting temperature of pure graphite, which leads to the formation of a tubular hollow structure of carbon .

In this research, all the mentioned effective factors from previous researches were adjusted to promote the efficiency of the process. First, the milling time, which is usually about 180 hours in the mechanothermal methods, was increased to 330 hours. As mentioned earlier, the metallic compounds of the vial that enter the powder during mechanical alloying are high potential regions for nucleation and growth of CNTs. Hence, a long milling time (330 h) and a high-alloy steel cup (Standard No 1.2550 key-to-steel) are selected for the mechanical activation step in this work. Most of the previous studies had utilized only one size of the balls [7, 15, 17], but using different dimensions of balls leads to a more random movement of balls and also more energy is transferred to the particles. Plus, the thickness of the powders layer on the surface of the balls and heterogeneity of the powders will be minimized [18]. So, we employed various sizes of balls to optimize the grinding process. As well as, what is not yet clear is the growth mechanism of CNTs in the mechanothermal method. In this paper, we also argue about the growth conditions of the nanotubes during the process.

Accordingly, the main purpose of the present work are the large-scale production of high-quality CNTs by applying the optimized factors and studying the growth mechanism of the carbon nanotubes.

2. MATERIALS AND METHODS

High purity graphite powder (15 μm size of flakes) was chosen as the precursor. The ball milling was carried out in a high-alloy steel vial (Standard No 1.2550 key-to-steel) at atmospheric pressure with 5 and 32 steel balls of 15 and 10 mm, respectively. The milling time was 330 h and BPR was kept at 20:1. The milling procedure was induced in a high-energy planetary ball mill under Argon at the cup speed of 300 rpm. In the next step, the ball-milled powders were placed in a furnace tube at 1400 ˚C for three hours in Argon to generate the CNTs. Finally, the obtained samples were placed in the furnace under the air atmosphere at the temperature of 330 ˚C for 132 min.

The structures of samples were studied by an X-ray diffractometer (Philips X'Pert, Cu-Kα, λ=0.1542 nm). Rietveld/MAUD refinement was used to measure the crystallite characteristics of the samples. The size distribution of the ball-milled graphite was measured by a zeta-seizer (ZEN3600). The morphologies of milled graphite particles were characterized by a scanning electron microscope (Cam Scan mv2300). The structure and size of the CNTs were analyzed by atomic force microscope (Autoprobe Cp, contact mode, 1 Hz rate of scan) and transmission electron microscope (LEO912-AB operated at 100 kV). The Raman spectroscopy (Takram P50C0R10, at 532 nm of laser wavelength) for analyzing the carbon nanotubes was carried out and DTA/TGA analyses (PC Luxx-NETZSCH) was taken in the air atmosphere to examine the mass loss profile and the thermal properties of the products.

3. RESULTS AND DISCUSSION

Figure 1 shows the XRD patterns of graphite particles during the ball milling process. There is a sharp and a broad peak at 26˚-27˚ and 43˚-46˚, respectively. These peaks are disappeared completely after the mechanical activation. The stable hexagonal phase is transformed gradually to the disordered and metastable amorphous phase and a noticeable reduction in crystallite size has occurred.

By increasing the activating times, both of the main peaks become broader because of the growing surface area of graphite particles, increasing and developing dislocations, creating sub-grain boundaries, and forming smaller grains. If the graphite grain size is reduced to about 3 nm, the crystal structure of graphite will transfer to the amorphous phase and this is related to the destruction of the graphite crystalline structure [12]. Based on the XRD profiles in Figure 1, the percentage of the produced amorphous phase, crystallite size, d002, the micro-strains were estimated by MAUD/Rietveld refinement, and then, these crystallographic data were put in Table 1.

The stable hexagonal close-packed (hcp) structure of carbon was still the dominant phase within the first 50 h of activation time. After 100 h of the ball-milling, the rate of destruction of the crystalline structure significantly decreased. Previous studies [13, 19] pointed out that no changes in the XRD pattern and the crystallite size have been observed after 170-1000 h of activation time. This is due to the creation of a balance between dislocation motion and recovery and recrystallization; thus cross slip does not cause the decrease in the grain size [18]. Actually, graphite sheets bent and converted to new

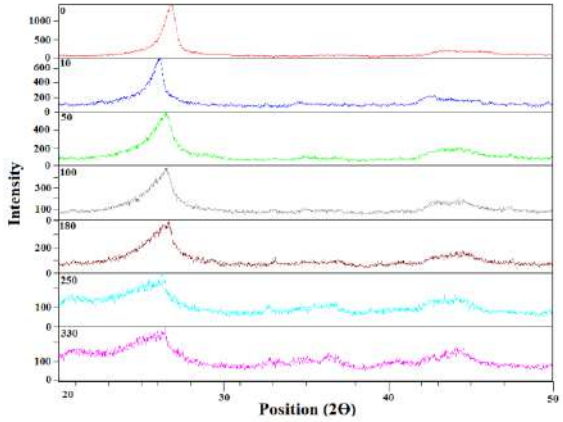

Figure 1. XRD patterns of graphite particles at different milling times

TABLE 1. The crystallographic data of graphite particles at different activation times

Milling Time (h)	Amorphous Phase (%)	Crystallite Size (nm)	d002 (nm)	Micro Strain (με)
0	0	390	0.332	0.00613
10	19	210.3	0.341	0.012
50	22	96	0.337	0.0175
100	69	58	0.337	0.0219
180	72	50.92	0.3376	0.0223
250	91	1.3	0.339	0.02507
330	93	1.3	0.339	0.02507

carbon-based nanostructures instead of a reduction in the crystallite size, owing to the high tenacity and flexibility of graphene plates and very strong σ bonds. These structures including carbon micro-tubes and carbon nanotubes [20, 21], ribbon nanostructures [22], and spherical and crustal structures of graphite [21]. Crumpled graphene sheets, hardly converted to nanotubes in the heat treatment stage due to high thermodynamic stability, toughness, and flexibility of the layers.

A key aspect of mechanical activation is the production of the amorphous phase as the precursor instead of these crumpled morphologies that are created at high milling speeds. In this study, instead of applying a high rotational speed, the normal speed (300 rpm) with high milling time was chosen to increase the percentage of the produced amorphous phase. As a result, we achieved to smallest crystallite size compared to similar works [6, 7, 23]. By increasing the milling time which leads to a long time of the process in the laboratory scale. This time can be reduced and the amount of initial graphite injected into the ball mill can be increased in order to achieve greater profitability by using industrial mills.

Generally, oxygen is slowing down the destructive process due to creating the saturated compounds with H_2, CO_2, and O_2, [24, 25]. In other words, Argon accelerates the reduction of the carbon grain size than Hydrogen and Oxygen under the same condition owing to its neutral nature [20].

The size distribution of the activated graphite for 330 h in a zeta-sizer analysis is depicted in Figure 2. The particle size distribution is in the range of 90-170 nm and the average particle is about 122 nm. The long-time of ball-milling transfers a high amount of energy to graphite particles which activation in all regions leads to the very fine and a none-wide distribution of the particles. This size distribution can facilitate the formation of the CNTs at the annealing step, since the uniform and very small particles by increasing the concentration gradient, have a positive impact on the formation of nanotubes.

Figure 3 illustrates the images of the scanning electron microscope of the initial graphite and the ball-milled graphite. The appearance of the spherical and the smaller graphite particles at 330 h of milling indicates structural changes and increasing the surface area of graphite particles due to high impact forces and severe plastic deformation. These ultra-activated turbostratic and amorphous particles with a high degree of agglomeration and free energy are the precursor materials and can be very effective on the quality and quantity of the CNTs which will be produced at the annealing step.

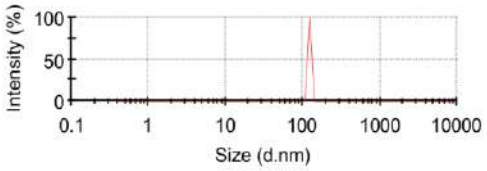

Figure 2. Size distribution of the milled graphite for 330 h

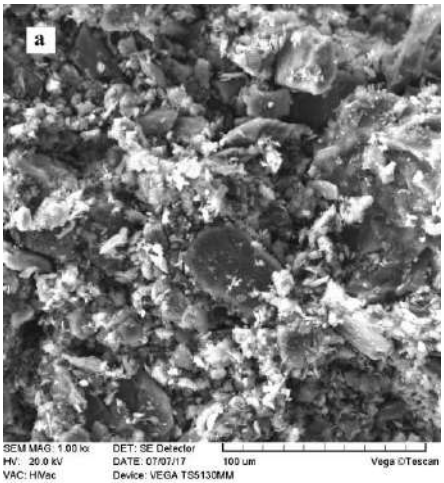

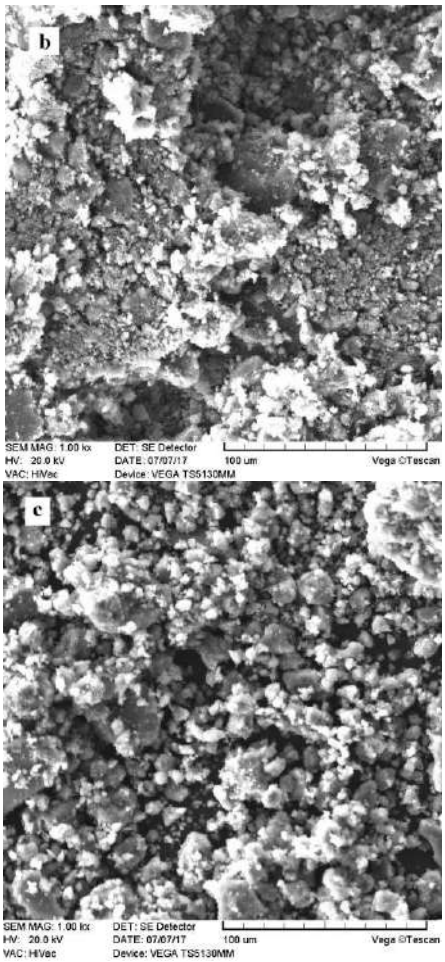

Figure 3. SEM images (a) initial graphite, (b) milled for 150 h, and (c)after 330 h of milling

EDX spectrum in Figure 4 reveals the different elements in the activated graphite for 330 h. These compositions such as iron contaminants play an important role in generating of CNTs, except the elements of Mg, Al, K, Ca, and Ti which come directly from the grid of SEM.

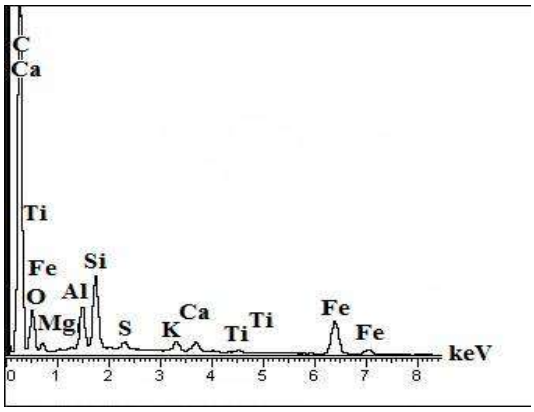

Figure 4. EDX of milled graphite for 330 h

TEM and AFM images of the fabricated CNTs after the thermal purification are demonstrated in Figure 5. The presence of a multitude number of carbon nanotubes in low magnification is a sign of the large-scale synthesis of the CNTs. The heat treatment and milling process are two major factors that determine the dimensions of the nanotubes. The distribution of 10-100 nm in diameter of carbon nanotubes and appropriate length (0.5-3 μm) indicate an approximately uniform size and dispersion of the metal catalyst particle which contaminates the powder during the ball milling process.

Nucleation and growth of CNTs are performing on catalyst particles according to the nucleation and the growth mechanism for the production of nanotubes in the presence of catalyst [26, 27]. By reducing the solubility and deposition of carbon atoms in the solution of carbon atoms and metal catalysts, carbon atoms by SP2 bonds are connected and finally, CNTs are formed. If carbon nanotubes grow upwards of the catalyst particles, the mechanism is labeled base-growth and if particles move at the head of the growing nanotubes, it is called tip-growth. Arrows in Figure 5 (c, d) illustrate catalyst particles that their possible endofullerenes and precipitates at the tips of the CNTs are obvious in the hypothetical tip-growth mechanism .

It seems during the mechanothermal process, first of all, amorphous carbons are attached to the catalyst particles and the nucleation stage is started. Next, the continuous longitudinal growth of nanotubes is taken by interfacial capillary forces and the diffusion of carbon atoms. Finally, the growth process continues as long as surface diffusion is supported by the concentration gradient and heat treatment. This finding corroborates the ideas of Chen et al. [16, 21] and Chadderton et al. [28]

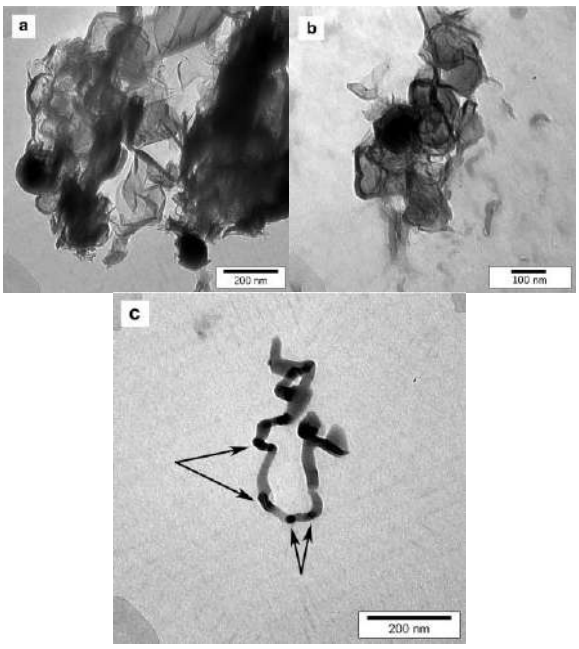

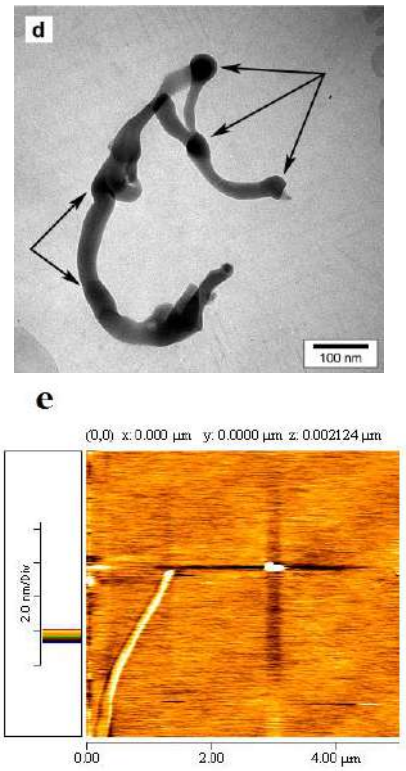

Figure 5. TEM (a, b, c, d, e) and AFM (d) images of synthesized carbon nanotubes by the heat treatment of ball-milled graphite after thermal purification (arrows show the catalyst particles)

who suggested that the growth of CNTs by the solid phase transformation is happened by surface diffusion. The growth of nanotubes entirely depends on the movement of the catalyst particle at the tip of the CNTs. Surface tensional forces, type, shape, and dimension of particle, heat and concentration gradient, and Van der Waals force between nanotubes are the most important factors which determine the direction of motion of the particle.

During the growth process, a competition between carbon atoms is created to form hexagons, heptagonal, and pentagons in the path of the particle. Hence, the length and width of the nanotubes are unpredictable and they are spring-like and bamboo-shaped with specific tubular hollow structures. The defects (heptagonal and pentagons) are preferred places for hydrogen storage [29-31]. As a result, synthesized curved nanotubes have a better performance for hydrogen storage compared to the straight nanotubes produced by other methods such as laser ablation or CVD. In addition, these manufactured nanotubes are probably more flexible than straight nanotubes and so they can be used for the production of high-strength nanocomposites by increasing the toughness of the matrix. Figure 6 provides information about the schematic diagram of the nucleation and growth of CNTs in the mechanothermal method .

The particles are larger than tubes and so it can therefore be assumed that the size of catalysts has a direct relationship with the diameter of the nanotubes, as previous reports [15, 32] confirmed an important impact of the milling time on the diameter of the CNTs. As a result, the long length and the relatively short diameter of the produced CNTs depict the usefulness of the long milling time and other applied factors in this study. Plus, furnace tube supplies the driving force for growing the nanotubes which this simple type of oven is economically more cost-effective than other methods such as laser ablation.

The X-ray diffraction pattern of the fabricated carbon nanotubes is shown in Figure 7. There are two main peaks. A sharp peak at 26˚ and a broad peak in the range of 41˚-43˚. According to Bragg's law [33], d002 was 0.342 nm, similar to d002 in multi-walled carbon nanotubes which is usually 0.34 nm [34].

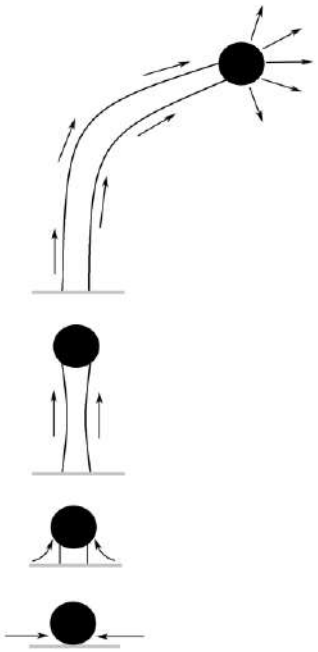

Figure 6. Schematic illustration of the proposed mechanism for the mechanothermal approach

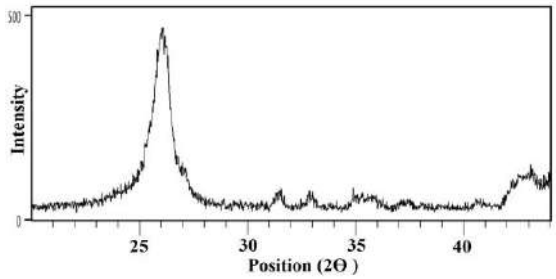

Figure 7. XRD diffraction pattern of the produced carbon nanotubes

In general, the d002 peak in CNTs is broadened, weakened, and shifted to the left side of the XRD profile by about half a degree (from 26.5˚ to 26˚), compared to pure graphite. This fact is related to the differences in the number of layers, changes in interlayer space, network distortion, and orientation of the carbon nanotubes against X-rays [35]. On the one hand, the diameter of the inner wall of multi-walled carbon nanotubes is more than 2 nm [36] and the obtained d002 is 0.342 nm. On the other, the number of walls usually has a one-to-one relationship with diameter according to Chiodarelli et al. [34]. As a result, it can be estimated that there are 20 to 50 walls in the synthesized CNT shown in Figure 5 with 20 nm in diameter. Overall, it is possible to hypothesize that a vast majority of the fabricated CNTs in this investigation have 10-40 walls, with attention to Chiodarelli's relation [34]. The strength of nanotubes is enhanced by increasing the number of walls whereas some of the other common methods such as laser ablation are unsuitable for the production of MWCNTs. Hence, the high number of walls of the prepared CNTs can makes them an ideal choice for the production of nanoalloys and nanocomposites.

Raman spectroscopy was performed for a more precise analysis of the quality and graphitization degree of the CNTs. The Raman spectra in Figure 8 indicate three main peaks. They are at 1349, 1566, and 2650 cm^{-1}, which are assigned to D, G, and G′ bands respectively. As well as, ID/IG and ID/IG′ were calculated 0.79 and 1.21, respectively.

The G-single-band (without Splitting) in Figure 8 is a strong sign of multi-walled carbon nanotubes. This fact is related to the non-split between G+ and G- bands due to the differences in the batches and diameters of MWCNTs [37]. The absence peak in radial breathing mode (100-200 cm^{-1}) is attributed to a large number of the walls (more than 20) and the inner diameter of CNTs (more than 2 nm), which make peaks immensely invisible and weak. The lack of any sharp peaks in this region shows a very small amount of generated single-walled carbon nanotubes (SWCNTs). D-band is concerned with asymmetry and disorders in the structure of graphite sheets including defects, impurities, and porosities that exist in carbon structures with sp2 hybridization [37-39]. The G′-band corresponds to the two-phonon process which its intensity depends on the purity of the sample and represents the long-range order of the CNTs [36, 40]. Thereby, ID/IG′ is a sensitive measure and less important than ID/IG for characterization of the quality and detecting the impurities of CNTs [41]. The obtained ID/IG and ID/IG′ ratios confirm ordered sp2 bonds and suitable quality of produced carbon nanotubes. It is also worth noting that the fabricated carbon nanotubes did not undergo any acid purification.

Figure 9 demonstrates the DTA/TGA analyses of the produced carbon nanotubes. The type of CNTs, quality,

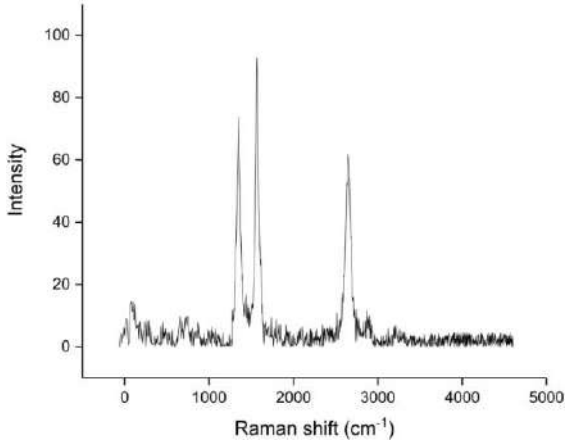

Figure 8. Raman spectrum of synthesized carbon nanotubes after thermal purification

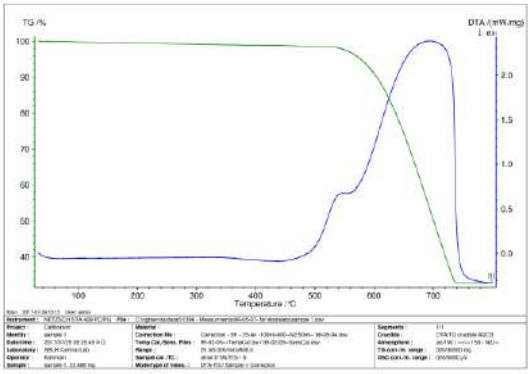

Figure 9. DTA/TG analyses of the fabricated CNTs

and purity of products can be determined regarding the initial temperature, oxidation temperature, residual mass, and weight loss in DTA/TGA. The oxidation temperature of amorphous carbon, SWCNTs, and MWCNTs are in the range of 200-300 ˚C, 350-500 ˚C, and 400-650 ˚C, respectively [36]. By comparing the weight percentage (vertical axis) and the temperatures (horizontal axis) with the mentioned oxidation temperature, the type and percentage of the produced nanotubes can be specified. As a consequence, one weight percentage of amorphous carbon, one weight percentage of single-walled carbon nanotubes, and more than 97 weight percentage of the initial amorphous carbon is converted to multi-walled carbon nanotubes .

The positive gradient in the DTA graph (450-700 ˚C) indicates the main exothermic reaction of MWCNTs with air. In some mechanothermal approaches, metal catalytic particles such as aluminum and yttrium, have been added to amorphous carbon to facilitate the fabrication of CNTs [42-44]. However, the obtained results show that the selected parameters without any additive catalyst are the optimal condition in the process .

On the one hand, common steel vials usually induce a lot of milling contaminants into the sample and the ceramic vials despite non-producing impurities, generates a small number of carbon nanotubes after heat treatment (due to non-metal catalyst) [43]. On the other hand, most of the elements in the chemical composition of the cup in this research including Fe, Si, S, Mn, Cr, and W were employed as the catalyst for the production of CNTs [17, 45-47]. Moreover, acid purification is a common step after the production of CNTs because it eliminates metal catalysts and increases the quality of nanotubes. Since no acid treatment was used in this study, a reasonable amount of iron contaminations is another sign of the appropriateness of the applied factors of milling. Especially when these results compare with other methods such as CVD which usually produce a very large percentage of metal impurities [3, 48]. Consequently, using this type of high-alloy steel in the vial, increasing the milling time, and selecting the different sizes of balls for complete amorphization of graphite, is proposed as a desirable way for the synthesizing of carbon nanotubes by the mechanothermal method.

4. CONCLUSION

In this study, by changing some effective variables in the mechanothermal approach, an attempt was made to optimize the efficiency of this method. First, the graphite powder was ball-milled for 330 h to maximize the amorphization. Subsequently, CNTs were produced by the annealing of amorphous carbon under the Ar atmosphere. A new tip-growth mechanism was recommend based on the random movement of the catalyst particles and it was shown that the direction of the growth does not follow a general movement according to the TEM images. The results of DTA/TG represent that by adjusting the effective variables, such as increasing milling time, select the appropriate temperature, using different sizes of the balls and special vial, mass production of carbon nanotubes (over 97%) is achieved by the mechanothermal way. This optimized method despite a long time of the process is very cost-effective and by applying the mentioned parameters, the quality and quantity of MWCNTs are increased simultaneously. The authors believe that this work has considerably developed the mechanothermal method and can be a starting point for future studies.

5. ACKNOWLEDGEMENTS

This study was funded by Shahid Bahonar University of Kerman and the author declares that they have no conflict of interest. It has not been published elsewhere and that it has not been submitted simultaneously for publication elsewhere.

6. REFERENCES

1. Chaudhary, S. and Singh, K., "Complex phenomenal growth of multi-walled carbon nanotubes in conventional arc discharge process", ***Transactions of the Indian Institute of Metals***, (2021), 1-6. DOI: 10.1007/s12666-021-02316-4
2. Ismail, R.A., Mohsin, M.H., Ali, A.K., Hassoon, K.I. and Erten-Ela, S., "Preparation and characterization of carbon nanotubes by pulsed laser ablation in water for optoelectronic application", ***Physica E: Low-dimensional Systems and Nanostructures***, Vol. 119, No. (2020), 113997. DOI: 10.1016/j.physe.2020.113997
3. Mirabootalebi, S.O. and Akbari, G.H., "Methods for synthesis of carbon nanotubes—review", ***International Journal of Bio-Inorganic Hybride Nanomaterials***, Vol. 6, No. 2, (2017), 49-57.
4. Li, Z., Yuan, D., Wu, H., Li, W. and Gu, D., "A novel route to synthesize carbon spheres and carbon nanotubes from carbon dioxide in a molten carbonate electrolyzer", ***Inorganic Chemistry Frontiers***, Vol. 5, No. 1, (2018), 208-216. DOI: 10.1039/C7QI00479F
5. Mirabootalebi, S., "A new method for preparing buckypaper by pressing a mixture of multi-walled carbon nanotubes and amorphous carbon", ***Advanced Composites and Hybrid Materials***, Vol. 3, No. 3, (2020), 336-343. DOI: 10.1007/s42114-020-00167-z
6. Manafi, S., Amin, M., Rahimipour, M., Salahi, E. and Kazemzadeh, A., "Large scale and low cost synthesis of multiwalled carbon nanotubes by mechanothermal absence catalysts", ***Advances in Applied Ceramics***, Vol. 109, No. 1, (2010), 25-30. DOI: 10.1179/174367609X414008
7. Manafi, S., Amin, M., Rahimipour, M., Salahi, E. and Kazemzadeh, A., "High-yield synthesis of multiwalled carbon nanotube by mechanothermal method", ***Nanoscale Research Letters***, Vol. 4, No. 4, (2009), 296-302. DOI: 10.1007/s11671-008-9240-3
8. Manafi, S., Rahimipour, M.R., Mobasherpour, I. and Soltanmoradi, A., "The synthesis of peculiar structure of springlike multiwall carbon nanofibers/nanotubes via mechanothermal method", ***Journal of Nanomaterials***, Vol. 2012, (2012), 15. DOI: 10.1155/2012/803546
9. Manafi, S., Rahimipour, M. and Soltanmoradi, A., "Ultra-high crystallinity millimeter long multiwall carbon nanotubes fabricated by mechanothermal method", ***Materials Science-Poland***, Vol. 30, No. 3, (2012), 226-230. DOI: 10.2478/s13536-012-0033-0
10. Boyrazlı, M. and Güler, S.H., "Synthesis of carbon nanostructures from corn stalk using mechano-thermal method", ***Journal of Molecular Structure***, Vol. 1199, (2020), 126976. DOI: 10.1016/j.molstruc.2019.126976
11. Chen, Y., Li, C.P., Chen, H. and Chen, Y., "One-dimensional nanomaterials synthesized using high-energy ball milling and annealing process", ***Science and Technology of Advanced Materials***, Vol. 7, No. 8, (2006), 839. DOI: 10.1016/j.stam.2006.11.014
12. Chen, Y., Fitz Gerald, J., Chadderton, L.T. and Chaffron, L., "Nanoporous carbon produced by ball milling", ***Applied Physics Letters***, Vol. 74, No. 19, (1999), 2782-2784. DOI: 10.1063/1.124012
13. Manafi, S., Amin, M., Rahimipour, M., Salahi, E. and Kazemzadeh, A., "Carbon nanotubes synthesized by mechanothermal method", ***New Carbon Materials***, Vol. 24, No. 1, (2009), 39-44. DOI: 10.1016/S1872-5805(08)60035-9
14. Güler, Ö. and Evin, E., "Carbon nanotubes formation by short-time ball milling and annealing of graphite", ***Optoelectronics and Advanced Materials***, Vol. 6, (2012), 183-187.
15. Evin, E., Güler, Ö., Aksoy, M. and Güler, S.H., "Effect of milling time on the formation of carbon nanotube by mechano-thermal

method", ***Bulletin of Materials Science***, Vol. 38, No. 4, (2015), 857-863. DOI: 10.1007/s12034-015-0952-6

16. Chen, Y., Conway, M., Gerald, J.F., Williams, J. and Chadderton, L., "The nucleation and growth of carbon nanotubes in a mechano-thermal process", ***Carbon***, Vol. 42, No. 8-9, (2004), 1543-1548. https://doi.org/10.1016/j.carbon.2004.02.003
17. Güler, Ö. and Evin, E., "Effect of milling type on formation of carbon nanostructures", ***Fullerenes, Nanotubes and Carbon Nanostructures***, Vol. 23, No. 5, (2015), 463-470.
18. Suryanarayana, C., "Mechanical alloying and milling", ***Progress in Materials Science***, Vol. 46, No. 1-2, (2001), 1-184.
19. Welham, N. and Williams, J., "Extended milling of graphite and activated carbon", ***Carbon***, Vol. 36, No. 9, (1998), 1309-1315. DOI: 10.1016/S0008-6223(98)00111-0
20. Li, J., Wang, L., Bai, G. and Jiang, W., "Carbon tubes produced during high-energy ball milling process", ***Scripta Materialia***, Vol. 54, No. 1, (2006), 93-97. DOI: 10.1016/j.scriptamat.2005.08.037
21. Chen, X., Yang, H., Wu, G., Wang, M., Deng, F., Zhang, X., Peng, J. and Li, W., "Generation of curved or closed-shell carbon nanostructures by ball-milling of graphite", ***Journal of Crystal Growth***, Vol. 218, No. 1, (2000), 57-61. DOI: doi.org/10.1016/S0022-0248(00)00486-3
22. Huang, Z., Calka, A. and Liu, H., "Effects of milling conditions on hydrogen storage properties of graphite", ***Journal of Materials Science***, Vol. 42, No. 14, (2007), 5437-5441.
23. Johan, M.R. and Moh, L.S., "Growth and optical study of carbon nanotubes in a mechano-thermal process", ***Carbon***, Vol. 8, (2013), 1047-1056.
24. Rietsch, J.-C., Gadiou, R., Vix-Guterl, C. and Dentzer, J., "The influence of the composition of atmosphere on the mechanisms of degradation of graphite in planetary ball millers", ***Journal of Alloys and Compounds***, Vol. 491, No. 1-2, (2010), L15-L19. DOI: 10.1016/j.jallcom.2009.10.193
25. Ong, T. and Yang, H., "Effect of atmosphere on the mechanical milling of natural graphite", ***Carbon***, Vol. 38, No. 15, (2000), 2077-2085. DOI: 10.1016/S0008-6223(00)00064-6
26. Purohit, R., Purohit, K., Rana, S., Rana, R. and Patel, V., "Carbon nanotubes and their growth methods", ***Procedia Materials Science***, Vol. 6, (2014), 716-728. DOI: 10.1016/j.mspro.2014.07.088
27. Lobo, L.S., "Nucleation and growth of carbon nanotubes and nanofibers: Mechanism and catalytic geometry control", ***Carbon***, Vol. 114, (2017), 411-417. https://doi.org/10.1016/j.carbon.2016.12.005
28. Chadderton, L.T. and Chen, Y., "A model for the growth of bamboo and skeletal nanotubes: Catalytic capillarity", ***Journal of Crystal Growth***, Vol. 240, No. 1-2, (2002), 164-169. https://doi.org/10.1016/S0022-0248(02)00855-2
29. Gayathri, V., Devi, N. and Geetha, R., "Hydrogen storage in coiled carbon nanotubes", ***international Journal of Hydrogen Energy***, Vol. 35, No. 3, (2010), 1313-1320. https://doi.org/10.1016/j.ijhydene.2009.11.083
30. Gayathri, V. and Geetha, R., "Hydrogen adsorption in defected carbon nanotubes", ***Adsorption***, Vol. 13, No. 1, (2007), 53-59. DOI: 10.1007/s10450-007-9002-z
31. Rajaura, R.S., Srivastava, S., Sharma, P.K., Mathur, S., Shrivastava, R., Sharma, S. and Vijay, Y., "Structural and surface modification of carbon nanotubes for enhanced hydrogen storage density", ***Nano-Structures & Nano-Objects***, Vol. 14, (2018), 57-65. https://doi.org/10.1016/j.nanoso.2018.01.005
32. Chen, Y., Conway, M. and Fitzgerald, J., "Carbon nanotubes formed in graphite after mechanical grinding and thermal annealing", ***Applied Physics A***, Vol. 76, No. 4, (2003), 633-636. https://doi.org/10.1007/s00339-002-1986-3
33. Ahmad, A., Pervaiz, M., Ramzan, S., Kiyani, M.Z., Khan, A., Ahmad, I. and Asiri, A.M., Role of xrd for nanomaterial analysis, in Nanomedicine manufacturing and applications. 2021, Elsevier.149-161. https://doi.org/10.1016/B978-0-12-820773-4.00008-1
34. Chiodarelli, N., Richard, O., Bender, H., Heyns, M., De Gendt, S., Groeseneken, G. and Vereecken, P.M., "Correlation between number of walls and diameter in multiwall carbon nanotubes grown by chemical vapor deposition", ***Carbon***, Vol. 50, No. 5, (2012), 1748-1752. DOI: 10.1016/j.carbon.2011.12.020
35. Mirabootalebi, S.O., Akbari Fakhrabadi, G.H. and Mirahmadi Babaheydari, R., "High-yield production of amorphous carbon via ball milling of graphite and prediction of its crystallite size through ann", ***Journal of Applied Organometallic Chemistry***, Vol. 1, No. 2, (2021), 76-85. http://dx.doi.org/10.22034/jaoc.2021.288020.1021
36. Lehman, J.H., Terrones, M., Mansfield, E., Hurst, K.E. and Meunier, V., "Evaluating the characteristics of multiwall carbon nanotubes", ***Carbon***, Vol. 49, No. 8, (2011), 2581-2602. https://doi.org/10.1016/j.carbon.2011.03.028I
37. Costa, S., Borowiak-Palen, E., Kruszynska, M., Bachmatiuk, A. and Kalenczuk, R., "Characterization of carbon nanotubes by raman spectroscopy", ***Materials Science-Poland***, Vol. 26, No. 2, (2008), 433-441.
38. Benoit, J., Buisson, J., Chauvet, O., Godon, C. and Lefrant, S., "Low-frequency raman studies of multiwalled carbon nanotubes: Experiments and theory", ***Physical Review B***, Vol. 66, No. 7, (2002), 073417. https://doi.org/10.1103/PhysRevB.66.073417
39. Antunes, E., Lobo, A., Corat, E. and Trava-Airoldi, V., "Influence of diameter in the raman spectra of aligned multi-walled carbon nanotubes", ***Carbon***, Vol. 45, No. 5, (2007), 913-921. https://doi.org/10.1016/j.carbon.2007.01.003
40. DiLeo, R.A., Landi, B.J. and Raffaelle, R.P., "Purity assessment of multiwalled carbon nanotubes by raman spectroscopy", ***Journal of Applied Physics***, Vol. 101, No. 6, (2007), 064307. https://doi.org/10.1063/1.2712152
41. Chakrapani, N., Curran, S., Wei, B., Ajayan, P.M., Carrillo, A. and Kane, R.S., "Spectral fingerprinting of structural defects in plasma-treated carbon nanotubes", ***Journal of Materials Research***, Vol. 18, No. 10, (2003), 2515-2521. https://doi.org/10.1557/JMR.2003.0350
42. Connan, H.G., Reedy, B.J., Marshall, C.P. and Wilson, M.A., "New nanocarbons: Rod milling and annealing of graphite in the presence of yttrium", ***Energy & Fuels***, Vol. 18, No. 6, (2004), 1607-1614. https://doi.org/10.1021/ef0400114
43. Rosas, G., Esparza, R., Liu, H., Ascencio, J. and Pérez, R., "Mechanical alloying synthesis of carbon nanotubes in the presence of alfe small clusters", ***Materials Letters***, Vol. 61, No. 3, (2007), 860-863. DOI: 10.1016/j.matlet.2006.06.032
44. Khazaei Feizabad, M., Khayati, G.R. and Pouresterabadi, S., "Design and synthesis of carbon nanotubes for adsorption utilities: An approach to direct preparation by mechanical milling at room temperature", ***Scientia Iranica***, Vol. 28, No. 3, (2021), 1884-1895. DOI: 10.24200/sci.2020.52977.2979
45. Das, D. and Roy, A., "Synthesis of diameter controlled multiwall carbon nanotubes by microwave plasma-cvd on low-temperature and chemically processed fe nanoparticle catalysts", ***Applied Surface Science***, Vol. 515, (2020), 146043. https://doi.org/10.1016/j.apsusc.2020.146043
46. Shah, K.A., Najar, F.A., Sharda, T. and Sreenivas, K., "Synthesis of multi-walled carbon nanotubes by thermal cvd technique on pt–w–mgo catalyst", ***Journal of Taibah University for Science***, Vol. 12, No. 2, (2018), 230-234. https://doi.org/10.1080/16583655.2018.1451114
47. Wang, J., Wang, W., Li, H., Tan, T., Wang, X. and Zhao, Y., "Carbon nanotubes/sic prepared by catalytic chemical vapor

deposition as scaffold for improved lithium-sulfur batteries", ***Journal of Nanoparticle Research***, Vol. 21, No. 6, (2019), 1-10. Doi:10.1007/s11051-019-4540-3

48. Aminayi, P., Allaedini, G. and Tasirin, S.M., "Hydrodynamic studies of fluidized bed chemical vapor deposition reactors to produce carbon nano tubes via catalytic decomposition over co/pd mgo", ***International Journal of Engineering***, Vol. 28, No. 12, (2016), 1693-1701. Doi: 10.5829/idosi.ije.2015.28.12c.01

Persian Abstract

چکیده

مولفه های موثر فراوانی در فرآیند مکانوترمال موثرند که عبارتند از سرعت آسیاب، نسبت اندازه گلوله به پودر و غیره. این موارد در کیفیت و کمیت نانولوله های کربنی تولیدی نقشی مهم دارند. در تحقیق پیش رو سعی شد تا با بهینه کردن پارامترهای اساسی؛ کیفیت ناتولوله های تولیدی افزایش یابد و همچنین مکانیزم رشد نانولوله ها نیز بررسی شد. بدین منظور آسیاکاری گرافیت در آسیاب گلوله ای و در کاپ با استاندارد ۱.۲۵۵۰ کلید فولاد انجام شد. سپس، ساختار ذرات آسیاکاری شده با آنالیزهایی نظیر زتاسایزر، میکروسکوپ الکترونی روبشی بررسی شدند. در گام بعدی، این پدرها تحت عملیات حرارتی در ۱۴۰۰ درجه سانتیگراد قرار گرفتند تا نانولوله های کربنی تولید شدند. مدلی خاص از رشد (tip-growth) بر اساس آنالیزهای محصولات فرآیند ارایه شد و همچنین راندمان روش بهینه شده مورد ارزیابی قرار گرفت.

International Journal of Engineering

Journal Homepage: www.ije.ir

An Investigation on Effects of Magnetic Parameter and Brownian Motion on Fluid Flow Between two Equal Plates: Application of Analytical Methods

P. Pasha[a], H. Nabi[a], M. M. Peiravi[b], M. Pourfallah[a], D. D. Ganji*[b]

[a] *Department of mechanical Engineering Mazandaran University of science and Technology, Babol, Iran*
[b] *Department of mechanical Engineering Babol Noshirvani University of Technology, Babol, Iran*

PAPER INFO

Paper history:
Received 26 july 2021
Received in revised form 28 August 2021
Accepted 29 August 2021

Keywords:
Adomian Decomposition Method
Brownian Motion
Hydrothermal Analysis
Thermo-phoretic

ABSTRACT

In the present paper, the heat transfer and fluid velocity between two horizontal plates is examined in existence of magnetic parameter. The parameters such as magnetic fluid flow, viscosity, Brownian motion, and thermo-phoretic have been investigated according to this analysis. The innovation of this paper is using two analytical methods to solve differential equations and compare the obtained results. In this paper, the effects of magnetic field on fluid flow for industrial use were investigated. The effects of magnetic field on fluid flow are surveyed by using Variation Iteration Method (VIM), Adomian Decomposition Method (ADM) and compare these methods with numerical Runge-Kutta method. According to results, increasing the values of magnetic parameter, the fluid velocity decreased and the fluid viscosity increased. Also, Brownian motion and thermo-phoretic parameters were directly related to the coefficient of friction. The Brownian motion of nanoparticles resulted in thermophoresis phenomenon and increasing both Brownian motion and thermophoresis causes an increase in temperature.

***doi**: 10.5829/ije.2021.34.10a.15*

NOMENCLATURE

H	distance the plates (m)	Nt	Thermo-phoretic parameter
C	Nano fluid concentration	Nb	Brownian motion
K	Dimensionless temperature	T_c	temperature of the cold wall (K)
x, y	coordinates (m)	ΔT	temperature difference
u,v	velocity components (m/s)	**Greek Symbols**	
θ	Dimensionless temperature	ρ	Density (kg/m^3)
ϑ	Kinematic viscosity (m^2/s)	$\boldsymbol{\mu}$	dynamic viscosity (kg/m. s)
C_p	Specific heat at constant pressure (J/kg.K)	$\boldsymbol{\beta}$	thermal expansion (1/K)
k	Thermal conductivity (W/m.K)	$\boldsymbol{\alpha}$	thermal diffusivity (m^2/s)
P^+	Modified fluid pressure	ν	Kinematic viscosity (m^2/s)
g_y	gravitational acceleration (m/s^2)	Ø	Dimensionless concentration
Pr	Prandtl number (υ/α)		

1. INTRODUCTION

Nanofluids are fluids containing Nano particle-sized fine particulate matter. Since these fluids have great heat transfer potential, special attention has been paid to this group of fluids as heat transfer environments.

Nanofluids have two parts. The first part is called the base fluid such as water and ethylene glycol, which is added to the mix. The second part of the Nanofluid is composed of Nanoparticles such as copper oxide and aluminum oxide. The major effects of Nanofluid and heat transfer through the Nanofluid can be attributed to the increase in energy efficiency, operating cost,

*Corresponding Author Institutional Email: ddg_davood@yahoo.com
(D. D. Ganji)

Please cite this article as: P. Pasha, H. Nabi, M. M. Peiravi, M. Pourfallah, D. D. Ganji, An Investigation on Effects of Magnetic Parameter and Brownian Motion on Fluid Flow Between two Equal Plates: Application of Analytical Methods, International Journal of Engineering, Transactions A: Basics Vol. 34, No. 10, (2021), 2341-2350

environmental clean up, or applications in the industry. The use of TiO_2-water nanofluids in the closed domain increases the Nusselt number by 23% and the friction factor by 42%. Grashof number is inversely related to increasing Nusselt number. mixed convection heat transfer from Al_2O_3-water nanofluid in W-shaped, copper tube cause the rate of heat transfer coefficient improved with Reynolds number for average wall temperatures of 50 and 60ºC. Magneto hydrodynamic nanofluid flow between two parallel analyzed and results showed concentration of nanofluid diminishes when Brownian movement increments whereas it increases with expands of thermophoretic parameter [1-20]. Gupta et al. [21] examined magneto convection in a nanofluid. Peiravi et al. [22] investigated the effect of variable Lorentz forces on nanofluid flow in movable parallel plates utilizing the analytical method. The results showed that increasing the Brownian motion parameter increased the temperature profile while increasing Brownian motion decreased the concentration profile. In the mentioned research, the influence of several factors, including skin friction coefficient, radiation parameter, and Weissenberg number was analyzed. An analytical investigation on mass and heat transfer of an MHD unsteady GO-water-squeezing nanofluid flow was carried out by Peiravi and Alinejad [23] between two infinite parallel moving plates. The novelty of this paper is the simultaneous simulation of two separate multi-phase nanofluids in two 3D enclosures under a heat flux boundary condition. Elsewhere, Pourmehran et al. [24] conducted an analytical study on squeezing unsteady nanofluid flow surrounded by parallel plates to which water (H_2O), as the base fluid mixed with several nanoparticles. Azimi and Mirzaei [25] performed an analytical study on the flow of Graphene oxide water nanofluid squeezed between parallel plates via RVIM. The results showed that the type of nanofluid is an important factor in the transfer of cooling and heating. As shown by Domairry Ganji et al. [26] the heat transfer rate increases in retention pools of nuclear waste. In another study by Hatami et al. [27] the differential quadrature method (DQM) was used to investigate the motion of a spherical particle in a fluid forced vortex. In this paper, the equations of particle motion in a forced vortex of fluid are calculated using the differential conversion method with Padé approximation. The velocity lines (angular and radial) and the path of a particle in a fluid vortex were examined in the present work. Rashidi et al. [28] investigated the flow point of the micropolar nanoscale. In this research, aluminum and copper oxides were used to prepare a mixture of water with basic liquids of Fe_3O_4 [29] nano cidal analysis in a porous environment under MHD. Modeling fluid and temperature fields were used the lattice Boltzmann approach based on the D2Q9 scheme. Jalilpour et al. [30] studied heat production at the MHD recession point of nanofluids to the porous tensile sheet. Hashemi Kachapi and Domairry Ganji [31] analyzed the nonlinear equations in fluids, progress in nonlinear science. In this work, they investigated various nonlinear equations by maple software. Aminoroayaie Yamini et al. [32] Mousavimehr et al. [33] Kostikov and Romanenkov [34] have examined the following issues. The first issue was the CFD model to investigate the hydraulic performance of the hole in the dam. In this research, the greatest speed for 100% opening of the door and Howell Bunger valve is almost 18 m/s within the area underneath the door, and the most extreme speed for 40% opening of the entryway is rise to 23.1 m/s. The second issue of article was the Performance Assessment of Shockwaves of Chute Spillways in Large Dams. In this article, the test arrangement of the shockwaves and their behavior along the chute and their lessening measures were displayed. The third subject of article was approximation of the multidimensional optimal control problem for the heat equation. The adomian decomposition method and variation iteration method are some of the most accurate tools for solving mathematical equations. These methods may be used to solve the ordinary differential equation and partial differential equation. In this paper, the nonlinear equations of velocity and temperature parameters were solved by using the adomian decomposition method (ADM) and Variation Iteration method. Also, it is tried to calculate the impacts of Brownian motion, viscosity factor, magnetic parameter, and thermophoretic factor on velocity and temperature. The innovations of this paper is the simulation of the results of Parameters the magnetic fluid flow, viscosity, Brownian motion, and thermo-phoretic using two numerical methods and compare these methods with the numerical method.

1. 1. Problem Definition Non-uniform flow is a flow that passes through two parallel plates and is affected by magnetic flux. Both the plate and the fluid stream rotate around y- axis. According to Figure 1, the plate is positioned at y=0 by two forces that are pulled to the opposite side of the plate. The direction of the magnetic flow is also along with the flow around the y-axis:

$$\frac{\partial u^+}{\partial x}+\frac{\partial v^+}{\partial y} \tag{1}$$

$$\rho_f\left(u^+\frac{\partial u^+}{\partial x}+V^+\frac{\partial u^+}{\partial y}\right)=-\frac{\partial P^+}{\partial x}+\mu\left(\frac{\partial^2 u^+}{\partial x^2}+\frac{\partial^2 u^+}{\partial y^2}\right)-\sigma B^2{}_0 u^+ \tag{2}$$

$$\rho_f\left(u^+\frac{\partial V^+}{\partial x}+V^+\frac{\partial V^+}{\partial y}\right)=-\frac{\partial P^+}{\partial y}+\mu\left(\frac{\partial^2 V^+}{\partial x^2}+\frac{\partial^2 V^+}{\partial y^2}\right) \tag{3}$$

$$\left(u^+\frac{\partial T^+}{\partial x}+V^+\frac{\partial T^+}{\partial y}\right)=\alpha\left(\frac{\partial^2 T^+}{\partial x^2}+\frac{\partial^2 T^+}{\partial y^2}\right)+\frac{(\rho C_p)_P}{(\rho C_P)_f}\times [D_B\left(\frac{\partial C^+}{\partial x}.\frac{\partial T^+}{\partial x}+\frac{\partial C^+}{\partial y}.\frac{\partial T^+}{\partial y}\right)+(\frac{D_T}{T_C^+})((\frac{\partial T^+}{\partial x})^2+\left(\frac{\partial T^+}{\partial y}\right)^2\Big] \tag{4}$$

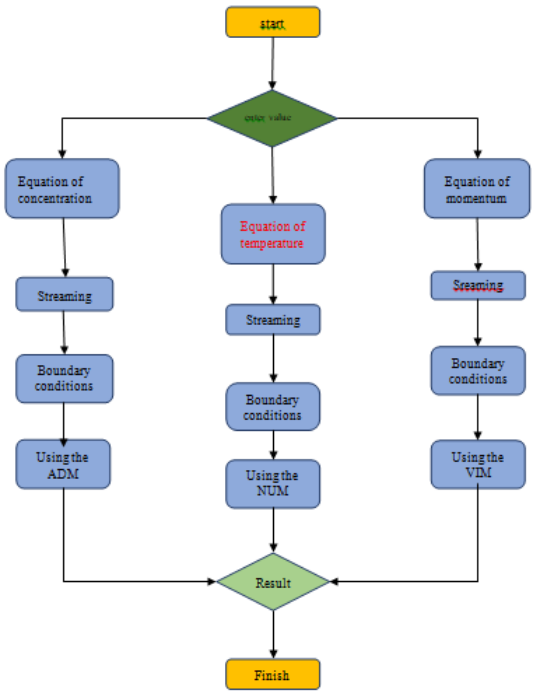

Figure 1. Flowchart of the problem

$$u^{+}\frac{\partial C^{+}}{\partial x}+V^{+}\frac{\partial C^{+}}{\partial y}=D_B\left(\frac{\partial^2 C^{+}}{\partial x^2}+\frac{\partial^2 C^{+}}{\partial y^2}\right)+\left(\frac{D_T}{T_0^{+}}\right)\left(\frac{\partial^2 T^{+}}{\partial x^2}+\frac{\partial^2 T^{+}}{\partial y^2}\right) \quad (5)$$

U^{+} And $V^{+}$are the velocities along the x-axis and y-axis, respectively. μ Denotes viscosity, $P^{+}$is modified fluid pressure, ρ_f is density,C^{+} is the specific heat of the nanofluid, K is the thermal conductivity, D_B is the diffusion coefficient of the diffusing species, and $T^{+}$is the temperature. The boundary conditions of these equations are as follows:

$$y=0 \leftrightarrow u^{+}=ax, T^{+}=T_h^{+}, V^{+}=0, C^{+}=C_h^{+} \quad (6)$$

$$y=h \leftrightarrow u^{+}=0, T^{+}=T_0^{+}, V^{+}=0, C^{+}=C_0^{+} \quad (7)$$

Non-dimensional variable in the above sentences is expressed as:

$$\eta=\frac{y}{h},\quad u^{+}=axf'(\eta),\quad V^{+}=-ahf(\eta),\quad \theta(\eta)=\frac{T^{+}-T_h^{+}}{T_0^{+}-T_h^{+}},\ \emptyset(\eta)=\frac{C^{+}-C_h^{+}}{C_0^{+}-C_h^{+}} \quad (8)$$

Now, we can write a genuine equation:

$$f^{(4)}-R(f'f''-ff'')-Mf''=0 \quad (9)$$

$$\theta''+PrRf\theta'+Nb\emptyset'\theta'+Nt\theta'^{2}=0 \quad (10)$$

$$\emptyset''+R\,.Scf\emptyset'+\frac{Nt}{Nb}\theta''=0 \quad (11)$$

The new boundary conditions are:

$$\eta=0\rightarrow f=0, f'=1, (\theta=1, \emptyset=1) \quad (12)$$

$$\eta=1\rightarrow f=1, (f'=0, \theta=0, \emptyset=0) \quad (13)$$

Dimensionless quantities: Nt is the thermo phoretic gauge, M is the magnetic gauge, Pr is a Prandtl number, R is the viscosity coefficient, Nb is the Brownian motion gauge and Sc is the Schmidt number.

$$R=\frac{ah^2}{\vartheta}, M=\frac{\sigma B_0 B_0 h^2}{\rho\vartheta}, Pr=\frac{\mu}{\rho_f\alpha}, Sc=\frac{\mu}{\rho_f D}, Nt=(\rho C)_P D_T(T_h^{+})/(\rho C)_f\alpha T_c^{+}, Nb=(\rho C)_P D_B(C_h)/(\rho C)_f\alpha \quad (14)$$

Nusselt number is defined as:

$$Nu=-\theta' \quad (15)$$

3. SIMULATION METHODOLOGY

3. 1. A. Adomian Decomposition Method (ADM)

A general nonlinear equation is considered in the form of [31]:

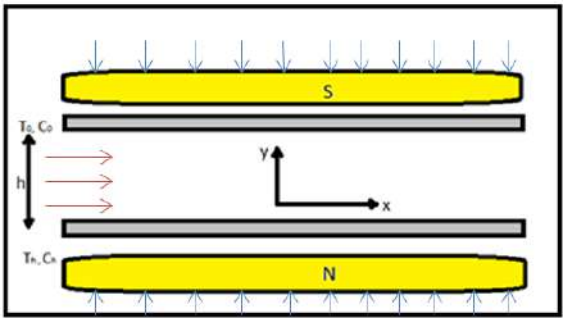

Figure 2. Schematic of magnetic effects between horizontal plates on Brownian motion

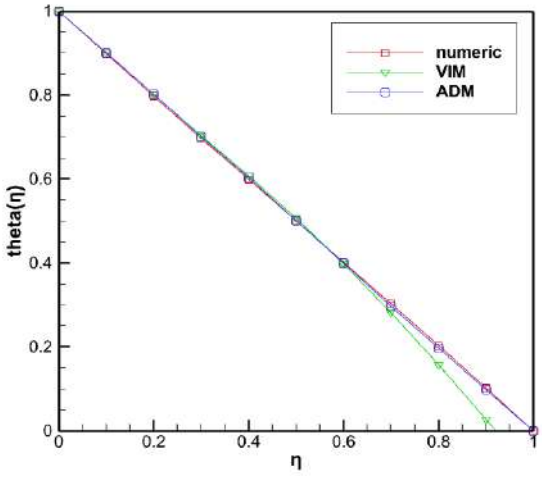

(a) Temperature profile

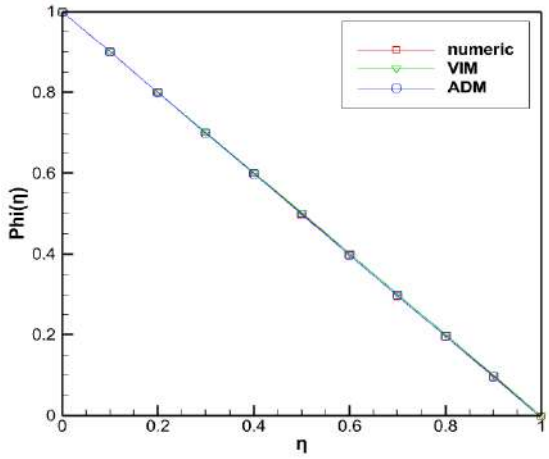

(b) Concentration profile

Figure 3. Comparison of a) the temperature and b) the concentration profile between ADM and VIM and Runge-Kutta methods at M=1, R=1, Sc=0.1, Nt=0.1, Nb=0.1, Pr=2.

$$L(u)+Ru+Nu=g(r) \quad (16)$$

Applying the inverse operator L^{-1} to both sides of (16) and using the given conditions [31]:

$$U=f(x)-L^{-1}(Ru)-L^{-1}(Nu) \quad (17)$$

For nonlinear differential equations, the nonlinear operator Nu=F(u) is observed in the Adomian decomposition method [5]:

$$F(u)=\sum_{m=0}^{\infty} A_m \quad (18)$$

The Adomian method defines the solution U(x) by the series [31]:

$$u=\sum_{m=0}^{\infty} u_m \quad (19)$$

$$F(u)=F(u_0)+F'(u_0)(u-u_0)+F''(u_0)\frac{(u-u_0)}{2!}+F'''(u_0)\frac{(u-u_0)}{3!}+\cdots \quad (20)$$

By equating terms, the first few Adomian polynomials $A_0, A_1, A_2,\ldots$[5]:

$$A_0=F(u_0) \qquad A_1=u_1F'(u_0) \qquad A_2=u_2F'(u_0)+\frac{1}{2!}u_1u_1F''(u_0) \quad (21)$$

3. 2. Application of ADM Based on ADM, the linear parts of the equation were divided and set it to 0. The differential equation with boundary conditions were solved.

$$\frac{d^4}{d\eta^4}f_0(\eta)=0 \quad (22)$$

$$\frac{d^2}{d\eta^2}\theta_0(\eta)=0 \quad (23)$$

$$\frac{d^2}{d\eta^2}\emptyset_0(\eta)=0 \quad (24)$$

$$f_0(\eta)=\eta^2-2\eta^2+\eta \leftrightarrow \theta_0(\eta)=\eta+1 \leftrightarrow \emptyset_0(\eta)=\eta+1 \quad (25)$$

Then, the non-linear differential equations are separated for Equation (9):

$$A_0=-R(3\eta^2-4\eta+1)(6\eta-4) \quad (26)$$

$$B_0=R(\eta^2-2\eta^2+\eta)(6\eta-4) \quad (27)$$

$$C_0=-M(6\eta-4) \quad (28)$$

$$A_1=(-R(6\eta-4)^2-6R(3\eta^2-4\eta+1))f_1(\eta) \quad (29)$$

$$B_1=(R(3\eta^2-4\eta+1)(6\eta-4)+6R(\eta^3-2\eta^2+\eta))f_1(\eta) \quad (30)$$

$$C_1=-6Mf_1(\eta) \quad (31)$$

For Equation (10):

$$D_0=-Pr\,R\,(\eta^3-2\eta^2+\eta) \quad (32)$$

$$D_1=-Pr\,R(3\eta^2-4\eta+1)\theta_1(\eta) \quad (33)$$

For Equation (11):

$$E_0=-R\,Sc\,(\eta^3-2\eta^2+\eta) \quad (34)$$

$$E_1=-R\,Sc(3\eta^2-4\eta+1)\emptyset_1(\eta) \quad (35)$$

According to the ADM method, the following statements of the parameters of the equations were written:

$$F_1(\eta)=R\left(\frac{3}{140}\eta^7-\frac{1}{10}\eta^6+\frac{11}{60}\eta^5-\frac{1}{6}\eta^4\right)-R\left(\frac{1}{280}\eta^8-\frac{2}{105}\eta^7+\frac{7}{180}\eta^6-\frac{1}{30}\eta^5\right)+M\left(\frac{1}{20}\eta^5-\frac{1}{6}\eta^4\right) \quad (36)$$

$$\theta_1(\eta)=-Pr\,R\left(\frac{1}{20}\eta^5-\frac{1}{6}\eta^4+\frac{1}{6}\eta^3\right)+\frac{1}{2}Nb\eta^2+\frac{1}{2}Nt\eta^2 \quad (37)$$

$$\emptyset_1(\eta)=-R\,Sc\left(\frac{1}{20}\eta^5-\frac{1}{6}\eta^4+\frac{1}{6}\eta^3\right) \quad (38)$$

Next, adding two sentences from each equation at M=1, Pr=2, R=1, Sc=0.1, Nt=0.1 and Nb=0.1 give:

$$F(\eta)=f_0(\eta)+f_1(\eta)\rightarrow f(\eta)=\eta^3-2\eta^2+\eta+\frac{17}{420}\eta^7-\frac{5}{36}\eta^6+\frac{4}{15}\eta^5-\frac{1}{3}\eta^4-\frac{1}{280}\eta^8 \quad (39)$$

$$\theta(\eta)=\theta_0(\eta)+\theta_1(\eta)\rightarrow\theta(\eta)=-\eta+1-\frac{1}{10}\eta^5+\frac{1}{3}\eta^4-\frac{1}{3}\eta^3+0.10\eta^2 \quad (40)$$

$$\emptyset(\eta)=\emptyset_0(\eta)+\emptyset_1(\eta)\rightarrow\emptyset(\eta)=-\eta+1-0.005\eta^5+0.016\eta^4-0.016\eta^3+0.000021\eta^9-0.000125\eta^8+0.00029\eta^7-0.00028\eta^6$$

3. 3. Variation Iteration Method (VIM) Where Ω is the frequency angle oscillator. The general formula for obtaining other sentences of u is defined by a coefficient λ as follows [31]:

$$u' + \Omega^2 = F(u)$$
$$F(u) = \Omega^2 u - \mathrm{f}(u) \quad (41)$$

Given the boundary equations:

$$u' = 0,$$
$$u(0) = \mathrm{A} \quad (42)$$

And the first functions:

$$u_0(\mathrm{t}) = \mathrm{A}\cos\Omega \quad (43)$$

$$\int_0^{\mathrm{T}} \cos\Omega \mathrm{t}[\Omega^2 \mathrm{u}_0 - \mathrm{f}(\mathrm{u}_0)]\mathrm{dt} = 0 \quad (44)$$

The λ coefficient is obtained by dividing the Laplace from the linear part of the equation. By different n definitions, the number of sentences is considered to obtain a better answer:

$$u_{n+1}(t) = u_n(t) + \int_0^{\mathrm{t}} \lambda \left\{ \frac{\mathrm{d}^2 \mathrm{u}_n}{\mathrm{d}\eta^2} + \Omega^2 \mathrm{u}_{\mathrm{n}}(\eta) - \mathrm{F}_n \right\} \mathrm{d}\eta \quad (45)$$

where λ is the Lagrange coefficient and F_n is considered various restricted:

$$\frac{d^2\lambda}{d\eta^2} + \Omega^2 \lambda(\eta) = 0 \quad (46)$$

$$\lambda(t) = 0, \quad (47)$$

$$1 - \frac{d\lambda}{dt} = 0 \quad (48)$$

The coefficient λ is calculated from the following formula:

$$\lambda = \frac{1}{\Omega} sin\Omega(\tau - t) \quad (49)$$

Then the formula is rewritten:

$$u_{n+1}(t) = u_n(t) + \int_0^t \frac{1}{\Omega} sin\Omega(\tau - t) \left\{ \frac{d^2 u_n}{d\eta^2} + F_n \right\} d\tau \quad (50)$$

3. 4. Application of VIM Based on the VIM method, the linear parts of the coupling equations are written as follows:

$$\frac{d^4}{d\eta^4} \mathrm{f}_0(\eta) = 0 \quad (51)$$

$$\frac{d^2}{d\eta^2} \theta_0(\eta) = 0 \quad (52)$$

$$\frac{d^2}{d\eta^2} \emptyset_0(\eta) = 0 \quad (53)$$

Then, the boundary conditions for the linear parts are expressed in the following:

$$F_0(0) = 0, \ f_0'(0) = 1, \ \theta_0(0) = 1, \ \emptyset_0(0) = 1 \quad (54)$$

$$f_0(1) = 0, \ \theta_0(1) = 0, \ \emptyset_0(1) = 0, \ f_0'(1) = 0 \quad (55)$$

The first sentences are given in terms of f and θ and $\emptyset$:

$$f_0(\eta) = \eta^3 - 2\eta^2 + \eta \ , \theta_0(\eta) = \eta + 1, \emptyset_0(\eta) = \eta + 1 \quad (56)$$

Then, by computing the linear parts of the equations, $\lambda_1, \lambda_2,$ and λ_3 are calculated as follows:

$$\lambda_1 = \frac{1}{6}(\tau - \eta)^3 \quad (57)$$

$$\lambda_2 = \tau - \eta \quad (58)$$

$$\lambda_3 = \tau - \eta \quad (59)$$

$$f_1(\eta) = \eta^3 - 2\eta^2 + \eta + \frac{1}{4}\left(-\frac{1}{6}R\left((3\eta^2 - 4\eta + 1)(6\eta - 4) - (\eta^3 - 2\eta^2 + \eta)(6\eta - 4)\right) - \frac{1}{6}M(6\eta - 4)\right)\eta^4 - \frac{1}{12}\eta^4\left(-R\left((3\eta^2 - 4\eta + 1)(6\eta - 4) - (\eta^3 - 2\eta^2 + \eta)(6\eta - 4)\right) - M(6\eta - 4)\right) \quad (60)$$

$$\theta_1(\eta) = -\eta + 1 - \frac{1}{2}\left(-Pr\ R(\eta^3 - 2\eta^2 + \eta) + Nb + Nt\right)\eta^2 \quad (61)$$

$$\emptyset_1(\eta) = -\eta + 1 + \frac{1}{2} R\ Sc\ (\eta^3 - 2\eta^2 + \eta)\eta^2 \quad (62)$$

Finally, by summing up the sentences at M=1, Pr=10, R=1, Sc=0.1, Nt=0.1, and Nb=0.1:

$$f(\eta) = f_1(\eta) \rightarrow f(\eta) = \eta^3 - 2\eta^2 + \eta + \frac{17}{12}\eta^7 - \frac{25}{12}\eta^6 + \frac{4}{3}\eta^5 - \frac{1}{3}\eta^4 - \frac{1}{4}\eta^8 \quad (63)$$

$$\theta(\eta) = (\eta + 0.8104) \times (\eta - 0.9203) \times (\eta - 1.4650) \times (\eta^2 - 0.4253) \times (\eta + 0.9153) \quad (64)$$

$$\emptyset(\eta) = \emptyset_1(\eta) \rightarrow \emptyset(\eta) = 0.5(\eta + 1.9029) \times (\eta - 1) \times (\eta - 2.4168) \times (\eta^2 - 0.4860) \times (\eta + 4.3490) \quad (65)$$

3. 5. Runge-Kutta Methods Runge-Kutta methods are a family of iterative methods used to match solutions to ordinary differential equations (OED). These methods use discretization in computing solutions in small steps. The next step Approximation is derived from the previous step by adding s terms. A problem of initial value should be specified as follows:

$$k_1 = h\, f(x_n, y_n) \quad (66)$$

$$k_2 = h\, f(x_n + \frac{1}{2}h\, , y_n + \frac{1}{2}k_1) \quad (67)$$

$$k_3 = h\, f(x_n + \frac{1}{2}h\, , y_n + \frac{1}{2}k_2) \quad (68)$$

$$k_4 = h\, f(x_n + h\,, y_n + k_3) \tag{69}$$

$$y_{n+1} = y_n + \frac{1}{6}k_1 + \frac{1}{3}k_2 + \frac{1}{3}k_3 + \frac{1}{6}k_4 + O(h^5) \tag{70}$$

k_1 is the slope at the start of the space using y. k_2 is the gradient in the middle of the range using y and k_1. k_3 is again the mid-course gradient but using y and k_2. k_4 is the slope at the end of the range utilizing y and k_3.

3. 6. Validation for Analytical Methods Figure 2 indicates the convergence graph of temperature and concentration profile in the range 0 to 1. Here, by applying two analytical solution methods and comparing the results with the numerical solution, the concentration and temperature parameters are evaluated. As shown in Figure 2, the ADM and numeric solutions converged on a line, but the VIM method initially had some numerical error, but began to converge on a line and converged with them. The third form converged without any computational error of all methods.

In this section for validation in accordance to Table 1, the present study compared to Derakhshan et al. [5]. The amount of computational error in our work is very low compared to others.

4. RESULTS AND DISCUSSION

In this research, the Nanofluids flow between two parallel plates is investigated using the ADM and VIM approach. Several diagrams according to Brownian motion, viscosity, thermophoresis factor, and magnetic influence relative to η were used to investigate fluid flow and heat transfer. A comparison was also made between the obtained results and the numerical method findings. The effect of the magnetic force having viscous impacts on Nanofluidic flow is presented in Figs. 4, 5, and 6. The comparative of results of ADM and NUM and VIM methods for investigating the effect of MHD and Viscosity on the temperature and velocity profiles. As can be seen in Figure 3, increasing the distance from the plate to the top, leads to a reduction in heat transfer and concentration. Based on Figure 4, by increasing the magnetic effects viscosity and velocity reduced and temperature is increased. Figure 5 shows the velocity changes of the fluid relative to viscosity changes. According to this graph, when the viscosity parameter increased, the fluid velocity decreased. Figure 6 shows the temperature changes of the fluid relative to viscosity changes. Based on this picture, the temperature profile reduces as a result of increasing the viscosity factor. Figure 7 shows the temperature changes of the fluid relative to thermophoretic parameter changes. The effects of the thermo-phoretic parameter and Brownian motion on the temperature are also presented in Figs. 7 and 8. The increase in thermo-phoretic parameters and Brownian motion has been found to increase temperature. The Brownian motion of nanoparticles results in the thermophoresis phenomenon, and increasing both Brownian motion and thermophoresis causes an increase in temperature. Figure 8 shows an increased concentration profile by increasing the viscosity factor. The heat transfer from fluid flow to surface increased by increasing concentration coefficient. Thermophoresis has caused by the Brownian motion of nanoparticles in fluids with a continuous temperature differential that is maintained externally. Because of the temperature disparity in the suspensions flow zone, tiny particles scatter faster in the hotter domain and slower in the colder domain. The cumulative impact of nanoparticle dispersion is migration from a hotter to a colder location of the fluid domain. According to Figure 9, by increasing the amount of viscosity the concentration parameter increased. This result is the same for both methods.

Figure 10 demonstrates the influences of the Schmidt number on the concentration profile (∅), and according

TABLE 1. Numerical comparison of non-dimensional temperature profile between present work with Derakhshan et al work [5]

η	$\theta_{Present}$	$\theta_{Derakhshan}$
0	1	1
0.1	0.9006990000	0.899450520215274
0.2	0.8018346666	0.798446158109890
0.5	0.5010416666	0.499408530656464
0.8	0.1970986666	0.203135052008296
0.9	0.09765100000e-1	0.102480354104553
1	0	0

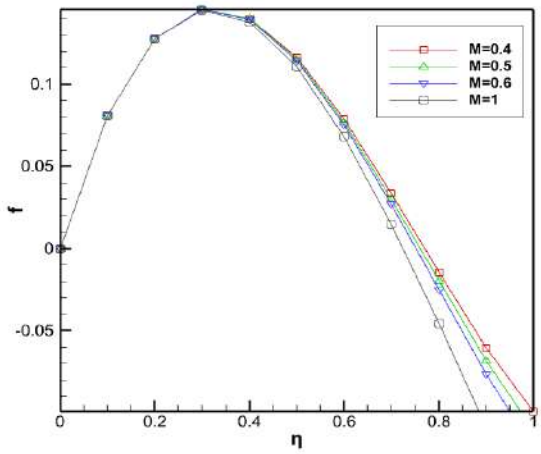

Figure 4. Effect of MHD on profile velocity by ADM at Pr=2, Sc=0.1, Nt=0.1, Nb=0.1

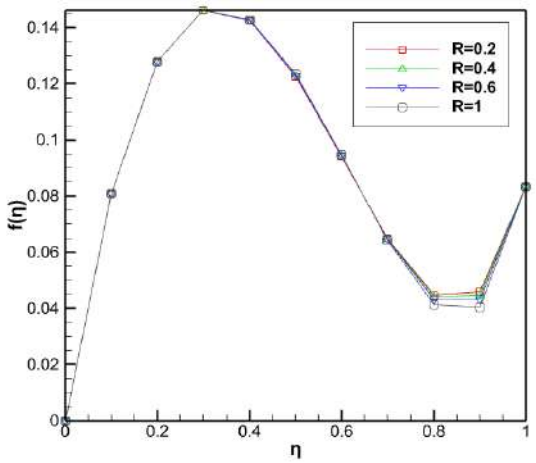

Figure 5. Effect of Viscosity on profile velocity by VIM at Pr=2, Sc=0.1, Nt=0.1, Nb=0.1

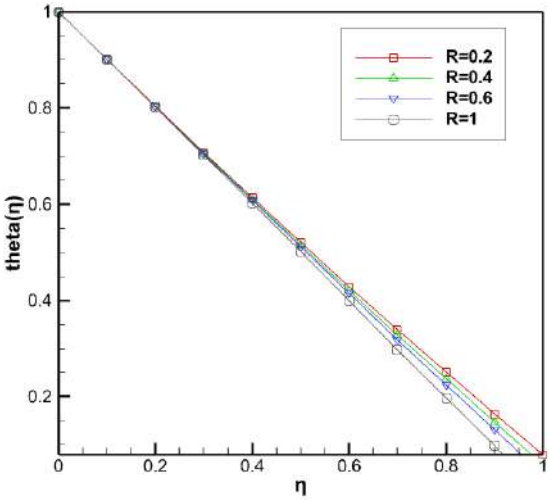

Figure 6. Effect of viscosity on profile temperature by ADM at Pr=2, M=1, Sc=0.1, Nt=0.1, Nb=0.1

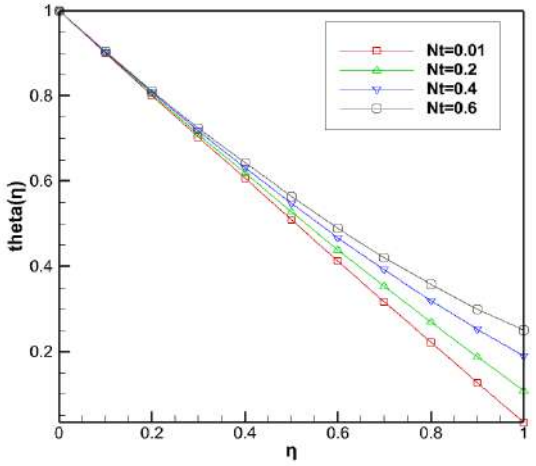

Figure 7. Effect of thermo-phoretic parameter on temperature by ADM method at Pr=2, M=1, Sc=0.1,Nb=0.1

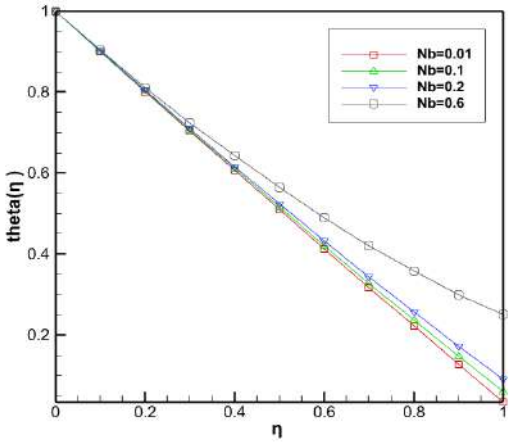

Figure 8. Influence of Brownian parameter on Temperature by ADM method at Pr=2, M=1, Sc=0.1, Nb=0.1

to the figure, by increasing the Schmidt number of fluid flow, the concentration parameter decreased.

Tables 2 and 3 summarized a numerical comparison of non-dimensional temperature and concentration

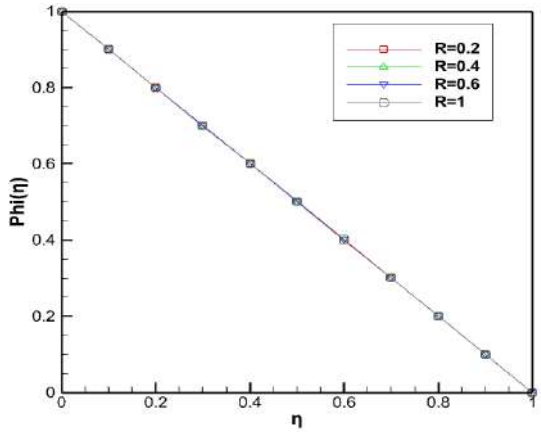

(a) ADM

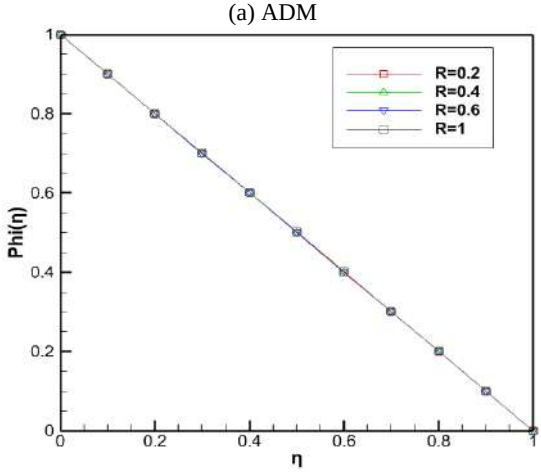

(b) VIM

Figure 9. Effect of viscosity on profile concentration by a) ADM and b) VIM at Pr=2, M=1, Sc=0.1, NT=0.1, Nb=0.1

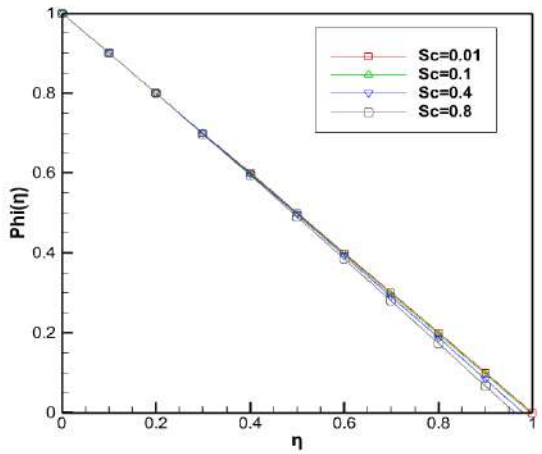

(a) ADM

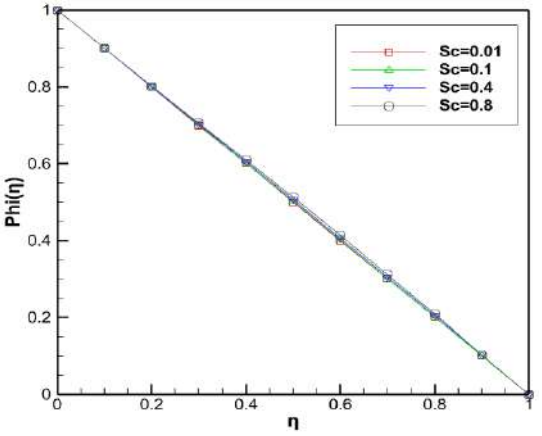

(b) VIM

Figure 10. Influence of Schmidt number on concentration by a) ADM and b) VIM method at Pr=2, M=1, Nt=0.1, Nb=0.1

TABLE 2. Numerical comparison of non-dimensional temperature between ADM, VIM and Runge-Kutta method

η	θ_{ADM}	θ_{VIM}	$\theta_{NUMERIC}$
0	1	1	1
0.1	0.9006990000	0.899450520215	0.899450
0.2	0.8018346666	0.798446158109	0.798446
0.5	0.5010416666	0.499408530656	0.499408
0.8	0.1970986666	0.203135052008	0.203135
0.9	0.0976510000	0.102480354104	0.102480
1	0	0	0

profile between ADM, VIM, and Runge-Kutta methods. In this section, all calculations are calculated with the least error.

According to Table 4, the specifications of the system used to solve the equations are as follows.

TABLE 3. Numerical comparison of non-dimensional Concentration profile between ADM, VIM and Runge-Kutta method

η	$\emptyset_{ADM}$	$\emptyset_{VIM}$	$\emptyset_{NUMERIC}$
0	1	1	1
0.1	0.8906990000	0.909450520215	0.909450
0.2	0.7918346666	0.808446158109	0.808446
0.5	0.4910416666	0.509408530656	0.499408
0.8	0.1970986666	0.203135052008	0.193135
0.9	0.0956510000	0.102480354104	0.972480
1	0	0	0

TABLE 4. comparison of CPU time between ADM and VIM

Numerical method	ADM	VIM
CPU time	2.77(s)	7.50(s)

Computer RAM =8, CPU=core i7. According to Table 3, the ADM method was obtained faster than VIM method.

5. CONCLUSION

In this paper, the heat transfer and fluid velocity between two horizontal plates is examined in existence of magnetic parameter. The parameters such as magnetic fluid flow, viscosity, Brownian motion, and thermo-phoretic have been investigated according to this analysis. The innovation of this paper is the using of two analytical methods for calculate differential equations and comparison these results with together. The results showed Temperature rise is accompanied by increases in the magnetic factor and reduction in concentration profile. Also, when Brownian motion increased, the viscosity parameter decreases. Brownian motion and thermo-phoretic parameters were directly related to the coefficient of friction.

- The velocity of the fluid between 2 plates with increasing the influence of the magnetic force from M=0.4 to M=1 is generally reduced.
- Influence of thermo-phoretic parameter on Temperature by ADM and VIM methods show that by increasing Nt=0.01 to Nt=0.6, The temperature increases from θ=0 to θ=0.28.
- By increasing the Schmidt number of fluid flow, the concentration parameter decreased.
- Thermophoresis is caused by the Brownian motion of nanoparticles in fluids with a continuous temperature differential that is maintained externally.

6. REFERENCES

1. Adibi, T., Razavi, S.E. and Adibi, O., "A characteristic-based numerical simulation of water-titanium dioxide nano-fluid in closed domains", ***International Journal of Engineering***, Vol. 33, No. 1, (2020), 158-163, doi: 10.5829/IJE.2020.33.01A.18.
2. Sadripour, S., "Investigation of flow characteristics and heat transfer enhancement in a nanofluid flow in a corrugated duct", ***Journal of Applied Mechanics and Technical Physics***, Vol. 59, No. 6, (2018), 1049-1057, doi: 10.1134/S002189441806010X.
3. Loganathan, P., Chand, P.N. and Ganesan, P., "Transient natural convective flow of a nanofluid past a vertical plate in the presence of heat generation", ***Journal of Applied Mechanics and Technical Physics***, Vol. 56, No. 3, (2015), 433-442, doi: 10. 1134/ s002189441503013x.
4. Razmara, N., "Microstructure of the poiseuille flow in a model nanofluid by molecular dynamics simulation", ***Journal of Applied Mechanics and Technical Physics***, Vol. 56, No. 5, (2015), 894-900, doi: 10.1134/S002189441505017X.
5. Derakhshan, R., Shojaei, A., Hosseinzadeh, K., Nimafar, M. and Ganji, D., "Hydrothermal analysis of magneto hydrodynamic nanofluid flow between two parallel by agm", ***Case Studies in Thermal Engineering***, Vol. 14, (2019), 100439, doi: 10.1016/j.csite.2019.100439.
6. Humphries, U., Govindaraju, M., Kaewmesri, P., Hammachukiattikul, P., Unyong, B., Rajchakit, G., Vadivel, R. and Gunasekaran, N., "Analytical approach of fe3o4-ethylene glycol radiative magnetohydrodynamic nanofluid on entropy generation in a shrinking wall with porous medium", ***International Journal of Engineering***, Vol. 34, No. 2, (2021), 517-527, doi. https://dx.doi.org/10.5829/ije.2021.34.02b.25
7. Mobadersani, F. and Bahjat, S., "Magnetohydrodynamic (mhd) flow in a channel including a rotating cylinder", ***International Journal of Engineering***, Vol. 34, No. 1, (2021), 224-233, doi. https://dx.doi:org/10.5829/ije.2021.34.01a.25
8. Akbarzadeh, P. and Fardi, A., "Natural convection heat transfer in 2d and 3d trapezoidal enclosures filled with nanofluid", ***Journal of Applied Mechanics and Technical Physics***, Vol. 59, No. 2, (2018), 292-302, doi: 10.1134/S0021894418020128.
9. Shahriari, A., Jahantigh, N. and Rakani, F., "Assessment of particle-size and temperature effect of nanofluid on heat transfer adopting lattice boltzmann model", ***International Journal of Engineering***, Vol. 31, No. 10, (2018), 1749-1759, doi: 10.5829/ije.2018.31.10a.18.
10. Alagappan, N. and Karunakaran, N., "Performance investigation of 405 stainless steel thermosyphon using cerium (iv) oxide nano fluid", ***International Journal of Engineering***, Vol. 30, No. 4, (2017), 575-581, doi: 10.5829/idosi.ije.2017.30.04a.16.
11. Akbari, M., Yavari, M., Nemati, N., Babaee Darband, J., Molavi, H. and Asefi, M., "An investigation on stability, electrical and thermal characteristics of transformer insulting oil nanofluids", ***International Journal of Engineering***, Vol. 29, No. 10, (2016), 1332-1340, doi: 10.5829/idosi.ije.2016.29.10a.02.
12. AJAY, K., "Performance evaluation of nanofluid (al2o3/h2o-c2h6o2) based parabolic solar collector using both experimental and cfd techniques", ***International Journal of Engineering***, Vol. 29, No. 4, (2016), 572-580, doi: 10.5829/idosi.ije.2016.29.04a.17.
13. Kheiri, M. and Davarnejad, R., "Numerical comparison of turbulent heat transfer and flow characteristics of sio2/water nanofluid within helically corrugated tubes and plain tube", ***International Journal of Engineering***, Vol. 28, No. 10, (2015), 1408-1414, doi: 10.5829/idosi.ije.2015.28.10a.02.
14. Khan, D., Hakim, M.A. and Alam, M., "Analysis of magneto-hydrodynamics jeffery-hamel flow with nanoparticles by hermite-padé approximation", ***International Journal of Engineering***, Vol. 28, No. 4, (2015), 599-607, doi: 10.5829/idosi.ije.2015.28.04a.15.
15. Goshtasbi Rad, E., "Experimental investigation of mixed convection heat transfer in vertical tubes by nanofluid: Effects of reynolds number and fluid temperature", ***International Journal of Engineering***, Vol. 27, No. 8, (2014), 1251-1258, doi: 10.5829/idosi.ije.2014.27.08b.11.
16. Mohammadi Ardehali, R., "Modeling of tio2-water nanofluid effect on heat transfer and pressure drop", ***International Journal of Engineering***, Vol. 27, No. 2, (2014), 195-202, doi: 10.5829/idosi.ije.2014.27.02b.04.
17. Rostami, M., Hassani Joshaghani, A., Mazaheri, H. and Shokri, A., "Photo-degradation of p-nitro toluene using modified bentonite based nano-tio2 photocatalyst in aqueous solution", ***International Journal of Engineering***, Vol. 34, No. 4, (2021), 756-762, doi. https://dx.doi.org/10.5829/ije.2021.34.04a.01
18. Siavashy, O.S., Nabian, N. and Rabiee, S., "Titanium dioxide nanotubes incorporated bioactive glass nanocomposites: Synthesis, characterization, bioactivity evaluation and drug loading", ***International Journal of Engineering***, Vol. 34, No. 1, (2021), 1-9, doi. https://dx.doi.org/10.5829/ije.2021.34.01a.01
19. Taheri, A.A. and Taghilou, M., "Towards a uncertainty analysis in thermal protection using phase-change micro/nano particles during hyperthermia", ***International Journal of Engineering***, Vol. 34, No. 1, (2021), 263-271, doi: 10.5829/ije.2021.34.01a.29.
20. Peiravi, M.M., Alinejad, J., Ganji, D. and Maddah, S., "Numerical study of fins arrangement and nanofluids effects on three-dimensional natural convection in the cubical enclosure", ***Challenges in Nano and Micro Scale Science and Technology***, Vol. 7, No. 2, (2019), 97-112, doi: 10.22111/tpnms.2019.27933.1164.
21. Gupta, U., Ahuja, J. and Wanchoo, R., "Magneto convection in a nanofluid layer", ***International Journal of Heat and Mass Transfer***, Vol. 64, (2013), 1163-1171, doi: 10.1016/j.ijheatmasstransfer.2013.05.035.
22. Peiravi, M.M., Alinejad, J., Ganji, D.D. and Maddah, S., "3d optimization of baffle arrangement in a multi-phase nanofluid natural convection based on numerical simulation", ***International Journal of Numerical Methods for Heat & Fluid Flow***, (2019), doi: 10.1108/HFF-01-2019-001.
23. Peiravi, M.M. and Alinejad, J., "Nano particles distribution characteristics in multi-phase heat transfer between 3d cubical enclosures mounted obstacles", ***Alexandria Engineering Journal***, Vol. 60, No. 6, (2021), 5025-5038, doi: 10.1016/j.aej.2021.04.013.
24. Pourmehran, O., Rahimi-Gorji, M., Gorji-Bandpy, M. and Ganji, D., *Retracted: Analytical investigation of squeezing unsteady nanofluid flow between parallel plates by lsm and cm*. 2015, Elsevier.
25. Azimi, A. and Mirzaei, M., "Analytical investigation of squeezing flow of graphene oxide water nanofluid between parallel plates using rvim", ***Journal of Computational and Theoretical Nanoscience***, Vol. 12, No. 2, (2015), 175-179, doi: 10.1166/jctn.2015.3711.
26. Domari, G.D., Peiravi, M. and Abbasi, M., "Evaluation of the heat transfer rate increases in retention pools nuclear waste", ***International Journal of Nano Dimension***, Vol. 6, No. 4, (2015), 385-398.
27. Hatami, M. and Ganji, D., "Motion of a spherical particle in a fluid forced vortex by dqm and dtm", ***Particuology***, Vol. 16, (2014), 206-212, doi: 10.1016/j.partic.2014.01.001.
28. Rashidi, M.M., Reza, M. and Gupta, S., "Mhd stagnation point flow of micropolar nanofluid between parallel porous plates with uniform blowing", ***Powder Technology***, Vol. 301, (2016), 876-885, doi: 10.1016/j.powtec.2016.07.019.

29. Peiravi, M.M. and Alinejad, J., "Hybrid conduction, convection and radiation heat transfer simulation in a channel with rectangular cylinder", ***Journal of Thermal Analysis and Calorimetry***, Vol. 140, No. 6, (2020), 2733-2747, doi: 10.1007/s10973-019-09010-0.

30. Jalilpour, B., Jafarmadar, S., Ganji, D., Shotorban, A. and Taghavifar, H., "Heat generation/absorption on mhd stagnation flow of nanofluid towards a porous stretching sheet with prescribed surface heat flux", ***Journal of Molecular Liquids***, Vol. 195, (2014), 194-204, doi: 10.1016/j.molliq.2014.02.021.

31. Ganji, D. and HashemiKachapi, S., "Analysis of nonlinear equations in fluids, progress in nonlinear science", ***Sian Academic***, , (2011), 1-294.

32. Aminoroayaie Yamini, O., Mousavi, S.H., Kavianpour, M. and Safari Ghaleh, R., "Hydrodynamic performance and cavitation analysis in bottom outlets of dam using cfd modelling", ***Advances in Civil Engineering***, Vol. 2021, (2021), doi: 10.1155/2021/5529792.

33. Mousavimehr, S., Yamini, O.A. and Kavianpour, M., "Performance assessment of shockwaves of chute spillways in large dams", ***Shock and Vibration***, Vol. 2021, (2021), doi: 10.1155/2021/6634086.

34. Kostikov, Y.A. and Romanenkov, A.M., "Approximation of the multidimensional optimal control problem for the heat equation (applicable to computational fluid dynamics (CFD))", ***Civil Engineering Journal***, Vol. 6, No. 4, (2020), 743-768, doi: 10.28991/cej-2020-03091506.

Persian Abstract

چکیده

در مقاله حاضر ، انتقال حرارت و سرعت سیال بین دو صفحه افقی با وجود پارامتر مغناطیسی بررسی شده است. پارامترهایی مانند جریان سیال مغناطیسی ، ویسکوزیته ، حرکت براونی و ترموفورتیک با توجه به این مورد بررسی شده است. نوآوری این مقاله استفاده از دو روش تحلیلی برای محاسبه معادلات دیفرانسیل و مقایسه این نتایج با هم میباشد.در این مقاله ، اثرات میدان مغناطیسی روی جریان سیال برای مصارف صنعتی مورد بررسی قرار گرفته است. اثرات میدان مغناطیسی جریان سیال با استفاده از روش تکرار تغییرات (VIM) و Adomian مورد بررسی قرار می گیرد و نتایج ان با روش نیومریک مقایسه میشود. مطابق با نتایج حاصله با افزایش اثرات مغناطیس ، سرعت جریان سیال کاهش می یابد و ویسکوزیته بیشتر میشود. همچنین ضریب نیروی براون با ضریب ترموفورتیک رابطه مستقیمی با ضریب اصطکاک دارند. نیروی براون نانوذرات نتایج ضریب ترموفورتیک هستند بطوریکه با افزایش نیروی براون و ترموفورتیک دما افزایش می یابد.

International Journal of Engineering

Journal Homepage: www.ije.ir

Influence of Various Design Parameters on Compressive Strength of Geopolymer Concrete: A Parametric Study by Taguchi Method

S. R. Raj[a], P. G. Arulraj[a], N. Anand*[a], K. Balamurali[a], G. Gokul[b]

[a] *Department of Civil Engineering, Karunya Institute of Technology and Sciences(KITS), Coimbatore, India*
[b] *Department of Physics, Karunya Institute of Technology and Sciences(KITS), Coimbatore, India*

PAPER INFO

Paper history:
Received 22 July 2021
Received in revised form 19 August 2021
Accepted 23 August 2021

Keywords:
Geo-polymer Concrete
Taguchi Method
Compressive Strength
OrdinaryPortland Cement

ABSTRACT

Global warming is one of the severe environmental effects, which are faced by the current generation. Studies show that Carbon dioxide (CO_2) is the major cause of global warming and is mainly due to the huge production of Ordinary Portland Cement (OPC). Supplementary cementitious materials can reduce this effect by reducing the required materials instead of OPC for construction purposes. Geopolymer Concrete (GPC) is a new generation concrete, which does not require OPC. In this study, Fly Ash (FA) was used to produce GPC. Various parameters were considered and the design of the experiment was made using Taguchi's method and developed an empirical relation to predicting the compressive strength of GPC based on the different parameters. Thirty-six mixes were cast to determine the effect of curing temperature, curing time, rest period, the ratio of Alkaline Activator solutions (AAs), ratio of activators to FA, the molarity of NaOH and replacement level of FA with OPC on the compressive strength. The contribution of each parameter was estimated by ANOVA. Results show that the addition of OPC had a significant effect on the compressive strength of GPC. The mix with 20% OPC, 14M NaOH, curing temperature of 60ºC, curing time of 36h, a rest period of 48h, AAs to FA ratio 0.3 and ratio of alkaline solutions 2.5 was found to have the maximum compressive strength. A regression equation is developed to determine the compressive strength of GPC concerning the parameters considered.

***doi**: 10.5829/ije.2021.34.10a.16*

1. INTRODUCTION

Global warming is one of the major environmental problems, which affects all living creatures. The liberation of greenhouse gases such as CO_2 has a major role in global warming [1]. The permitted level of CO_2 in the atmosphere is 0.04% [2]. When the level of CO_2 increases beyond the permissible limit, global warming happens. OPC is one of the major binding materials that liberates CO_2 around 5-7% [3]. There are several research works undertaken to develop sustainable concrete by replacing OPC with other supplementary cementitious materials like industrial by-products. The production of cement releases greenhouse gas. The heating of limestone releases CO_2 directly, while the burning of fossil fuels to heat the kiln indirectly results in CO_2 emissions. The environmental issues associated with greenhouse gases, in addition to the depletion of natural resources, play a leading role in the sustainable development of the cement and concrete industry during this century. Due to scarcity of natural resources or growing concern over greenhouse gases or both, a time will come when the production of cement will have to be curtailed or cannot be increased to maintain the ecological balance [4]. Therefore, it is necessary to look for sustainable materials for the production of concrete. About 13-22% of CO_2 emission from OPC production can be reduced by using sustainable binding materials blended with OPC [3]. The Indian coal is of low grade having a high ash content of the order of 30 - 45% producing a large quantity of FA at coal/lignite based thermal power stations. The management of FA has been troublesome because of its disposal due to its potential of causing pollution of air and water. In the past decade,

*Corresponding Author Institutional Email: nanand@karunya.edu (N. Anand)

Please cite this article as: S. R. Raj, P. G. Arulraj, N. Anand, K. Balamurali, G. Gokul, Influence of Various Design Parameters on Compressive Strength of Geopolymer Concrete: A Parametric Study by Taguchi Method, International Journal of Engineering, Transactions A: Basics Vol. 34, No. 10, (2021), 2351-2359

there has been a tremendous increase in the generation of FA; coal-based thermal power plants meet more than 70% of country's demand for electricity. At present, India produces approximately 180 million-tons of FA every year. Some of the problems associated with FA are large area of land required for disposal and toxicity associated with heavy metals leached to groundwater. FA was treated as a waste material and a source of air and water pollution until the last decade. However, at present it is considered as a resource material to produce different useful binding products. By increasing the utilization of FA, the emission of CO_2 can be reduced.

In the year 1987, Davidovits developed a new generation binding material, which is produced through the polymerization process of alumina-silicate source materials like FA, bottom ash, GGBS, etc., with the aid of AAs, and it is termed as GPC [2]. The production of GPC will reduce the emission of CO_2 by 80%. Two major environmental pollutions CO_2 emission and open landfill of FA are reduced by the production of FA-based GPC. The main constituents of GPC are silicon and aluminum that are provided by thermally activated natural materials (e.g. kaolinite or rice husk ash) or industrial by-products (e.g. FA or slag) and an alkaline activating solution, which polymerizes these materials into molecular chains and networks to create a hardened binder. It is termed alkali-activated concrete or inorganic polymer concrete [5-7]. Ambient cured GPC was made by using different alumino-silicate source materials such as slag, fly ash, etc. at CBRI, Roorkee. Also, they introduced lightweight GP sheets, solid bricks, hollow blocks, foamed bricks and solid blocks made of GPC. The production of GPC at ambient conditions by using different aluminosilicate source materials such as slag, FA, etc. resulted in the production of readymade lightweight GP sheets, solid bricks, hollow blocks, foamed bricks and solid blocks [8]. Dr. Genichi Taguchi observed that the ratio of time and money spending for engineering experiments and testing is higher than the efforts taken for making products. He felt that the process of inspection, screening and salvaging could not improve poor quality. This moved Taguchi to develop a new optimization method of the processes of engineering experimentation. He said that "Cost is more important than quality but the quality is the best way to reduce cost". He developed a statistical technique known as the Taguchi method [9]. Taguchi method is now used for different disciplines such as optimization of concrete mix, finding the optimum values for the ingredients in a mixture, etc [10,11]. Only a limited number of works are done by the Taguchi method to optimize the parameters according to different properties of Geopolymer concrete [11-13]. ANOVA was used to find the percentage of effect of each parameter. Partial replacement of FA was found to give good mechanical properties when compared with other proportions [14]. By the addition of cement in GPC, hardened properties increase whereas fresh properties decrease. Also, the concrete becomes more dense and compact. The optimum replacement level for OPC was found to be 10% [15, 16]. OPC provides excellent early and final compressive strength in the GPC mix in the absence of heat curing, but beyond 10% OPC addition reduced strength from 82.5% to 24.4% [17-19]. The combination of $NaOH+Na_2SiO_3$ was found to have high compressive strength and is suitable for structural applications. GPC mix having AAs to FA ratio of 0.35 to 0.45 and 12M & 16M NaOH solution, the ratio of AAs as 2.5 at a curing temperature of 90^{o}C for 12h provided more than 60MPa strength with the curing period of 24 h at 60^{o}C. Beyond 16h of curing time and more than 120^{o}C temperature of curing time had no significant improvement on the strength of GPC [20]. A rest time of 30 minutes for the activator solution and increases in curing time provides good mechanical properties than the resting time of 24 h. Porosity and water absorption were found to decrease [15]. 14M NaOH solution provides a strength of 25-30 MPa. 90% of the compressive strength was achieved at a temperature of 70^{o}C to 90^{o}C and at a curing time of 18 to 24 h. According to [21] strength of the concrete reduces beyond 150^{o}C due to overheating. The optimum value for activators to FA ratio was found 0.40 and beyond 16M NaOH solution does not provide strength to the concrete due to the improper polymerization [22].

The mechanical properties of FA-based GPC were investigated by the Taguchi method. Considered parameters include calcium aluminate cement (CAC) replacement (5, 10 and 20%), the concentration of NaOH (10, 12 and 14M) and activator to binder ratio (35, 40 and 45%). It was found that mix with 10M NaOH solution, 5% CAC replacement and 45% of activator to binder ratio exhibited good workability. In addition, 14M NaOH solution, 10% CAC replacement and 35% of activator to binder ratio exhibited maximum compressive strength of 56.8 MPa at 28 days of ambient curing. It was concluded that the CAC replacement ratio had a significant influence on the strength, whereas the workability of the concrete mix was influenced by the activator to binder ratio [23]. The mechanical properties of GPC with GGBS were examined at ambient curing conditions by Taguchi method and the considered parameters include binder content (400, 450 and 500 kg/m^3), AA to Binder content (Al/Bi) ratio (0.35, 0.45 and 0.55), sodium silicate to sodium hydroxide ratio (1.5, 2.0 and 2.5) and concentration of NaOH solution (10, 12 and 14M). Maximum compressive strength (60.4 MPa) was obtained after 7 days at ambient curing condition and the optimum value for each of the considered parameters are binder content of 450 kg/m^3, Al/Bi ratio of 0.35, sodium silicate to sodium hydroxide ratio of 2.5 and 14M NaOH solution. The addition of GGBS in the FA-based GPC has the advantage that heat curing can be avoided [12]. An investigation was carried out on the compressive strength of GPC by using the Taguchi method. It was found that

30% of GGBS, 50% of M-sand and activators to binder ratio of 0.40 showed maximum compressive strength [11]. Compressive strength and water absorption properties of FA-based GPC were investigated by Taguchi method carried out considering various parameters like OPC as FA replacement, NaOH concentration and curing temperature. It was found that maximum compressive strength of 64.39 MPa at 7 days of curing was obtained for the mix with 20% OPC, 15M NaOH solution and 70°C for 24 h. Similarly, minimum water absorption was obtained for the mix with 20% OPC, 10M NaOH solution and 80°C for 24h. Mechanical and durability properties of GPC were found to depend on the concentration of NaOH, amount of AAs, AAs to FA ratio, curing period and curing temperature [13]. In earlier studies, researchers have replaced FA with a maximum cement content of 15%. In this study, 20% FA was replaced. Parameters are not considered together in the earlier research works. In this research, seven parameters are considered together. Normally when considering more number of parameters together more experiments are needed for testing. But to reduce the number of experiments, Taguchi's method can be used. In the Taguchi method, the minimum number of experiments can be found which will provide the effects of all the parameters accurately at a low cost. This method was adopted for various engineering analysis to optimize various influencing parameters [6]. Taguchi experimental design reduces the cost, improves the quality and provides robust design solutions. The advantages of the Taguchi method over the other methods are that numerous factors can be simultaneously optimized and more quantitative information can be extracted from fewer experimental trials. From the critical analysis of the literature, it is evident that different parameters will influence the compressive strength of FA-based GPC. An attempt has been made to carry out a parametric study on the factors influencing the compressive strength of GPC.

2. DETAILS OF THE EXPERIMENT

2. 1. Materials

2. 1. 1. Fly Ash FA used in this research was obtained from the Mettur Thermal power plant, which is located in Salem, India. The obtained FA was found to contain 59.93% SiO_2, 19.66% Al_20_3, 2.82% Fe_2O_3, 3.33% CaO, 1.12% MgO, 0.22% K_2O, and 0.34% Na_2O through X-ray Diffraction (XRD) analysis. Following its chemical composition obtained, FA contains low Calcium content. Therefore, the obtained FA is termed as low calcium FA or Class-F FA. The specific gravity of Mettur FA was determined as 2.31 and the specific surface area of FA particle was found to be 320m^2/kg.

2. 1. 2. Ordinary Portland Cement (OPC) OPC 53 grade obtained from a local source was used for this research as an external calcium source for the setting GPC. The chemical properties of FA and OPC are given in Table 1.

2. 1. 3. Aggregates Manufactured Sand (M-Sand) was obtained from local supplies. Density, water absorption and specific gravity of M-Sand were found to be 1670 kg/m^3, 1.35% and 2.7, respectively. Coarse Aggregate (CA) was also obtained from the local source. Crushed stone aggregates of nominal diameter between 10mm and 20mm with density, water absorption and Specific gravity of CA were found to be 1760 kg/m^3, 0.5% and 2.9, respectively.

2. 1. 4. Alkaline Activator Solution Activator solution was made by combining the commercially available Sodium hydroxide (NaOH) pellets and Sodium Silicate (Na_2SiO_3) solution. NaOH solution was prepared by mixing the required quantity of 97-98% pure NaOH pellets with distilled water to get the desired molarity and kept for 24h to expel the heat produced during the mixing process. Na_2SiO_3 solution obtained from the local source was used in this research. Na_2SiO_3 has a pH value of 10-13, a specific gravity of 1.45-1.55g/cm^3 and a density of 1450-1550 kg/m^3. The total solid content present in the available sodium silicate solution is 45-55% by mass.

2. 2. Test Parameters

The number of parameters considered and the levels for those factors were selected based on the literature review. In this research, seven different parameters were considered which can influence the compressive strength of GPC. The parameters considered are curing temperature, curing time, rest period, a ratio of AA solutions, a ratio of activators to FA, the molarity of NaOH and replacement level of FA with OPC. The details of considered parameters and the levels of each parameter are given in Table 2.

TABLE 1. The chemical composition of OPC and FA

Constituent	OPC (%)	FA (%)
Silica Oxide(SiO_2)	21.28	59.93
Aluminum Oxide(Al_2O_3)	4.33	19.66
Iron Oxide(Fe_2O_3)	1.85	2.82
Calcium Oxide(CaO)	64.30	3.33
Magnesium Oxide(MgO)	1.81	1.12
Sodium Oxide(Na_2O)	0.17	0.34
Potassium Oxide(K_2O)	0.71	0.22
Loss of ignition(LOI)	1.50	1.56

TABLE 2. Parameters and levels for compressive strength

Parameters	Level 1	Level 2	Level 3
OPC content (%)	0	10	20
Molarity of NaOH (M)	10	12	14
Curing temperature (°C)	60	80	100
Curing time (h)	12	24	36
Rest period (h)	24	48	-
AAs to FA ratio	0.30	0.35	0.40
The ratio of alkaline solutions	2	2.5	3

2. 3. Design of Experiment Taguchi method was used to develop the Design of Experiments (DOE) and to determine the minimum number of experiments to be carried out to completely understand the influence of these seven parameters [13, 24-27]. A robust design of the L_{36} orthogonal array was developed for compressive strength experimentation. Table 3 shows the different parametric combinations obtained by the Taguchi method to carry out the experiments. Thirty-six sets of experiments with different levels of factors were designed as per the Taguchi method and the developed L_{36} matrix is given in Table 3.

TABLE 3. L_{36} Matrix designed as per Taguchi method

Trial mixture	Rest Period (h)	Curing Temperature (°C)	Curing Time (h)	Ratio of Alkaline Solution	Molarity of NaOH (M)	Ratio of Activators to FA	Percentage of Cement (%)
T_1	24	60	12	2	10	0.3	0
T_2	24	80	24	2.5	12	0.35	10
T_3	24	100	36	3	14	0.4	20
T_4	24	60	12	2	10	0.35	10
T_5	24	80	24	2.5	12	0.4	20
T_6	24	100	36	3	14	0.3	0
T_7	24	60	12	2.5	14	0.3	10
T_8	24	80	24	3	10	0.35	20
T_9	24	100	36	2	12	0.4	0
T_{10}	24	60	12	3	12	0.3	20
T_{11}	24	80	24	2	14	0.35	0
T_{12}	24	100	36	2.5	10	0.4	10
T_{13}	24	60	24	3	10	0.4	10
T_{14}	24	80	36	2	12	0.3	20
T_{15}	24	100	12	2.5	14	0.35	0
T_{16}	24	60	24	3	12	0.3	0
T_{17}	24	80	36	2	14	0.35	10
T_{18}	24	100	12	2.5	10	0.4	20
T_{19}	48	60	24	2	14	0.4	20
T_{20}	48	80	36	2.5	10	0.3	0
T_{21}	48	100	12	3	12	0.35	10
T_{22}	48	60	24	2.5	14	0.4	0
T_{23}	48	80	36	3	10	0.3	10
T_{24}	48	100	12	2	12	0.35	20
T_{25}	48	60	36	2.5	10	0.35	20
T_{26}	48	80	12	3	12	0.4	0
T_{27}	48	100	24	2	14	0.3	10
T_{28}	48	60	36	2.5	12	0.35	0
T_{29}	48	80	12	3	14	0.4	10
T_{30}	48	100	24	2	10	0.3	20
T_{31}	48	60	36	3	14	0.35	20
T_{32}	48	80	12	2	10	0.4	0
T_{33}	48	100	24	2.5	12	0.3	10
T_{34}	48	60	36	2	12	0.4	10
T_{35}	48	80	12	2.5	14	0.3	20
T_{36}	48	100	24	3	10	0.35	0

2. 4. Preparation of Test Specimens For the desired concentration of NaOH solution for each trial mix, NaOH pellets were dissolved in distilled water. Prepared NaOH solution was added with Na_2SiO_3 solution and mixed thoroughly. Thirty minutes after the preparation of AAs solution, dry materials such as aggregates and binders were mixed in a mechanical mixer for about 2 minutes. After dry mixing of materials, AA solution was poured slowly into the dry mix along with the required water and mixed continuously. The materials were mixed for about 2 minutes until the concrete appears to be homogeneous. After the mixing, the GPC mixture was poured into the compressive strength cube mold of size 150mm × 150mm. The preparation of specimens and the slump details are shown in Figures 1 and 2, respectively. The specimens were cast and kept at room temperature for the corresponding rest period given in Table 3. After the completion of the rest period, the specimens were de-molded and kept in an electric furnace as per the specification given in Table 3. The inner dimensions of the furnace are 500mm × 500mm × 500mm. The sides and top of the furnace were lined with electrical heating coils embedded in refractory bricks. The specimens were heated uniformly on three sides [28]. Heat curing of specimens is shown in Figure 1A. Once the curing of specimens is completed, the specimens were allowed to cool naturally and the specimens were kept at ambient temperature until testing.

2. 5. Testing Method For determining the compressive strength, cubical GPC specimens were tested in a Compressive strength Testing Machine (CTM) of capacity 2000kN at the age of 28 days specimens is shown in Figure 1B. The load was applied to the specimen gradually and continuously at a rate of 14/N/mm^2/minute [29]. Three specimens were tested for each trial mix and the results were given as their average.

3. RESULT AND DISCUSSION

3. 1. Analysis of the Results During the present investigation, 108 cube specimens were tested. Workability for OPC blended GPC mix was tested following IS- 10262-2019 and slump of the mixes were maintained in the range of 100mm to 150mm [30]. The hardened properties of the OPC blended GPC specimens were tested following IS-516 [29]. From table 3, it can be seen that almost all the mixtures have 28 days compressive strength values above 30 MPa. The specimens correspond to 20% OPC as FA replacement, 10M concentration of NaOH solution, curing temperature of 60°C for 36 h, rest period of 48 h, AA ratio of 2.5 and activator solution to FA ratio of 0.35. Minimum compressive strength was observed for the T_{15} specimen with an average strength value of 22.89 MPa. These specimens correspond to 14M concentration of NaOH solution, curing temperature of 100°C for 12 h, rest period of 24h, alkaline solution ratio of 2.5 and activator solution to FA ratio of 0.35, cement content was zero for this mix. From the experimental results, it can be seen that the compressive strength of GPC increases with the increasing percentage of OPC.

According to Table 3, specimens having a rest period of 48h give better strength than the specimens having 24h rest period. This shows that the polymerization process continuous up to 48h. It is found that the specimens cured at 60°C and 80°C for 36h had higher than those of the specimens cured under other conditions. But specimens cured at 100°C for 12h also show good compressive strength. This is following the findings of [20, 29]. They reported that the higher strength was observed at 90°C for a curing period of 12 to 18h. From Figure 2, it can be seen that maximum strength was obtained for the specimens having 20% OPC replacement. It is reported that a 20% OPC replacement level was optimum [5]. Increasing the OPC level beyond this resulted in a decrease in the strength of the GPC due to extra calcium in the mix [30]. From Figure 2, it can also be seen that the variation in the concentration of NaOH between 10M and 14M was found to have a small effect on the compressive strength of GPC and 12M solution resulted in higher strength than the other molar solutions. This is following the findings of [20]. They observed that 12M NaOH solutions yielded maximum strength. Maximum strength was found when the ratio of AAs was 2.5 and the ratio of activators to FA was 0.35. This is following the finding of [20]. They reported that maximum strength was observed when the ratio of AAs was 2.5 and the activator to FA ratio was 0.35.

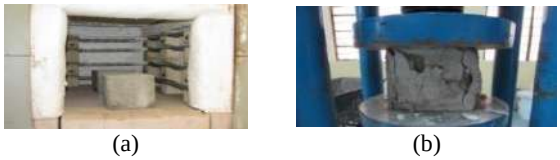

(a) (b)

Figure 1. (a) Heat curing of test specimens (b) Compression test on GPC cube

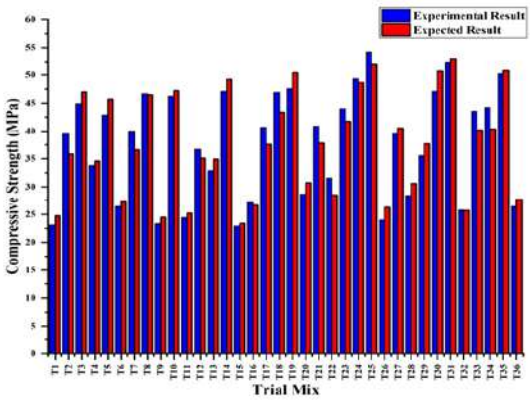

Figure 2. Comparison of the estimated and experimental compressive strength of GPC

Figures 3 (A, C, D, E and G) indicate the increase in the rest period, curing time, AA ratio, the concentration of NaOH, and addition of Additives (OPC) increase the compressive strength of GPC, whereas Figures 4B and 4F show that increase in curing temperature and AA-FA ratio declines the compressive strength of GPC decreases [15].

3. 2. Mathematical Model Based on the results, compressive strength for each parameter were described in Table 4. The main objective of this analysis is to find out the impact of considered key parameters and their contribution, i.e. OPC addition, molarity of NaOH, curing temperature, curing time, rest period, AA-FA ratio and ratio of activators solution on the compressive strength of GPC. From the ANOVA results for compressive strength of GPC, it is observed that addition of OPC as FA replacement is the most significant parameter with the highest contribution of 77.44%, whereas other parameters such as rest period, curing temperature, curing time, a ratio of alkaline solutions, the molarity of NaOH and ratio of activators to FA have the contributions of 2.12%, 0.21%, 2.38%, 1.82%, 1.37% and 0.96%, respectively. The compressive strength of GPC can be increased by the addition of OPC. Calcium oxide is a major compound in OPC which provides strength to the concrete. Calcium tends to react with the alkalis which result in additional hydration products and heat [31]. The produced heat also helps to improve the compressive strength of GPC by enhancing the curing temperature of the system. Beyond the 20% replacement level, the compressive strength of GPC decreases due to the utilization of available water for the hydration of OPC. The maximum increase in the compressive strength of OPC blended GPC was found to be 57.78% more than that of the GPC containing 0% OPC. An expression for the compressive strength of GPC was developed using a regression equation based on the obtained experimental results. The compressive strength (denoted by S), rest period (denoted by R), curing temperature (denoted by T), curing time (denoted by C), a ratio of alkaline solutions (denoted by A), the molarity of NaOH (denoted by M), a ratio of activators to FA (denoted by F) and addition of OPC as FA replacement (denoted by P) and the expression is given below.

$$S = 15.7 + 0.1319R - 0.0268T + 0.1630C - 0.41A + 0.761M - 25.0F + 1.133P \quad (1)$$

The result of the mathematical model was compared with the experimental results and the details are shown in Figure 2. From the figure, it can be seen that the developed mathematical model can predict the compressive strength of GPC accurately. The percentage errors in predicting the compression strength of GPC concerning the various parameters are shown in Figure 3. From Equation (1) it can be seen that the regression model can be used to predict the strength of GPC accurately. The percentage error is found to be less than 10.

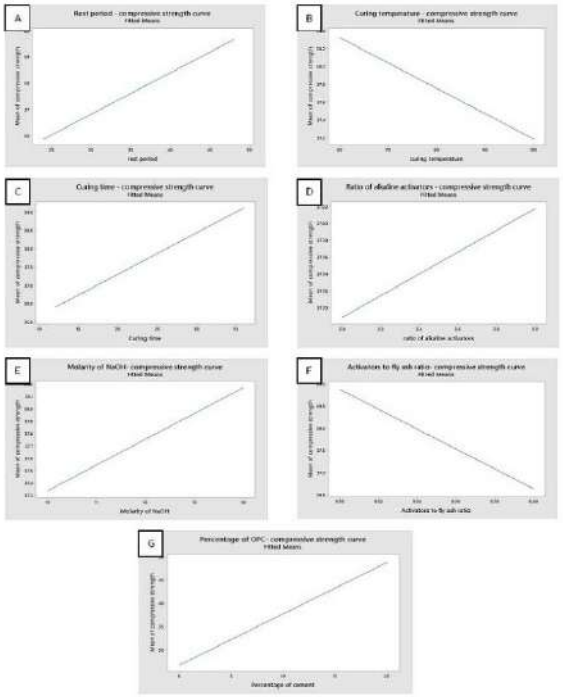

Figure 3. software stimulation of compressive strength of GPC Vs. Rest period, curing temperature, curing time, AA ratio, the concentration of NaOH, activator-FA ratio, the addition of additives

TABLE 4. ANOVA for compressive strength

Source	Sum of squares	Degree of freedom	Mean square	F-value	Contribution (%)
Rest Period(h)	90.22	1	90.22	3.39	2.12
Curing temperature(°C)	8.77	2	4.39	0.16	0.21
Curing time(h)	101.62	2	50.81	1.91	2.38
Ratio of Alkaline solutions	77.48	2	38.74	1.46	1.82
Molarity of NaOH(M)	58.41	2	29.20	1.10	1.37
Ratio of Activators to FA	41.03	2	20.51	0.77	0.96
OPC (%)	3302.92	2	1651.46	62.11	77.44
Error	584.96	22	26.59		13.71
Total	4265.41	35			100.00

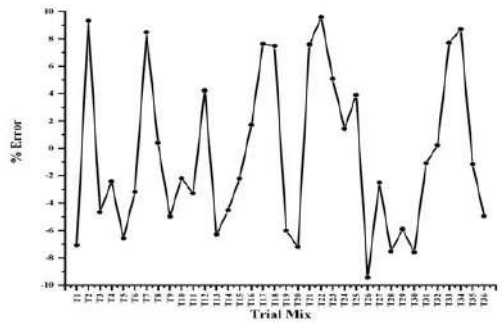

Figure 4. Percentage error for the estimated and experimental compressive strength of GPC

3. 3. Signal–to–noise Ratio (SN Ratio)

Optimum combination for the levels of the considered factors determined by using signal to noise ratio was calculated by using the following equations:

$$\frac{S}{N} = -10log\left(\frac{\bar{y}^2}{s^2}\right) \quad (2)$$

$$\frac{S}{N} = -10log\frac{1}{n}\sum y^2 \quad (3)$$

$$\frac{S}{N} = -10log\frac{1}{n}\sum\frac{1}{y^2} \quad (4)$$

The highest ratio of signal to noise ratio was considered as better for the optimum parametric combination [16]. SN ratio was calculated using Equation (4) and the best optimum combination were shown in Figure 5. It was observed that compressive strength of the mixture increases with the addition of OPC until 20% replacement, increases with a rest period of 48 h and molarity of NaOH of 14M. Maximum strength was achieved with the ratio of alkaline solutions of 2, activators to FA ratio of 0.3 and curing temperature of 60ºC for 36h.

When a higher concentration of NaOH solution is added with FA, it liberates a higher amount of silica and alumina. These two compounds influence the strength of the whole system. Also by the addition of OPC, induces the additional hydration products accompanied with a geo-polymeric binder to form the concrete [31]. From the SN ratio graph, the optimum parametric combination for higher strength of GPC was observed to be 20% OPC, 14M NaOH, curing temperature 60ºC, curing time 36h, rest period 48h, AA to FA ratio 0.3 and ratio of alkaline solutions 2.

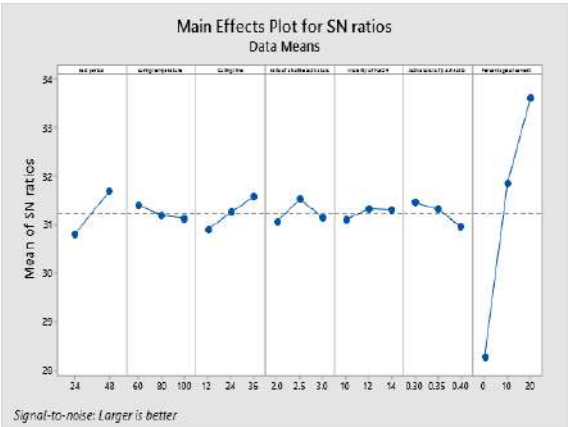

Figure 5. S-N ratio graph for compressive strength

4. CONCLUSIONS

Seven parameters that were expected to influence the compressive strength of GPC were considered for the parametric study. Taguchi method was used to design the experiment and a mathematical model was developed by using experimental results. The replacement of FA with OPC significantly improves the compressive strength of GPC. The optimum replacement level FA with OPC for GPC is 20%. The strength of the GPC mix was found to increase by 57.78% when OPC content was increased from 0 to 20%. From ANOVA, the addition of OPC was found to be the most significant factor for activating the required strength. From the research, the strength contributions of considered parameters are OPC (77.44%), curing time (2.38%), rest period (2.12%), the ratio of alkaline solutions (1.82%), molarity of NaOH (1.37%), a ratio of activators to FA (0.96%) and curing temperature (0.21%). The regression equations arrived with a high degree of accuracy can be utilized for the determination of the compressive strength of GPC with the considered parameters. The mix with 20% OPC, 14M NaOH, curing temperature 60ºC, curing time 36h, rest period 48h, AAs to FA ratio 0.3 and ratio of alkaline solutions 2 was found to have the maximum compressive strength.

5. ACKNOWLEDGMENT

The authors acknowledge the research facility provided by the Department of Civil Engineering, Karunya Institute of technology and sciences, Coimbatore, India for carrying out the research presented in this paper.

6. REFERENCES

1. E. Hache, M. Simoen, G.S. Seck, Bonnet, Clé, A. Jabberi, S. Carcanague, "The impact of future power generation on cement demand: An international and regional assessment based on climate scenarios", ***International Economics***, (2020), DOI: 10.1016/ j.inteco.2020.05.002.
2. D.K. Panesar, R. Zhang, "Performance comparison of cement replacing materials in concrete: Limestone fillers and supplementary cementing materials – A review", ***Construction and Building Materials***, Vol. 251, 118866, (2020). DOI: 10.1016/j.conbuildmat.2020.118866

3. L.K. Turner, F.G. Collins, "Carbon dioxide equivalent (CO_2-e) emissions: A comparison between geopolymer and OPC cement concrete", ***Construction and Building Materials***, Vol. 43, (2013), 125-130. DOI:10.1016/j.conbuildmat.2013.01.023
4. F. Delaram, Y. Mohammadi, M. R. Adlparvar, "Evaluation of the Combined Use of Waste Paper Sludge Ash and Nanomaterials on Mechanical Properties and Durability of High Strength Concretes", ***International Journal of Engineering, Transactions A: Basics***, Vol. 34, No. 7, (2021), 1653-1666. DOI: 10.5829/IJE.2021.34.07A.10
5. E. Sharifi, S.J. Sadjadi, M.R. Aliha, A. Moniri, "Optimization of high-strength self-consolidating concrete mix design using an improved Taguchi optimization method", ***Construction and Building Materials***, Vol. 236, (2020), 117547. DOI:10.1016/j.conbuildmat.2019.117547
6. T. Fantous, A. Yahia, "Effect of viscosity and shear regime on stability of the air-void system in self-consolidating concrete using Taguchi method", ***Cement and Concrete Composites***, 103653, (2020). DOI:10.1016/j.cemconcomp.2020.103653
7. H. Tanyildizi, M. Şahin, "Taguchi optimization approach for the polypropylene fiber reinforced concrete strengthening with polymer after high temperature", ***Structural and Multidisciplinary Optimization***, Vol. 55, No. 2, (2016), 529-534. DOI:10.1007/s00158-016-1517-z
8. B. Singh, G. Ishwarya, M. Gupta, S.K. Bhattacharyya, "Geopolymer concrete: A review of some recent developments", ***Construction and Building Materials***, Vol. 85, (2015), 78-90. DOI: 10.1016/j.conbuildmat.2015.03.036
9. Genichi Taguchi, S. Konishi, Y. Wu, "Taguchi methods: orthogonal arrays and linear graphs. Tools for quality engineering", ***Dearborn, Michigan: American Supplier Institute***, (1987).
10. M. A. Ahmed Al-dujaili, I. A. Disher Al-hydary, Z. Zayer Hassan, "Optimizing the Properties of Metakaolin-based (Na, K)-Geopolymer Using Taguchi Design Method", ***International Journal of Engineering, Transactions A: Basics***, Vol. 33, No. 4, (2020), 631-638. DOI: 10.5829/ije.2020.33.04a.14
11. C. Jithendra, S. Elavenil, "Effects of Parameters on Slump and Characteristic Strength of Geopolymer Concrete using Taguchi Method", ***International Journal of Engineering, Transactions C: Aspects***, Vol. 34, No. 03, (2021), 629-635. DOI**:** 10.5829/ije.2021.34.03c.06
12. M.N.S. Hadi, N.A. Farhan, M.N. Sheikh, "Design of geopolymer concrete with GGBFS at ambient curing condition using Taguchi method", ***Construction and Building Materials***, Vol. 140, (2017), 424-431. DOI:10.1016/j.conbuildmat.2017.02.131
13. A. Mehta, R. Siddique, B.P. Singh, S. Aggoun, G. Łagód, D. Barnat-Hunek, "Influence of various parameters on strength and absorption properties of fly ash based geopolymer concrete designed by Taguchi method", ***Construction and Building Materials***, Vol. 150, (2017), 817-824. DOI: 10.1016 /j. conbuildmat. 2017 . 06 . 066
14. H.K. Shehab, A.S. Eisa, A.M. Wahba, "Mechanical properties of fly ash based geopolymer concrete with full and partial cement replacement", ***Construction and Building Materials***, Vol. 126, (2016), 560-565. DOI: 10.1016/j.conbuildmat.2016.09.059
15. A.A. Aliabdo, A.E.M. Abd Elmoaty, H.A. Salem, "Effect of cement addition, solution resting time and curing characteristics on fly ash based geopolymer concrete performance", ***Construction and Building Materials***, Vol. 123, (2016), 581-593. DOI: 10.1016/j.conbuildmat.2016.07.043
16. A. Mehta, R. Siddique, "Properties of low-calcium fly ash based geopolymer concrete incorporating OPC as partial replacement of fly ash", ***Construction and Building Materials***, Vol. 150, (2017). 792-807. DOI:10.1016/j.conbuildmat.2017.06.067
17. L. Assi, S. Ghahari, E. Deaver, D. Leaphart, P. Ziehl, "Improvement of the early and final compressive strength of fly ash-based geopolymer concrete at ambient conditions", ***Construction and Building Materials***, Vol. 123, (2016), 806-813. DOI: 10.1016/j.conbuildmat.2016.07.069
18. M. Askarian, Z. Tao, G. Adam, B. Samali, "Mechanical properties of ambient cured one-part hybrid OPC-geopolymer concrete", ***Construction and Building Materials***, Vol. 186, (2018). 330-337. DOI: 10.1016/j.conbuildmat.2018.07.160
19. B.B. Jindal, "Investigations on the properties of geopolymer mortar and concrete with mineral admixtures: A review", ***Construction and Building Materials***, Vol. 227, (2019). DOI: 10.1016/j.conbuildmat.2019.08.025
20. P. Nath, P.K. Sarker, "Effect of GGBFS on setting, workability and early strength properties of fly ash geopolymer concrete cured in ambient condition", ***Construction and Building Materials***, Vol. 66, (2014), 163-171. DOI: 10.1016/j.conbuildmat.2014.05.080
21. C.D. Atiş, E.B. Görür, O. Karahan, C. Bilim, S. İlkentapar, E. Luga, "Very high strength (120MPa) class F fly ash geopolymer mortar activated at different NaOH amount, heat curing temperature and heat curing duration", ***Construction and Building Materials***, Vol. 96, (2015), 673-678. DOI: 10.1016/j.conbuildmat.2015.08.089
22. A.A. Aliabdo, A.E.M. Abd Elmoaty, H.A. Salem, "Effect of water addition, plasticizer and alkaline solution constitution on fly ash based geopolymer concrete performance", ***Construction and Building Materials***, Vol. 121, (2016), 694-703. DOI: 10.1016/j.conbuildmat.2016.06.062
23. Y.F. Cao, Z. Tao, Z. Pan, R. Wuhrer, "Effect of calcium aluminate cement on geopolymer concrete cured at ambient temperature", ***Construction and Building Materials***, Vol. 191, (2018), 242-252. DOI: 10.1016/j.conbuildmat.2018.09.204
24. M.N. Hadi, H. Zhang, S. Parkinson, "Optimum mix design of geopolymer pastes and concretes cured in ambient condition based on compressive strength, setting time and workability", ***Journal of Building Engineering*** Vol. 23, (2019), 301-313. DOI: 10.1016/j.jobe.2019.02.006.
25. S.V. Patankar, Y.M. Ghugal, S.S. Jamkar, "Mix design of fly ash based geopolymer concrete" ***In Advances in Structural Engineering***, (2015), 1619-1634. DOI: 10.1007/978-81-322-2187-6_123
26. A. Hassan, M. Arif, M. Shariq, "Effect of curing condition on the mechanical properties of fly ash-based geopolymer concrete" ***SN Applied Sciences***, Vol. 1, No. 12, (2019), 1694. DOI: 10.1007/s42452-019-1774-8.
27. Y. Ling, K. Wang, X. Wang, S. Hua, "Effects of mix design parameters on heat of geopolymerisation, set time, and compressive strength of high calcium fly ash geopolymer", ***Construction Building Material***, Vol. 228, (2019), 116763. DOI**:** 10.1016/j.conbuildmat.2019.116763.
28. D. P. Thanaraj, N. Anand, P. Arulraj, "Experimental investigation of mechanical properties and physical characteristics of concrete under standard fire exposure" ***Journal of Engineering, Design and Technology***, (2019), 878-903. DOI**:** 10.1108/jedt-09-2018-0159.
29. IS: 516-1959 (Reaffirmed -2004), "Method of tests for strength of concrete", Bureau of Indian Standards, New Delhi.
30. IS: 10262:2019, "*Concrete Mix proportioning Guidelines", New Delhi*.
31. D. Hardjito, C.C. Cheak, C.H. Lee Ing, "Strength and Setting Times of Low Calcium Fly Ash-based Geopolymer Mortar", ***Modern Applied Science***, Vol. 2, No. 4, (2008). DOI: 10.5539/mas.v2n4p3

Persian Abstract

چکیده

گرمایش جهانی یکی از اثرات شدید زیست محیطی است که نسل کنونی با آن روبرو شده است. مطالعات نشان می دهد که دی اکسید کربن (CO_2)عامل اصلی گرم شدن کره زمین است و عمدتا به دلیل تولید عظیم سیمان پرتلند معمولی (OPC)است. مواد سیمانی تکمیلی می تواند با کاهش مواد مورد نیاز به جای OPC برای اهداف ساختمانی ، این اثر را کاهش دهد. بتن Geopolymer (GPC) یک بتن نسل جدید است که نیازی به OPC ندارد. در این مطالعه از Fly Ash (FA) برای تولید GPC استفاده شد. پارامترهای مختلفی در نظر گرفته شد و طراحی آزمایش با استفاده از روش تاگوچی انجام شد و یک رابطه تجربی با پیش بینی مقاومت فشاری GPC بر اساس پارامترهای مختلف ایجاد کرد. سی و شش مخلوط برای تعیین تأثیر دمای عمل آوری ، زمان پخت ، دوره استراحت ، نسبت محلول های فعال کننده قلیایی (AA)، نسبت فعال کننده ها به FA ، مولار NaOH و سطح جایگزینی FA با OPC بر روی فشار مورد استفاده قرار گرفت. استحکام – قدرت. سهم هر پارامتر توسط ANOVA برآورد شد. نتایج نشان می دهد که افزودن OPC تأثیر قابل توجهی بر مقاومت فشاری GPC داشت. مخلوط با ۲۰٪ OPC، ۱۴ M NaOH ، دمای عمل آوری 60°C ، زمان پخت ۳۶ ساعت ، یک دوره استراحت ۴۸ ساعت ، نسبت AA به FA 0.3 و نسبت محلولهای قلیایی ۲.۵ دارای حداکثر مقاومت فشاری بود. یک معادله رگرسیونی برای تعیین مقاومت فشاری GPC در مورد پارامترهای مد نظر ایجاد شده است.

International Journal of Engineering

Journal Homepage: www.ije.ir

Any-time Randomized Kinodynamic Path Planning Algorithm in Dynamic Environments with Application to Quadrotor

E. Taheri*

Electrical Engineering Department, Malek Ashtar University of Technology, Tehran, Iran

P A P E R I N F O

Paper history:
Received 24 May 2021
Received in revised form 30 August 2021
Accepted 05 September 2021

Keywords:
Kinodynamic Path Planning
Rapidly-exploring Random Trees
Quadrotor
Collision Avoidance
Dynamic Obstacles

A B S T R A C T

Kinodynamic path planning is an open challenge in unmanned autonomous vehicles and is considered an NP-Hard problem. Planning a feasible path for vertical take-off and landing quadrotor (VTOL-Q) from an initial state to a target state in 3D space by considering the environmental constraints such as moving obstacles avoidance and non-holonomic constraints such as hard bounds of VTOL-Q is the key motivation of this study. To this end, let us propose the any-time randomized kinodynamic (ATRK) path-planning algorithm applicable in the VTOL-Q. ATRK path-planning algorithm is based on the Rapidly-exploring random trees (RRT) and consists of three main components: high-level, mid-level, and low-level controller. The high-level controller utilizes a randomized sampling-based approach to generate offspring vertices for rapid exploring and expanding in the configuration space. The mid-level controller uses the any-time method to avoid collision with moving obstacles. The low-level controller with a six-DOF dynamic model accounts for the kinodynamic constraints of VTOL-Q in the randomized offspring vertices to plan a feasible path. Simulation results on three different test-scenario demonstrate the kinodynamic constraints of the VTOL-Q are integrated into the randomized offspring vertices. Also, in presence of moving obstacles, the ATRK re-plans the path in the local area as through an any-time approach.

***doi**: 10.5829/ije.2021.34.10a.17*

NOMENCLATURE

$\eta = [\eta_1\ \eta_2]$	Quadrotor position and orientation in the E-frame.	M_B	System inertia matrix.
$v = [v_1\ v_2]$	Quadrotor linear and angular velocity in the B-frame.	C_B	Coriolis-centripetal matrix.
$J: R^6 \to R^{6\times 6}$	Coordinate transformation matrix relating the two frames.	$\Lambda = [f_B\ \ \tau B]^T$	Quadrotor force and torque.

1. INTRODUCTION

In the last decade, a dramatic interest has appeared in vertical take-off and landing quadrotors. In fact, these vehicles are already becoming a portion of everyday reality, especially in modern societies. Several huge potential domains for stakeholders such as surveillance and inspection, search and rescue, military and defence, civil, agriculture, payload delivery, environmental protection, etc. require these vehicles to perform special missions in unpredictable and time-variable situations [1-6]. Current status and future perspectives on the development of quadrotors were studied in literature [7, 8]. One of the standing problems in the field of quadrotor autonomy is the achievement of real-time guidance, navigation, and control (GNC) system. To meet the need for autonomy in the quadrotor, many public and private attempts are made with regard to the path planning issues in these vehicles. Path planning is defined as a vital requirement in autonomous robotics which is described by algorithms that transform high-level demand (mission) into low-level demand (movement) [9, 10]. Thanks to robotic science, the path planning problem has important applications in areas such as drug design, animation design, assist surgeons, graphics, games theory, virtual and augmented reality, very-large-scale

*Corresponding Author Institutional Email: taheri.ehsan@mut-es.ac.ir (E. Taheri)

Please cite this article as: E. Taheri, Any-time Randomized Kinodynamic Path Planning Algorithm in Dynamic Environments with Application to Quadrotor, International Journal of Engineering, Transactions A: Basics Vol. 34, No. 10, (2021), 2360-2370

integration (VLSI) design, etc. In this context, various studies conducted and number of methods have been proposed. Detailed articles survey were accomplished to define the current state of the art of path planning problem in literature [11-13]. For motion planning and autonomy subjects, numerous researches exist in different manuscripts and number of methods are being presented. The intelligent path planning method based on the artificial neural network for the quadrotor is proposed by Khosravian and Maghsoudi [14]. The position and attitude control with considering the under actuated constraints through the recurrent neural network based on non-linear PID is the main evolution of this study. Also, the path planning module is proposed in this paper as a high-level controller. The decentralized fuzzy adaptive sliding mode algorithm for the multi-quadrotor is proposed by Manouchehri et al. [15]. In this approach, affine nonlinear agents with nonlinear control gain are considered. The proposed method is used to plan the formation between a groups of quadrotors. Performance of this method is evaluated through the numerical simulation. Parameters of a target tracker robot are identified through the particle swarm optimization (PSO) algorithm by Sangdani and Tavakolpour-Saleh [16]. Motion equations of robot are described with considering flexible joints. For this purpose a non-linear spring and damper system are defined. Parameters of this system is identified and evaluated though the experimental results. A variable-step RRT* path planning algorithm is proposed for a quadrotor to increase the convergence rate and efficiency in a below-canopy environment [17]. A cost function is used in the variable-step RRT* to optimize the offspring vertices connection and the Bezier curve is utilized to smooth the path. Allen and Pavone [18] proposed a real-time path planning algorithm that is applied on a physical quadrotor operating in an indoor area. The proposed algorithm utilizes an offline-online computation procedure, a machine-learning approach, an optimal cost distance metric function, and trajectory smoothing to plan a path. A chaos-based logistic map is integrated with the particle swarm optimization algorithm to improve the path optimality for an autonomous unmanned aerial vehicle (UAV) [19]. The optimal controller is proposed by Mashadi et al. [20] for tracking the predefined path with application to the integrated driver/vehicle system. Controller parameters are designed through the LQR and GA algorithm. Hence, controller performance is appropriated in the various driving styles, road conditions and initial errors of vehicle position and orientation. The integrated driver/DYC control system is presented to overcome the vehicle path tracking problems with considering the vehicle active safety [21]. In this controller, the heading error and the lateral deviation between the real and desired path are received as inputs and then the steering angle and a direct yaw moment are designed as outputs. PID coefficients are optimized through the heuristic approach. Hence, the performance of the driver/DYC controller is acceptable on lane-change maneuvers, double-lane changes, J-turn and other desired tracks. Finally, Monte-Carlo simulation is utilized to assess the performance of this method. Gao et al. [22] introduced the path planning problem which is divided into front-end path searching and back-end path filtration.

The path is planned by the sampling-based informed method and the planned path is optimized through the penalty functions. This approach is implemented in a lightweight quadrotor platform and is evaluated in unknown cluttered indoor and outdoor workspaces. In, The optimal path planning algorithm was proposed by Heidari and Saska [23] for a quadrotor by considering various objective functions, such as energy efficiency. The necessary conditions of optimality are formulated here as a normal form of a two-point boundary-value problem using Pontryagin's minimum principle. The control forces were added into the artificial potential field (APF) to plan an optimal path for a quadrotor [24]. The slack variables in this paper are used to change the constrained optimization problem to an unconstrained problem. However, there are many various criteria to classify the path planning algorithms such as 1) complete algorithms, 2) probabilistic-complete algorithms, 3) deterministic algorithms, 4) randomized algorithms, 5) optimal algorithms, 6) suboptimal or asymptotically optimal algorithms, 7) global algorithms (map-based), 8) local algorithms (sensor-based), 9) real-time algorithms, 10) kinodynamic algorithms, etc. [25-30]. These path planning algorithms are developed through the three main groups of classical, heuristic, andmeta-heuristic [31]. Figure 1 illustrates classical algorithms including family of bug-based (Bug 1 & 2, I-Bug, K-bug, and Tangent-bug), roadmap-based, graph-based, cell decomposition-based, sampling-based, potentialfield-based, etc. Most of the classical algorithms are complete and deterministic. Hence, these are sensitive to parameter tuning and computational-complexity of them increase in the order O (n^2) by

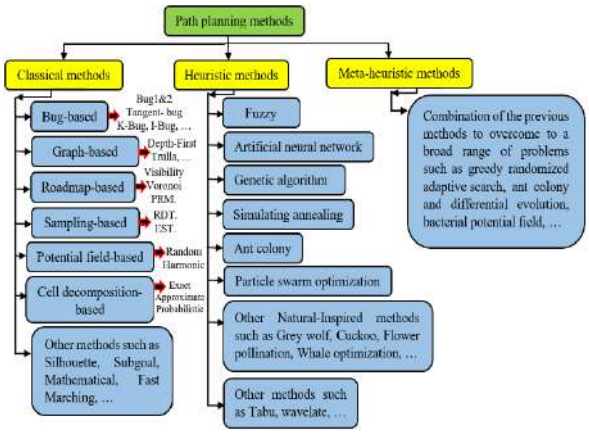

Figure 1. Classification of path planning methods

increasing the density of obstacles, workspace dimensions, numbers of kinodynamic constraints, etc. While this can be proved the most heuristic and meta-heuristic algorithms are probabilistic-complete.

Remark 1. Probabilistic-complete means that a probability of designing a path goes to one if one path exists and time goes to infinity.

Among the most path planning algorithms mentioned above, the external (kinematic) constraints are considered in the path planning procedure but the internal (differential) constraints are seldom considered. Thus they usually cannot be able to plan a feasible path. This challenge becomes harder when unknown or moving obstacles have appeared in the kinodynamic path planning problem. Also, computational and time complexity of the kinodynamic path planning problem increase in the order O (n^2) by increasing numbers of moving obstacles, kinodynamic constraints, degrees of freedoms, and C-space dimension. These challenges of real-time kinodynamic planning can be formulated into two questions that serve as the key motivation of this study.

Motivating Question 1. Can we propose an any-time path planning algorithm that takes into account both kinematics (moving obstacles avoidance) and dynamics (velocity and acceleration) constraints for VTOL-Q in a simultaneous manner?

Motivating Question 2. Given such a generalized method to kinodynamic path planning, can we utilize a randomized sampling-based approach to reduce the computational and time complexity of the problem?

In response to such motivating questions, this article proposes the any-time randomized kinodynamic (ATRK) path-planning algorithm here as the state-of-the-art in this field applicable in the VTOL-Q. In a nutshell, the main contributions of this article can be summarized as follows:

1) In the proposed ATRK path planning algorithm the reachability of each offspring vertex which is planned through the rapidly-exploring random trees (RRT) method is assessed to assure the quadrotor kinodynamic (kinematic and dynamic) constraints are considered in the planned path. Hence, both dynamic and kinematic (kinodynamic) constraints are integrated into the designed path and it's followed through the quadrotor properly.

2) In the proposed ATRK the randomized sampling-based approach is utilized to reduce the computational and time complexity of the problem. The search tree is expanded in the configuration space in a random manner here. In this way, the total number of vertices is reduced in the search tree compare to the conventional methods. It is worth to be mentioned that the computational and time complexity in the complete path planning algorithm increase in the order O (n^2) by increasing numbers of moving obstacles, kinodynamic constraints, degrees of freedoms, and C-space dimension.

3) The any-time reactive event-based method re-plans the path in the local areas to avoid collision with moving obstacles and prevents trapping the path in the local minima problem.

The rest of this manuscript is organized as follows: a brief background of the quadrotor dynamic model and sampling-based path planning algorithm is presented in section 2. The any-time randomized kinodynamic (ATRK) path-planning algorithm consists of three main components that are presented in section 3. These components are: high-level, mid-level, and low-level controller. Performance and effectiveness of the proposed path planning algorithm in presence of moving and unknown obstacles are assessed through the two different scenarios in section 4, and finally, the conclusion is given in section 5.

2. OVERVIEW OF QUADROTOR DYNAMIC AND SAMPLING-BASED ALGORITHM

2. 1. Quadrotor Kinematic and Dynamic

Typically, the structure of a quadrotor is rigid and symmetric, in which four rotors are attached at the ends of arms in a plus or cross-configurations. The desired forces and moments are generated on the quadrotor through the counter-clockwise rotating in front and back propellers (numbers 1 and 3 in Figure 2) and clockwise rotating in right and left propellers (numbers 2 and 4 in Figure 2). The Euler-Lagrange and Newton-Euler are conventional methods that are utilized to explain dynamics behaviours for a quadrotor [32-35]. Before explaining the dynamic model of a quadrotor, it is necessary to explain the reference frames and kinematic equations. Two reference frames are used to derive the

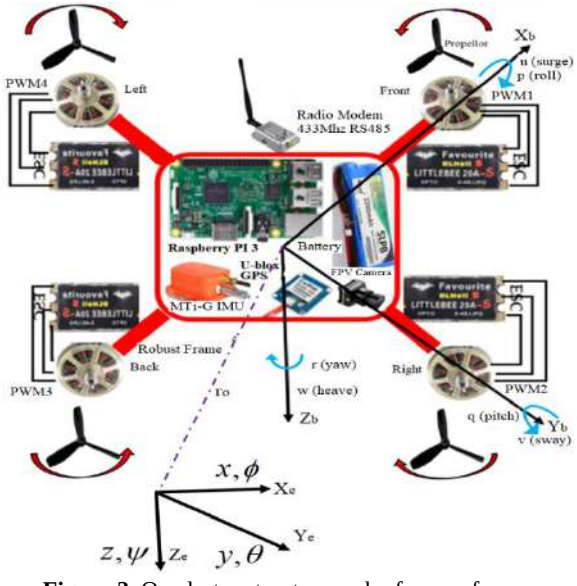

Figure 2. Quadrotor structure and reference frames

dynamic model (Figure 2): The fixed (Earth) frame (E-frame), the mobile (Body) frame (B-frame).

Six DOF are required in 3D-space to explain the quadrotor translation and rotation movement. The quadrotor position and orientation ($\eta \in R^6$) in the E-frame is presented by:

$$\eta = [\eta_1\ \eta_2] = (x, y, z, \\ \phi \in [-\pi, \pi], \theta \in [-\pi/2, \pi/2], \psi \in [-\pi, \pi]) \in R^6 \quad (1)$$

and the quadrotor linear and angular velocity ($v \in R^6$) in the B-frame is presented through the following vector:

$$v = [v_1\ v_2] = (u, v, w, p, q, r) \in R^6 \quad (2)$$

Quadrotor kinematic motion equations by considering the geometric aspects of motion are defined in the following form where J is $R^6 \to R^{6\times 6}$:

$$\dot{\eta} = J(\eta)v \to \begin{bmatrix} \dot{\eta}_1 \\ \dot{\eta}_2 \end{bmatrix} = \begin{bmatrix} J_1(\eta_2) & 0_{3\times 3} \\ 0_{3\times 3} & J_2(\eta_2) \end{bmatrix} \begin{bmatrix} v_1 \\ v_2 \end{bmatrix} \quad (3)$$

where, $\eta_1 \& \eta_2 \in R^3$ presents the position and orientation, and vectors $v_1 \& v_2 \in R^3$ presents the linear and angular velocities in the body coordinate system. Relation between the position and linear velocities is explained through the $J_1(\eta_2) = C_z(\psi).C_y(\theta).C_x(\phi) \in SO(3)$:

$$J_1(\eta_2) = \\ \begin{bmatrix} c\psi & -s\psi & 0 \\ s\psi & c\psi & 0 \\ 0 & 0 & 1 \end{bmatrix} \begin{bmatrix} c\theta & 0 & s\theta \\ 0 & 1 & 0 \\ -s\theta & 0 & c\theta \end{bmatrix} \begin{bmatrix} 1 & 0 & 0 \\ 0 & c\phi & -s\phi \\ 0 & s\phi & c\phi \end{bmatrix} = \\ \begin{bmatrix} c\psi c\theta & -s\psi c\phi + c\psi s\theta s\phi & s\psi s\phi + c\psi s\theta c\phi \\ s\psi c\theta & c\psi c\phi + s\psi s\theta s\phi & -c\psi s\phi + s\psi s\theta c\phi \\ -s\theta & c\theta s\phi & c\theta c\phi \end{bmatrix} \quad (4)$$

and the correlation between the orientation and angular velocities is defined through the $J_2(\eta_2)$:

$$J_2(\eta_2) = \begin{bmatrix} 1 & s\phi t\theta & c\phi t\theta \\ 0 & c\phi & -s\phi \\ 0 & s\phi/c\theta & c\phi/c\theta \end{bmatrix} \quad (5)$$

Consequently, the quadrotor kinematic motion is defined as below:

$$\dot{x} = w[s\phi s\psi + c\phi c\psi s\theta] - v[c\phi s\psi - c\psi s\phi s\theta] + \\ u[c\psi c\theta]\ \dot{y} = v[c\phi c\psi + s\phi s\psi s\theta] - w[c\psi s\phi - \\ c\phi s\psi s\theta] + u[c\theta s\psi]\ \dot{z} = w[c\phi c\theta] - u[s\theta] + \\ v[c\theta s\phi]\ \dot{\phi} = p + r[c\phi t\theta] + q[s\phi t\theta]\ \dot{\theta} = q[c\phi] - \\ r[s\phi]\ \dot{\psi} = r\frac{c\phi}{c\theta} + q\frac{s\phi}{c\theta} \quad (6)$$

Using the Newton-Euler equation, and by making the following assumptions: 1- The quadrotor frame is supposed to be rigid and symmetrical, 2- The centre of mass and the body-fixed frame origin are assumed to coincide, 3- The propellers are supposedly rigid, 4- Thrust and drag are proportional to the square of the propellers speed, 5- The dynamics of the rotors and propellers are negligible. 6- The inertia matrix (I) is diagonal, in other words, the axes of the B-frame coincide with the body principal axes of inertia, the dynamic model is written in the following form.

Newton's law and Euler's law are stated to explain the total forces and the total torques that are applied to the quadrotor:

$$Newton's\ law \Rightarrow m(v_2 \wedge v_1 + \dot{v}_1) = f_B \\ = [f_X f_Y f_Z]^T \in R^3 \\ Euler's\ law \Rightarrow I.\dot{v}_2 + v_2 \wedge (I.v_2) = \tau_B \\ = [\tau_X \tau_Y \tau_Z]^T \in R^3 \quad (7)$$

where m=2.1kg is the quadrotor mass,^ is the cross product,

$I = [I_{xx} = 0.00612 kg\,m^2, I_{yy} = 0.00612 kg\,m^2, \\ , I_{zz} = 0.0137 kg\,m^2]^T$

is the inertia matrix, f_B is the quadrotor force, and τ_B is the quadrotor torque. These equations are defined in the state-space in the following form:

$$\begin{bmatrix} mI_{3\times 3} & 0_{3\times 3} \\ 0_{3\times 3} & I \end{bmatrix} \begin{bmatrix} \dot{v}_1^B \\ \dot{v}_2^B \end{bmatrix} + \begin{bmatrix} v_2^B \times (mv_1^B) \\ v_2^B \times (Iv_2^B) \end{bmatrix} = \begin{bmatrix} f_B \\ \tau_B \end{bmatrix} \quad (8)$$

The dynamic model is described in a matrix form:

$$M_B \dot{v} + C_B(v)v = \Lambda = \begin{bmatrix} f_B & \tau B \end{bmatrix}^T \\ M_B = \begin{bmatrix} mI_{3\times 3} & 0_{3\times 3} \\ 0_{3\times 3} & I \end{bmatrix}, C_B = \begin{bmatrix} 0_{3\times 3} & -mS(v_1^B) \\ 0_{3\times 3} & S(Iv_2^B) \end{bmatrix} \quad (9)$$

where M_B is the diagonal and constant system inertia matrix, C_B is the Coriolis-centripetal matrix which is tabulated in Table 1. S (.) is the skew-symmetric operator which is defined as below:

$$S(k) = -S^T(k) = \begin{bmatrix} 0 & -k_3 & k_2 \\ k_3 & 0 & -k_1 \\ -k_2 & k_1 & 0 \end{bmatrix} \quad (10)$$

Inertia and Coriolis-centripetal matrix are defined as bellow:

TABLE 1. Quadrotor Parameters of dynamic model

$m = 2.1kg$	$b = 3.21\times 10^{-5} kg\,m^2$
$I_{xx} = I_{yy} = 0.00612 kg\,m^2$	$d = 6.45\times 10^{-7} kg\,m^2$
$I_{zz} = 0.0137 kg\,m^2$	l=0.2m
$J_r = 1.23\times 10^{-5} kg m^2$	g=9.81 $m\,s^{-2}$

$$M_B=\begin{bmatrix}2.1&0&0&0&0&0\\0&2.1&0&0&0&0\\0&0&2.1&0&0&0\\0&0&0&0.00612&0&0\\0&0&0&0&0.00612&0\\0&0&0&0&0&0.0137\end{bmatrix}$$

$$C_B=\begin{bmatrix}0&0&0&0&2.1w&-2.1v\\0&0&0&-2.1w&0&2.1u\\0&0&0&2.1v&-2.1u&0\\0&0&0&0&0.0137r&-0.00612q\\0&0&0&-0.0137r&0&0.00612p\\0&0&0&0.00612q&-0.00612p&0\end{bmatrix} \quad (11)$$

$\Lambda=\begin{bmatrix} f_B & \tau B\end{bmatrix}^T$ in the quadrotor (Equation (9)) consists of three components:

$$\begin{aligned}&\Lambda=G_B(\eta)+O_B(v)\Omega+E_B\Omega^2\\&\Omega^{Overall}=-\Omega_1^{front}+\Omega_2^{right}-\Omega_3^{back}+\Omega_4^{left}\\&\Omega=[\Omega_1,\Omega_2,\Omega_3,\Omega_4]^T\end{aligned} \quad (12)$$

where $\Omega(rad_S{}^{-1})$ is the propellers speed, G_B is the gravitational force that is generated due to the gravitational acceleration,

$$G_B(\eta)=\begin{bmatrix}mgs\theta,-mgc\theta s\phi,-mgc\theta s\phi,0,0,0\end{bmatrix}^T \quad (13)$$

O_B is the gyroscopic torque that is produced due to the propeller rotation (overall rotors speed is an imbalance or the quadrotor has the roll or pitch),

$$O_B(v)=J_{TP}\begin{bmatrix}0&0&0&0\\0&0&0&0\\0&0&0&0\\q&-q&q&-q\\-p&p&-p&p\\0&0&0&0\end{bmatrix} \quad (14)$$

$J_{TP}[NmS^2]\rightarrow total\ inertia\ of\ rotors$

and E_B is the main forces and torques that the $l(m)$ is the distance between the centre of the quadrotor mass and the centre of any propeller, the $d(kg\,m^2)$ is drag factor, and the $b(kg\,m^2)$ is thrust factor.

$$E_B=\begin{bmatrix}0&0&0&0\\0&0&0&0\\b&b&b&b\\0&-bl&0&bl\\-bl&0&bl&0\\-d&d&-d&d\end{bmatrix} \quad (15)$$

From Equations (9) and (12) it is possible to write:

$$\dot{v}=M_B^{-1}(-C_B(v)v+G_B(\xi)+O_B(v)\Omega+E_B\Omega^2) \quad (16)$$

The quadrotor dynamic in the body frame is defined as follows:

$$\begin{aligned}&\dot{u}=(vr-wq)+gs\theta\\&\dot{v}=(wp-ur)-gc\theta s\phi\\&\dot{w}=(uq-vp)-gc\theta s\phi+\frac{U_1}{m}\\&\dot{p}=\frac{I_{yy}-I_{zz}}{I_{xx}}qr-\frac{J_{TP}}{I_{xx}}q\Omega+\frac{U_2}{I_{xx}}\\&\dot{q}=\frac{I_{zz}-I_{xx}}{I_{yy}}pr+\frac{J_{TP}}{I_{yy}}p\Omega+\frac{U_3}{I_{yy}}\\&\dot{r}=\frac{I_{xx}-I_{yy}}{I_{zz}}pq+\frac{U_4}{I_{zz}}\end{aligned} \quad (17)$$

The control signal $U=\begin{bmatrix}U_1,U_2,U_3,U_4\end{bmatrix}^T\in R^4$ is defined as below:

$$\begin{aligned}&U_1=b(\Omega_1^2+\Omega_2^2+\Omega_3^2+\Omega_4^2)\\&U_2=lb(-\Omega_2^2+\Omega_4^2)\\&U_3=lb(-\Omega_1^2+\Omega_3^2)\\&U_4=d(-\Omega_1^2+\Omega_2^2-\Omega_3^2+\Omega_4^2)\end{aligned} \quad (18)$$

By Equations (17) and (4) the dynamic model in hybrid-frame (linear equations in the E-frame and angular equations in the B-frame) is possible to write:

$$\begin{aligned}&\ddot{x}=(s\psi s\phi+c\psi s\theta c\phi)\frac{U_1}{m}\\&\ddot{y}=(-c\psi s\phi+s\psi s\theta c\phi)\frac{U_1}{m}\\&\ddot{z}=-g+(c\theta c\phi)\frac{U_1}{m}\\&\dot{p}=\frac{I_{yy}-I_{zz}}{I_{xx}}qr-\frac{J_{TP}}{I_{xx}}q\Omega+\frac{U_2}{I_{xx}}\\&\dot{q}=\frac{I_{zz}-I_{xx}}{I_{yy}}pr+\frac{J_{TP}}{I_{yy}}p\Omega+\frac{U_3}{I_{yy}}\\&\dot{r}=\frac{I_{xx}-I_{yy}}{I_{zz}}qp+\frac{U_4}{I_{zz}}\end{aligned} \quad (19)$$

Remark 2. If the rotation movement in the quadrotor is achieved with the small angles, the dynamic model (Equation (19)) can be more simplified. That is to say, the dot product between the angular velocities and the inertia of each rotor are negligible.

2. 2. Sampling-based Path Planning Algorithms

Sampling-based path planning algorithms have been proposed since late 90s for NP-hard problems in the high-dimensional workspace and for high-degree-of-freedom robots that are out of reach for deterministic, complete methods [36-38]. The Rapidly-exploring random trees (RRT) is one of the most famous and most studied algorithms for sampling-based path planning issue. The RRT is able to apply the robot's dynamics in the path

planning procedure. Also, due to the randomized nature of RRT, the computational and time complexity of the problem are reduced. In a nutshell, RRT is a simple and fast method which is appropriate for real-time and kinodynamic applications.

Remark 3. Here, the kinodynamic term means that both kinematics and dynamics (velocity and acceleration) constraints are taken into account during the path planning procedure in a simultaneous manner. Hence, the planned path through this method is feasible (flyable) for the VTOL-Q. Also, the any-time term means that the quality of initial path improves during the planning time remains. Hence, the VTOL-Q can be avoid collision by unknown or moving obstacles in the local area.

Algorithm 1: The pseudo-code of the standard RRT

1: $(x, x_{free}) \leftarrow$ Configuration/Free space
2: $V \leftarrow \{q_{ini}, q_{goal}\}$
3: $E \leftarrow \{\emptyset\}$
4: $R(V,E) \leftarrow$ Search Tree
5: $(N, \beta) \leftarrow$ Max. number of iteration and threshold of goal vertex.
6: $R_c \leftarrow L^2 norm(q_{goal}, q_{new})$
7: **while** $i < N$ **and** $R_c \geq \beta$ **do**
8: $q_{rand} \leftarrow$ The random sampling is generated through the function number 1 (x_{free}).
9: $V_{near} \leftarrow$ The best candidate parent vertices are determined through the function # 3.
10: $q_{parent} \leftarrow$ The parent vertex is determined through the function number 2. $\triangleright$ $byEq.(20)$.
11: $[q_{new}, \Im] \leftarrow$ The edge and new vertex are generated through the function # 4.
12: **if** $(q_{new}, \Im)$ located in x_{free} **then** $\triangleright$ $byFun.\#5$
13: $V \leftarrow \{V \bigcup q_{new}\}$
14: $E \leftarrow \{E \cup \Im\}$
15: $R \leftarrow$Update(R)
16: **endif**
17: $R_c \leftarrow$ Update (R_c)
18: **endwhile**

Standard RRT framework consists of five main components: 1) Sampling function, 2) Metric function, 3) Branch function, 4) Neighbors function and 5) Collision detection function which are introduced briefly as follows [31]:

1- Sampling function: Random offspring vertices (q_{rand}) are generated by this function to expanding the search tree $R(V,E)$ in the configuration space. Where, (R) is the search tree in free space $C_{free} = C / C_{obstacle}$, (E) is the set of tree edges, and (V) is the set of tree vertices. The random offspring vertices can be guided toward the goal state by adding bias, bridge test, M-Line axis, boundary layer, or other techniques.

2- Metric function: The performance of this function can have a significant influence on the path planning ability. The various strategies are defined: Manhattan, Chessboard, Weighted Euclidean, Adaptive, Diagonal, etc. The metric function (γ) is defined as follows:

$$\gamma(q_{rand}) = g(q_{\text{int}}, q_{parent}) + h(q_{parent}, q_{rand}) \quad (20)$$

3- Neighbors function: This function receives the (q_{rand}) and $\gamma(q_{rand})$ as inputs and determines a subset of the best candidate vertices (Vnear⊂V) among the all available vertices of the search tree (V).

4- Branch function: This function receives the (q_{rand}) and (q_{parent}), then plans an edge $(\Im)$ as an output. If the random offspring vertex is out of reach for the search tree, the new vertex is generated.

5- Collision detection function: The output of the sampling (q_{rand}) and branch functions $(q_{new}, \Im)$ are assessed through this function for located in the free configuration space (c_{free}). The pseudo-code of the standard RRT is presented in Algorithm 1 and also the concept of this is illustrated in Figure 3 [9].

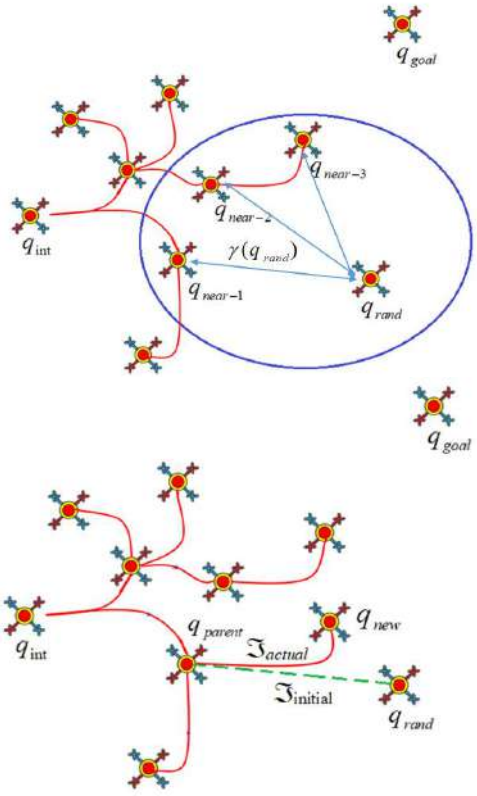

Figure 3. Conceptual representation of RRT path planning algorithm

3. PROPOSED ANY-TIME RANDOMIZED KINODYNAMIC (ATRK) PATH-PLANNING

Here, the ATRK path planning algorithm is proposed to increase the autonomy level in the considered VTOL-Q. The ATRK utilizes the randomized sampling-based method to reduce the time complexity of the path planning problem. By reducing the time complexity, the ATRK is able to rapid re-plan the path in the local areas to avoid collision with moving obstacles. Furthermore, the ATRK integrates both kinematic and dynamic constraints of VTOL-Q in the generated vertices. So, the planned path is feasible for the VTOL-Q. ATRK consists of three main components: high-level, mid-level, and low-level controller which are introduced as follows.

3. 1. High-level Controller The high-level controller utilizes the RRT approach to generate offspring vertices for rapid exploring and expanding in the configuration space. For this purpose, in each iteration, the high-level controller receives several initial parameters such as the configuration space, mission requirements, terminate condition and etc. and then generated a set of vertex and edge in a random manner. In this way, the search tree is expanded in the configuration space until the VTOL-Q reaches the target state threshold. The feasibility of each vertex and edge in the search tree for the VTOL-Q is assessed through the low-level controller as follows, (lines 8-11 Algorithm 2).

3. 2. Low-level Controller The Low-level controller with a six-DOF dynamic model integrates the kinodynamic constraints of VTOL-Q in the randomized offspring vertices to plan a feasible path. The offspring vertices in the low-level controller are converted to the desired references and the control signal is computed to apply to the rotors, (lines 15-16 Algorithm 2). A discrepancy between the output of the high-level controller $\left[q_{new}, \Im\right]$ and the output of the low-level controller $\left[q_{Flyable}, \Im_{Flyable}\right]$ is appeared due to either motion constraints or insufficient time.

3. 3. Mid-level Controller The mid-level controller uses the any-time reactive method to avoid collision with moving obstacles. For this purpose, first, the collision point (CP) and local goal (LG) are determined, then the local search tree is expanded from the current location of VTOL-Q to the LG. The local search tree in comparison to the initial search tree has high priority.

4. TEST-CASES

Performance and effectiveness of the proposed path planning algorithm are evaluated through the three different scenarios as follows:

Scenario 1: It is assumed that the configuration space in the first test-case is a narrow passage in, Figure 4(a) and is a maze-shaped space in, Figure 4(b).

Algorithm 2: Proposed ATRK

1: $(x, x_{free}) \leftarrow$ Configuration/Free space
2: $V \leftarrow \{q_{ini}, q_{goal}\}$
3: $E \leftarrow \{\emptyset\}$
4: $R(V, E) \leftarrow$ Search Tree
5: $(N, \beta) \leftarrow$ Max. number of iteration and threshold of goal vertex.
6: $R_c \leftarrow L^2 norm(q_{goal}, q_{new})$
7: **while** $i < N$ **and** $R_c \geq \beta$ **do**
8: $q_{rand} \leftarrow$ The random sampling is generated through the function number 1 (x_{free}).
9: $V_{near} \leftarrow$ The best candidate parent vertices are determined through the function number 3.
10: $q_{parent} \leftarrow$ The parent vertex is determined through the function number 2. $\triangleright$ $byEq.(20)$.
11: $\left[q_{new}, \Im\right] \leftarrow$ The edge and new vertex are generated through the function # 4.
12: **if** $(q_{new}, \Im)$ located in x / x_{free} **then**
13: go to line 8
14: **else**
15: $\left[U_1, U_2, U_3, U_4\right] \leftarrow Low-level\ controller(q_{parent}, q_{new}, \Im)$
16: $\left[q_{Flyable}, \Im_{Flyable}\right] \leftarrow 6DoF \bmod el\left[U_1, U_2, U_3, U_4\right]$ $\triangleright$ $byEq.(19)$
17: **endif**
18: **if** $(q_{Flyable}, \Im_{Flyable})$ located in x_{free} **then**
19: $V \leftarrow \{V \bigcup q_{Flyable}\}$
20: $E \leftarrow \{E \cup \Im_{Flyable}\}$
21: $R \leftarrow$Update(R)
22: **endif**
23: $R_c \leftarrow$ Update (R_c)
24: **endwhile**

Scenario 2: It is assumed that the configuration space in the second test-case is a cluttered space with two unknown static obstacles.

Scenario 3: It is assumed that the configuration space in the third test-case is a cluttered space with four unknown moving obstacles.

Remark 4. The results are performed on MATLAB software, which is fitted with an ASUS laptop comprising a Core i7 CPU with 16 GB of RAM and a 256 GB SSD.

The following results are summarized from Figures 4-6: In the first scenario position of all obstacles are known for VTOL-Q. However, two different test-case with different complexity (narrow passage and a maze-shaped space) are considered to path planning.

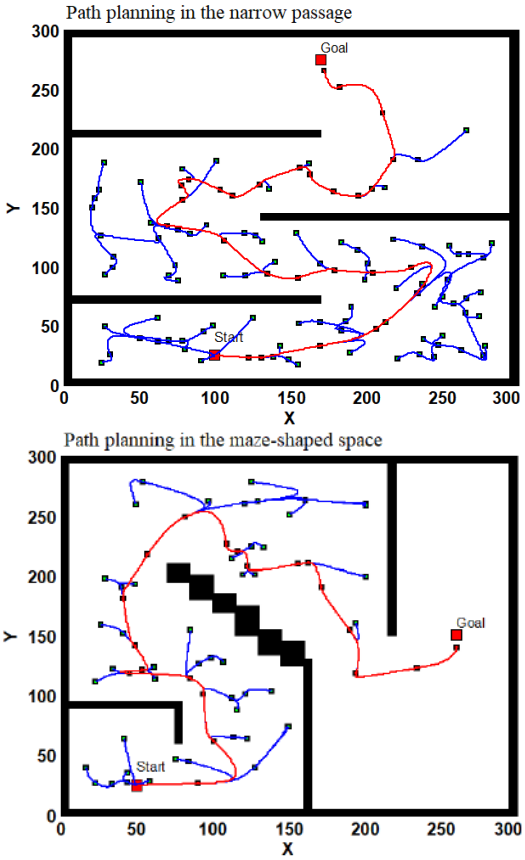

Figure 4. VTOL-Q path planning through the ATRK algorithm in the narrow passage and a maze-shaped space. It is assumed that the all obstacles position are known in the scenario #1

The ATRK path planning algorithm plans a path in the both configuration space by considering kinodynamic constraints of VTOL-Q, (lines 15-16 Algorithm 2).

Hence the planned path is feasible and VTOL-Q tracks the path. In the second scenario, the VTOL-Q detects pre-unknown obstacles during the planned path. In order to avoid collision with them, the collision point (CP) and local goal (LG) are determined. Then the local search tree is expanded from the current location of VTOL-Q to the LG. The VTOL-Q re-plans the path to avoid collision by the first unknown obstacle in the local area. Nevertheless, in the presence of the second unknown obstacle, the VTOL-Q could not reach the first local goal; hence the second local goal is planned. In the third scenario, four moving obstacles are considered which are depicted by a-d in Figure 6. The VTOL-Q predicts collision point by the moving obstacle #b, (lines 12-13 Algorithm 2). Hence re-plans the path in the local area. In a nutshell, path planning through the proposed any-time randomized kinodynamic (ATRK) path planning algorithm in the two types of static known environment with different complexities: 1-narrow passage, and 2-maze-like space is considered in the first scenario and their results are shown in Figure 4 a & b.

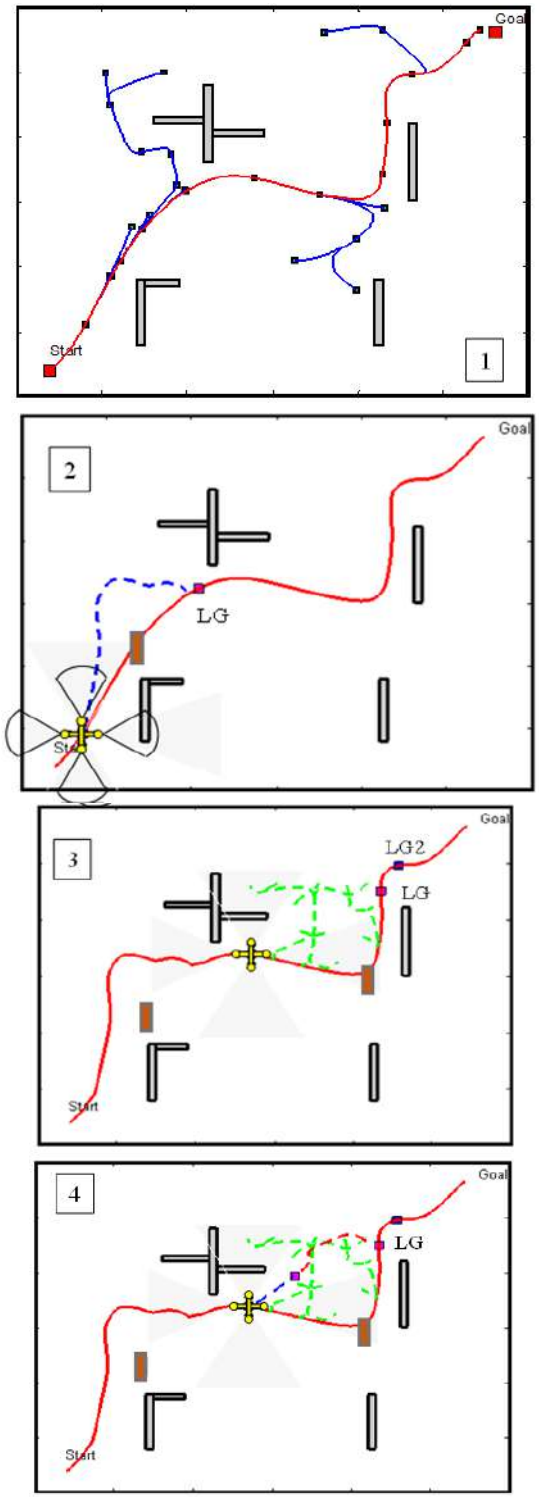

Figure 5. VTOL-Q path planning through the ATRK algorithm in presence pre-unknown static obstacles, (scenario #2)

In both configuration space, the initially planned path is illustrated through the blue line and the optimized path with the triangular inequality is illustrated through the red line. The number of the vertices (waypoints) in the

final path (red path) with the triangular inequality is reduced in comparison with the initial path (blue path). Due to the randomized nature of the proposed ATRK the optimized path is sub-optimal. Path planning through the proposed ATRK in the unknown static configuration space is considered in the second scenario. Its related results are shown in Figure 5. The local search tree with green edges is shown in this scenario to avoid collision by the unknown static obstacles. In the third scenario, four unknown moving obstacles are considered in the simulations. Moving obstacles #b has collided with the initially planned path. Hence, the initial path is re-planed in the local area that is shown by the blue edges in Figure 6. Furthermore, the features of proposed ATRK are compared with the standard RRT in Table 2.

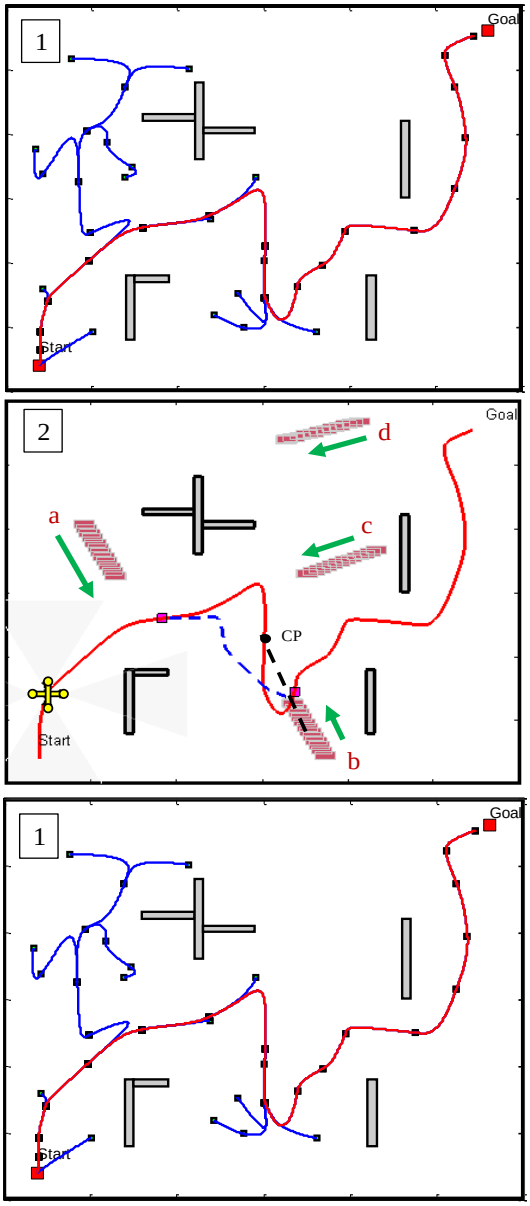

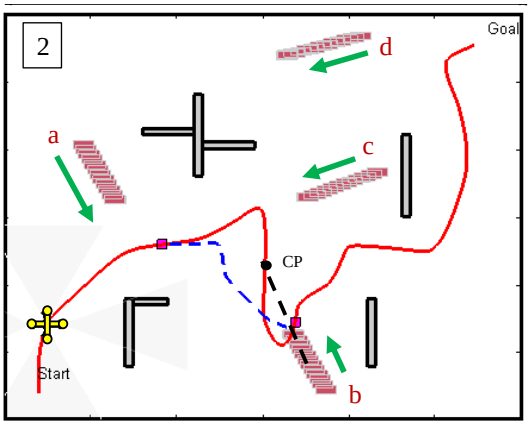

Figure 6. VTOL-Q path planning through the ATRK algorithm in presence pre-unknown moving obstacles, (scenario #3)

TABLE 2. Comparison of the proposed ATRK with the standard RRT

Features	Standard RRT	Proposed ATRK
Execution time and Memory consumption	High	Low
Path optimality	Non-optimal	Sub-optimal
Type of Constraints	Kinematic	Kinodynamic
Training and query phases	Offline-Offline	Offline- Online
Type of Obstacles	Known- Static	Unknown-Moving
Total number of vertices in the search tree	High	Low

5. CONCLUSION

This paper focuses on the study of an any-time kinodynamic path planning framework to plan a feasible path for a VTOL-Q by considering both kinematic and dynamic constraints in the presence of pre-unknown moving obstacles. To this end, let us propose the any-time randomized kinodynamic (ATRK) path-planning algorithm applicable in the VTOL-Q, (Algorithm #2). ATRK path-planning algorithm is based on the RRT and consists of three main components: high-level, mid-level, and low-level controller. The high-level controller utilizes a randomized sampling-based approach to generate offspring vertices for rapid exploring and expanding in the configuration space, (lines 8-11 Algorithm #2). The mid-level controller uses the any-time method to avoid collision with moving obstacles. Low-level controller with a six-DOF dynamic model accounts for the kinodynamic constraints of VTOL-Q in the randomized offspring vertices to plan a feasible path, (lines 15-16 Algorithm #2). In some cases, a discrepancy between the output of the high-level controller and the

output of the low-level controller is appeared due to either motion constraints or insufficient time. Simulation results on three different scenarios demonstrate the kinodynamic constraints of the VTOL-Q are integrated into the randomized offspring vertices, hence the proposed ATRK path-planning algorithm is able to plan a feasible path, and the VTOL-Q tracks the planned path appropriately. Also, in presence of moving obstacles, the ATRK re-plans the path in the local areas through the any-time approach. The local search tree in comparison to the initial search tree has a high priority to execute. In a nutshell, the ATRK in all three scenarios is able to integrate the kinodynamic constraints of VTOL-Q in the randomized offspring vertices. Furthermore, the local search trees are expanded in the local areas through the any-time method to avoid collision by moving obstacles.

6. REFERENCES

1. Campana, S., "Drones in archaeology. State-of-the-art and future perspectives", ***Archaeological Prospection***, Vol. 24, No. 4, (2017), 275-296, https://doi.org/10.1002/arp.1569.
2. Yang, K., Keat Gan, S. and Sukkarieh, S., "A gaussian process-based rrt planner for the exploration of an unknown and cluttered environment with a uav", ***Advanced Robotics***, Vol. 27, No. 6, (2013), 431-443, https://doi.org/10.1080/01691864.2013.756386.
3. Pizetta, I.H.B., Brandão, A.S. and Sarcinelli-Filho, M., "Avoiding obstacles in cooperative load transportation", ***ISA Transactions***, Vol. 91, (2019), 253-261, https://doi.org/10.1016/j.isatra.2019.01.019.
4. da Silva, M.F., Honorio, L.M., Marcato, A.L.M., Vidal, V.F. and Santos, M.F., "Unmanned aerial vehicle for transmission line inspection using an extended kalman filter with colored electromagnetic interference", ***ISA Transactions***, Vol. 100, (2020), 322-333, https://doi.org/10.1016/j.isatra.2019.11.007.
5. Shobeiry, P., Xin, M., Hu, X. and Chao, H., "Uav path planning for wildfire tracking using partially observable markov decision process", in AIAA Scitech 2021 Forum. (2021), 1677, https://doi.org/10.2514/6.2021-1677.
6. Mohammed, H., Romdhane, L. and Jaradat, M.A., "Rrt*n: An efficient approach to path planning in 3d for static and dynamic environments", ***Advanced Robotics***, Vol. 35, No. 3-4, (2021), 168-180, https://doi.org/10.1080/01691864.2020.1850349.
7. Floreano, D. and Wood, R.J., "Science, technology and the future of small autonomous drones", ***Nature***, Vol. 521, No. 7553, (2015), 460-466, https://doi.org/10.1038/nature14542.
8. Villasenor, J., "“Drones” and the future of domestic aviation [point of view]", ***Proceedings of the IEEE***, Vol. 102, No. 3, (2014), 235-238, DOI: 10.1109/JPROC.2014.2302875.
9. Taheri, E., Ferdowsi, M.H. and Danesh, M., "Closed-loop randomized kinodynamic path planning for an autonomous underwater vehicle", ***Applied Ocean Research***, Vol. 83, (2019), 48-64, https://doi.org/10.1016/j.apor.2018.12.008.
10. Barraquand, J., Langlois, B. and Latombe, J.-C., "Numerical potential field techniques for robot path planning", ***IEEE Transactions on systems, Man, and Cybernetics***, Vol. 22, No. 2, (1992), 224-241, DOI: 10.1109/21.148426.
11. Cabreira, T., Brisolara, L. and Ferreira Jr, P.R., "Survey on coverage path planning with unmanned aerial vehicles", ***Drones***, Vol. 3, No. 1, (2019), https://doi.org/10.3390/drones3010004.
12. Rubí, B., Pérez, R. & Morcego, B., "A survey of path following control strategies for uavs focused on quadrotors", ***Journal of Intelligent & Robotic Systems***, Vol. 98, No. 2, (2020), 241–265, https://doi.org/10.1007/s10846-019-01085-z.
13. Heidari, H. and Saska, M., "Trajectory planning of quadrotor systems for various objective functions", ***Robotica***, Vol. 39, No. 1, (2021), 137-152, https://doi.org/10.1017/S0263574720000247.
14. Khosravian, E. and Maghsoudi, H., "Design of an intelligent controller for station keeping, attitude control, and path tracking of a quadrotor using recursive neural networks", ***International Journal of Engineering, Transactions B: Applications***, Vol. 32, No. 5, (2019), 747-758. doi: 10.5829/ije.2019.32.05b.17
15. Manouchehri, P., Ghasemi, R. and Toloei, A., "Distributed fuzzy adaptive sliding mode formation for nonlinear multi-quadrotor systems", ***International Journal of Engineering, Transactions B: Applications***, Vol. 33, No. 5, (2020), 798-804, DOI: 10.5829/IJE.2020.33.05B.11.
16. Sangdani, M. and Tavakolpour-Saleh, A., "Particle swarm optimization based parameter identification applied to a target tracker robot with flexible joint", ***International Journal of Engineering, Transactions C: Aspects***, Vol. 33, No. 9, (2020), 1797-1802, DOI: 10.5829/IJE.2020.33.09C.14.
17. Liu, B., Feng, W., Li, T., Hu, C. and Zhang, J., "A variable-step rrt* path planning algorithm for quadrotors in below-canopy", ***IEEE Access***, Vol. 8, (2020), 62980-62989, DOI: 10.1109/ACCESS.2020.2983177.
18. Allen, R.E. and Pavone, M., "A real-time framework for kinodynamic planning in dynamic environments with application to quadrotor obstacle avoidance", ***Robotics and Autonomous Systems***, Vol. 115, (2019), 174-193, https://doi.org/10.1016/j.robot.2018.11.017.
19. Shao, S., Peng, Y., He, C. and Du, Y., "Efficient path planning for uav formation via comprehensively improved particle swarm optimization", ***ISA Transactions***, Vol. 97, (2020), 415-430, https://doi.org/10.1016/j.isatra.2019.08.018.
20. Mashadi, B., Mahmoodi-K, M., Kakaee, A.H. and Hosseini, R., "Vehicle path following control in the presence of driver inputs", ***Proceedings of the Institution of Mechanical Engineers, Part K: Journal of Multi-body Dynamics***, Vol. 227, No. 2, (2013), 115-132, https://doi.org/10.1177/1464419312469755.
21. Mashadi, B., Mahmoudi-Kaleybar, M., Ahmadizadeh, P. and Oveisi, A., "A path-following driver/vehicle model with optimized lateral dynamic controller", ***Latin American Journal of Solids and Structures***, Vol. 11, No. 4, (2014), 613-630, https://doi.org/10.1590/S1679-78252014000400004.
22. Gao, F., Lin, Y. and Shen, S., "Gradient-based online safe trajectory generation for quadrotor flight in complex environments", in 2017 IEEE/RSJ international conference on intelligent robots and systems (IROS), IEEE. (2017), 3681-3688, DOI: 10.1109/IROS.2017.8206214.
23. Heidari, H. and Saska, M., "Trajectory planning of quadrotor systems for various objective functions", ***Robotica***, Vol. 39, No. 1, (2020), 137-152, https://doi.org/10.1017/S0263574720000247.
24. Chen, Y.-b., Luo, G.-c., Mei, Y.-s., Yu, J.-q. and Su, X.-l., "Uav path planning using artificial potential field method updated by optimal control theory", ***International Journal of Systems Science***, Vol. 47, No. 6, (2016), 1407-1420, https://doi.org/10.1080/00207721.2014.929191.
25. Frazzoli, E., Dahleh, M.A. and Feron, E., "Real-time motion planning for agile autonomous vehicles", ***Journal of Guidance, Control, and Dynamics***, Vol. 25, No. 1, (2002), 116-129, https://doi.org/10.2514/2.4856.
26. Gong, W., "Probabilistic model based path planning", ***Physica A: Statistical Mechanics and its Applications***, (2021), 125718, https://doi.org/10.1016/j.physa.2020.125718.

27. Le, A.V., Arunmozhi, M., Veerajagadheswar, P., Ku, P.-C., Minh, T.H.Q., Sivanantham, V. and Mohan, R.E., "Complete path planning for a tetris-inspired self-reconfigurable robot by the genetic algorithm of the traveling salesman problem", ***Electronics***, Vol. 7, No. 12, (2018), 344, https://doi.org/10.3390/electronics7120344.

28. Zheng, S. and Liu, H., "Improved multi-agent deep deterministic policy gradient for path planning-based crowd simulation", ***IEEE Access***, Vol. 7, (2019), 147755-147770, DOI: 10.1109/ACCESS.2019.2946659.

29. Kimmel, A., Shome, R. and Bekris, K., "Anytime motion planning for prehensile manipulation in dense clutter", ***Advanced Robotics***, Vol. 33, No. 22, (2019), 1175-1193, https://doi.org/10.1080/01691864.2019.1690207.

30. Wang, W., Xu, X., Li, Y., Song, J. and He, H., "Triple rrts: An effective method for path planning in narrow passages", ***Advanced Robotics***, Vol. 24, No. 7, (2010), 943-962, https://doi.org/10.1163/016918610X496928.

31. Taheri, E., Ferdowsi, M.H. and Danesh, M., "Fuzzy greedy rrt path planning algorithm in a complex configuration space", ***International Journal of Control, Automation and Systems***, Vol. 16, No. 6, (2018), 3026-3035, https://doi.org/10.1007/s12555-018-0037-6.

32. Bouabdallah, S., Noth, A. and Siegwart, R., "Pid vs lq control techniques applied to an indoor micro quadrotor", in 2004 IEEE/RSJ International Conference on Intelligent Robots and Systems (IROS) (IEEE Cat. No.04CH37566). Vol. 3, (2004), 2451-2456 vol.2453, DOI: 10.1109/IROS.2004.1389776.

33. Bresciani, T., "Modelling, identification and control of a quadrotor helicopter", ***M. Sc. Thesis***, Vol., No. 0280-5316, (2008), http://lup.lub.lu.se/student-papers/record/8847641.

34. Sabatino, F., "Quadrotor control: Modeling, nonlinearcontrol design, and simulation", KTH, School of Electrical Engineering (EES), Automatic Control., (2015), http://urn.kb.se/resolve?urn=urn:nbn:se:kth:diva-175380.

35. Das, A., Lewis, F. and Subbarao, K., "Dynamic inversion with zero-dynamics stabilisation for quadrotor control", ***IET Control Theory & Applications***, Vol. 3, No. 3, (2009), 303-314, DOI: 10.1049/iet-cta:20080002.

36. Kuffner, J.J.a.L., Steven M, "Rrt-connect: An efficient approach to single-query path planning", Proceedings 2000 ICRA. Millennium Conference. IEEE International Conference on Robotics and Automation. Symposia Proceedings (Cat. No. 00CH37065), Vol. 2, (2000), 995-1001, DOI: 10.1109/ROBOT.2000.844730.

37. Wang, J., Chi, W., Li, C., Wang, C. and Meng, M.Q.H., "Neural rrt*: Learning-based optimal path planning", ***IEEE Transactions on Automation Science and Engineering***, Vol. 17, No. 4, (2020), 1748-1758, DOI: 10.1109/TASE.2020.2976560.

38. Richter, C., Bry, A. and Roy, N., Polynomial trajectory planning for aggressive quadrotor flight in dense indoor environments, in ***Robotics Research***, 2016.649-666, https://doi.org/10.1007/978-3-319-28872-7_37.

Persian Abstract

چکیده

طراحی مسیر سینودینامیکی برای ربات های بدون سرنشین خودمختار به عنوان یک چالش باز تحقیقاتی و یک مسئله NP_Hard شناخته می‌شود. هدف از این تحقیق طراحی یک مسیر قابل اجرا برای یک ربات عمود پرواز از موقعیت و سرعت ابتدایی به موقعیت و سرعت نهایی با درنظر گرفتن همزمان قیدهای سینماتیکی همچون موانع متحرک و قیدهای دینامیکی همچون محدودیت‌های حرکت در یک فضای کاری سه بعدی می‌باشد. برای این منظور الگوریتم طراحی مسیر تصادفی سینودینامیکی هر لحظه زمان، برای ربات مد نظر در این مقاله پیشنهاد می‌گردد. الگوریتم طراحی مسیر پیشنهادی از خانواده الگوریتم‌های طراحی مسیر درخت جستجویی سریع تصادفی می‌بوده و از سه زیر سیستم اصلی تشکیل می‌گردد. سه زیرسیتم اصلی به ترتیب عبارتند از: کنترل‌کننده سطح بالا، کنترل کننده میانی و کنترل کننده سطح پایین. کنترل کننده سطح بالا وظیفه نمونه برداری تصادفی به منظور تولید گره‌های فرزند تصادفی در فضای کاری مد نظر و هدایت و گسترش درخت جستجو را برعهده دارد. کنترل کننده میانی به کمک الگوریتم هر لحظه وظیفه رشد درخت‌های جستجوی محلی جهت اجتناب از برخورد با موانع از پیش ناشناخته متحرک را برعهده دارد. همچنین وظیفه حرص شاخه‌های نامتناسب درخت جستجو و طراحی یک مسیر زیربهینه نیز با این واحد می‌باشد. کنترل کننده سطح پایین به کمک مدل دینامیکی شش درجه آزادی ربات وظیفه اعمال قیدهای حرکتی ربات در فرآیند رشد شاخه‌ها و گره‌های درخت جستجو را بر عهده خواهد داشت. بدین ترتیب درخت مشتمل بر شاخه‌ها و گره‌هایی خواهد شد که پیشتر قیدهای حرکتی در انها لحاظ شده و از قابل رهگیری بودن انها توسط ربات اطمینان حاصل شده است. الگوریتم طراحی مسیر پیشنهادی در طی سه سناریو تست متفاوت ارزیابی می‌گردد. نتایج نشان می‌دهد که الگوریتم پیشنهادی نه تنها قادر به طراحی مسیر با قابلیت رهگیری توسط ربات می‌باشد بلکه حجم محاسبات نیز به خاطر عملکرد تصادفی روش کاهش چشمگیری داشته و از برخورد با موانع متحرک نیز به کمک رشد درخت‌های جستجوی محلی اجتناب شده است.

IJE TRANSACTIONS A: Basics Vol. 34, No. 10, (October 2021) 2371-2378

International Journal of Engineering

Journal Homepage: www.ije.ir

Microstructure and Mechanical Properties of Polyamid 6/Acrylonitrile-butadiene Rubber Nanocomposites Fabricated by Friction Stir Process

A. Ghorbankhan, M. R. Nakhaei*

Facility of Mechanics and Energy, Shahid Beheshti University, Tehran, Iran

PAPER INFO

Paper history:
Received 10 August 2021
Received in revised form 05 September2021
Accepted 08 September2021

Keywords:
*Polyamid6/*Acrylonitrile-butadiene Rubber*/ Clay*
Nanocomposite
Modulus Strength
Eessential Work of Fracture
Response Surface Methodology

ABSTRACT

Thermoplastic elastomer (TPE) based on polyamid 6 (PA6)/ acrylonitrile-butadiene rubber (NBR) containing 5 wt % nanoclay (Closite 30B) have been prepared via friction stir process (FSP). In this study, the essential work of fracture (EWF) approach was employed to investigate the fracture behavior of PA6/NBR nanocompsites. Also, the modulus strength of specimens was modeled by response surface methodology (RSM), considering three input variables including rotational speed (ω), traverse speed (S), and shoulder temperature (T). Thus, a quadratic mathematical model between input variables (ω, S and T) and response (modulus strength) of PA6/NBR/clay nanocomposites was achieved. Moreover, the morphology of the PA6/NBR blends containing 5 wt % was investigated by x-ray diffraction (XRD), scanning electron microscopy (SEM), and transmission electron microscopy (TEM). The results show that a sample of PA6/NBR thermoplastic elastomer (TPE) containing 5 wt % nanoclay at maximum tensile strength exhibited the maximum specific essential work of fracture (w_e) and specific non-essential work of fracture (w_p). Also, the results of RSM method demonstrate that the optimum condition of the process including rotational speed (ω), traverse speed (S), and shoulder temperature (T) were 1200 rpm, 25mm/min, and 146℃, respectively. Thus, under optimum condition, maximum modulus strength of 658 MPa was obtained.

***doi**: 10.5829/ije.2021.34.10a.18*

1. INTRODUCTION

Thermoplastic elastomers (TPEs) are defined as a collection of copolymers (such as plastic and rubber) that consist of materials with both elastic (related to rubber phase) and strength (related to plastic phase) properties [1, 2]. They have a wide application in industry due to their ability to stretch, to moderate elongation and return to their near original shape, excellent thermal, mechanical, and chemical resistances [3, 4]. In recent years, a lot of articles reported on mechanical properties and fracture mechanisms of TPE blends [5-7]. The fracture toughness of PA6/NBR/Hallosite nanotube (HNTs) nanocomposite was investigated by Paran et al. [8]. Their results showed that the work of inner fracture zone (w_e) decreased with addition of HNTs into the PA6/NBR blend and, at the same time, the non-essential work of fracture (w_p) increased. Mahallati et al. [9] have investigated the effect of the NBR content and nanoclay loading on the microstructure and thermal behavior of PA6/NBR nanocomposites. They found that the storage modulus and oil resistance increased with the loading of the nanoclay. Paran et al. [10] have studied the effect of HNT on the mechanical and morphology properties of PA6/NBR blend. They concluded that the storage modulus, Young's modulus, and yield stress increased with increasing HNT content. The friction stir process is a new method for produce polymer nanocomposite [11]. The high rotational speed of the tool in this process leads to great shear stress in the process zone. The high shear stress leads to better nanofiller dispersion in the polymeric systems and improvement in the mechanical properties such as tensile, modulus strength, and fracture behavior. In this study, the effect of input variables such as shoulder temperature, rotational speed, and traverse speed on the total work of fracture and modulus strength of PA6/NBR/Clay are investigated by EWF and RSM approach, respectively. Also, the morphology of

*Corresponding Author Institutional Email: m_nakhaei@sbu.ac.ir (M. R. Nakhaei)

Please cite this article as: A. Ghorbankhan M. R. Nakhaei, Microstructure and Mechanical Properties of Polyamid 6/Acrylonitrile-butadiene Rubber Nanocomposites Fabricated by Friction Stir Process, IJE TRANSACTIONS A: Basics Vol. 34, No. 10, (October 2021) 2371-2378

PA6/NBR/Clay nanocomposites is studied by x-ray diffraction (XRD), transmission electron microscopy (TEM), and scanning electron microscopy (SEM).

2. Experimental design and procedure

2. 1. Materials To fabricate the specimens, polyamide 6 (PA6), nitrile butadiene rubber (NBR), and nanoclay (Cloisite 30B) were supplied from Kolon plastic co., Korea, Kumbo polymer Co., Korea, and Southern clay Co., USA, respectively. Chemical and physical characterizations of these materials are summarized in Table 1.

2. 2. TPE Nanocomposite Preparation The thermoplastic elastomer (TPE) nanocomposites based on PA6/NBR containing PA6 (70%) and NBR (30%) were prepared using a Brabender internal mixer at a process temperature of 230 ℃ with a screw speed of 80 rpm for 6 minutes. The workpiece sheets with 200×160×3.2 mm dimensions were achieved using a Mini Test Press operating at 130MPa.

2. 3. FSP Tool Johns describes many models to manufacture an FSP tool for polymers [11, 12]. Therefore, john's tool design is the model for the current tooling used at BYU. The FSP tool consists of two main functions: localized heating and material flow [13, 14]. Figure 1 shows the schematic of the FSP tools was used in this study. The FSP tool used in the study consist of a cylindrical threaded pin, a ball bearing, a heater, and a Teflon-coated shoulder (Figure 1).

To fabricate PA6/NBR/clay nanocomposite, a Deckel milling machine (M.S.T Co, Iran) was employed. The primary components were fixed on a milling machine, and a grove of 2.25 mm depth was machined in the middle of the workpiece. The nanoclay particles were placed in the groove, and they compressed. To obtain the height of the improvised nanoclay particle (h_n) in the groove, Equation (1) can be used:

$$h_n = \frac{A_g}{T_g . D_r} \quad (1)$$

where A_g and T_g are the cross-sectional area of groove and groove width, respectively. Also, D_r is the density ratio achieved by diving nanoparticles density by TPE composite density. Finally, the rotating tool along the groove moved to distribute nanoclay particles on the PA6/NBR blend.

In this study, the statistical and probabilistic methods of RSM with Box-Behnken three-level design is used to analyze the effect of input variables on mechanical properties. The ranges of input variables at three levels are shown in Table 2. Based on this design, fifteen experiments were carried to obtain the mathematical models, as shown in Table 3.

TABLE 1. Raw material properties used in nanocomposites

Material	Characteristics	Value	Units
PA6	Density	1.14	g/cm^3
	Melting point	220	℃
	Melt flow index (MFI)	31.4	g/10 min
	Mooney viscosity ML(1+4)125˚C	41	M
NBR	Bound Acrylonitrile	34	%
	Density	0.98	g/cm^3
Cloisite 30B	Modifier Concentration	90	Meq/100g
	Density	1.98	g/cm^3
	d-Spacing	18.4	Å

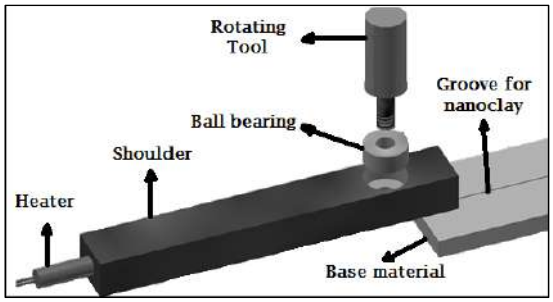

Figure 1. Schematics of friction stir process tool

2. 5. EWF Method One of the successful methods to investigate fracture behavior of nanocomposites is to use the essential work of fracture (EWF) method. This method is suitable for soft materials with low strength, such as polymers [15, 16]. In calculating fracture toughness of polymer nanocomposites, the EWF test, due to simple preparation of specimens and easy calculations has attracted considerable interest in academia and industries. In this method, to characterize the resistance to damage process occurring during tensile tests in outer fracture process zone (OPZ) and resistance to crack propagation in inner fracture process zone (IPZ), tensile test of double-edge notched tension (DENT) specimens with various values of ligament length (13, 15, 17 and 19 mm) were carried, based on ISO 293 protocol. Figure 2 demonstrates the schematic of the DENT specimens, FPZ, and OPZ [16, 17]. Using obtained load vs. displacement curves from tensile tests, EWF parameters can be achieved. The total work of fracture (W_f), which is calculated by the integral of F-D curves, consists of the applied work in a direction perpendicular to the ligament length (W_e) and plastic work in upper and lower areas of ligament length (W_p). The form of the formulation used for this parts is:

$$W_f = W_e + W_p \quad (2)$$

TABLE 2. The selected input variables and their limits

Parameters	Unit	Notations	Limits		
			–1	0	+1
Rotational speed	rpm	ω	800	100	1200
Traverse speed	mm/min	S	20	30	40
Shoulder temperature	℃	T	125	150	175

TABLE 3. Design matrix and the measured response

Run Order	ω (rpm)	S (mm/min)	T (℃)	Modulus Strength (MPa)
1	1200	20	150	645
2	1000	40	175	513
3	800	40	150	556
4	1200	30	175	613
5	1000	40	125	535
6	1000	20	125	543
7	800	30	125	533
8	800	20	150	549
9	1000	30	150	593
10	1200	30	125	626
11	1200	40	150	584
12	800	30	175	583
13	1000	30	150	595
14	1000	20	175	581
15	1000	30	150	597

Since the fracture toughness of polymer materials does not depend on the dimensions of specimens, Equation (2) can be rewritten by specific terms, as follows:

$$W_f = w_e.Lt + \beta L^2 t.w_p \quad (3)$$

$$w_f = \frac{W_f}{L} = w_e + \beta L.w_p \quad (4)$$

where $w_f, w_e, and\ w_p$ are specific work of fracture, specific essential work of fracture, and specific non-essential work of fracture, respectively. Also, β is the shape factor, and t is specimen thickness.

In other definition, the energy required to break, which is absorbed or consumed, can be defined by applied work in yielding (W_y) and necking + tearing (W_n) regions as follow:

$$W_f = W_y + W_n \quad (5)$$

By introducing Equation (3) into Equation (5), specific measurements of EWF parameters is written as follow:

$$w_f = (w_{e,y} + \beta L.w_{p,y}) + (w_{e,n} + \beta L.w_{p,n}) \quad (6)$$

where $w_{e,y}$, and $w_{e,n}$ are the specific yielding-related essential work of fracture and specific necking and tearing-related essential work of fracture, respectively. Also, $w_{p,y}$, and $w_{p,n}$ are specific plastic work of fracture in yielding and necking+ tearing zones, respectively [15, 17].

2. 6. Characterization The microstructures and phase morphology of the produced specimens were characterized using a Philips XL30 scanning electron microscope (Joel co., USA). For increasing the nanocomposite surface conductivity. Experimental measurements of nanoparticles distance were calculated by x-ray diffraction test. The aim of this test is to illustrate and compare the penetration of polyme chain between nanoclay layers in different samples of nanocomposites. For this work, using Philips X'Pert diffractometer with kα radiation of wavelength λ=1.540598 A°, the XRD curves of nanocomposites specimens were achieved. The dispersion of clay in the PA6/NBR blends was investigated using a transmission electron microscope (TEM) by a Philips EM208S at 100 kV. TEM samples were prepared by microtoming 80 nm thick using a diamond knife in an Ultracut Uct microtome (Leica Company, Austria). In order to investigate tensile properties of nanocomposites samples, tensile tests were performed using a Zuker tensile testing machine (Zwick Co., Germany). These experiments were performed at room temperature with crosshead speed of 1mm/min. Furthermore, the dimensions of specimens were determined based on the ASTM D256 standard [16]. Table 4 shows the average of three measurements of tensile tests for each run.

3. RESULTS

3. 1. Analysis of Variance (ANOVA) Depending on acceptable experimental data, analysis of variance (ANOVA) is a good technique for input variables screening which has the most effect on the output variables. In this method, the input variables with more F-value and less P-value (less 5% with 95% confidence level) have the most effect on the output variables. Therefore, they can be selected as the main variables with regard to their roles in the experimental data [2, 18]. The ANOVA table for the input and output variable are shown in Table 4. According to both columns F-value and P-value in Table 4, terms of shoulder temperature (T), rotational speed (ω), and traverse speed (S) as the linear effects are significant. Also, terms of quadratic and interaction effects of input variables such as ω^2, S^2, T^2 and ω×S, ω×T, S×T, can be regarded in the mathematical model. Due to the above results, the mathematical models for modulus strength are illustrated in Equations (7) and (8).

(a) In terms of coded factors:

$$\text{Modulus strength (MPa)} = 595 + 30.87\times\omega - 16.25\times S + 6.63\times T - 17\times\omega\times S - 15.75\times\omega\times T - 15\times S\times T + 17.13\times \omega^2 - 28.62\times S^2 - 23.38\times T^2 \quad (7)$$

(b) In term of actual factors:

$$\text{Modulus strength (MPa)} = -1218.85 + 0.025\times\omega + 33.05\times S + 16.43\times T - 0.0085\times\omega\times S - 0.0035\times\omega\times T - 0.06\times S\times T + 0.00042\times\omega^2 - 0.28\times S^2 - 0.037\times T^2 \quad (8)$$

3. 1. 1. Validation Equations (7) and (8) present the mathematical models of modulus strength with regard to 15 experimental tests. The accuracy and predictive capabilities of mathematical models can be assessed by comparing them with experimental results for various conditions [1, 11]. Therefore, the validation of mathematical models is investigated using three confirming experiments. The actual measurements, predicted values, and the percentage of error for three experiments with the new conditions are given in Table 5.

TABLE 4. ANOVA analysis for the modulus strength model

Source	Sum of Squares	df	Mean Square	F–Value	P-value
Model	19449.8	9	2161.0	87.3	< 0.0001
Rotational speed	7625.1	1	7626.1	306.1	< 0.0001
Traverse speed	2112.5	1	2112.5	85.3	0.0002
Shoulder	351.1	1	351.3	14.1	0.0131
ω×S	1156.0	1	1156.0	46.7	0.0010
ω×T	992.2	1	992.2	40.1	0.0014
S×T	90.0	1	900.0	36.3	0.0018
ω^2	1082.8	1	1082.8	43.7	0.0012
S^2	3025.4	1	3025.4	122.2	0.0001
T^2	2017.4	1	2017.4	81.5	0.0003
Residual	123.7	5	24.7		
Lack of Fit	115.7	3	38.5	9.65	0.0954
Pure Error	8.0	2	4.0		
Cor Total	19573.6	14			

TABLE.5. Validation of test results.

Run	Process parameters			Modulus Strength (MPa)
	ω	S	T	
1	1000	40	150	Actual: 550 Predict: 559 Error (%): 1.1
2	800	30	150	Actual: 581 Predict: 562 Error (%): 3.2
3	1200	20	175	Actual: 630 Predict: 661 Error (%): 4.9

According to the RSM method, the maximum and minimum modulus strength of PA6/NBR blends containing 5% wt nanoclay by different input variables values are given in Table 6. According to values of modulus strength in Table 6, the maximum modulus strength, which occurs at 1200 rpm (related to rotational speed), 25 mm/min (related to traversing speed), and 146℃ (related to shoulder temperature), is 658 MPa (TPO5-1 sample). Moreover, the minimum modulus strength of PA6/NBR/Clay nanocomposite is 521 MPa, which occurs at 800 rpm, 20 mm/min, and 130℃, respectively (TPO5-2 sample). Comparing mechanical properties of the TPO5-1 sample fabricated by FSP in this study with PA6/NBR/Clay produced by an internal mixer [9] shows that addition of nanoclay in the PA6/NBR blend increased the modulus strength of the nanocomposite from 378 to 658 and 630 MPa, respectively. Also, with addition of nanoclay to the PA6/NBR blend, the tensile strength of nanocomposites produce by the internal mixer decreased, whereas the tensile strength of FSP samples increased.

3. 2. Morphological Studies

3. 2. 1. XRD Analysis The corves of the XRD diffraction patterns for clay platelets and two samples of TPO5-1 and TPO5-2, as shown in Figure 2. Using calculating d-space from Bragg's law can be illustrated the rate of distribution of nanoclay in the matrix.

$$d = \frac{n\lambda}{2sin\theta} \quad (9)$$

where d, λ, and θ are the intergallery distance of clay, the x-ray wavelength, and angle related to the maximum point of the first peak, respectively. Also, n is the diffraction sequence [11]. As shown in Figure 2, the diffraction peak of neat clay appears at 2θ= 2.5°, corresponding to d_{001} basal spacing of 35.29 A° by Equation 11. In the XRD pattern of the TPO5-1 sample, the characteristic peak did not appear. This illustrates that the clay platelets in the matrix were exfoliated excellently in this sample. According to the researches, the size of clay particles on PP/EPDM thermoplastic elastomer reduced due to the higher rotational speed [1, 2]. On the other hand, the TPO5-2 sample exhibited an apparent peak at 2θ=2.3° (d= 38.36 A°). Thus, the observation above shows that the input variables (T, ω, and S) will determine the distribution quality of clay particles on PA6/NBR blends. According to the XRD results,

TABLE 6. Mechanical properties of TPO5-1 and TPO5-2 sample

Run	Process parameters			Tensile Strength (MPa)	Modulus Strength (MPa)	Impact Strength (j/m)
	ω	S	T			
TPO5-1	1200	25	146	32.9	658	69
TPO5-2	800	20	130	27.4	521	62

comparing X-ray diffraction patterns of the samples fabricated by FSP in this study and internal mixer [3, 9] shows that the correct choice of friction stir process parameters can have a great effect on nanoparticle dispersion on the polymer matrix.

3. 2. 2. SEM Figures 3 show the SEM micrographs of samples of TPO5-1 and TPO5-2. It was shown that the size of the NBR particles of the TPO5-1 sample is less than the TPO5-2 sample. Moreover, the amount of decrease in the size of NBR particles depends on the rotational speed values. Thus, as shown in Figure 3 that as rotating speed increases, shear stress increases, and the sizes of elastomer phases decreased [8, 10]. The size of the elastomeric phase in TPO5-2, observed as dark zones by scanning electron microscopy, was reduced with increasing rotational speed. Therefore, the decrease of NBR particles was well correlated with increasing the ω observed by SEM micrographs.

3. 2. 3. TEM The TEM micrographs of samples of TPO5-1 and TPO5-2 are illustrated in Figure 4. As shown in Figure 4, the PA6 and NBR phases are illustrated by gray and light areas, respectively. Also, the clay platelets on PA6/NBR blends are shown by dark lines. As shown in Figures 4a and 4b, the exfoliated rate of the TPO5-2 sample (Figure 4a) is better than the TPO5-1 sample (Figure 8b) on the PA6/NBR blend.

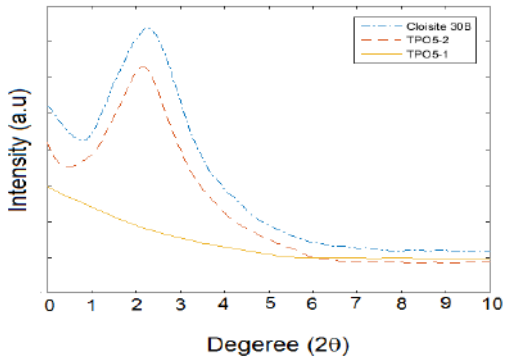

Figure 2. XRD Spectra of Closite 30B and PA6/NBR/Clay nanocomposites

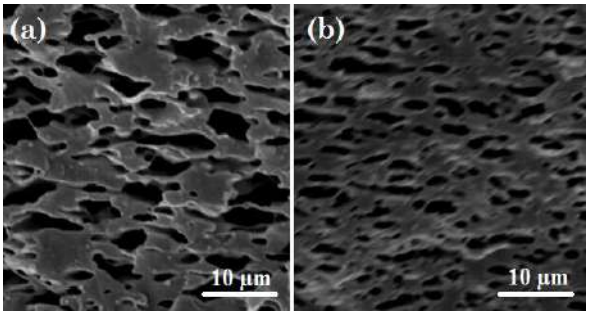

Figure 3. SEM micrograph of PA6/NBR nanocomposite (a) TPO5-2 and (b). TPO5-1

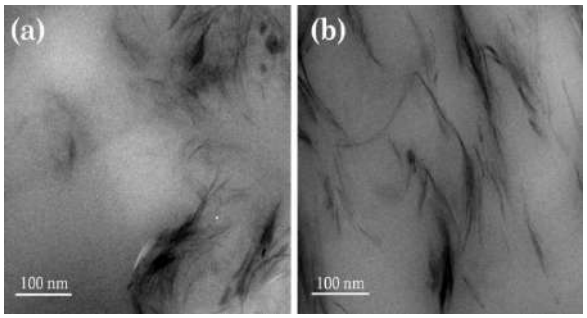

Figure 4. TEM micrograph of PA6/NBR nanocomposite (a) TPO5-2 and (b). TPO5-1

Following this reasoning, the potential energy for bond formation in interfaces of elastomeric and thermoplastic phases is great in TPO5-2 specimen compared to TPO5-1 specimen. On the other hand, an increase in modulus strength and fracture toughness of nanocomposites is dependent on the extent of exfoliation of nanoparticles in the matrix [11]. Thus, this result is in agreement with the fracture behavior and modulus strength of the specimens and could be an indication of comparatively stronger interactions between the clay nanoparticles and the PA6/NBR matrix in TPO5-2 sample.

3. 2. 4. EWF Test Due to the EWF test and DENT specimens with different ligament lengths (L), the load-displacement curves of PA6/NBR thermoplastic elastomers (TPEs) and TPO5-1 and TPO5-2 samples were illustrated in Figure 5. Figure 5a shows the load-displacement curve of the PA6/NBR blend containing 0% wt of nanoclay. Also, Figures 5b and 5c show the load-displacement curves of TPO5-1 and TPO5-2 samples, respectively. As indicated in Figure 5, the yielding parts in all samples have the same shapes, although this is not the same for all necking + tearing sections. Moreover, the integral of load-displacement curves for each sample increases with increasing ligament length. The maximum stress values (σ_{xax}) curves of PA6/NBR blend, TPO5-1, and TPO5-2 nanocomposites with different ligament lengths are illustrated in Figure 6. According to the ESIS stress criterion and Hills plasticity criterion, the maximum stress (σ_{xax}) values for each specimen should be in the range of 0.9-1.1 of the average of maximum stress. These criteria show that the fracture process of nanocomposite samples in the plane stress condition occurred. Therefore, Figure 4 shows that the application of the EWF theory in PA6/NBR/Clay nanocomposites is validated [2, 16].

EWF measurement for the yielding and necking + tearing sections are listed in Table 7. The results show that a sample of TPO5-2 exhibited the maximum specific essential work of fracture and specific non-essential work of fracture. This topic is clear thanks to good load transfer between matrix and nanoparticles due to better distribution of nanoparticles in the matrix, and less agglomeration compare with other samples [16].

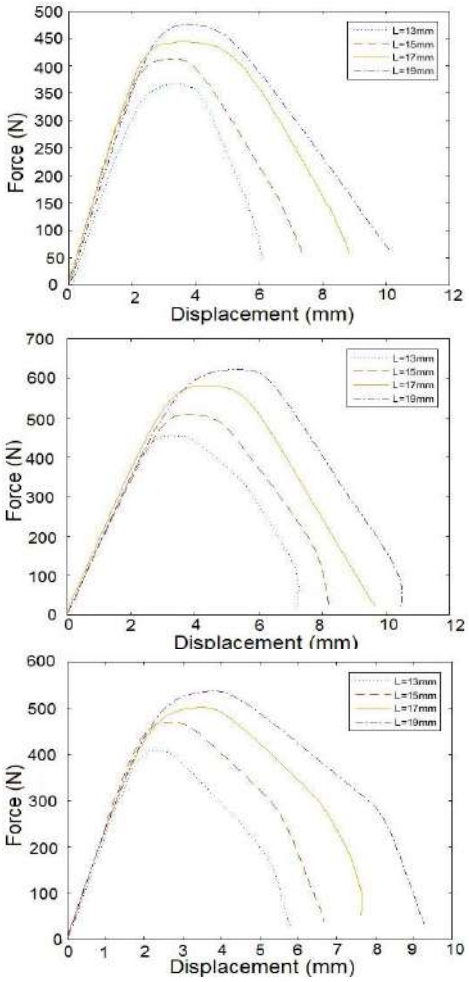

Figure 5. Force versus displacement curves for the three tested materials (a) PA6/NBR (b) TPO5-2 and (c).TPO5 – 1

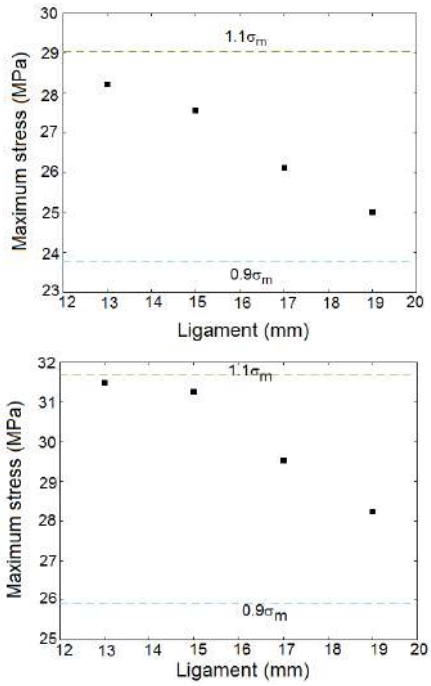

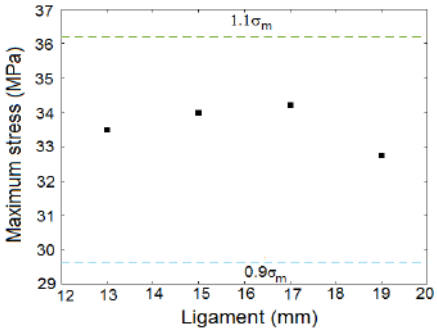

Figure 6. Maximum stress versus ligament length of (a) PA6/NBR (b) TPO5-2 and (c). TPO5-1

TABLE 7. The results of essential and non-essential work of fracture PA6/NBR, TPO5-1, and TPO5-2

Sample	W_e	βW_P	$W_{e,y}$	$\beta w_{p,y}$	$W_{e,n}$	$\beta w_{p,n}$
PA6/NBR	27.35	7.35	10.5	1	16.85	6.35
TPO5-1	12.8	8.1	6.2	2.1	6.6	6
TPO5-2	41.5	8.75	13.7	2.4	27.45	6.35

4. CONCLUSION

PA6/NBR nanocomposites containing 5% wt nanoclay Closite 30B were provided by friction stir process. The essential work of fracture (EWF) approach was used to investigate the fracture behavior of PA6/NBR/clay nanocomposites. Also, for modeling purposes and find the relationship between input variables and response (modulus strength), the RSM method was employed successfully. Moreover, using x-ray diffraction (XRD), transmission electron microscopy (TEM) scanning electron microscopy (SEM) were investigated the morphology of PA6/NBR blends containing 5 wt% nanoclay. The obtained result leads to the following conclusions.

1. Response surface methodology (RSM) is well applicable for modeling modulus strength of PA6/NBR/clay nanocomposite by mathematical models.
2. The modulus strength can be improved by increasing rotational speed in all encoded rang of the Box-Behnken design. Thus, the rotational speed has a the most effective on the modulus strength.
3. The results of the RSM method demonstrate that the optimum condition of the process was found to be at including rotational speed (ω), traverse speed (S), and shoulder temperature (T) of 1200 rpm, 25mm/min, and 146 ℃, respectively.
4. The total work of fracture increased with the presence of nanoclay. The sample of PA6/NBR TPE containing 5% wt nanoclay at maximum tensile strength exhibited the maximum specific essential work of fracture and the specific non-essential work of fracture.

5. The XRD results showed that the better distribution of nanoclay layers on PA6/NBR blend obtained for TPO5-2 sample.
6. SEM micrographs confirmed that amount of decrease in size of NBR particles depend on the rotational speed values, as well as, the higher rotational speed in FSP lead to higher shear stress and decreases size of NBR particles. Also, TEM images showed that an exfoliated and intercalated morphologies were obtained for the TPO5-2 sample.

5. REFERENCES

1. Nakhaei, M. and Naderi, G., "Modeling and optimization of mechanical properties of pa6/nbr/graphene nanocomposite using central composite design", ***International Journal of Engineering, Transactions C: Aspects***, Vol. 33, No. 9, (2020), 1803-1810. doi: 10.5829/IJE.2020.33.09C.15
2. Nakhaei, M.R., Mostafapour, A., Dubois, C., Naderi, G. and Reza Ghoreishy, M.H., "Study of morphology and mechanical properties of pp/epdm/clay nanocomposites prepared using twin-screw extruder and friction stir process", ***Polymer composites***, Vol. 40, No. 8, (2019), 3306-3314. doi: 10.1002/PC.25188
3. Yudhanto, F., Jamasri, J., Rochardjo, H. S. B., and Kusumaatmaja, A., "Experimental Study of PVA Nanocomposite Film Reinforced by Cellulose Nanofibers from Agave Cantala" I***nternational Journal of Engineering, Transactions A: BAsics,*** Vol. 34, No. 4, (2021) 987-998. doi: 10.5829/IJE.2021.34.04A.25
4. Qiu, Y., Wang, J., Wu, D., Wang, Z., Zhang, M., Yao, Y. and Wei, N., "Thermoplastic polyester elastomer nanocomposites filled with graphene: Mechanical and viscoelastic properties", ***Composites Science and Technology***, Vol. 132, (2016), 108-115. doi: 10.1016/J.COMPSCITECH.2016.07.005
5. Azdast, T. and Hasanzadeh, R., "Tensile and morphological properties of microcellular polymeric nanocomposite foams reinforced with multi-walled carbon nanotubes", ***International Journal of Engineering, Transactions C: Aspects***, Vol. 31, No. 3, (2018), 504-510. doi: 10.5829/IJE.2018.31.03C.14
6. Rashahmadi, S., Mosalman, S. and Hasanzadeh, R., "The effect of tio2 nanoparticles on mechanical properties of poly methyl methacrylate nanocomposites (research note)", ***International Journal of Engineering, Transactions B: Applications***, Vol. 30, No. 5, (2017), 807-813. doi: 10.5829/IDOSI.IJE.2017.30.05B.22
7. Ghasemi, F.A., Niyaraki, M.N., Ghasemi, I. and Daneshpayeh, S., "Predicting the tensile strength and elongation at break of pp/graphene/glass fiber/epdm nanocomposites using response surface methodology", ***Mechanics of Advanced Materials and Structures***, Vol. 28, No. 10, (2021), 981-989. doi: 10.1080/15376494.2019.1614702
8. Paran, S., Naderi, G., Ghoreishy, M. and Dubois, C., "Essential work of fracture and failure mechanisms in dynamically vulcanized thermoplastic elastomer nanocomposites based on pa6/nbr/xnbr-grafted hnts", ***Engineering Fracture Mechanics***, Vol. 200, (2018), 251-262. doi: 10.22063/JIPST.2020.1732
9. Mahallati, P., Arefazar, A. and Naderi, G., "Thermoplastic elastomer nanocomposites based on pa6/nbr", ***International Polymer Processing***, Vol. 25, No. 2, (2010), 132-138. doi: 10.3139/217.2311
10. Paran, S.R., Naderi, G. and Ghoreishy, M.R., "Effect of halloysite nanotube on microstructure, rheological and mechanical properties of dynamically vulcanized pa6/nbr thermoplastic vulcanizates", ***Soft Materials***, Vol. 14, No. 3, (2016), 127-139. doi: 10.1080/1539445X.2016.1157694
11. Nakhaei, M., Naderi, G. and Mostafapour, A., "Effect of processing parameters on morphology and tensile properties of pp/epdm/organoclay nanocomposites fabricated by friction stir processing", ***Iranian Polymer Journal***, Vol. 25, No. 2, (2016), 179-191. doi: 10.1007/S13726-015-0412-6
12. Zinati, R.F. and Razfar, M.R., "Finite element simulation and experimental investigation of friction stir processing of polyamide 6", ***Proceedings of the Institution of Mechanical Engineers, Part B: Journal of Engineering Manufacture***, Vol. 229, No. 12, (2015), 2205-2215. doi: 10.1177/0954405414546705
13. Goli Bidgoli, M., Ranjbaran, A., Mirzavand, K., Shajari, Y., Seyedraoufi, Z. S., Porhonar, M., "Investigation of Carbon Fiber Reinforced Polymer Composite Welding with a New Tool in Friction Stir Welding Method" I ***International Journal of Engineering, Transactions C: Aspects***, Vol. 32, No. 6, (2019) 860-865. doi: 10.5829/IJE.2019.32.06C.09
14. Huang, Y., Meng, X., Xie, Y., Wan, L., Lv, Z., Cao, J. and Feng, J., "Friction stir welding/processing of polymers and polymer matrix composites", ***Composites Part A: Applied Science and Manufacturing***, Vol. 105, (2018), 235-257. doi: 10.1016/J.COMPOSITESA.2017.12.005
15. Hafiz, T., "Influence of temperature and moisture on the compressive strength of carbon fiber reinforced polymers", ***International Journal of Engineering, Transactions B: Applications***, Vol. 33, No. 5, (2020), 916-922. doi: 10.5829/IJE.2020.33.05B.24
16. Khodabandelou, M., Aghjeh, M.K.R. and Mazidi, M.M., "Fracture toughness and failure mechanisms in un-vulcanized and dynamically vulcanized pp/epdm/mwcnt blend-nanocomposites", ***RSC Advances***, Vol. 5, No. 87, (2015), 70817-70831. doi: 10.1039/C5RA12087J
17. Bárány, T., Czigány, T. and Karger-Kocsis, J., "Application of the essential work of fracture (ewf) concept for polymers, related blends and composites: A review", ***Progress in Polymer Science***, Vol. 35, No. 10, (2010), 1257-1287. doi: 10.1016/J.PROGPOLYMSCI.2010.07.001
18. Sahith Reddy, S., "Optimization of calcined bentonite caly utilization in cement mortar using response surface methodology", ***International Journal of Engineering, Transactions A: BAsics***, Vol. 34, No. 7, (2021), 1623-1631. doi: 10.5829/IJE.2021.34.07A.07

Persian Abstract

چکیده

ترموپلاستیک الاستومرهای بر پایه پلی آمید 6/ نیتریل بوتادین رابر (PA6/NBR) شامل 5 ٪ وزنی نانو ذرات خاک رس با فرایند اصطکاکی اغتشاشی (FSP) ساخته شد. در این تحقیق از کار ضروری شکست (EWF) برای بررسی رفتار شکست ترکیب های PA6/NBR با 0% و 5% درصد وزنی خاک رس استفاده شد.همچنین مدول کششی نمونه ها با استفاده از روش پاسخ سطح (RSM) مدلسازی شد که سه پارامتر ورودی شامل سرعت چرخشی ابزار (ω)، سرعت خطی (S) و دمای شولدر (T) مورد نظر قرار گرفت. بنابراین یک معادله ریاضی درجه دوم بین متغییرهای ورودی و پاسخ بدست آمد. علاوه بر این، ریز ساختار ترکیب PA6/NBR شامل 5% نانو ذرات خاک رس با پراش اشعه ایکس (XRD)، میکروسکوپ الکترونی روبشی (SEM) و میکروسکوپ الکترونی عبوری (TEM) مورد بررسی قرار گرفت. نتایج نشان می دهد که نمونه دارای بیشترین استحکام کششی دارای بیشترین کار ضروری و کار غیر ضروری شکست است. همچنین نتایج حاصل از RSM نشان داد که بیشترین مدول کششی زمانی بدست خواهد آمد که سرعت چرخشی، سرعت خطی و دمای شولدر ابزار به ترتیب برابر با 1200 rpm، 25 mm/min و 146 °C است که در این شرایط بهینه، مدول کششی برابر 658 MPa بدست خواهد.

AIMS AND SCOPE

The objective of the International Journal of Engineering is to provide a forum for communication of information among the world's scientific and technological community and Iranian scientists and engineers. This journal intends to be of interest and utility to researchers and practitioners in the academic, industrial and governmental sectors. All original research contributions of significant value focused on basics, applications and aspects areas of engineering discipline are welcome.

This journal is published in three quarterly transactions: Transactions A (Basics) deal with the engineering fundamentals, Transactions B (Applications) are concerned with the application of the engineering knowledge in the daily life of the human being and Transactions C (Aspects) - starting from January 2012 - emphasize on the main engineering aspects whose elaboration can yield knowledge and expertise that can equally serve all branches of engineering discipline.

This journal will publish authoritative papers on theoretical and experimental researches and advanced applications embodying the results of extensive field, plant, laboratory or theoretical investigation or new interpretations of existing problems. It may also feature - when appropriate - research notes, technical notes, state-of-the-art survey type papers, short communications, letters to the editor, meeting schedules and conference announcements. The language of publication is English. Each paper should contain an abstract both in English and in Persian. However, for the authors who are not familiar with Persian, the publisher will prepare the latter. The abstracts should not exceed 250 words.

All manuscripts will be peer-reviewed by qualified reviewers. The material should be presented clearly and concisely:

- *Full papers* must be based on completed original works of significant novelty. The papers are not strictly limited in length. However, lengthy contributions may be delayed due to limited space. It is advised to keep papers limited to 7500 words.
- *Research* notes are considered as short items that include theoretical or experimental results of immediate current interest.
- *Technical notes* are also considered as short items of enough technical acceptability with more rapid publication appeal. The length of a research or technical note is recommended not to exceed 2500 words or 4 journal pages (including figures and tables).

Review papers are only considered from highly qualified well-known authors generally assigned by the editorial board or editor in chief. Short communications and letters to the editor should contain a text of about 1000 words and whatever figures and tables that may be required to support the text. They include discussion of full papers and short items and should contribute to the original article by providing confirmation or additional interpretation. Discussion of papers will be referred to author(s) for reply and will concurrently be published with reply of author(s).

INSTRUCTIONS FOR AUTHORS

Submission of a manuscript represents that it has neither been published nor submitted for publication elsewhere and is result of research carried out by author(s). Presentation in a conference and appearance in a symposium proceeding is not considered prior publication.

Authors are required to include a list describing all the symbols and abbreviations in the paper. Use of the international system of measurement units is mandatory.

- On-line submission of manuscripts results in faster publication process and is recommended. Instructions are given in the IJE web sites: www.ije.ir-www.ijeir.info
- Hardcopy submissions must include MS Word and jpg files.
- Manuscripts should be typewritten on one side of A4 paper, double-spaced, with adequate margins.
- References should be numbered in brackets and appear in sequence through the text. List of references should be given at the end of the paper.
- Figure captions are to be indicated under the illustrations. They should sufficiently explain the figures.
- Illustrations should appear in their appropriate places in the text.
- Tables and diagrams should be submitted in a form suitable for reproduction.
- Photographs should be of high quality saved as jpg files.
- Tables, Illustrations, Figures and Diagrams will be normally printed in single column width (8cm). Exceptionally large ones may be printed across two columns (17cm).

PAGE CHARGES AND REPRINTS

The papers are strictly limited in length, maximum 6 journal pages (including figures and tables). For the additional to 6 journal pages, there will be page charges. It is advised to keep papers limited to 3500 words.

Page Charges for Papers More Than 6 Pages (Including Abstract)	
For International Author ***	**$55 / per page**
For Local Author	**100,000 Toman / per page**

AUTHOR CHECKLIST

- Author(s), bio-data including affiliation(s) and mail and e-mail addresses).
- Manuscript including abstracts, key words, illustrations, tables, figures with figure captions and list of references.
- MS Word files of the paper.

International **J**ournal of **E**ngineering, P.O. Box 13145-1659, Tehran, I.R. Iran
Materials and Energy Research Center, 5 Ahuramazda St., Alvand Ave., Argentina Sq., Tehran, Islamic Republic of Iran
www.merc.ac.ir - www.emerc.ac.ir

THOMSON REUTERS

WEB OF SCIENCE

Scopus®

CAS®
A DIVISION OF THE
AMERICAN CHEMICAL SOCIETY

Google
Scholar